Seamount Morphology, Distribution, and Structure of the Southwest Indian Ridge

Lily Muller

Thesis submitted to the University of Oxford
for the degree of Doctor of Philosophy
in
Earth Sciences



Department of Earth Sciences
and University College,
University of Oxford

Trinity, 2017

Supervised by Prof. Tony Watts FRS

Declaration

The contents of this thesis are all my own work, except where otherwise stated. The views and opinions expressed herein are mine and not necessarily those of any other person or body unless so attributed.

Citation: Lily Muller (2017), Seamount Morphology, Distribution, and Structure of the Southwest Indian Ridge, D.Phil. Thesis, University of Oxford, Department of Earth Sciences, Oxford, UK.

Keywords:

This thesis has been typeset using LaTeX 2_ε and references were compiled using BibTeX. Many of the figures and calculations were produced using GMT(Wessel and Smith, 1991).

Copyright ©, by Lily Muller, 2017.
All rights reserved.

No part of the material protected by this copyright notice may be reproduced or utilised in any form or by any means, electronic or mechanical, including photocopying, recording or by any information storage and retrieval system, without written permission from the copyright owner.

Printed in the United Kingdom.

Abstract

Seamount Morphology, Distribution, and Structure of the Southwest Indian Ridge

Lily Muller
University College, Oxford

Trinity, 2017

Ultra-slow spreading ridges have a full spreading rate of less than 20 mm yr^{-1}, and show deviations from the fundamental characteristics identified at faster spreading rates; however, they are poorly studied compared to faster spreading ridges. In this thesis we aim to build on previous studies in order to further characterise the unique processes occurring at the ultra-slow spreading Southwest Indian ridge (SWIR). This is an exploratory study utilising novel and existing bathymetry, gravity, video imagery data to understand tectonic and volcanic processes along the ridge crest from triple junction to triple junction. We conduct a series of studies which focus on the axial valley morphology, large seamount morphology, the distribution of small seamounts and large seamounts on the ridge, and admittance studies.

We show that the long wavelength trends in geophysical data, geochemical data, and axial valley morphology are well correlated. These variations reflect along-axis changes in the crustal and mantle structure, governed by the thermal structure of the ridge. Seamounts provide important morphological evidence of the volcanic and tectonic processes beneath the Earth's surface. We use detailed morphological investigations to show that volcanic and erosional processes on six large seamounts are controlled by the local faulting and melt migration mechanisms. We investigate the distribution of seamounts on the ridge using a numerical algorithm, and demonstrate a lower seamount density than faster spreading ridges. We show that the seamount population statistics vary along the ridge due to changes in the degree of partial melting, magma conduit availability, and melt focussing mechanisms; the locations of three proximal hotspots coincide with increases in the estimated magmatic flux. Finally, best fit elastic thicknesses are determined using a 3D windowed admittance technique, which was tested using synthetic data. We construct a combined convection-flexure model to account for misfits between the observed data and existing flexural theoretical models. The average elastic thickness varies between 7 km and 12 km, and we show a strong dependence on spreading rate.

Extended Abstract

Seamount Morphology, Distribution, and Structure of the Southwest Indian Ridge

Lily Muller

University College, Oxford

Morphological studies of mid-ocean ridges have shown a dichotomy between the fast spreading East Pacific Rise and slow spreading Mid-Atlantic Ridge. Further investigation of the mid-ocean ridge system have subsequently shown that slow spreading ridges (spreading rates less than 60 mm yr^{-1}) are generally characterised by axial valleys superimposed on a broad ridge; fast spreading ridges (spreading rates greater than 80 mm yr^{-1}) are generally characterised by narrow axial rises. These ridge types all share several fundamental characteristics: (*i*) they have a relatively consistent crustal thickness, on average between 6 and 7 km, (*ii*) they consist of volcanic accretionary segments separated by transform or non-transform discontinuities, (*iii*) they generate elongate fault bound abyssal hills which have a strike perpendicular to the spreading direction.

More recent investigations have revealed the existence of a new type of mid-ocean ridge: ultra-slow ridges, with full spreading rates of less than 20 mm yr^{-1}. These ultra-slow spreading ridges, which make up 10% of our global mid ocean ridge system, show

deviations from the fundamental characteristics identified at faster spreading rates. In this thesis we aim to build on previous studies in order to further characterise the unique processes occurring at the ultra-slow spreading Southwest Indian ridge (SWIR). This thesis is an exploratory study utilising marine geophysical data comprised of existing data from 392 cruises, and novel bathymetry, gravity, video, and rock sample data collected between 2011 and 2013. Previous studies at the SWIR have shown that areas of the ridge crest have anomalously thin crust, a high percentage of peridotite on the seafloor, and anomalously deep axial depths; however these studies are confined to small areas of the ridge. The motivation for this thesis is to elucidate the variation in tectonic and volcanic processes along the ridge crest from triple junction to triple junction. In order to do this, we conduct a series of studies which focus on: the axial valley morphology, detailed studies of large seamount morphology on the ridge crest, the distribution of small seamounts on the axial valley floor, the distribution of large seamounts on the ridge flanks and admittance calculations to determine elastic thickness variations along the ridge crest.

Initially, we review existing literature on the long wavelength geophysical variation along the ridge. These are used to form a framework for interpretation for other geophysical trends observed elsewhere in this thesis. These long wavelength geophysical trends clearly show the influence of nearby hotspots and the degree of ridge obliquity. Numerical studies have shown that a combination of brittle-plastic and viscous rheologies undergoing extension at slow rates produces an axial valley morphology. We test the applicability of a simple lithospheric spreading model to the SWIR by examining the relationship between regional along axis depths and the size and shape of the axial valley. We find that the shape of the axial valley shows systematic variation with the long wavelength bathymetric and gravity signatures at the SWIR; axial highs along the ridge are characterised by shallow, narrow axial valleys, while axial lows are characterised by deep, wide axial valleys. This relies on the assumption that the

regional axial valley depths are solely dependent on the temperature structure of the lithosphere, and does not take into account geochemical mantle heterogeneity. In order to establish the relationship between the lithosphere rheology and axial valley widths, irrespective of the lithosphere temperature structure, we directly compare the axial valley widths with the elastic thickness (T_e), which is a proxy for lithospheric strength. We show that there is a positive correlation between elastic thickness and axial width, indicating that the width of the axial valley is governed by the lithosphere rheology and thus the lithospheric stretching model is applicable at very low spreading rates.

The smaller scale segmentation on the ridge is investigated, using along axis axial bathymetry and gravity profiles to divide the ridge into segments, separated by first and second order discontinuities. The axial valley morphology of these segments was analysed through profiles, maps and 3D visualisation and the segments divided into four groups. Each group represents a distinct morphological type based on the axial profile, length, gravity signature and shape of the axial valley. We show that the majority of the segments are analogous with those found on the slow spreading Mid-Atlantic Ridge (MAR); however a fourth segment type is identified and described. This segment type appears to be unique to the melt poor regions of ultra-slow ridges.

The next two sections of the thesis investigate seamounts, which are important windows into the volcanic and tectonic processes occurring on and beneath the Earth's surface. We present novel bathymetry data of 5 seamounts and 1 oceanic core complex collected during 2011 and 2012. This multibeam bathymetry is supplemented by backscatter acoustic data, ROV imagery and rock samples (available for 5 out of the 6 edifices), which are used to groundtruth the observations at a variety of scales.

We show that the predominant constructive features observed are flank rift zones, which form irregular edifice geometries. An analysis of the correlations between flank rift zone length and other geometric parameters shows that the formation of flank rift zones is

primarily controlled by the height of the edifice, followed by the lava eruption rate. The orientations of these flank rift zones, which provide an indication of the principle directions of crustal stress, have a strong correlation with the distance between the seamount and the nearby spreading axis and transform faults. We use this to argue that some of the seamounts formed on the ridge flanks, while others formed in the axial valley and subsequently moved off axis. Fault controlled melt migration is proposed as the mechanism for the formation of these large flank seamounts, outside of the axial valley.

The dominant destructive features observed are slope failures, which produce two types of observed morphology; large slope failures, which cause significant modification to the edifice geometry, and small gullies, which do not. The large slope failures exhibit morphological features consistent with both debris avalanches and slumping. Therefore, we propose a combined process in which slow slumping creates the initially steep fault scarp, and the over steepened slope subsequently fails as a debris avalanche, which leaves the characteristic chute structure and debris field.

The distribution of seamounts along the ridge provides an indication of the variation in magmatic output over different parts of the ridge. We utilise a numerical algorithm to distinguish volcanic edifices from background topography. This algorithm was tested using a one-at-a-time sensitivity analysis and the results calibrated against similar seamount distribution studies.

We initially apply the algorithm to four areas of the axial valley floor with complete swath bathymetry coverage, distributed over different parts of the ridge. The results show that the observed seamount density on the SWIR is between 21 and 44 % of that observed on the MAR indicating that the SWIR is comparatively melt poor, as predicted from upwelling models. The seamount populations are characterised using a maximum likelihood model, which has been shown to be more suitable than least

squares models. We show that variation in the seamount population characteristics between the different study sections reflect the changes in the regional degree of partial melting of that part of the ridge, the magma conduit availability in that section of the ridge, and the degree to which melt focussing mechanisms are operating. Analogies may be drawn between the seamount populations on the SWIR and those on the ultraslow spreading Gakkel Ridge in the Arctic, indicating that these volcanic patterns may be characteristic of ultra-slow spreading ridges.

We then analyse the distribution of large seamounts on the ridge crest and flanks using integrated shipboard and satellite derived bathymetry grids. We apply the algorithm to the wider Southwest Indian Ridge region in order to compare the results with subsets of the results from previous global seamount distribution studies. This comparison shows that there is good agreement between the studies, which indicates that the implementation of the algorithm was successful in distinguishing seamounts from background abyssal hill morphology. The variation in the number of seamounts along the ridge crest shows that this is primarily governed by magma conduit availability. Areas of the ridge with faster effective spreading rates or a large number of transform faults have the highest large flank seamount density. The total seamount volume, which does not always correlate with the number of seamounts, is representative of the local magma supply. The total seamount volume is used to estimate the time integrated magmatic flux along the ridge, which shows a positive correlation with the axial bathymetry. Three broad highs in the magmatic flux correspond to the axial high bathymetry at the locations of the Marion, Bouvet and Crozet hotspots, and are attributed to the increase in magma supply due to the influx of material from these hotspots. A small number of large volume seamounts found in close proximity to the transforms are attributed to magma migration along these zones of weakness.

The seamount distribution and long wavelength bathymetry and gravity data indicate changes in the rheology of the lithosphere along the ridge. We can directly assess these

changes in lithospheric strength through the calculation of admittance. Admittance studies utilise the relationship between bathymetry and gravity in order to calculate an observed admittance. This observed admittance may be compared with the admittance derived from theoretical flexural models in order to determine the best fit elastic thickness, which is a proxy for lithospheric strength. We assess variation in the strength of the lithosphere at an ultra-slow spreading ridge by calculating the elastic thickness (T_e) for a series of windows along the length of the ridge. These are then interpreted in terms of the long wavelength variation on the SWIR and compared against faster spreading ridges.

Synthetic bathymetry and gravity data consisting of Gaussian shaped seamounts on a plane are used to test the windowed admittance technique. This testing showed a number of sources of error for the windowed admittance, including the latitude of the study location, the finite nature of the windows and the presence of thermally subsiding ridge topography at slow and ultra-slow spreading rates. These sources of error were corrected for using different grid projections, and empirical corrections determined from synthetic testing.

Using the improved method, we calculate the admittance for 15 windows along the SWIR. This admittance is used to calculate isostatic response functions (IRFs) for each window, allowing windows with different water depths to be compared more easily. We fit a flexural model, derived from elastic plate theory, to the observed IRFs using least squares fitting to determine the best fit T_es. Two main sources of misfit are identified: long wavelength positive anomalies and mid-wavelength rollover, which have been previously attributed to the effects of mantle convection. A combined flexural-convection model is derived from convection equations and fitted to the observed IRFs. This combined flexural-convection model reduces the misfits observed between the flexural model and the IRFs, particularly at the long wavelengths. The average non-convecting lithospheric lid thicknesses, recovered from fitting of the combined model,

vary between 31 km and 91 km. These lid thicknesses show a strong positive correlation with the best fit T_e, which we attribute to variation in the thermal structure of the ridge.

The T_es derived from both models are compared and the pattern along the ridge examined. We show that the average T_e of the ridge varied between 7 and 12 km, however the faster spreading ridge crests at the triple junctions, and the Andrew Bains fracture system produced anomalously low and high T_es respectively. We show that the T_e varies systematically with the other long wavelength geophysical trends observed.

Previous studies have suggested that the T_e increases with decreasing spreading rate. We present windowed admittance calculations for the Mid-Atlantic and East Pacific Rises in order to compare the T_es for different spreading rates using a consistent methodology. We show that there is a systematic increase in T_e with decreasing spreading rate, which we attribute to the systematic variation in thermal structure with spreading rate.

Contents

Abstract **i**

Extended Abstract **iii**

Table of Contents **xi**

List of Figures **xv**

List of Tables **xxxiii**

Abbreviations Glossary **xxxv**

Acknowledgments **xxxvii**

1 Introduction **1**
1.1 Ultra-slow Spreading Ridges 1
1.2 Southwest Indian Ridge 5
1.3 Thesis Structure 7

2 Data Acquisition and Processing **11**
2.1 Geophysical Measurements at Sea 12
2.1.1 Shipboard Bathymetry 13
2.1.2 Shipboard Gravity 15
2.1.3 Shipboard Magnetics 20
2.2 RRS James Cook Cruise 22
2.2.1 Navigation 24
2.2.2 Bathymetry 24
2.2.3 Gravity 26
2.2.4 ROV profiles and sampling 26
2.3 R/V Marion Dufresne and R/V Meteor cruises 28
2.3.1 Navigation 28
2.3.2 Bathymetry 29
2.3.3 Gravity 30
2.3.4 Magnetics 30
2.4 Other cruise data 31
2.4.1 Bathymetry 31

2.4.2 Gravity . . . 32
2.4.3 Magnetics . . . 33
2.5 Satellite data . . . 34
2.5.1 Satellite derived gravity . . . 35
2.5.2 Satellite derived Bathymetry . . . 37
2.6 Combining datasets . . . 38
2.7 Chapter Summary . . . 40

3 Ridge Crest Morphology 41
3.1 Long Wavelength Geophysical Variation . . . 42
3.1.1 Constructing Along Axis Bathymetry and Gravity Profiles . . . 43
3.1.2 Along Axis Profile Results . . . 50
3.1.3 Causes of Long Wavelength Variation . . . 57
3.2 Axial Valley Morphology . . . 69
3.2.1 Across Axis Bathymetry Profiles . . . 71
3.2.2 Correlation between Axial Width and Elastic Thickness . . . 78
3.2.3 Ridge segmentation . . . 80
3.3 Chapter Summary . . . 96

4 Seamount Morphology 99
4.1 Seamounts on Mid Ocean Ridges . . . 99
4.2 Criteria for Identifying Morphological Features . . . 100
4.2.1 Constructive Volcanic Features . . . 101
4.2.2 Slope Failures . . . 103
4.2.3 Truncated Summits . . . 103
4.2.4 Faulting and Fractures . . . 104
4.2.5 Substrate Analysis . . . 104
4.3 Morphological Descriptions . . . 105
4.3.1 Coral Seamount . . . 106
4.3.2 Melville Bank . . . 110
4.3.3 Middle of What Seamount . . . 114
4.3.4 Sapmer Bank . . . 119
4.3.5 Atlantis Bank . . . 123
4.3.6 Vera Seamount . . . 128
4.4 Morphological Features . . . 134
4.4.1 Surface Geology . . . 134
4.4.2 Flank Rift Zones . . . 142
4.4.3 Slope Failures . . . 155
4.5 Chapter Summary . . . 174

5 Seamount Distribution 177
5.1 The Modified Basal Outlining Algorithm . . . 178
5.2 Axial Valley Floor Seamounts . . . 182
5.2.1 Data and Methods . . . 182
5.2.2 Results . . . 188

5.2.3 Discussion . . . 204
5.2.4 Patterns of Magmatism . . . 208
5.3 Ridge Flank Seamounts . . . 210
5.3.1 Data and Methods . . . 211
5.3.2 Results . . . 226
5.4 Chapter Summary . . . 239

6 Admittance and Elastic Thickness 243
6.1 Isostatic Models . . . 245
6.1.1 Elastic Plate Model . . . 247
6.1.2 Modelling Gravity Anomalies . . . 255
6.1.3 Gravitational Admittance . . . 256
6.1.4 Determination of Best Fit Elastic Thickness . . . 260
6.2 Synthetic Testing . . . 262
6.2.1 Synthetic Data . . . 264
6.2.2 Synthetic T_e Recovery . . . 269
6.2.3 Admittance of the Ridge . . . 279
6.3 Admittance Results . . . 281
6.3.1 Isostatic Response Functions . . . 281
6.3.2 Recovered T_e . . . 294
6.3.3 Comparison with other Mid Ocean Ridges . . . 296
6.4 Chapter Summary . . . 301

7 Conclusions 305
7.1 Future Work . . . 309

Bibliography 311

List of Figures

1.1 Igneous crustal thickness plotted against full spreading rate for seismic measurements corrected for the effect of thin crust at fracture zones. Crustal thicknesses range between 5.5 km and 7.5 km except for ultra-slow spreading rates (less than 20 mm yr^{-1}). Modified from Bown and White (1994). 3

1.2 Global plate boundaries (grey lines) defined by Bird (2003). Coloured lines represent oceanic spreading ridges: Fast spreading (full spreading rate greater than 60 mm yr^{-1}) shown as green lines, Ultra-slow spreading (full spreading rate less than 20 mm yr^{-1}) shown as red lines. All other ridge segments shown as yellow lines. Ultra-slow spreading ridges are names: GR = Gakkel Ridge, LT = Lena Trough, KR = Knipovich Ridge, MR = Mohns Ridge, CT = Cayman Trough, AAR = American Antarctic Ridge, SWIR = Southwest Indian Ridge. Adapted from Snow and Edmonds (2007). 4

1.3 Location map showing bathymetry of the Southwest Indian region from the GEBCO 2014 30'' x 30'' global bathymetry grid (IOC et al., 2003). Spreading ridges are shown in red. The location of present hotspots, characterised by bathymetric swells and active volcanism, are represented by grey dots and the hotspot name given. 6

2.1 Bathymetry of the Southwest Indian Ridge region from the GEBCO 2014 30 x 30 global bathymetry grid (IOC et al., 2003). Cruise tracks for the JC066 RRS James Cook cruise in 2011 (black line), and MD192 R/V Marion Dufresne and M101-2 Meteor cruises in 2012 and 2013 (red line). 12

2.2 Bathymetry map of the world's oceans produced by John Murray following the Challenger Expedition (Murray and Hjort, 1912) 14

2.3 Schematic diagram of a La Coste-Romberg sea gravimeter (LaCoste, 1959; Micro-G LaCoste, n.d.) modified from Jones (1999) 16

2.4 Figure showing the processing of gravity data from the JC066 cruise. The bathymetry is shown at the top (black line) for reference as it should be well correlated with the final free-air anomaly. The labels at the top indicate the ship activity and illustrate the change in gravity correction required when the ship is in transit vs on station. The Q-C gravity (blue line) is the raw gravity anomaly, prior to Eötvös and cross-coupling corrections. The Eötvös correction (red line) is correlated with the speed and heading of the ship (shown in green and blue respectively) from which it is calculated. In particular, the sign of the Eötvös correction changes with changing heading of the ship with respect to the rotation of the Earth. The cross-coupling error (light blue) increases with ship speed due to increased ship motion. The free-air anomaly calculated by applying the Eötvös and cross-coupling errors to the QC-gravity is shown in black, and shows a good correlation to the shipboard bathymetry. 19

2.5 Bathymetry of the Southwest Indian Ridge region from the GEBCO 2014 30 x 30 global bathymetry grid (IOC et al., 2003). Cruise tracks for the JC066 RRS James Cook cruise in 2011 (black line). 23

2.6 Bathymetry survey over Melville seamount showing cruise track in black. Bathymetry data shown here is raw data and so shows significant artefacts. These were subsequently removed using MB-system software. . . 25

2.7 Swath bathymetry of Coral Seamount showing transits of ROV (Remotely Operated underwater Vehicle) as a blue line and SHRIMP (Seabed High Resolution Imaging Platform) as a yellow line. 27

2.8 Bathymetry of the Southwest Indian Ridge region from the GEBCO 2014 30 x 30 global bathymetry grid (IOC et al., 2003). Cruise track of cruise RHUM-RUM aboard the R/V Marion Dufresne, which was repeated for cruise M101/2 aboard the R/V Meteor shown as a black line. 29

2.9 Bathymetry of the Southwest Indian Ridge region from the GEBCO 2014 30 x 30 global bathymetry grid (IOC et al., 2003). Shiptracks of cruises which collected multibeam and single beam bathymetry data used in this thesis shown in black. 32

2.10 Sandwell and Smith satellite gravity (Sandwell and Smith, 1997). Shiptracks of cruises which collected shipboard gravity data used in this thesis are shown in black 33

2.11 Crustal ages based on the Müller et al. (1997) age grid. Shiptracks of cruises which collected shipboard magnetic data used in this thesis are shown in black. 34

2.12 Figure showing the composite bathymetry map. The shipboard multibeam bathymetry, gridded using GMT's Nearneighbor (Wessel and Smith, 1991), is highlighted. The background is from the GEBCO 2014 30'' x 30'' global bathymetry grid (IOC et al., 2003). 39

3.1 Bathymetry map from the GEBCO 2014 30'' x 30'' grid, contoured at 2000 m. The black boxes outline the 7 Sections of the ridge identified using along axis geophysical and geochemical profiles. These Sections are labelled A to G and are referred to throughout this chapter. 43

3.2 Two dimensional magnetic anomaly profiles from existing cruise data; cruise tracks are shown in the inset map. Observed magnetic anomaly profiles (solid black lines) are compared to calculated magnetic anomaly profiles (dashed red lines) predicted using a full spreading rate of 14 mm yr^{-1} increasing to 16 mm yr^{-1} after 4 Ma, a 0.5 km thick source layer draped over the topography, and magnetisation of 18 A m^{-1} and 4 A m^{-1} on and off axis respectively. The graphic below the profiles show the seafloor spreading model draped over the topography, which is derived from the centre beam of the multibeam bathymetry for each shiptrack. The grey band represents the extent of the Bruhnes anomaly used to define the zero-age track. 45

3.3 Magnetic anomaly picks derived from shipboard magnetic profiles across the ridge. The following anomaly picks are shown: 1n (black circles); 2An (red circles); 5n (blue circles); 6n (green circles). The grey line shows the zero-age track constructed using the picks of the Bruhnes anomaly. 46

3.4 Series of maps showing the calculation of mantle Bouguer anomalies. The panels show the free-air gravity anomaly (panel A); gravity effect of the crust-water interface (panel B); gravity effect of the crust-mantle interface (panel C); the combined gravity effect of these two interfaces (panel D); the combined gravity effect subtracted from the free-air gravity anomaly to produce the mantle Bouguer anomaly (panel E). 48

3.5 Differences between a series of profiles sampled along zero-age for different calculated mantle Bouguer anomalies. For each difference profile, all assumed densities and thicknesses are the same as the original profile, except for the one being tested. Panel A shows the original mantle Bouguer anomaly profile for reference (thin black line) and the profile with a median filter with a wavelength of 5° of longitude (thick black line). The original profile assumes a crustal thickness of 5 km, crustal density of 2800 kg m^{-3}, and a mantle density of 3300 kg m^{-3}. Panel B shows the difference between the MBA profile in panel A and MBA profiles with crustal thicknesses of 3 km (blue) and 7 km (red). Panel C shows the difference between the MBA profile in panel A and an MBA profile with a mantle density of 3180 kg m^{-3} (red). Panel D shows the difference between the MBA profile in panel A and MBA profiles with crustal densities of 2700 kg m^{-3} (red) and 2900 kg m^{-3} (blue). 49

3.6 Along-ridge profiles of bathymetry, mantle Bouguer anomaly, variation in $Na_{8.0}$ composition of basalt glasses dredged along the SWIR axis and shear wave velocity heterogeneities. These were sampled along a zero-age track, which was determined using magnetic anomaly picks (see Figure 3.3). Panel 1 shows the division of the ridge into seven Sections based on geophysical and geochemical characteristics. Panel 2 shows the bathymetry (black line) sampled from shipboard bathymetry where available and the GEBCO 2014 30'' x 30'' grid elsewhere. The red line is the bathymetry filtered using a median filter with a wavelength of 5° longitude. Panel 3 shows the free-air gravity anomaly (black line) sampled from the Sandwell and Smith altimetry derived 1' x 1' marine gravity grid v.23.1 (Sandwell and Smith, 2008). Panel 4 shows the mantle Bouguer anomaly (black line) sampled from the MBA grid described above and the median filtered MBA (green line). The median filtered MBA grid calculated using a reduced mantle density of 3180 kg m^{-3} is shown in orange. Panel 5 shows the variation in $Na_{8.0}$ composition of basalt glasses dredged along the SWIR axis from Cannat et al. (2008) and Standish et al. (2008). Panel 6 shows shear wave velocity heterogeneities at 75 km depth, sampled from the tomographic model of Debayle et al. (2005). These are in percentage difference relative to PREM (V_s = 4.39 km s^{-1}). The grey vertical bars show the locations of fracture zones: BO = Bouvet, IO = Islas Orcadas, SH = Shaka, DT = DuToit, AB = Andrew Bains, MA = Marion, PE = Prince Edward, ES = Eric Simpson, DII = Discovery II, IN = Indomed, GA = Gallieni, AII - Atlantis II, ME = Melville. 52

3.7 Graph showing the variation in effective spreading rate along the ridge, calculated using the method of Dick et al. (2003). Red bars show the average effective spreading rate for each Section, which are labelled A-G, and are defined in Figures 3.6 and 3.1. Blue bars show the effective spreading rates for individual segments following broad 1st and 2nd order segmentation illustrated in Figure 3.16. The illustration of the ridge above shows the difference between the ridge strike (black line) and spreading direction (red arrows), determined using normal earthquake mechanisms and the orientation of transform faults. 58

3.8 A) Segmentation interpretation for Section B, superimposed on bathymetric contours. Segmentation illustrated reflects the 1st and 2nd order discontinuities only. Some morphologies such as oblique shear basins, which are interpreted to represent discontinuities, have been included in the segments in order to produce a continuous axial trace as has been done in other along axis studies (e.g. Lin et al., 1990; Cannat et al., 2008). B) Bathymetry data consisting of shipboard multibeam data and, where multibeam was unavailable the GEBCO 2014 30'' x 30'' grid (IOC et al., 2003). Superimposed on the bathymetry are the normal fault solutions for well-located earthquakes since 1977 with magnitudes >4.5 from the Global Centroid Moment Tensor database. C) Mantle Bouguer anomalies calculated by removing the gravity effect of the crust-water and moho interfaces assuming a consistent crustal density of 5 km and densities of 1030 kg m^{-3}, 2800 kg m^{-3} and 3300 kg m^{-3} for the water, crust and mantle respectively. 61

3.9 A) Segmentation interpretation for Section A, superimposed on bathymetric contours. Segmentation illustrated reflects the 1st and 2nd order discontinuities only. Some morphologies such as oblique shear basins, which are interpreted to represent discontinuities, have been included in the segments in order to produce a continuous axial trace as has been done in other along axis studies (e.g. Lin et al., 1990; Cannat et al., 2008). B) Bathymetry data consisting of shipboard multibeam data and, where multibeam was unavailable the GEBCO 2014 30'' x 30'' grid (IOC et al., 2003). Superimposed on the bathymetry are the normal fault solutions for well-located earthquakes since 1977 with magnitudes >4.5 from the Global Centroid Moment Tensor database. C) Mantle Bouguer anomalies calculated by removing the gravity effect of the crust-water and moho interfaces assuming a consistent crustal density of 5 km and densities of 1030 kg m^{-3}, 2800 kg m^{-3} and 3300 kg m^{-3} for the water, crust and mantle respectively. 64

3.10 A) Segmentation interpretation for Section D, superimposed on bathymetric contours. Segmentation illustrated reflects the 1st and 2nd order discontinuities only. Some morphologies such as oblique shear basins, which are interpreted to represent discontinuities, have been included in the segments in order to produce a continuous axial trace as has been done in other along axis studies (e.g. Lin et al., 1990; Cannat et al., 2008). B) Bathymetry data consisting of shipboard multibeam data and, where multibeam was unavailable the GEBCO 2014 30'' x 30'' grid (IOC et al., 2003). Superimposed on the bathymetry are the normal fault solutions for well-located earthquakes since 1977 with magnitudes >4.5 from the Global Centroid Moment Tensor database. C) Mantle Bouguer anomalies calculated by removing the gravity effect of the crust-water and moho interfaces assuming a consistent crustal density of 5 km and densities of 1030 kg m^{-3}, 2800 kg m^{-3} and 3300 kg m^{-3} for the water, crust and mantle respectively. 67

3.11 The upper and lower bathymetry maps show the location of across axis profiles, which were sampled to produce the ensemble average profile for the western and eastern parts of the ridge respectively . The profiles on the right show the individual profiles for Section G (marked on the lower bathymetry map), and the resultant ensemble averaged profile at the bottom. 72

3.12 Schematic diagram showing the definition of measurements taken of the axial valley bathymetric profiles. 73

3.13 Ensemble averaged axial profiles for Sections A to G of bathymetry (black line). Red dashed line shows the predicted bathymetry for subsidence following the plate cooling model of Parsons and Sclater (1977). The standard Parsons and Sclater (1977) model has been vertically shifted for each profile, so that the model zero age depth varies, in order to account for the long wavelength changes in axial depth. 75

3.14 Ensemble average profile of Section B including: All profiles (black line), profiles across magmatic segments (red line), profiles across amagamtic segments (blue line). 77

3.15 Right map shows the location of boxes for used for the admittance analysis (see chapter 6 for more detail). The red line shows the trace of the ridge axis. The contours are bathymetric contours with an interval of 2,000 m. Left graph shows the axial width averaged over the length of the admittance box against the best fit elastic thickness. Error bars are calculated using a percentage RMS error cut off of 20%. Black lines shows the theoretical relationship between elastic thickness and distance between first and second breaks for a broken plate model, given in equation 3.1. The assumed mantle density is 3300 kg m^{-3}, and assumed infill density is 0 kg m^{-3} (dotted line), 1030 kg m^{-3} (solid line) and 2800 kg m^{-3} (dashed line). 79

3.16 Example of along axis bathymetry and mantle Bouguer anomaly profiles between 42° E and 53° E. Dashed vertical lines represent the boundaries between segments. Shaded segments are discontinuities (either transform or non-transform), which have an along axis width due to the continuous nature of the profile track. These are excluded from the segments to remove source of bias from the measurements of segment length and axial relief. 82

3.17 Upper map shows bathymetry of segment 11 on the SWIR, an example of a Group I type segment. Contour interval is 100 m. Lower map shows the interpreted structural geomorphology, which was constructed using visual examination of 3D multibeam bathymetry and mantle Bouguer anomaly maps in Fledermaus software. Hashed area - inner valley area, dotted area - off axis basins, grey stippled area - axial volcanic ridge, black circles - volcanic cones. 84

3.18 Upper map shows bathymetry of segment 41 on the SWIR, an example of a Group I type segment. Contour interval is 100 m. Lower map shows the interpreted structural geomorphology, which was constructed using visual examination of 3D multibeam bathymetry and mantle Bouguer anomaly maps in Fledermaus software. Hashed area - inner valley area, dotted area - off axis basins, grey stippled area - axial volcanic ridge, black circles - volcanic cones. 85

3.19 Upper map shows bathymetry of segment 52 on the SWIR, an example of a Group II type segment. Contour interval is 100 m. Lower map shows the interpreted structural geomorphology, which was constructed using visual examination of 3D multibeam bathymetry and mantle Bouguer anomaly maps in Fledermaus software. Hashed area - inner valley area, dotted area - off axis basins, grey stippled area - axial volcanic ridge, black circles - volcanic cones. 87

3.20 Upper map shows bathymetry of segment 55 on the SWIR, an example of a Group III type segment. Contour interval is 100 m. Lower map shows the interpreted structural geomorphology, which was constructed using visual examination of 3D multibeam bathymetry and mantle Bouguer anomaly maps in Fledermaus software. Hashed area - inner valley area, dotted area - off axis basins, black circles - volcanic cones. 88

3.21 Upper map shows bathymetry of segment 8 on the SWIR, an example of a Group IV type segment. Contour interval is 100 m. Lower map shows the interpreted structural geomorphology, which was constructed using visual examination of 3D multibeam bathymetry and mantle Bouguer anomaly maps in Fledermaus software. Hashed area - inner valley area, dotted area - off axis basins, black circles - volcanic cones. 90

3.22 Schematic conceptual diagrams illustrating the proposed structure and processes occurring at the different segment Group types. 93

4.1 Examples of flank rift zones from Hawaii. Figure A, adapted from Fiske and Jackson (1972), shows topography of the onshore flank rift zones and offshore continuation, which forms a linear volcanic ridge. The dark shaded area represents the area above sea level, the white dotted areas show the locations of onshore volcanic rifts. Contour interval is 1000 ft (305 m). Figure B, adapted from Smith et al. (2002), shows a bathymetric map of the Puna Ridge, Hawaii, contoured at 50 m. The bathymetry shows lava terraces (T), volcanic cones (C), and craters (black dots). 102

4.2 Comparison of substrate interpretation and backscatter along an ROV transect draped over a topographic profile of distance along a transect plotted against depth measured using a USBL on the ROV. Lower profile shows substrate interpretation; upper profile shows backscatter sampled from a backscatter grid (Figure 4.21). Light shades represent high backscatter, dark shades represent low backscatter. 105

4.3 Bathymetry map and bathymetric profiles showing Coral Seamount in regional context. 106
4.4 Bathymetry map (contour interval 100 m) of Coral Seamount from cruise JC066. Blue tracks show the ROV transects, yellow tracks show the SHRIMP transects, and white tracks show the HyBIS transects. White circles denote lithology sampling locations, letters correspond to the ROV images in Figure 4.26 and profile locations in Figure 4.28. 107
4.5 3D perspective image of the summit of coral seamount. A colour gradient representing bathymetry is applied between the depths of 400 m and 150 m. The mesh grid reflects the underlying bathymetry. The bathymetry data have been illuminated by an artificial sun in the south and the contour interval is 25 m. 108
4.6 Perspective view of Coral Seamount from the north (azimuth 5°, elevation 5°). The mesh grid shows the regional bathymetry derived from the GEBCO 2014 30'' x 30'' global bathymetry grid (IOC et al., 2003). The coloured image shows the shipboard bathymetry from cruise JC066. The bathymetry data have been illuminated by an artificial sun in the southwest and the contour interval is 25 m. 109
4.7 Bathymetry map and bathymetric profiles showing Melville Bank in regional context. 110
4.8 Bathymetry map (contour interval 100 m) of Melville Bank from cruise JC066. Blue tracks show the ROV transects, yellow tracks show the SHRIMP transects, and white tracks show the HyBIS transects. White circles denote lithology sampling locations, letters correspond to the ROV images in Figure 4.26 and profile locations in Figure 4.28. 111
4.9 12 kHz backscatter sonar of Melville Bank. Dark shades are low backscatter, light shades are high backscatter. Bathymetric contours at an interval of 200 m are overlain. 112
4.10 Perspective view of Melville Bank from the southwest (azimuth 210°, elevation 40°). The mesh grid shows the regional bathymetry derived from the GEBCO 2014 30'' x 30'' global bathymetry grid (IOC et al., 2003). The coloured image shows the shipboard bathymetry from cruise JC066. The bathymetry data have been illuminated by an artificial sun in the southwest and the contour interval is 25 m. 113
4.11 Bathymetry map and bathymetric profiles showing Middle of What Seamount in regional context. 114
4.12 Bathymetry map (contour interval 100 m) of Middle of What Seamount from cruise JC066. Blue tracks show the ROV transects, yellow tracks show the SHRIMP transects, and white tracks show the HyBIS transects. White circles denote lithology sampling locations, letters correspond to the ROV images in Figure 4.26 and profile locations in Figure 4.28. . . 115
4.13 12 kHz backscatter sonar of Middle of What Seamount. Dark shades are low backscatter, light shades are high backscatter. Bathymetric contours at an interval of 200 m are overlain. 116

4.14 Upper panel shows a tectonic interpretation map of Middle of What Seamount. Bathymetric contours (thin black lines) are plotted at 100 m intervals. Thick black lines show the positions of faults inferred from bathymetry, backscatter and slope maps. Summit bathymetry (above 1300 m depth) is shaded to show the dissection of the summit regions due to faulting. Lower panel shows a bathymetric profile across the seamount along the red line on the map. Faults and volcanic cones are labelled. 117
4.15 Bathymetry map and bathymetric profiles showing Sapmer Bank in regional context. 119
4.16 Bathymetry map (contour interval 100 m) of Sapmer Bank from cruise JC066. Blue tracks show the ROV transects, yellow tracks show the SHRIMP transects, and white tracks show the HyBIS transects. White circles denote lithology sampling locations, letters correspond to the ROV images in Figure 4.26 and profile locations in Figure 4.28. 120
4.17 12 kHz backscatter sonar of Sapmer Bank. Dark shades are low backscatter, light shades are high backscatter. Bathymetric contours at an interval of 200 m are overlain. 121
4.18 Perspective view of Sapmer Bank from the south (azimuth 160°, elevation 40°). The mesh grid shows the regional bathymetry derived from the GEBCO 2014 30'' x 30'' global bathymetry grid (IOC et al., 2003). The coloured image shows the shipboard bathymetry from cruise JC066. The bathymetry data have been illuminated by an artificial sun in the northeast and the contour interval is 25 m. 123
4.19 Bathymetry map and bathymetric profiles showing Atlantis Bank in regional context. 124
4.20 Bathymetry map (contour interval 100 m) of Atlantis Bank from cruise JC066. Blue tracks show the ROV transects, yellow tracks show the SHRIMP transects, and white tracks show the HyBIS transects. White circles denote lithology sampling locations, letters correspond to the ROV images in Figure 4.26 and profile locations in Figure 4.28. Inset shows greyscale bathymetry of northern slope failure illuminated by an artificial sun in the northwest showing small scale morphology. 125
4.21 12 kHz backscatter sonar of Atlantis Bank. Dark shades are low backscatter, light shades are high backscatter. Bathymetric contours at an interval of 200 m are overlain. 127
4.22 Perspective view of Atlantis Bank from the south (azimuth 160°, elevation 40°). The mesh grid shows the regional bathymetry derived from the GEBCO 2014 30'' x 30'' global bathymetry grid (IOC et al., 2003). The coloured image shows the shipboard bathymetry from cruise JC066. The bathymetry data have been illuminated by an artificial sun in the northeast and the contour interval is 25 m. 128
4.23 Bathymetry map and bathymetric profiles showing Vera Seamount in regional context. 129

4.24 Bathymetry map (contour interval 100 m) of Vera Seamount from cruise MD192. 130

4.25 Perspective view of Vera Seamount from the south (azimuth 160°, elevation 40°). The mesh grid shows the regional bathymetry derived from the GEBCO 2014 30'' x 30'' global bathymetry grid (IOC et al., 2003). The coloured image shows the shipboard bathymetry from cruise MD192. The bathymetry data have been illuminated by an artificial sun in the northeast and the contour interval is 25 m. 131

4.26 A series of still images taken from ROV video imagery showing some of the different substrates observed on the seamounts. The location of each image is shown on the bathymetry maps in the previous sections and ROV transect profiles in Figure 4.28. White scale bars are 50 cm long. (A) Coarse clastic sand (B) Sand with rounded volcaniclastic cobbles (C) Carbonate platform with surficial plates (D) Coral framework (E) Fine volcanic ash during coring operations (F) Beach conglomerate (G) Pillow lavas (H) Folded lava flows with banding (I) Intrusive gabbros (J) Angular volcanic tallus boulders (K) Tectonised gabbros (L) Dark fine grained rock, cut through by hydrothermal veins. 136

4.27 Photomicrographs of thin sections from lithological samples taken using the ROV grab arm and HyBIS rock grab. Scale is on the bottom right of each micrograph. (1) Fine grained limestone with thick walled benthic forams, molluscan material and algae fragments (2) Contact between limestone and altered gabbro (3) Tholeiitic basalt with plagioclase phenocrysts (4) Olivine dolerite with sub-euhedral resorbed phenocrysts (5) Tectonised gabbro with abundant amphibole (6) Coarse grained olivine gabbro. 138

4.28 ROV transects across the five seamounts showing the different lithological interpretations based on ROV imagery and petrological samples. Locations of ROV transects are shown in the earlier seamount bathymetry maps. Lithological interpretations are draped over a topographic profile of distance along transect plotted against depth measured using a USBL on the ROV. Figure illustrates rock type on the seafloor only, with no constraints on lithology thickness. Letters correspond to the ROV images in Figure 4.26. 140

4.29 Geometry of flank rift zone orientations, illustrated as circular azimuthal histograms of unweighted frequencies for the four different tectonic settings. Tectonic settings are illustrated schematically below each polar histogram, not to scale. Label n=x, where x is the number of flank rift zones measured in this particular tectonic setting. The label in the bottom right corner indicates the magnitude represented by each concentric circle on the azimuthal histogram. 145

4.30 Schematic diagram illustrating hypothetical mechanism for off-ridge volcanism. Inferred isotherms (red dashed lines), solidus (thick red dashed line) and Moho (black line) geometry from seismic experiments of Li et al. (2015). Grey vertical lines and ellipses reflect dykes and pillow lavas respectively. Solid black lines indicate a stylised representation of ridge topography and sub-surface faults. Red areas represent hypothetical magma packets. Red arrows show the migration of magma along the impermeable boundary at the top of the melt column. 150
4.31 Plot of edifice height against crustal age for seamounts described in this chapter (red crosses) and other seamounts on the SWIR (black crosses). All seamounts represented by black crosses show no flank rift zone structures. Bathymetric contours for the seamounts in this chapter (red crosses) are overlain to illustrate the seamount geometry. Crustal ages are determined using magnetic anomaly picks. 152
4.32 Plot of edifice volume against flank rift zone length for seamounts described in this chapter (red crosses). Bathymetric contours for the seamounts in this chapter (red crosses) are overlain to illustrate the seamount geometry. Seamount volumes were determined using a basal contour to define the extent of the seamount (see chapter 5). 154
4.33 Bathymetric profile through the slope failure on Melville Banks southwest flank (red line) and adjacent unfailed flank (black line). Slope failure volume was calculated by comparing the two profiles in conjunction with contour parallel profiles to estimate a total volume of material removed. The volume of material removed is within 0.15 km^3 of the estimated volume of the debris deposit, suggesting little loss of material. 156
4.34 Map showing locations of bathymetric profiles used for exponential curve fitting (black lines) overlain over bathymetry data. Profiles start at the edge of the shelf break to eliminate wave eroded platforms and are 12 km in length. Clusters of profiles are oriented parallel to the average maximum dip direction of the sector being investigated. Each sector is classified into slope failure or unfailed flank based on morphological data. Bathymetry data are shipboard bathymetry overlain by regional bathymetry from the Sandwell and Smith global predicted bathymetry v.23.1 (Sandwell and Smith, 2008). Significant discrepancies between these two bathymetric data sets occur in some sectors of the seamounts. 159
4.35 Ensemble average profiles of bathymetry for a single sector of Coral Seamount. Profiles used to calculate the average are individually displayed (black lines) and stacked at the bottom (grey lines). Resultant average profile is overlain in red. 160
4.36 Selected bathymetric profiles from Melville Bank and Atlantis Bank (black line) and the fitted exponential curve (red line).The exponential coefficient (b) and root mean square (RMS) error for each profile is included. Profiles reflect a range of b coefficients and RMS errors calculated across the seamounts. Profiles 11 and 6 represent slope failure sectors while profiles 7 and 20 represent unfailed volcanic sectors. . . . 162

4.37 Comparison of exponential coefficient (b) and RMS error for each profile. Slope failure profiles (triangles), which are identified using bathymetry and backscatter, generally have b>0.6 and RMS error <80 while volcanic unfailed sectors (black circles) have b<0.6 and a wide range of RMS errors. A notable exception in the lower left shows a sector interpreted as a slope failure with a low b coefficient. This slope failure is interpreted as a collapsed caldera. 163

4.38 Schematic diagram illustrating the two-stage slope failure process proposed to explain the steep upper slope, mid-slope chute structure, and downslope debris fields observed at Melville Seamount and Atlantis Bank. 165

(a) Initial unfailed slope. 165

(b) First stage: slumping causing slow movement of consolidated material along fault. 165

(c) Second stage: failure of the surficial material of the over steepened slump scar forming a debris avalanche. 165

4.39 Windrose diagrams illustrating the average slope gradient along different azimuths for each seamount. Slope gradients range from 7° to 40°. Blue sectors indicate no slope failures, green sectors indicates small scale gully features which do not significantly modify the edifice geometry, red sectors indicate tectonic features such as fault scarps which affect the slope gradient. Major slope failures are indicated with black arrows, numbers correspond to table 4.2. 169

4.40 Plot showing the relationship between edifice height and the degree of slope failures present on the seamounts described in this chapter (red crosses). Bathymetric contours for the seamounts in this chapter (red crosses) are overlain to illustrate the seamount geometry. Base axis shows a qualitative description of the degree of slope failure based on bathymetry and backscatter data. 170

5.1 Reproduced from Bohnenstiehl et al. (2012). Panel A shows the locations of topographic profiles passing through the topographic peak, distributed azimuthally. Panels B and C show N-S and E-W profiles. White circles show the incremented steps as the basal contour is modified down slope. Red circles show the termination point of the basal contour modification for these profiles. 179

5.2 Reproduced from Bohnenstiehl et al. (2012). Schematic diagram showing the incrementation of the basal contour, and the subsequent changes in the ratio of the cross sectional area and outlining perimeter, which is primarily used to determine the location of the base of the seamount. . 181

5.3 Bathymetric map showing location of four study areas: oblique, orthogonal, central, eastern. Study areas are outlined by black boxes. Bathymetry data is derived from the GEBCO 2014 30'' x 30'' global bathymetry grid (IOC et al., 2003) and contoured at 2000 m. 183

5.4 Bathymetric map of the axial valley gridded at 50 m using swath bathymetry. White circles of fixed diameter are used to show the locations of seamounts detected which are greater than 50 m in height. The map is contoured at 250 m so seamounts between 50 and 100 m may not be clearly visible on the bathymetry. 184
5.5 Bathymetric map of the MAR axial valley and flanking highs between 25.5° and 27.5° N gridded at 50 m derived from multibeam bathymetry. This represents a subset of the entire analysis area which extends between 24° and 30° N. Black boxes show the areas in which the MBOA was used to detect seamounts. Red circles show the locations of seamounts detected on the axial valley floor greater than 50 m in height. White circles show the location of seamounts detected on the flanking highs greater than 50 m in height. The bathymetry is contoured at 250 m. . . 185
5.6 Cumulative count of seamounts plotted against height for the axial valley floor of the MAR from 24° N to 30° N. Black solid circles show the observed height distribution, black line shows the maximum likelihood model fit to the data. 186
5.7 Bathymetry map of the oblique Section based on multibeam bathymetry. Black boxes outline the areas used in the analysis to detect seamounts. Red circles show the locations of seamounts with height greater than 50 m in the axial valley floor. White circles show the location of seamounts with height greater than 50 m on the rim flanks. Bathymetry data was used to identify the limits of the axial valley floor to calculate the observed seamount densities. 188
5.8 Cumulative count of seamounts plotted against height for the axial valley floor of the oblique Section. Black solid circles show the observed height distribution, black line shows the maximum likelihood model fit to the data. 189
5.9 Seamount distribution along the axial valley of the oblique Section. Lower graph shows the number of seamounts binned in intervals of 0.2° longitude. Upper graph shows the axial bathymetry along zero-age. . . 191
5.10 Cumulative count of seamounts plotted against height for the axial valley floor of the three segments types in the oblique Section, a) Amagmatic, b) Shallow c) Magmatic. Black solid circles show the observed height distribution, black line shows the maximum likelihood model fit to the data. 192
5.11 Bathymetry map of the orthogonal Section based on multibeam bathymetry. Black boxes outline the areas used in the analysis to detect seamounts. Red circles show the locations of seamounts with height greater than 50 m in the axial valley floor. White circles show the location of seamounts with height greater than 50 m on the rim flanks. 194
5.12 Cumulative count of seamounts plotted against height for the axial valley floor of the orthogonal Section. Black solid circles show the observed height distribution, black line shows the maximum likelihood model fit to the data. 195

5.13 Seamount distribution along the axial valley of the orthogonal Section. Lower graph shows the number of seamounts binned in intervals of 0.2° longitude. Upper graph shows the axial bathymetry along zero-age crust. 196

5.14 Polar histogram of the seamount phase angles, which form a non-dimensional representation of the seamount position with respect to the segment centre and bounding discontinuities. An angle of 0° corresponds to the discontinuity, while an angle of 180° corresponds to the centre of the segment. 197

5.15 Bathymetry map of the central Section based on multibeam bathymetry. Black boxes outline the areas used in the analysis to detect seamounts. Red circles show the locations of seamounts with height greater than 50 m in the axial valley floor. White circles show the location of seamounts with height greater than 50 m on the rim flanks. 198

5.16 Cumulative count of seamounts plotted against height for the axial valley floor of the central Section. Black solid circles show the observed height distribution, black line shows the maximum likelihood model fit to the data. 199

5.17 Polar histogram of the seamount phase angles, which form a non-dimensional representation of the seamount position with respect to the segment centre and bounding discontinuities. An angle of 0° corresponds to the discontinuity, while an angle of 180° corresponds to the centre of the segment. 200

5.18 Seamount distribution along the axial valley of the central Section. Lower graph shows the number of seamounts binned in intervals of 0.2° longitude. Upper graph shows the axial bathymetry along zero-age crust. 201

5.19 Bathymetry map of the eastern Section based on multibeam bathymetry. Black boxes outline the areas used in the analysis to detect seamounts. Red circles show the locations of seamounts with height greater than 50 m in the axial valley floor. White circles show the location of seamounts with height greater than 50 m on the rim flanks. 202

5.20 Seamount distribution along the axial valley of the eastern Section. Lower graph shows the number of seamounts binned in intervals of 0.2° longitude. Upper graph shows the axial bathymetry along zero-age crust. 203

5.21 Schematic block diagrams illustrating the three different styles of volcanism observed on different areas of the SWIR axial valley. 209

5.22 Series of graphs showing the variation in different output parameters due to varying the e-fit, while other parameters are held at base case values. The output parameters measured are (a) seamount number (b) average seamount height (c) total seamount height (d) total seamount volume (e) average seamount ellipticity, calculated using the ratio of the long and short axes (f) average seamount volume 217

5.23 Series of graphs showing the variation in different output parameters due to varying the contour interval, while other parameters are held at base case values. The output parameters measured are (a) seamount number (b) average seamount height (c) total seamount height (d) total seamount volume (e) average seamount ellipticity, calculated using the ratio of the long and short axes (f) average seamount volume (g) range of azimuths exhibited by the best fitting ellipses 218

5.24 Series of graphs showing the variation in different output parameters due to varying the maximum basal dimension, while other parameters are held at base case values. The output parameters measured are (a) seamount number (b) average seamount height (c) total seamount height (d) total seamount volume (e) average seamount ellipticity, calculated using the ratio of the long and short axes (f) average seamount volume (g) range of azimuths exhibited by the best fitting ellipses 220

5.25 Series of graphs showing the variation in different output parameters due to varying the maximum elliptical ratio, while other parameters are held at base case values. The output parameters measured are (a) seamount number (b) average seamount height (c) total seamount height (d) total seamount volume (e) average seamount ellipticity, calculated using the ratio of the long and short axes (f) average seamount volume (g) range of azimuths exhibited by the best fitting ellipses 222

5.26 Series of graphs showing the variation in different output parameters due to varying the minimum slope threshold, while other parameters are held at base case values. The minimum slope threshold is expressed in the graphs as minimum height-radius ratio i.e. $tan(slope)$. The output parameters measured are (a) seamount number (b) average seamount height (c) total seamount height (d) total seamount volume (e) average seamount ellipticity, calculated using the ratio of the long and short axes (f) average seamount volume (g) range of azimuths exhibited by the best fitting ellipses 223

5.27 Graph illustrating the number of seamounts detected for the same synthetic grid split up into different size grids. The number of seamounts lost along the margin is equal to the difference between the number of detected seamounts for the grid being investigated and the full grid (20° x 20°) 226

5.28 Maps showing locations of seamounts located in the SWIR region from (a) Hillier and Watts (2007) (0.1 to 6.7 km in height), (b) Wessel (2001) (2 to 7 km in height), (c) this study (∼0.3 to 7 km in height). The seamount locations from the other two studies were sampled from global data sets. 227

5.29 Log number of seamounts plotted against height for the Southwest Indian Ridge region (-10 to 70° E, 25 to 60° S).Blue line shows the results from this study. Red line shows the results from a subset of the global study of Hillier and Watts (2007) taken over the same SWIR region. . . 229

5.30 Profiles of seamount counting statistics along the ridge crest of the Southwest Indian Ridge. Panel A shows the number of seamounts binned in 1° intervals. Panel B shows the total volume of seamounts binned in 1° intervals. Panel C shows the total volume-seamount count ratio for each 1° bin. Panel D shows the magmatic flux calculated by integrating the total seamount volume over the crustal age. This assumes that all seamounts formed on zero-age crust. 231

5.31 Polar histogram of the seamount phase angles, which form a non-dimensional representation of the seamount position with respect to the segment centre and bounding discontinuities. (a) includes transform discontinuities (b) does not include transform discontinuities. An angle of 0° corresponds to the discontinuity, while an angle of 180° corresponds to the centre of the segment. 236

(a) Phase distribution including transform discontinuities 236

(b) Phase distribution neglecting transform discontinuities 236

5.32 Seamount number and total volume binned in 1° increments of longitude (SWIR) or latitude (EPR and MAR) for (a) Southwest Indian Ridge (b) Mid-Atlantic Ridge (c) East Pacific Rise. 238

6.1 Schematic diagram illustrating the flexure of an elastic beam due to bending moments applied at either end of the beam. Adapted from Watts (2001). 248

6.2 Schematic diagram illustrating the stresses experienced by an element of a cross section of a flexed beam. Adapted from Watts (2001). 249

6.3 Schematic diagram illustrating the moments acting on an element of the beam and the shear forces acting on the boundary of the element. Adapted from Watts (2001). 250

6.4 Schematic diagram illustrating the forces applied to the top and bottom of the element of the beam. Adapted from Watts (2001). 251

6.5 Schematic diagram illustrating the simple crustal model used for the relationship between topography and flexure, given in equation 6.26. . . 254

6.6 Schematic diagram illustrating the simple crustal model used to derive the equations for gravitation admittance due to flexure. 257

6.7 The coherence, phase and admittance determined from the spectral analysis of bathymetry and free-air gravity anomalies for a window on the Southwest Indian Ridge crest. The inset shows the location and topographic features of the window. The red points on the admittance graph show the data used to estimate the slope. The blue line shows the best fit slope. 260

6.8 Top panel shows the IRFs for two different windows (centred on 15° E and 65° E at the ridge axis) with different T_e in blue and red. The black lines are the theoretical flexural IRFs for T_e between 0 and 40 km. The bottom left panel shows the RMS error minima used to determine best fit T_e. The bottom right panel shows an enlarged image of the RMS minima illustrating the constant difference cut off of 20% of the minimum RMS error value, which is used to determine upper and lower bonds for the best fit T_e 263

6.9 Panel A shows a sample of synthetic bathymetry. Panels B, C and D show the corresponding gravity data for T_e of 2 km, 6 km and 10 km respectively. 265

6.10 Power spectra for the topography of synthetic bathymetry using base-height ratios between 2 and 11.7 (black), between 1 and 5.85 (blue) and between 3 and 23.4 (red). 266

6.11 Schematic diagram illustrating the two layer crustal model used to calculate the gravity anomaly for the topography and flexed synthetic surfaces. 268

6.12 Isostatic response functions and best fit T_e from least squares fitting for windows with a Mercator projection. Top left panel shows the position of the windows and the variation in window size with latitude. Top right panel shows the IRFs for synthetic T_e of 2 km (red), 6 km (green) and 10 km (blue). Bottom panel shows the recovered T_e (solid circles) compared to the input T_e (coloured lines) for synthetic T_e of 2 km (red), 6 km (green) and 10 km (blue). Error bars are derived from the RMS errors as detailed in Figure 6.8. 270

6.13 Isostatic response functions and best fit T_e from least squares fitting for windows with an equal area projection. Top left panel shows the position of the windows. Top right panel shows the IRFs for synthetic T_e of 2 km (red), 6 km (green) and 10 km (blue). Bottom panel shows the recovered T_e (solid circles) compared to the input T_e (coloured lines) for synthetic T_e of 2 km (red), 6 km (green) and 10 km (blue). Error bars are derived from the RMS errors as detailed in Figure 6.8. 274

6.14 Comparison of synthetic input T_e and recovered T_e illustrating the systematic underestimation of T_e, which increases with T_e. Dotted line shows the relationship between synthetic input and recovered T_e if the T_e is recovered perfectly. The black dots show the average recovered T_e over a series of windows for a given synthetic input T_e. The black line shows the fit of the cubic equation describing the downward bias. The grey line shows the bias curve used in Kalnins and Watts (2009). 276

6.15 Figure showing the difference between input T_e and recovered T_e using synthetic topography and gravity for different window sizes. The solid black line shows the input T_e. The five coloured circles show the recovered T_e for the same input T_e using different window sizes. 277

6.16 Comparison of input synthetic T_e and recovered T_e for windows over a synthetic ridge. The top panel shows results for a synthetic ridge with a spreading rate of 14 mm yr^{-1} typical of the SWIR. The top panel shows results for a synthetic ridge with a spreading rate of 25 mm yr^{-1} typical of the MAR. The top panel shows results for a synthetic ridge with a spreading rate of 140 mm yr^{-1} typical of the EPR. 280
6.17 Bathymetry map sampled from the GEBCO 2014 30'' x 30'' grid. The locations of the admittance windows on the Southwest Indian Ridge are outlined in black 281
6.18 Fit of theoretical flexure model to observed IRF data for 4 different windows on the SWIR. The raw data is represented by the blue dots, the error bars are determined using the admittance error. The solid black line is the theoretical flexural model with the best fit T_e determined by least squares fitting. 283
6.19 Comparison of the McKenzie (2010) model and the model used in this study. 285
6.20 Flexural response function, $\phi(k)$ 290
6.21 Fit of theoretical flexure-convection model to observed IRF data for 4 different windows on the SWIR. The raw data is represented by the blue dots, the error bars are determined using the admittance error. The solid black line is the theoretical flexural model with the best fit T_e determined by least squares fitting. The dotted black line is the new combined flexure-convection model. 291
6.22 Relationship between best fit T_e and lithospheric lid thickness for the windows along the Southwest Indian Ridge. 292
6.23 Isostatic response functions for windows at 0° and 5° longitude. Blue circles show the observed data, black shows the flexural model fit. Error bars are determined using the admittance error. 293
6.24 Variation in elastic thickness along the Southwest Indian Ridge crest. Top panel shows the position of the windows. Upper graph shows the best fit T_e using the combined flexure-convection model. Lower graph shows the best fit T_e using the purely flexural model. 295
6.25 Variation in elastic thickness along the Mid-Atlantic Ridge crest. Top panel shows the position of the windows. Upper graph shows the best fit T_e using the combined flexure-convection model. Lower graph shows the best fit T_e using the purely flexural model. 297
6.26 Variation in elastic thickness along the East Pacific Rise. Top panel shows the position of the windows. Upper graph shows the best fit T_e using the combined flexure-convection model. Lower graph shows the best fit T_e using the purely flexural model. 299
6.27 Comparison of best fit T_e and spreading rate. Red circles - SWIR, blue squares - MAR, green triangles - EPR, pink circles - data for the MAR and EPR from Cochran (1979), yellow diamonds - data for a global set of ridges from Luttrell and Sandwell (2012). Grey boxes show the range expected for the MAR and EPR from Cochran (1979). 301

List of Tables

2.1 List of multibeam surveys carried out over seamounts on cruise JC066 . 25

3.1 Characteristics of the ensemble average bathymetry profiles for Sections A to G. 74

4.1 Summary of SWIR study seamount characteristics 132
4.2 Characteristics of slope failures identified on the six seamounts. 167
4.3 Characteristics of the edifices and truncated summits identified on the six seamounts. 172

5.1 Seamount population statistics for different studies between 24° N and 30° N on the axial valley floor of the Mid-Atlantic Ridge 187
5.2 Input parameters for the Modified Basal Outlining Algorithm 212
5.3 Input parameter statistics 213
5.4 Importance, sensitivity and elasticity indexes from one-at-time sensitivity analysis on the input parameters for the Modified Basal Outlining Algorithm 215
5.5 Final values selected as input parameters for the Modified Basal Outlining Algorithm 224

6.1 Layer thicknesses and densities used in crustal model 269
6.2 Notation for Vincenty's Formula 272
6.3 Parameters used in combined flexure-convection model 286

Abbreviations and Symbols Glossary

AVR - Axial Volcanic Ridge

BTJ - Bouvet Triple Junction

CIR - Central Indian Ridge

EPR - East Pacific Rise

FRZ - Flank Rift Zone

HyBIS - Hydraulic Benthic Interactive Sampler

IRF - Isostatic Response Function

LVR - Linear Volcanic Ridge

Ma - Millions of years ago

MAR - Mid Atlantic Ridge

NDGC - National Geophysical Data Center

NOAA - National Oceanic and Atmospheric Administration

OCC - Oceanic Core Complex

ROV - Remotely Operated underwater Vehicle

RTJ - Rodriguez Triple Junction

SAAR - South American Antarctic Ridge

SEIR - Southeast Indian Ridge

SHRIMP - Seabed High Resolution Imaging Platform

SWIR - Southwest Indian Ridge

T_e - Elastic Thickness

USBL - Ultra Short BaseLine

Acknowledgements

First and foremost I would like to thank my supervisor Tony Watts. I'm incredibly grateful for his continuous guidance and enthusiasm for the project, without which it would not have succeeded. His lifetime of scientific curiosity is infectious. To my family, I couldn't have survived this PhD without your unquestioning love and support; to my parents, for their unfailing confidence in me, my partner Thomas, who helped me enjoy life outside my PhD, and to Harriet, who always believed I would succeed. I'd like to thank the scientists and crew aboard my three research cruises, particularly those on board JC066 for supporting a novice at sea, and the PhD students for all the good times. Thanks also to Brook T, Rebecca, Brook K, Dirk, Maria, Johnny, Dan, Lara, and Tristan in the Marine Lab, for good humour, empathy, and the endless office games. I am grateful to Henry Dick and to Jian Lin for sharing of their research insights on the Southwest Indian Ridge during my stay at Woods Hole Oceanographic Institute, and for the welcome and hospitality I received; and to James Moore for his continued guidance and support with the admittance studies in this thesis. Finally, a special thank you to Mr Purser, my school geology teacher, who first set me on the road to a love of geology.

Chapter 1

Introduction

1.1 Ultra-slow Spreading Ridges

Mid-ocean ridges have been studied using bathymetric measurements since the HMS Challenger expedition (1872-1876), which identified a north-south rise in the middle of the Atlantic Ocean: the Mid-Atlantic Ridge. Since the Second World War, advances in technology and increased marine activity have led to increasingly detailed seafloor surveys revealing a global mid-ocean ridge system. These surveys have allowed mid-ocean ridges to be classified based on their morphological, structural and volcanological features. Early morphological studies (e.g. Heezen, 1960; Menard, 1960) showed a dichotomy between the, fast spreading, East Pacific Rise and, slow spreading, Mid-Atlantic Ridge. Further investigation of the mid-ocean ridge system showed that slow spreading ridges (spreading rates less than 60 mm yr^{-1}) are generally characterised by axial valleys superimposed on a broad ridge; fast spreading ridges (spreading rates greater than 80 mm yr^{-1}) are generally characterised by narrow axial rises (e.g. Macdonald, 1982). Intermediate spreading ridges, with spreading rates between fast and slow spreading rates are characterised by variable axial morphology(Behn et al., 2004). These ridge types all share several fundamental characteristics: (i) They have a relatively consistent crustal thickness, on average between 6 and 7 km (Raitt, 1963)

(*ii*) They consist of volcanic accretionary segments separated by transform or non-transform discontinuities (Lin et al., 1990; Sempere et al., 1993) (*iii*) They generate elongate fault bound abyssal hills which have a strike perpendicular to the spreading direction (Macdonald, 1982).

These changes in morphological characteristic are often interpreted in terms or spreading rate. However, anomalous areas of the mid-ocean ridge system such as the Australian Antarctic Discordance and Reykjanes Ridge, which are anomalously deep and shallow respectively, have been related to convective up and downwellings in the mantle. This shows that these morphological variations are dependent on the temperature structure, which is itself dependent on the spreading rate along with other variables.

In the late 1980s and 1990s bathymetric mapping and dredge sampling continued on the global mid-ocean ridge system, revealing some anomalous observations on very slow spreading ridges in the Arctic and Indian Oceans. Multibeam bathymetry studies of the axial crest morphology (e.g. Cannat et al., 1999; Cochran et al., 2003) showed that some segments of these ridges were anomalously deep and not oriented perpendicular to the spreading directions. These isolated axial deep areas were attributed to anomalously cold mantle temperatures similar to the Australian Antarctic Discordance (Cannat et al., 1999). Basalts sampled at these anomalously deep segments were found to be K-enriched alkali basalts and hawaiites (le Roex et al., 1992), incompatible with the degree of partial melting and crustal accretion mechanisms attributed to slow spreading ridges. The unusual geochemical signature of these basalts was attributed to a very low degree of partial melting (3-5 wt%) at a greater depth than predicted by mid-ocean ridge melting models (le Roex et al., 1992). These low degrees of partial melting should produce a thinner crust than the 6 to 7 km observed at other mid-ocean ridges (see Figure 1.1). Seismic studies over anomalously deep segments of the Gakkel Ridge showed dramatically thinner crust, between 2 and 3 km thick (Jackson et al., 1982).

Another change in the ideas of crustal accretion at very slow spreading ridges occurred through dredging at ridge-transform intersections. These dredges showed abundant

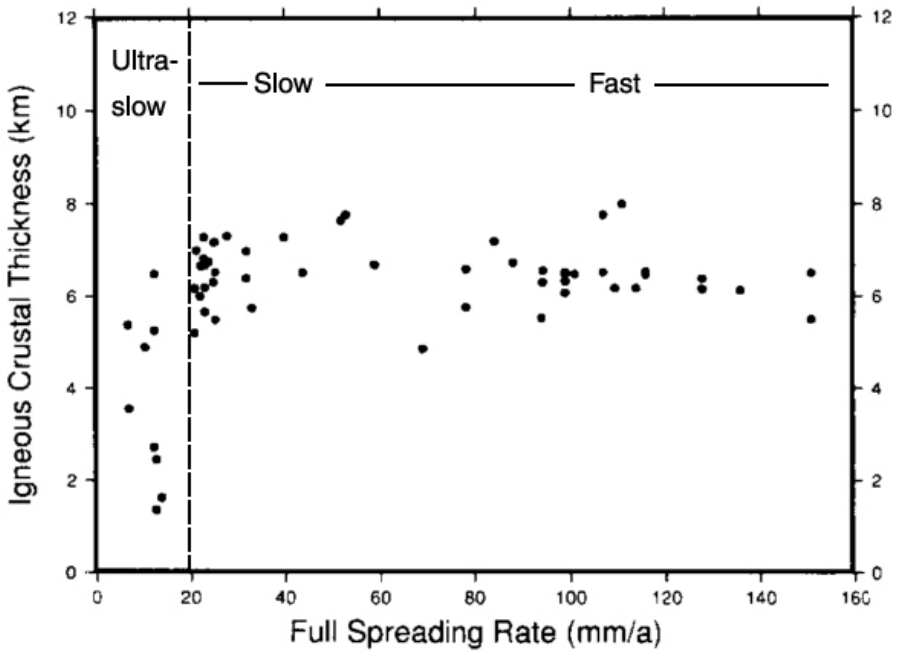


Figure 1.1: Igneous crustal thickness plotted against full spreading rate for seismic measurements corrected for the effect of thin crust at fracture zones. Crustal thicknesses range between 5.5 km and 7.5 km except for ultra-slow spreading rates (less than 20 mm yr^{-1}). Modified from Bown and White (1994).

lower crustal and upper mantle rocks exposed at the seafloor, which could not be accounted for by the vertical displacement observed at the inside transform corner highs (Dick et al., 1991). Further dredging of the anomalously deep regions away from the ridge-transform intersections reveals a higher than expected abundance of peridotite (Cannat et al., 2006; Dick et al., 2003). These observations suggest a large proportion of mantle and lower crustal rocks are exposed at the seafloor in the deep areas of these ridges. It has subsequently been shown that the seismic structure derived from seismic experiments in the Arctic (Jackson et al., 1982) could be satisfied by a thin layer of serpentinite overlying mantle rocks, suggesting that the magmatic crust may be entirely absent.

The inferred low degree of partial melting on these ridges, thin magmatic crust and anomalously deep bathymetry were all attributed to the effects of very slow spreading rates, less than 20 mm yr^{-1}, leading to the proposal of a new class of mid-ocean ridge:

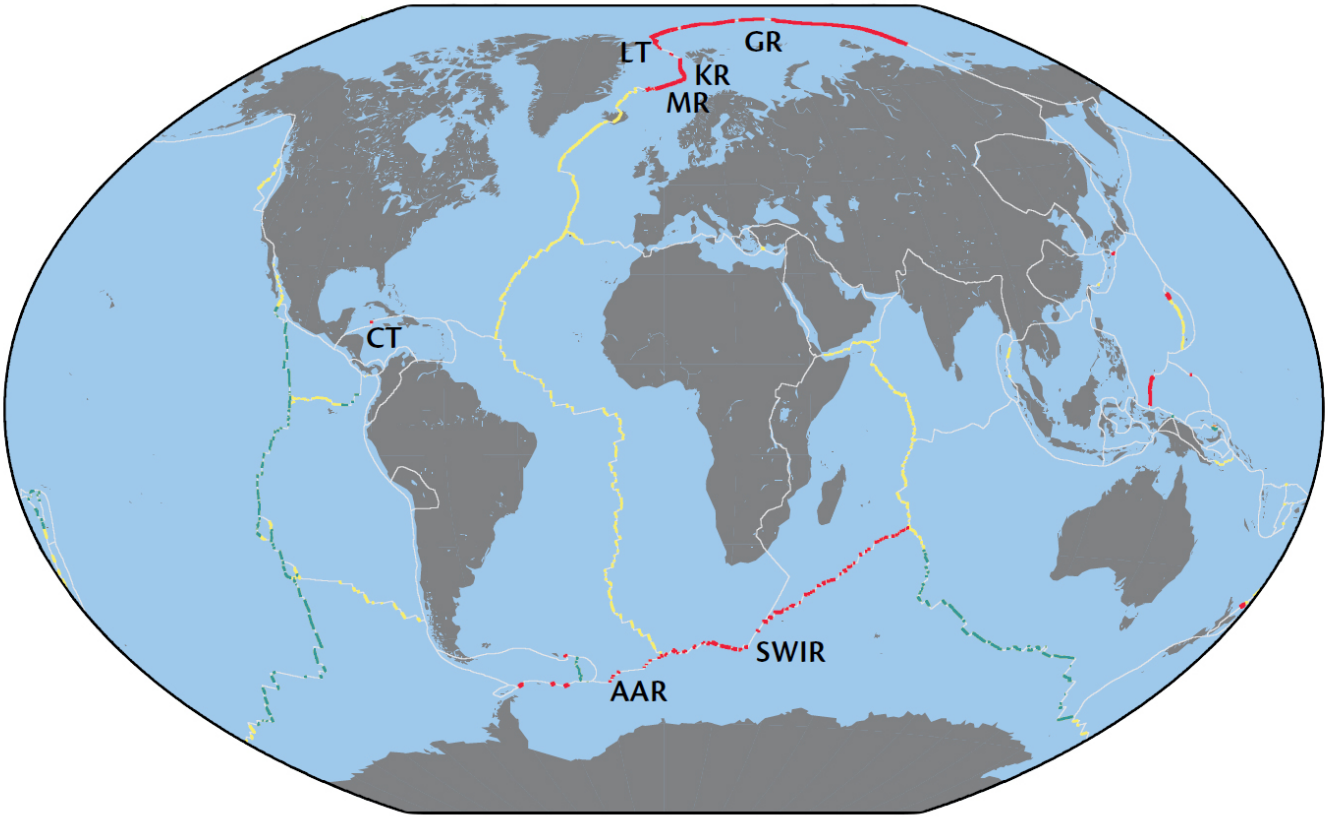


Figure 1.2: Global plate boundaries (grey lines) defined by Bird (2003). Coloured lines represent oceanic spreading ridges: Fast spreading (full spreading rate greater than 60 mm yr^{-1}) shown as green lines, Ultra-slow spreading (full spreading rate less than 20 mm yr^{-1}) shown as red lines. All other ridge segments shown as yellow lines. Ultra-slow spreading ridges are names: GR = Gakkel Ridge, LT = Lena Trough, KR = Knipovich Ridge, MR = Mohns Ridge, CT = Cayman Trough, AAR = American Antarctic Ridge, SWIR = Southwest Indian Ridge. Adapted from Snow and Edmonds (2007).

ultra-slow spreading(Dick et al., 2003). Ultra-slow spreading rates, defined as less than 20 mm yr^{-1} occur on the Southwest Indian Ridge, Gakkel and other Arctic Ridges, the Mid-Cayman Spreading Centre and sections of the South American Antarctic Ridge (see Figure 1.2). These ultra-slow spreading ridges make up 10 % of our global mid ocean ridge system, however they have until recently remained poorly studied due to inaccessibility. There has been renewed interest in the last decade which has led to a number of studies on ultraslow spreading ridges, however, these ridges still remain data poor compared to well-studied ridges such as the Mid-Atlantic Ridge and East Pacific Rise. As a result, many of the studies are concentrated on particular areas of

the ridge and do not give a complete understanding of the processes across the ridge as a whole.

1.2 Southwest Indian Ridge

The Southwest Indian Ridge (SWIR), shown in Figure 1.3, represents a divergent plate boundary between the African and Antarctic plates. The ridge extends 7700 km between the Bouvet Triple Junction (BTJ) in the southern Atlantic Ocean and the Rodriguez Triple Junction (RTJ) in the Indian Ocean. These are both ridge-ridge-ridge intersections between the SWIR and the southern tip of the Mid Atlantic Ridge and eastern South American Antarctic Ridge in the east (0° 40'E 55° S) and the Central and Southwest Indian Ridges in the west (70° E 25° 30'S). The SWIR has a full spreading rate of ∼14 mm yr^{-1}, which varies slightly along the ridge length (Patriat et al., 1997; Chu and Gordon, 1999; Demets et al., 2010). The ridge has a highly oblique orientation (∼60° from north) relative to the plate spreading direction which varies between 0° and 44° from north).

Numerous studies of segmentation, geochemistry, and geophysical variations along the axis of the Southwest Indian Ridge have led to the division of the ridge into three main sections (Grindlay et al., 1998; Dick et al., 2003; Standish et al., 2008; Cannat et al., 2003; Sauter and Cannat, 2010). The western section of the ridge from the Bouvet Triple Junction to 25° E has a roughly E-W orientation though the spreading direction varies between 44° and 10° from north. The western most portion of this section, around the triple junction, is influenced by the Bouvet hotspot (Mitchell and Livermore, 1998) and has a few widely spaced transforms. In contrast, there are no transforms east of the Shaka transform, where the ridge forms two segments, one oblique and one orthogonal which are connected by non-transform discontinuities (Grindlay et al., 1998; Dick et al., 2003). The central portion of the ridge, which is the least well-studied, extends from the Andrew-Bains transform (35°) to the Melville transform (61°) and is influenced by

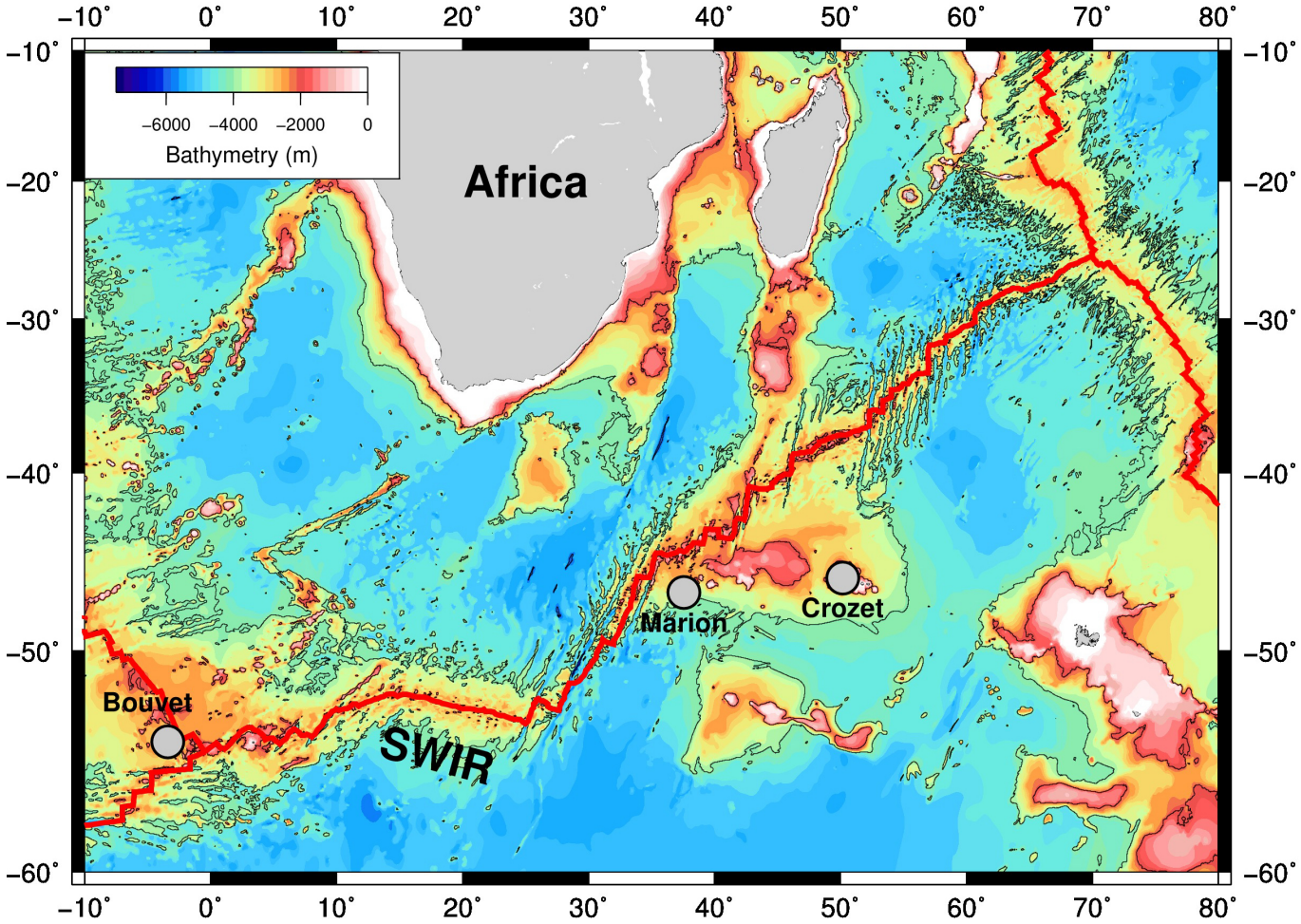


Figure 1.3: Location map showing bathymetry of the Southwest Indian region from the GEBCO 2014 30'' x 30'' global bathymetry grid (IOC et al., 2003). Spreading ridges are shown in red. The location of present hotspots, characterised by bathymetric swells and active volcanism, are represented by grey dots and the hotspot name given.

the Marion (Georgen et al., 2001) and possibly Crozet hotspots (Sauter et al., 2009) forming a long wavelength decrease in axial depth, named the Marion Rise. There are numerous transforms in this section of the ridge, often closely spaced as well as large non-transform discontinuities, which form large oblique shear basin structures. The eastern part of the ridge, which has been the subject of numerous studies, has no transform faults; the segmentation is instead defined by non-transform discontinuities, which separate long oblique segments with the deepest average axial depths along the ridge (Cannat et al., 1999; Mendel et al., 1997). These ridge segments are proposed to

be amagmatic and are punctuated by three distinctly magmatic segments with shallow axial depths and volcanic topography (Cannat et al., 2006).

1.3 Thesis Structure

This thesis consists of an exploratory study on the SWIR, and as such does not set out to answer any one specific question; instead, this thesis aims to increase our understanding of tectonic and volcanological processes occurring on the ultra-slow Southwest Indian Ridge using novel marine geophysical data acquired over 3 cruises, in addition to archive data from previous cruises.

Chapter 2 Data Acquisition and Processing

In this chapter, we present new marine geophysical data collected over three cruises in 2011, 2012 and 2013. These data include shipboard bathymetry, gravity, magnetics, ROV video imagery and rock sampling. This chapter details the methods and theory used during acquisition and processing of these data and assesses the data quality. Archive shipboard bathymetry, gravity and magnetics data are collated from 329 cruises to form a database of marine geophysical data for the Southwest Indian Ridge region. Some areas of the ridge contain significant data gaps, particularly in the central region, therefore satellite derived bathymetry and gravity data are integrated with shipboard data to provide complete coverage.

Chapter 3 Ridge Crest Morphology

In chapter 3, we initially review the long wavelength geophysical and geochemical variation along the ridge. These long wavelength variations form the framework for interpretations of other geophysical trends identified along the ridge. We use across axis profiles to characterise the variation in the shape and size of the axial valley morphology and relate these to the long wavelength geophysical variations along the ridge. The elastic thickness, a proxy for the lithospheric strength, is compared to the

axial valley width to assess the applicability of lithospheric stretching models at the SWIR. We finally use detailed swath bathymetry to classify the segmentation on the ridge and discuss the implications for the volcanic and tectonic processes in the axial rift valley.

Chapter 4 Seamount Morphology

In chapter 4, we present an integrated morphological study of six seamounts surveyed primarily on cruise JC066 in 2011 and MD192 in 2012. We use swath bathymetry to produce detailed 3D maps, the interpretations of which are aided by the use of backscatter to determine the substrate nature. These backscatter interpretations are ground-truthed using ROV video imagery collected in transects across the seamounts, as well as rock samples, which are used to confirm lithological interpretations from video imagery. These data are used to interpret the morphology of each seamount and identify the major constructive and destructive morphological features. We discuss the processes that form these morphological features, and the relationship between the seamount morphology and local tectonic setting.

Chapter 5 Seamount Distribution

In chapter 5, swath bathymetry and satellite derived bathymetry are used to assess the spatial distribution of seamounts within the axial valley and along the ridge crest. Seamounts are located using the modified basal outlining algorithm (MBOA) of Bohnenstiehl et al. (2012). Testing on both synthetic and real bathymetry data is undertaken, in order to determine the parameter values which best separate volcanic edifices from tectonically generated highs. Two separate studies are carried out using the MBOA: The first study uses swath bathymetry to compare the distribution of small seamounts (at least 50 m tall) in the axial valley, where detailed swath bathymetry of the whole valley floor is available. The second study uses integrated swath bathymetry and satellite derived bathymetry to locate large seamounts (greater than 300 m tall) on the ridge crest across the whole of the ridge length. The first study is used to draw inferences about the magmatic accretion processes occurring in the axial valley

on different sections of the ridge. The second study is used to assess the variation in magmatism along the length of the ridge and is interpreted in terms of hotspot influence, spreading obliquity and variations in mantle temperature.

Chapter 6 Admittance and Elastic Thickness

In chapter 6, we use bathymetry and gravity data to calculate the gravitation admittance for a series of windows centred on the ridge crest. These gravitational admittances are then used to estimate elastic thickness (T_e), which is a proxy for lithospheric strength. The admittance method is tested using synthetic bathymetry and gravity data in order to correct for factors such as large changes in latitude, finite window bias and the effect of the ridge topography. The resultant best fit elastic thicknesses along the ridge are interpreted in the context of the large scale geophysical variations described in chapter 3. Elastic thickness calculations are also carried out for a series of windows along the Mid-Atlantic Ridge and East Pacific Rise in order to assess the relationship between spreading rate and lithospheric strength.

Chapter 2

Data Acquisition and Processing

This chapter outlines the acquisition and processing of marine geophysical data used in this thesis. Shipboard bathymetry, gravity and magnetic data were acquired over three cruises on the RRS James Cook (2011), the R/V Marion Dufresne (2012) and the R/V Meteor (2013). Seafloor samples and imagery were also acquired during the RRS James Cook cruise.

These shipboard data form the core of this thesis, supplemented by other cruise data from the NOAA National Centers for Environmental Information (formerly NDGC) located in Boulder, Colorado. In areas with sparse shipboard data, global bathymetry and gravity anomaly grids derived from satellite altimetry are used.

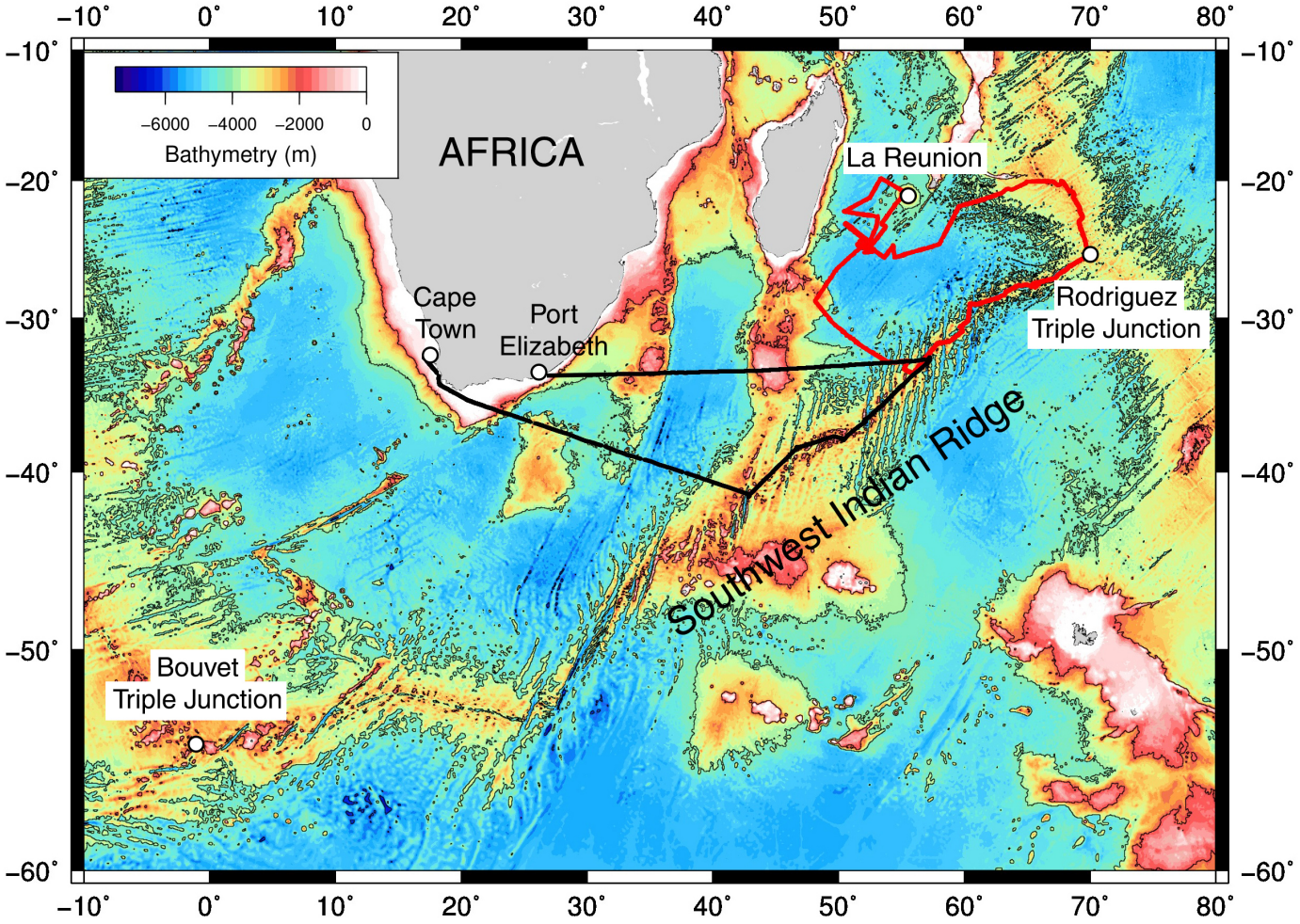


Figure 2.1: Bathymetry of the Southwest Indian Ridge region from the GEBCO 2014 30 x 30 global bathymetry grid (IOC et al., 2003). Cruise tracks for the JC066 RRS James Cook cruise in 2011 (black line), and MD192 R/V Marion Dufresne and M101-2 Meteor cruises in 2012 and 2013 (red line).

2.1 Geophysical Measurements at Sea

Only a few percent of the seafloor has been surveyed using multibeam bathymetry due to the inherent challenges involved in surveying vast areas overlain by up to 5 km of water (Smith and Sandwell, 2004). In the last few decades major advances in technology have led to greater coverage and an increase in data quality of shipboard surveys. In the next section we review a brief history of bathymetric, gravity and marine magnetic data acquisition and the main technologies used.

2.1.1 Shipboard Bathymetry

Bathymetric surveys have been conducted throughout history for the purposes of navigation. From the simple lines with sounding-lead found on Mediterranean ship wrecks dating from the 6th century BC (Johnson and Nurminen, 2007), to the earliest surviving chart to feature simple point depth soundings drawn in 1584 (Johnson and Nurminen, 2007). These early bathymetric surveys consist of a sparse number of data points along a single cruise track, and subsequent technological advancements have improved the accuracy and resolution of bathymetric surveys. The invention of mechanical wire sounding machines in the 19th century, and an increase in the number of government sponsored expeditions, increased the area of the seafloor surveyed, though the poor resolution allowed only the broad shape of the ocean basins to be established. One of the most scientifically prolific expeditions was that of the HMS Challenger, which took oceanographic measurements, including 363 depth soundings across the world's oceans from 1872-6 (Theberge, 1989). These depth soundings, which were continued throughout the 19th and 20th by the British admiralty, were used to identify key features of the ocean floor such as the Mid-Atlantic Ridge and Marianas Trench.

A major breakthrough in the field of bathymetry was inadvertently discovered during echo-sounding experiments to detect icebergs, following the sinking of the HMS Titanic in 1912. The Canadian inventor Reginald Fessenden, whilst conducting one of these experiments, noted that in addition to the return echo from the iceberg, a second echo was received from the seafloor 1.5 km below the ship (Bates et al., 1982). The outbreak of WWI in 1914 and WWII in 1939 led to the rapid development of echo-sounding technology for use in submarine navigation and detection, and it was during this time that the first submarine volcano survey was published (Smith, 1937). Following WWII, academic and military marine cruises continued to utilise single beam echo-sounding, though the wide spacing of ship tracks in the open ocean and navigational uncertainty limited the use of these data. In an attempt to mitigate the issue of poor coverage, academic groups shared bathymetric data, forming the basis of today's bathymetric

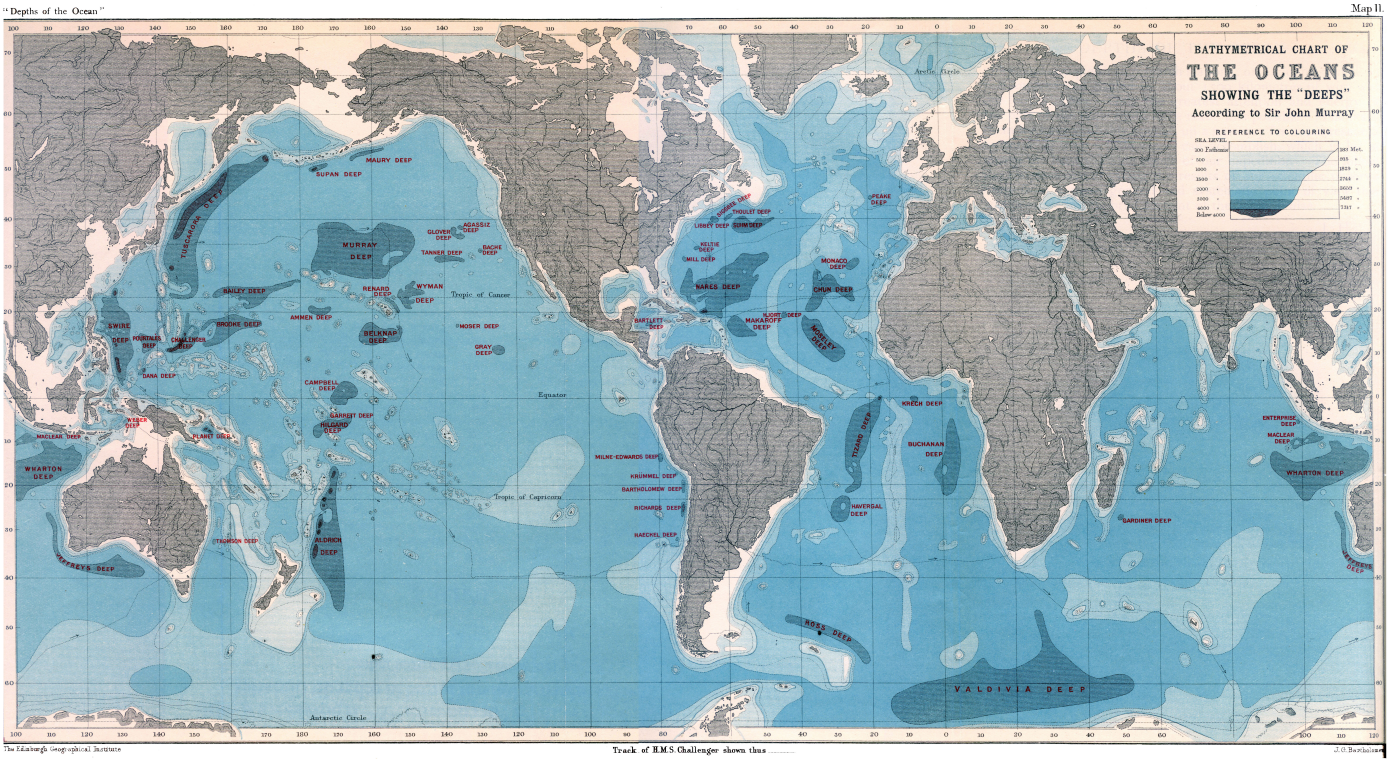


Figure 2.2: Bathymetry map of the world's oceans produced by John Murray following the Challenger Expedition (Murray and Hjort, 1912)

databases (Carpine-Lancre et al., 2003). The final major technological breakthrough came during the 1960s when the General Instruments Corporation of the United States developed a multibeam swath bathymetry system (Theberge, 1989). This system, which built upon the early single beam echo-sounding technology, utilised a line of echo-sounding beams oriented perpendicular to the direction of the vessel's heading, generated by an array of transducers on the vessel's hull (Jones, 1999). These echo beams reflect from the seafloor and are detected by a separate array of receivers. The resultant two-way travel time is then calculated, and converted into depths based on sound velocity profiles obtained using vertical measurements of sea water temperature and salinity. These multibeam systems permitted a large swath of the seafloor to be surveyed in a single transect, producing a map of the seafloor, in contrast to the simple profiles produced by single beam echo sounders. The first commercially available SeaBeam system became available in the early 1970s and was rapidly adopted by marine research vessels.

Recognising the importance of bathymetric data for use in marine research, General Bathymetric Charts of the Oceans (GEBCO) released a 1 minute resolution global bathymetric grid in 2003 based on shipboard bathymetric data (Carpine-Lancre et al., 2003). GEBCO's most recent bathymetric grid (GEBCO 2014) has a resolution of 30 arc-second intervals and was released in December 2014.

2.1.2 Shipboard Gravity

Gravity measurements at sea are a more recent endeavour than bathymetric surveys. One of the main challenges to accurate gravity measurements is measuring accelerations in the order of a few milligals, on a ship which experiences horizontal and vertical accelerations several orders of magnitude greater due to the effects of wave motion. One of the most influential geophysicists in early marine gravity studies was Vening Meinesz. Vening Meinesz's native country, the Netherlands, has particularly unstable soil, introducing horizontal accelerations during gravity measurements. In order to remove these unwanted effects, Vening Meinesz developed a system of two pendulums swinging in opposite phase, allowing the vertical accelerations to be measured but cancelling out much of the horizontal acceleration. Using this new gravimeter, the first successful marine gravity measurements were taken by Vening Meinesz in 1923 aboard a submarine (Vening Meinesz, 1929). The submarine was not subject to the large wave and wind forces on the surface, and had a fewer vibrations due to electric motors as opposed to diesel engines, allowing measurements with an accuracy of 4 to 5 mGal to be obtained (Vening Meinesz, 1929). Following WWII, these apparatus were fitted to 27 submarines, and a global gravity survey was carried out by Worzel, forming the basis of our marine gravity database today (Worzel and Harrison, 1963). However, access to submarines was limited so an alternative solution was needed to take measurements from a standard vessel. The development of the spring gravimeter, independently pioneered by LaCoste and Graf during the late 1950s, allowed marine gravity measurements to be taken continuously along track on a surface ship, with

measurements within 3 mGal of the Vening Meinesz submarine apparatus (Worzel, 1959; LaCoste, 1959).

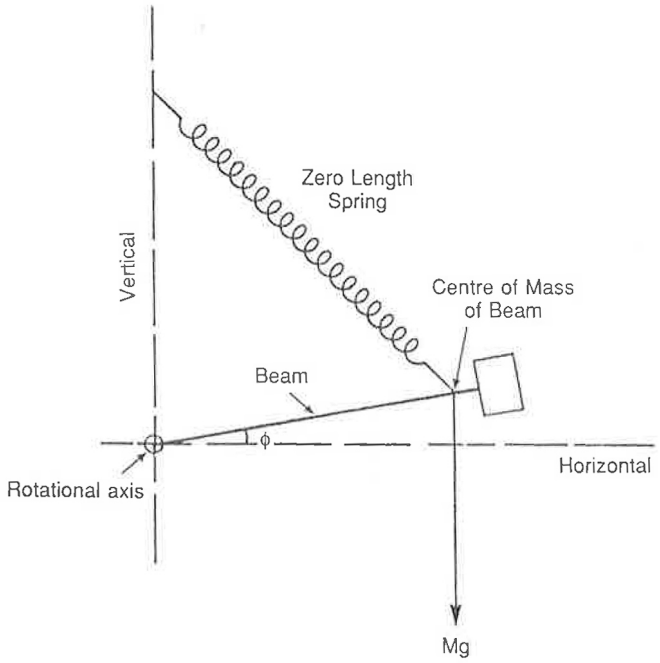


Figure 2.3: Schematic diagram of a La Coste-Romberg sea gravimeter (LaCoste, 1959; Micro-G LaCoste, n.d.) modified from Jones (1999)

These gravimeters measure the deflection from horizontal of a heavily damped beam attached to the casing by a spring, and form the basis of modern sea gravimeters such as those made by Micro-G LaCoste. Modern sea gravimeters use a zero length spring supporting a weighted beam, the deflection of which is tracked over time (typically 180 seconds) and averaged (LaCoste, 1959). From these measurements the average acceleration due to gravity may be calculated using

$$\overline{g} = \frac{d}{dt} \int_{t_1}^{t_2} (u'' + 2h\omega u' + \omega^2 u)\, dt + ay \tag{2.1}$$

where $\overline{g}$ is the average acceleration due to gravity, t is time, h is damping coefficient, ω is the angular oscillation frequency of the beam, a accounts for the force exerted by the spring on the beam when it is in the null position and y is the null position of the beam (LaCoste, 1959).

The instrument is mounted on a gyro-stabilised platforms to reduce the effect of ship movement and retain a broadly horizontal position. In addition, dedicated accelerometers are mounted on the platform, measuring any remaining horizontal accelerations which can then be removed in post-processing. The specified accuracy of these spring gravimeters is ± 0.5 mGal and have a working accuracy of ± 1 mGal at sea (Micro-G LaCoste, n.d.).

Eötvös correction

Despite the extensive damping applied to the gravimeter to compensate for ship motion, one error which cannot be corrected for during measurement is the Eötvös error (Eotvos, 1919). This is caused by the centripetal force experienced by the ship due to the spin of the Earth. When the ship moves eastward, the centripetal force increases causing a negative error in the measured acceleration due to gravity, requiring a positive correction. Conversely westward ship movement requires a negative Eötvös. This correction therefore depends on the ship's speed, heading and latitude and may be corrected using

$$E_c = 7.503S \sin H \cos \phi + 0.004154S^2 \tag{2.2}$$

where E_c is the Eötvös correction, S is the ships speed in knots, H is the heading and ϕ is the latitude (Eotvos, 1919).

Other errors

Cross-coupling errors arise due to the coupling that exists between the vertical and horizontal accelerations of the beam and those of the ship (Talwani et al., 1966). These errors increase in rough weather, since the gyro stabilised platform no longer keeps the instrument horizontal. The horizontal accelerations of the instrument relative to the beam are recorded during the cruise by accelerometers mounted on the instrument platform, and may be removed in post processing. Cross-coupling errors are more

common on older data (pre-1980s) due to less optimised design (Worzel and Harrison, 1963).

Gravimeters are subject to instrumental drift over time, which if linear may easily be corrected using the absolute gravity measurements taken at base station tie-ins at either end of the cruise.

Reduction to gravity anomalies

Marine gravimeters are relative instruments, meaning gravity measurements must be converted to absolute values before being reduced to gravity anomalies. Relative gravity measurements are taken at the start and end of a cruise at a location where gravity has previously been measured using an absolute gravimeter (a gravity base station), and then immediately on the wharf near the ships gravimeter. The marine relative values may then be converted to absolute values, taking into account the difference in relative readings between the wharf and base station. It is worth noting that additional instrumental and human errors may be introduced during base station tie-ins, particularly due to inconsistent temperature affecting the spring constant of the gravimeter and levelling errors. Repeated readings at the gravity base station and the wharf are taken, and averaged to reduce such errors.

The resulting absolute gravity measurements must then be corrected for the effect of height above the geoid, using the free-air correction (FAC). Since the average sea surface height approximates the geoid this correction is usually negligible, however areas of strong geoid anomaly such as deep sea trenches require a correction of up to 10 to 20 mGal (Chapman and Talwani, 1982).

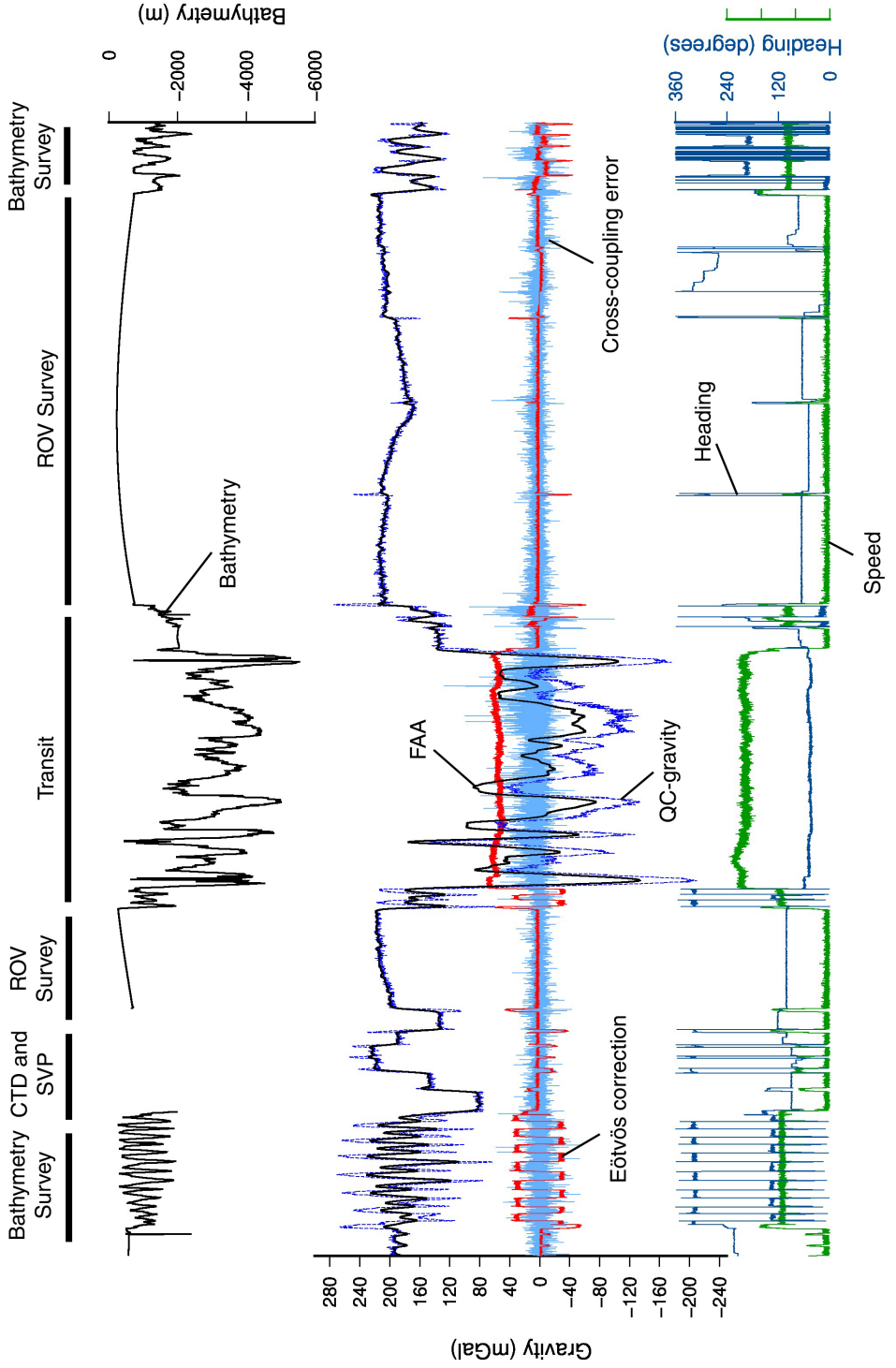


Figure 2.4: Figure showing the processing of gravity data from the JC066 cruise. The bathymetry is shown at the top (black line) for reference as it should be well correlated with the final free-air anomaly. The labels at the top indicate the ship activity and illustrate the change in gravity correction required when the ship is in transit vs on station. The Q-C gravity (blue line) is the raw gravity anomaly, prior to Eötvös and cross-coupling corrections. The Eötvös correction (red line) is correlated with the speed and heading of the ship (shown in green and blue respectively) from which it is calculated. In particular, the sign of the Eötvös correction changes with changing heading of the ship with respect to the rotation of the Earth. The cross-coupling error (light blue) increases with ship speed due to increased ship motion. The free-air anomaly calculated by applying the Eötvös and cross-coupling errors to the QC-gravity is shown in black, and shows a good correlation to the shipboard bathymetry.

This study area lacks strong geoid anomalies, thus the free air correction may be considered to be 0 mGal. The free-air gravity anomaly is defined as

$$\Delta g_{FAA} = (g_{obs} + FAC) - g_{\phi} \tag{2.3}$$

where g_{obs} is the observed gravity, FAC is the free-air correction and g_{ϕ} is the gravity of the reference ellipsoid, which is defined by the Geodetic Reference System as

$$g_{\phi} = g_e\big(1 + Asin^2(\phi) - Bsin^2(2\phi)\big) \tag{2.4}$$

where ϕ is the geographic latitude, g_e is the gravity measured at the equator, and A and B are parameters selected to produce a good fit to true gravity. For the GRS80 reference system, the values of A and B are 0.0053024 and 0.0000058 respectively.

2.1.3 Shipboard Magnetics

The Earth's magnetic field has been used for navigation since the invention of the compass, records of which exist as early as 1044 in China (Needham, 1994). Early observations of declination date from 1538, and provide a general representation of the Earth's magnetic field (Bullard and Mason, 1963). In order to define the magnetic field at a particular point, three quantities are required: the strength of the magnetic field, and two field components or two angles giving the direction of the field relative to the Earth's axis (Bullard and Mason, 1963). Most early historical measurements are of the declination and occasionally inclination; the first charts of horizontal component and field strength were published in 1819 (Bullard and Mason, 1963). At this time the transition from wooden to iron and steel ships in the 19th century made full 3-component magnetic measurement at sea problematic, due to the magnetic field of the ship itself, though a number of dedicated surveys were made in specially built non-magnetic ships and aircraft (e.g. Vestine, 1960). To avoid this problem, the majority of modern marine magnetic measurements today use a magnetometer which is towed

behind the ship. These magnetometers typically measure the total magnetic field vector, since practical limitations in orienting three vector magnetometer sensors at right angles leads to a loss of precision (Marine Magnetics Corp, 2007).

Modern magnetometers use proton precession physics to measure the total magnetic field strength (Jones, 1999). Protons suspended in a fluid are artificially aligned (polarised) by an external applied magnetic field or other polarising force. When this external polarising force is removed, they relax to align with the ambient magnetic field. During this relaxation process, the protons precess with a frequency (known as the Larmor frequency), which is proportional to the magnetic field strength, and may be measured as a small induced electrical signal. Older proton-precession magnetometers polarised the protons using an induced magnetic field, which requires a large current input and produces a low magnitude output signal. These have now been superseded by Overhauser magnetometers, which use electron-proton coupling to achieve polarisation (Marine Magnetics Corp, 2007). A chemical containing a free radical atom is added to the proton rich fluid, leading to unbound electrons within the fluid. These electrons are stimulated by low-frequency RF radiation of a specific frequency. The energy imparted on the electrons is transferred to nearby protons through electron-proton coupling, polarising the protons. The polarisation of the protons is dependent not on the strength of the applied magnetic field, but on the chemistry of the added free radical chemical as the spin of the protons may be expressed by

$$\frac{N_+}{N_-} = 1 + \frac{h(\omega_s - \omega_i)}{kT} \tag{2.5}$$

where N_+ and N_- are the number of protons with positive and negative spins respectively, h is Planks constant, ω_s is the electron spin angular frequency and ω_i is the proton spin angular frequency (Marine Magnetics Corp, 2007). This relationship reduces the need for high power input and produces a higher magnitude signal. The removal of the low-frequency RF radiation leads to relaxation of the protons and an induced electrical current proportional to the total magnetic field strength as in proton-

precession magnetometers. In addition, the low-frequency RF radiation has a frequency which does not interfere with that of the precession signal, allowing simultaneous measurement and polarisation.

Reduction of magnetic data

The reduction of magnetic data to magnetic anomalies involves a number of corrections followed by a removal of the regional magnetic field (Ramsey, 1950).

Magnetic measurements of total field strength must be corrected for diurnal variation, caused by the changes in the external component of the Earth's magnetic field due to interaction between the sun and ionosphere (Egedal, 1947). A continuous magnetic record from a land base station for the duration of the cruise may be used to isolate the diurnal variation, and apply a correction to the data. This may also be used to correct for any linear instrument drift. Depending on the length of the survey, a longer period secular variation correction may also be calculated from base station records (Bloxham and Gubbins, 1985).

A normal field correction is necessary for marine surveys to correct for the variations in the magnetic field with latitude and longitude. This correction is made using the International Geomagnetic Reference Field (IRGF) (Thebault et al., 2015). The magnetic measurements are reduced to magnetic anomalies by the removal of the regional field, which for large scale marine surveys is the IGRF (Thebault et al., 2015).

2.2 RRS James Cook Cruise

On the 7th November 2011, the RRS James Cook left Cape Town, South Africa to undertake a 44 day cruise (JC066) to five seamounts on the Southwest Indian Ridge (SWIR) crest. The primary aim of the cruise was to study the benthic biology of these seamounts, particularly in relation to cold-water coral reefs and concerns re-

garding over-fishing. In addition to the marine biological research, ocean chemistry, physical oceanography and geophysical surveys were undertaken at each seamount. A total of ∼7000 km of continuous multibeam bathymetry and shipboard gravity was collected during the cruise including dedicated swath mapping surveys at the each of the seamounts.

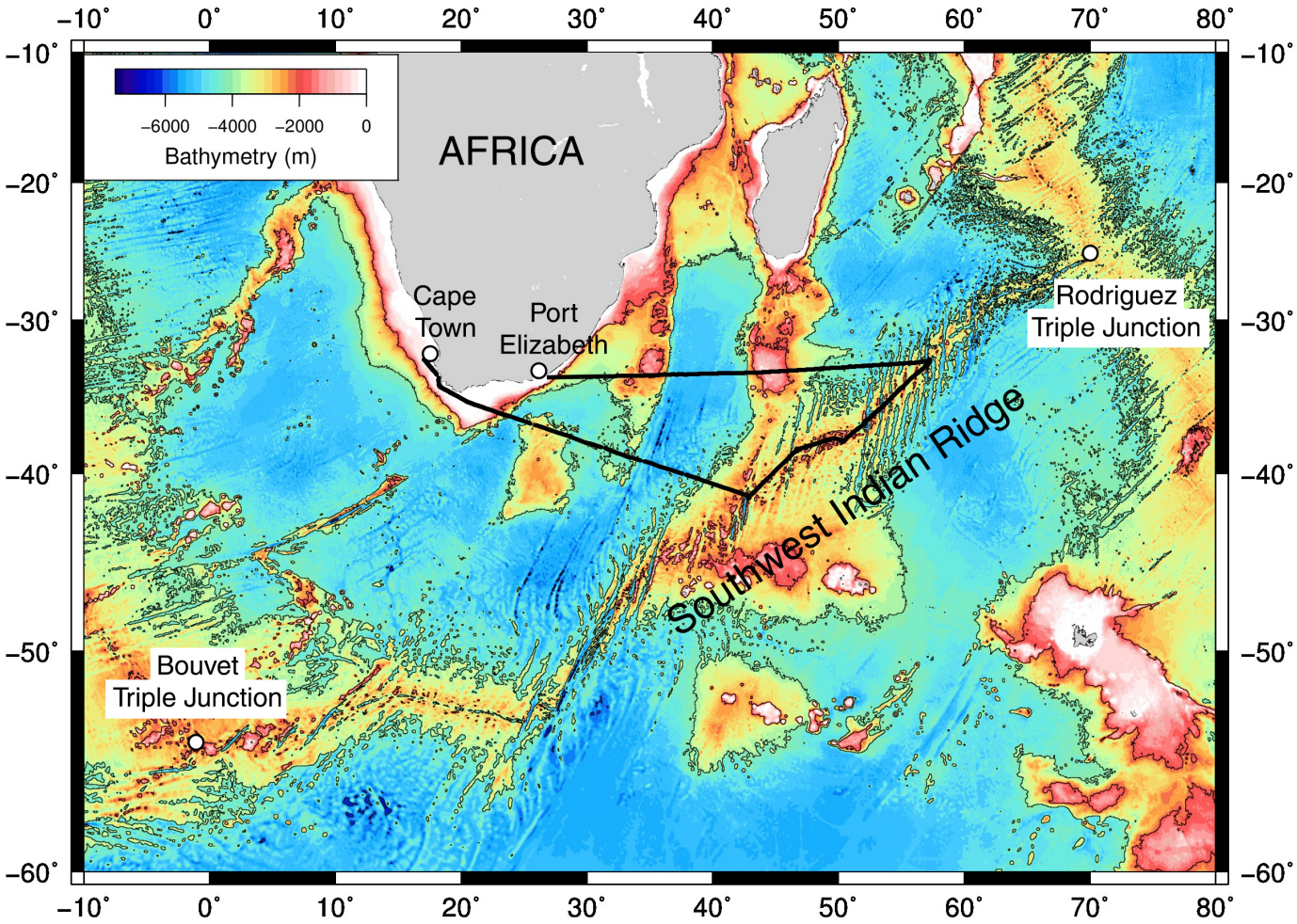


Figure 2.5: Bathymetry of the Southwest Indian Ridge region from the GEBCO 2014 30 x 30 global bathymetry grid (IOC et al., 2003). Cruise tracks for the JC066 RRS James Cook cruise in 2011 (black line).

A 4 day sub-cruise (JC067) was undertaken to study the benthic fauna associated with the Dragon vent field on the SWIR. The RRS James Cook arrived back into Port Elizabeth (South Africa) on the 21st December 2011 having successfully completed surveys of all five seamounts.

2.2.1 Navigation

Navigation for the RRS James Cook was provided by a fully continuous satellite GPS system POSMV (Applanix Position and Orientation Systems for Marine Vessels). This provides measurements of ships location, velocity, attitude, heave and angular rate vectors which were passed into the multibeam and gravity systems. POSMV specifications give an accuracy of 0.5 to 2 m (Applanix, n.d.). In order to assess the scatter for the ship GPS system, GPS locations were recorded whilst stationary in Cape Town port. Plotting these locations show random scatter of up to 0.55 m from the true location of the ship, which was determined by averaging a number of different GPS systems over several days.

2.2.2 Bathymetry

Swath bathymetry surveys were conducted over 5 seamount sites at different locations along the Southwest Indian Ridge crest. Surveys were designed to record swath with significant overlap between survey lines to reduce the effects of bubble entrainment (see below) and to minimise shadow zones caused by rapid shallowing over the summits. Each survey included multiple tie-ins and a sound velocity profile in order to calibrate the swath system and to accurately convert two-way travel times to depths.

The RRS James Cook has two hull mounted Kongsberg swath systems, a SIMRAD EM120 for deep water swath and a SIMRAD EM710 for shallow water swath. The EM120 was used for the majority of the cruise. This multibeam system operates at a frequency of 12 kHz and was used with the maximum 191 beams, giving 150° coverage. Any pings from beam angles greater than 120° were discounted to reduce errors. The system has a reported accuracy of 0.2% of water depth Kongsberg (n.d.) equating to $\sim$4 m at the base of the seamounts and $\sim$20 cm at the summits, though these errors increase in adverse weather. The errors in multibeam bathymetry were assessed by comparing the results from overlapping beams on an area of undeformed seafloor. This

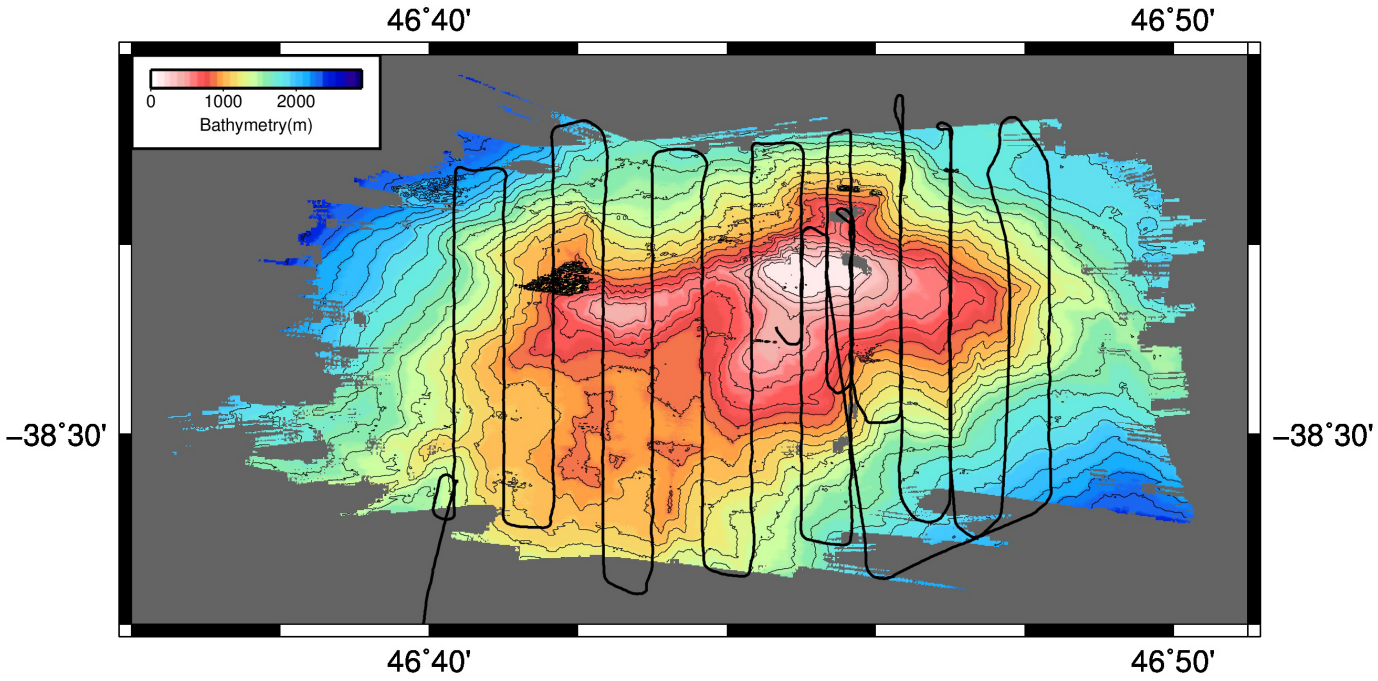


Figure 2.6: Bathymetry survey over Melville seamount showing cruise track in black. Bathymetry data shown here is raw data and so shows significant artefacts. These were subsequently removed using MB-system software.

comparison yielded errors of ±3.1 m. One particular problem encountered was bubble entrainment over the echo sound receivers reducing the number and quality of the pings received during bad weather. This was mitigated by reducing speed to 4 knots during surveys and ensuring greater overlap between survey lines, however backscatter data from Coral Seamount and Melville Bank was unusable. Raw multibeam data was subsequently processed to remove spurious data points using MB-System v.5.3. Pings which returned depths below the seafloor or required a non-plausible gradient in the seafloor were discounted using visual inspection.

Table 2.1: List of multibeam surveys carried out over seamounts on cruise JC066

Seamount	Date of survey	Swath Bathymetry	Backscatter
Coral Seamount	15/11/2011	Yes	No (adverse weather)
Melville Bank	21/11/2011	Yes	No (adverse weather)
Middle of What Seamount	01/12/2011	Yes	Yes
Sapmer Bank	06/12/2011	Yes	Yes
Atlantis Bank (OCC)	09/12/2011; 11/12/2011	Yes	Yes

2.2.3 Gravity

Shipboard gravity was recorded continuously during the cruise using a Lacoste Air-Sea Gravity System II. This gravimeter is mounted on a gyro-stabilised platform to minimise acceleration experienced by the beam due to ship movement, and to keep the system horizontal. A dedicated accelerometer mounted on the gravimeter recorded any accelerations not damped by the platform. The gravimeter has a specified accuracy of 1 to 5 mGal at sea Micro-G LaCoste (n.d.) though errors increase during rough conditions, particularly if ship motions exceed the tipping capacity of the stabilisation platform. Crossover analysis of 2727 points gave a root mean square error of $\pm$ 8.4 mGal which is reasonable for the conditions experienced.

Base station tie-ins were conducted at absolute gravity stations in Cape Town and Port Elizabeth using a Worden Land Gravimeter. Repeat readings were taken to increase reliability and these results use to convert the relative gravity readings at sea to absolute values. These readings were also used to calculate an instrument drift correction of 13 mGal over the 44 day cruise.

A loss of power to the gravimeter during the cruise resulted in the loss of gravity data over a 7 day period including the gravity survey of Coral seamount.

Ship velocity and heading data recorded using the ships GPS system were used to calculate the Eötvös correction. The Eötvös correction and cross-coupling correction were applied to data, instrumental drift removed and the free-air correction applied to produce free-air anomalies (FAA).

2.2.4 ROV profiles and sampling

At each seamount benthic profiles were taken using a Remotely Operated underwater Vehicle (ROV), the Kiel 3000 or one of two image platforms: Hydraulic Benthic Interactive Sampler (HyBIS) and Seabed High Resolution IMaging Platform (SHRIMP).

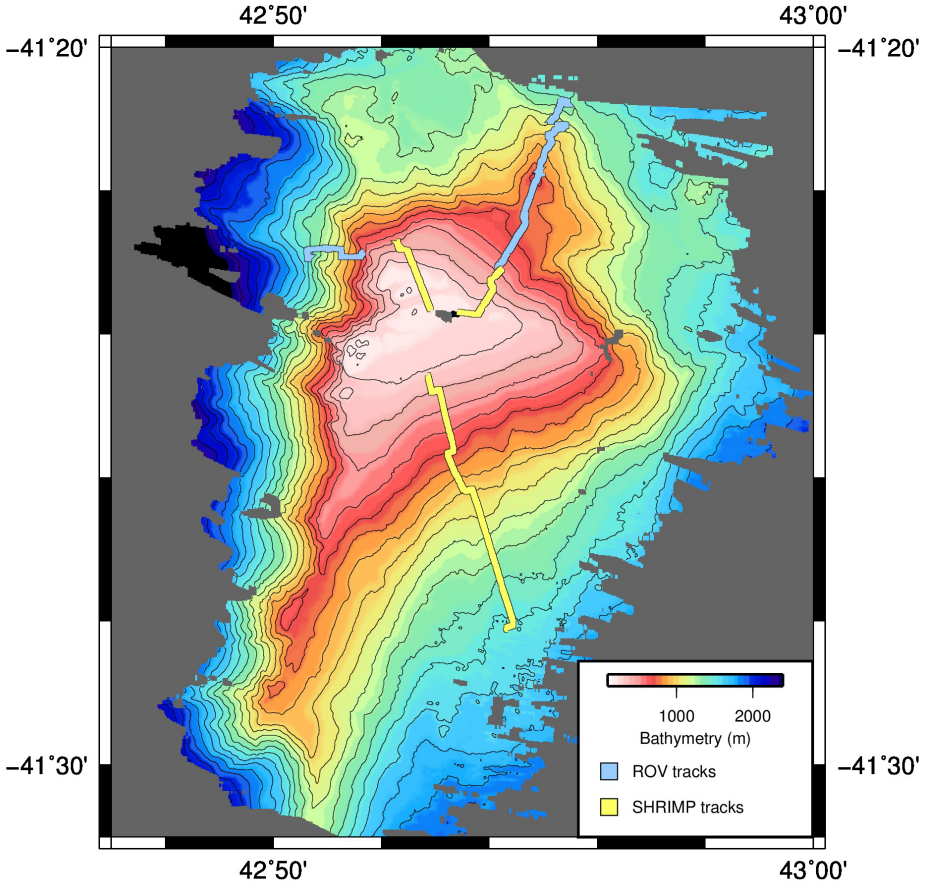


Figure 2.7: Swath bathymetry of Coral Seamount showing transits of ROV (Remotely Operated underwater Vehicle) as a blue line and SHRIMP (Seabed High Resolution Imaging Platform) as a yellow line.

The Kiel 3000 was placed around 1 m above the seabed at a speed of 0.2 knots, though some areas of extreme topography prevented close observation. The Kiel ROV recorded continuous HD video footage, as well as HD still images when the ROV was stationary; 3 parallel lasers 0.1 m apart provided scale for the images. In addition to imagery data, two manipulator arms permitted the collection of rock and fauna samples, which were transported to the surface in boxes.

The SHRIMP towed camera system was used to collected video and still imagery of the seabed using downward and forward facing cameras. The nature of the connection to the ship meant that the SHRIMP could not observe the seafloor as closely as the ROV and was subject to the vertical motions of the ship, reducing the quality of the

images. A laser scale mounted on the camera provided scale for the images.

The HyBIS was used primarily in areas of extreme topography as the on-board thrusters allowed for a greater freedom of movement. Video footage was provided by downward and forward facing cameras, though a lack of lighting and laser scale made the images less easy to interpret. HyBIS also has a hydraulic grab system which was used to sample sediment and loose rocks from the seabed.

2.3 R/V Marion Dufresne and R/V Meteor cruises

The next two cruises were part of the RHUM-RUM project, a French-German collaborative passive seismic experiment to image the Reunion hotspot plume. The first cruise aboard the R/V Marion Dufresne departed La Port (La Reunion, France) on 23rd September deploying 57 ocean-bottom seismometers (OBS) around La Reunion Island and along the Southwest Indian Ridge before returning to La Reunion on 26th October. 12 months later the R/V Meteor departed Port Louis (Mauritius) on 23rd October and followed the same cruise track to retrieve the OBS returning to La Port (La Reunion, France) with all the OBS on 4th December.

During both cruises continuous swath bathymetry, shipboard gravity and magnetic data were recorded. Magnetic and bathymetric data acquisition was paused during OBS retrieval operations.

2.3.1 Navigation

The R/V Marion Dufresne and R/V Meteor were both equipped with modern continuous satellite GPS navigation systems which provided ships location, velocity, and attitude information for all scientific equipment on board.

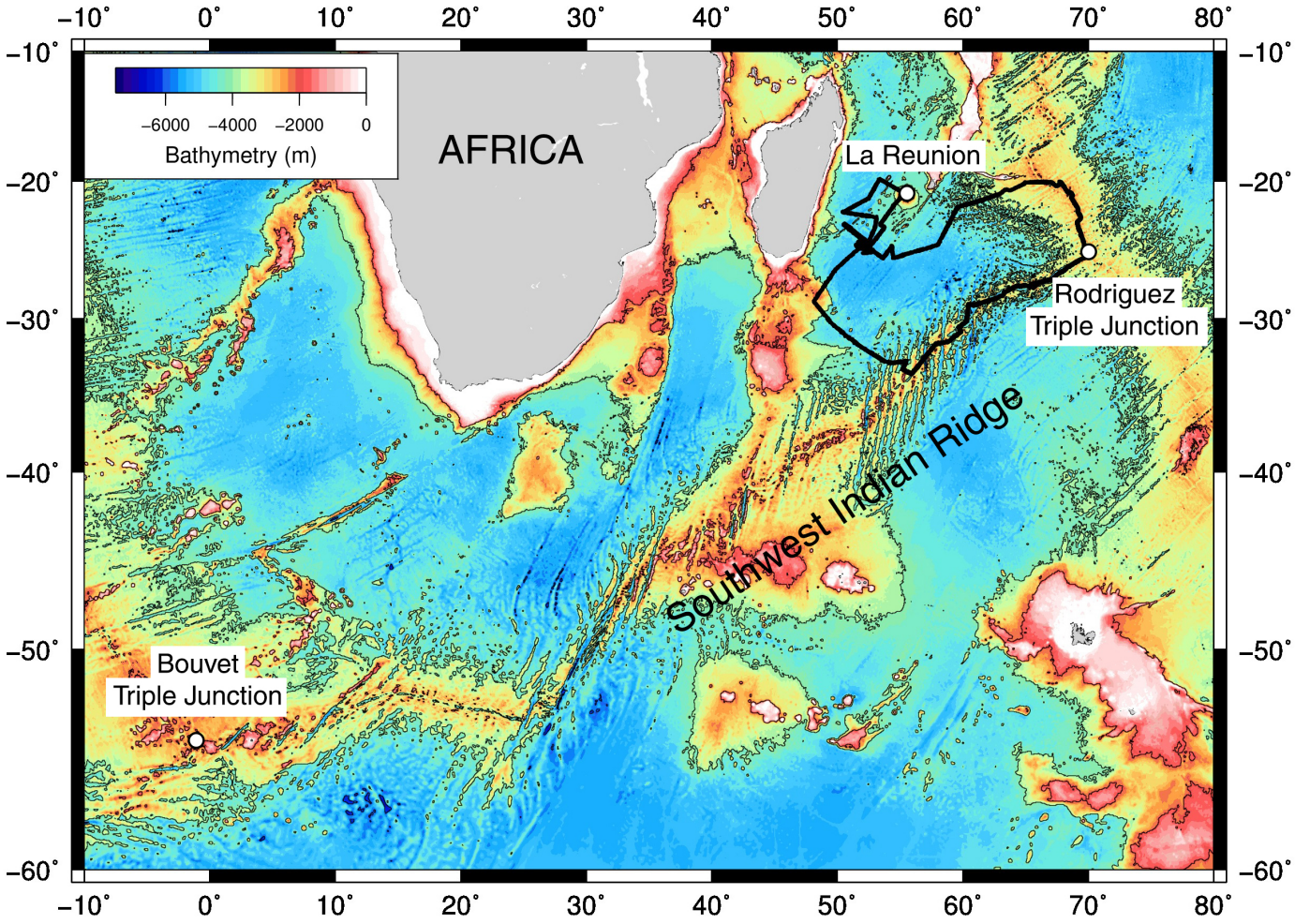


Figure 2.8: Bathymetry of the Southwest Indian Ridge region from the GEBCO 2014 30 x 30 global bathymetry grid (IOC et al., 2003). Cruise track of cruise RHUM-RUM aboard the R/V Marion Dufresne, which was repeated for cruise M101/2 aboard the R/V Meteor shown as a black line.

2.3.2 Bathymetry

A total of ∼15000 km of swath bathymetry was acquired on each of the RHUM-RUM cruises including a dedicated survey of a large seamount situated in the SWIR axial valley. Data were generally acquired during transits between OBS sites at a speed of 9-12 knots, though this was reduced for the SWIR seamount survey. The travel-times were converted into depth soundings using sound velocity profiles taken at 10 sites along the cruise.

The R/V Marion Dufresne is equipped with a unique Thomson Seafalcon 11 multibeam system, which uses a 12kHz carrier and 5 separate multibeam arrays to reduce data gaps. Specified accuracy is 0.4% of the water depth (Barruol, 2013). This data was processed using the CARAIBES software to remove spurious data.

The R/V Meteor is equipped with two Kongsberg systems, EM120 and EM710 as found on the RRS James Cook. The deep water EM120 was used for the majority of the cruise. This system used a 12 kHz frequency, 120° beam angle and double pinging frequency. This data was processed using MB-System v.5.3 and Fledermaus software, where spurious data points were removed using visual identification.

2.3.3 Gravity

Marine gravity measurements were taken on the first of the RHUM-RUM cruises. The R/V Marion Dufresne was equipped with a Lacoste Air-Sea Gravity System II which recorded continuous gravity measurements throughout the cruise. These relative measurements were corrected for Eötvös error using ship's speed and heading from the GPS, and cross coupling error using readings from the accelerometers mounted on the instrument platform. Base station tie-ins were performed at the start and end of the cruise at the Saint Denis astronomic station to convert from relative to absolute gravity.

2.3.4 Magnetics

A SeaSpy Overhauser magnetometer was deployed for both RHUM-RUM cruises. This provided continuous magnetic data throughout the cruise, except during OBS deployment or retrieval and two maintenance days due to shark activity. Magnetic data were relayed in real time to the ship allowing continuous observation to ensure high data quality. The magnetometer was towed 250 m behind the ship at 100 m depth to ensure minimal contamination from the ship's hull.

The raw data was corrected for diurnal and secular variation during the cruise using

base station readings from Mauritius. Magnetic anomalies were collected by removing the regional background field, in this case the International Geomagnetic Reference Field (IGRF v.11).

2.4 Other cruise data

The cruise data collected during JC066 and the RHUM-RUM cruises was supplemented with data from the National Centers for Environmental Information (formerly the National Geophysical Data Center) in Boulder, Colorado. Swath bathymetry, shipboard gravity and magnetic data were collated from 392 cruises from 1956 to 2000. Much of the cruise data from this area is French in origin, and this French data from more recent years is not openly available; however two grids calculated using multibeam bathymetry from the GALLiENi cruise (Sauter et al., 2001) were also used.

2.4.1 Bathymetry

Swath and single beam bathymetry from a total of 368 cruises was collated for the SWIR region. Multibeam surveys are often restricted to areas of interest such as ridges, leaving large areas of deep ocean with sparse data. While this is true for the Southwest Indian Ridge, where the majority of dedicated surveys are located along the ridge crest, the importance of this region as a transit zone to the remote French Territorial Islands and to sites of scientific interest in Antarctica has at least ensured some coverage off-ridge. Bathymetry data was reviewed to remove cruises with instrument or data recording issues, however the data were not processed for bad pings using MB-System as the vast majority of cruises had already undergone at least a basic level of editing.

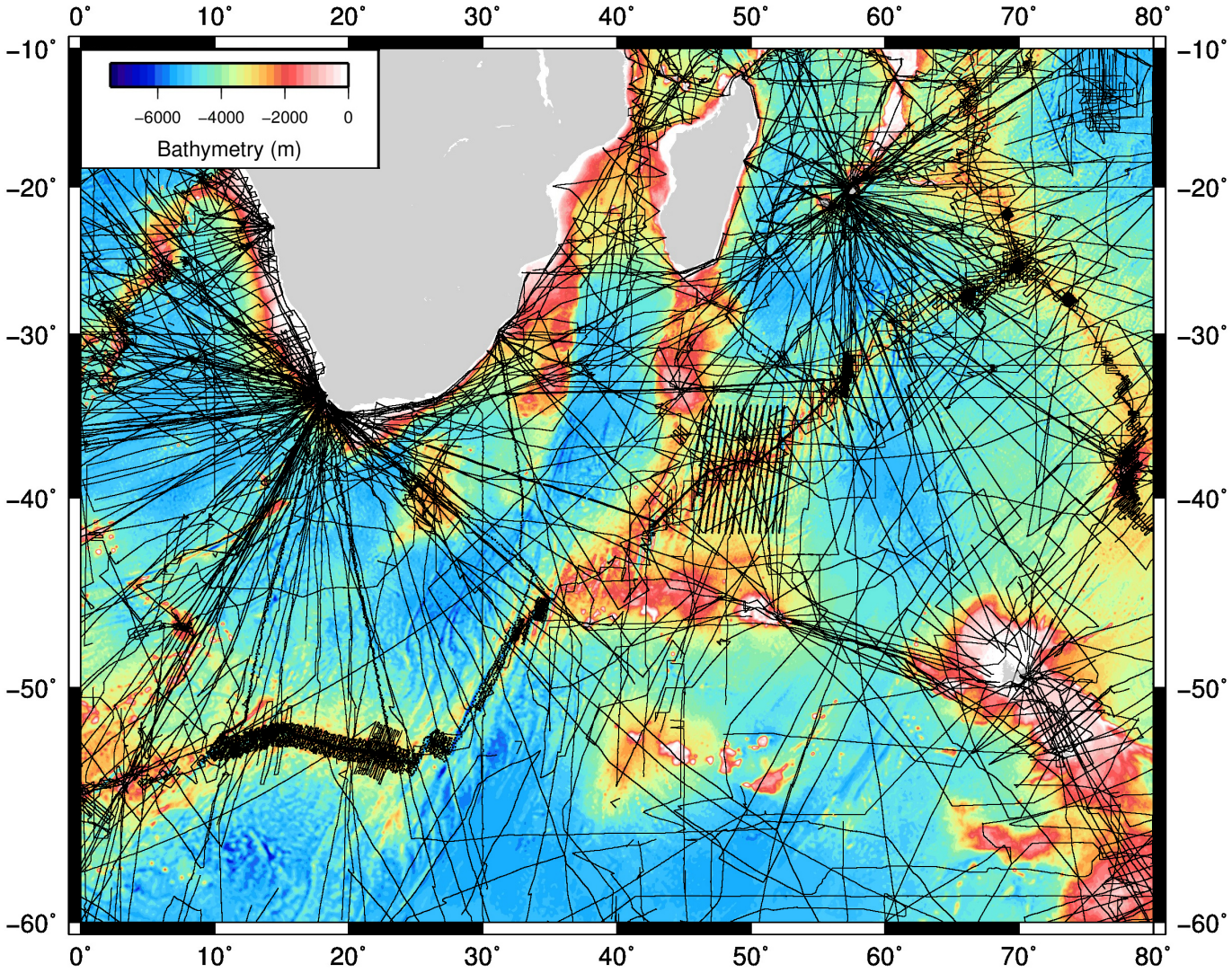


Figure 2.9: Bathymetry of the Southwest Indian Ridge region from the GEBCO 2014 30 x 30 global bathymetry grid (IOC et al., 2003). Shiptracks of cruises which collected multibeam and single beam bathymetry data used in this thesis shown in black.

2.4.2 Gravity

Shipboard gravity data from 129 cruises was collated for this study. It should be noted that, older gravimeters are more prone to cross-coupling errors due to less efficient damping (Worzel and Harrison, 1963), however retrospective corrections are difficult to make.

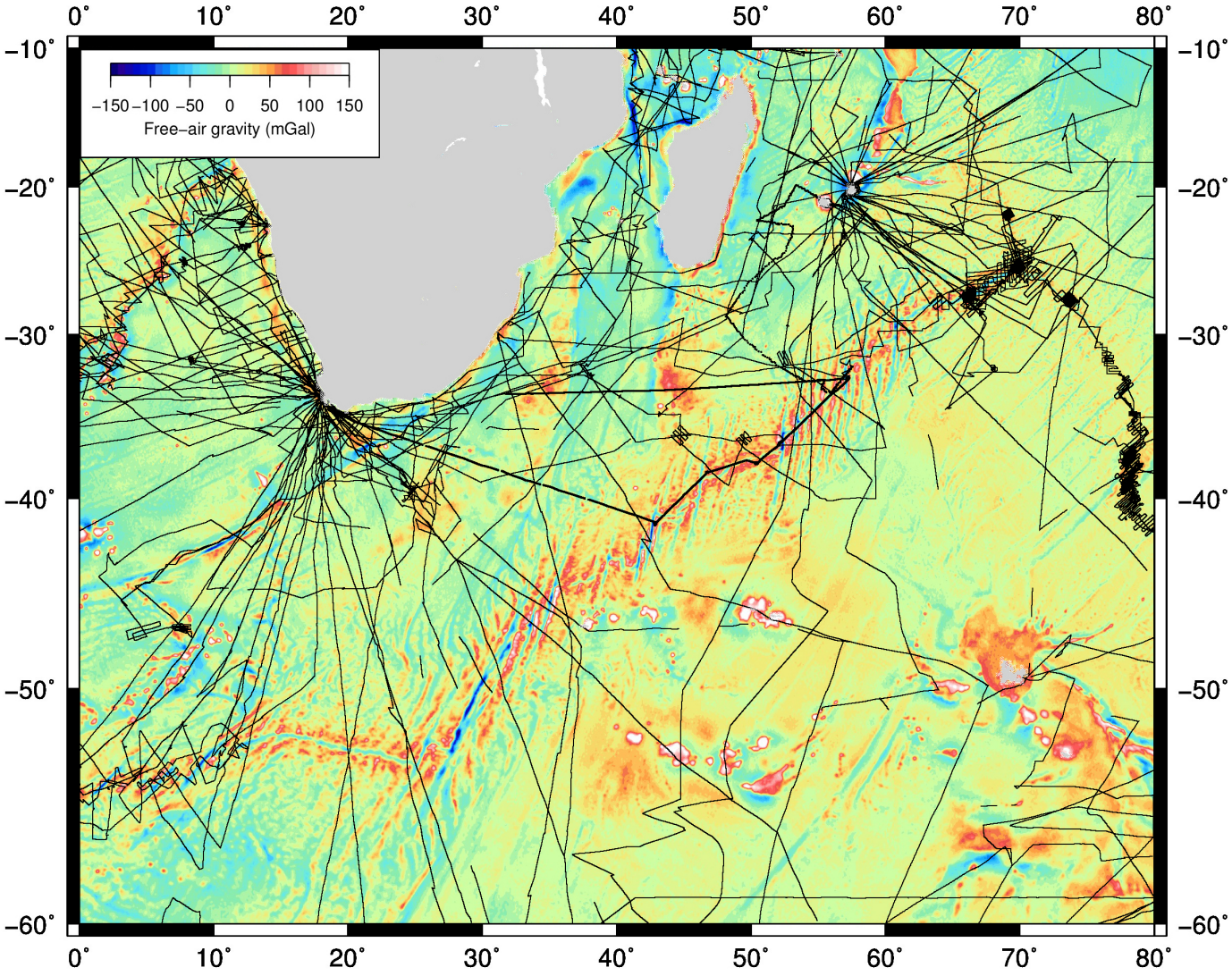


Figure 2.10: Sandwell and Smith satellite gravity (Sandwell and Smith, 1997). Shiptracks of cruises which collected shipboard gravity data used in this thesis are shown in black

2.4.3 Magnetics

Magnetic data from a total of 217 cruises was collated, however unlike bathymetry and gravity data the simple number of tracks are less important than their location. Closely spaced profiles across the ridge crest are important for estimating crustal ages and spreading rates. As well as the profiles across, there are a number of dedicated magnetic surveys over the ridge crest, particularly at the eastern end.

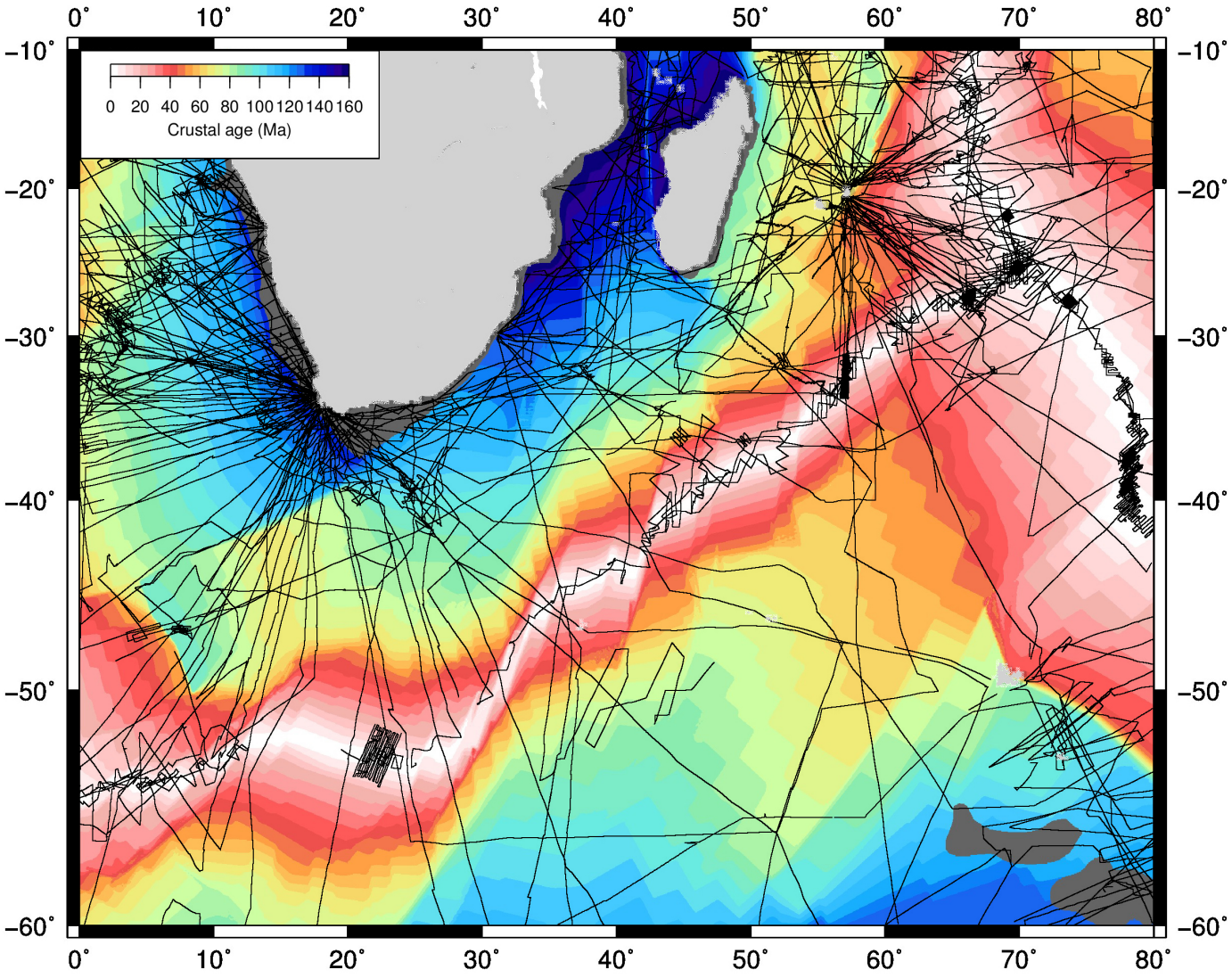


Figure 2.11: Crustal ages based on the Müller et al. (1997) age grid. Shiptracks of cruises which collected shipboard magnetic data used in this thesis are shown in black.

2.5 Satellite data

Shipboard data are an invaluable tool for marine research; however a very small percentage of the oceans have been surveyed since research began (Smith and Sandwell, 2004). The advent of satellite technology in the early 1970's opened a new avenue for data collection in even the remotest ocean regions. Early geodetic satellite missions (eg. GEOS-3 launched in 1975 (Stanley, 1979)) provided global data coverage for sea surface altimetry for the first time. Satellite methods have two major disadvantages.

The first is that the resolution of the data obtained is much poorer (1-5 minutes) than measurements taken at sea (on the order of metres). The second is the inability to measure seafloor bathymetry directly due to the rapid attenuation of altimetry radar in water.

2.5.1 Satellite derived gravity

Satellites such as SEASAT (launched 1978 (Born et al., 1979)) and ERS 1 (launched 1991 (Duchossois, 1991)) uses pulse-limited radar to measure the distance between the satellite and the closest sea surface point. The equipotential sea surface approximates the geoid, however the satellite altimetry measurement includes the instantaneous sea surface height caused by waves and wind. This sea surface height is removed using an independent measurement of the height of the satellite above the ellipsoid obtained using GPS. This provides a measure the mean height of the equipotential sea surface, which approximates the geoid. The raw sea surface altimetry data undergo a number of corrections including tidal motion, removal of ice and land outliers and removal of data showing high significant wave height (Sandwell and Smith, 1997). The resulting data is then low-pass filtered and individual profiles differentiated along track with respect to time, to produce along-track vertical deflections (Sandwell and Smith, 1997).

$$\eta(\mathbf{x}) \equiv -\frac{\partial N}{\partial x} \cong -\frac{1}{g_0}\frac{\partial U}{\partial x} \tag{2.6}$$

$$\xi(\mathbf{x}) \equiv -\frac{\partial N}{\partial y} \cong -\frac{1}{g_0}\frac{\partial U}{\partial y} \tag{2.7}$$

where $N(\mathbf{x})$ is the geoid height, $U(\mathbf{x}, z)$ is the gravitational potential. These deflections are gridded to form grids of north (ξ) and east (η) vertical deflections (e.g. Sandwell and Smith, 1997).

Since the Brun's formula gives a first order relationship between the geoid height $N(\mathbf{x})$

and gravity potential $U(\mathbf{x}, z)$ by (e.g. Sandwell and Smith, 1997)

$$N(\mathbf{x}) \cong \frac{1}{g_0} U(\mathbf{x}, 0) \tag{2.8}$$

and the gravity anomaly $\Delta g(\mathbf{x})$ is related to the vertical derivative of the gravity potential $U(\mathbf{x}, z)$ by (e.g. Sandwell and Smith, 1997)

$$\Delta g(\mathbf{x}) = -\frac{\partial U(\mathbf{x}, 0)}{\partial z} \tag{2.9}$$

The grid of vertical deflections may be used to calculate the gravity anomaly using Laplace's equation $\nabla^2 U = 0$ to relate the vertical deflection, gravity potential and gravity anomaly. Substituting 2.6, 2.7 and 2.8 into Laplace's equation gives the relationship between the vertical gravity gradient and the sum of the x and y derivatives of the east and north vertical deflections (e.g. Sandwell and Smith, 1997)

$$\frac{\partial \Delta g}{\partial z} = -g_0 \left(\frac{\partial \eta}{\partial x} + \frac{\partial \xi}{\partial y} \right) \tag{2.10}$$

This differential equation may then reduced to an algebraic equation in the wavenumber domain using Fourier transformation following Haxby et al. (1983)

$$\frac{\partial \Delta g(\mathbf{k}, z)}{\partial z} = -2\pi i g_0 [k_x \eta(\mathbf{k}) + k_y \xi(\mathbf{k})] \tag{2.11}$$

Upward continuation may be used to relate the gravity anomaly at the Earth's surface to a height z (e.g. Sandwell and Smith, 1997)

$$\Delta g(\mathbf{k}, z) = \Delta g(\mathbf{k}, 0) \mathrm{e}^{-2\pi |\mathbf{k}| z} \tag{2.12}$$

Taking previous equation and deriving it with respect to z, then evaluating for z=0 gives the relationship between the Fourier transform of the gravity anomaly and the

sum of the Fourier transforms of the two components of vertical deflections, thus allowing the gravity anomaly grid to be calculated from the grid of vertical deflections (e.g. Sandwell and Smith, 1997)

$$\Delta g(\mathbf{k}, 0) = \frac{ig_0}{|\mathbf{k}|}[k_x \eta(\mathbf{k}) + k_y \xi(\mathbf{k})] \tag{2.13}$$

Finally, the spherical harmonic gravity model is added to give the long wavelength gravity field. The resolution of the gravity grids produced increased with the density of the coverage as more missions were flown, so that by 1997 Sandwell and Smith had produced a global 2 minute gravity grid (Sandwell and Smith, 1997) and by 2009 this was replaced by a 1 minute resolution grid. Comparison of shiptrack gravity data and the 2009 1 minute global grid yielded differences of 2 to 4 mGal (Sandwell and Smith, 2009).

Other satellites such as GRACE (launched in 2002) and GOCE (launched in 2009) measure gravity directly. GRACE uses a two satellite system where the distance between them is used to measure the variation in gravity, allowing it measure the gravity of the geoid up to 2 mGal accuracy Grace (2013). GOCE measures the difference in acceleration of two masses 50 cm apart. These direct gravity measurements have the caveat that they cannot resolve features <200 km due to upward continuation over 400 km (Smith and Sandwell, 2004).

2.5.2 Satellite derived Bathymetry

Since altimetry radar signals attenuate in water, seafloor bathymetry is not directly measurable by satellite methods. However, Parker (1972), showed that the topography associated with a given gravity anomaly can be calculated in the wave domain. Following this, Dixon et al. (1983) used profiles of geoid height data from Seasat tracks to infer ocean depths for an area with existing conventional bathymetry measurements. This showed that the prediction is strongly dependant on the assumed form of iso-

static compensation as well as topographic features out of the profile plane. Smith and Sandwell (2004) used gravity-topography ratios for wavelengths between 15 km and 160 km, estimated by applying a linear regression method to gridded ship soundings and gravity data, to provide the relationship between gravity and topography. Following this, Sandwell and Smith used an iterative inversion to solve Parkers equation to estimate the bathymetry from the 1 minute global gravity anomaly grid to produce the Sandwell and Smith global bathymetry grid (Sandwell and Smith, 2008). Comparisons with multibeam bathymetry showed that 50% of the differences are less than 25 m (Sandwell and Smith, 2008), however the resolution is poor compared to that of multibeam bathymetry.

2.6 Combining datasets

As outlined in the sections above, many of the marine geophysical datasets have a trade-off between coverage and resolution, small high resolution datasets or global coverage datasets with limited resolution. In this work a combination of these datasets are used, depending on the suitability for the analysis being performed.

Detailed morphological studies (chapters 3 and 4) and high resolution seamount distribution studies (chapter 5) use solely shiptrack bathymetry, as a high resolution is necessary. Low resolution morphological studies (chapter 3) and seamount distribution studies over a large area (chapter 5) utilise a combined dataset (shown in Figure 2.12). This consists of shipboard bathymetry where available, elsewhere, the global GEBCO grid is used. Isostatic studies (chapter 6) use both bathymetry and gravity data, meaning that the bathymetry data must be unrelated to the gravity data to avoid introducing a circular relationship. Therefore, the GEBCO bathymetric grid is used, as opposed to gravity derived bathymetry (Sandwell and Smith, 2008), as GEBCO is based solely on ship track bathymetry.

Shipboard and global datasets were combined to produce regional maps of bathymetry

and gravity, where areas of sparse shipboard data are supplemented using the global grids. It is noted that gridding processes will affect the statistical distribution of the data points (Smith, 1993).

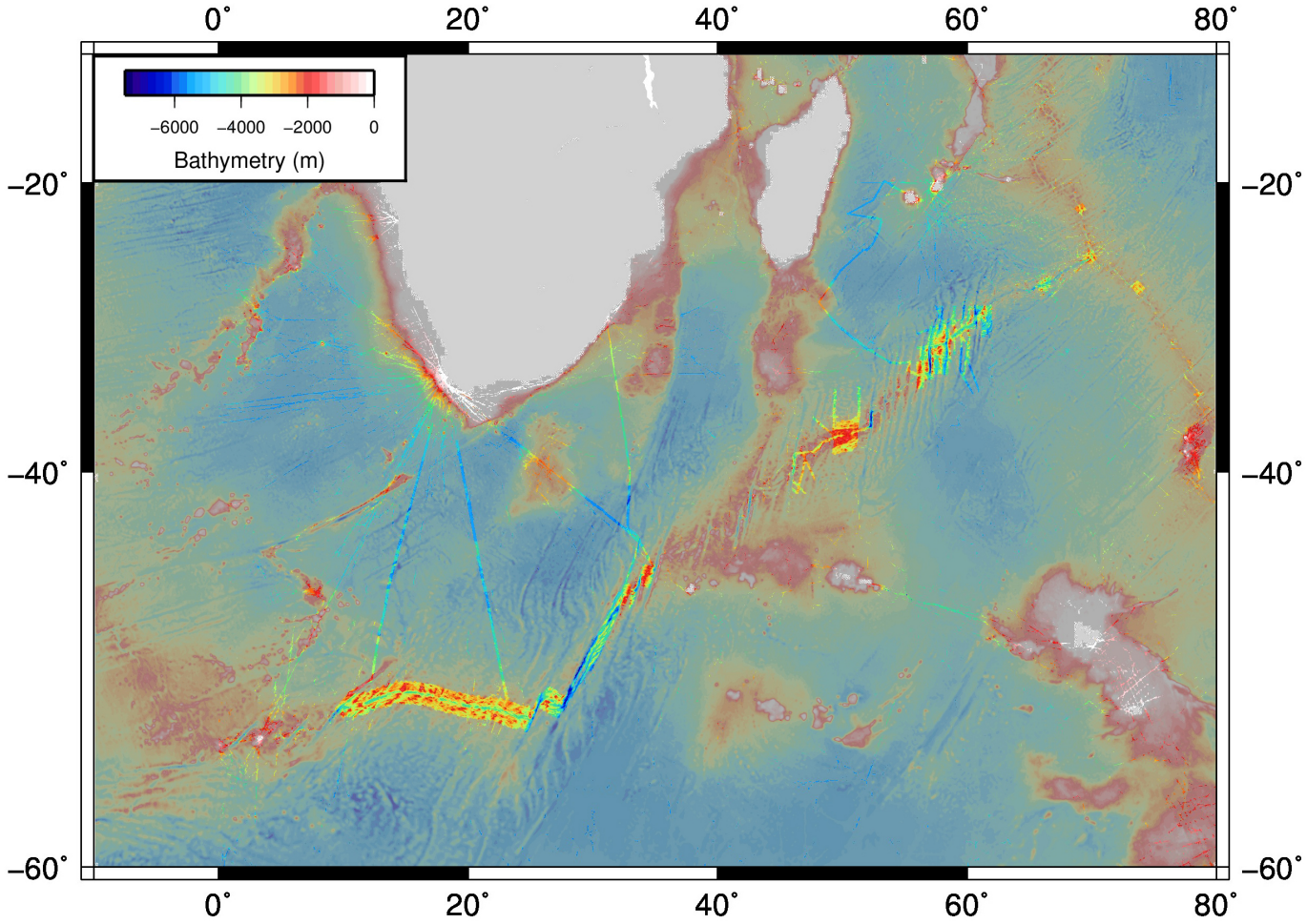


Figure 2.12: Figure showing the composite bathymetry map. The shipboard multibeam bathymetry, gridded using GMT's Nearneighbor (Wessel and Smith, 1991), is highlighted. The background is from the GEBCO 2014 30'' x 30'' global bathymetry grid (IOC et al., 2003).

2.7 Chapter Summary

Over this chapter we have reviewed how data used in this thesis was collected, collated and processed. We note the following key points:

- Shipboard bathymetry, gravity and magnetic data were acquired over three cruises between 2011 and 2013, forming the core data set for this thesis.
- Bathymetry data was processed to remove spurious points using MB-System v5.3, CARAIBES and Fledermaus.
- Relative gravity data collected at sea were converted from relative to absolute values using base station tie-ins. These gravity data were reduced to gravity anomalies by removing the gravity effect of the reference ellipsoid. Corrections for the Eötvös error, cross coupling errors and linear instrumental drift were finally applied.
- Magnetic data were reduced to magnetic anomalies by removing the IGRF v.11 and corrected for diurnal variation and linear instrumental drift using base station readings from Mauritius.
- Cruise data from 368 cruises were collated for the Southwest Indian region including shipboard bathymetry, gravity and magnetic data, though it is noted that older data sets will be less accurate, particular with regards to navigation.
- Global satellite data including gravity and predicted bathymetry grids were reviewed. All global grids had a poorer resolution than shipboard data, and upward continuation effects mean direct gravity measurements are unable to resolve smaller features.
- Global datasets and shipboard data were combined to produce regional data grids of bathymetry and gravity for analysis, including small scale morphological studies, seamount counting and isostatic studies.

Chapter 3

Ridge Crest Morphology

Slow and ultra-slow spreading ridges are typically characterised by an axial valley morphology (Heezen, 1960). Numerical modelling studies (e.g. Chen and Jason Morgan, 1990) have shown that a combination of brittle-plastic and viscous rheologies undergoing extension at slow rates produced an axial valley morphology. These studies show that the axial valley morphology is dependent on the ridge rheology, which is dependent on a number of factors including the ridge thermal structure. Observations of the axial valley morphology, therefore, provide information on the sub-axial structure of the ridge and its influencing factors.

In this chapter we initially review the causes of long wavelength variation in geophysical and geochemical data from published literature. This provides the framework for new observations during this thesis. We then use axial bathymetry profiles to investigate the applicability of a simple model for the formation of axial valley morphology along the ridge. These findings are further confirmed by comparing predictions of models with best fit elastic thicknesses (a proxy for lithospheric strength) with the axial valley widths along the ridge. Finally, we use swath bathymetry and along axis profiles to divide the ridge into segments. These segments are classified into Groups and the variation in axial valley processes between these Groups is discussed.

For clarity the word 'Section', where it refers to one of the seven areas of the ridge identified from geophysical profiles, is capitalised. These Sections consist of a number of segments, which are defined as lengths of the ridge axis separated by bounding discontinuities. These segments are later classified into 'Groups', which are based on the segment characteristics and not the segment location or Section.

3.1 Long Wavelength Geophysical Variation

The long wavelength variation in geophysical and geochemical data along the Southwest Indian Ridge has been previously discussed in a number of studies (e.g. Cannat et al., 1999, 2008; Sauter and Cannat, 2010). The following section of this thesis reviews these data and uses them to split the ridge into seven Sections, which reflect the long wavelength geophysical variation along the ridge. We outline some of the main influences on the ridge morphology such as the proximity of hotspots and ridge spreading obliquity.

Previous studies have used along-axis profiles to illustrate the long wavelength geophysical variation along the SWIR (e.g. Cannat et al., 1999; Sauter and Cannat, 2010). These profiles have been constructed by sampling bathymetry and gravity data along the deepest part of the axial valley. However, instead of sampling along maximum depth, we sample the data along zero-age crust, which is located using magnetic data. This should enable us to a produce a more accurate illustration of the current variations along the ridge crest, as previous studies (Malinverno, 1990) have argued that variation in axial depths along a segment may be attributed to variation in zero-age profiles.

The following section of this thesis describes the construction of the new along axis profiles for bathymetry and mantle Bouguer anomaly data. These data are described and compared with published seismic and geochemical data in order to establish the long wavelength variations along the ridge.

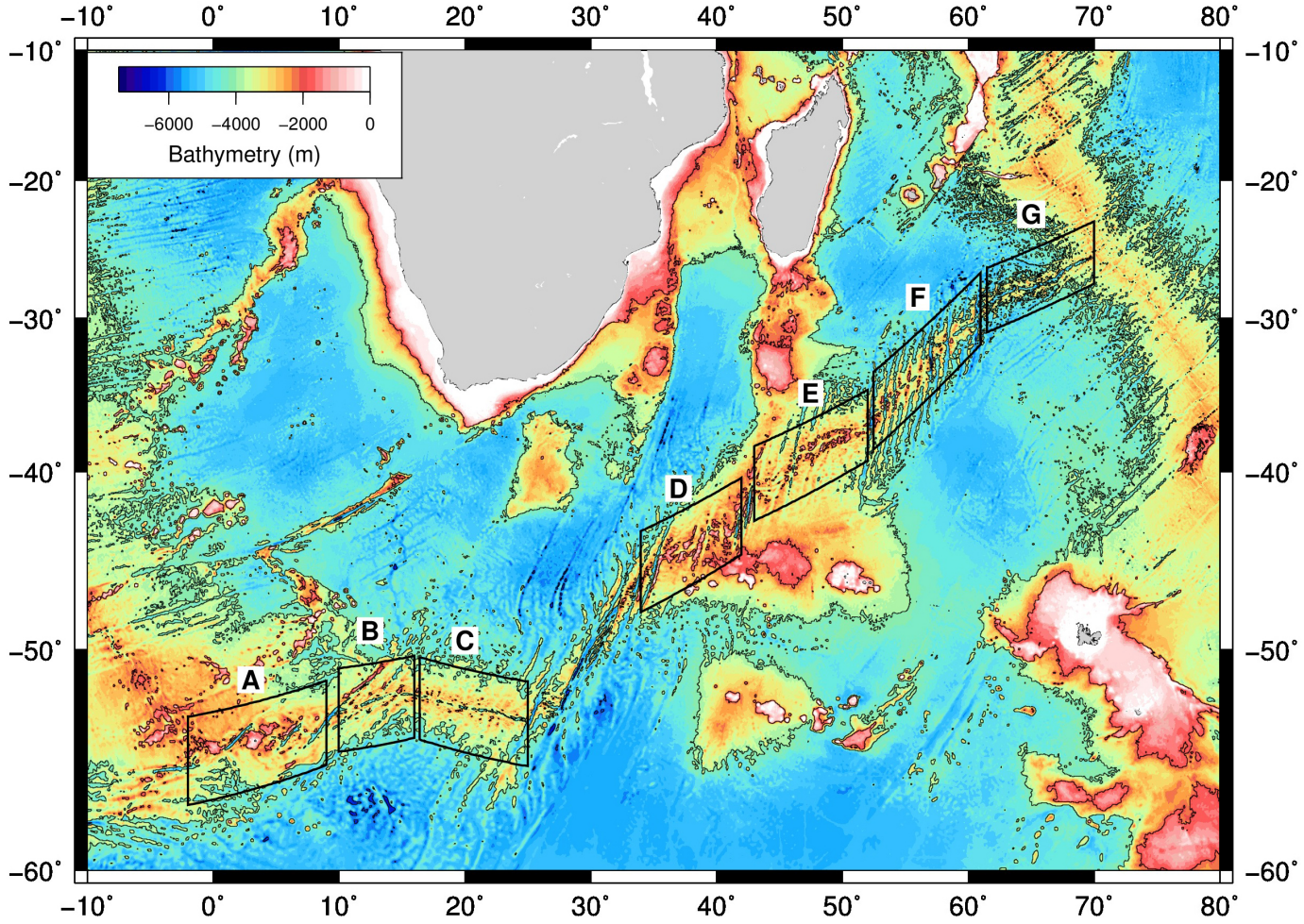


Figure 3.1: Bathymetry map from the GEBCO 2014 30'' x 30'' grid, contoured at 2000 m. The black boxes outline the 7 Sections of the ridge identified using along axis geophysical and geochemical profiles. These Sections are labelled A to G and are referred to throughout this chapter.

3.1.1 Constructing Along Axis Bathymetry and Gravity Profiles

Profiles of bathymetry and mantle Bouguer anomaly were constructed along the ridge axis. Mantle Bouguer anomalies were calculated from the free-air gravity anomalies since, while free-air gravity anomalies at the axis primarily reflect the changes in axial bathymetry, mantle Bouguer anomalies reflect changes in mantle density and/or crustal thickness. The profiles were sampled from 30'' x 30'' gridded data along a

track following zero-age, which was identified using shipboard magnetic data crossing the ridge.

In order to identify the seafloor spreading anomalies in the magnetic data, a theoretical magnetic profile was constructed using MODMAG software (Mendel et al., 2005). A set of parameters including full spreading rate, source layer thickness, and magnetisation both on and off axis were fitted iteratively, in order to reproduce the magnetic anomalies observed across different areas of the ridge as closely as possible. The MODMAG model was then compared with shipboard magnetic profiles across the ridge, in order to pick the anomalies consistently along the ridge. An example of the two-dimensional magnetic profiles and fitted MODMAG model for the area between 48° E and 52° E is shown in Figure 3.2. These magnetic anomalies were best reproduced using a full spreading rate of 14 mm yr^{-1}, increasing to 16 mm yr^{-1} after 4 Ma, a 0.5 km thick source layer draped over the topography and an on-axis magnetisation of 18 A m^{-1} decreasing to 4 A m^{-1} off-axis. Tisseau and Patriat (1981) showed that at ultraslow spreading rates the boundaries between normal and reverse polarity boundaries are sloped. In order to correct for this effect, the width of the magnetic blocks is reduced by a factor called the contamination coefficient, relative to each point on the calculated profile in turn. A contamination coefficient of 0.6 is used to account for the contamination between different polarity blocks. These spreading rate, magnetisation, and contamination coefficient were varied for different areas of the ridge, since there is significant variation in spreading obliquity, asymmetry and different magnetisation amplitudes of amagmatic regions (Sauter et al., 2008). The parameters used for different areas of the ridge are in good agreement with previous magnetic studies in those regions (Bronner et al., 2014; Searle and Bralee, 2007; Hosford et al., 2003). In general, the anomalies showed reasonable fits to the forward model with respect to the Bruhnes anomaly and anomaly 2An, which is generally well defined on both the north and south sides. Anomalies 3Bn and 3n are observed sporadically on the south side but are small amplitude or absent on the north side. The 5n anomaly is generally high amplitude and well defined to the north and sometimes present in the south. The anomaly picks

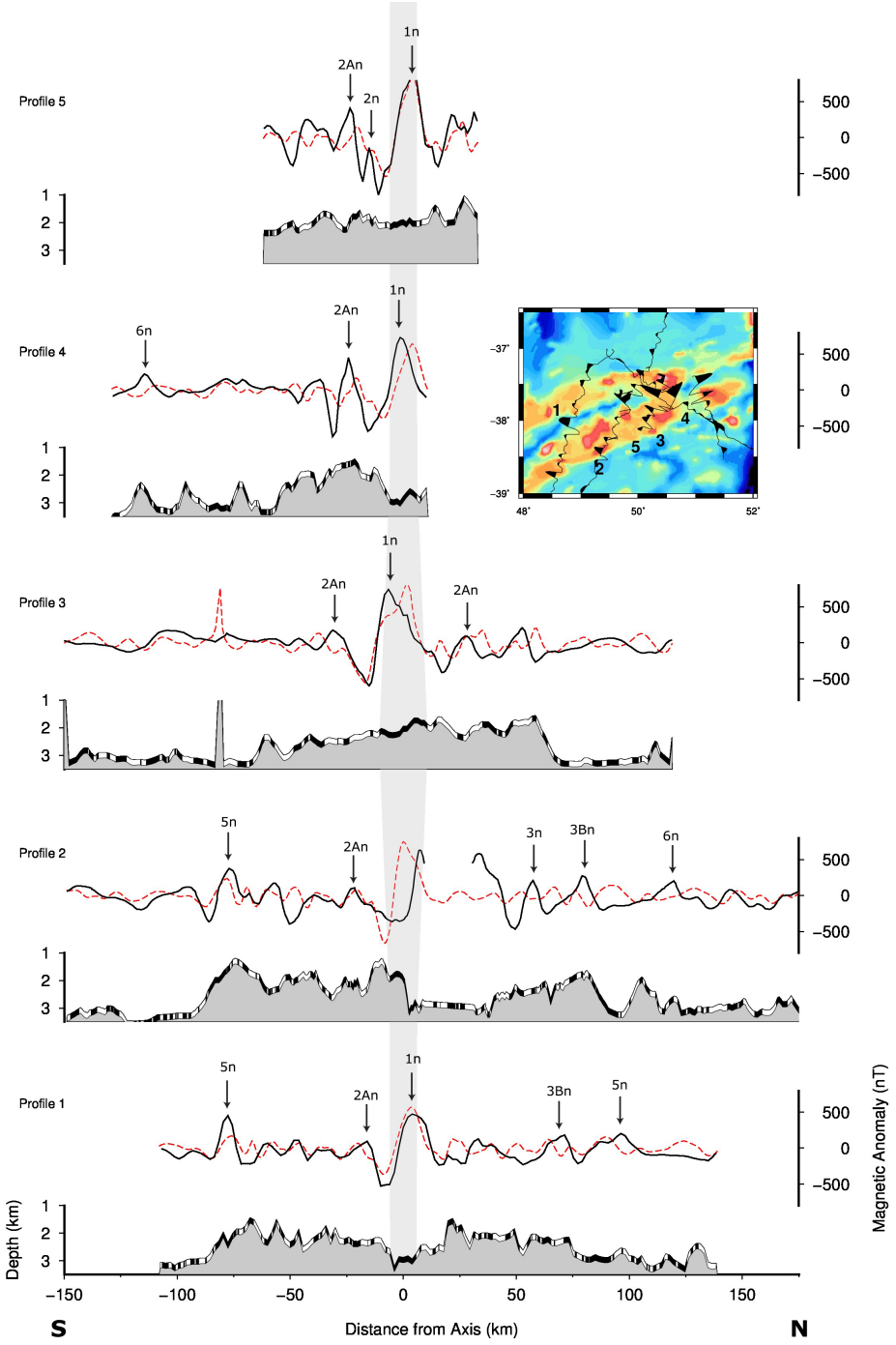


Figure 3.2: Two dimensional magnetic anomaly profiles from existing cruise data; cruise tracks are shown in the inset map. Observed magnetic anomaly profiles (solid black lines) are compared to calculated magnetic anomaly profiles (dashed red lines) predicted using a full spreading rate of 14 mm yr^{-1} increasing to 16 mm yr^{-1} after 4 Ma, a 0.5 km thick source layer draped over the topography, and magnetisation of 18 A m^{-1} and 4 A m^{-1} on and off axis respectively. The graphic below the profiles show the seafloor spreading model draped over the topography, which is derived from the centre beam of the multibeam bathymetry for each shiptrack. The grey band represents the extent of the Bruhnes anomaly used to define the zero-age track.

were compared with good pre-existing studies for the SWIR (e.g. Bronner et al., 2014; Hosford et al., 2003) and showed good agreement.

These magnetic profiles were used to identify up to anomaly 6 (~20.5 Ma) where the profile length, azimuth, and data quality permitted. The anomaly picks are shown in Figure 3.3. The picks of the Bruhnes anomaly were used to plot a track of zero-age along the ridge crest, extrapolated in areas of sparse profiles using the Müller et al. (1997) global age grid, the axial volcanic ridge where present, which is assumed to denote the neovolcanic zone, and the deepest axial valley bathymetry.

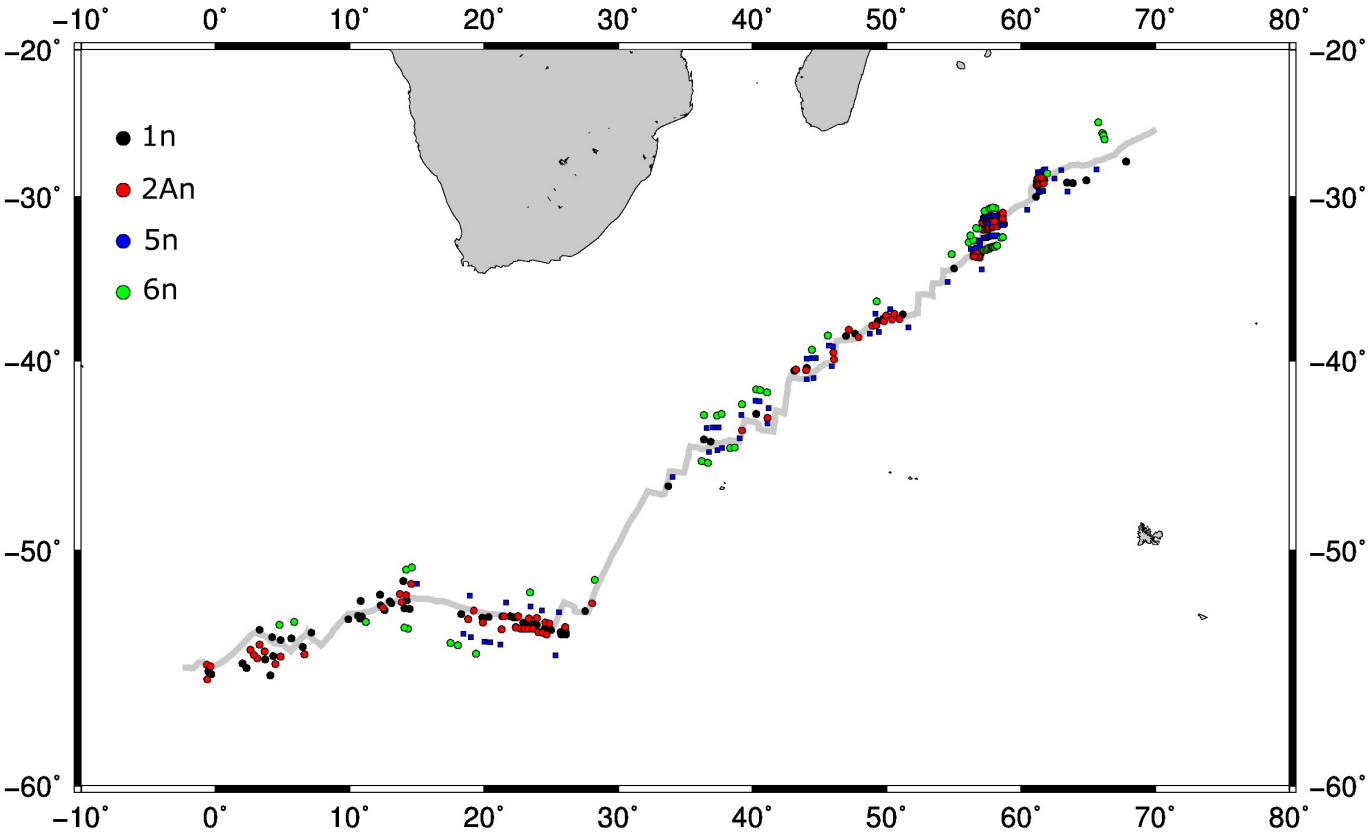


Figure 3.3: Magnetic anomaly picks derived from shipboard magnetic profiles across the ridge. The following anomaly picks are shown: 1n (black circles); 2An (red circles); 5n (blue circles); 6n (green circles). The grey line shows the zero-age track constructed using the picks of the Bruhnes anomaly.

This zero-age track was used to sample the integrated shipboard and satellite bathymetry data described in chapter 2, in order to produce the along axis profiles in Figure 3.6.

Mantle Bouguer anomalies (MBAs) were calculated following the method of Kuo and Forsyth (1988), removing the gravity effects of the topography and base of the crust to produce an anomaly, which reflects changes in crustal thickness and mantle density. The gravity effects of the water-crust interface (Figure 3.4-B) and crust-mantle interface (Figure 3.4-C) were calculated using the Fast Fourier Transform (FFT) method of Parker (1972). Initially, a constant crustal thickness of 5 km was assumed, and densities of 1030 kg m^{-3}, 2800 kg m^{-3} and 3300 kg m^{-3} were used for the water, crust and mantle respectively. The gravity effects of these two surfaces were then subtracted from the observed free-air gravity to produce mantle Bouguer anomalies (Figure 3.4-E). These anomalies reflect (*i*) lateral changes in crustal thickness, generally associated with short wavelength MBA variation (*ii*) lateral changes in mantle density, generally associated with long wavelength MBA variation.

There are uncertainties in the assumed crustal and mantle densities, and crustal thickness, used to calculate the mantle Bouguer anomalies. In particular, the sub-axial mantle density at mid-ocean ridges is expected to be lower than beneath older oceanic lithosphere, and the crustal thickness is expected to be thinner than at faster spreading ridges (Reid and Jackson, 1981). The lack of representative seismic surveys along the Southwest Indian Ridge means that these assumptions are poorly constrained. In order to assess the degree of uncertainty caused by these assumptions on the final MBA, MBAs for a variety of densities and crustal thicknesses were calculated and the results compared with the original MBA profile. Figure 3.5 shows the effect of varying crustal densities between 2700 kg m^{-3} and 2900 kg m^{-3}, mantle densities between 3180 kg m^{-3} and 3300 kg m^{-3}, and crustal thicknesses between 3 km and 7 km. The results show that the differences between the MBAs are within 10 mGal (mostly within 5 mGal), and do not change the long wavelength MBA trend.

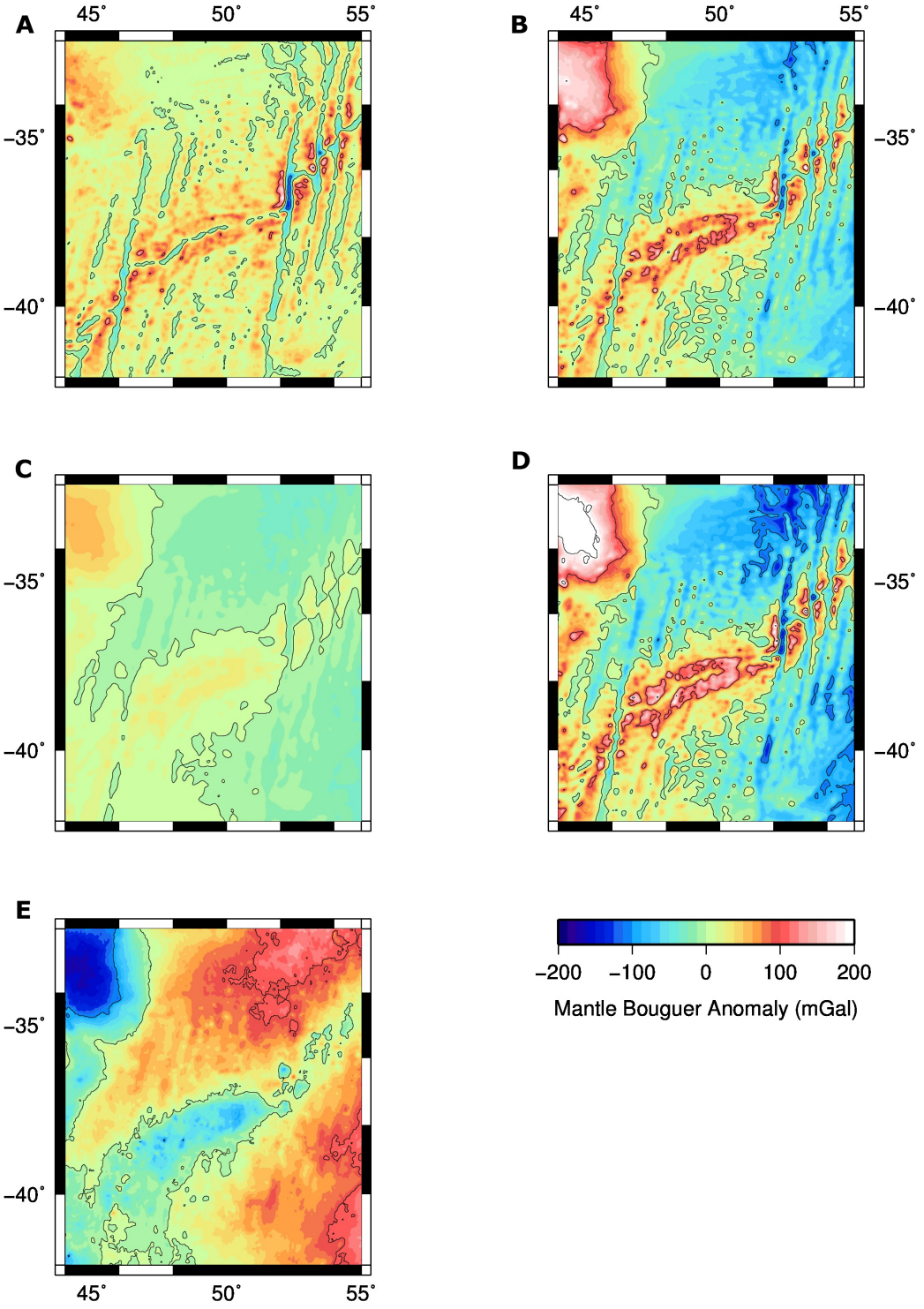


Figure 3.4: Series of maps showing the calculation of mantle Bouguer anomalies. The panels show the free-air gravity anomaly (panel A); gravity effect of the crust-water interface (panel B); gravity effect of the crust-mantle interface (panel C); the combined gravity effect of these two interfaces (panel D); the combined gravity effect subtracted from the free-air gravity anomaly to produce the mantle Bouguer anomaly (panel E).

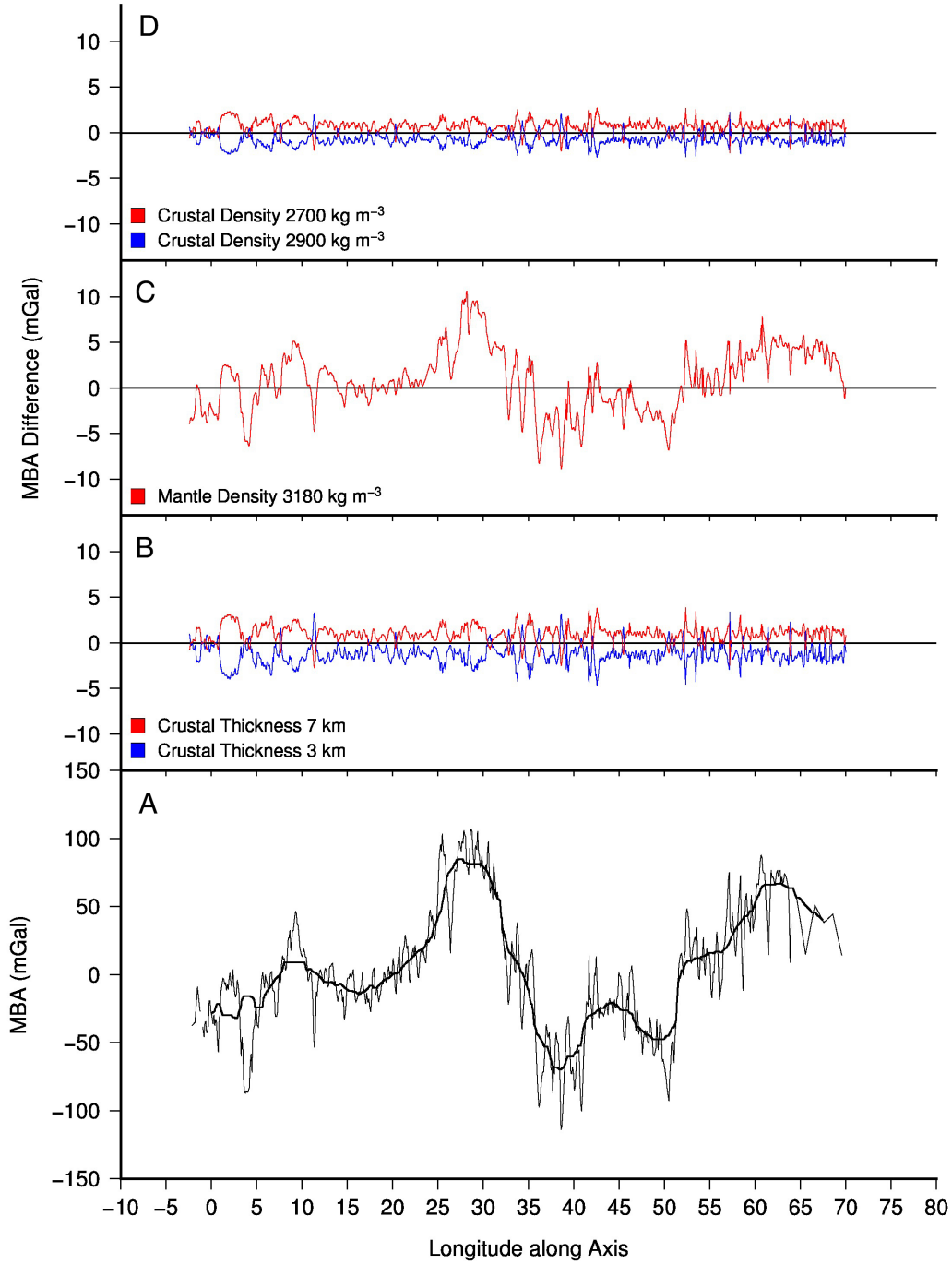


Figure 3.5: Differences between a series of profiles sampled along zero-age for different calculated mantle Bouguer anomalies. For each difference profile, all assumed densities and thicknesses are the same as the original profile, except for the one being tested. Panel A shows the original mantle Bouguer anomaly profile for reference (thin black line) and the profile with a median filter with a wavelength of 5° of longitude (thick black line). The original profile assumes a crustal thickness of 5 km, crustal density of 2800 kg m^{-3}, and a mantle density of 3300 kg m^{-3}. Panel B shows the difference between the MBA profile in panel A and MBA profiles with crustal thicknesses of 3 km (blue) and 7 km (red). Panel C shows the difference between the MBA profile in panel A and an MBA profile with a mantle density of 3180 kg m^{-3} (red). Panel D shows the difference between the MBA profile in panel A and MBA profiles with crustal densities of 2700 kg m^{-3} (red) and 2900 kg m^{-3} (blue).

The greatest difference is caused by a reduction in mantle density from 3300 kg m^{-3} to 3180 kg m^{-3}, reflecting the increased temperature in the sub-axial mantle. Profiles calculated using mantle densities of both 3300 kg m^{-3} and 3180 kg m^{-3} are shown in the final along axis profiles (see Figure 3.6) for comparison.

Comparison of mantle Bouguer anomaly maps with those from previous studies (e.g. Georgen et al., 2001; Grindlay et al., 1998) show good agreement. The final mantle Bouguer anomaly grid was sampled along the zero-age track to produce the gravity profile in Figure 3.6.

3.1.2 Along Axis Profile Results

The long wavelength variations in the axial bathymetry and gravity profiles calculated in this study are the same as for previously published profiles (Cannat et al., 1999; Sauter and Cannat, 2010). There are differences in the bathymetry profiles at shorter wavelength caused by the sampling along zero-age as opposed to the deepest part of the axial valley. These are significant when identifying the short wavelength segmentation on the ridge, as discussed in thesis section 3.2.3.

The compilation of bathymetry and mantle Bouguer anomaly data along axis show large scale variations along the length of the ridge (Cannat et al., 1999; Georgen et al., 2001). Figure 3.6 shows the along axis profiles for different geophysical and geochemical datasets. The correlations between these allow us to draw conclusions about the changes in the crustal structure and mantle properties along the ridge (e.g. Cannat et al., 1999, 2008; Sauter and Cannat, 2010). Three geophysical data sets are used: (*i*) the bathymetry reflects regional changes in axial depth, (*ii*) the MBA reflect the density changes in the upper mantle and/or changes in crustal thickness along the ridge (Kuo and Forsyth, 1988), (*iii*) the lateral variation in shear wave velocity sampled from the surface wave tomography of fundamental and higher mode Rayleigh waves (Debayle et al., 2005) are particularly sensitive to mantle temperature (Priestley and Mckenzie, 2013), and so provide insight into the thermal structure of the upper mantle

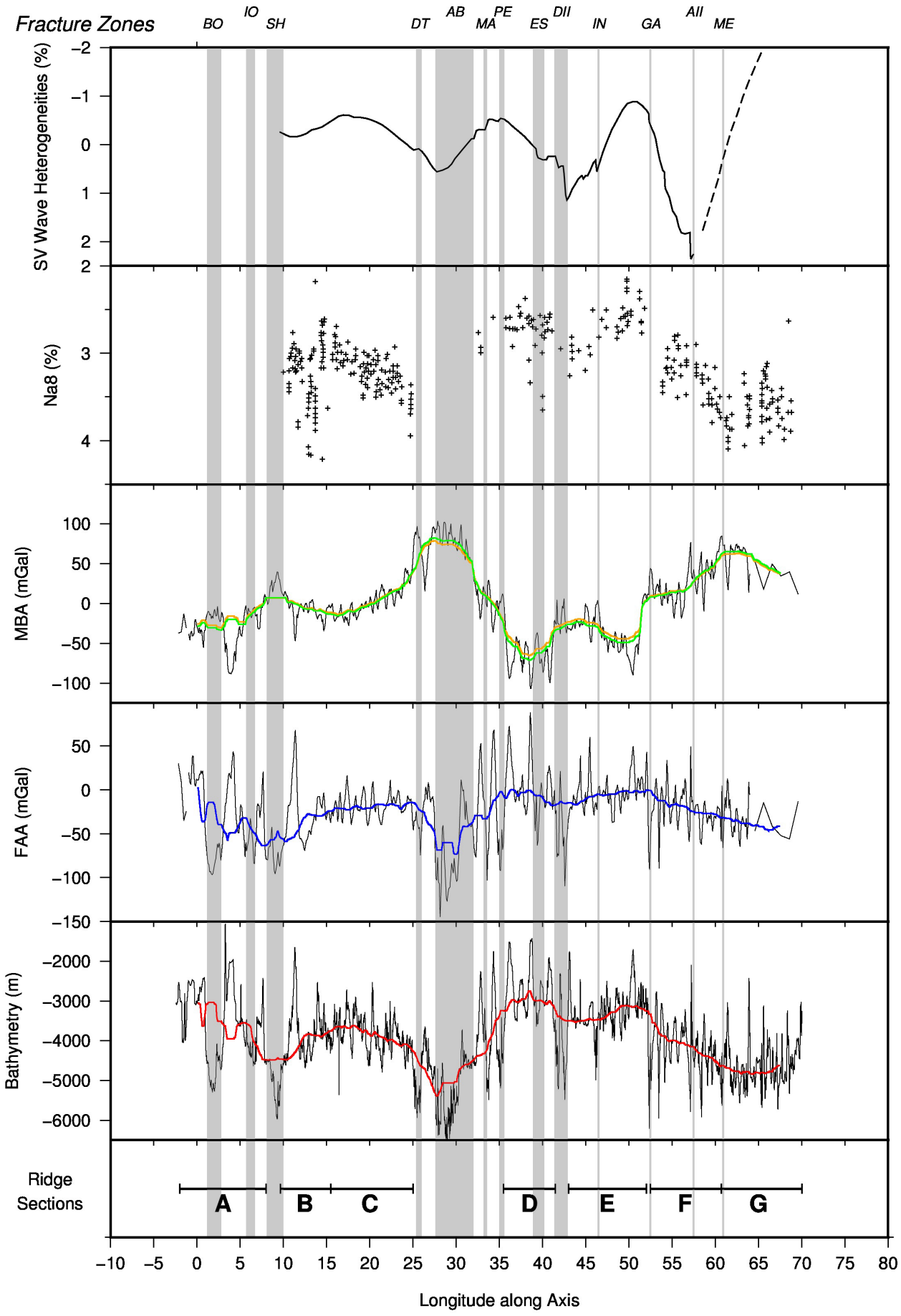

Fracture Zones
BO
IO
SH
DT
AB
MA
PE
ES
DII
IN
GA
AII
ME
SV Wave Heterogeneities (%)
Na8 (%)
MBA (mGal)
FAA (mGal)
Bathymetry (m)
Ridge Sections
A
B
C
D
E
F
G
Longitude along Axis

Figure 3.6: Along-ridge profiles of bathymetry, mantle Bouguer anomaly, variation in $Na_{8.0}$ composition of basalt glasses dredged along the SWIR axis and shear wave velocity heterogeneities. These were sampled along a zero-age track, which was determined using magnetic anomaly picks (see Figure 3.3). Panel 1 shows the division of the ridge into seven Sections based on geophysical and geochemical characteristics. Panel 2 shows the bathymetry (black line) sampled from shipboard bathymetry where available and the GEBCO 2014 30'' x 30'' grid elsewhere. The red line is the bathymetry filtered using a median filter with a wavelength of 5° longitude. Panel 3 shows the free-air gravity anomaly (black line) sampled from the Sandwell and Smith altimetry derived 1' x 1' marine gravity grid v.23.1 (Sandwell and Smith, 2008). Panel 4 shows the mantle Bouguer anomaly (black line) sampled from the MBA grid described above and the median filtered MBA (green line). The median filtered MBA grid calculated using a reduced mantle density of 3180 kg m^{-3} is shown in orange. Panel 5 shows the variation in $Na_{8.0}$ composition of basalt glasses dredged along the SWIR axis from Cannat et al. (2008) and Standish et al. (2008). Panel 6 shows shear wave velocity heterogeneities at 75 km depth, sampled from the tomographic model of Debayle et al. (2005). These are in percentage difference relative to PREM (V_s = 4.39 km s^{-1}). The grey vertical bars show the locations of fracture zones: BO = Bouvet, IO = Islas Orcadas, SH = Shaka, DT = DuToit, AB = Andrew Bains, MA = Marion, PE = Prince Edward, ES = Eric Simpson, DII = Discovery II, IN = Indomed, GA = Gallieni, AII - Atlantis II, ME = Melville.

(Sauter et al., 2009). Figure 3.6 shows the shear wave heterogeneities expressed as a percentage relative to PREM (V_s = 4.39 km s^{-1} at 75 km) sampled at 75 km depth. In addition to geophysical data, geochemical data from basalt glasses sampled along the ridge provide important constraints on melt supply and mantle pressures. Two main geochemical proxies are used. The sodium content ($Na_{8.0}$) of SWIR basalt glasses (corrected for the effect of low pressure fractional crystallisation to an MgO content of 8 wt% (Klein and Langmuir, 1987)) is commonly used as a proxy for degree of partial melting and therefore melt supply at mid-ocean ridges (Klein and Langmuir, 1987). Iron content ($Fe_{8.0}$) of SWIR basalt glasses (also corrected to an MgO content of 8 wt%) is commonly used as a proxy for the mean pressure of mantle melting, as well as degree of melting (Klein and Langmuir, 1987).

The small wavelength variations in bathymetry are well correlated with changes in the free-air gravity anomaly, which primarily reflect the density contrast at the water-crust interface. Figure 3.6 shows that over long wavelengths the bathymetry is well anti-correlated with the mantle Bouguer anomaly (Georgen et al., 2001), indicating that the relief is compensated by along axis changes in mantle density or crustal thickness

(Phipps Morgan et al., 1987; Lin and Phipps Morgan, 1992; Kuo and Forsyth, 1988). This suggests that areas with a greater average depth have thinner crust or denser sub-axial mantle than areas with a shallower average depth.

This is significant, as the bathymetry sampled along zero-age has a mean depth of 3924 m and a standard deviation of 922 m, indicating large changes in axial depth along the ridge. Over small wavelengths, the axial depth variation is caused by segmentation, in which segments form axial highs that are separated by axial lows at transform faults and non-transform discontinuities. These short wavelength variations cause extreme deeps such as the Andrew Bains fracture zone (6700 m depth) and extreme highs such as the Joseph Mayes seamount (1250 m depth), and are superimposed on large wavelength variation.

These large scale variations were used to divide the ridge into seven Sections, as shown in the bottom panel of Figure 3.6. The following section briefly describes the main geophysical and geochemical parameters of each Section of the ridge. These are used to provide a framework in which to interpret the changes in the ridge crest morphology, discussed later in this chapter.

Section A shows a regional bathymetric high (on average 3000 m depth) away from the fracture zones, which is well correlated with a regional MBA low, indicating a hot, low density mantle and/or crustal thickening (assuming the crust has a constant density). The increase in axial depth and MBA across the Islas Orcadas transform suggests that the source of this increased mantle temperature lies to the west of this transform. Assuming that the reduction in MBA over this Section is solely due to crustal thickening, we can estimate the magnitude of the crustal thickening using the Bouguer slab formula: $\Delta g = 2\pi\Delta\rho G\Delta L$, where Δg is the change in MBA, $\Delta\rho$ is the density contrast at the moho, G is the gravitational constant and ΔL is the change in crustal thickness. This assumes that the crust and mantle have constant densities. The change in MBA over Section A, shown in Figure 3.6, is approximately 45 mGal; assuming that $\Delta\rho$ is 380 kg m^{-3}, the change in crustal thickness is $\sim$ 2.8 km.

Section B, known in literature (e.g. Dick et al., 2003) as the 'oblique Section', is associated with a sharp deepening in regional bathymetry, despite having the highest bathymetric peak on the ridge (Joseph Mayes seamount). The accompanying MBA high suggests crustal thinning or a decrease in mantle temperature between Sections A and B. The shear wave velocity is low compared with surrounding Sections, which indicates a colder mantle. The $Na_{8.0}$ content of basalt glasses along this Section of the ridge show a wide range of values. This is attributed to differences in the upwelling processes between amagmatic and volcanic segments (Cannat et al., 2008), which are discussed further in section 3.1.3, as well as a possible two lithology mantle source (Standish et al., 2008).

Section C, known in literature (e.g. Grindlay et al., 1998) as the 'orthogonal Section', has an intermediate to high axial depth, which decreases towards the du Toit-Andrew Bains fracture zone system, mirrored by the MBA low, which becomes more positive towards the fracture zones. This suggests an increase in crustal thickness and/or mantle temperature relative to the adjacent oblique Section and fracture zone system. The bathymetric shallowing also coincides with a decrease in shear wave velocity, inferring a hotter sub-axial mantle than Section B. The $Na_{8.0}$ content for SWIR basalts in this Section are well correlated with axial depths, with values between 3.4% and 2.3%, greater than the surrounding Sections but not as low as the values obtained in the central part of the ridge (Standish et al., 2008). This suggests that this Section of the ridge has an intermediate degree of partial melting relative to the rest of the ridge (Sauter and Cannat, 2010). The $Fe_{8.0}$ content for basalts in this region show a decrease of 0.7% from east to west indicating greater melt supply in the western part of this Section (Standish et al., 2008).

The Du Toit-Andrew Bains fracture zone system, though not a named Section, is associated with a distinct change in the geophysical and geochemical trends along the ridge. The fracture zone system is associated with a decrease in zero-age depth, including the deepest point on the ridge at the Andrew-Bains fracture zone (6700 m

depth). The corresponding increases in the MBA, as well as the increased shear wave velocity, indicate that the area beneath the fracture zone system has a colder mantle regime. This is also proposed to be the boundary between Atlantic-type and Indian-type mantle sources based on isotopic compositions (Janney et al., 2005).

Section D, which lies to the east of the Du Toit-Andrew Bains fracture zone system, shows a large axial high, which reaches its peak between 35° E and 41° E, forming the apex of the Marion Rise. This rise corresponds to a long wavelength MBA low, reduced shear wave velocities and low $Na_{8.0}$ content in basalt glasses (Cannat et al., 2008). Other geochemical proxies for the degree of partial melting such as Sm/Yb and CaO/Al_2O_3 support increased partial melting in this region (Font et al., 2007; Meyzen et al., 2003). These correlations suggest a hotter mantle regime and thicker crustal structure over this Section. Application of the Bouguer slab formula (described above) to the reduction in MBA of ∼75 mGal observed over Section D yields an increase in crustal thickness of ∼4.7 km.

Section E, which extends from the Discovery II to the Gallieni transform faults, consists of two subsections separated by the Indomed transform. The area between the Discovery II and Indomed transforms shows a localised decrease in axial depth relative to the surrounding Sections, though not as low as the oblique Section or easternmost part of the SWIR. This is correlated with higher $Na_{8.0}$ content in basalt glasses, coupled with an increase in the MBA and a sharp increase in the shear wave velocities, all of which indicate a colder mantle with reduced partial melting. In contrast, the area of Section E between the Indomed and Gallieni transform faults shows a localised increase in axial depth similar to that observed over the Marion Rise in Section D. The lower $Na_{8.0}$ content in basalts, decrease in the MBA, and decrease in the shear wave velocities all suggest that the mantle temperature and degree of partial melting increase east of the Indomed transform fault.

Section F, which is characterised by a series of closely spaced transform faults, is associated with sharp decreases in the axial depth, which continue through from Section

G to the Rodriguez Triple Junction (RTJ). The increase in $Na_{8.0}$ basalt content, and positive increases in the MBA and shear wave velocity, all indicate a colder mantle. The increase in shear wave velocity is very sharp, suggesting that this represents a finite density boundary within the mantle, as opposed to a gradual change. The decrease in shear wave velocity to the east of the Atlantis II fracture zone is attributed to a lack of resolution in the tomographic imagery, and to the influence of the hotter mantle regimes associated with the faster spreading Southeast and Central Indian Ridges (Debayle et al., 2005). It is, therefore, not considered representative of the Southwest Indian Ridge system.

Section G, which extends from the Melville transform to the Rodriguez Triple Junction (RTJ), exhibits the deepest average axial depths across the whole ridge. These extreme depths are mirrored in the high MBAs in this Section. The $Na_{8.0}$ content of basalts along this Section shows significant variation but are, on average, the highest along the ridge (Sauter et al., 2009). This correlates with a decrease in the $Fe_{8.0}$ content (Meyzen et al., 2003) indicating a decrease in mean pressure of the mantle and colder mantle temperatures to the east (Cannat et al., 1999). This is corroborated by Cr/(Cr+Al) ratios in spinel samples between 61° E and 64° E, which infer very low degrees of melting (Seyler, 2003). The decreased shear wave velocity in this Section, as explained above, is not considered to reflect the Southwest Indian Ridge system (Sauter and Cannat, 2010). Application of the Bouguer slab formula (described above) to the increase in MBA of ∼50 mGal observed over Sections F and G yields a decrease in crustal thickness of ∼3.1 km.

In summary, the axial bathymetric and mantle Bouguer anomaly profiles allow the ridge to be divided into seven Sections, which may be grouped according to their characteristics:

- Sections A, D and the eastern part of Section E: Areas with anomalously shallow axial depths, low MBAs suggesting thickened crust, and low shear wave velocities indicating an anomalously hot, low density upper mantle. Geochemical proxies

indicate greater degrees of partial melting.

- Sections B, F and G: Areas with anomalously deep axial depths, high MBAs suggesting thin crust. Section F and G show high shear wave velocities indicating an anomalously cold, high density upper mantle, while Section B shows only intermediate velocities. Geochemical proxies indicate lower degrees of partial melting in all three Sections.

- Sections C and the western part of E: Areas with intermediate axial depths, MBAs, and shear wave velocities suggesting normal crustal thicknesses and mantle densities along these Sections. While these characteristics are normal for the Southwest Indian Ridge, they may differ from normal characteristics for other slow spreading ridges such as the Mid-Atlantic Ridge. The geochemical proxies along these Sections indicate intermediate degrees of partial melting, compared to other Sections on the SWIR.

3.1.3 Causes of Long Wavelength Variation

This section of the thesis discusses two influences on the mantle and crustal structure of the ridge based on the observation above, ridge spreading obliquity and the influence of hotspots.

Ridge Spreading Obliquity

At many mid-ocean ridges, the spreading direction is orthogonal to the strike of the ridge axis; however this is not the case at the Southwest Indian Ridge. The majority of the ridge is spreading slightly obliquely (5 to 10° from orthogonal), while some areas of the ridge are spreading more obliquely (up to 32°) (Grindlay et al., 1998; Cannat et al., 2008). The increase in spreading obliquity increases the length of the ridge per unit lithosphere created and mantle upwelling must slow accordingly, due to conservation of mass (Dick et al., 2003). This decrease in mantle upwelling is expressed as the

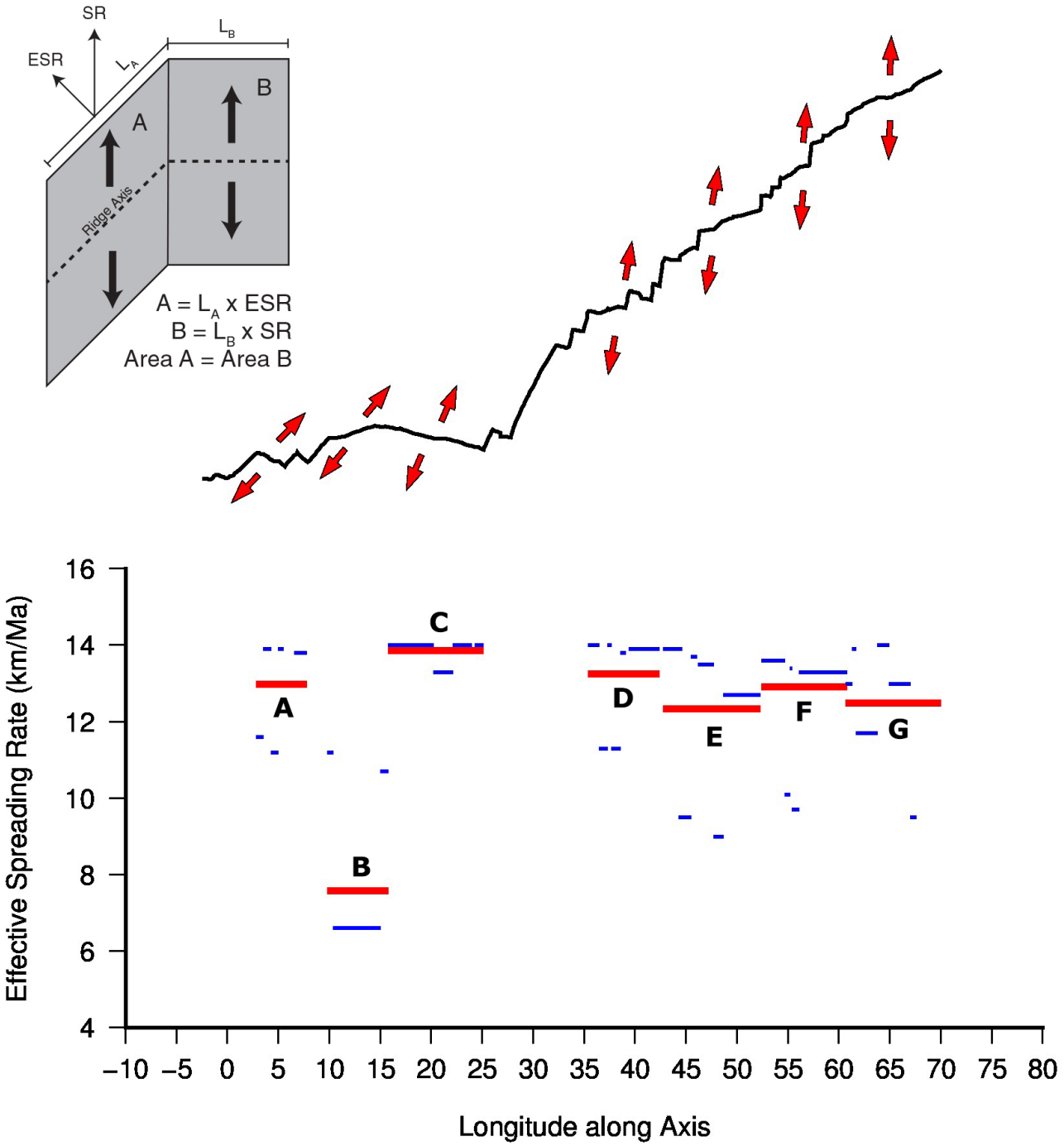


Figure 3.7: Graph showing the variation in effective spreading rate along the ridge, calculated using the method of Dick et al. (2003). Red bars show the average effective spreading rate for each Section, which are labelled A-G, and are defined in Figures 3.6 and 3.1. Blue bars show the effective spreading rates for individual segments following broad 1st and 2nd order segmentation illustrated in Figure 3.16. The illustration of the ridge above shows the difference between the ridge strike (black line) and spreading direction (red arrows), determined using normal earthquake mechanisms and the orientation of transform faults.

component of spreading perpendicular to the ridge axis, termed the effective spreading rate (ESR) (Dick et al., 2003; Cannat et al., 2008).

The effective spreading rate (ESR) was calculated for each segment along the ridge using the method of Dick et al. (2003). The ridge trend was estimated using the magnetic anomalies to define the Bruhnes anomaly and the orientation of the axial valley. The spreading direction was estimated using the orientation of transform offsets and the orientation of normal earthquake mechanisms from the Global Centroid Moment Tensor database. The difference between the ridge trend and spreading direction was used to calculate the ridge obliquity. This was then used to calculate the effective spreading rate, assuming a full spreading rate of 14 mm yr^{-1} for orthogonal spreading (Patriat et al., 1997). The variation in effective spreading rate along the ridge is illustrated in Figure 3.7.

Figure 3.7 shows that, with the exception of Section B, the Sections on the ridge have average effective spreading rates between 12.3 mm yr^{-1} and 13.9 mm yr^{-1}. Section B, in contrast, is up to 28° oblique and has an average effective full spreading rate of 7.6 mm yr^{-1}.

As described above, Section B (see Figure 3.1 for location) shows deep axial depths on the ridge but lacks the high shear wave velocities associated with a regional cold mantle. The geochemical proxies for partial melting show a wide range of results, reflecting the segment scale changes in this Section. Dick et al. (2003) mapped the segmentation of this Section, and showed that the majority of the Section is dominated by amagmatic spreading punctuated with two magmatic segments, the Joseph Mayes segment and the Narrowgate segment (see Figure 3.8).

Changes in spreading rate, or in this case effective spreading rate, exert a kinematic first order control on the rate of deformation and the regional thermal mantle structure (Small, 1998), both of which affect the formation of topography at the axis. These changes in spreading rate should therefore be reflected in the morphology.

This change between magmatic and amagmatic segments is apparent in the large variations in axial valley depth, where amagmatic segments are characterised by deep well defined axial valleys, and magmatic segments are characterised by poorly defined, shallow axial valleys.

The amagmatic segments (1, 3-6, 8) have well-defined, deep, wide axial valleys, with localised axial valley floor topography. Segments 1, 3 and 4 are the deepest (on average 4600 m), while segments 5, 6 and 8 are shallower (on average 4300 m). Detailed mapping by Dick et al. (2003) showed that flanking topography is generally linear with continuous ridges parallel to the ridge trend, though they curve towards the spreading direction towards the end of the ridges. These asymmetric ridges, which vary between 600 m and 1700 m in height, are defined by inward facing normal faults and continue along strike up to 150 km. Dredges of this segment show large proportions of serpentinized peridotite, suggesting that there is thin or no igneous crust on this segment (Dick et al., 2003). These flank topographic features are therefore likely tectonic in origin. These morphological features are all indicative of a reduced melt supply forming tectonically generated structures, which is consistent with the reduced upwelling caused by the spreading obliquity.

Segments 2 and 7 have a contrasting morphology to the amagmatic segments on this part of the ridge. Segment 7 has a significantly reduced obliquity compared to other segments on this Section, while segment 2 has a reduced spreading obliquity compared to segments 3-6, but similar orientation to segments 1 and 8. The axial valley shallows rapidly across a non-transform offset which forms a boundary between the segments 1 and 2. Segment 2 has a poorly defined, shallow axial valley with an average depth of $\sim$3600 m, and has large areas of irregular topography defined by a series of ridge trend parallel normal faults (Dick et al., 2003). This segment is dominated by the Joseph Mayes seamount, which fills the axial valley at the segment centre, reaching $\sim$1500 m depth. The edifice morphology of Joseph Mayes seamount illustrates the disparity between the spreading direction and ridge strike, since the orientation of volcanic rift

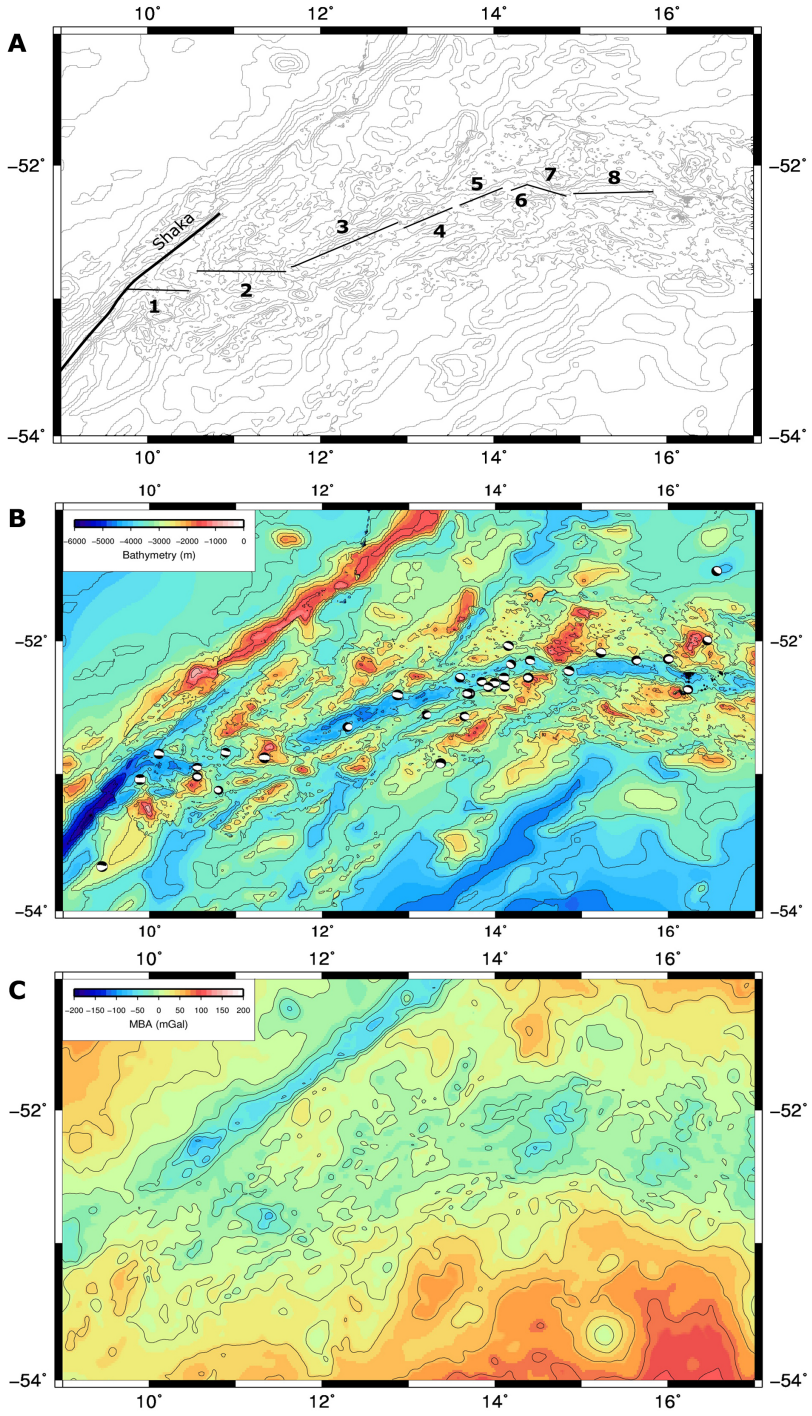


Figure 3.8: A) Segmentation interpretation for Section B, superimposed on bathymetric contours. Segmentation illustrated reflects the 1st and 2nd order discontinuities only. Some morphologies such as oblique shear basins, which are interpreted to represent discontinuities, have been included in the segments in order to produce a continuous axial trace as has been done in other along axis studies (e.g. Lin et al., 1990; Cannat et al., 2008). B) Bathymetry data consisting of shipboard multibeam data and, where multibeam was unavailable the GEBCO 2014 30'' x 30'' grid (IOC et al., 2003). Superimposed on the bathymetry are the normal fault solutions for well-located earthquakes since 1977 with magnitudes >4.5 from the Global Centroid Moment Tensor database. C) Mantle Bouguer anomalies calculated by removing the gravity effect of the crust-water and moho interfaces assuming a consistent crustal density of 5 km and densities of 1030 kg m^{-3}, 2800 kg m^{-3} and 3300 kg m^{-3} for the water, crust and mantle respectively.

systems can be used to deduce the orientation of average tectonic stress in a region (Nakamura, 1977). The edifice morphology of the Joseph Mayes seamount shows two principle orientations. On the south side of the seamount it is dominated by ridge parallel features including a large normal fault; on the northwest flank there are a number of spreading direction perpendicular fault traces. Segment 7 shows a similar shallowing in axial depth from 4400 m to 2800 m, as seen in segment 2, and is accompanied by a large, off axis linear high trending in the spreading direction. The northern end of this broad ridge shows rounded volcanic edifice structures, suggesting that this ridge is formed by volcanic accretion which is in direct contrast to the tectonically generated flank topography on the amagmatic segments. This linear ridge suggests that there has been a sustained period of magmatic input on this segment of the ridge. These segments show morphologies associated with robust magmatic activity and high melt supply. On segment 7 this increased melt supply can be attributed to the strike of the ridge, which is almost orthogonal to the spreading direction, meaning that the effective spreading rate is higher than that of the adjacent segments. The strongly negative mantle Bouguer anomaly centred on segment 7 supports this. However segment 2, which appears to have a greater level of magmatic activity than segment 7, has a similar ridge strike to the amagmatic segments 1 and 8 and a less negative mantle Bouguer anomaly than segment 7. The ridge obliquity, therefore, is not the sole cause for the contrasting morphologies along this Section of the ridge.

The discontinuity located at 13° E marks a change in the average depth of the axial valley. A linear bathymetric low cuts across the flanking topography extending over 200 km from the ridge axis, striking parallel to the Shaka fracture zone. This is interpreted as the flank disruption caused by the non-transform discontinuity at 13.5° E indicating that this is a long-lived discontinuity. The segments to the west of this discontinuity are deeper than the segments to the east of the discontinuity. A geochemical study by Standish et al. (2008) showed that basalts dredged from the amagmatic segments were characterised by slightly enriched MORB signatures (compared to segments from Section C), consistent with a depressed melt column and reduced melt supply. Basalts

from the magmatic segments were found to have more enriched MORB signature, despite having a high melt supply. Standish et al. (2008) attributed this to melt migration away from the amagmatic segments towards the magmatic segments. Cannat et al. (2008) suggested that this melt focussing is achieved through melt migration along an upward sloping thermal barrier at the base of the lithosphere and rapid injection through established dykes. The discontinuity at 13° E represents the boundary between regions of melt focussing.

There is evidence that the position and number of these magmatic segments may fluctuate over time. Significant broad linear ridges, which strike in the spreading direction, can be seen on the flanks of segment 3 at 12°E 45' and segment 5 at 16°E 15' often accompanied by a slight shallowing of the axial valley. Though these segments are now clearly amagmatic, these ridges may represent the location of waning magmatic centres.

Influence of Hotspots

Many oceanic ridges are influenced by the presence of nearby mantle plumes, inducing physical and chemical anomalies on the ridge. Evidence for hotspot-ridge interaction include anomalous geochemistry due to mixing of mantle sources, anomalous axial shallowing, increased crustal thickness and decreases in both MBAs and shear wave velocities. These are attributed to the delivery of hot, low density material towards the mid-ocean ridge axis, and are reviewed in Ito et al. (2003). Many studies of plume-ridge interaction focus on relatively accessible locations such as Iceland and the Galapagos Islands, whereas the interaction between the Southwest Indian Ridge and nearby hotspots is the subject of fewer studies (e.g. Georgen et al., 2001; Sauter et al., 2009).

The Southwest Indian Ridge is proximate to two mantle plumes, the Marion plume and the Bouvet plume. The volcanically active, Marion island, which is situated 250 km from the ridge axis on 28 Ma crust (Müller et al., 1997), represents the current position

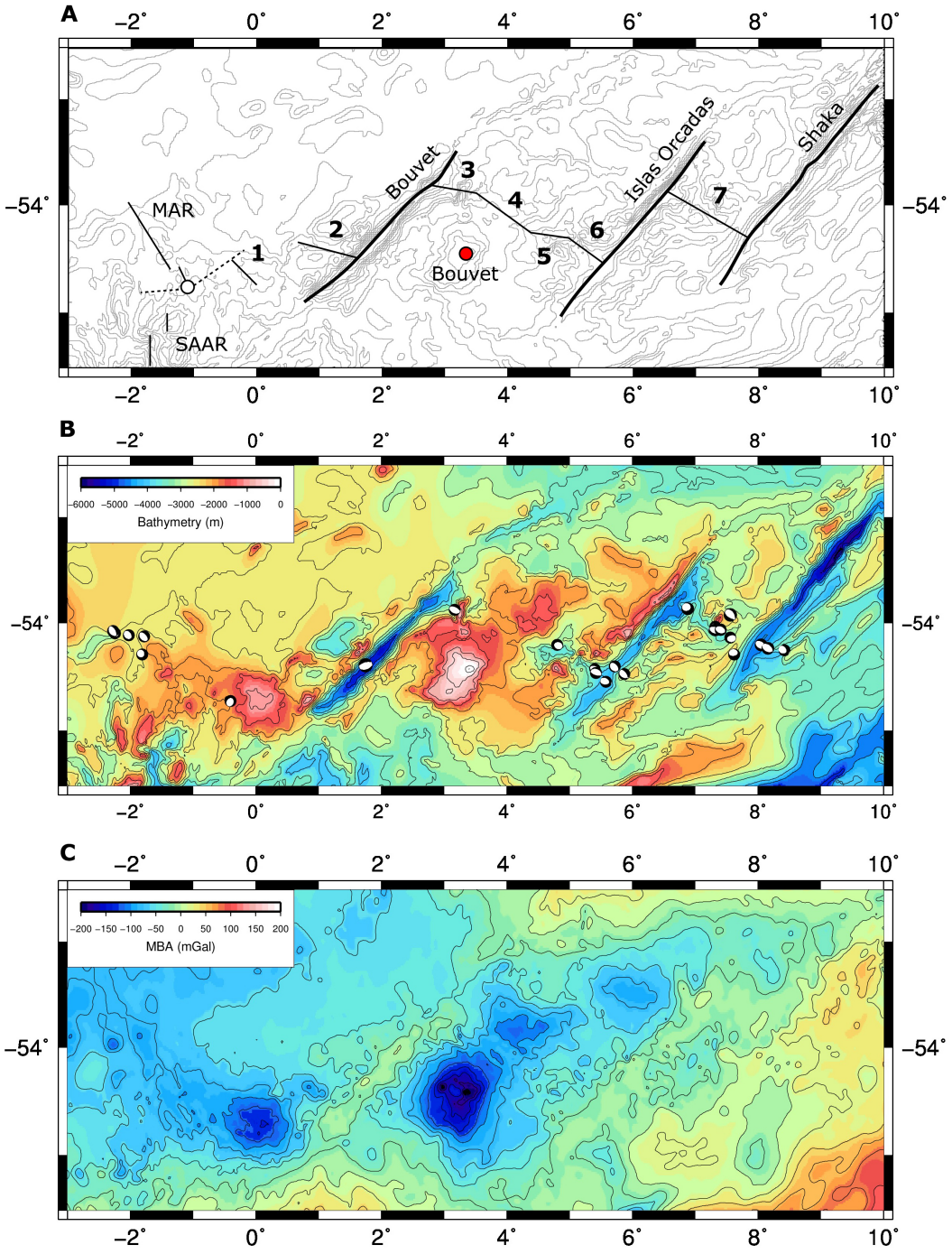


Figure 3.9: A) Segmentation interpretation for Section A, superimposed on bathymetric contours. Segmentation illustrated reflects the 1st and 2nd order discontinuities only. Some morphologies such as oblique shear basins, which are interpreted to represent discontinuities, have been included in the segments in order to produce a continuous axial trace as has been done in other along axis studies (e.g. Lin et al., 1990; Cannat et al., 2008). B) Bathymetry data consisting of shipboard multibeam data and, where multibeam was unavailable the GEBCO 2014 30'' x 30'' grid (IOC et al., 2003). Superimposed on the bathymetry are the normal fault solutions for well-located earthquakes since 1977 with magnitudes >4.5 from the Global Centroid Moment Tensor database. C) Mantle Bouguer anomalies calculated by removing the gravity effect of the crust-water and moho interfaces assuming a consistent crustal density of 5 km and densities of 1030 kg m^{-3}, 2800 kg m^{-3} and 3300 kg m^{-3} for the water, crust and mantle respectively.

of the Marion plume (Duncan, 1981; Morgan, 1981). Bouvet island is situated 55 km from the ridge axis on 7 Ma crust (Müller et al., 1997), and Speiss seamount forms part of the ridge axis to the west of the Bouvet transform fault (Mitchell and Livermore, 1998). There has been debate as to whether the current position of the Bouvet plume is represented by Bouvet Island or Speiss Seamount (Mitchell and Livermore, 1998; Ligi et al., 1997). This question remains unresolved, so for the purpose of this study we will assume that the Bouvet plume is located under Bouvet Island. The Bouvet and hotspots are located 55 km and 250 km south of the ridge axes of Sections A and D respectively (see Figure 3.1). These two Sections have the shallowest zero-age depths along any portion of the ridge, on average 3000 m deep (up to 1400 m depth including volcanic topography).

Section A extends from the Bouvet Triple Junction (BTJ) at $\sim$ 1° W, 54.8° S (Sclater et al., 1976) to the Shaka transform at 8° E. The bathymetry, mantle Bouger anomalies and segmentation are shown in Figure 3.9. Unlike the rest of the ridge, the first two segments are not defined by an axial valley, as would be expected at an ultra-slow spreading rate. Near the triple junction, magnetic profiles (Sclater et al., 1976) and earthquake mechanisms have been used to indicate that the poorly defined axis forms an axial high following the Speiss ridge in segment 1 (Mitchell and Livermore, 1998). Segment 2 is defined by a clear axial high rising $\sim$1400 m above the flanking topographic lows. Axial high morphologies have been observed on slow spreading ridges under the influence of a hotspot (Searle et al., 1998; Canales et al., 1997; Malinverno, 1993). This transition from axial valley to axial high is attributed to the increase in temperature, which weakens the lithosphere. Numerical modelling studies suggest that when the lithosphere is weak compared to the extensional stresses, an isostatically supported high forms (Madsen et al., 1984; Phipps Morgan et al., 1987).

The influence of the Bouvet plume is reflected in the MBA, which shows a broad negative between -200 mGal and -50 mGal attributed to crustal thickening and/or lower density underlying material from the hotspot. The most negative anomalies

are associated with Bouvet Island and the Spiess Ridge topography, both of which have been proposed as the current position of the Bouvet plume. Geochemical studies indicate that both of these features were formed by the Bouvet hotspot (Kurz et al., 1998).

An axial valley is established to the east of the Bouvet transform, however it is wider and shallower than the axial valley topography elsewhere on the ridge. The transition from an axial high to an axial valley across the Bouvet transform suggests that the influence of the Bouvet plume is greater to the west, despite the presence of Bouvet Island to the east of the transform. This perhaps suggests that the Speiss Ridge represents the current position of the Bouvet plume and that the Bouvet transform represents a thermal barrier diminishing the influence of the hotspot further east. The trend of increasing axial depth and more positive MBAs is repeated across the Islas Orcadas transform to the east.

Section D, which lies 250 km to the north of the Marion hotspot, shows similar morphological features to Section A. The bathymetry, mantle Bouger anomalies and segmentation are shown in Figure 3.10. The average axial valley depth is approximately 1000 km shallower than the magmatically robust segments of Section C, and almost 2000 m shallower than the deepest parts of the SWIR. This forms a large scale high, called the Marion Rise, which extends from 35° E to 52° E along the axis.

The axial morphology along this Section consists of alternating, shallow axial valleys with significant off-axis, anomalously shallow topography, and oblique basins with anomalously deep topography which continues off-axis. The anomalously shallow segments are characterised by narrow axial valleys (between 31 km and 42 km across) with very little axial relief (between 800 m and 400 m deep). The flanking topography extends up to 150 km off-axis, generally trends parallel to the strike of the nearby transforms, and does not follow a plate cooling subsidence trend. The westernmost shallow segment has flanking topography, which forms a V-shape topographic anomaly extending east from the shallowest part on the axial valley. This is attributed to the

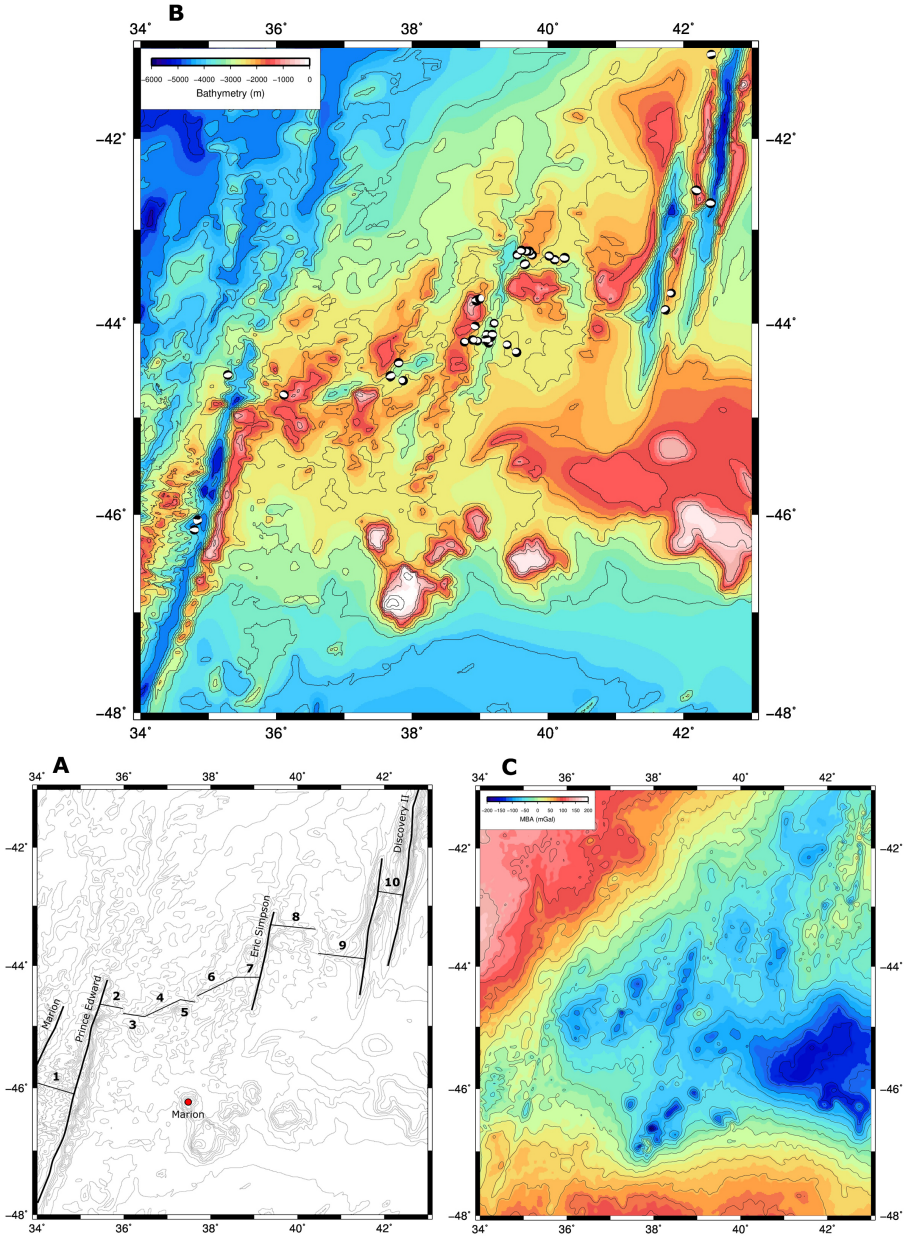


Figure 3.10: A) Segmentation interpretation for Section D, superimposed on bathymetric contours. Segmentation illustrated reflects the 1st and 2nd order discontinuities only. Some morphologies such as oblique shear basins, which are interpreted to represent discontinuities, have been included in the segments in order to produce a continuous axial trace as has been done in other along axis studies (e.g. Lin et al., 1990; Cannat et al., 2008). B) Bathymetry data consisting of shipboard multibeam data and, where multibeam was unavailable the GEBCO 2014 30'' x 30'' grid (IOC et al., 2003). Superimposed on the bathymetry are the normal fault solutions for well-located earthquakes since 1977 with magnitudes >4.5 from the Global Centroid Moment Tensor database. C) Mantle Bouguer anomalies calculated by removing the gravity effect of the crust-water and moho interfaces assuming a consistent crustal density of 5 km and densities of 1030 kg m^{-3}, 2800 kg m^{-3} and 3300 kg m^{-3} for the water, crust and mantle respectively.

westward propagation of an area of anomalous melt generation. Detailed multibeam on this Section of the ridge is sparse, however, the available data of these flanking shallow features show that they consist of rounded topographic highs, suggesting that these are volcanic in origin. If individual isolated topographic highs are ignored, the background regional depths are higher on the southern side of the axis than the northern side of the axis. This is particularly noticeable on segment 8, which has a large ridge defining the southern flank and very subdued relief on the northern flank.

Separating these shallow segments are oblique basins, which have an axial depth, on average, 1500 m deeper than the shallow segments. These basins strike 75° from north (25° oblique to the spreading direction), and offset the spreading axis between ∼30 km and ∼50 km. The off-axis bathymetry shows linear anomalous lows, which trend parallel to the strike of the adjacent transforms and generally decrease in width away from the axis. These oblique shear basins are interpreted as discontinuities originating in the upper mantle, separating the accretionary segments. The off-axis traces indicate that these discontinuities are long-lived and stable. The decrease in the width of the off-axis traces suggests that the shear stresses across the discontinuity were originally accommodated by a narrow zone of deformation i.e., a transform discontinuity; however, magnetic profiles in this Section are too sparse to confirm this. These upper mantle discontinuities may act as thermal barriers, causing material to be diverted either side of the discontinuities, resulting in increased melt supply on the accretionary segments, which forms the observed volcanic topography.

The ridge discontinuity between segments 8 and 9 is offset in the reverse direction to other offsets (both non-transform and transform) along the ridge. This may represent a migration of the ridge towards the hotspot source due to asymmetric spreading, as has been observed at other ridge-hotspot systems (Small, 1995).

This segmentation pattern and the influence of the Marion hotspot is reflected in the MBAs, which are dominated by a broad negative across Marion Island and the ridge axis. Linear concentrated lows, which cross cut the ridge axis, correspond to the large

relief topography on the ridge flanks. The off axis traces of the oblique shear basin discontinuities are clearly shown in the MBAs, which show linear highs extending away from the ridge, corresponding to the bathymetric lows. These suggest that the crust under these traces is thinner, which is consistent with the diversion of melt away from these colder mantle discontinuities. There are abrupt increases in the MBAs across the Prince Edward and Discovery II transform faults, indicating that these transforms act as thermal barriers preventing along axis melt migration from the hotspot influenced region (Georgen et al., 2001).

A series of common features, such as elevated regional axial depths, negative MBAs and asymmetric ridge axis profiles are identified on Sections A and D, and attributed to the interaction between the Bouvet and Marion hotspots respectively, and the ridge axis. This study and other morphological studies (Mitchell and Livermore, 1998) suggest that the Bouvet hotspot forms discrete channel flows, forming large plateaus and ridges, while in contrast, the Marion hotspot has a broader influence, where existing upper mantle discontinuities govern the migration of hotspot material.

3.2 Axial Valley Morphology

Slow and ultra-slow spreading ridges are characterised by an axial valley morphology at the ridge crest (Heezen, 1960; Macdonald, 1982). While studying continental rifting, Vening Meinesz (1950) used a simple mechanical model to explain the formation of a rift valley due to extension. He showed that increasing horizontal tensile forces applied to the crust caused an initial normal fault break across a tilted plane. The initial faulting caused effective loading on the hanging wall, producing downward flexure until a second fault break occurs. Following the broken plate model of Bullard (1936), the distance between the first and second break, x_0, is given by

$$x_0 = \frac{\pi}{4\lambda} \tag{3.1}$$

where λ is a parameter which determines the amplitude and wavelength of the deformation and is given by:

$$\lambda = \left[\frac{(\rho_m - \rho_{infill})g}{4D}\right]^{1/4} \tag{3.2}$$

where D is the flexural rigidity, which is dependent on the rheology of the lithosphere, g is the acceleration due to gravity, and ρ_{infill} and ρ_m are the densities of the infill and mantle respectively.

There have been a number of models proposed for the formation of the axial valley in an oceanic spreading centre setting. Early researchers suggested that the axial valley was created by a loss of hydraulic head (Sleep, 1969) due to the fractional forces acting on the sides of a conduit along which magma rises. This decrease in pressure causes the topographic depression observed as the axial valley. However maintaining such a conduit in the primarily horizontal thermal regime of a mid ocean ridge is difficult (Phipps Morgan et al., 1987), particularly in a melt-poor system. Subsequent models were based on the simple wedge model of Vening Meinesz (1950), in which increasing horizontal tension applied to a plate causes thinning of the lithosphere and normal faulting in the brittle upper crust (Tapponnier and Francheteau, 1978). Evidence supporting this model includes the presence of axial valley topography at fossil ridges e.g. Coral and Labrador Seas (Watts, 1982) and seismicity studies, which show that the maximum depth of fault-related seismicity occurs at the ridge axis, where the largest faults would be expected (e.g. Tooney et al., 1988; Kong et al., 1992).

Numerical modelling of mid ocean ridges (e.g. Phipps Morgan et al., 1987; Lin et al., 1990; Chen and Jason Morgan, 1990) has shown that a combination of brittle-plastic and viscous rheologies undergoing extension at slow rates produces an axial valley morphology consistent with those observed on slow spreading ridges such as the Mid-Atlantic Ridge. These numerical models show that the thermal structure of the lithosphere governs the rheology of the lithosphere, which determines the size and shape of

the axial valley (Chen and Jason Morgan, 1990). Colder, stronger lithosphere is able to support a wider, deeper axial valley compared to hotter weaker lithosphere. As discussed in section 3.1 variations in the regional along axis depths may be attributed to changes in the mantle density and crustal thickness. Regional axial highs are underlain by less dense mantle and/or thicker crust, both of which indicate a hotter temperature regime. We can therefore use the relationship between the along axis regional depths and axial valley morphology as a simple indication of the applicability of the lithospheric wedge model to the ultra-slow spreading Southwest Indian Ridge.

3.2.1 Across Axis Bathymetry Profiles

In order to examine the relationship between regional along axis depths and axial morphology, we need to compare bathymetric profiles of the axial valley with the regional along axis depth. However, active processes such as faulting and constructive volcanism occurring at a spreading plate boundary zone lead to highly variable small scale topography within the axial valley and on the rift flanks. To ascertain the broad variations in axial valley morphology over different Sections of the Southwest Indian Ridge, the characteristic features of the axial valley must be determined. A series of across-axis profiles (shown in Figure 3.11) centred on the axis every 0.25° longitude, 400 km in length and trending parallel to the spreading direction, were sampled from the bathymetry data, described in chapter 2, as shown in Figure 3.11. An ensemble averaging technique (Bassett and Watts, 2015) was used to isolate an average profile containing features common between the profiles for a given Section of the ridge, and removing features which did not appear on multiple profiles. This technique utilises Fourier transforms to calculate a frequency spectrum for each profile. The individual Fourier transform coefficients for each profile are used to calculate an average frequency spectrum, which is then inverse Fourier transformed to produce an average bathymetric profile. Ensemble average profiles of bathymetry for each of the ridge Sections, defined in Figure 3.6, are shown in Figure 3.13.

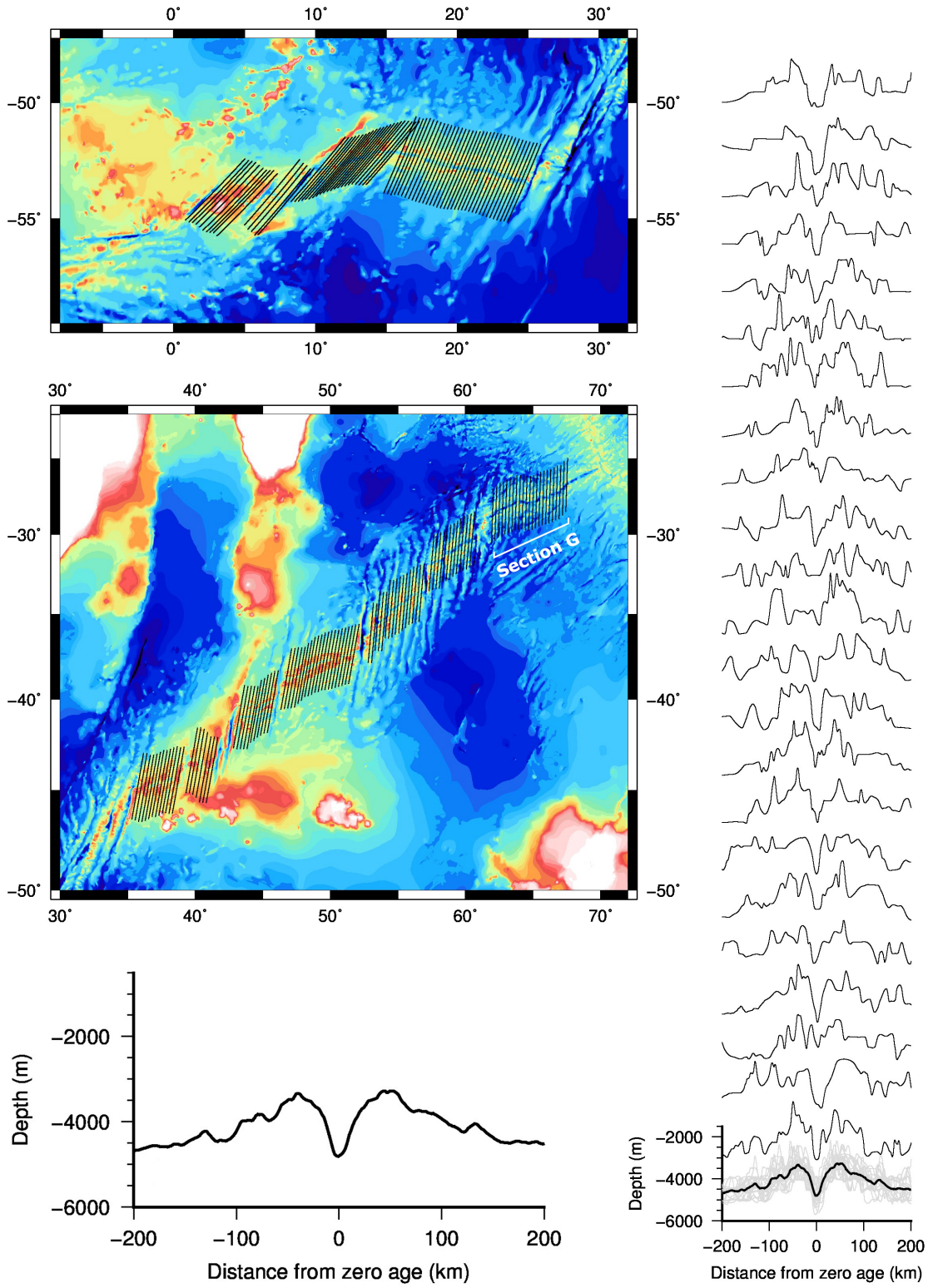


Figure 3.11: The upper and lower bathymetry maps show the location of across axis profiles, which were sampled to produce the ensemble average profile for the western and eastern parts of the ridge respectively . The profiles on the right show the individual profiles for Section G (marked on the lower bathymetry map), and the resultant ensemble averaged profile at the bottom.

It should be noted that, while the ensemble average isolates the common features between profiles, if there is a high degree of morphological variation between the profiles, the resulting profile will not be representative of either morphology. For most Sections along the ridge the morphology is consistent, however this is not the case for Section B. This is discussed further in the descriptions below.

All of the ensemble average profiles show a clear axial valley at zero-age and flanking rim uplifts though the amplitude, shape and asymmetry of the valleys varies between Sections. In order to quantify the changes in axial morphology, a number of measurements were taken as shown in Figure 3.12.

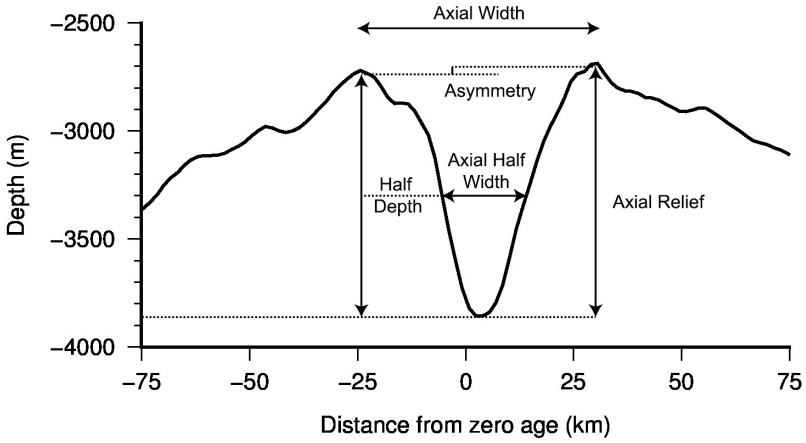


Figure 3.12: Schematic diagram showing the definition of measurements taken of the axial valley bathymetric profiles.

The morphological characteristics of the average axial valley for each Section are detailed in table 3.1.

Sections C and E, which were associated with intermediate melt supply and thermal regime compared to the rest of the ridge in thesis section 3.1, are both characterised by axial relief between 1000 m and 1500 m, and full and half widths of ∼54 km and ∼22 km respectively. Comparison of the off axis bathymetry with the predicted bathymetry using the plate cooling model of Parsons and Sclater (1977) shows a good fit for the general subsidence trend. This suggests that the thermal regimes at these

Table 3.1: Characteristics of the ensemble average bathymetry profiles for Sections A to G.

Section	**Maximum Depth (m)**	**Maximum Axial Relief (m)**	**Minimum Axial Relief (m)**	**Asymmetry (m)**	**Axial Width (km)**	**Axial Half Width (km)**
A	3226	818	670	148 (S)	37	17
B	3751	897	665	232 (N)	60	27
C	3857	1169	1137	32 (N)	55	23
D	2791	772	426	346 (S)	35	17
E	3150	1002	829	110 (S)	53	20
F	4156	1289	1235	54 (N)	54	26
G	4806	1548	1479	69 (N)	81	34

Sections of the ridge are not affected by anomalous mantle temperatures. Section E has a greater asymmetry than Section C, which is attributed to anomalously shallow topography south of the axis on the eastern part of Section E. Sauter et al. (2004) used bathymetry and magmatic anomaly data to suggest that this shallow topography was due to a melting anomaly caused by the influence of the Crozet hotspot.

Sections A and D, which were associated with increased crustal thickness and low mantle densities in section 3.1, are both characterised by anomalously low axial relief (on average between 600 m and 750 m), and the full and half axial valley widths are both the narrowest along the ridge. The reduced axial width is consistent with a weaker lithosphere, since wide axial valleys cannot be supported when the lithosphere is weak. This is most likely due to an increase in temperature at the ridge axis, as expected from the geochemical proxies, which indicate an increased degree of partial melting. The axial valley is slightly shallower and narrower on Section D than Section A, indicating that temperatures are higher along this Section of the ridge, or that this morphology is more consistently represented across the ridge Section. This may reflect

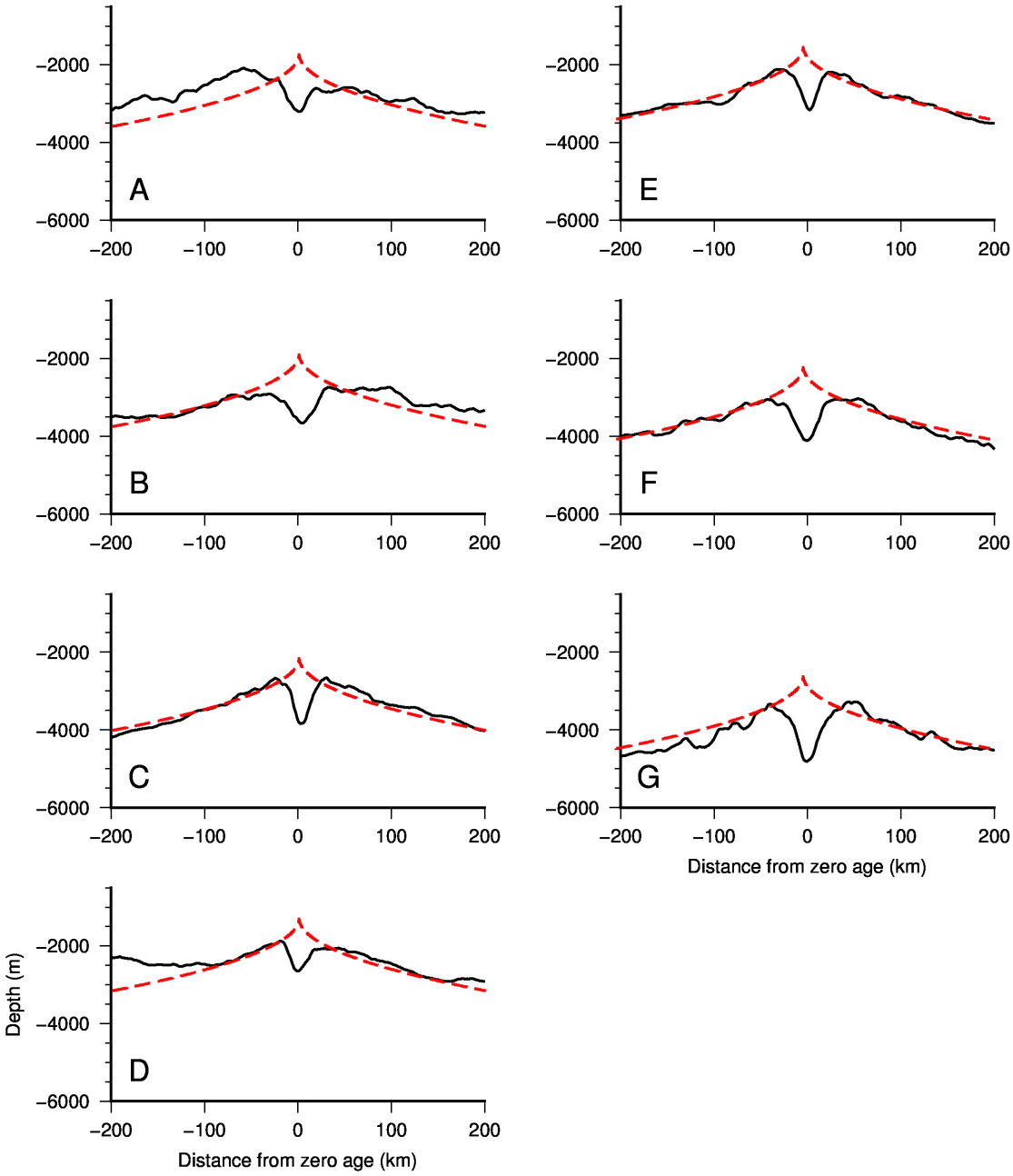


Figure 3.13: Ensemble averaged axial profiles for Sections A to G of bathymetry (black line). Red dashed line shows the predicted bathymetry for subsidence following the plate cooling model of Parsons and Sclater (1977). The standard Parsons and Sclater (1977) model has been vertically shifted for each profile, so that the model zero age depth varies, in order to account for the long wavelength changes in axial depth.

the broader region of influence of the Marion hotspot compared to the Bouvet hotspot, as indicated by the broad Marion Rise. Both Sections A and D show strong asymmetry

to the south, suggesting that the sources of these increased mantle temperatures lie to the south of the ridge axis on both Sections. This is consistent with the proposed current locations of the Marion and Bouvet hotspots, which are both situated south of the ridge axis.

Sections F and G, which were associated with decreased crustal thickness and high mantle densities in Figure 3.6, are characterised by anomalously high axial relief (on average between 1250 m and 1500 m). The axial valley widths for Section G are significantly wider than other Sections of the ridge, while Section F has similar axial widths to Sections B, C and E. The deep, wide axial valley morphology on Section G indicates that the lithosphere is strong and cold in order to support the large axial valley. The narrower axial valley profile for Section F is due to the high concentration of transform faults in this Section. The tectonic highs associated with transform-ridge intersections, which form transverse ridges parallel to the transform, extend into the axis forming narrow axial valleys, thus reducing the average axial valley width. The deep axial morphology on Section G indicates that the lithosphere is stronger than on other Sections on the ridge. This is also the case on Section F, but to a lesser degree. This is consistent with the gradual increase in axial depth and MBA from west to east across these Sections. Neither of these Sections is particularly asymmetric.

Section B, which was associated with decreased crustal thickness but a normal mantle density in section 3.1, shows a different axial morphology to Sections F and G. Section B has significant changes in morphology at a segment scale between deep, oblique amagmatic segments and shallow magmatic segments. Figure 3.14 shows the ensemble average profiles for the whole Section (black line), the magmatic segments only (red line) and amagmatic segments only (blue line). The variation in ensemble average profiles between the segments reflects the difference in effective spreading rate between the segments as discussed in section 3.1.3. Obliquely spreading segments with reduced upwelling produce deep, wide axial valley profiles, while the orthogonal, magmatic segments produce shallow, narrow axial valley profiles with volcanic structures.

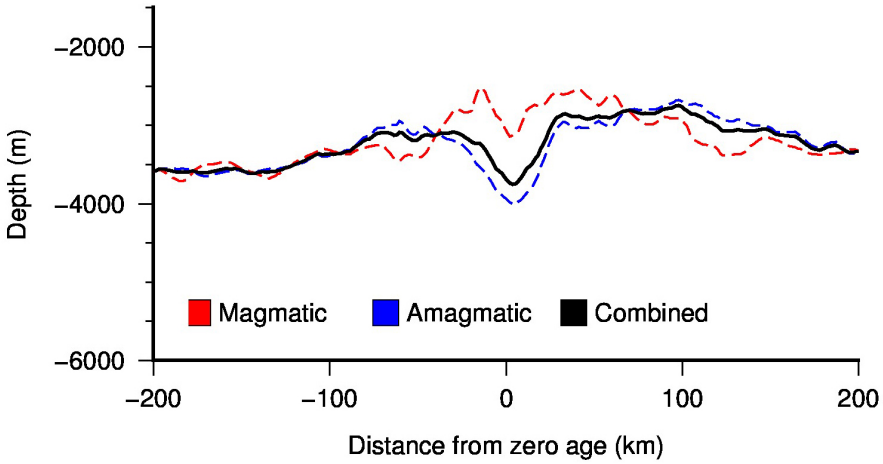


Figure 3.14: Ensemble average profile of Section B including: All profiles (black line), profiles across magmatic segments (red line), profiles across amagamtic segments (blue line).

These observations show a clear correlation between the along axis depth and axial morphology. In areas of the ridge with colder mantle temperatures and low melt supply forming a stronger lithosphere, the axial valley has a greater vertical relief, greater widths and deeper axial depths. Conversely, in areas with anomalously hot mantle or increased melt supply, which weakens the lithosphere, the axial valley has less vertical relief, reduced width and shallower axial valley depths. This suggests that the simple lithospheric stretching model, which is dependent on the lithosphere thermal structure, is applicable to the ultra-slow spreading SWIR. This assumes that the variation in along axis depths is caused by changes in the thermal structure of the ridge. Zhou and Dick (2013) proposed that the Marion Rise, the largest positive axial swell along the ridge, is not supported by hot mantle. They suggest that the geophysical and geochemical observations made over the Marion Rise may be attributed to mantle geochemistry heterogeneity caused by depletion from the African super plume. Therefore, we need a different way to assess the variation in the lithospheric strength, that does not depend on the thermal structure. The next section compares the axial valley width with the elastic thickness, a proxy for the strength of the lithosphere.

3.2.2 Correlation between Axial Width and Elastic Thickness

The elastic thickness, T_e, is a proxy for the integrated strength of the lithosphere (Burov and Diament, 1995; Kirby, 2014). More details on elastic plate theory and the determination of elastic thickness along the SWIR are provided in chapter 6. Strong lithosphere is characterised by high T_e, while weaker lithosphere is characterised by lower T_e. The T_e at a mid-ocean ridge reflects the thermal and mechanical structure of the ridge axis (Cochran, 1979). Seafloor topography is created at the ridge axis, where the T_e is 'frozen' in and carried away by seafloor spreading. Thus, studies of gravity and topography off-ridge provide information on the long-term strength of the ridge axis. The T_e at mid-ocean ridges are generally low, since T_e increases with crustal age due to lithospheric cooling and thickening (Watts, 1978). In this section, we compare the axial valley widths, which represents the distance between first and second break in Bullard's broken plate model (equation 3.1), and elastic thickness for different locations along the ridge.

Figure 3.15 shows a plot of axial valley width against elastic thickness (T_e) for a series of 9° x 9° windows along the ridge (see chapter 6 for further details). This figure shows a general trend of increasing axial valley width with increasing T_e. This confirms the inference that the areas of colder sub-axial mantle, and consequently increased lithospheric strength, support wider axial valley widths. The three lines in Figure 3.15 show the theoretical distance between first and second breaks of the broken plate model of Bullard (1936), given in equations 3.1 and 3.2 for different infill densities, ρ. The observed axial valley width on the SWIR generally shows a greater T_e than predicted by the Bullard model.

This may be attributed to a number of causes. The definition and measurement of the axial valley is subjective, and may not necessarily represent the location of the first and second plate breaks. Macdonald et al. (1975) used a series of across axial valley profiles across the Mid-Atlantic Ridge to show the presence of an inner and outer axial valley, both bound by normal faults. For some areas of the ridge, admittance calculations may

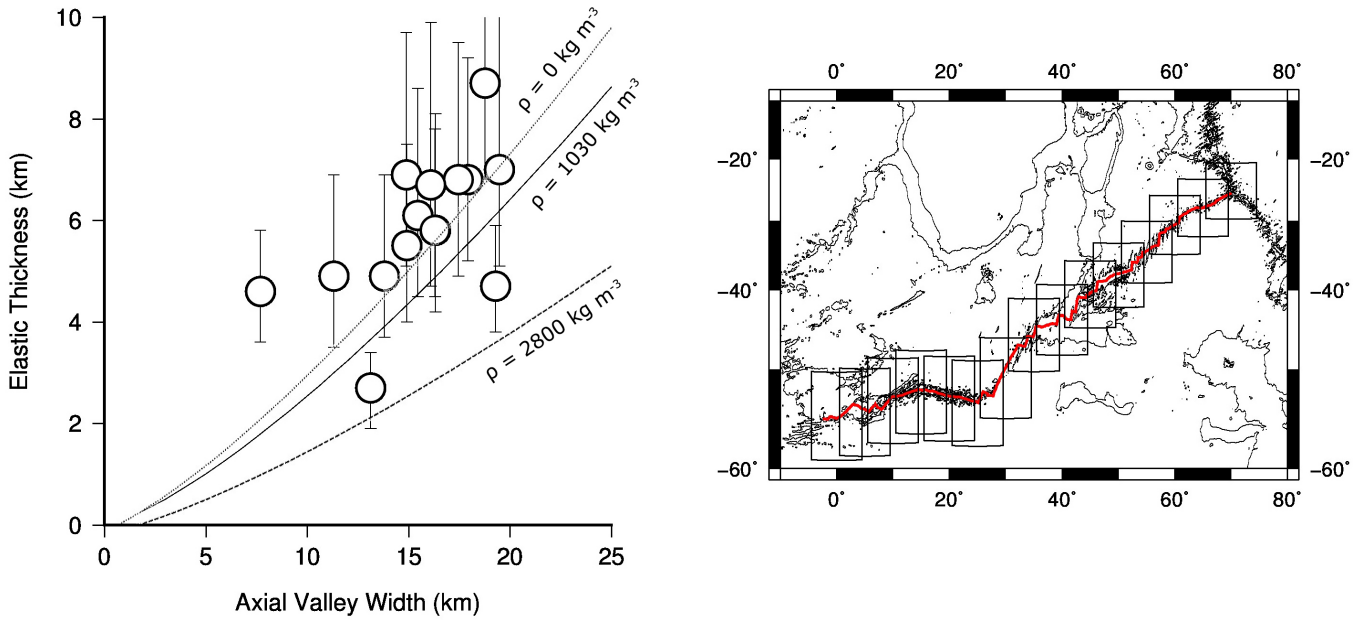


Figure 3.15: Right map shows the location of boxes for used for the admittance analysis (see chapter 6 for more detail). The red line shows the trace of the ridge axis. The contours are bathymetric contours with an interval of 2,000 m. Left graph shows the axial width averaged over the length of the admittance box against the best fit elastic thickness. Error bars are calculated using a percentage RMS error cut off of 20%. Black lines shows the theoretical relationship between elastic thickness and distance between first and second breaks for a broken plate model, given in equation 3.1. The assumed mantle density is 3300 kg m^{-3}, and assumed infill density is 0 kg m^{-3} (dotted line), 1030 kg m^{-3} (solid line) and 2800 kg m^{-3} (dashed line).

include areas of crust which did not form at the ridge crest, such as Marion Island, the del Cano rise and the aseismic Madagascar ridge. It has been suggested that all of these features formed due to hotspot volcanism away from the ridge crest. This older crust has a higher T_e than the ridge crest, due to lithospheric cooling, and therefore biases the T_e towards higher values (Watts, 1978). Finally, Neumann and Forsyth (1993) used 2D admittance studies of profiles along strike within the MAR axial valley to show that the T_e of the axial valley is ∼2 km, significantly less than the ∼6-13 km, predicted by Cochran (1979) using across-axis profiles. The T_e in this study reflects the whole of the ridge crest, and therefore is higher than the predicted T_e in the axial valley itself.

While the axial width measured at the shallowest point on the axial valley is correlated with T_e, the axial width measured at a depth half way between the axial rim mountains and the deepest point of the axial valley does not vary significantly with T_e. This is attributed to the presence of an inner and outer wall morphology, first observed by Macdonald et al. (1975) on the Mid-Atlantic Ridge. This is particularly obvious in the axial valley profile of Section G (see Figure 3.13) where the upper slopes of the axial valley are defined by a set of terraces formed of a series of fault blocks while the lower slopes of the axial valley steepen and are defined by an inner graben.

The systematic changes in the axial valley width and morphology with elastic thickness and along axis depths indicate that the axial morphology is controlled by the lithosphere rheology, which is primarily controlled by the thermal structure. The lithospheric wedge models applied at the MAR appear, based on these simple relationships, to be applicable to the ultra-slow spreading SWIR; however full numerical modelling is necessary to confirm this.

3.2.3 Ridge segmentation

Along axis profiles of bathymetry and gravity show that mid-ocean ridge axes may be divided into segments separated by discontinuities. This segmentation reflects the three-dimensional accretionary processes that occur at divergent plate boundaries (e.g. Schouten and White, 1980). At slow spreading ridges, such as the Mid-Atlantic Ridge, these segments vary between 10 km and 100 km long and are associated with bathymetric highs, which shallow towards the centre of the segments (e.g. Sempere et al., 1993; Grindlay et al., 1998; Tolstoy et al., 1993). The separating discontinuities are defined by bathymetric deeps, and include both transform and non-transform discontinuities (Grindlay et al., 1991). This bathymetric pattern is anti-correlated with along axis profiles of mantle Bouguer anomalies, which are low at segment centres, forming a characteristic bullseye pattern, and high at the discontinuities (Kuo and Forsyth, 1988). This correlation has been used to infer crustal thickness variations, showing

that segment centres are associated with thick crust and high melt supply, while non-transform discontinuities are associated with thin crust and low melt supply (Lin et al., 1990; Cannat et al., 1999). Studies of segmentation on the Southwest Indian Ridge have concentrated on the easternmost Section (Section G), the oblique Section (Section B), and the orthogonal Section (Section C) all of which show a different pattern of segmentation (e.g. Mendel and Sauter, 1997; Cannat et al., 1999; Grindlay et al., 1998).

This section aims to redefine segmentation in a consistent way along the whole ridge using along axis bathymetry and gravity. This segmentation is based on first and second order (transform and non-transform) discontinuities, as it is not possible to distinguish third and fourth order discontinuities from the available data.

Short wavelength variations in the along axis bathymetry and mantle Bouguer anomaly profiles were used to define 74 segments along the Southwest Indian Ridge. These were defined using a continuous axial valley profile, similar to profiles used in comparable studies on the MAR (Lin et al., 1990). In order to avoid the contamination of the accretionary segments by the adjacent discontinuities, large offset transforms and wide non-transform discontinuities are defined as having an along axis width as opposed to a finite boundary. This allows the segments to be defined as representing the portions of the ridge limited by axial discontinuities as defined by Macdonald et al. (1988). As such the segmentation differs slightly from previous studies on the SWIR, such as those of Cannat et al. (1999) and Grindlay et al. (1998).

General Segment Characteristics

Segments, defined by transforms and non-transform discontinuities, vary between 18 km and 163 km in length, though the majority of segments are between 20 km and 90 km in length. The axial depth profile along the axis exhibits axial reliefs ranging between 40 m and 2400 m, measured from peak to trough (see Figure 3.16). Discontinuities are defined by depth maxima, which are greatest for transform faults and

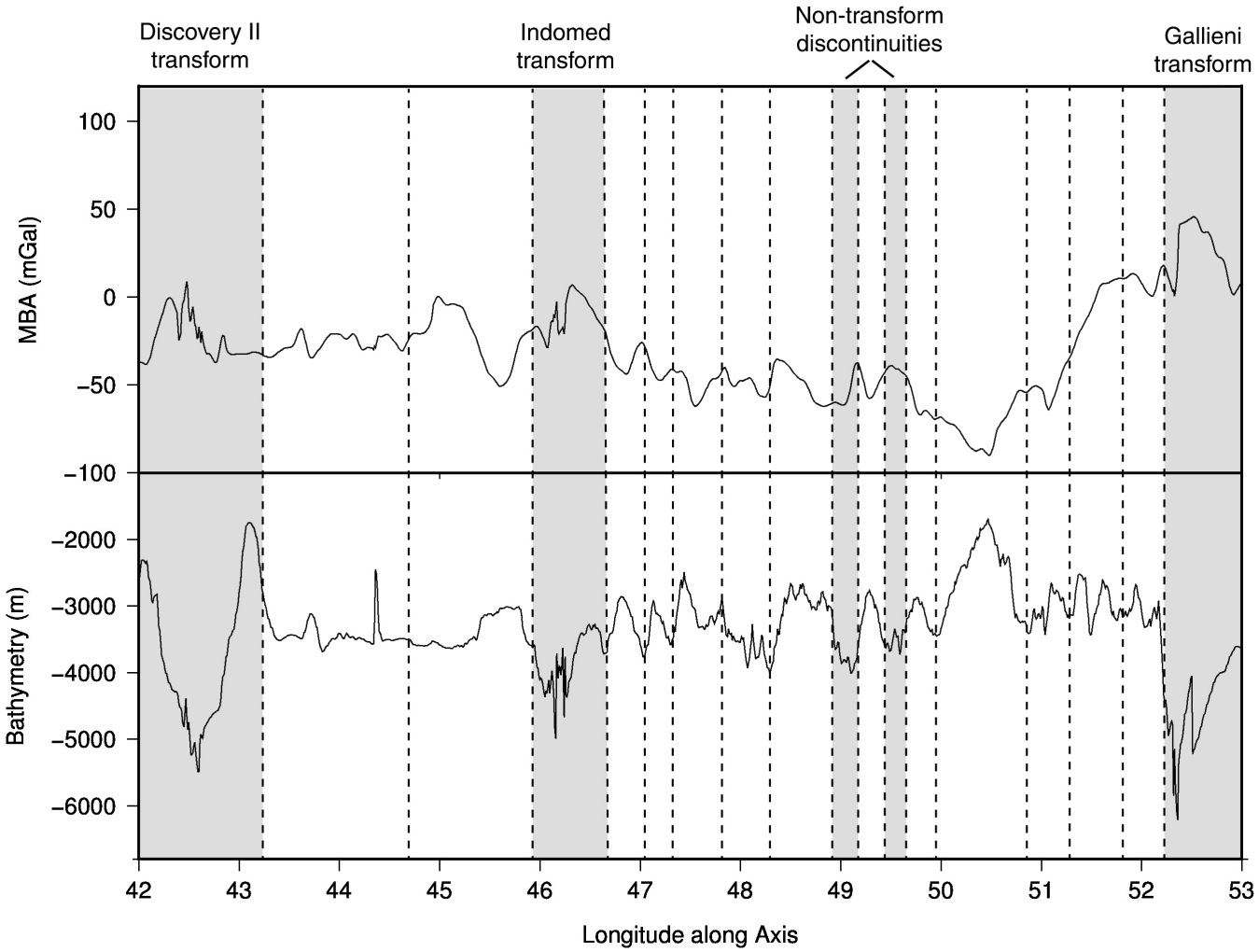


Figure 3.16: Example of along axis bathymetry and mantle Bouguer anomaly profiles between 42° E and 53° E. Dashed vertical lines represent the boundaries between segments. Shaded segments are discontinuities (either transform or non-transform), which have an along axis width due to the continuous nature of the profile track. These are excluded from the segments to remove source of bias from the measurements of segment length and axial relief.

shallower over non-transform discontinuities. These depth variations are similar to those observed along both the EPR (Macdonald and Sempere, 1984) and the MAR (Sempere et al., 1993) and appear to be a fundamental characteristic of mid-ocean ridges across a range of spreading rates.

The ridge segments were grouped into four distinct Groups, which were defined by the axial relief, segment length, MBA magnitude and axial morphology, following the method of Sempere et al. (1993). The first two segments west of the Bouvet transform

are excluded, due to the axial rise morphology and uncertainty over the location of the ridge axis (Mitchell and Livermore, 1998). The last segment on the eastern-most end of the SWIR is also excluded due to the local influence of the hotter mantle under the Southwest and Central Indian Ridges.

The magnitudes of the axial relief and mantle Bouguer anomalies for each segment were measured from peak to trough. In order to eliminate anomalous reliefs due to the presence of volcanic peaks and other very short wavelength topography, the peak value was taken as the ninetieth percentile value of the axial depths for any given segment. This removed the effects of short wavelength topography without significantly reducing the axial relief in segments with no short wavelength topography.

Segment Types

Group I segments are defined by large amplitude along-axis relief, between 1400 m and 2400 m, from peak to trough. Bathymetry examples of two endmembers of Group I type segment morphology (Segments 11 and 41) are shown in Figures 3.17 and 3.18. These segments generally correspond to strong MBA lows between -20 mGal and -60 mGal below the average MBA for the Section. These MBAs become increasingly negative toward the segment centres, forming a symmetric, circular 'bullseye' at the shallowest part of the segment. On most segments, the axial valley is narrower in the centre of these segments and widens in the area adjacent to the bounding discontinuities, forming an 'hourglass morphology' as shown in Figure 3.17. These segments exhibit robust axial volcanic ridges in the centre of the segment. On some segments, the axial valley and axial volcanic ridge is replaced with an axial high or very low relief axial valley as shown in Figure 3.18. The small-scale morphology within the axial valley at these segments is rounded and lacks evidence of major fault scarps, indicating that this is due to volcanic accretion and not an isostatically supported high such as that seen at the EPR. The flanking rift mountains consist of continuous linear ridges, which are parallel to the ridge strike. These ridges are occasionally truncated by the off-axis

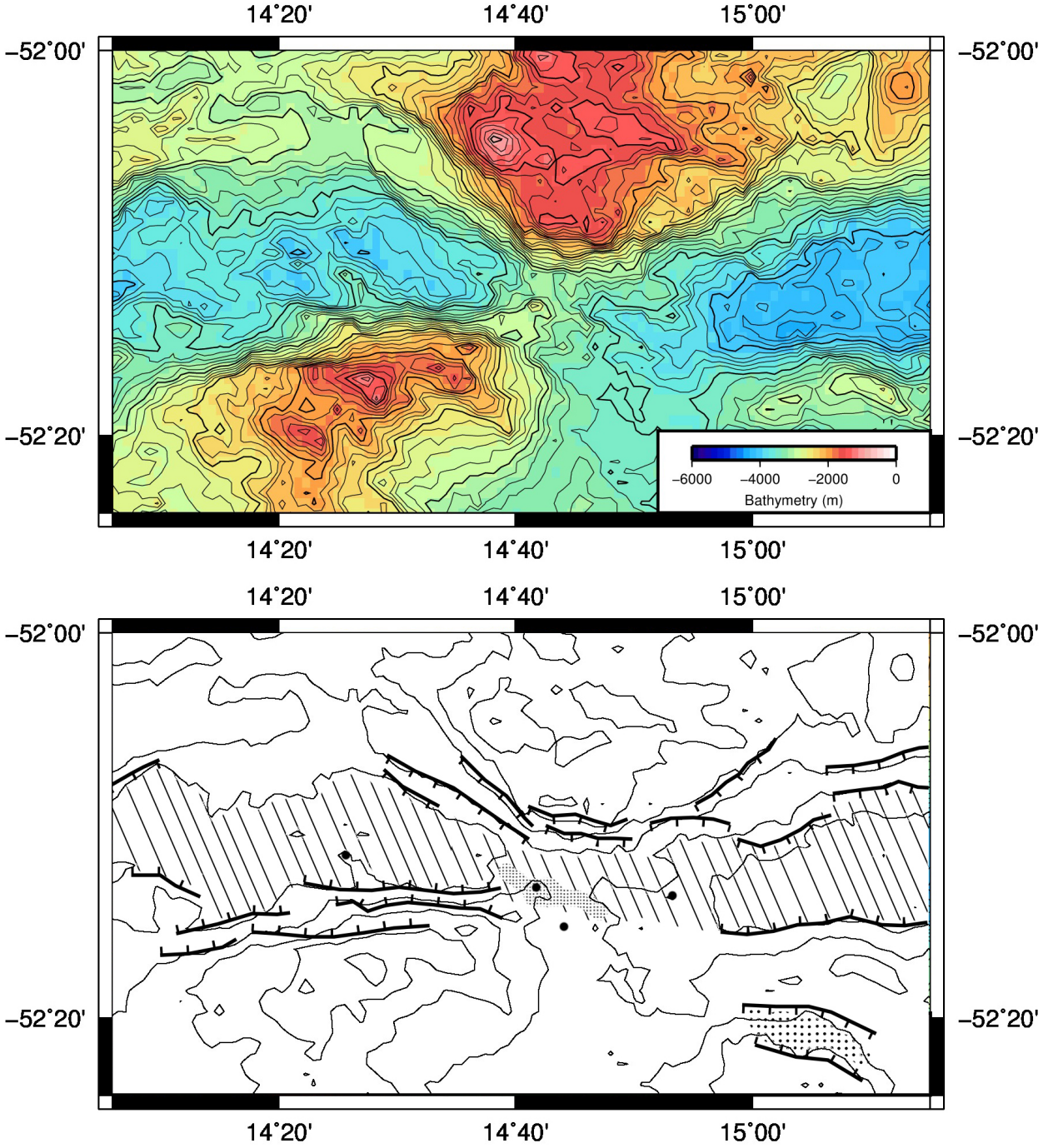


Figure 3.17: Upper map shows bathymetry of segment 11 on the SWIR, an example of a Group I type segment. Contour interval is 100 m. Lower map shows the interpreted structural geomorphology, which was constructed using visual examination of 3D multibeam bathymetry and mantle Bouguer anomaly maps in Fledermaus software. Hashed area - inner valley area, dotted area - off axis basins, grey stippled area - axial volcanic ridge, black circles - volcanic cones.

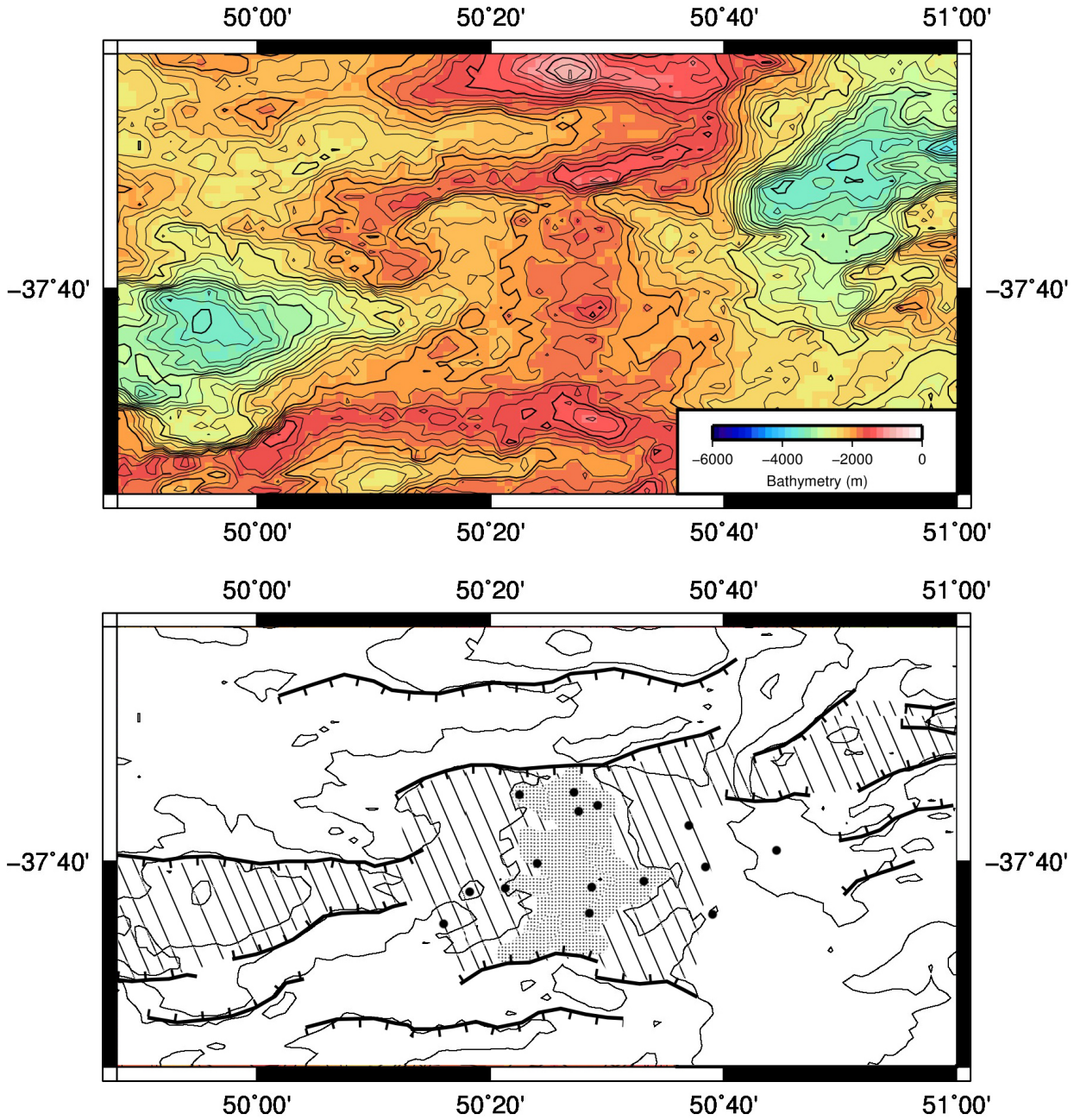


Figure 3.18: Upper map shows bathymetry of segment 41 on the SWIR, an example of a Group I type segment. Contour interval is 100 m. Lower map shows the interpreted structural geomorphology, which was constructed using visual examination of 3D multibeam bathymetry and mantle Bouguer anomaly maps in Fledermaus software. Hashed area - inner valley area, dotted area - off axis basins, grey stippled area - axial volcanic ridge, black circles - volcanic cones.

traces of non-transform discontinuities. The decrease in depth, narrowing of the axial

valley and circular gravity anomalies towards the centre of the segment suggest that the mantle upwelling beneath these segments is focused, and that the crustal thickness increases towards the segment centre. These segments represent magmatically robust segments with a high melt supply compared to the rest of the ridge.

Group II segments are defined by intermediate along-axis relief, between 700 m and 1400 m from peak to trough, and range in length between 60 km and 160 km. An example of a Group II type segment (Segment 52) is shown in Figure 3.19.

The mantle Bouguer anomalies along these segments show greater variation than Group I segments. The ridge axis, is defined by mantle Bouguer anomaly lows along the axis, which increase with distance from the axis; however these may be linear in form, or form circular mantle Bouguer anomaly lows at the centre of the segments. The axial valley shows a slight narrowing at the centre of the segment forming an hourglass morphology, though not as pronounced or consistent as that seen on Group I segments. Axial volcanic ridges are generally robust, reaching up to 400 m high, and form narrow linear ridges, often near the segment centre. These do not extend to the axial valley walls, and partial filling of the axial valley due to volcanic accretion is not observed on these segments. The flanking morphology consists of linear ridges as in Group I segments, however these have less relief, reflecting the reduction in volcanic accretion in the neo-volcanic zone. The axial relief and magnitude of the mantle Bouger anomalies associated with Group II segments indicate that these have an intermediate melt supply, compared to other segments on the ridge. There is variation in the melt supply between segments within Group II segments, which is reflected in changes in axial volcanic ridge morphology between segments. Some of the segments show morphological signs of focussed upwelling as seen in Group I segments, such as narrowing of the axial valley and circular mantle Bouguer anomalies at the segment centres, though not all segments.

Group III segments are defined by intermediate to low along-axis relief, between 300 m and 1000 m from peak to trough. They are generally shorter than Group II segments,

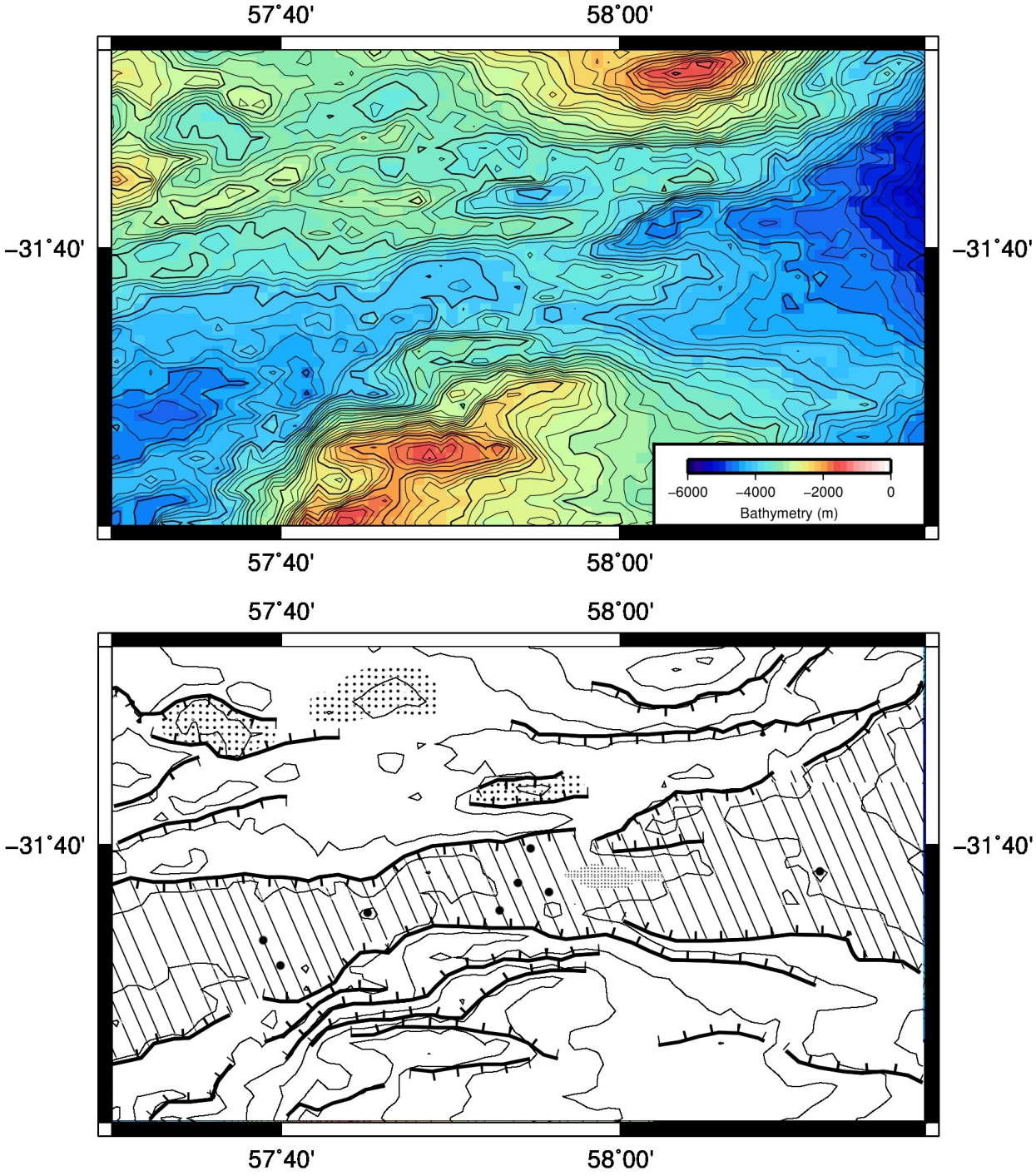


Figure 3.19: Upper map shows bathymetry of segment 52 on the SWIR, an example of a Group II type segment. Contour interval is 100 m. Lower map shows the interpreted structural geomorphology, which was constructed using visual examination of 3D multibeam bathymetry and mantle Bouguer anomaly maps in Fledermaus software. Hashed area - inner valley area, dotted area - off axis basins, grey stippled area - axial volcanic ridge, black circles - volcanic cones.

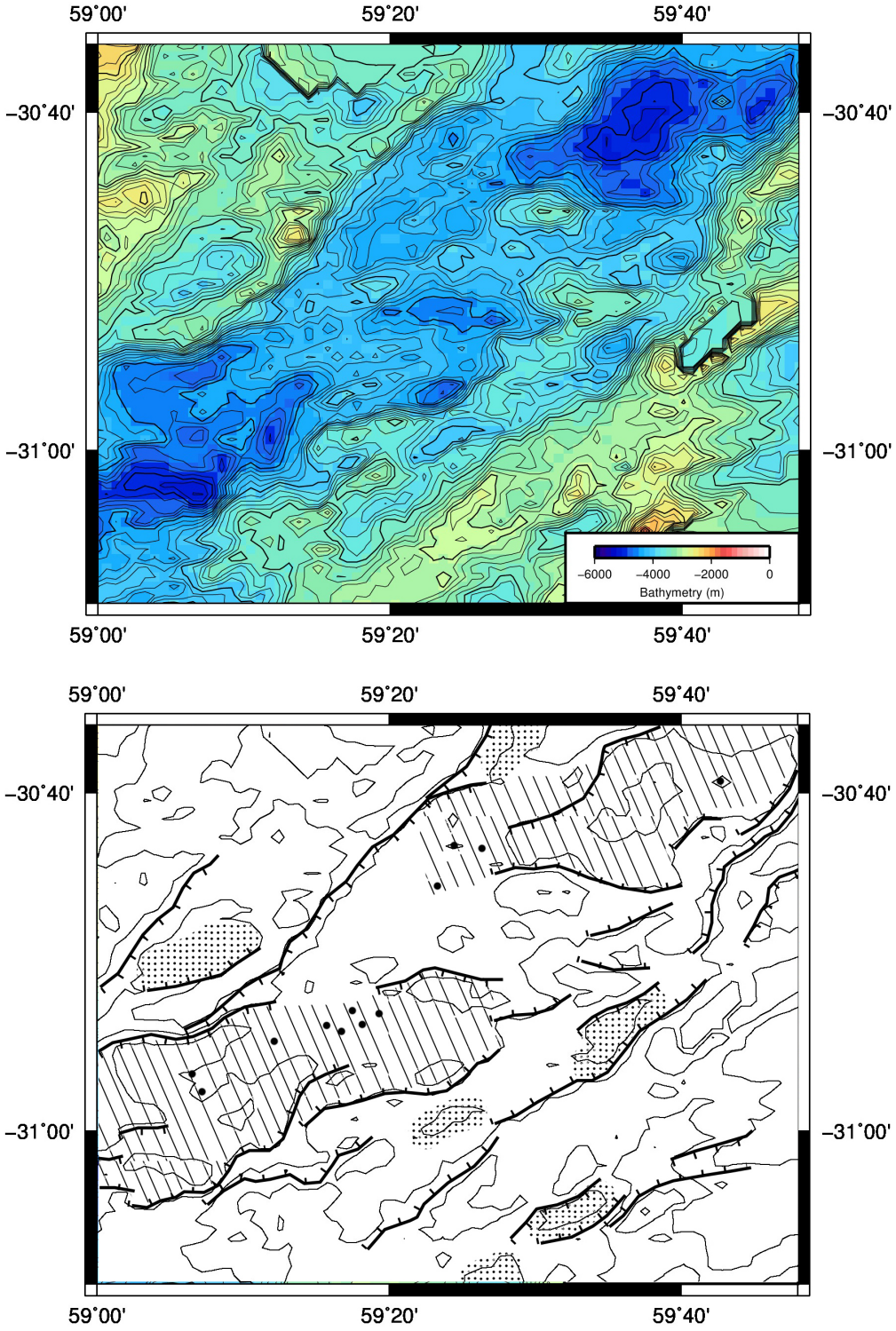


Figure 3.20: Upper map shows bathymetry of segment 55 on the SWIR, an example of a Group III type segment. Contour interval is 100 m. Lower map shows the interpreted structural geomorphology, which was constructed using visual examination of 3D multibeam bathymetry and mantle Bouguer anomaly maps in Fledermaus software. Hashed area - inner valley area, dotted area - off axis basins, black circles - volcanic cones.

ranging in length between 20 km and 80 km. An example of a Group III type segment (Segment 55), which is divided by a non-transform discontinuity at 59° 25', is shown in Figure 3.20. There is no evidence of circular mantle Bouguer anomaly lows at these segment centres, and the values of the mantle Bouguer anomalies are more positive, varying between 0 mGal and -20 mGal. The axial valley width remains generally constant throughout the segment, and lacks the narrowing towards the centre of the segment observed in Group I and II segments. In contrast the axial valley floor is wide and deep, with short wavelength topographic variations. The topographic fabric of the axial valley floor generally strikes perpendicular to the spreading direction, and lacks the rounded volcanic edifices observed on Group I and II segments. These structures are interpreted as tectonically generated. Axial volcanic ridges are largely absent or, when present, have relief less than 100 m. The flanking morphology is more disrupted than that observed in Groups I and II, and consists of a series of fault generated, isolated basins and ridges, which are not continuous along strike. These segments have a lower melt supply than either Group I or Group II segments, resulting in reduced axial relief, more positive mantle Bouguer anomalies, and minimal axial volcanic relief. The presence of axial volcanic ridges on some of these segments indicates that magmatic activity still occurs, though tectonic processes are most likely dominant.

Group IV segments are defined by low along-axis relief, between 50 m and 400 m from peak to trough, and range between 25 km and 100 km in length. An example of a Group IV type segment (Segment 8) is shown in Figure 3.21. The along-axis relief, in contrast to all the other segment types, deepens towards the centre of the segment. This is attributed to the increase in magmatism on segments on either side of the ridge. The axial deeps associated with non-transform discontinuities, which bound the segment, form part of the deep wide axial valley. The mantle Bouguer anomalies are linear, following the strike of the ridge axis. In contrast to the gravity lows associated with other segment types, the anomalies along Group IV segments form isolated positives (between 0 mGal and 20 mGal) along the deepest parts of the segment. These are flanked by linear negative anomalies between -30 mGal and 0 mGal, corresponding to

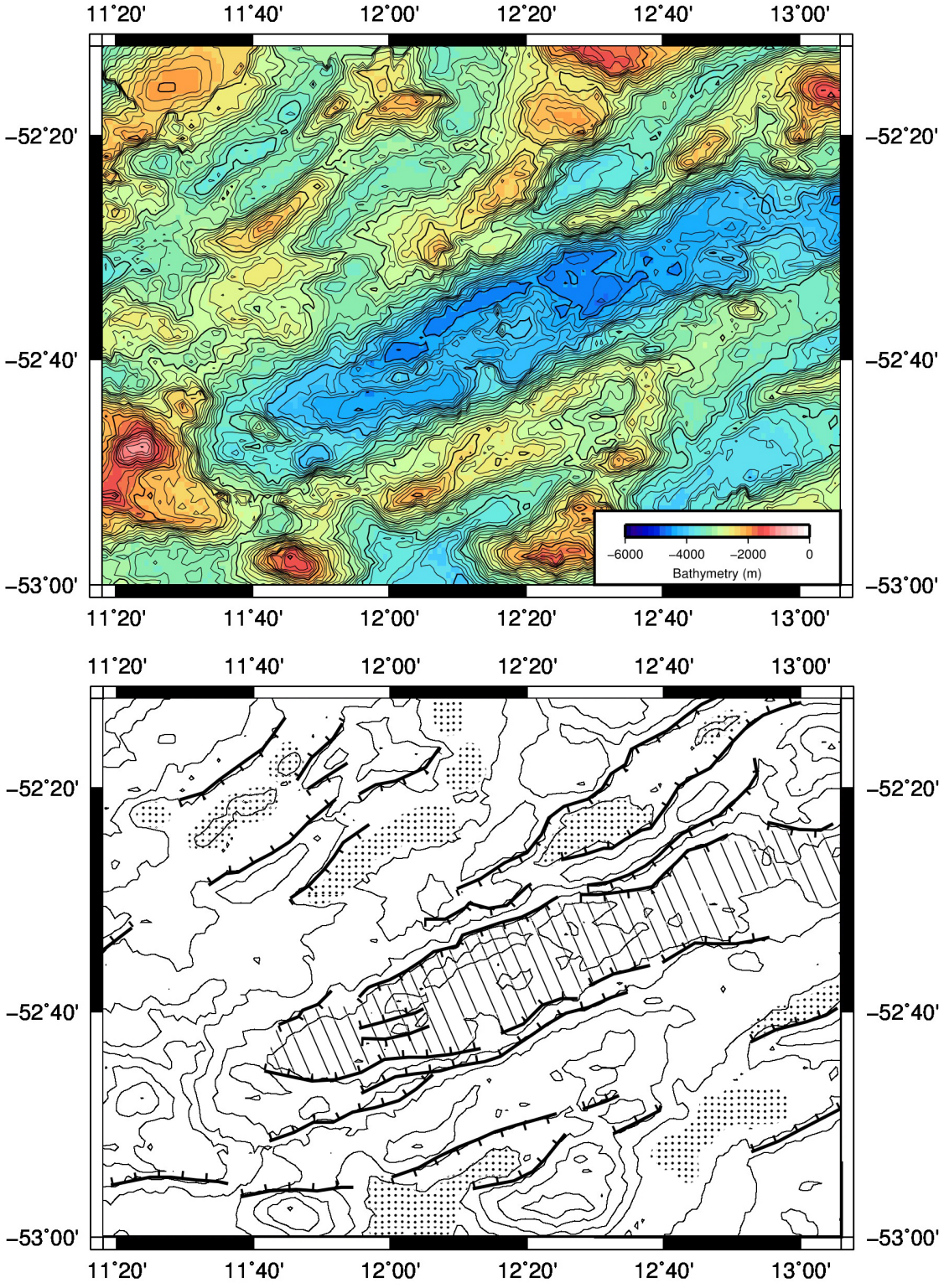


Figure 3.21: Upper map shows bathymetry of segment 8 on the SWIR, an example of a Group IV type segment. Contour interval is 100 m. Lower map shows the interpreted structural geomorphology, which was constructed using visual examination of 3D multibeam bathymetry and mantle Bouguer anomaly maps in Fledermaus software. Hashed area - inner valley area, dotted area - off axis basins, black circles - volcanic cones.

the flanking highs. The axial valley width remains generally constant throughout the segment, even widening slightly at the centre of the segment. The axial valley floor is wide and deep, ranging from 5200 m to 4000 m depth, approximately 500 m deeper than other segments. The axial valley floor topography consists of a series of basins and low relief highs that strike along the ridge axis. These are bound by faults and interpreted as tectonically generated topography. Axial volcanic ridges are not present and volcanic cones are rare. The flanking morphology is chaotic, consisting of fault generated, isolated basins and ridges. Group IV segments have a unique morphology, unlike any of the other segment Groups. The increase in axial depth towards the segment centre indicates a lack of melt focussing beneath these segments. This is consistent with positive mantle Bouguer anomalies and morphological structures dominated by tectonic processes, as opposed to volcanic accretion.

Intra-segment Variation

The axial valley bathymetry of Group I and Group II type segments show a number of common morpho-tectonic features. The width of the axial valley generally decreases towards the centre of the segment by up to 8 km, coinciding with in a decrease in axial valley depth between 700 m and 1400 m. In contrast, approaching the bounding discontinuities, the axial valley widens and deepens. This is analogous with intra-segment patterns observed on the MAR (Sempere et al., 1993), however the along-axis relief at the SWIR has a much steeper gradient. Seismic studies on the MAR (Kong et al., 1992) showed that these variations along an individual segment correspond to a shallowing of the brittle-ductile transition from the end of the segments towards the segment centre. Since the depth of the brittle-ductile transition reflects the 3D thermal structure of the sub-axial lithosphere, the morpho-tectonic changes along a segment reflect an increase in the sub-axial lithospheric temperature at the segment centre at

Group I and II type segments.

In contrast, Group IV type segments exhibit a reversed morphology. The width of the axial valley increases by up to 5 km and the axial valley deepens by up to 400 m towards the centre of the segment. Approaching the bounding discontinuities, which separate these segments from more magmatic segments, the axial valley narrows and the axial depths decrease. These observations suggest that the brittle-ductile transition may be at its deepest below these segments.

Group III type segments show little variation in axial valley width along their length. They generally increase in axial relief towards the centre of the segment, however the magnitude of this increase is approximately 400 m less than that observed at Group II segments.

Figure 3.22 shows conceptual diagrams of the different structures and processes occurring at the different segment types, which lead to the observed bathymetric variation. We attribute these variations to the regional degree of partial melt and the redistribution of melt. Group II and III type segments are analogous to the 'V' and 'U' shaped segments on the MAR respectively (Sempere et al., 1993). On Group II segments, melt migrates from the discontinuities towards the centre of the segment. This causes thickened volcanic crust towards the centre of the segment as evidenced by the bullseye gravity anomalies, which are also seen on the MAR (Lin et al., 1990). Group III segments have a more even melt distribution, most likely to due to the shorter segment length reducing the volume of melt migration. Group I and IV type segments do not have clear analogues on the MAR, and show greater melt-supply excesses and deficits than Group II and III segments. These are attributed to strongly focussed upwelling and multi-segment scale melt migration towards and away from segment types I and IV respectively. Seismic experiments at a Group I type segment centred on 50.5° E have shown the increased melt supply leads to crustal thicknesses of up 9.5 km, 5.5 km greater than the surrounding segments (Li et al., 2015). Seismic experiments across melt-poor Group IV type segments show reduced seismic thicknesses between 3.5 km

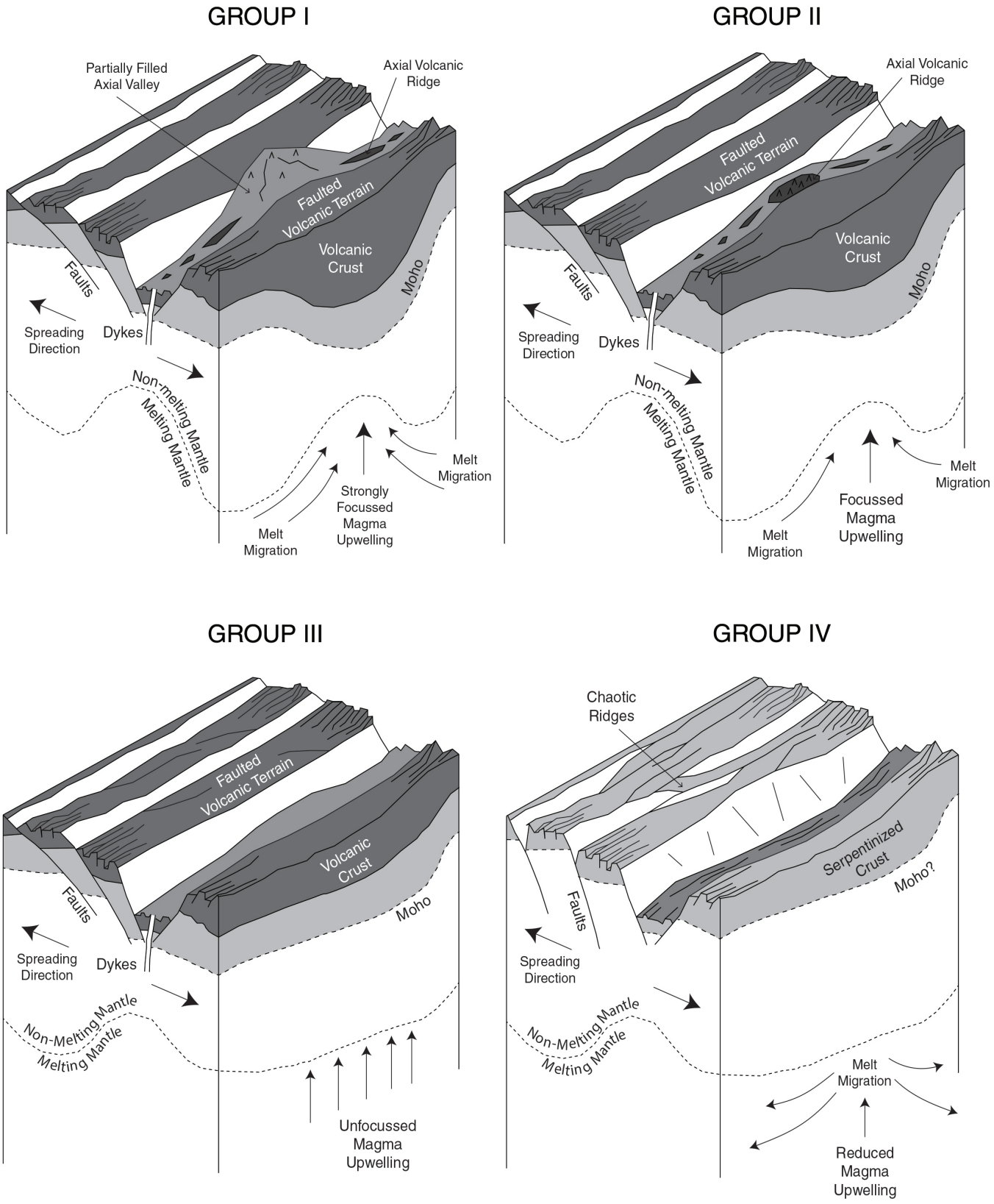


Figure 3.22: Schematic conceptual diagrams illustrating the proposed structure and processes occurring at the different segment Group types.

and 6 km at the segment mid-points (Muller et al., 1999; Minshull et al., 2006). Amagmatic segments on the Gakkel ridge, which are analogous to Group IV segments have been shown to have even thinner crustal thicknesses, between 1.9 km and 3.3 km (Jokat et al., 2003). Further seismic experiments are needed to confirm the variation in crustal structure beneath the different ridge segments, particularly Group II and Group III type segments.

Distribution of segment types along the ridge

Group I segments represent robust magmatic segments with a high melt supply. These segments occur in two distinct settings along the SWIR. A large number of Group I segments are present along Section D and Section A in the regions influenced by the Marion and Bouvet hotspot plumes. These areas of the ridge show a series of Group I segments separated by transform and non-transform discontinuities. The rapid shallowing between the segment boundaries and segment centre indicate that, although the plume provides a regional increase in temperature and melt supply, this melt is strongly focussed towards the centre of the segments. Grindlay et al. (1998) suggested that the segmentation pattern of the orthogonal Section (Section C) resulted from pattern of upper mantle discontinuities with a wavelength between 200 km and 300 km. The segmentation observed over these plume influenced regions show a similar pattern, though unlike in the orthogonal Section, the discontinuities have a greater along axis length than the accretionary segments.

In contrast to these areas with multiple adjacent Group I segments, some areas of the ridge have Group I segments in isolation. These occur on the oblique Section (Section B) and easternmost part of the SWIR (Section F) both of which are among the melt poorest parts of the ridge. These Group I segments form isolated magmatic segments surrounded by amagmatic (Group IV) segments. The axial valley is often partially filled or filled at these segments, indicating a robust magmatic system with a large melt supply. Dick et al. (2003) and Cannat et al. (2008) suggested that the uneven

distribution of magma in these areas of the ridge are due to strong magma focussing mechanisms. This was further supported by geochemical observations that revealed highly enriched MORB lava compositions, despite the inferred high degree of partial melting at these magmatic segments (Standish et al., 2008).

Group II and III segments are distributed along the majority of the ridge, with the exception of the oblique Section (Section B), where Group I and Group IV segments are juxtaposed, and the Sections influenced by hotspots (Sections A and D), which consist mostly of Group I segments. Group II segments are generally slightly more prevalent than Group III segments to the west of the Atlantis II transform, while the opposite is true to the east. This is attributed to the reduction in melt supply to the east of the Atlantis II transform, since Group III segments have less axial relief and minimal MBA gravity signatures compared to the Group II segments. These segments represent an intermediate melt supply with no strong melt focussing either towards or away from these segments.

Group IV segments represent very low or even absent magmatic upwelling. These segments are primarily found on the oblique Section (Section B) and easternmost part of the SWIR (Section F), which have the lowest supply on the ridge. The cause of the low melt supply is reflected in the long wavelength geophysical and geochemical signatures (discussed in section 3.1) and is attributed to oblique spreading in Section B and cold mantle temperatures in Section F. These Sections do, however, show some magmatic activity restricted to particular segments. This contrast between amagmatic and magmatic segments has been attributed to very focussed mantle upwelling (Sauter et al., 2004; Cannat et al., 2008). In contrast to the segment scale melt migration inferred at the centre of Group II segments, this requires magma to be redistributed over long distances. Sauter et al. (2004) suggested that this is achieved through a combination of melt migration along the base of the lithosphere, which forms a thermal barrier to hot melt, and rapid injection through dykes, which are established in these high melt focussed regions.

The distribution of the segment types show that the dominance of magmatic versus tectonic processes at an individual ridge segment is influenced by the long wavelength mantle and crustal structure. Sections of the ridge in which geochemical proxies indicate increased degrees of partial melting have a greater proportion of magmatically dominated Group I and Group II type segments; Sections of the ridge in which geochemical proxies indicate decreased partial melting have a greater proportion of tectonically dominated Group III and Group IV type segments. Areas of the ridge with an intermediate melt supply exhibit both Group II and Group III type segments, the proportions of which change depending on the relative melt supply; areas of higher intermediate melt supply have a greater proportion of more magmatic Group II segments compared to more tectonic Group III segments, and visa versa. While the long wavelength melt supply clearly has an influence on the segment type, it does not preclude the presence of isolated amagmatic, tectonic segments in regions of high melt supply or isolated magmatic segments in regions of low melt supply. This is attributed to the strong melt focussing mechanisms discussed in the section above.

3.3 Chapter Summary

This chapter presents bathymetry and gravity data along and across the ridge axis, which is used to show the long wavelength variations in mantle and crustal structure and the relationships between axial valley morphology and long wavelength trends. The key points are as follows:

- We reconstruct along axis bathymetry and mantle Bouguer anomaly profiles using magnetic data to identify the location of zero-age. Comparison to existing profiles in published literature show similar long wavelength variation, but differences in small scale segmentation.

- Long wavelength variations in along axis bathymetry, mantle Bouguer anomalies, mantle shear wave velocities and geochemical proxies show systematic correla-

tions, which are interpreted as changes in mantle density and crustal thickness along the ridge axis.

- The inferred changes in mantle density and crustal thickness are attributed two causes: influence of hotspots and changes in the spreading obliquity of the ridge. Areas of high mantle temperatures, increased crustal thickness and increased degree of partial melting are attributed to the influence of the Marion and Bouvet hotspots. Areas of decreased crustal thickness and reduced degrees of partial melting, despite a normal mantle density are attributed to reductions in effective spreading rate due to ridge obliquity.

- We show that axial valley morphology is well correlated with changes in along axis depths. This is attributed to the common governing factor for the rheology and axial valley depths: the thermal structure of the ridge.

- Since some axial valley depths may be attributed to mantle geochemical heterogeneity, the axial valley widths are directly compared to the elastic thickness, a proxy for lithospheric strength. We show a positive correlation between axial valley widths and lithospheric strength, suggesting that a lithospheric wedge model is applicable at the SWIR.

- We use along axis bathymetry and mantle Bouguer anomalies to divide the ridge into segments. These segments are divided into four distinct types based on the morphology and geophysical signatures.

- The morphological variations between the segment types are used to infer changes in crustal structure and melt migration mechanisms. Strong melt focussing is used to explain the melt excesses and deficits observed at the different segment types.

- We show that the long wavelength variation in mantle and crustal structure on the ridge influences the distribution of the segment types, however a mix of segment types is observed on most areas of the ridge.

Chapter 4

Seamount Morphology

4.1 Seamounts on Mid Ocean Ridges

It was once believed that the ocean floor was featureless, lacking any significant topography, however we now know that the seafloor is littered with seamounts. An increase in the availability of seafloor bathymetry data and advances in technologies during World War II led to the discovery of seamounts; first in the ocean basins (Hess, 1946) and subsequently on mid-ocean ridges (Heezen, 1960; Menard, 1960).

Volcanoes at mid-ocean ridges are typically low relief (50 m to 200 m) circular edifices, 1 km to 2 km across (Batiza and Vanko, 1984) that form on the flanks of the axial rise in fast spreading settings, or in the neo-volcanic zone of the axial valley in slow spreading ridges (Small, 1998). In contrast, a small number of larger seamounts (up to 3000 m in height (Hillier and Watts, 2007; Wessel, 2001)) are found in the flanks of slow-spreading mid-ocean ridges (see chapter 5).

Seamount morphology has previously been used as an important tool to understand the tectonic, volcanic and erosional processes occurring in a region (Nakamura, 1977). A proportion of these studies involve volcanic islands in an intra-plate settings (e.g. Fiske and Jackson, 1972; Mitchell et al., 2002). The majority of the small seamounts

found at mid-ocean ridges have relatively uniform morphology and individually give little indication of tectonic processes. In contrast, the seamounts chosen for this study are large volume (>2000 km^3), high relief (>1500 m) and exhibit complex geometries similar to those observed on large oceanic islands. These seamount morphologies may be used to assess the different tectonic, volcanic and erosional processes occurring under the influence of the local setting on the ridge crest.

Previous work on seamounts at mid-ocean ridges has either focused on (*i*) the number and distribution of small volcanic cones in the axial valley at fast, slow and ultra-slow spreading ridges (e.g. Smith and Cann, 1992; Mendel and Sauter, 1997) or (*ii*) large seamount morphology studies at non ultra-slow spreading ridges (e.g. Johnson and Embley, 1990; Fornari and Ryan, 1984). This chapter studies large seamount morphology across six seamounts on the ultra-slow Southwest Indian Ridge. Swath bathymetry surveys and seafloor video transects were carried out over four seamounts and one oceanic core complex in 2011 (cruise JC066) and swath bathymetry acquired over one seamount in 2012 (cruise M101-2).

The oceanic core complex, Atlantis Bank, is studied as a topographic feature and irrespective of tectonic or volcanic origin the term 'seamount' is used to describe the edifice.

4.2 Criteria for Identifying Morphological Features

A number of distinct morphological features are present on the Southwest Indian Ridge seamounts in this study; however the criteria by which these features have previously been identified and classified differ between studies (e.g. Vogt and Smoot, 1984; Batiza and Vanko, 1984; Smith et al., 2002; Acosta et al., 2003). The following section details the criteria used to distinguish particular morphological features in this study.

4.2.1 Constructive Volcanic Features

Constructive volcanic features are defined as features formed by the addition of magmatic material to the surface of the ocean crust. These features, which make up the majority of seamount edifices, include flank rift zones (FRZs) expressed as linear ridges, lava terraces, lava flows and volcanic cones. Flank rift zones (FRZs) form due to the concentration of dykes in oceanic islands and seamounts to form dyke swarms (Walter et al., 2005). Sustained intrusive and extrusive activity along FRZs form ridges, which extend away from or subparallel to the main edifice of the seamount, as shown in Figure 4.1. FRZs are distinguished from elongate lava terraces by their high degree of ellipticity ($>\frac{1}{3}$) and their pyramidal profile in cross-section. These ridges are characterised by high backscatter on the ridge summit, which decreases slightly on the ridge slopes due to rough volcanic morphology and steep slopes scattering the acoustic signal. Lava terraces form due to the ponding of lava flows, the frontal lobe of which cools forming a rim that becomes the edge of the terrace (Smith et al., 2002). Lava terraces are identified by sharp breaks in slope on the volcanic edifice, forming flat plateau structures, as shown in Figure 4.1. These correspond to regions of high backscatter and occasionally have rim craters. Large lava flows can be distinguished using bathymetry and are most distinct on the steepest flanks of the seamounts, where they form discrete protrusions from the edifice. These massive lavas are characterised by high backscatter, however the steep gradient of the volcanic flanks may lead to low backscatter shadows obscuring the high backscatter signature of the lavas. Further evidence of lava flows includes the presence of volcanic cones at the source, and occasionally, levees at the margins. Volcanic cones are defined as circular or sub-circular conical structures between 10 m and 200 m in height, shown in Figure 4.1, and are characterised by small circular areas of high backscatter. Some of these cones have summit craters, some are flat and some are conical; they often merge with other cones to form agglomerate structures.

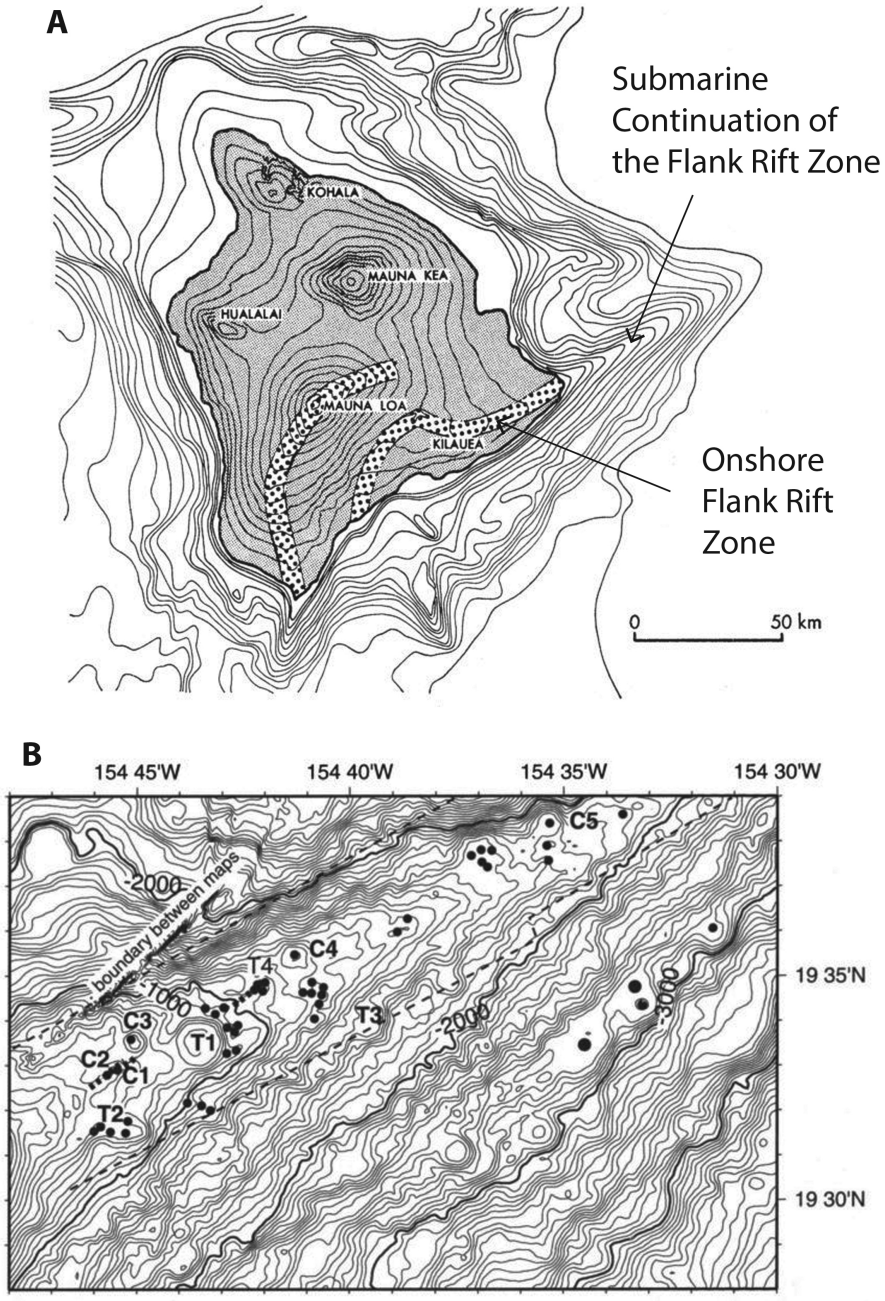


Figure 4.1: Examples of flank rift zones from Hawaii. Figure A, adapted from Fiske and Jackson (1972), shows topography of the onshore flank rift zones and offshore continuation, which forms a linear volcanic ridge. The dark shaded area represents the area above sea level, the white dotted areas show the locations of onshore volcanic rifts. Contour interval is 1000 ft (305 m). Figure B, adapted from Smith et al. (2002), shows a bathymetric map of the Puna Ridge, Hawaii, contoured at 50 m. The bathymetry shows lava terraces (T), volcanic cones (C), and craters (black dots).

4.2.2 Slope Failures

Slope failures and their resultant morphological features have been identified on many seamounts and ocean islands (e.g. Moore et al., 1989; Mitchell, 2003; Masson et al., 2002). The term 'slope failure' is a general term, encompassing a wide variety of processes in which material moves downslope under gravitational forces. Slope failures at volcanic islands fall into two broad categories classified according to Varnes (1978): (*i*) debris avalanches - rapid granular rock flows; (*ii*) slumps - slow movement of material along a plane of weakness. Debris avalanches are identified by arcuate elliptical or sub-circular head scars at the source area, a smooth elongate valley-like chute and a hummocky debris deposit consisting of sediment and boulders (Siebert, 1984). Slumps are identified by a sharp break in slope followed be a resumption of rugged volcanic topography further downslope (Varnes, 1978). Most studies involve slope failures from large seamounts and oceanic islands such as Hawaii and the Canaries, however, Moore et al. (1989) showed that these landslides show similar characteristic features at both large and small scales. In addition to the large slope failures described above, side scan sonar images commonly show small gully features on the very steep flanks of a volcano (Fornari and Ryan, 1984). This is most likely caused by small slope failures, which are of insufficient volume to indent the seamount flank (Mitchell, 2003).

4.2.3 Truncated Summits

The summits of seamounts can become truncated by a variety of mechanisms (Mitchell, 2001), including eruptive ring dykes, caldera infill, and wave erosion. Truncated summits are identified by distinct breaks in slope and a summit plateau with a gradient of less than 1°. Summit relief between 10 m and 200 m in height may be subsequently imposed on the flat plateau due to volcanic or sedimentary processes, however the break in slope remains identifiable in slope profiles.

4.2.4 Faulting and Fractures

Faults and fractures are identified by linear breaks in slope, which cut across the contours of an edifice (Batiza and Vanko, 1984). These form steep bathymetric scarps sometimes hundreds of metres in height, characterised by bright linear reflectors on backscatter data. Maps of slope gradient and 3D bathymetry illuminated relief maps, produced using Fledermaus software, were used to identify these scarps. Pelagic sediment drape may conceal fault traces at the surface, though small gullies may be present on the surface due to fault movement at depth. Fractures are more difficult to detect on bathymetry data as they do not form scarp structures, and require high resolution acoustic imaging to detect (Smith et al., 2002).

4.2.5 Substrate Analysis

Substrate analyses based on backscatter interpretations were made using the methodology of Blondel and Murton (1997).To ensure that this methodology was applicable to the seamounts in this study, remotely operated underwater vehicle (ROV) video imagery was used to identify the major substrates and ground-truth the backscatter data interpretations. Petrological thin sections of rock samples collected at specific outcrops were used to confirm lithological interpretations made using visual identification from ROV imagery on the outcrop scale. Low backscatter (dark areas) corresponds to unconsolidated sediments, which attenuate the 12 kHz signal (Mitchell, 1993), as well as very rough volcanic morphologies and areas with slope gradient $>20^{\circ}$ where the acoustic signal is deflected or scattered. High backscatter (light areas) corresponds with smooth hard lithologies such as massive lavas and carbonate platforms. Areas with slope gradients $<3^{\circ}$ have lighter backscatter than might be expected, due to the reduced scattering of the acoustic signal. Intermediate or mixed areas of backscatter often occur in slope failure debris deposits, where the acoustic signal is attenuated by thick sediment and reflected by large blocks and boulders (Masson et al., 2002).

Figure 4.2 shows the relationship between the backscatter and lithological interpretations from an example ROV transect. In general, the areas of unconsolidated sediments correspond to low backscatter (dark) areas while igneous lithologies correspond to high backscatter (light) areas. The small scale variations in lithology observed along such a profile are not always reflected in the corresponding backscatter, however when viewed in context as a map, the broad areas of high and low backscatter will define areas of common substrate.

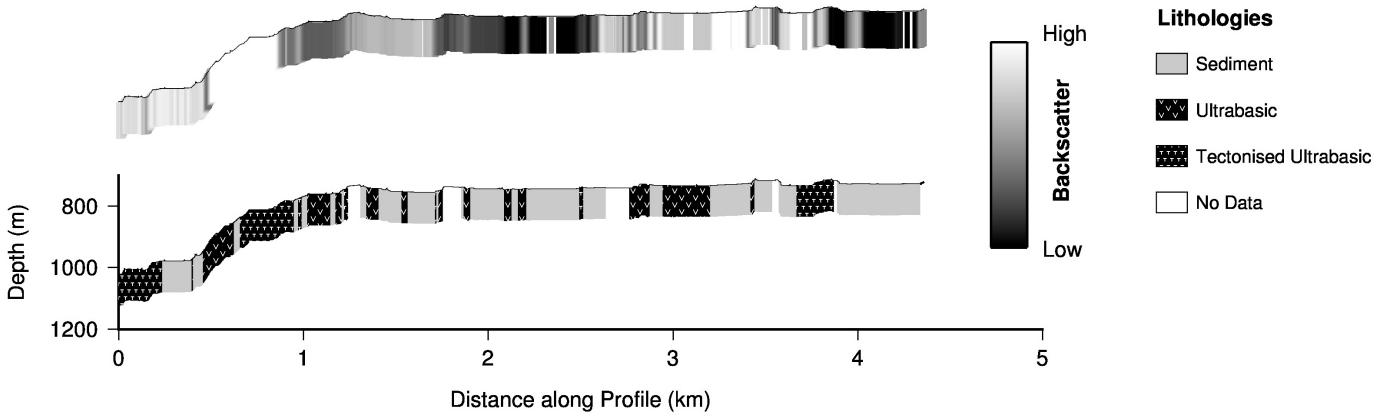


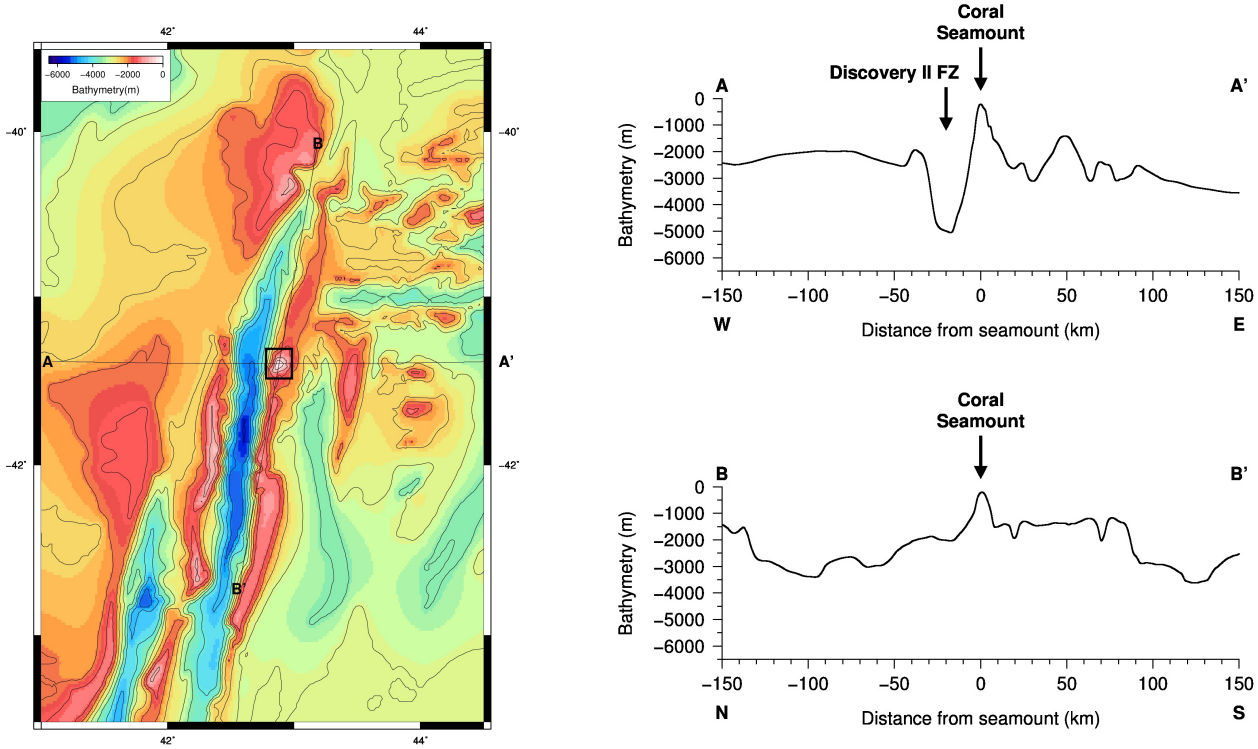
Figure 4.2: Comparison of substrate interpretation and backscatter along an ROV transect draped over a topographic profile of distance along a transect plotted against depth measured using a USBL on the ROV. Lower profile shows substrate interpretation; upper profile shows backscatter sampled from a backscatter grid (Figure 4.21). Light shades represent high backscatter, dark shades represent low backscatter.

4.3 Morphological Descriptions

Each of the seamounts surveyed along the ridge show a distinct morphology influenced by their volcanic history, tectonic setting and erosional history. This section contains a detailed description of the morphology of each seamount.

4.3.1 Coral Seamount

Coral Seamount (41.402° S, 42.883° E) is situated on the Southwest Indian Ridge crest on the east flank of the Discovery II fracture zone. The seamount is constructed on a transverse ridge associated with the adjacent transform, as shown in Figure 4.3. Swath bathymetry data were acquired over the seamount; however backscatter data were not used for analysis due to large errors introduced by bubble entrainment under the hull during poor weather conditions.



(a) Bathymetry from the GEBCO 2014 30'' x 30'' global bathymetry grid (IOC et al., 2003) of the region surrounding Coral Seamount. The black box marks the location of Coral Seamount; the lines A-A' and B-B' mark the locations of the context profiles in Figure 4.3b.

(b) Bathymetric profiles derived from sampling the GEBCO 2014 30'' x 30'' global bathymetry grid (IOC et al., 2003) along a ridge parallel azimuth (A-A') and a transform parallel azimuth (B-B') intersecting at Coral Seamount (see Figure 4.3a for profile locations). Major topographic features are labelled.

Figure 4.3: Bathymetry map and bathymetric profiles showing Coral Seamount in regional context.

Coral Seamount, shown in Figure 4.4, has a roughly triangular geometry, elongated in the north-south direction, extending 11.2 km from east to west and 17.6 km from

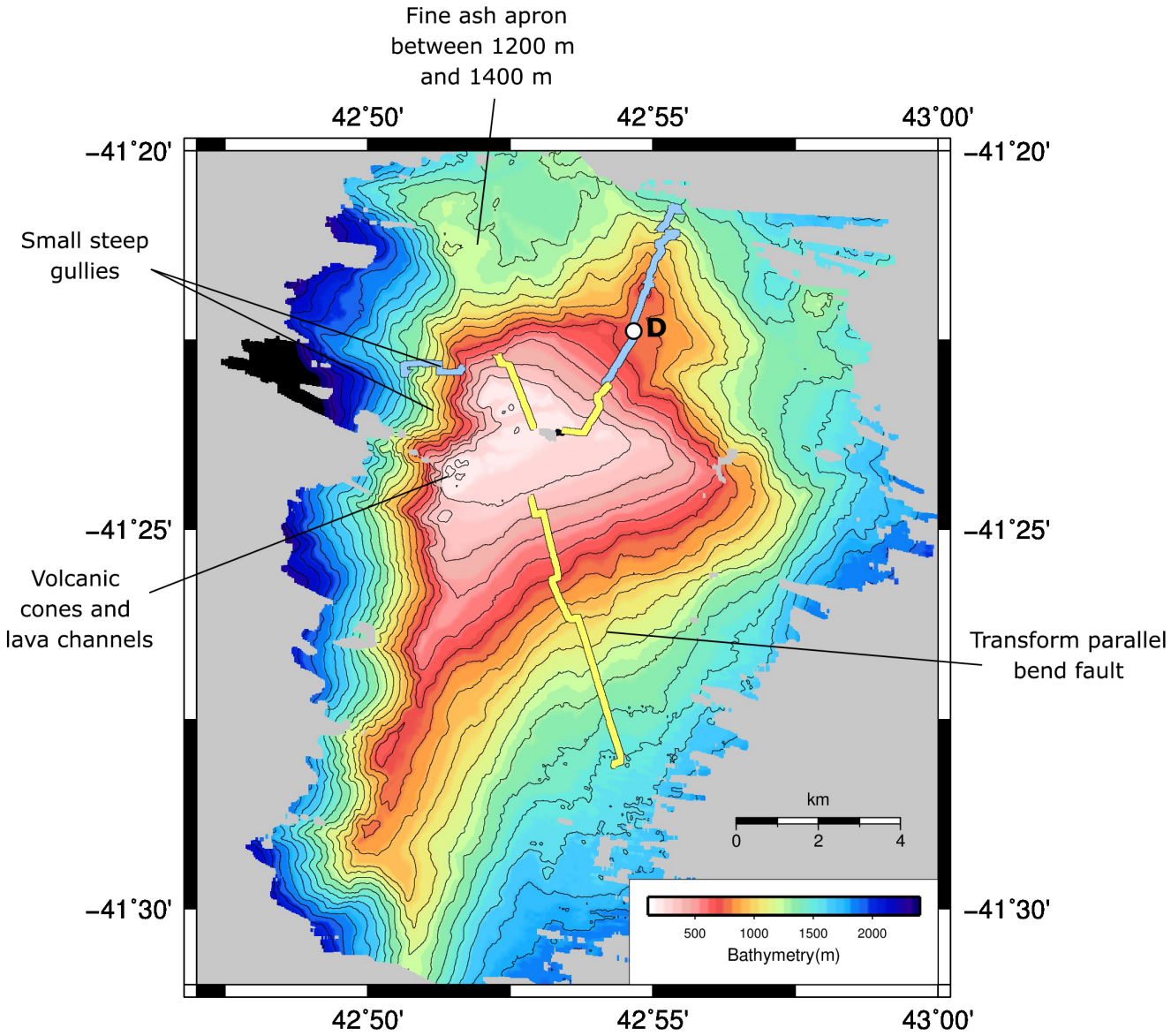


Figure 4.4: Bathymetry map (contour interval 100 m) of Coral Seamount from cruise JC066. Blue tracks show the ROV transects, yellow tracks show the SHRIMP transects, and white tracks show the HyBIS transects. White circles denote lithology sampling locations, letters correspond to the ROV images in Figure 4.26 and profile locations in Figure 4.28.

north to south. The seamount has a gently dipping truncated summit with some local relief. The southwest area of the summit, is smooth and has a dip of $<3^{\circ}$ towards the southwest. There are a number of vents, represented by eight summit cones between 40 and 70 m tall, mostly clustered along the summit's western edge. A number of leveed

lava channels up to 90 m deep separate the summit cones, and all extend in a radial pattern from a point at the top of the western flank (see Figure 4.5). ROV observations discount the possibility of these summit structures being carbonate in origin.

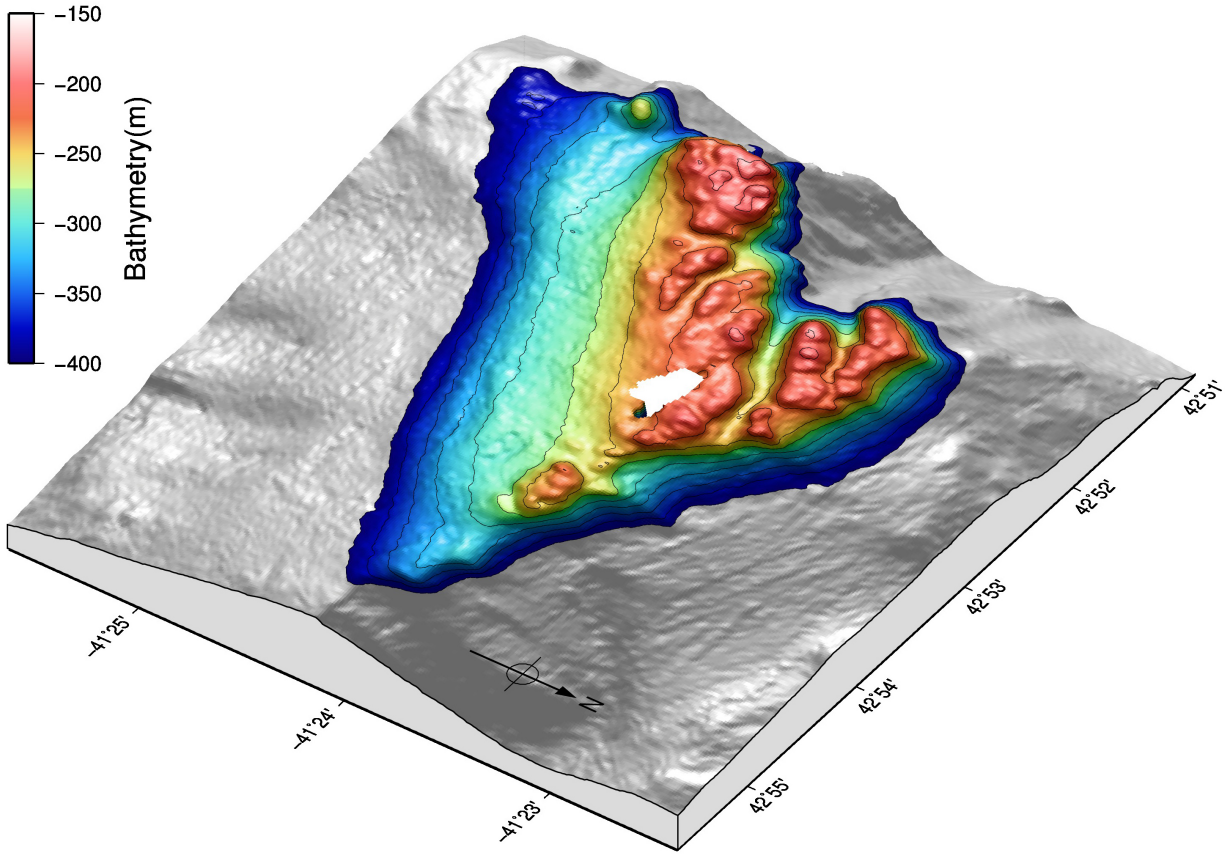


Figure 4.5: 3D perspective image of the summit of coral seamount. A colour gradient representing bathymetry is applied between the depths of 400 m and 150 m. The mesh grid reflects the underlying bathymetry. The bathymetry data have been illuminated by an artificial sun in the south and the contour interval is 25 m.

The average slope gradient and morphology varies between the different flanks of the seamount. The western flank is the steepest with average gradients of 20° to 30°, though the upper parts of the slopes are locally up to 50° steep. This steep face shows numerous arcuate gully structures: these are interpreted as small volume slope failures, which do not modify the slope gradient. Positive protrusions from the slope overlying the gullies are interpreted as lava flows issuing from the volcanic cones on the summit. The less steep southeastern flank has an average gradient of 5° to 10° and a smooth surface,

more typical for a seamount (Smith and Jordan, 1988). ROV imagery shows that this slope is covered by unconsolidated sediment and coral framework, which conceals any volcanic structures. A small number of volcanic outcrops were observed, usually extrusive lavas with little distinct small scale morphology. A series of linear breaks in slope, which cut across the contours of the southeast slope, are interpreted as fault scarps. These faults are parallel to the adjacent Gallieni transform fault, shown in Figure 4.6, and are therefore most likely bend faults resulting from tension caused by flexure due to thermal bending moments on the margins of the transform (Parmentier and Haxby, 1986).

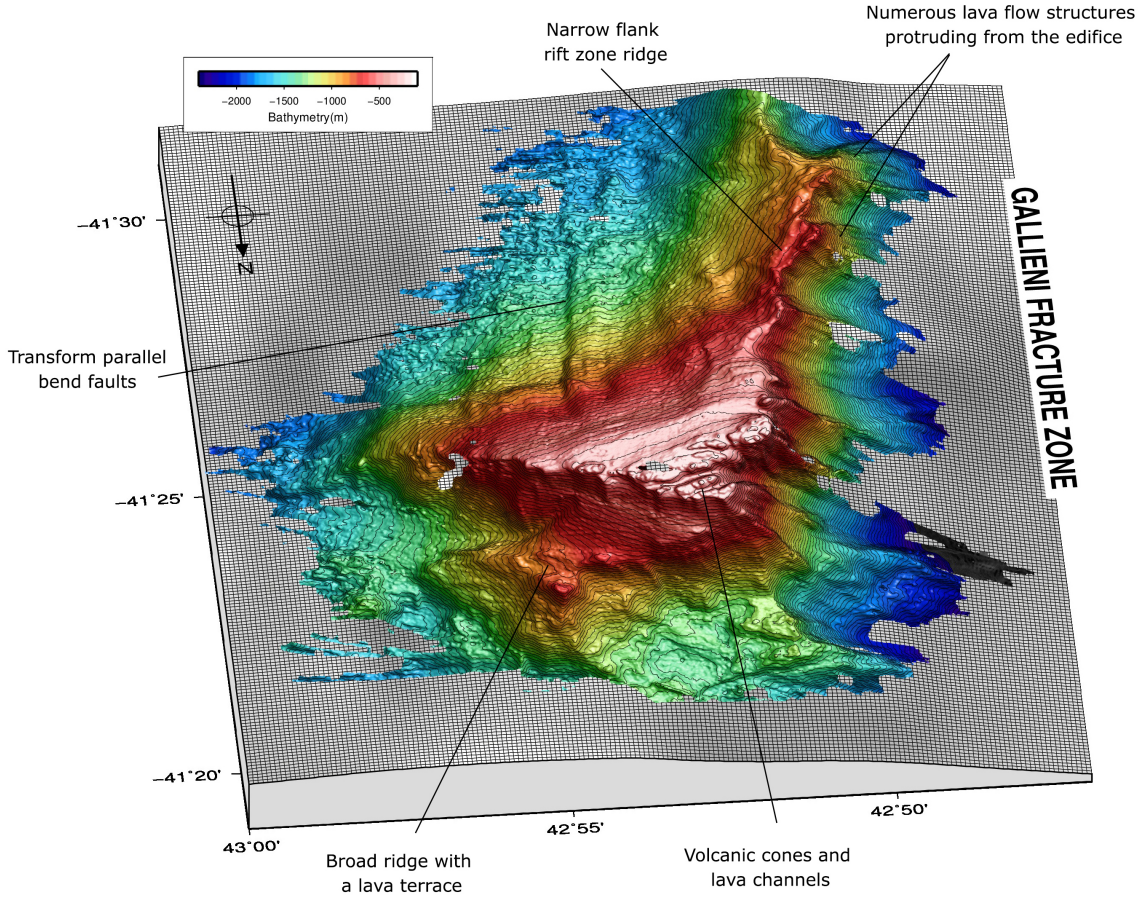
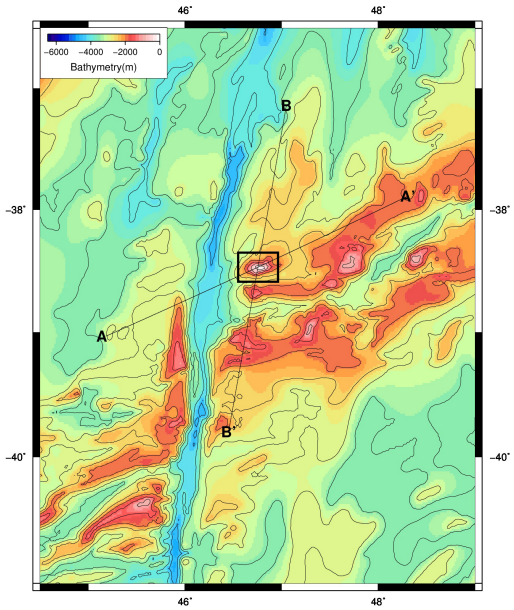


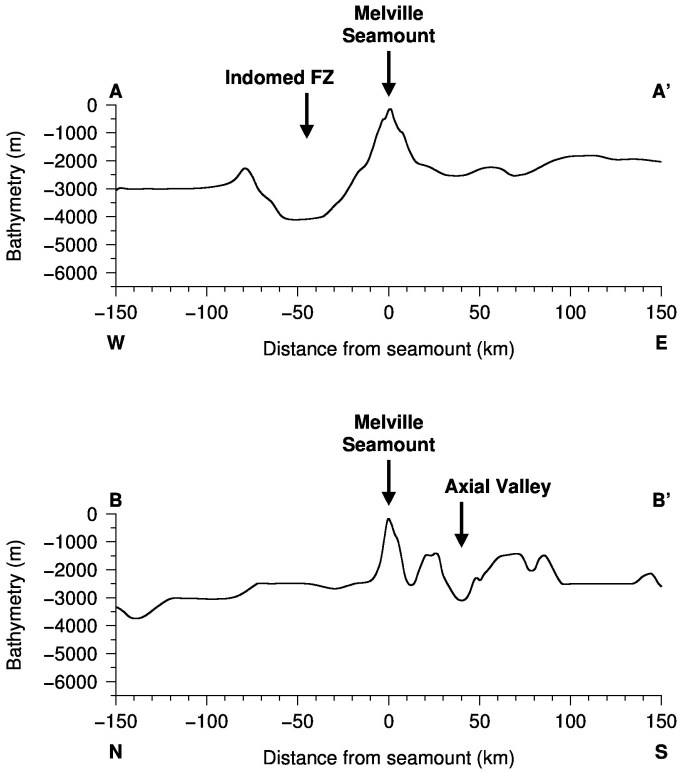
Figure 4.6: Perspective view of Coral Seamount from the north (azimuth 5°, elevation 5°). The mesh grid shows the regional bathymetry derived from the GEBCO 2014 30'' x 30'' global bathymetry grid (IOC et al., 2003). The coloured image shows the shipboard bathymetry from cruise JC066. The bathymetry data have been illuminated by an artificial sun in the southwest and the contour interval is 25 m.

4.3.2 Melville Bank

Melville Bank (38.467° S, 46.758° E) is situated 45 km north of the axial valley, just beyond the axial rim mountains, shown in Figure 4.7. The seamount is on the outside transform corner of the northern trace of the Indomed fracture zone, which is located 45 km to the west of Melville Bank. Swath bathymetry and backscatter data were acquired over the seamount, however the backscatter data contains noise due to poor weather during the survey.



(a) Bathymetry from the GEBCO 2014 30'' x 30'' global bathymetry grid (IOC et al., 2003) of the region surrounding Melville Bank. The black box marks the location of Melville Bank; the lines A-A' and B-B' mark the locations of the context profiles in Figure 4.7b.



(b) Bathymetric profiles derived from sampling the GEBCO 2014 30'' x 30'' global bathymetry grid (IOC et al., 2003) along a ridge parallel azimuth (A-A') and a transform parallel azimuth (B-B') intersecting at Melville Bank (see Figure 4.7a for profile locations). Major topographic features are labelled.

Figure 4.7: Bathymetry map and bathymetric profiles showing Melville Bank in regional context.

Melville Bank, shown in Figure 4.8, has an elongate stellate geometry with well de-

veloped flank rift zones (FRZs) forming volcanic ridges in the four cardinal directions. The geometry created by these FRZs is further enhanced by slope failures between the constructive sectors. The seamount is elongated in the east-west direction, extending 13.3 km from east to west and 7.4 km from north to south. The summit is truncated at a depth of 130 m and is characterised by high bathymetry indicative of volcanic or consolidated carbonate substrate, punctuated with swaths of low backscatter corresponding to unconsolidated sediment observed in ROV imagery. The summit has negligible local relief (<20 m) with a gradient <1°.

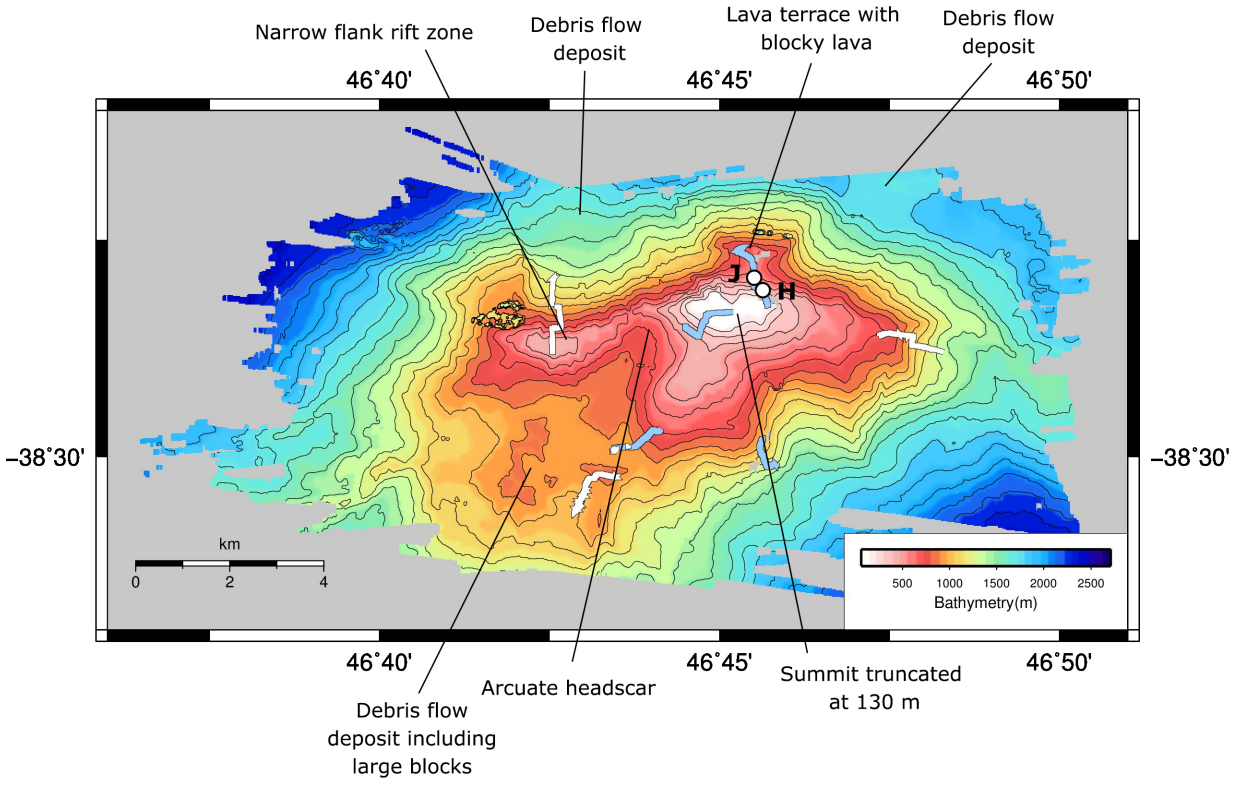


Figure 4.8: Bathymetry map (contour interval 100 m) of Melville Bank from cruise JC066. Blue tracks show the ROV transects, yellow tracks show the SHRIMP transects, and white tracks show the HyBIS transects. White circles denote lithology sampling locations, letters correspond to the ROV images in Figure 4.26 and profile locations in Figure 4.28.

The eastern, southern and western FRZs are separated by deep embayments caused by slope failures. The western FRZ is expressed as a narrow volcanic ridge, with steep flanks and lava flows issuing from the summit of the ridge. The other FRZs have broader

ridges and have multiple volcanic cones, lava terraces and flow structures. Three of the ridges are characterised by high backscatter in accordance with their volcanic substrate surrounded by a low backscatter region, interpreted as a volcanic ash apron at the base of the steep volcanic flanks (shown in Figure 4.9). The low backscatter observed on the lava terrace on the northern FRZ corresponds to blocky jointed lavas observed on ROV imagery, which scatter the acoustic signal.

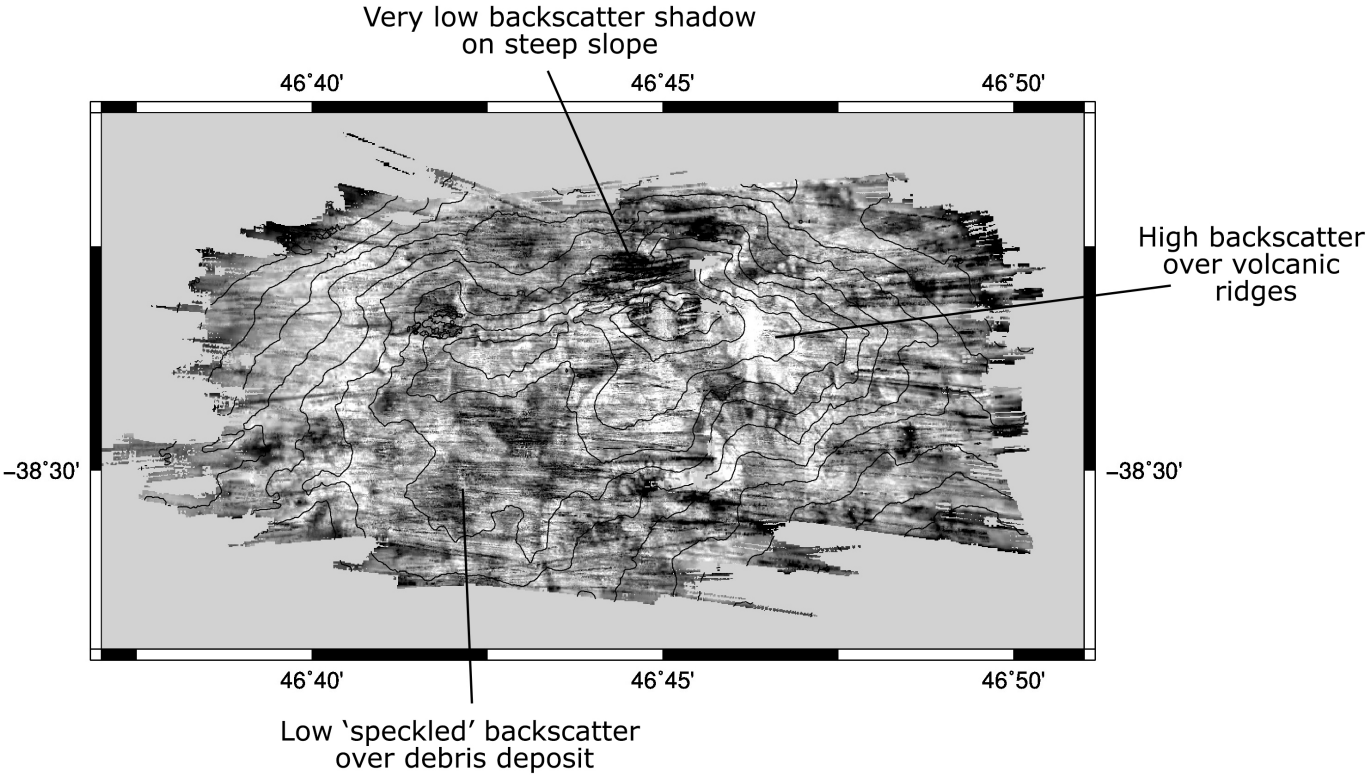


Figure 4.9: 12 kHz backscatter sonar of Melville Bank. Dark shades are low backscatter, light shades are high backscatter. Bathymetric contours at an interval of 200 m are overlain.

A number of slope failures are evident from the bathymetry; a major embayment on the southwest flank and several minor embayments in the northwest and northeast flanks, shown in Figure 4.8. The source areas on the edifice are all defined by smooth high backscatter embayments in the edifice, often preceded upslope by an arcuate headscar between 0.9 and 1.5 km across. These embayments widen downslope to form wide smooth depressed chute structures, sometimes bound by volcanic ridges.

The northwest and northeast slope failures show a reversal in bathymetric contours downslope, indicating a debris deposit. The large slope failure on the southwest flank exhibits lobate contours outlining a hummocky debris field approximately 250 m thick. All three debris fields coincide with low 'speckled' backscatter. Some larger boulders up to 40 m across are visible on the bathymetry. The total volume of the slope failure, estimated by comparing profiles from the slope failure sector and adjacent unfailed volcanic flank sectors, is 1.25 km^3.

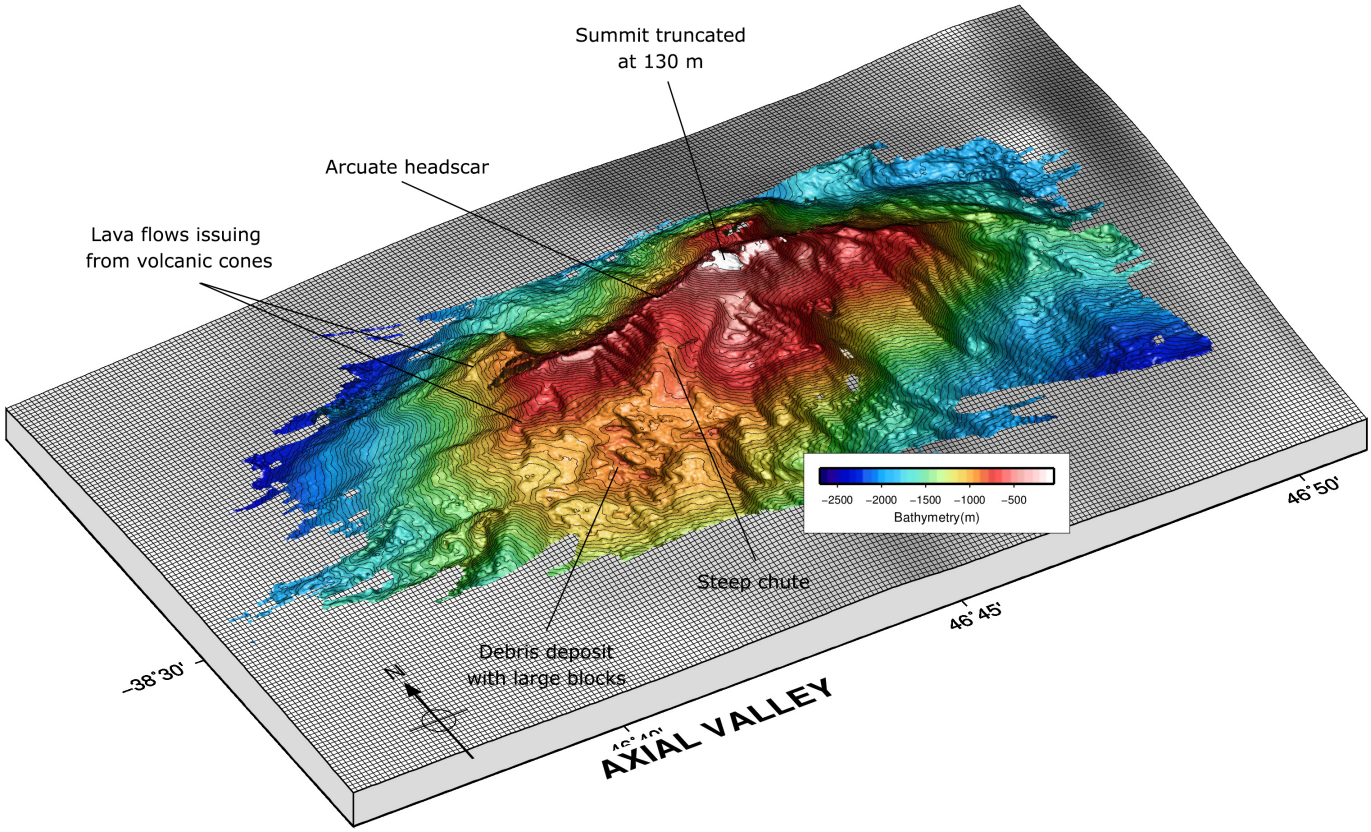
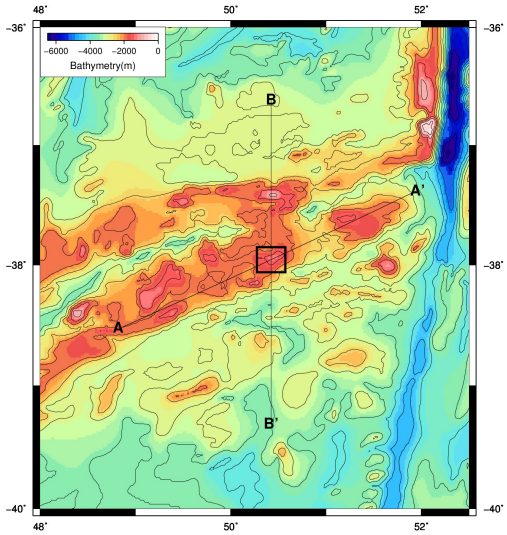


Figure 4.10: Perspective view of Melville Bank from the southwest (azimuth 210°, elevation 40°). The mesh grid shows the regional bathymetry derived from the GEBCO 2014 30'' x 30'' global bathymetry grid (IOC et al., 2003). The coloured image shows the shipboard bathymetry from cruise JC066. The bathymetry data have been illuminated by an artificial sun in the southwest and the contour interval is 25 m.

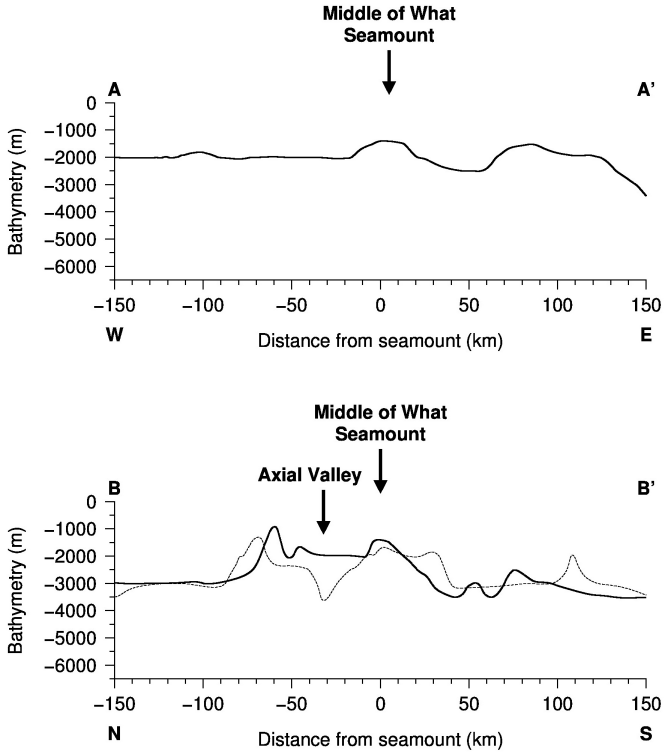
No linear tectonic structures such as fault traces were observed on this seamount, though they may be obscured by volcanism or sediment cover.

4.3.3 Middle of What Seamount

Middle of What Seamount (37.958° S, 50.416° E) is situated 30 km south of the axial valley, and forms part of the axial rim mountains, shown in Figure 4.11. Unlike the other seamounts, Middle of What is located on a mid-segment over 200 km from the nearest transform fault. The ridge axis shows a relative axial high adjacent to the seamount, an increase of approximately 1700 m above the surrounding axial valley depth. Swath bathymetry and backscatter data were acquired over the seamount.



(a) Bathymetry from the GEBCO 2014 30'' x 30'' global bathymetry grid (IOC et al., 2003) of the region surrounding Middle of What Seamount. The black box marks the location of Middle of What Seamount; the lines A-A' and B-B' mark the locations of the context profiles in Figure 4.11b.



(b) Bathymetric profiles derived from sampling the GEBCO 2014 30'' x 30'' global bathymetry grid (IOC et al., 2003) along a ridge parallel azimuth (A-A') and a transform parallel azimuth (B-B') intersecting at Middle of What Seamount (see Figure 4.11a for profile locations). The dotted line shows the average regional profile, since the axial valley near Middle of What Seamount is partially filled due to anomalous volcanism. Major topographic features are labelled.

Figure 4.11: Bathymetry map and bathymetric profiles showing Middle of What Seamount in regional context.

Middle of What Seamount, shown in Figure 4.12, has an elliptical geometry, is dissected

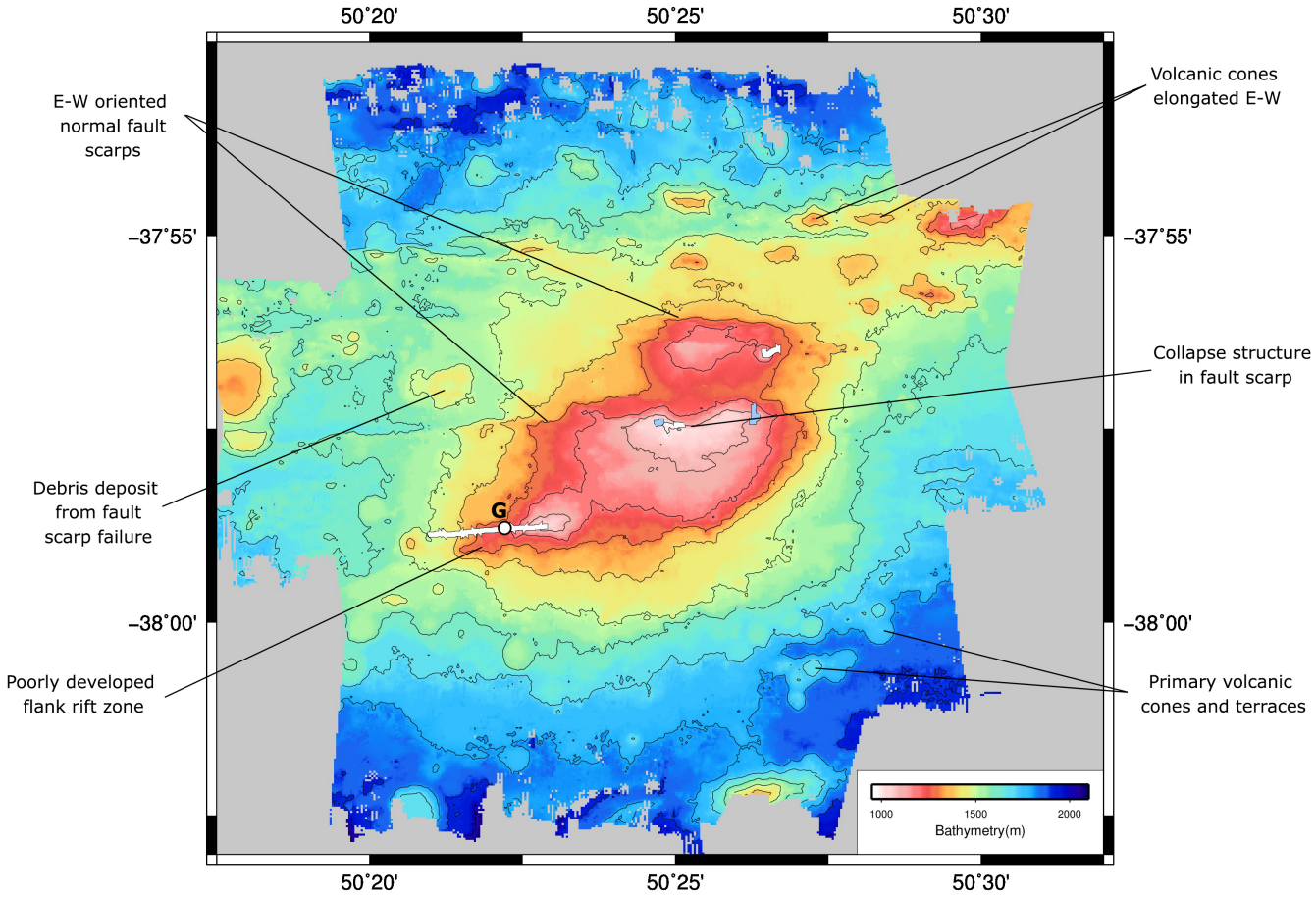


Figure 4.12: Bathymetry map (contour interval 100 m) of Middle of What Seamount from cruise JC066. Blue tracks show the ROV transects, yellow tracks show the SHRIMP transects, and white tracks show the HyBIS transects. White circles denote lithology sampling locations, letters correspond to the ROV images in Figure 4.26 and profile locations in Figure 4.28.

by a series of normal faults, and extends 11.8 km from east to west and 8.8 km from north to south. Middle of What Seamount has much lower relief (1023 m) and a deeper summit (977 m depth) than the other seamounts. The summit has a domed morphology dipping at a gradient of 5° to the south. ROV imagery shows that the summit is covered with sediment. Summit relief consists of a small number of volcanic cones and a small east-west oriented fault scarp. The northern edge of the summit is linearised due to a large normal fault separating it from a secondary eruptive centre to the north.

The north and south flanks show different morphological features, though the slopes

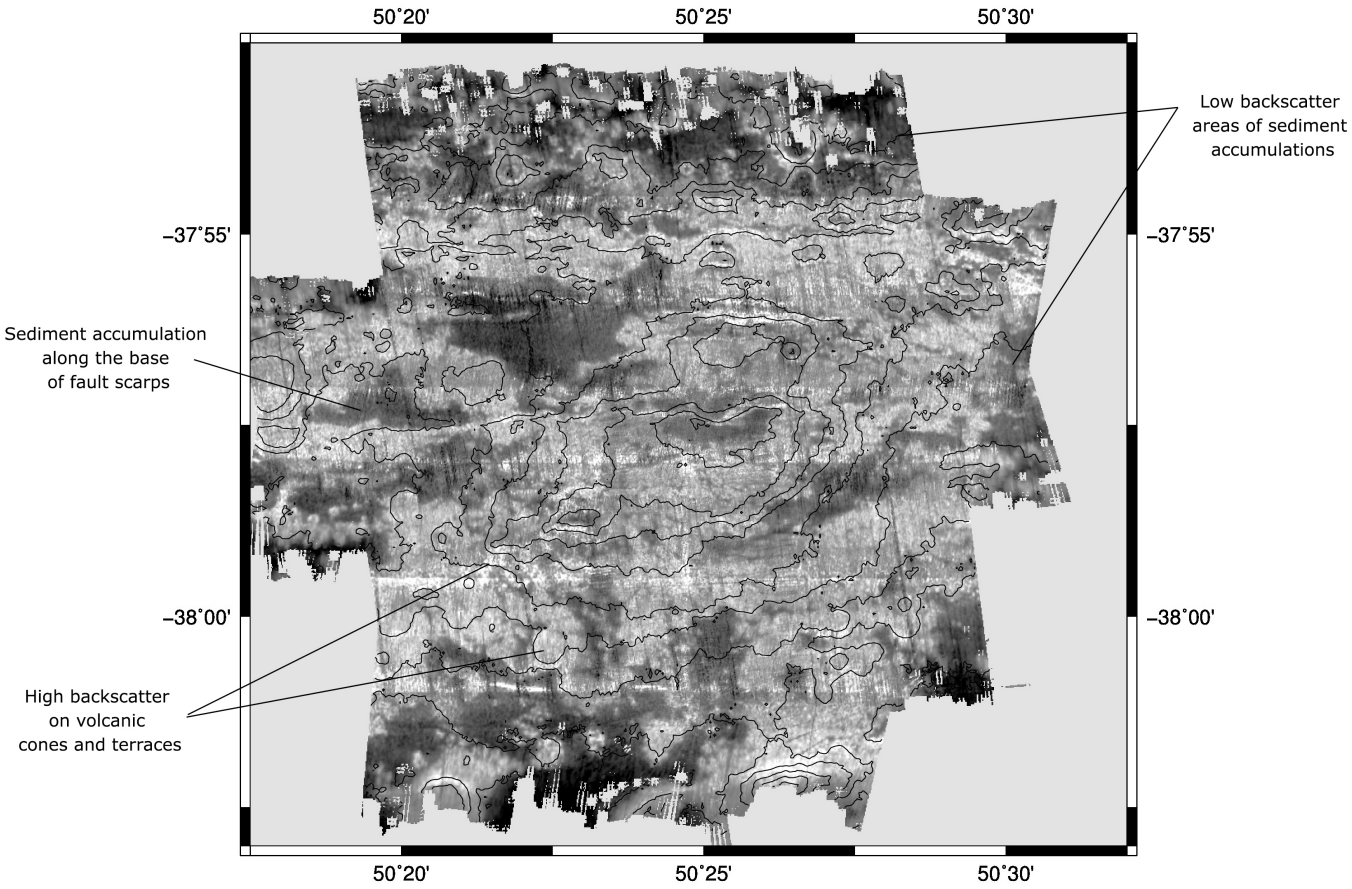


Figure 4.13: 12 kHz backscatter sonar of Middle of What Seamount. Dark shades are low backscatter, light shades are high backscatter. Bathymetric contours at an interval of 200 m are overlain.

have similar gradients (5°). The southern flank consists of lobate lava terraces and volcanic cones, some with small summit craters, extending radially out from the summit.

These features are generally characterised by high backscatter, particularly the volcanic cones, however areas of low backscatter may distinguish areas of sediment accumulation, shown in Figure 4.13. Very strong currents were experienced by the ROV at this seamount; these aid in the transport of sediment, which collects at the base of fault scarps. The southwest flank of the seamount exhibits a small ridge representing a flank rift zone in the early stage of evolution.

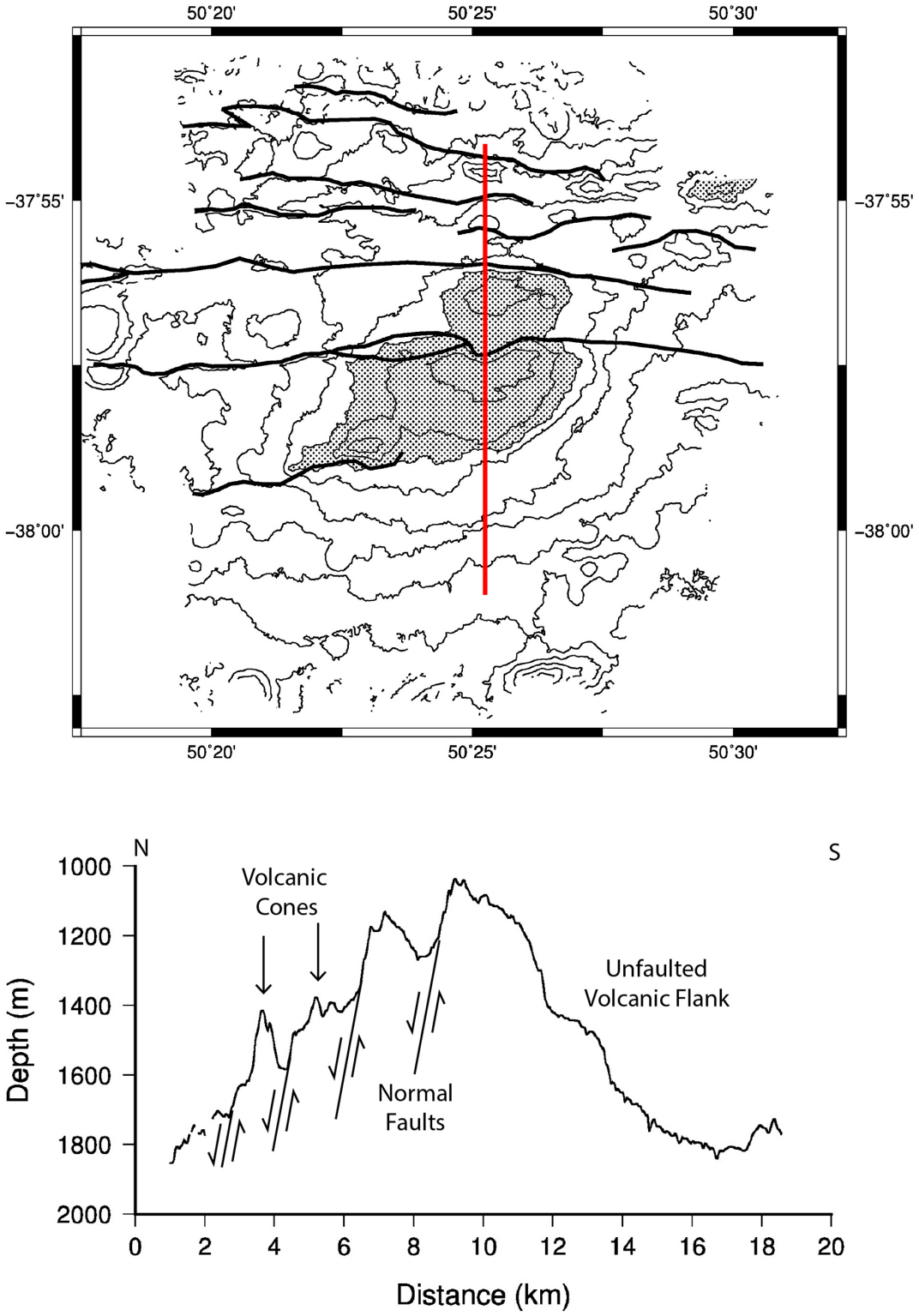


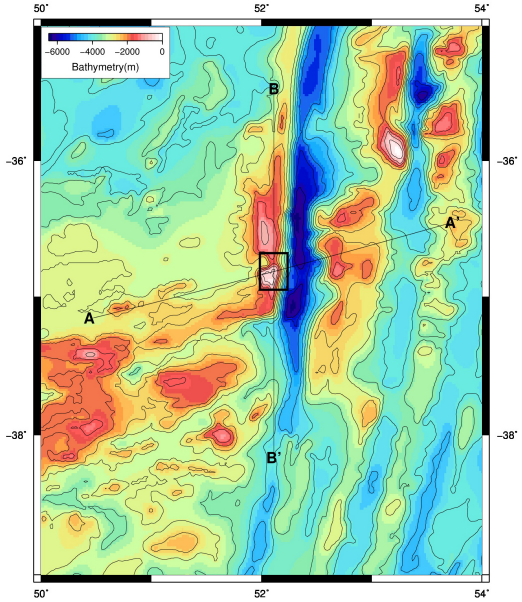
Figure 4.14: Upper panel shows a tectonic interpretation map of Middle of What Seamount. Bathymetric contours (thin black lines) are plotted at 100 m intervals. Thick black lines show the positions of faults inferred from bathymetry, backscatter and slope maps. Summit bathymetry (above 1300 m depth) is shaded to show the dissection of the summit regions due to faulting. Lower panel shows a bathymetric profile across the seamount along the red line on the map. Faults and volcanic cones are labelled.

The northern flank, in contrast, is dominated by a large number of east-west trending (axial valley parallel) normal faults, dissecting the original volcanic morphology (shown in Figure 4.14). The three major normal faults across the summit area have fault scarps measuring 230 m, 180 m and 90 m in height, and are normal faults with the downthrown side to the north. Some cone structures are cut through by faults while some are not, indicating that volcanic activity occurred both before and after faulting. Volcanic cones on the northern flank are elongated east-west and are aligned with the east-west trending fault trace suggesting these faults act as magma conduits. The abundance of normal faults on the northern flank and absence on the southern flank is similar to the fault patterns observed at sub-aerial volcanoes such as Fieale in the Asal Rift of the East African Rift zone (De Chabalier and Avouac, 1994; van Wyk de Vries and Merle, 1996). These fault patterns result from the tectonic dismemberment of the edifice during spreading separating the original edifice into two edifices, which move apart during spreading, retaining the original volcanic morphology on the furthest flank. Middle of What Seamount is situated approximately 30 km south of the axial valley, and regional bathymetry derived from the GEBCO 2014 grid (IOC et al., 2003) (Figure 4.11) shows a corresponding high 30 km north of the axial valley, possibly originally part of the edifice prior to separation during spreading. This symmetrical pattern resulting from the dismemberment of a volcanic edifice in the axial valley has been observed at other mid-ocean ridge seamounts, such as the Lucky Strike seamount on the Mid-Atlantic Ridge (Escartín et al., 2014).

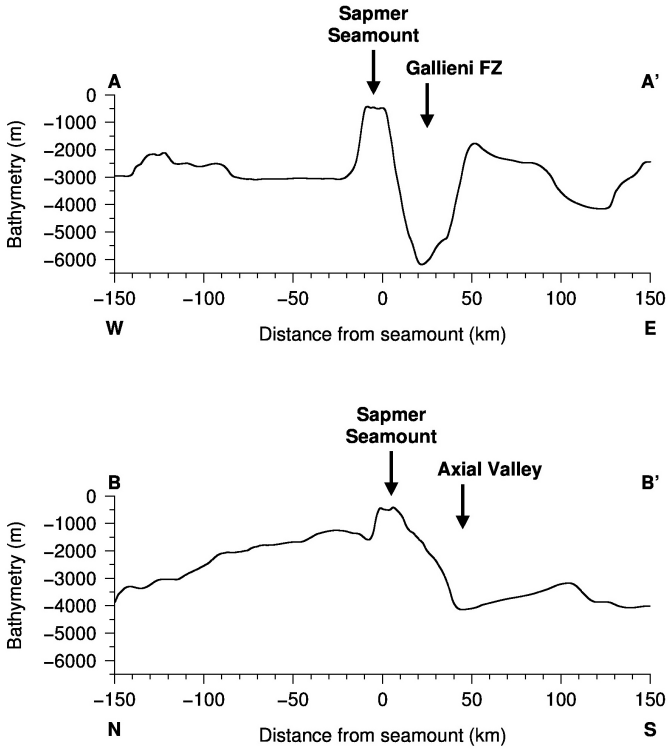
No major slope failure features are observed on this seamount. A small arcuate depression in the fault trace of the largest fault is interpreted as a small slope failure, possibly caused by a splay in the main fault. The subparallel fault blocks have channelled the resulting debris westward to form a deposit defined by an area of low backscatter northwest of the summit.

4.3.4 Sapmer Bank

Sapmer Bank (36.816° S, 52.116° E) is situated on the inside transform corner on the west flank of the Gallieni transform, shown in Figure 4.15. This seamount forms part of the high topography associated with the intersection of the transform fault and mid-ocean ridge axis, which lies 50 km south of the seamount. Swath bathymetry and backscatter data were acquired over the seamount.



(a) Bathymetry from the GEBCO 2014 30'' x 30'' global bathymetry grid (IOC et al., 2003) of the region surrounding Sapmer Bank. The black box marks the location of Sapmer Bank; the lines A-A' and B-B' mark the locations of the context profiles in Figure 4.15b.



(b) Bathymetric profiles derived from sampling the GEBCO 2014 30'' x 30'' global bathymetry grid (IOC et al., 2003) along a ridge parallel azimuth (A-A') and a transform parallel azimuth (B-B') intersecting at Sapmer Bank (see Figure 4.15a for profile locations). Major topographic features are labelled.

Figure 4.15: Bathymetry map and bathymetric profiles showing Sapmer Bank in regional context.

Sapmer Seamount, shown in Figure 4.16, has a roughly rectangular geometry, modified by a slope failure on the southeast flank and flank rift zones forming volcanic ridges to the north and south. The seamount extends 17.2 km from north to south and 13.5 km

from east to west at its widest point.

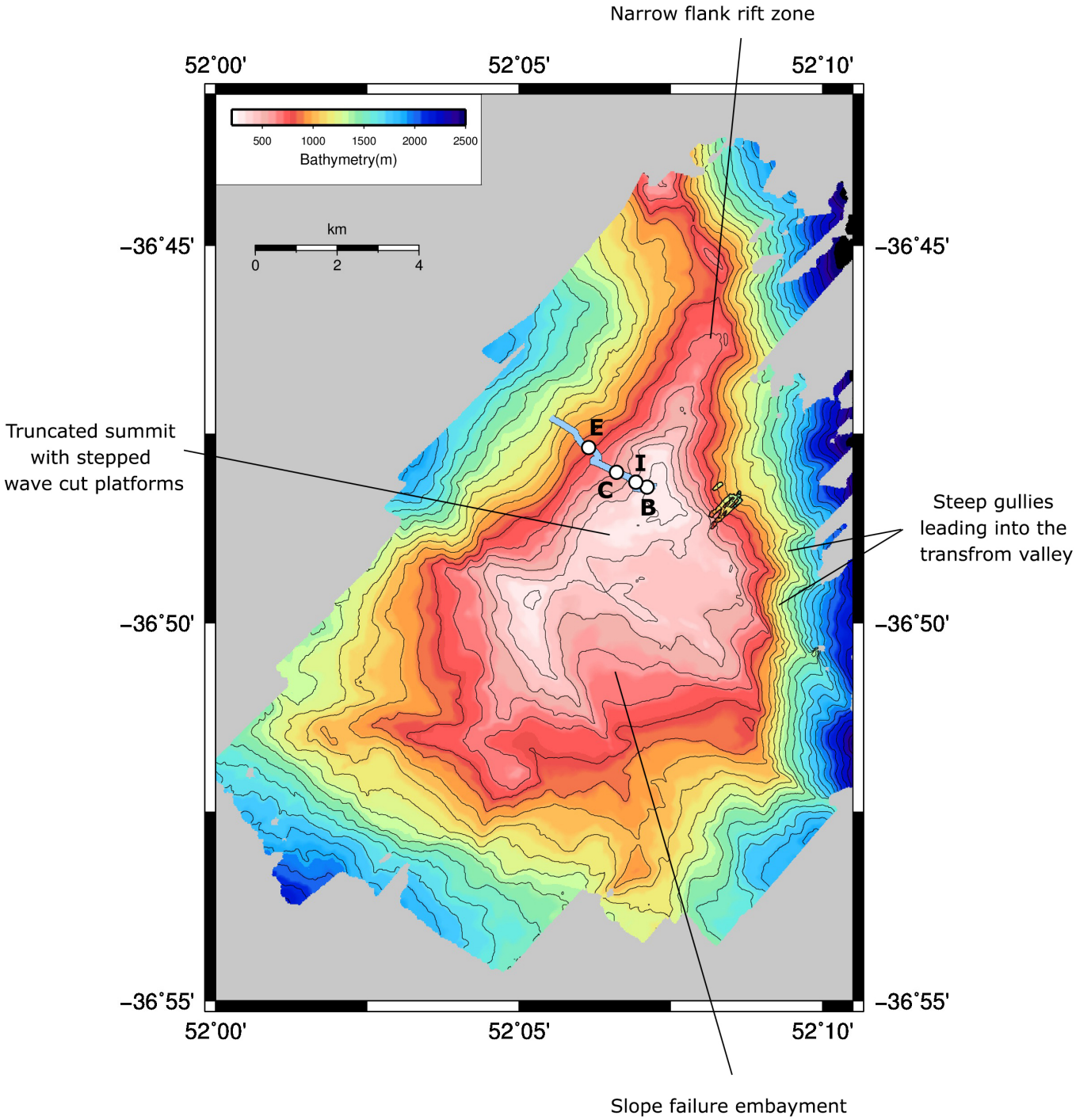


Figure 4.16: Bathymetry map (contour interval 100 m) of Sapmer Bank from cruise JC066. Blue tracks show the ROV transects, yellow tracks show the SHRIMP transects, and white tracks show the HyBIS transects. White circles denote lithology sampling locations, letters correspond to the ROV images in Figure 4.26 and profile locations in Figure 4.28.

The summit is defined by a break in slope at 350 m depth, which leads to a summit dipping 4° to the southeast. The summit is characterised by high backscatter, which corresponds to a consolidated carbonate platform observed on ROV imagery. The summit has significant local relief with two domed areas approximately 60 m high, separated by a small saddle ridge, which forms the top of an embayment in the edifice.

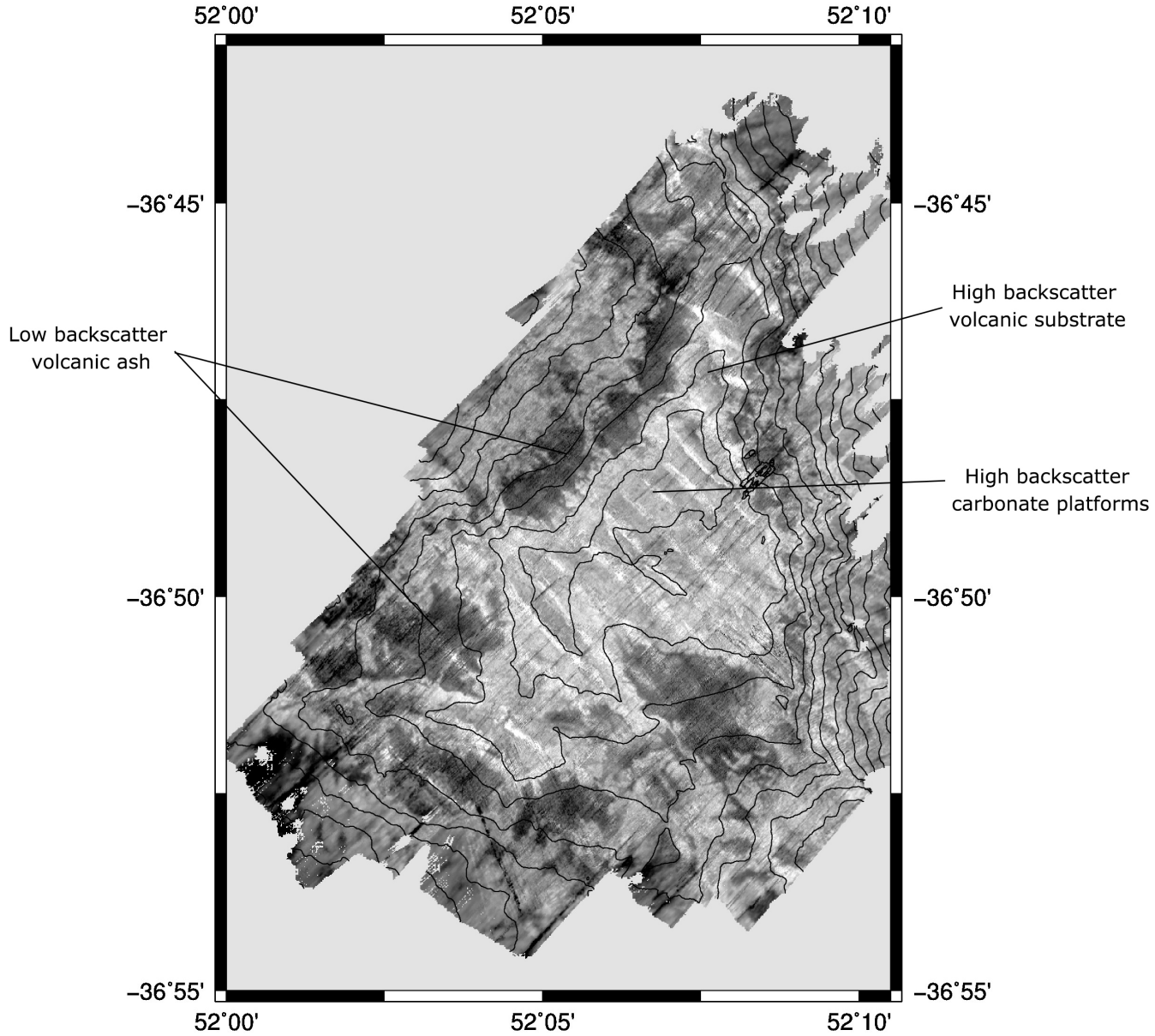


Figure 4.17: 12 kHz backscatter sonar of Sapmer Bank. Dark shades are low backscatter, light shades are high backscatter. Bathymetric contours at an interval of 200 m are overlain.

The gradient of the flanks differ significantly across the seamount. The steep east flank (20°) to 30°) is situated directly adjacent to the Gallieni transform and is probably oversteepened due to flexure associated with thermal bending moments on the margins of the transform (Parmentier and Haxby, 1986).

This eastern flank shows numerous lava flows issuing from the volcanic cone at the tip of the central ridge, extending southeast from the main summit. Small indentations in relief, between 5 m and 30 m are interpreted as small volume slope failures, though no debris deposits are observed due to the adjacent transform valley. The west flank, which has a less steep gradient (15°) to 20°), has a smooth morphology due to unconsolidated sediment cover. ROV imagery shows that this sediment is a fine volcanic ash. This corresponds to an apron of low backscatter, which forms a band around the seamount between 600 m and 1000 m. The radial nature of this deposit at a constant depth suggests that this is a fall deposit from explosive volcanism occurring in shallow submarine eruptions. A number of linear indentations on the west flank, shown in Figure 4.18, approximately 60 m in depth, may be surface expressions of buried faults, which trend northwest-southeast, oblique to the ridge and transform.

The southeast flank is significantly modified by slope failure processes. An arcuate headscar, extending 180° around the top of the feature and measuring 2.5 km across, dominates the southeast flank. This slope failure does not show the same characteristic slope failure features observed at other seamounts in this study or elsewhere (Moore et al., 1989; Masson et al., 2002; Mitchell, 2003). The embayment is broad and shallow, lacking a steep chute or debris field, though this would most likely be lost in the adjacent transform valley. The extensive rim suggests that this may have been a large caldera, which has subsequently collapsed on the southeast side.

Sapmer Seamount exhibits a number of flank rift zones expressed as volcanic ridges. A narrow ridge extends north-northeast, following the trend of the main edifice, before bending round to the northwest at the northern tip. A series of broader northwest-southeast trending flank rift zones intersect the main edifice forming a series of volcanic

ridges with volcanic cones at the tip.

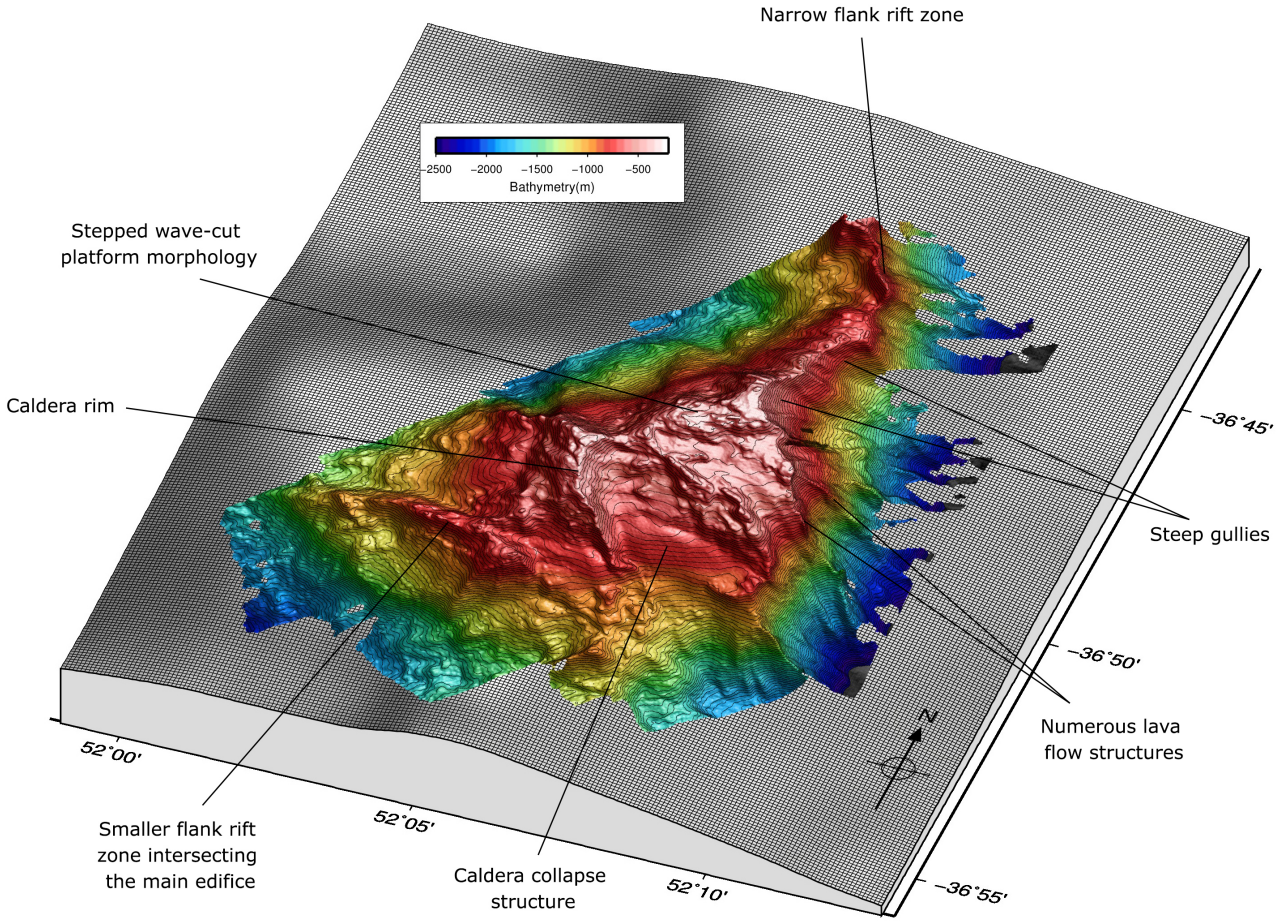
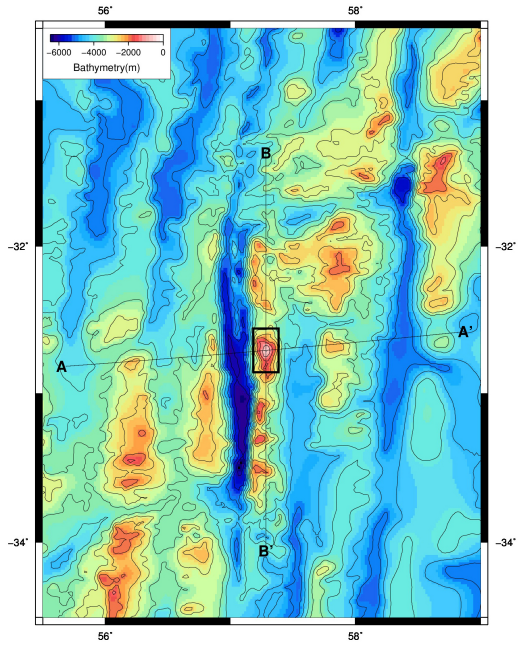


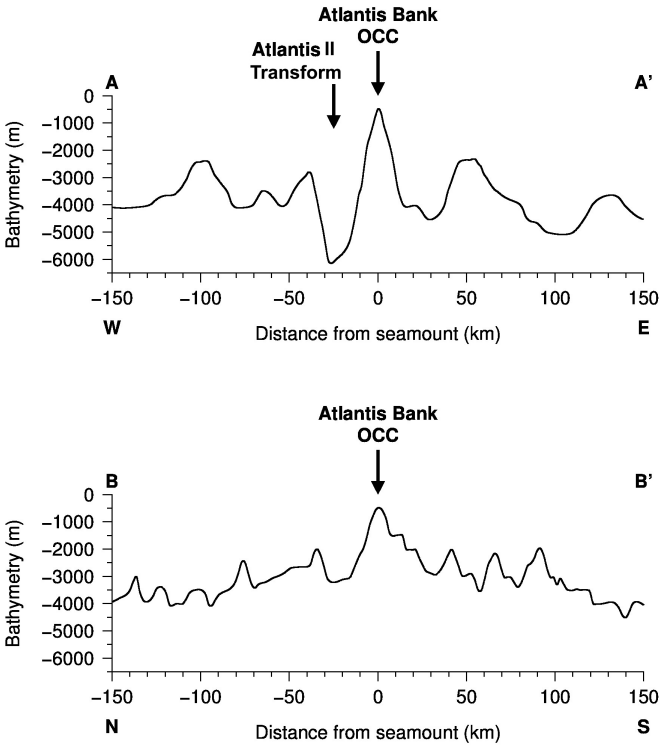
Figure 4.18: Perspective view of Sapmer Bank from the south (azimuth 160°, elevation 40°). The mesh grid shows the regional bathymetry derived from the GEBCO 2014 30'' x 30'' global bathymetry grid (IOC et al., 2003). The coloured image shows the shipboard bathymetry from cruise JC066. The bathymetry data have been illuminated by an artificial sun in the northeast and the contour interval is 25 m.

4.3.5 Atlantis Bank

Atlantis Bank (32.708° S, 57.300° E) is a 12 Ma old plutonic oceanic core complex situated on the eastern flank of the Atlantis II transform (Dick et al., 2000), shown in Figure 4.19. The composition, structure and origin of Atlantis Bank have been well discussed in the literature (e.g. Dick et al., 2000; Baines et al., 2003; Muller et al.,



(a) Bathymetry from the GEBCO 2014 30'' x 30'' global bathymetry grid (IOC et al., 2003) of the region surrounding Atlantis Bank. The black box marks the location of Atlantis Bank; the lines A-A' and B-B' mark the locations of the context profiles in Figure 4.19b.



(b) Bathymetric profiles derived from sampling the GEBCO 2014 30'' x 30'' global bathymetry grid (IOC et al., 2003) along a ridge parallel azimuth (A-A') and a transform parallel azimuth (B-B') intersecting at Atlantis Bank (see Figure 4.19a for profile locations). Major topographic features are labelled.

Figure 4.19: Bathymetry map and bathymetric profiles showing Atlantis Bank in regional context.

2000). The work presented here is concerned with Atlantis Bank as a morphological feature and the volcanic, tectonic and erosional processes which affect it.

Atlantis Bank, shown in Figure 4.20, has an elongate geometry, initially broad in the north, narrowing to a ridge in the south. The domal morphology associated with normal detachment faulting at oceanic core complexes is truncated by a large transform parallel fault. This fault scarp is ∼700 m high, with a slope gradient between 45° and 30°, and extends at least 14 km along strike. ROV observations of the fault scarp reveal dark, tectonised rocks interpreted to be ultrabasic crustal lithologies. Previous submersible dives have observed striae and shingle structures, which indicate a normal sense of motion on these faults (Matsumoto et al., 2003). This fault does not show the

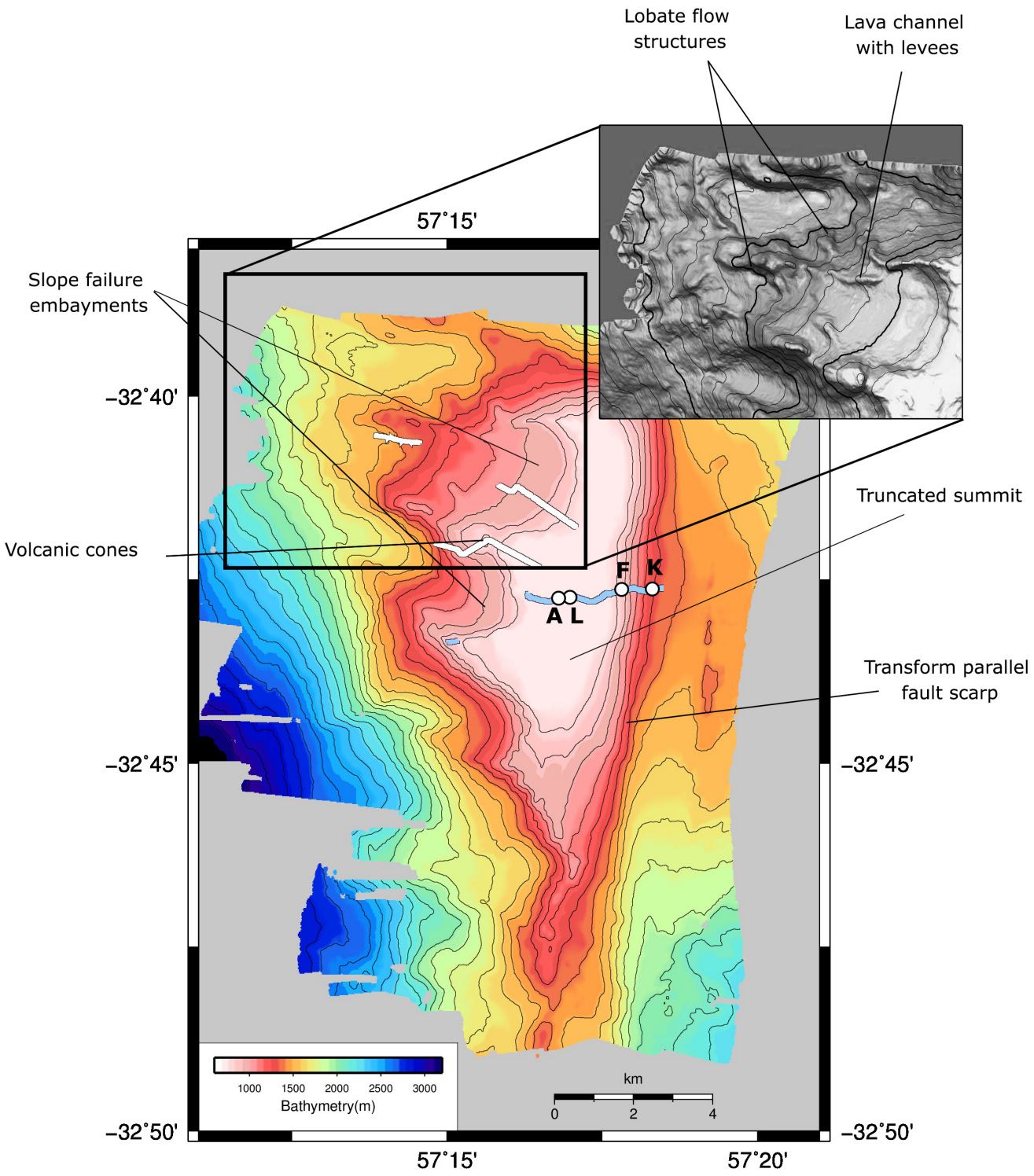


Figure 4.20: Bathymetry map (contour interval 100 m) of Atlantis Bank from cruise JC066. Blue tracks show the ROV transects, yellow tracks show the SHRIMP transects, and white tracks show the HyBIS transects. White circles denote lithology sampling locations, letters correspond to the ROV images in Figure 4.26 and profile locations in Figure 4.28. Inset shows greyscale bathymetry of northern slope failure illuminated by an artificial sun in the northwest showing small scale morphology.

corrugated surfaces observed on the E-W trending detachment fault (Macleod et al., 1998) to the north of the edifice (beyond the area of swath bathymetry). Regional bathymetry shows a second fault scarp to the east of the first. These form part of a series of transform parallel and perpendicular faults observed in the region surrounding Atlantis Bank (Baines et al., 2003).

The western flank of the seamount, which is the focus of this study, has been significantly modified by slope failure processes and has 4 embayments decreasing in size from 3.3 km across in the north to 1.2 km in the south. These embayments are characterised by arcuate headscars and steep embayed chute structures, shown in Figure 4.22. The northern and southern most embayments also show opposing convex and concave contours downslope of the chute, indicative of debris deposits. The backscatter data, shown in Figure 4.21, which is used to define the extent of slope failure debris deposits is less clear at Atlantis Bank than the other seamounts. There is an apron of low backscatter between 800 m and 1200 m, indicating unconsolidated sediments, which extend around the whole seamount, including the eastern fault scarp. The continuous nature and consistent depth of this low backscatter band is similar to the volcanic ash fall deposits observed at the other seamounts.

Downslope of the northern slope failure are areas of high backscatter, cutting across the low backscatter to form lobate structures. These high backscatter areas coincide with smooth bathymetry, defined by linear margins similar to the leveed lava channels observed on Hawaii (Clague et al., 2000).

ROV imagery of sheet lavas confirms the interpretation of these high backscatter areas as volcanic extrusive lithologies, issuing from the cone structures either side of the slope failure. Geological evidence has suggested that magmatism persists during active detachment faulting, though the exact relationship between magmatism and tectonism is still unclear (MacLeod et al., 2009). Studies suggest that magma intrusion at oceanic core complexes is preferentially accommodated by intrusive activity (Olive et al., 2010) with a large proportion (20 to 40%) of the magma captured in the detachment footwall

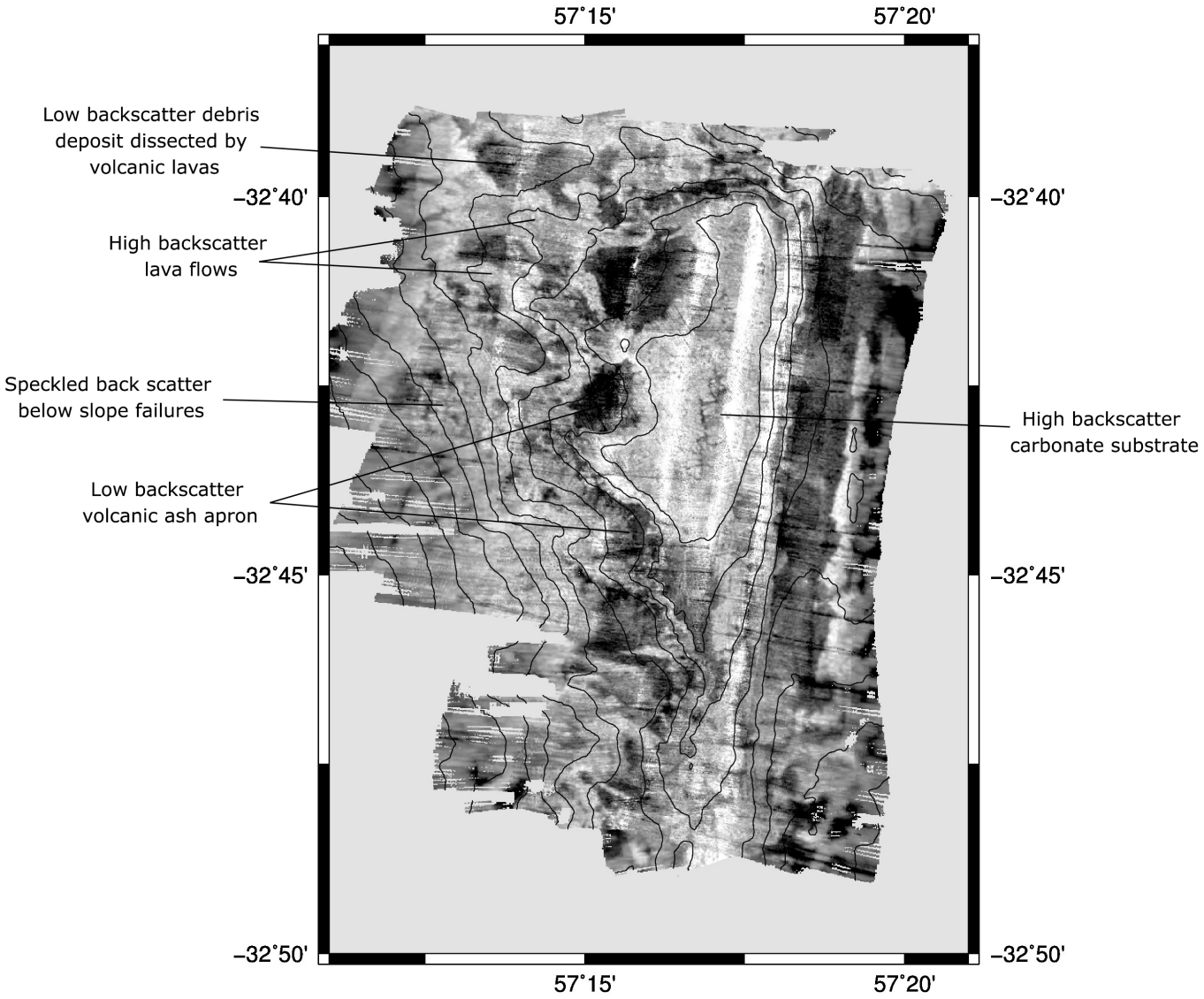


Figure 4.21: 12 kHz backscatter sonar of Atlantis Bank. Dark shades are low backscatter, light shades are high backscatter. Bathymetric contours at an interval of 200 m are overlain.

(Kelemen et al., 2007). The presence of extrusive volcanic structures on the western flank of Atlantis Bank, however, is clear evidence of extrusive volcanism at an oceanic core complex. This is likely due to the large network of major strike slip and normal faults observed around Atlantis Bank (Baines et al., 2003), which provide multiple pathways for magma to ascend to the surface.

The summit of Atlantis Bank is truncated at a depth of 700 m with a small amount

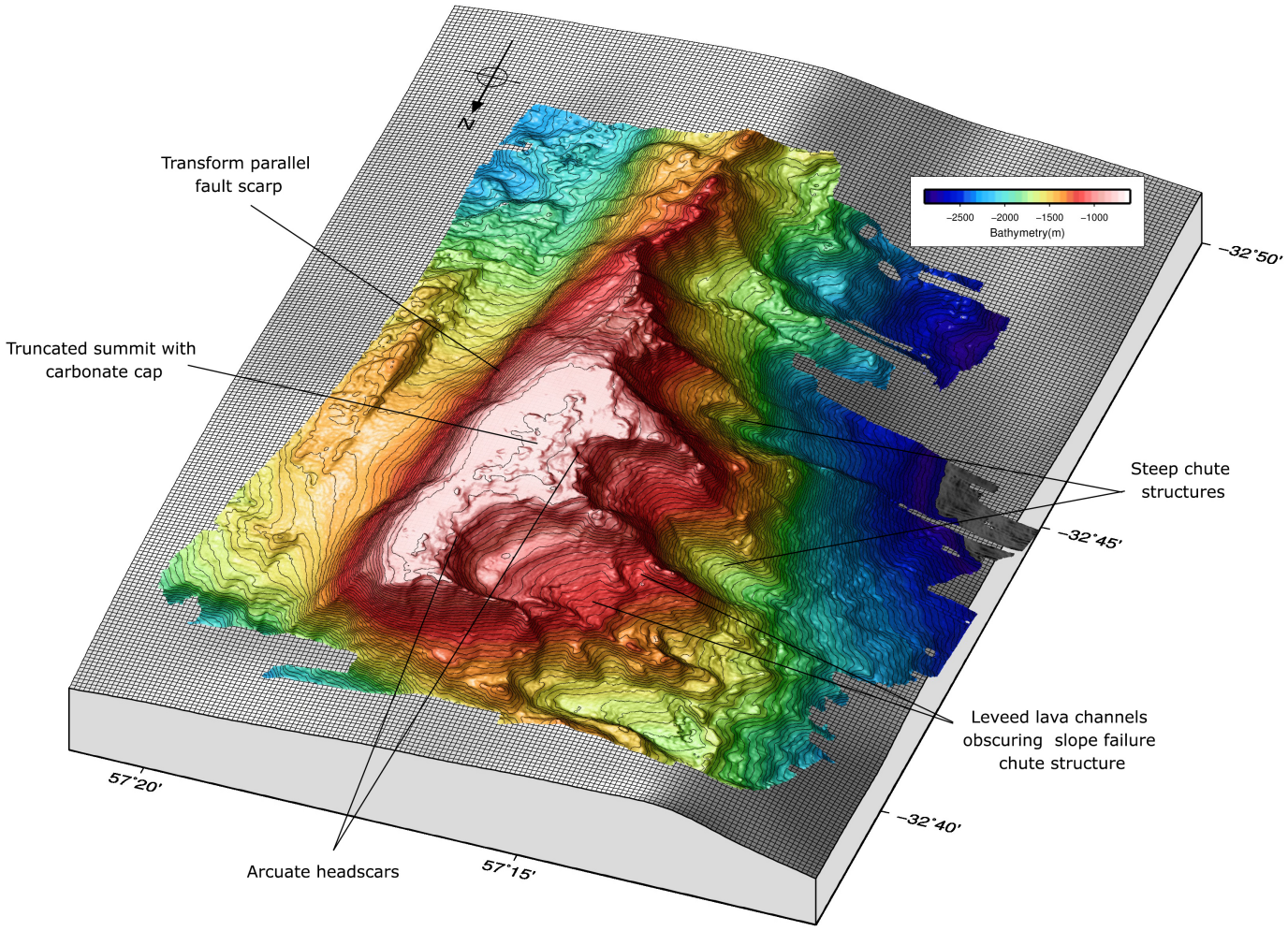


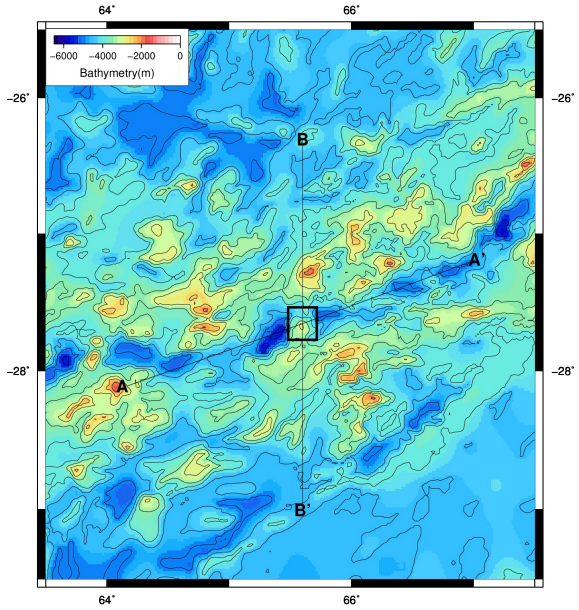
Figure 4.22: Perspective view of Atlantis Bank from the south (azimuth 160°, elevation 40°). The mesh grid shows the regional bathymetry derived from the GEBCO 2014 30'' x 30'' global bathymetry grid (IOC et al., 2003). The coloured image shows the shipboard bathymetry from cruise JC066. The bathymetry data have been illuminated by an artificial sun in the northeast and the contour interval is 25 m.

of local topography up to 20 m in height, increasing toward the centre of the summit. The summit is dominated by areas of bare rock covered in sediment observed on ROV imagery.

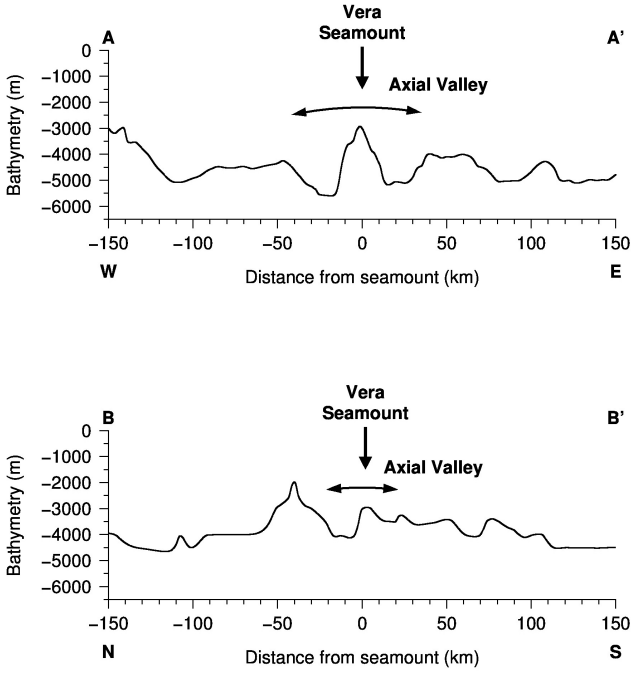
4.3.6 Vera Seamount

Vera Seamount (27.650° S, 65.616° E) is situated on the Southwest Indian Ridge crest in the axial valley. The seamount spans the width of the axial valley forming a shallow

point on the axis, shown in Figure 4.23. Swath bathymetry and backscatter data were acquired over the seamount.



(a) Bathymetry from the GEBCO 2014 30'' x 30'' global bathymetry grid (IOC et al., 2003) of the region surrounding Vera Seamount. The black box marks the location of Vera Seamount; the lines A-A' and B-B' mark the locations of the context profiles in Figure 4.23b.



(b) Bathymetric profiles derived from sampling the GEBCO 2014 30'' x 30'' global bathymetry grid (IOC et al., 2003) along a ridge parallel azimuth (A-A') and a transform parallel azimuth (B-B') intersecting at Vera Seamount (see Figure 4.23a for profile locations). Major topographic features are labelled.

Figure 4.23: Bathymetry map and bathymetric profiles showing Vera Seamount in regional context.

Vera Seamount, shown in Figure 4.24, is situated in the axial valley rising from the unusually deep axial valley depth of 5000 m to 2734 m at the summit. This seamount spans the width of the axial valley, extending 12 km from north to south and 22 km from east to west. The young age of this seamount reveals detailed small scale volcanic constructive features, which are obscured by sediment cover at the older seamounts in this study.

In contrast to small conical seamounts normally found in the axial valley, Vera Seamount, shown in Figure 4.25, shows complex morphology with numerous flank rift zones (FRZs). FRZs extend east, south-southwest and northwest from the main edifice,

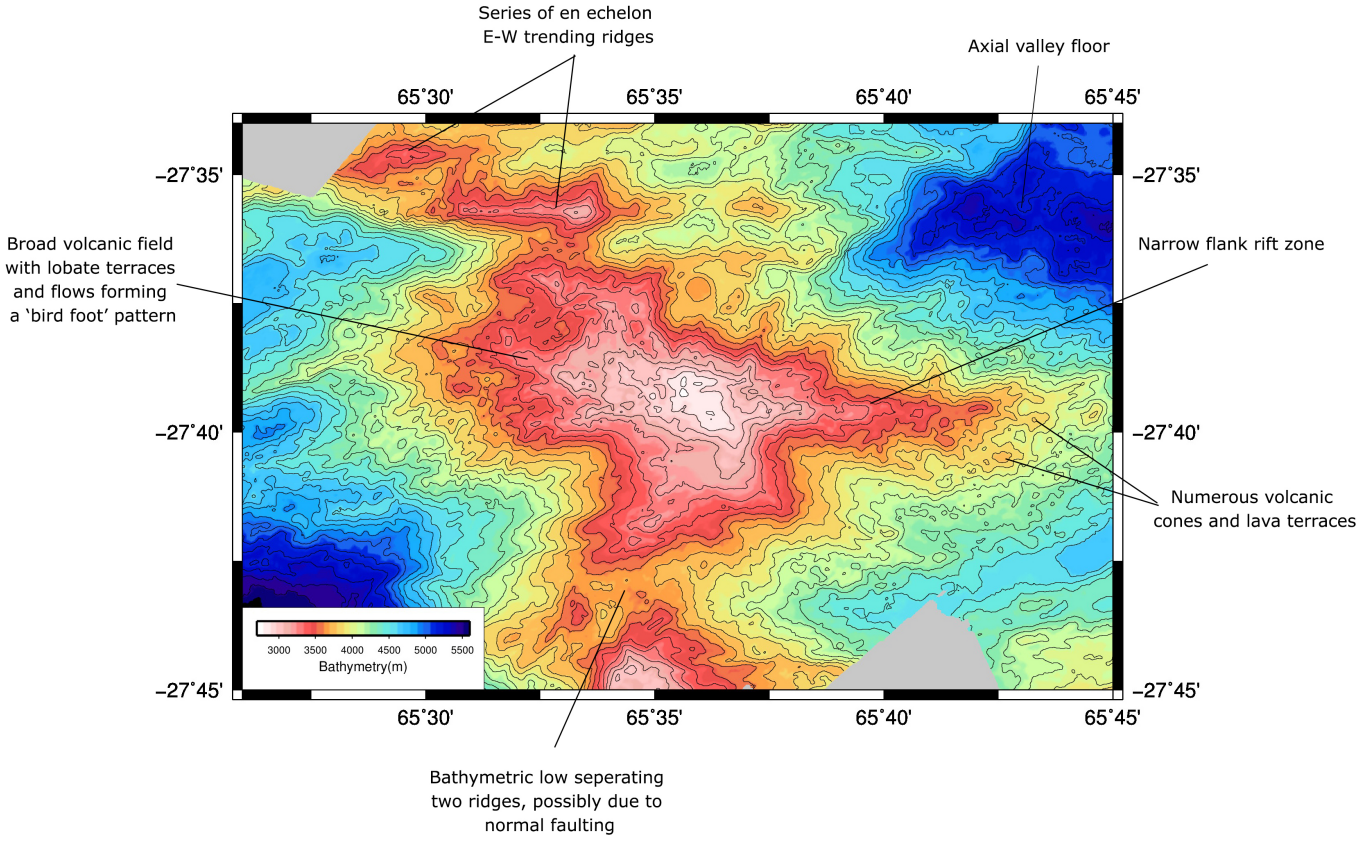


Figure 4.24: Bathymetry map (contour interval 100 m) of Vera Seamount from cruise MD192.

each with different morphological forms. The eastern FRZ is characterised by a 9.0 km long ridge, measuring 2.2 km across. The steep slopes of the eastern ridge along with small lava terrace and cone features are consistent with an intrusive dyke complex. This dyke complex forms the core of the ridge, which grows through inflation and fissure eruptions as seen at the Puna Ridge in Hawaii (Smith et al., 2002). The steep along-ridge gradient (87 m/km) is consistent with the longitudinal slope required to drive the dyke intrusion along the length of the rift (Fialko and Rubin, 1998). The east-west trend of this FRZ indicates that it is likely underlain by a ridge-parallel normal fault.

The south-southwestern FRZ is broader (4.3 km across) and extends only 6.9 km from the main edifice. A topographic high to the south of the seamount is most

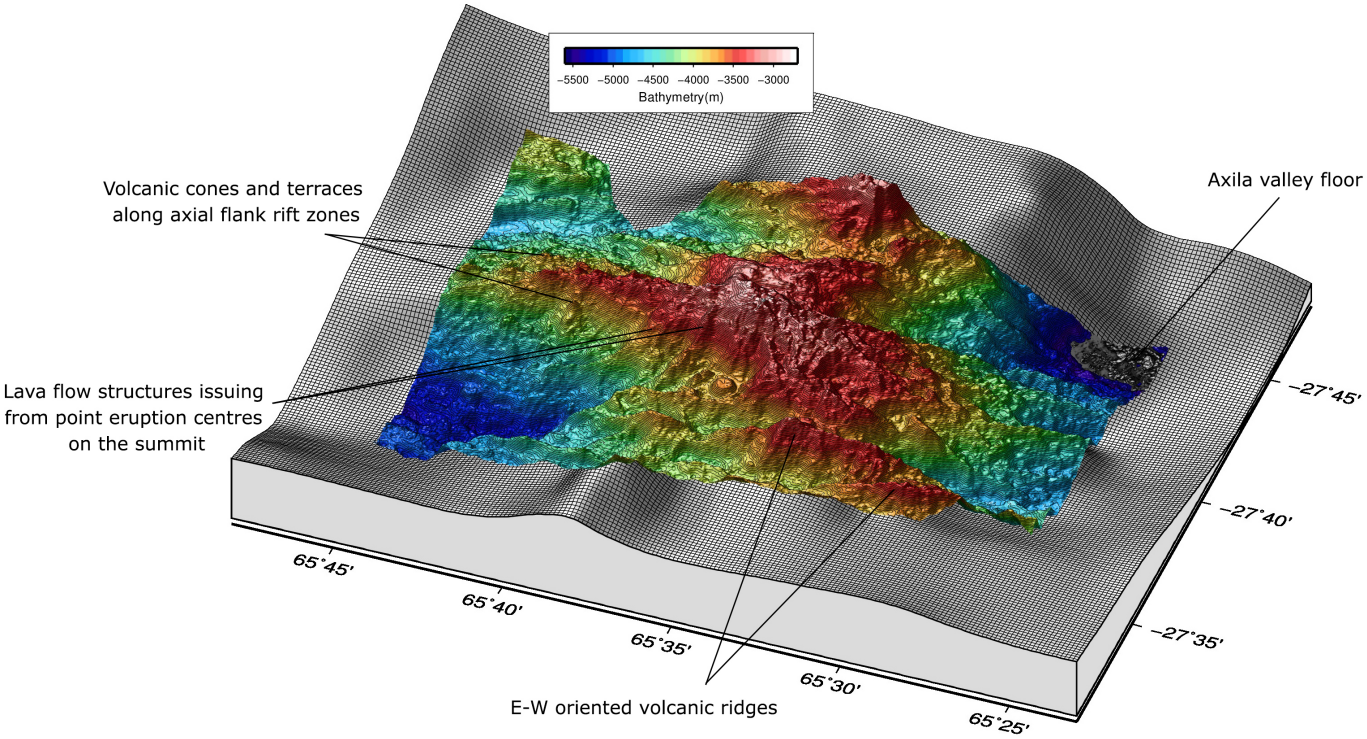


Figure 4.25: Perspective view of Vera Seamount from the south (azimuth 160°, elevation 40°). The mesh grid shows the regional bathymetry derived from the GEBCO 2014 30'' x 30'' global bathymetry grid (IOC et al., 2003). The coloured image shows the shipboard bathymetry from cruise MD192. The bathymetry data have been illuminated by an artificial sun in the northeast and the contour interval is 25 m.

likely a continuation of this FRZ topography, dissected as the seamounts is pulled apart by normal faulting in the axial valley walls. The northwestern FRZ forms an elevated broad volcanic field, leading downslope to a number of small non-parallel flow structures spreading out along the lower flanks in bird-foot pattern. The numerous cones and small ridges are consistent with point source eruptions feeding lava flows, which travel downslope to build up this composite volcanic morphology.

The summit of the seamount consists of rough volcanic morphology forming two eruption centres capped by several volcanic cones up to 140 m high. The backscatter data, which have significant noise, bears no relation to the morphology observed in the bathymetry and are assumed to be a series of artifacts.

Table 4.1: Summary of SWIR study seamount characteristics

Seamount Name	**Location**	**Minimum Depth (m)**	**Shelf Break Depth (m)**	**Base depth (m)**	**Morphology**	**Tectonic Features**	**Backscatter (BS)**	**Crustal Age (Ma)**
Coral	41° 24' S, 42° 52' E	190	310	2700	N-S volcanic ridge. Broad summit with volcanics.	Transform parallel bend fault	N/A	6.1
Melville Bank	38° 28' S, 46° 45' E	107	130	2400	Predominant E-W volcanic ridge, smaller NNE-SSW ridges. Large slope failure on SW flank.		High BS defining volcanic ridges, low BS defining debris lobes from slope failures	7
Middle of What	37° 58' S, 50° 24' E	977	-	2000	Circular edifice with numerous volcanic cones and normal fault scarps	Numerous ridge-parallel normal faults	Mostly high BS, small areas of low BS defining areas of thick sediment	3.5

Sapmer Bank	36° 50' S, 52° 06' E	267	330	3000	Volcanic axial ridges trending NE-SW and NW-SE. Caldera collapse scar.	Shallow gullies possibly buried faults on the SW flank	High BS on the summit, low BS on the flanks with the exception of volcanic ridges	8
Atlantis Bank (OCC)	32° 43' S, 57° 17' E	700	750	3000	Linear edifice parallel to Atlantis II fracture zone. Significant slope failures on W flank	Transform parallel normal faults dissecting the E flank	Low BS below headscars, overlain downslope by areas of high BS	12 (Dick et al., 2000)
Vera Seamount	27° 42' S, 65° 36' E	2734	-	5300	Well developed flank rift zones, multiple volcanic cones and flows	Normal fault blocks at the N and S edges	Dominated by artifacts unrelated to the morphology	0

4.4 Morphological Features

Table 4.1 summarises the morphological features observed on the seamounts described above.

4.4.1 Surface Geology

The substrates on the seamounts were identified using backscatter analysis, ROV video imagery and petrological samples. There are three main types of substrate: sedimentary, igneous and biogenic.

Sedimentary Lithologies

Five main sedimentary substrates were observed on the seamounts, two consolidated lithologies: limestone and beach conglomerate; three non-consolidated lithologies: coarse clastic sand, fine volcanic ash and poorly sorted debris deposits.

Limestones were observed only on the summit and upper flanks of the seamounts (within 150 m of the shelf break) which also had truncated summits, corresponding to the photic zone when these seamounts were near the sea surface. These limestones were often associated with wave cut platform structures. In thin section these limestones show thick walled rotalids, agglutinates and fragments of algae indicating a benthic shallow water environment (Figure 4.27-1). Sparry calcite clasts lack zoning and appear to be primary phreatic features. The combination of juvenile and adult microfauna show that these limestones were not laid down in hydrostatic equilibrium indicating a moderately high energy environment. These observations are consistent with those made by Palmiotto et al. (2013), who concluded that the Atlantis Bank limestones were deposited on a 100 to 200 m deep platform, in a mixture of high and low energy environments. A sample of the limestone-igneous contact demonstrates that the limestone was laid down on cold igneous material as fragile thin walled globigerinoides are undeformed despite being millimetres from the contact (Figure 4.27-2). The distribution and petrology suggests that these shallow water limestones were formed on the seamounts which in the past emerged as volcanic islands. These limestone for-

mations are analogous to those found on other tectonically drowned islands, observed near the Vera and Romanche fracture zones in the Atlantic (Palmiotto et al., 2013). As shoreline erosion occurred, limestones formed on the flanks and the summit as it became fully submerged during subsidence. The stepped terraces observed at Sapmer Seamount (Figure 4.28) are a result of repeated stages of subsidence and limestone formation.

A clast rich conglomerate lithology was only observed at one location at the edge of the summit of Atlantis Bank. The rock is clast supported with dark pebble to cobble sized clasts presumed to be of igneous lithology (Figure 4.26-F). The clasts are well rounded with no preferred orientation apparent. This outcrop is interpreted as beach conglomerate formed by wave erosion of igneous clasts on a shoreline. The surrounding limestones and hydrothermal fluids provide ample sources for matrix cement. This lithology was not observed during sampling by Palmiotto et al. (2013) and may be very localised.

Of the three non-consolidated lithologies observed, the most ubiquitous was a coarse clastic sand (Figure 4.26-A). This sand was typically light coloured, gravel to sand sized and reasonably well sorted. This sand was often mixed with either biogenic rubble or rounded volcanic cobbles (Figure 4.26-B), which most likely result from wave erosion. This sand was observed at all depths and the distribution is likely to be primarily a function of strong currents, as demonstrated on Middle of What Seamount, where it has accumulated at the base of normal fault scarps (Figure 4.13).

A fine ash lithology was observed primarily on Sapmer Bank, Atlantis Bank and Coral Seamount. This light coloured sediment was very fine grained and formed a thick suspension in the water during coring operations using the ROV (Figure 4.26-E). These deposits occur in a band between 600 m and 1000 m depth (e.g. Figure 4.28) which corresponds to an apron of low backscatter surrounding the seamount (e.g. Figure 4.17). These are interpreted as fine material fall deposits from explosive phreatic eruptions. The lack of volcanic ash deposits above 600 m indicates that either vigorous

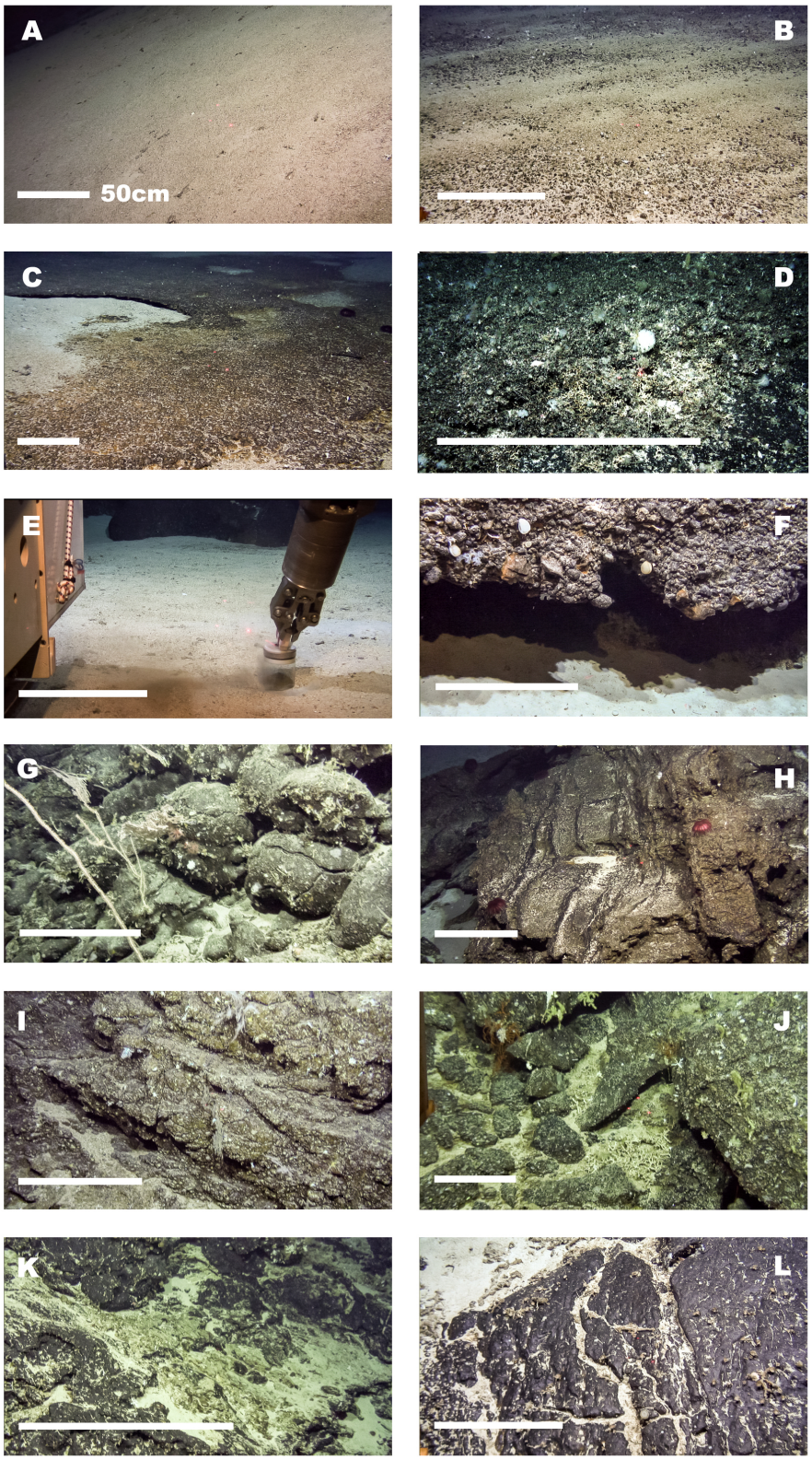


Figure 4.26: A series of still images taken from ROV video imagery showing some of the different substrates observed on the seamounts. The location of each image is shown on the bathymetry maps in the previous sections and ROV transect profiles in Figure 4.28. White scale bars are 50 cm long. (A) Coarse clastic sand (B) Sand with rounded volcaniclastic cobbles (C) Carbonate platform with surficial plates (D) Coral framework (E) Fine volcanic ash during coring operations (F) Beach conglomerate (G) Pillow lavas (H) Folded lava flows with banding (I) Intrusive gabbros (J) Angular volcanic tallus boulders (K) Tectonised gabbros (L) Dark fine grained rock, cut through by hydrothermal veins.

eruptions did not occur above this depth or that the deposits have since been eroded or overlain.

The final unconsolidated sediment type occurs in areas downslope of slope failures and consists of the edifice material, transported due to gravity following failure along a plane of weakness. These debris deposits are sometimes characterised by 'speckled' backscatter (Figure 4.9) due to thick accumulations of sediment mixed with large entrained boulders, as observed at other oceanic island slope failures (e.g. Masson et al., 2002). If thick enough, these poorly sorted deposits may correspond to a lobe-like feature on the bathymetry (Figure 4.10).

Igneous Lithologies

The majority of the igneous rocks observed on these seamounts are extrusive volcanic lavas which show a number of different morphologies including pillow lavas, lobate flows, folded flows, blocky lavas and leveed channels. Thin sections of these lavas show that they are fine grained holocrystalline basalts with plagioclase phenocrysts up to 2 mm in size (Figure 4.27-3). A number of these samples were significantly hydrothermally altered.

The different lava morphologies were not distinguishable using backscatter or bathymetry data except the very rough blocky lithology, which exhibited slightly lower backscatter, and large leveed lava channels, which could be identified using bathymetry data (Figure 4.20). The overall distribution of these different lava morphologies is, therefore, only known for areas sampled by ROV transects.

The majority of lava flows observed on the seamounts had a massive morphology with a smooth top surface, often occurring as bands or flows separated by sediments or coral substrate. These occurred ubiquitously across the seamounts.

Pillow lavas (Figure 4.26-G) had rounded elliptical structures, often piled on top of each other. Individual pillows ranged between 30 cm and 50 cm across and exhibited

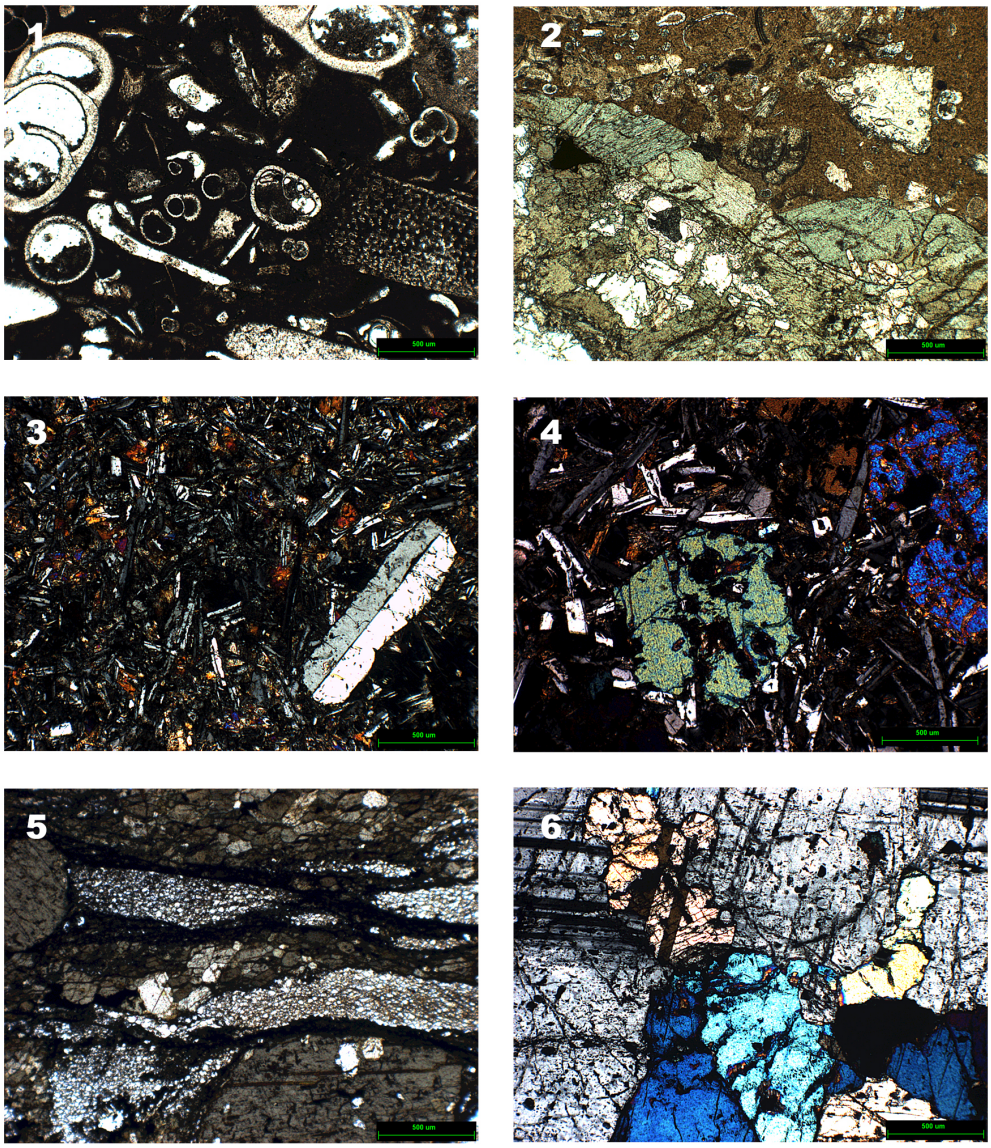


Figure 4.27: Photomicrographs of thin sections from lithological samples taken using the ROV grab arm and HyBIS rock grab. Scale is on the bottom right of each micrograph. (1) Fine grained limestone with thick walled benthic forams, molluscan material and algae fragments (2) Contact between limestone and altered gabbro (3) Tholeiitic basalt with plagioclase phenocrysts (4) Olivine dolerite with sub-euhedral resorbed phenocrysts (5) Tectonised gabbro with abundant amphibole (6) Coarse grained olivine gabbro.

characteristic curving cracks, remnants of the cooling crust cracking as further lava is injected into the pillow. Pillow lavas occur primarily on Middle of What Seamount (Figure 4.28) most likely due to the low slope gradients, which promote pillow lava formation (Gregg and Fink, 1995). The presence of pillow lavas suggests that volcanism

on this seamount had a relatively low effusion rate promoting the formation of pillow structures over lobate flows. Small areas of pillow lavas are observed on the gentlest slopes on Melville seamount, though these are small outcrops surrounded by lobate flows. Where the effusion rate increased or slope gradient exceeded 5° these pillow lavas gave way to lobate flows which form large irregular masses with a metre scale botryoidal surface texture.

Folded flows (Figure 4.26-H) exhibit metre-scale banding, formed as the advancing lava deforms the overlying thin crust into parabolic folds, with the hinge toward the flow direction (Batiza and White, 2000). These folded flows were only observed in three locations so their distribution on the seamounts is unclear; however wax analog experiments suggest that these morphologies form at intermediate flow rates and slope gradients of at least 10° (Gregg and Fink, 1995).

Massive blocky lavas with a very rough morphology were observed on several seamounts. These lavas are dominated by metre-scale fractures and joints between 5 cm and 10 cm wide forming irregular angular blocks between 0.5 m and 2 m wide. These blocky morphologies are primarily observed on the large flat lava terraces (Figure 4.28) slightly downslope from the summit, such as the terrace on the north side of Melville seamount. These may have formed due to contraction of lava ponds during cooling, though the fractures are not as regular as might be expected from cooling joints.

Large lava channels surrounded by levees are observable on swath bathymetry (Figure 4.20). The lavas observed form smooth sheets in the centre of the channel grading to tumbled chaotic morphology on the margins. This variation across the channel is caused by greater cooling of lava at the margins compared with the centre of the flow. These large lava channels occur primarily on steep slopes (>20°) and generally indicate high effusion rates (Gregg and Fink, 1995).

Intrusive rock outcrops are not common on the surface of the seamounts, with the exception of Atlantis Bank. These intrusive outcrops have a rough surface texture scattered with resistant phenocrysts and appear slightly green in colour. Thin sections

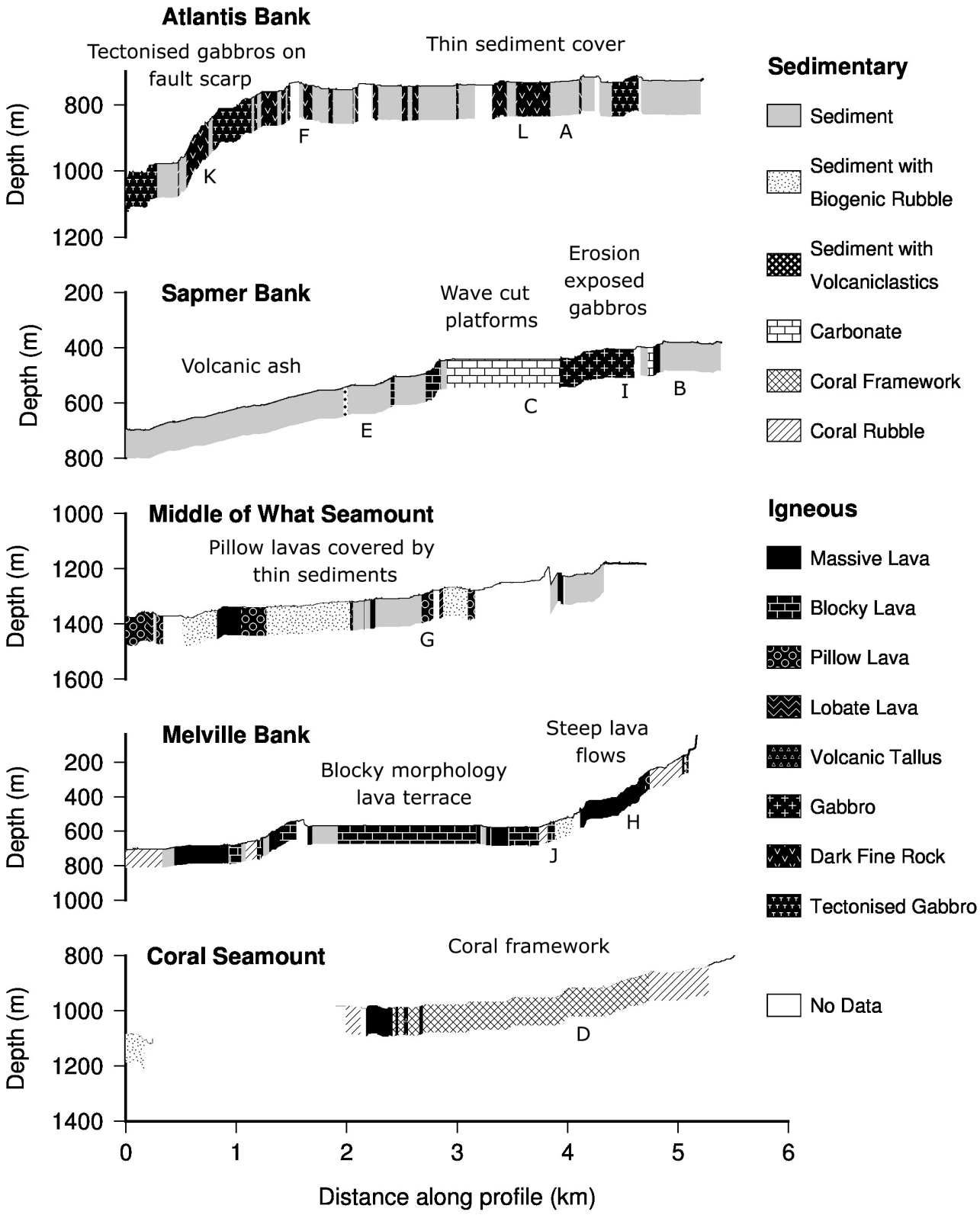


Figure 4.28: ROV transects across the five seamounts showing the different lithological interpretations based on ROV imagery and petrological samples. Locations of ROV transects are shown in the earlier seamount bathymetry maps. Lithological interpretations are draped over a topographic profile of distance along transect plotted against depth measured using a USBL on the ROV. Figure illustrates rock type on the seafloor only, with no constraints on lithology thickness. Letters correspond to the ROV images in Figure 4.26.

(Figure 4.27-4,6) show two main lithologies. (*i*) A holocrystalline medium grained dolerite with subhedral olivine phenocrysts showing resorption textures (*ii*) A holocrystalline coarse grained olivine gabbro with an anhedral texture. These two different lithologies may reflect either crystallisation at different depths or different parts of an intrusive structure such as a dyke, though the resorption texture observed in the olivine dolerite indicate different crystallisation depths. The outcrops occur primarily at the edge of wave eroded platforms on the summits of some of the seamounts such as Sapmer Seamount (Figure 4.28), where erosion has exposed the interior of the seamount. It is possible that slope failures have exposed intrusive lithologies along the chutes, however these features are generally covered by a thin layer of sediment.

Dredges and IODP drilling at Atlantis Bank, which is an oceanic core complex, have shown that the main edifice is composed of olivine gabbros, often with tectonised microstructures and hydrothermal veins (e.g. Dick et al., 2000; Kinoshita et al., 2001; Macleod et al., 1998). Peridotites have also been dredged high on the transform wall (Dick et al., 2000). Two lithologies were identified using ROV imagery, a fine grained dark rock (Figure 4.26-L) often cross cut with hydrothermal veins and a tectonised gabbro (Figure 4.26-J). The petrology of the fine grained dark rock is uncertain as no sample was obtained. In thin section (Figure 4.27-5) the tectonised gabbro shows strongly foliated bands of pyroxene and plagioclase, and a large proportion of amphibole suggesting the influence of hydrothermal fluids. The presence of fluids is further inferred from the rapid gradation from fine to coarse grained texture within the sample.

Biogenic Lithologies

The biogenic lithologies observed consisted of coral framework, formed of macroscopic skeletal framework (Figure 4.26-D), and biogenic rubble, which results from breakdown of the coral framework. These corals require hard substrates for attachment such as bedrock or cobbles (Rogers et al., 2007) indicating that areas of coral are most likely underlain by primary volcanic substrate. Deep sea corals are typically slow growing

and have the potential to live for thousands of years (Andrews et al., 2005) and so can, in theory, act as an indicator of recent volcanic and tectonic quiescence for any given slope section. A number of abrupt transitions from coral framework to bare slopes were initially thought to be indicators of transition between old volcanic morphology and slope failures or fresh volcanic flows. The subsequent discovery of trawling equipment and scrape marks on the seafloor led to the conclusion that these areas of the seamount were scraped clean by fishing trawlers, and the features observed are anthropogenic.

This section shows the distribution of sedimentary, igneous and biogenic lithologies on the seamounts. These lithologies are associated with bathymetric or backscatter characteristics, allowing the substrate interpretation to be extended beyond the ROV survey tracks. The lithology distributions across the seamounts are primarily controlled by depth, slope gradient and erosional processes such as sub-aerial erosion and slope failures.

4.4.2 Flank Rift Zones

Flank rift zones (FRZs) are well developed on most of the seamounts, expressed as linear ridges which define the seamount geometry. These rifts are expressed as three different ridge morphologies. Type 1: Steep sloped, narrow ridges extending away from the main edifice of the seamount with an average width-length ratio of 0.45; Type 2: Broad, short ridges adjacent to the main edifice with an average width-length ratio of 0.90; Type 3: Proto-ridges consisting of raised areas of discontinuous topography extending in a linear trend away from the seamount. Each seamount exhibits some combination of these three rift morphologies, except Middle of What Seamount which has only poorly developed type 3 proto-ridges.

The narrow type 1 ridges occur on four out of the five seamounts, and generally have rough volcanic morphology. On the seamounts situated on older crust, small-scale distinguishing features on these ridges are limited to small gullies and indistinct flow structures issuing from the summit of the ridge. This is likely due to pelagic drape

obscuring the original volcanic morphology. Vera Seamount, which is situated on much younger crust, lacks this pelagic drape and therefore allows us to examine the small scale volcanic morphology. The narrow type 1 ridge extending eastwards from Vera's summit, consists of a series of cones and terraces similar to those observed on the Puna Ridge, Hawaii (Smith et al., 2002). Individual cones range from conical to flat-topped and reach up to 200 m tall. A small number of narrow elongate structures on the ridge crest may have originated from fissure eruptions, or may result from exposure of the intrusive dyke core. These volcanic structures are consistent with an intrusive dyke complex forming the observed ridges through inflation and fissure eruptions. Fiske and Jackson (1972) suggested that these dyke swarms exploited pre-existing weaknesses and fault systems. A number of these ridges end with an arcuate embayment similar to those observed on from FRZ ridges in Hawaii (Smith et al., 2002), though it is unclear whether these structures are small slope failures or volcanic in origin.

The broader type 2 ridges occur on only two of the seamounts but are distinguished from the type 1 ridges based on their large width-length ratio. These ridges are capped by multiple eruption sites represented by wide shallow cones reaching 600 m across, situated on broad summits. These cones are frequently flat topped and even cratered in the centre. The ridge flanks are steep and consist of a series of narrow lobe-shaped lava terraces connected by flow structures. The volcanic morphology observed is consistent with point eruptions from central cones which then flow downslope, building up the volcanic edifice. In contrast with the narrow type 1 ridges, these wider ridges are likely to be underlain by a small magma source or fed by a dyke from the main magma chamber; however this dyke does not propagate along the ridge.

The proto-ridges occur on three out of the five seamounts, in particular it is the only ridge type observed on Middle of What Seamount, which has low relief. These are not strictly ridges as they are made of discontinuous topography in a linear pattern however they are most likely pre-cursers to a well-developed FRZ. These discrete areas of relief represent small eruption centres exploiting the same pre-existing weakness such

as a faults or fractures. These ridges have lower relief (<200 m) when compared with well-developed FRZs.

Flank Rift Zone Orientation

This section explores the factors affecting the orientations of flank rift zones developing on these seamounts, particularly the effect of nearby transform faults on the local stress field. The orientation of volcanic rift systems can be used to deduce the orientation of average tectonic stress in a region (Nakamura, 1977). This stress may be tectonic or gravitational in origin (Fiske and Jackson, 1972). In a system without pre-existing structural weaknesses or tectonic stresses a pattern of three rifts 120° apart (Mercedes symbol) is the expected fracture pattern, caused by upward directed forces exerted from a magma chamber on the overlying edifice (Luongo et al., 1991; Carracedo, 1994).

The orientations of flank rift zones were inferred from the orientations of the ridges formed. It should be noted that although dykes are commonly thought to indicate the orientations of stress axes, a recent dyke intrusion event measured with InSAR showed strike-slip motion occurring during the event (Ruch et al., 2016). It is unclear, however, how representative this event was. We therefore continue on the assumption that the flank rift zone orientations are an accurate indicator of the crustal stress axes. These orientations were measured and classified into tectonic settings based on the seamount's relation to the axial valley and active transforms. The orientation of the FRZs on the flank of a seamount differs according to which of the four local tectonic settings it is situated in:

1. Mid-Segment: Located at least 50 km from any transform fault or fracture zone
2. Transform Adjacent: Located within 50 km of an active transform fault but at least 50 km from the axial valley
3. Inside Transform Corner: Located within 50 km of a fracture zone and within 50 km of the axial valley

4. Outside Transform Corner: Located within 50 km of an active transform fault and within 50 km of the axial valley

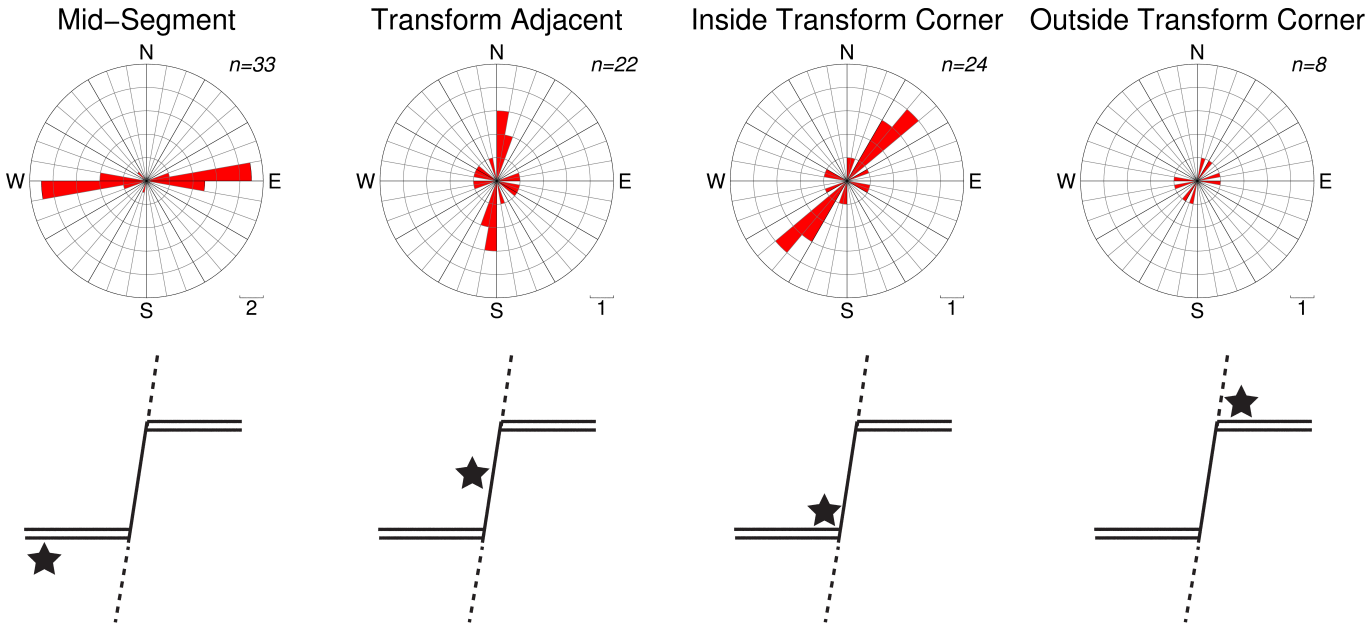


Figure 4.29: Geometry of flank rift zone orientations, illustrated as circular azimuthal histograms of unweighted frequencies for the four different tectonic settings. Tectonic settings are illustrated schematically below each polar histogram, not to scale. Label n=x, where x is the number of flank rift zones measured in this particular tectonic setting. The label in the bottom right corner indicates the magnitude represented by each concentric circle on the azimuthal histogram.

The majority of flank rift zones on seamounts in a mid-segment setting, shown in Figure 4.29, have an east-west orientation perpendicular to the spreading direction. This is parallel to the regional ridge-parallel extensional stress field resulting from plate cooling of young oceanic lithosphere (Sandwell, 1986; Turcotte, 1974). A number of FRZs in mid-segment settings, in particular those observed on Vera Seamount and the proto-rift on Middle of What Seamount, do not follow this east-west orientation for which there may be several explanations. Vera Seamount, which is a large volume seamount located in the rift valley, has three FRZs almost equidistant at 90°, 190° and 315° from north. The ridges generated along these FRZs span the width of the axial valley, in line with the observations of Standish and Sims (2010), who showed evidence

of volcanism occurring up to the margins of the axial valley. This is similar to the fracture pattern predicted in the absence of tectonic stresses, aside from those exerted by an underlying magma chamber (Luongo et al., 1991; Carracedo, 1994). Therefore, while there are almost certainly extensional tectonic stresses acting at Vera Seamount, these may have less influence than the local stresses introduced by magma injections in the subsurface. This upward buoyant force may be enhanced by large local changes in crustal thickness. Vera Seamount is located on a magmatic segment in a predominately amagmatic part of the ridge. These areas have been associated with large local changes in crustal thickness (Schlindwein and Schmid, 2016; Li et al., 2015). The thicker, low density crust beneath this segment of the ridge forms a buoyant upward force similar to that introduced by magma injections in the subsurface (Artyushkov, 1973), resulting in the observed FRZ orientations.

Seamounts in transform fault settings exhibited a small number of FRZs perpendicular to the spreading direction, however the majority were oriented parallel to the transform fault, shown in Figure 4.29. The stress of the lithosphere in close proximity to transform faults may be described by a biaxial stress field with extension parallel to both the ridge and transform fault (Gudmundsson, 1995). It has been suggested that the transform parallel extensional stress is caused by thermal stresses associated with the juxtaposition of young and old lithosphere (Sandwell, 1984; Choi et al., 2008), flexural stress in response to differences in spreading direction (Pockalny et al., 1996), and seafloor subsidence (Neves et al., 2004). It is likely that the stress is generated by a combination of these sources. This localised transform parallel extension leads to the formation of faults parallel to the transform, such as those observed on the flanks of Coral Seamount. These faults act as conduits creating 'least work' pathways for magma, forming FRZs. Local gravitational stresses may also contribute to a transform parallel preferred orientation. During studies of the Hawaiian rift zones, Fiske and Jackson (1972) found that the development of a new magma pathway was strongly influenced by the gravitational forces of the edifice. These forces encourage the edifice to spread out, promoting dyke injection parallel to regional topographic contours. While

the seamounts in this study are much smaller volumetrically, and unlikely to generate such forces, they are built on transverse ridges formed by forces operating across the fracture zones (Bonatti, 1978). These transverse ridges have a sufficient volume to generate gravitational forces, which promote transform parallel dyke injection.

Seamounts in an inside transform corner setting, shown in Figure 4.29, exhibited the majority of FRZs trending NE-SW, rotated from spreading rate perpendicular or transform parallel orientations. These FRZs are subject to perturbation of the regional extensions stress field due to shearing along the active transform, which has been quantified in numerical modelling studies (e.g. Fujita and Sleep, 1978; Phipps Morgan and Parmentier, 1984). The interaction between the tectonic stresses generated by these two features are observed at other ridges in the curvature of normal faults towards the offset direction (Gracia et al., 1999), ridge and transform oblique fault traces (Karson and Dick, 1983) and teleseismic events with oblique normal mechanisms towards the end of mid-ocean ridge segments (Huang and Solomon, 1987). Behn et al. (2002) examined the effect of coupling across the transform fault, using element boundary calculations to show that coupling of 5% produced a rotation of fault mechanisms consistent with the orientations of the FRZs observed at the seamounts in this study. These FRZs exploit the rotated fault planes as magma conduits leading to the NE-SW orientation observed. Sapmer Seamount, which is located on an inside transform corner, exhibits a NE-SW broad geometry, following the trend described above. There are, however, a number of smaller FRZs intersecting the main edifice at a perpendicular angle. These may be related to stresses experienced by the crust due to inside transform corner uplift (Severinghaus and Macdonald, 1988) or caused by dyke swarms propagating along the steep slope gradients on the edge of the transforms (Fialko and Rubin, 1998).

Seamounts forming in an outside transform corner setting, shown in Figure 4.29, exhibited FRZs, which are both perpendicular to the spreading direction and rotated orientations trending northeast-southwest, but the sample number here was smaller

and therefore the results less robust. However; they are reflective of the fault mechanism rotations predicted by Behn et al. (2002) for an outside transform corner setting. The lower number of FRZs in this setting is consistent with microseismicity studies, which show that inside transform corner settings are more seismically active than outside transform corner settings (Wolfe et al., 1995).

On-ridge and Off-ridge Volcanism

A large proportion of extrusive volcanism at mid-ocean ridges takes place in the 1 km to 2 km wide neovolcanic zone on the ridge axis (Macdonald, 1982), though evidence from the SWIR shows that at ultra-slow spreading rates, this neovolcanic zone may extend across the width of the axial valley floor up to 10 km wide (Standish and Sims, 2010). Off-axis volcanism has been observed, particularly at slower spreading rates, which has been attributed to the greater availability of fracture zone conduit systems (Batiza, 1981). The morphological and lithological evidence described in the previous two sections suggest that some of the seamounts in this study may have formed off-axis (Coral Seamount, Melville Bank and Sapmer Bank), while others formed in the neovolcanic zone (Vera and Middle of What Seamounts).

Vera Seamount clearly formed on axis, since it has not moved from the neovolcanic zone where it formed. Middle of What Seamount, which is located 50 km off-axis shows large areas of pillow basalts, which typify the effusive eruptions onto the shallowly dipping slopes of the neovolcanic axis (Fornari et al., 1985). The FRZ orientation analysis shows predominantly east-west trending structures including lineated volcanic cones and faulting. In the previous section, these structures were attributed to the extensional stresses, which are dominant in a mid-segment setting. The extensive east-west faulting on the northern flank is similar to the pattern of faulting exhibited by the Fieale volcano in the East African Rift, which formed on the axis and is now being pulled into two parts. A bathymetric high, directly north of Middle of What Seamount on the other side of the axial valley, was probably originally joined with Middle of

What Seamount in the neovolcanic axis.

Coral Seamount, Melville Bank and Sapmer Bank do not show east-west trending tectonic or volcanic features. In contrast, the orientations of such features on these seamounts are determined by the crustal stresses in their local tectonic settings

The morphological and lithological evidence above suggests that these seamounts may be divided into two groups based on their formation. One group, consisting of Middle of What and Vera Seamounts, formed in the neovolcanic axis of magmatic segments while the other group, consisting of Coral Seamount, Melville Bank and Atlantis Bank, formed off-axis. The exact distance from the axis is not clear, however it is likely to be beyond the axial valley walls (at least 10 km off axis).

For seamounts forming in the neovolcanic zone, such as Vera Seamount, magma is supplied through rapid dyke injection mechanisms (Cannat et al., 1999). However, for seamounts forming off-axis in transform fault settings, an alternative mechanism of magma transport is needed (Figure 4.30). The FRZ orientations strongly suggest that these seamounts are supplied by melt migrating along deep seated faults, however these seamounts are often located in melt-poor fracture zone locations. 3D seismic tomography studies at the SWIR axis (50° E) by Li et al. (2015) have shown significant along-axis and lateral variations in crustal thickness, from 9.5 km to 4 km thickness over <30 km. Magma transport occurs along an impermeable boundary at the top of melt column, where buoyant forces drive the magma upslope (e.g. Sparks and Parmentier, 1994). Therefore these areas of anomalously thick crust, which depress the melt column, may provide a mechanism for discrete magma packets to move towards the melt-poor, thin crust areas. While most of the magma packets will freeze due to the colder temperatures, some may be captured by the deep seated faults associated with the fracture zones, providing a pathway to the surface. These are then erupted along fault lines oriented according to the local tectonic settings, resulting in the FZR orientations observed on these seamounts. Further evidence from gabbro cumulates on a magmatic segment of the SWIR (Meyer et al., 1989), show that the crust is created from small

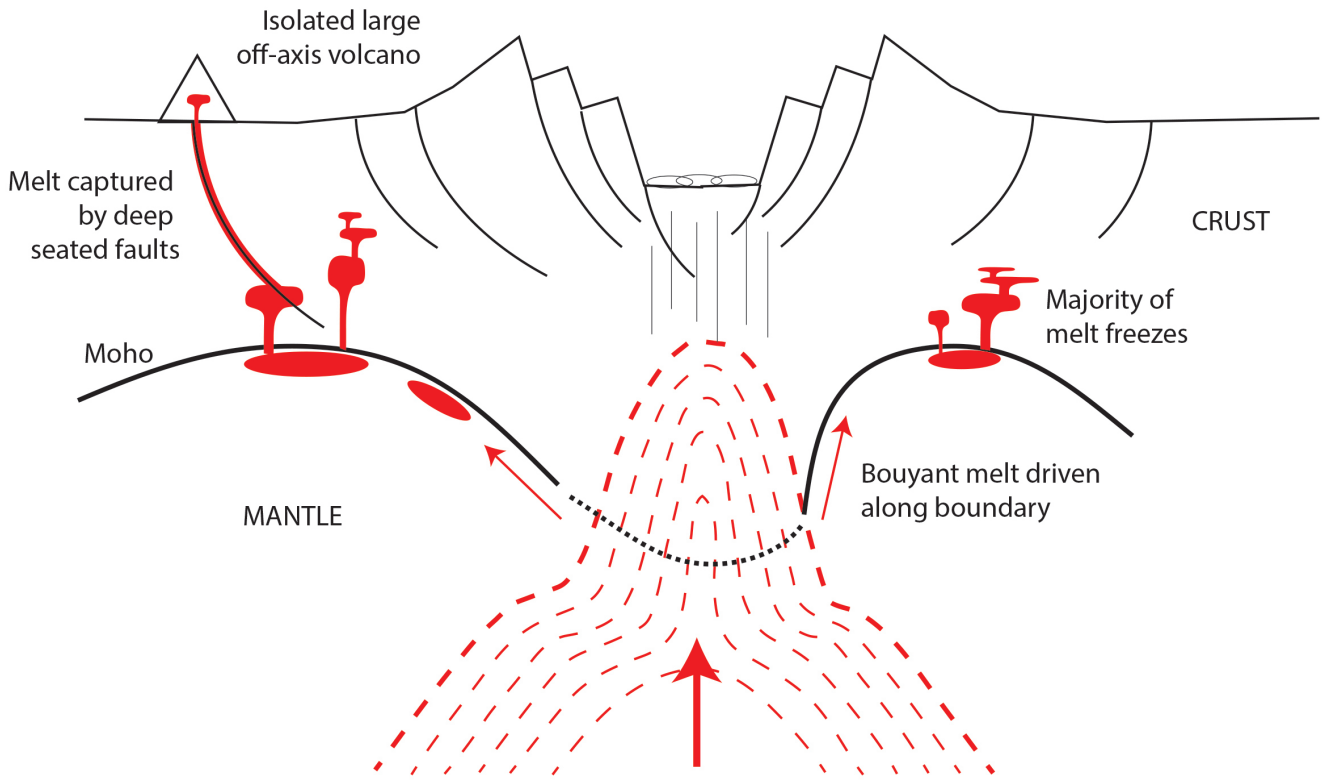


Figure 4.30: Schematic diagram illustrating hypothetical mechanism for off-ridge volcanism. Inferred isotherms (red dashed lines), solidus (thick red dashed line) and Moho (black line) geometry from seismic experiments of Li et al. (2015). Grey vertical lines and ellipses reflect dykes and pillow lavas respectively. Solid black lines indicate a stylised representation of ridge topography and sub-surface faults. Red areas represent hypothetical magma packets. Red arrows show the migration of magma along the impermeable boundary at the top of the melt column.

batches of melt, which either rise rapidly to the surface or become entrained in the shallow crust. In a system with a typically cold thickened lithosphere, fault captures provides a mechanism for this rapid ascent through the crust. Thermal heating from repeated magma entrainment along a fault plane decreases the viscosity differential between the conduit walls and injected magma, increasing the percentage of magma reaching the surface (Macdonald, 1982).

Flank Rift Zone Evolution

The development and evolution of flank rift zones has been studied at the Hawaiian islands (e.g. Fiske and Jackson, 1972), Pacific Guyots (Vogt and Smoot, 1984), Canary islands (Mitchell et al., 2002) and many other seamount groups. As a result of these studies, a variety of factors affecting rift zone development have been proposed. The following section explores factors affecting the FRZ development at the seamounts in this study including edifice height, edifice volume and crustal age.

Four out of the five seamounts (all except Middle of What Seamount) show well developed FRZs of varying length and orientation. Middle of What Seamount has an incipient FRZ expressed as a proto-ridge on the southwest flank, however it is not well developed, as in the other seamounts.

Edifice Height

Edifice height was measured from the shallowest point on the summit to the base of the edifice defined using multibeam bathymetry. Many of the seamounts are constructed on raised topographic features such as transverse ridges and inside transform corner topography. In these cases the edifice base is defined as the break in slope where the edifice rests upon the underlying topography. In addition, the current edifice height is a minimum height due to truncation from wave erosion. As a result in some cases the edifice heights are likely to be underestimates when determining factors such as the depth of magma chamber and height of the magma column.

Figure 4.31 shows the relationship between edifice height, crustal age and FRZ development. Bathymetric contours are superimposed for the seamounts described earlier in this chapter to provide an indication of the shape and extent of the FRZs, while black crosses represent seamounts lacking FRZs identified using swath bathymetry. The seamounts are clearly divided into two groups: (*i*) those with edifice heights above 2000 m, which have well developed rift zones (*ii*) those with edifice heights below 2000 m, which lack well developed rift zones. This development in FRZs above 2000 m in

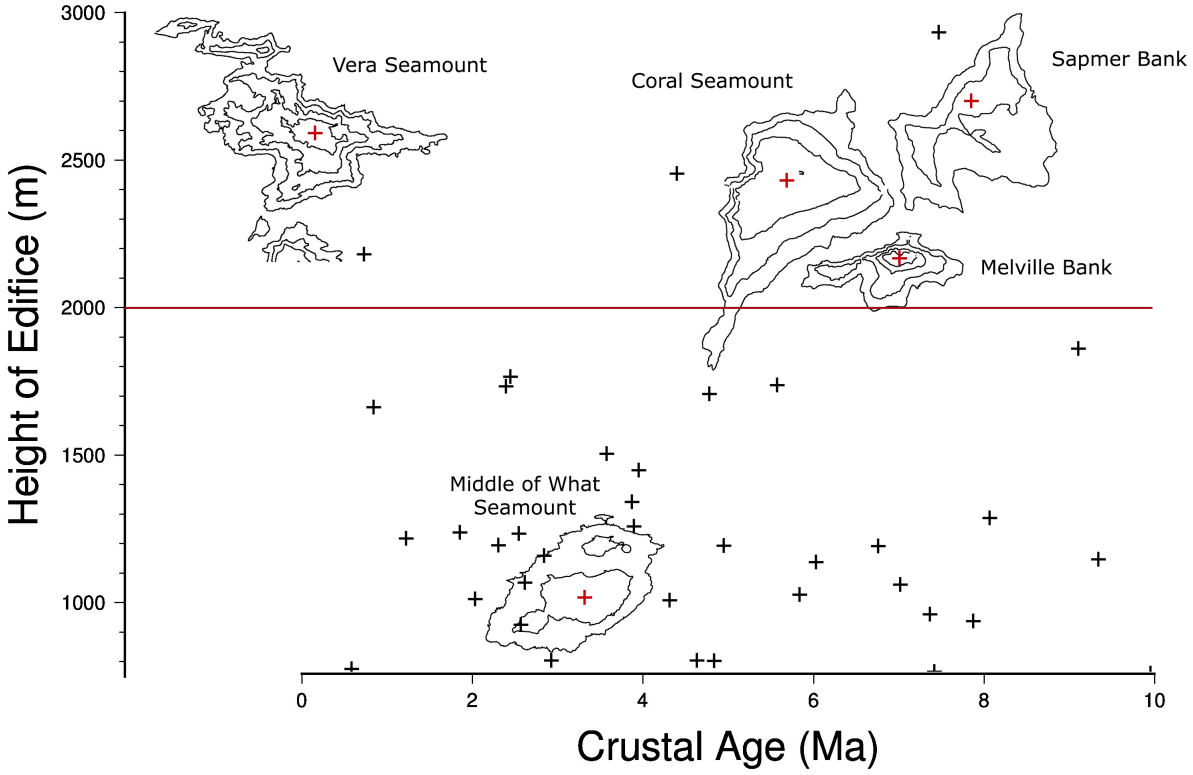


Figure 4.31: Plot of edifice height against crustal age for seamounts described in this chapter (red crosses) and other seamounts on the SWIR (black crosses). All seamounts represented by black crosses show no flank rift zone structures. Bathymetric contours for the seamounts in this chapter (red crosses) are overlain to illustrate the seamount geometry. Crustal ages are determined using magnetic anomaly picks.

height is not simply a consequence of edifice age as crustal age (which is used as an indicator of the maximum age) does not appear to determine the development of FRZs, since both Vera Seamount, located in the neovolcanic zone, and seamounts located on older crust have well developed FRZs.

Mitchell (2001) showed that seamounts in a variety of tectonic settings showed a general transition from circular to stellate forms due to FRZ formation and slope failure at edifice heights between 2 km to 4 km. This does not hold true for all seamounts (e.g. Binard et al., 1992) indicating that there is variation in the degree to which the

mechanisms involved affect any given seamount. The transition height observed at the seamounts in this study is at lower end of the range inferred by Mitchell (2001) as FRZs are well developed in edifices just over 2000 m, though embayments caused by slope failures between FRZs will lead them to appear more well developed than they are. Mitchell (2001) attributed the transition from circular to stellate geometry to the upward movement of the magma chamber within the edifice, which occurs as the horizon of neutral density moves upwards due to the increasing density difference between the magma and overlying rock (Ryan, 1987). While this is the case for magma chambers in large isolated edifices such as Hawaii (Ryan et al., 1981), magma chambers at mid-ocean ridges lie deeper than the horizon of neutral density (Hooft and Detrick, 1993), particularly at slow spreading ridges, where hydrothermal circulation cools the upper lithosphere (Purdy et al., 1992). The presence of faults and fractures, which promote hydrothermal circulation, also provide conduits along which magma can migrate through the crust. It has been suggested that an increase in local magma supply along these faults would increase the pressure at the base of the magma column, promoting the sideways movement of magma into FRZs (Vogt and Smoot, 1984). It is unclear whether, in areas with a high number of faults and fractures, the cooling due to hydrothermal circulation or the exploitation of weaknesses by ascending magma is dominant; however, the presence of flank rift zones, predominantly on seamounts greater than 2 km tall, is clear.

Edifice Volume

Figure 4.32 shows a positive correlation between edifice volume and maximum flank rift zone length. The seamount volumes were isolated using a basal contour to define the edifice and calculated using GMT's `grdvolume` on the bathymetric data. There are a number of factors which are known to influence FRZ length including edifice height, underlying topography and the number of existing FRZs.

Vogt and Smoot (1984) showed that in a system with a consistent magmatic supply such as intraplate oceanic islands, the maximum rift flank length depends on the pres-

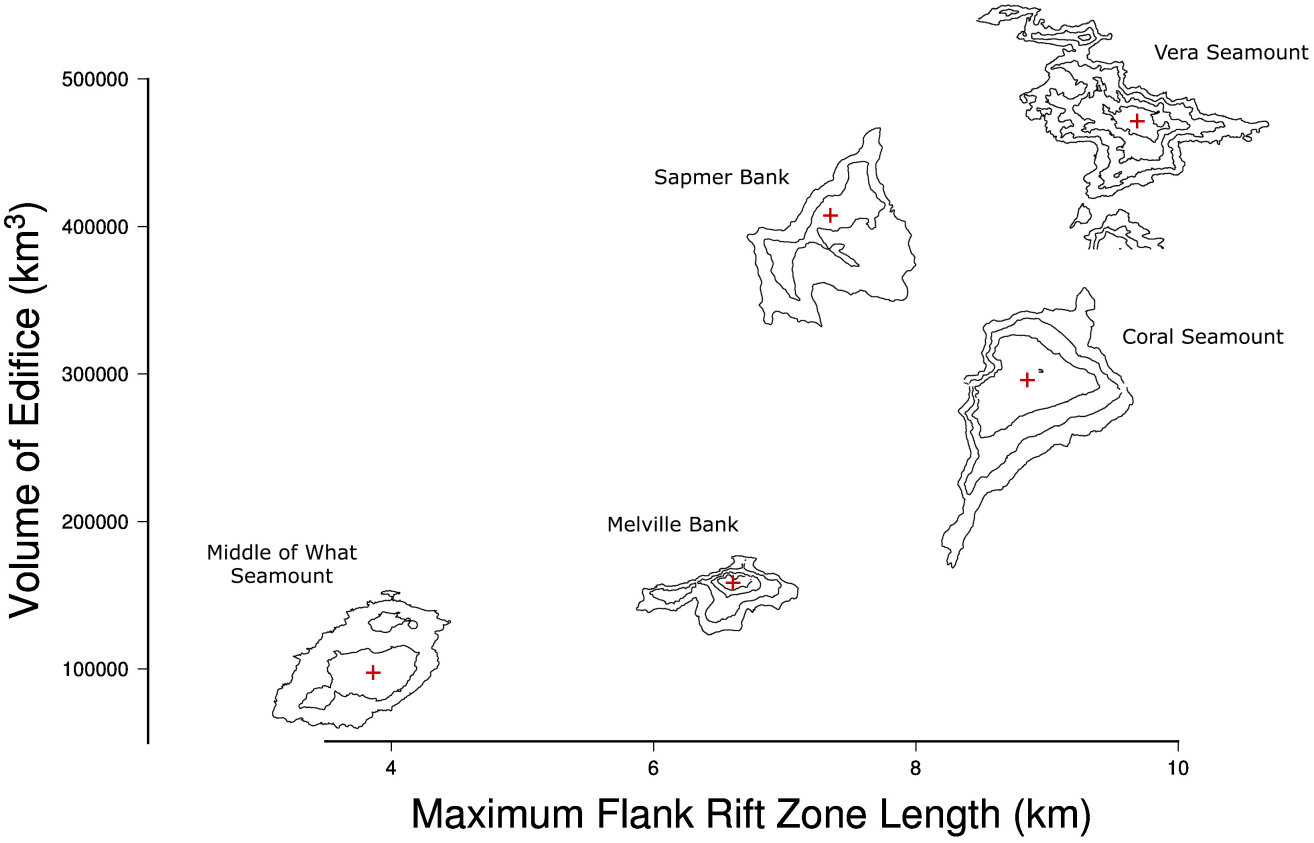


Figure 4.32: Plot of edifice volume against flank rift zone length for seamounts described in this chapter (red crosses). Bathymetric contours for the seamounts in this chapter (red crosses) are overlain to illustrate the seamount geometry. Seamount volumes were determined using a basal contour to define the extent of the seamount (see chapter 5).

sure differential between the base of the magma column and the hydrostatic pressure at an equivalent depth. In the case of the seamounts in this study, the positive correlation between flank rift zone length and edifice volume instead of height suggests that the availability of magma is a limiting factor. Vera Seamount, which is located in the neovolcanic zone with a relatively high magma supply, has the greatest volume and longest flank rift zones despite its young age. Sapmer Bank, which has a greater edifice height, and therefore greater magma-hydrostatic pressure differential (particularly when taking into account the transform corner topography on which the seamount lies), has FRZs on average 2 km shorter than those observed at Vera Seamount.

This pattern may be further perturbed by the number of FRZs on a seamount, and the basement topography on which it lies. Over any given period of time, seamounts with fewer FRZs (such as Coral Seamount) will have a proportionally larger volume of magma injected through dyking in the same FRZ, increasing its length, while those with more FRZs (such as Sapmer Seamount) will have a proportionally smaller volume of magma material injected into each FRZ. It is not clear why some seamounts have fewer RFZs than others, as this does not appear to be affected by age or edifice height (Vogt and Smoot, 1984). It is possible that some magma conduits may become preferred due to thermal memory effects, in which repeated magma injections decrease the viscosity differential between the newly injected magma and conduit walls (Macdonald, 1982). The basement topography may also influence the ease of dyke injection and the maximum length of any given FRZ. Steep longitudinal slope gradients, such as those found on the edges of the rift valley and transform fault systems, will promote dyke propagation as gravitational forces drive along-axis flow of dykes, increasing the potential FRZ length (Fialko and Rubin, 1998).

This section shows that the development of flank rift zones on a seamount edifice is controlled primarily by edifice height, with seamounts above 2000 m showing well developed flank rift zones. This is attributed to an increase in the lithostatic pressure at the base of the melt column promoting lateral intrusion. While other studies suggest that edifice height is also the primary control on flank rift zone length, data presented above suggests that on these seamounts, edifice volume is the governing factor. This indicates that the availability of magma supply is a limiting factor at these seamounts.

4.4.3 Slope Failures

The slope failure features observed on the seamounts in this study are of two main types. Some seamounts have major slope failures, which indent the seamount edifice and are characterised by deeply embayed headscars, erosional chutes and debris deposits. Other seamounts show steep gullies, which do not significantly indent the edifice or modify

the slope gradient. Several seamounts show a combination of these two styles of slope failure. Slope failures occur on some but not all of the seamounts in this study. Slope failures were not observed on Middle of What Seamount (aside from a small fault scarp collapse) or Vera Seamount. There are also no major slope failures on Coral Seamount except small scale gully structures on the steepest face. Middle of What Seamount and Vera Seamount have lower relief and less steep slope gradients that the other seamounts, accounting for the lack of slope failures; However, Coral Seamount has similar relief and slope gradients to seamounts which have major slope failures, so additional factors must be affecting the presence or absence of slope failures on these seamounts. It is possible that past slope failures on Coral Seamount have been obscured by subsequent volcanism or sedimentation. Melville Bank, Sapmer Bank and Atlantis Bank all exhibit features associated with major slope failures. Of these three seamounts, only the slope failure on the southwest flank of Melville Bank shows a complete set of features: arcuate headscar, smooth chute and downslope debris deposit.

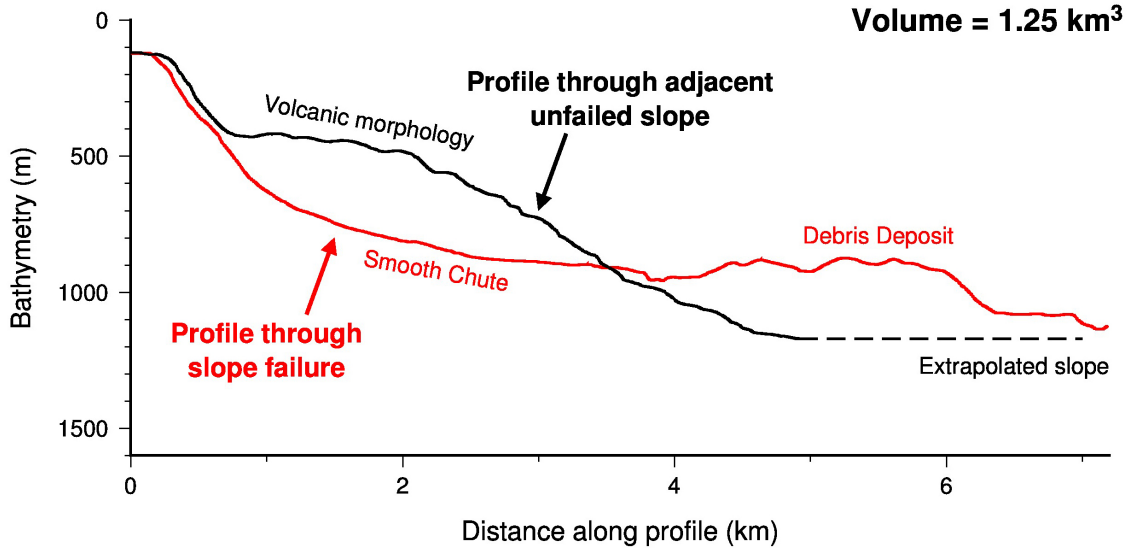


Figure 4.33: Bathymetric profile through the slope failure on Melville Banks southwest flank (red line) and adjacent unfailed flank (black line). Slope failure volume was calculated by comparing the two profiles in conjunction with contour parallel profiles to estimate a total volume of material removed. The volume of material removed is within 0.15 km^3 of the estimated volume of the debris deposit, suggesting little loss of material.

Taking the slope failure on the southwest flank of Melville Bank as an example (shown

in Figure 4.10), it is possible to compare profiles through the slope failure and adjacent unfailed slope (Figure 4.33). This shows the section of the edifice which has been removed and deposited downslope during the failure, measuring approximately 1.25 km^3. This is significantly smaller than many of the slope failures studied on large oceanic islands such as the Canaries (Watts and Masson, 1995; Masson et al., 2002) and Hawaii (Moore et al., 1989), however previous work has shown that slope failures at extreme scales show a similar set of features (Moore et al., 1989). Slope failures on Sapmer Bank and Atlantis Bank exhibit arcuate headscars and steep smooth chute structures but no major debris deposits were observed. There are two possible reasons for this: either, the slope failure runout length is greater than the multibeam bathymetry coverage or the debris deposit has been channelled away from the seamount by the extreme topography associated with the ridge and transform faults. Downslope of the slope failures on Sapmer Bank and Atlantis Bank are the Gallieni and Atlantis II transforms respectively, so it is likely that any debris flows from these slope failures were deposited in the transform valleys. Some of the slope failure sectors show small along strike scarps, represented by discontinuous breaks in the slope, which are interpreted as small slump structures.

Exponential Slope Fitting

Without debris deposits, it is difficult to distinguish between embayments caused by slope failures and the natural embayments in the edifice between volcanic ridges. Adams et al. (1998) showed that slope failures follow an exponential pattern due to the exponential decrease in transport capacity with distance from the source. This approach was applied to the slope failures at El Hierro in the Canary islands by Gee et al. (2001), who showed that an exponential model had a good fit with slope failure sectors compared to unfailed flank areas. This does not hold true for all slope failures though, such as some of those observed on Hawaii (Moore et al., 1989). Exponential curves were fitted to profiles from all six seamounts in order to determine if there are

any statistical differences between unfailed volcanic sectors and slope failure sectors on the mid-ocean ridge seamounts in this study.

A series of bathymetric profiles were constructed for each seamount. These profiles were initially constructed as 12 km radial profiles extending from a fixed point at the centre of the seamount summit with azimuths incremented every 5°. These were sampled at an interval 10 m from shipboard bathymetry from the JC066 and MD192, with a grid spacing of 20 m. Visual examination and preliminary model fitting of these profiles showed that they were not representative of the seamount morphology for two reasons. The first is that some of the seamounts have truncated summits due to wave erosion, causing significant breaks in slope unrelated to volcanic or slope failure processes. The second reason is that, due to the ellipticity of some of the edifices, the radial profiles did not follow the line of maximum dip along the slope, biasing the profiles towards shallower gradients. In order to remove these two effects, a series of profiles were constructed originating along a contour at the summit shelf break depth. Clusters of profiles were oriented parallel to the average maximum dip direction of the sector being investigated. The multibeam data coverage was not sufficient to produce profiles of suitable length, therefore the shipboard multibeam data were combined with regional bathymetry extracted from a global bathymetry grid. Comparisons of both the GEBCO 2014 30'' x 30'' global bathymetry grid (IOC et al., 2003) and the Sandwell and Smith 1 x 1 minute predicted bathymetry grid (Sandwell and Smith, 2008) with the shipboard multibeam showed significant bathymetric differences, illustrated in the individual profiles in Figure 4.34. These differences arise from the inability of the global grids to resolve small wavelength extreme topography as accurately as the shipboard multibeam (Marks and Smith, 2006). Of these two global grids, the Sandwell and Smith grid shows the least differences when compared to the multibeam bathymetry as these seamounts are located in remote regions, in which the shiptrack data used to construct the GEBCO grid is sparse.

The differences between the shipboard multibeam and Sandwell and Smith predicted

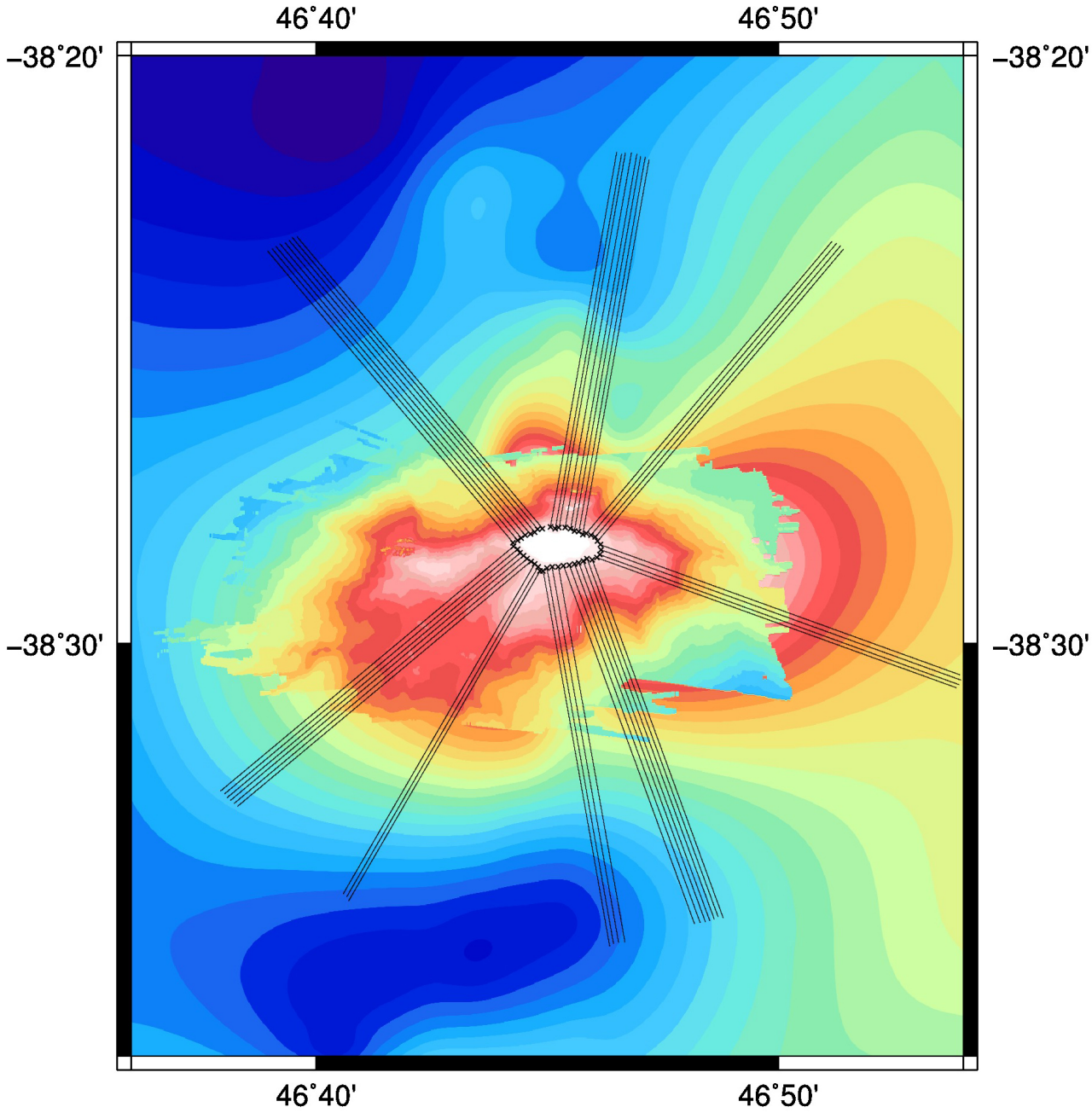


Figure 4.34: Map showing locations of bathymetric profiles used for exponential curve fitting (black lines) overlain over bathymetry data. Profiles start at the edge of the shelf break to eliminate wave eroded platforms and are 12 km in length. Clusters of profiles are oriented parallel to the average maximum dip direction of the sector being investigated. Each sector is classified into slope failure or unfailed flank based on morphological data. Bathymetry data are shipboard bathymetry overlain by regional bathymetry from the Sandwell and Smith global predicted bathymetry v.23.1 (Sandwell and Smith, 2008). Significant discrepancies between these two bathymetric data sets occur in some sectors of the seamounts.

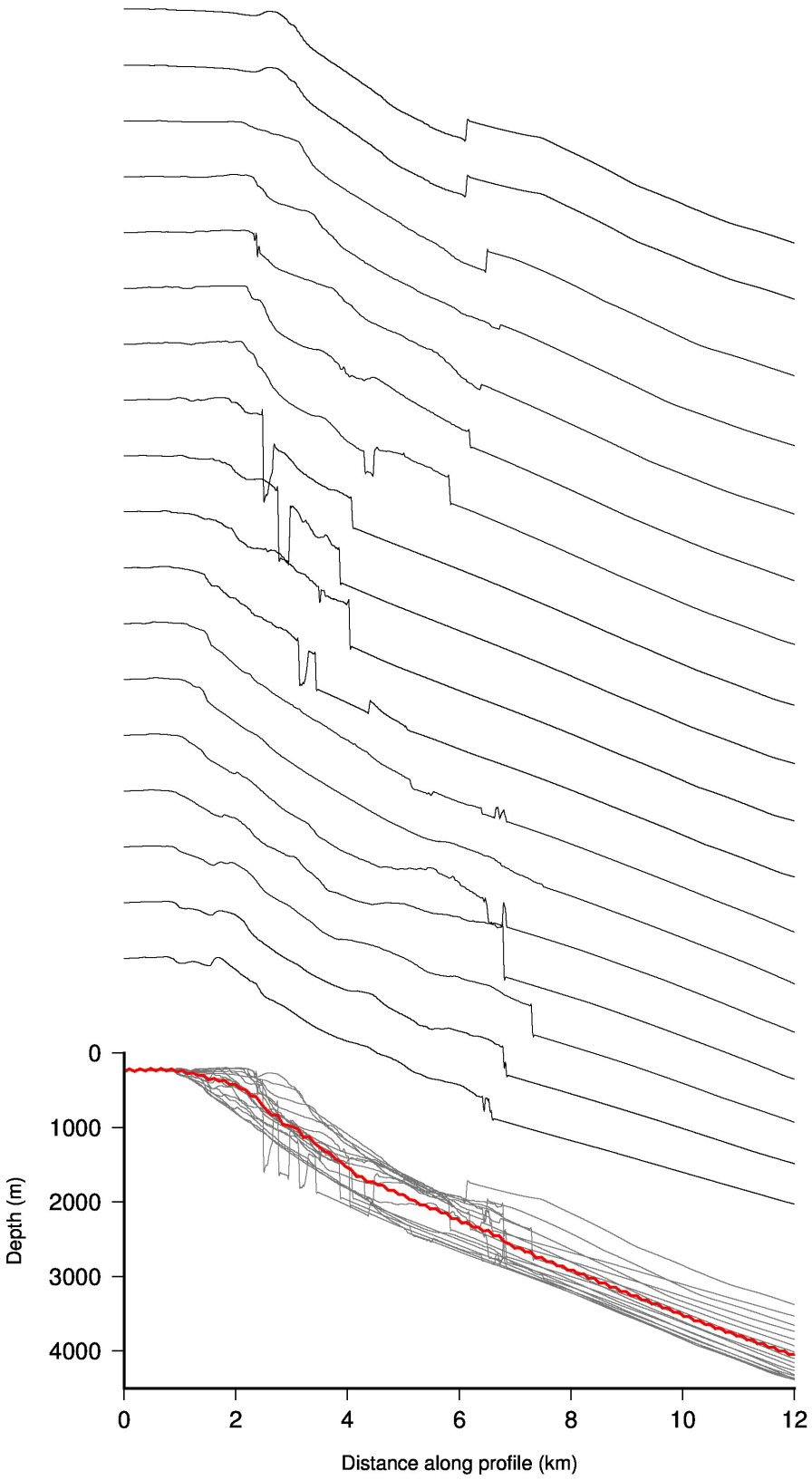


Figure 4.35: Ensemble average profiles of bathymetry for a single sector of Coral Seamount. Profiles used to calculate the average are individually displayed (black lines) and stacked at the bottom (grey lines). Resultant average profile is overlain in red.

bathymetry produces step artifacts in the bathymetry profiles where the two datasets adjoin. In order to remove these artifacts, an ensemble averaging technique was used to isolate an average profile containing features common between the profiles and remove those which differ between profiles (Bassett and Watts, 2015). This technique utilises Fourier transforms to calculate a frequency spectrum for each profile. These are then used to calculate an average frequency spectrum using each profile's individual Fourier coefficients. This average frequency spectrum is then inverse Fourier transformed to produce an average bathymetry profile (shown in Figure 4.35). This ensemble average technique is particularly relevant as the number of profiles being averaged is small (between 4 and 18). Bassett and Watts (2015) showed that for averaging >30 profiles, ensemble averaging and traditional arithmetic averaging (stacking) are comparable. However, for smaller numbers of profiles, as is the case with this study, the ensemble averaging is better able to isolate the common bathymetric features.

These profiles of distance versus depth were fitted to the exponential model of Gee et al. (2001), given by the equation

$$y = ae^{-bx} + c \tag{4.1}$$

where y is the depth, x is the distance along the profile and a, b, and c are constants. The model is fitted using a non-linear least squares optimisation, choosing parameters a, b and c so that the residuals of the model are minimised.

Figure 4.36 shows four representative profiles of distance along the profile against bathymetry (black) and their best fit exponential models (red). Profiles 11 and 6 are sampled from sectors with arcuate headscars, chutes and other slope failure features while profiles 7 and 20 are sampled from unfailed volcanic sectors. The exponential model fits the profiles from slope failure sectors well, leading to low root mean square (RMS) errors. These profiles are steeper over the proximal 2 km and have a greater curvature (rate of change of slope) than profiles in unfailed sectors. Deviations from

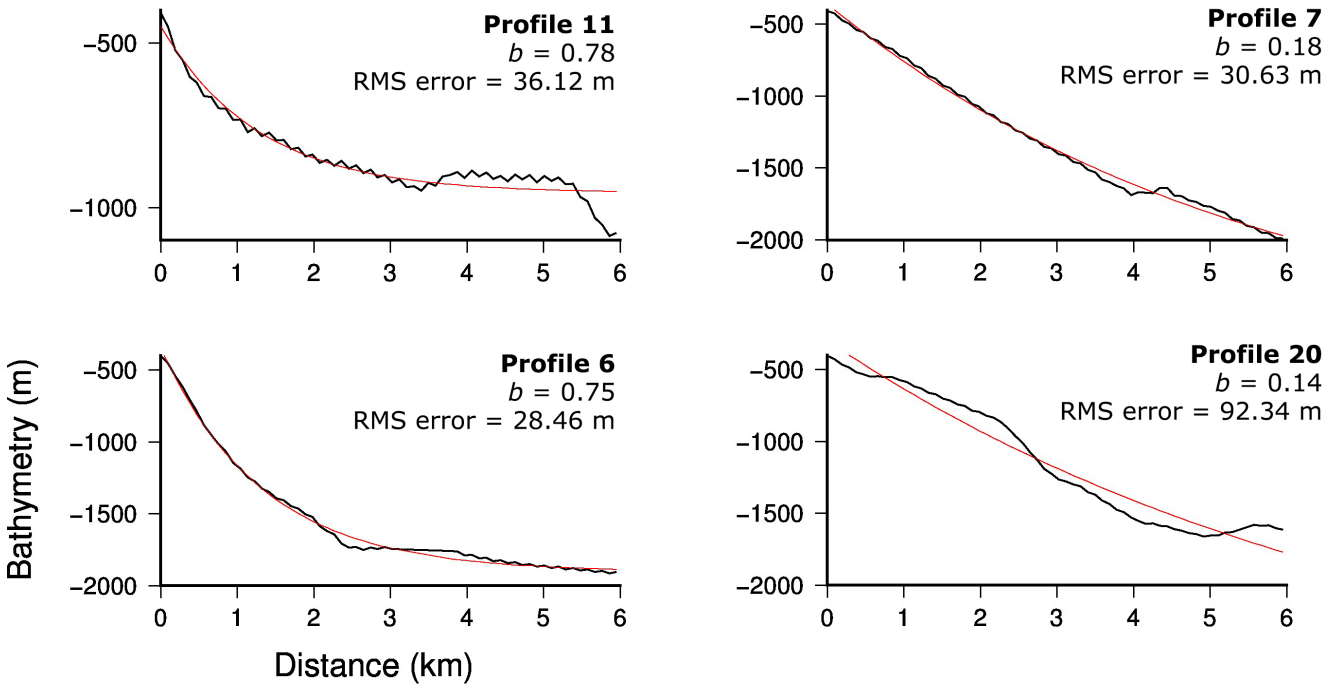


Figure 4.36: Selected bathymetric profiles from Melville Bank and Atlantis Bank (black line) and the fitted exponential curve (red line).The exponential coefficient (b) and root mean square (RMS) error for each profile is included. Profiles reflect a range of b coefficients and RMS errors calculated across the seamounts. Profiles 11 and 6 represent slope failure sectors while profiles 7 and 20 represent unfailed volcanic sectors.

the model in these slope failure sectors occur either as slight breaks in slope at the base of the chutes, as seen in profile 6, or due to debris deposits, as seen in profile 11. These slope failure profiles are, however, in general smoother than those in unfailed sectors. The unfailed profiles, do not show an exponential shape, though stretching of the exponential model to form an almost linear fit, as seen in profile 7, can lead to deceptive low RMS errors. In the majority of profiles irregularity of the unfailed volcanic slope lead to deviations from the model and RMS errors over 50 m, as seen in profile 20.

Gee et al. (2001) found that landslide sectors at El Hierro in the Canary Islands could be distinguished from unfailed volcanic sectors by comparing the b coefficient against RMS error of the exponential model fit for each profile. A comparison of b coefficients and RMS errors for each profile in this study shows that slope failure and unfailed

sectors form two distinct groups (shown in Figure 4.37).

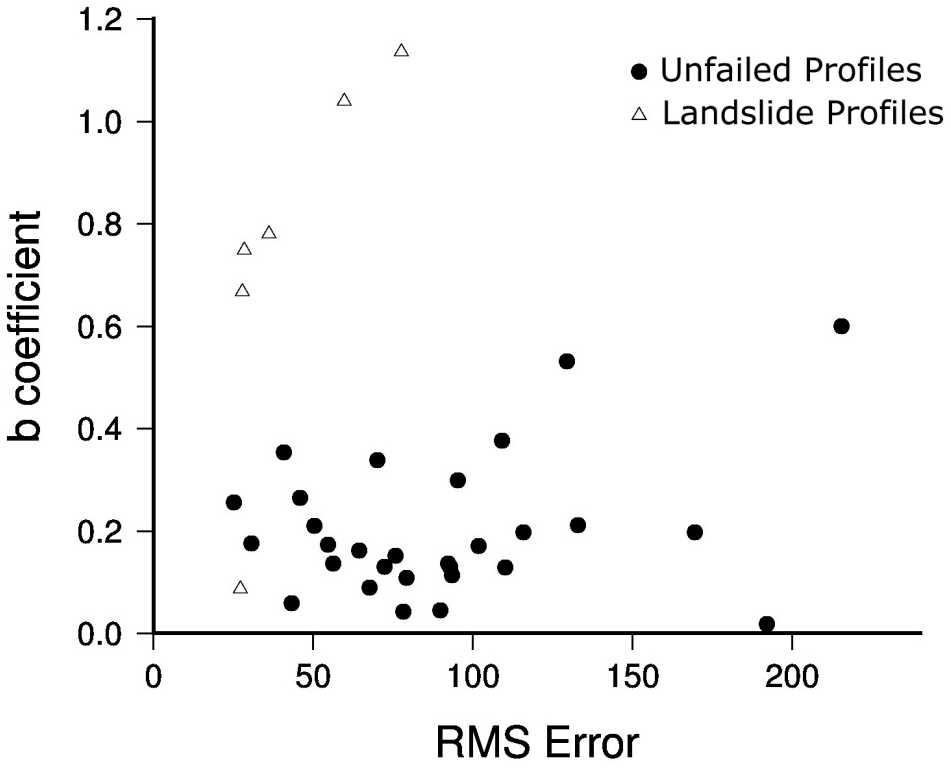


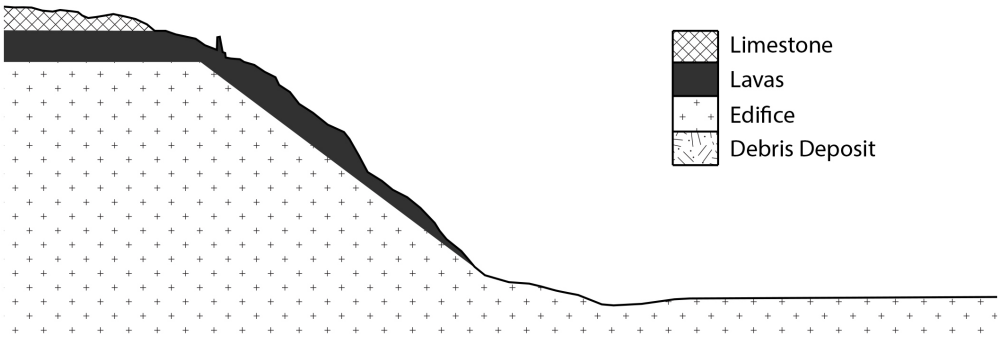
Figure 4.37: Comparison of exponential coefficient (b) and RMS error for each profile. Slope failure profiles (triangles), which are identified using bathymetry and backscatter, generally have b>0.6 and RMS error <80 while volcanic unfailed sectors (black circles) have b<0.6 and a wide range of RMS errors. A notable exception in the lower left shows a sector interpreted as a slope failure with a low b coefficient. This slope failure is interpreted as a collapsed caldera.

Slope failure sector profiles in this study have high b coefficients and low RMS errors, while unfailed volcanic sector profiles have low b coefficients and variable RMS errors. One anomalous slope failure sector profile has the low b coefficient, similar to those of unfailed volcanic profiles. This anomalous profile shows an arcuate headscar and so was classified as a slope failure sector, however, this slope failure (from the southwest flank of Sapmer Seamount) is interpreted as caldera collapse rather than a debris avalanche and so does not show the exponential profile shape expected.

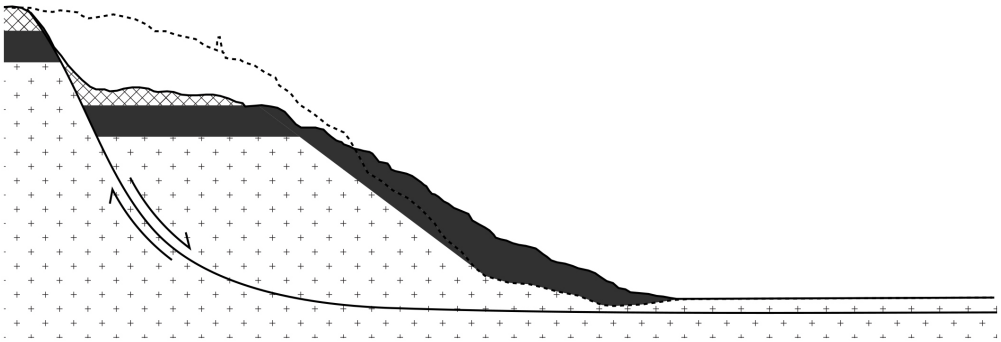
In contrast the results observed on the seamounts in this study, Gee et al. (2001) found that slope failure sectors at El Hierro were characterised by a low b coefficient, though

both slope failure sectors on the seamounts in this study and at El Heirro were characterised by low RMS errors. The high b coefficients for the SWIR seamount slope failures reflect steeper upper slopes, and an increased degree of curvature compared to the slope failures observed at El Hierro. This difference is due to variation in the slope failure processes between the two edifices. Slope failures in this study exhibit features which are consistent with slumping processes such as steepened upper slopes (leading to the diagnostic higher b coefficients), small scarp features due to block rotation and sometimes a break in slope at the base of the chute. These same slope failures also exhibit features consistent with debris avalanches such as amphitheatre headscars, narrow smooth chutes and thick hummocky debris deposits. In order to reconcile these features, a two stage process is inferred (Figure 4.38) in which the unfailed volcanic flank undergoes initial slumping (Figure 5.31b), most likely along a deep seated fault, causing the slow movement of consolidated material downslope. Dislocations and rotations within the slump material during movement cause the small scarps which trend for a short distance along slope. The surficial material on the now over-steepened slump face undergoes further failure, forming a fluidised debris deposit, which travels downslope (Figure 4.38c). The failure point is often distinguished by an amphitheatre headscar, which leads to a smooth chute and further downslope a hummocky debris deposit in some slope failures. The lack of seismic data across these slope failures means that the internal structure shown in Figure 4.38 is speculative.

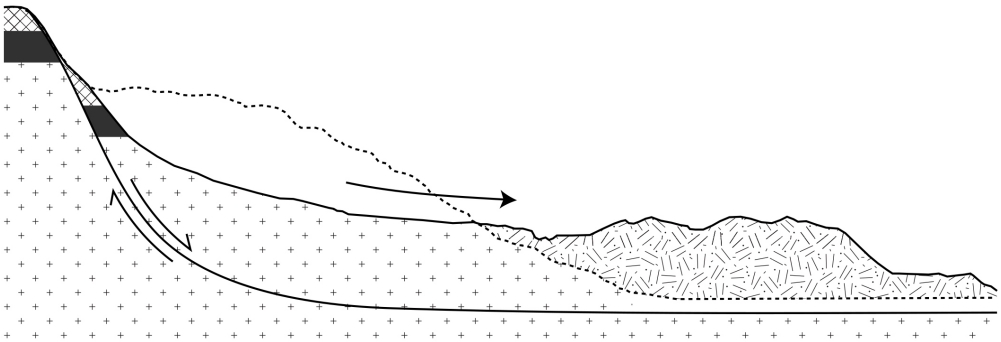
The runout distance of any given slope failure depends on various factors, including but not limited to height, volume, density of material, loss of shear strength during failure, and the presence of surrounding topography leading to channelization or obstruction of the flow (Hampton et al., 1996). The runout distances observed at the SWIR are short with height-length ratios between 0.12 and 0.15. The short run out of these debris deposits is attributed to the small volume of dense material involved in the slope failures, and the obstruction of the flows by surrounding topography. The combination of slumping and fluidised debris avalanches observed at these seamounts is similar to some of the slope failures observed at Hawaii (Moore and Normark, 1994).



(a) Initial unfailed slope.



(b) First stage: slumping causing slow movement of consolidated material along fault.



(c) Second stage: failure of the surficial material of the over steepened slump scar forming a debris avalanche.

Figure 4.38: Schematic diagram illustrating the two-stage slope failure process proposed to explain the steep upper slope, mid-slope chute structure, and downslope debris fields observed at Melville Seamount and Atlantis Bank.

In considering the applicability of this exponential slope fitting method to the seamounts in this study, there are a number of issues. The method was able to distinguish the slope failure sectors from the unfailed sectors based on their steep exponential profile shape with a high curvature. However, while this holds true for these particular seamounts as evidenced by the multibeam bathymetry and backscatter data , this does not follow the pattern of slope failures at El Hierro (Gee et al., 2001). This is attributed to a difference in the landslide processes occurring on the seamounts in this study and those on EL Hierro. As such, this method could not be applied indiscriminately unless the type of slope failure, and therefore the expected shape was known. In a system with a combination of several different slope failure processes this would become increasingly problematic. Slope failures at both the Canaries and the seamounts in this study were characterised by low RMS errors due to their exponential profiles, which contrast in particular with the unfailed volcanic sectors on the seamounts in this study. However, anomalously low RMS errors can be generated for unfailed sectors as the exponential model may be manipulated to fit an almost linear slope profile, as seen in Profile 7. RMS error may therefore be used only as a general indicator.

Using the methodology above in conjunction with multibeam bathymetry and backscatter observations, eight major slope failures were identified at Melville seamount, Sapmer Bank and Atlantis Bank. Minor slope failures in the form of steep gullies were also identified on Coral Seamount and Sapmer Bank. The characteristics of these slope failures and their associated edifices are summarised in table 4.2.

Causes of Slope Failure

The factors affecting the triggering of slope failures at oceanic islands and seamounts are reviewed in Keating and McGuire (2000), and may be attributed to physical edifice characteristics, endo-edifice effects occurring within the edifice, and exo-edifice effects occurring outside of the edifice.

Physical characteristics of the edifice which effect the slope failure potential include

Table 4.2: Characteristics of slope failures identified on the six seamounts.

Slope Failure	**Edifice Height**	**Estimated Original Height**[1]	**Crustal Age**	**Embayment**	**Chute**	**Debris Lobe**	**Debris Deposit**	**Embayment Width**	**Headscar Depth**
Coral W flank	2410	2888	6.1	Gullies	-	-	-	1.5 (average)	610 (average)
Melville 1 (NE flank)	2170	2761	7	Y	Y	Y	Y	0.9	500
Melville 2 (SW flank)	2170	2761	7	Y	Y	Y	Y	2.1	430
Melville 3 (NW flank)	2170	2761	7	Y	N	Y	Y	2.8	450
Sapmer 1 (SW flank)	2733	3312	8	Y	Y	N	Y	2.5	400
Sapmer E flank	2733	3312	8	Gullies	-	-	-	0.8 (average)	470 (average)

[1]Calculated using equation 4.2

Atlantis 1 (W flank)	2300	-	12	Y	N	Y (misaligned)	Y	2.9	800
Atlantis 2 (W flank)	2300	-	12	Y	Y	N	Y	2.1	750
Atlantis 3 (W flank)	2300	-	12	Y	Y	N	N	2.4	800
Atlantis 4 (W flank)	2300	-	12	Y	N	Y	N	1.5	1070

slope angle (Siebert, 1984), edifice height (Mitchell, 2003) and lithology (Moore and Fiske, 1969).

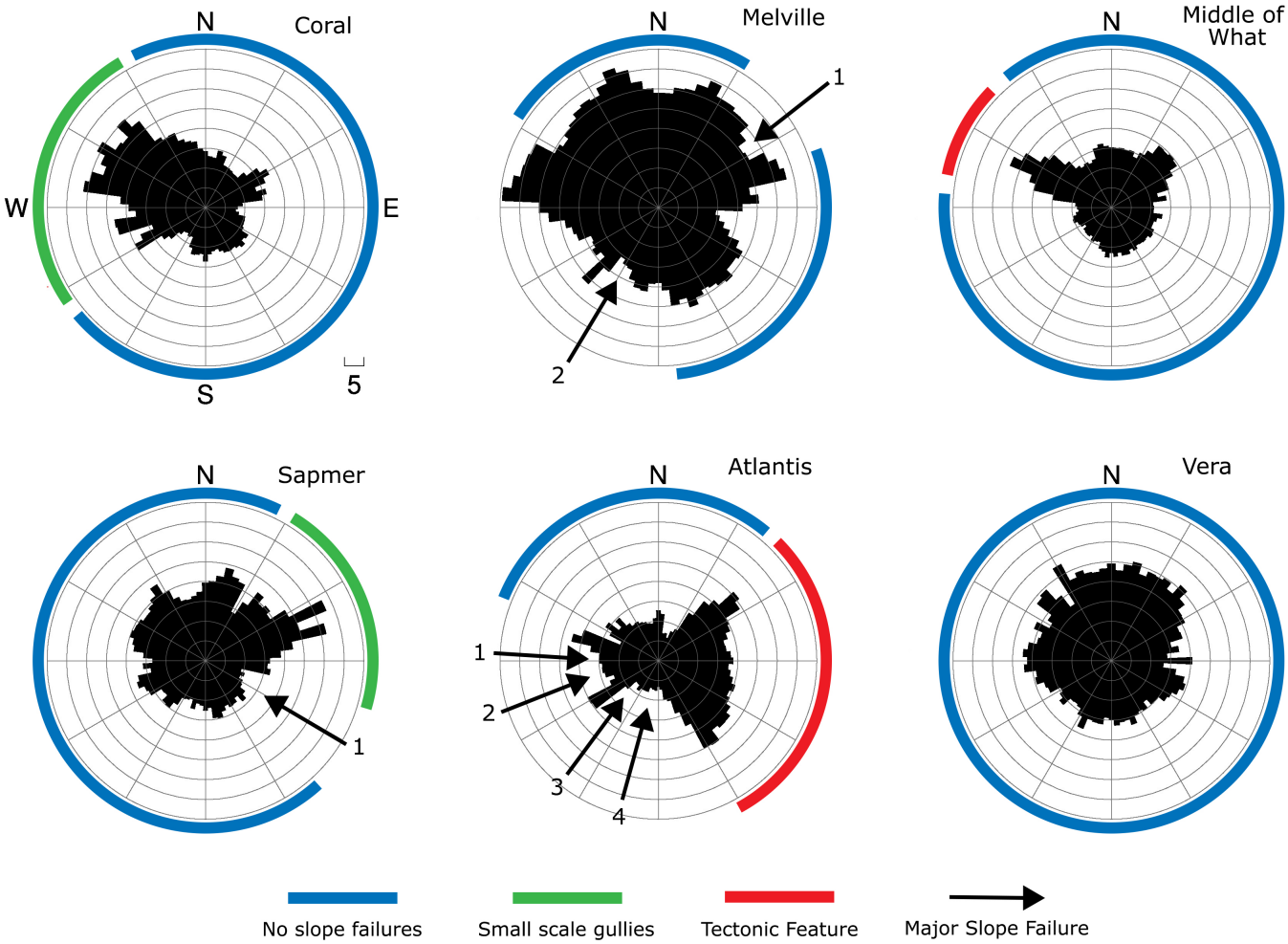


Figure 4.39: Windrose diagrams illustrating the average slope gradient along different azimuths for each seamount. Slope gradients range from 7° to 40°. Blue sectors indicate no slope failures, green sectors indicates small scale gully features which do not significantly modify the edifice geometry, red sectors indicate tectonic features such as fault scarps which affect the slope gradient. Major slope failures are indicated with black arrows, numbers correspond to table 4.2.

There is a correlation between slope angle and the frequency of major slope failures at Quaternary volcanoes (Siebert, 1984), with edifice modifying slope failures occurring at slope gradients >20° (Keating and McGuire, 2000). The average slope gradient for profiles at different azimuths from a centre point on each seamount were calculated (shown in Figure 4.39). Of the six seamounts, Melville shows the steepest slope gradients, however these are biased by the steep cliffs leading up to the summit which locally exceed 50°. The majority of the seamount slope gradients vary between 7° and

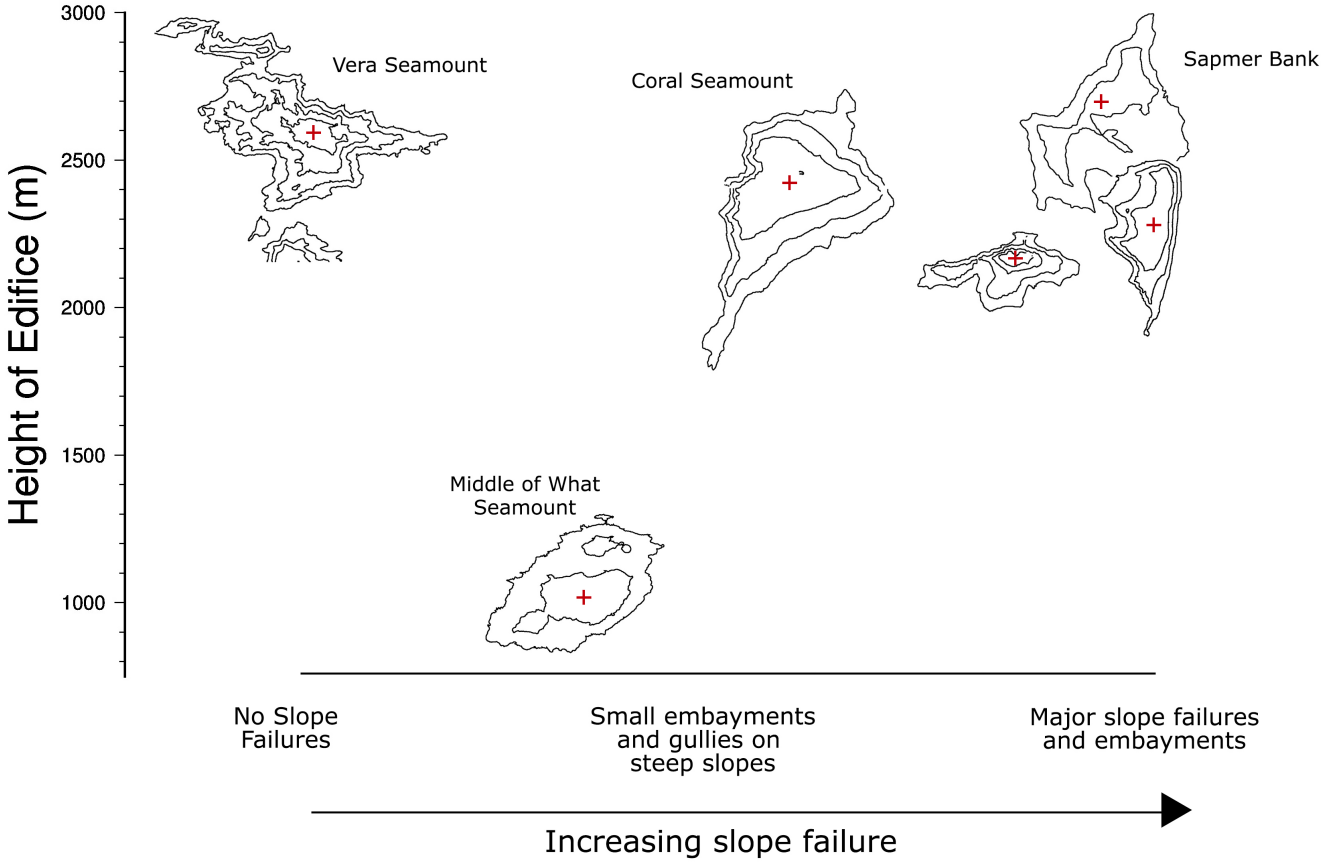


Figure 4.40: Plot showing the relationship between edifice height and the degree of slope failures present on the seamounts described in this chapter (red crosses). Bathymetric contours for the seamounts in this chapter (red crosses) are overlain to illustrate the seamount geometry. Base axis shows a qualitative description of the degree of slope failure based on bathymetry and backscatter data.

28°, though the ellipticity of some of the seamounts, in particular Atlantis Bank means that some profiles do not follow the maximum dip of the slope leading to underestimations of the average slope gradient. Tectonic features such as fault scarps introduce anomalously high slope gradients and so are marked on Figure 4.39 in red. Slope failure sectors (shown as black arrows in Figure 4.39) are characterised by comparatively low slope gradients, though the slope gradients for unfailed sectors adjacent to them have higher gradients between 15° and 20°. The steepest slope gradients generally correlate with a steep gullied morphology consisting of a series of small embayments <200 m

in depth. These gullies are the result of small volume slope failures, which do not significantly modify the slope gradient or edifice morphology. The two seamount flanks which exhibit this gully morphology are on Sapmer Bank (northwest flank) and Coral Seamount (west flank), which are adjacent to the Gallieni and Discovery II transform faults respectively. Steeply dipping fractures caused by shear stresses associated with the adjacent transform may cause the slope to break more frequently along shallow steep planes of weakness as opposed to larger deeper failures, as seen elsewhere on these edifices.

In a study of seamounts on young lithosphere including 44 mid-ocean ridge seamounts Mitchell (2003) showed that major slope failures were common on edifices greater than 2500 m and rare on edifices below this threshold of instability. Though the present day edifice heights of the seamounts are below the 2500 m threshold of instability, all three of the seamounts with major slope failures have truncated summits. Assuming that these truncated summits were caused by wave erosion and are not a primary volcanic feature the original edifice heights may be estimated. Vogt and Smoot (1984) used observations of modern oceanic volcanoes to show that the original volcanic island height prior to erosion (h), and summit plateau area (A) following erosion, are related by the following empirical formula:

$$log_{10}h = 2.5 + 0.25 \cdot log_{10}A \tag{4.2}$$

Estimations of the original volcanic island heights using this formula are listed in table 4.3, though this approach cannot be applied to Atlantis Bank as it is a tectonically generated oceanic core complex. Taking into account these estimated volcanic island heights, the maximum edifice height of all of the seamounts except for Middle of What and Vera Seamounts exceed 2500 m. The lack of major slope failures on Coral Seamount, despite its large edifice height, is attributed to the low slope gradients, which range between 7° and 12°, while Middle of What Seamount lacks sufficient edifice height to produce major slope failures.

Table 4.3: Characteristics of the edifices and truncated summits identified on the six seamounts.

Seamount	**Truncated Summit**	**Minimum Depth**	**Shelf Break Depth**	**Summit Plateau Area**	**Estimated Volcanic Island Height**
Coral	Y	190 m	310 m	5.223 km^2	478 m
Melville	Y	107 m	130 m	1.833 km^2	368 m
Middle of What	N	977 m	-	-	-
Sapmer	Y	267 m	330 m	11.260 km^2	579 m
Atlantis	Y	700 m	750 m	21.309 km^2	N/A
Vera	N	2734 m	-	-	-

The seamount lithology has a number of different effects on the slope failure potential, either forming planes of weakness along which slides may occur or highly porous and permeable layers increasing the circulation of seawater within the edifice (Keating and McGuire, 2000). Submarine volcanic eruptions at shallow depths often result in violent magma-water interaction causing lava flow material to fragment, forming poorly consolidated, porous hyaloclastite and lava rubble deposits (Moore and Fiske, 1969). For tholeiitic basalts the transition from effusive extrusion to fragmental processes occurs between 200 m to 100 m, becoming more fragmented with decreasing depth (Kokelaar, 1986). The truncated summit morphology, carbonates, and wave cut platforms indicate that all of the seamounts with major slope failures were once oceanic islands which have subsequently undergone erosion and subsidence. Comparing the shelf break depth (see Table 4.3), which represents the most recent location of the subaerial-subaqueous transition on the edifice, with the depth of slope failure headscars shows that the slope failures occur within 370 m of this subaqueous subaerial transition depth. This range is well within the depths over which phreatic eruption material would be deposited. The depths of the slope failure headscars are consistent across any given edifice (within

100 m) possibly indicating a common hyaloclastite rubble layer with low mechanical strength along which slope failures may occur (Mitchell, 2003). These highly porous layers also permit a greater depth of seawater circulation within the seamount edifice, which causes positive interstitial pore pressures, increasing the slope failure potential (Keating and McGuire, 2000).

Endo-edifice effects which affect the slope failure potential include dyke injections (Elsworth and Voight, 1995), eruptions and volcanogenic earthquakes. Without detailed mapping of dyke intrusions and information on the relative chronology of slope failures and eruptive phases, it is difficult to assess the influence of these effects at these seamounts.

Exo-edifice effects which affect the slope failure potential include rainfall and tectonic seismicity. Rainfall is an important factor in the failure potential of sub-aerial landslides as it increases the alteration of rocks to clays and increases pore pressure (Keating and McGuire, 2000). Morphological and lithological evidence shows that some of the seamounts in this study were near the sea surface and may have been volcanic islands. If so, any slope failures which were initiated in the sub-aerial environment may have been affected by rainfall. However, studies have shown that the highly permeable nature of oceanic island lithologies compared with sub-aerial lithologies means that the water table remains close to sea level and increased rainfall has little effect on the slope stability (McGuire, 1996; Mitchell, 2003). Seismic and gravitational accelerations generated by nearby earthquakes cause short lived stresses which exceed the cohesive strength of the rock (Newmark, 1965), triggering slope failures. These seamounts are situated in seismically active tectonic settings in close proximity to the spreading axis and active transforms as shown by microseismicity studies (Schlindwein and Schmid, 2016). Without real time monitoring, however, it is not possible to link the triggering of specific slope failures with specific seismic events. There are numerous examples of landslides triggered by earthquakes (e.g. Hampton et al., 1996), however some areas such as the seismically active Azores show few landslides (Mitchell, 2003), though more

have recently been discovered. This suggests that seismic waves may be a trigger for slope failures but if the slope is not already close to failure, the seismic waves alone are insufficient to cause a slope failure on their own.

This sections shows that the slope failure profiles exhibited morphological features associated with both slumping and debris avalanche processes. These features are attributed to a two-stage failure process in which slumping along deep seated faults is followed by collapse of the surficial material on the over steepened slope. The precise causes of any given slope failure are uncertain, however slope gradient, edifice height and lithology appear to be consistent factors across the seamounts.

4.5 Chapter Summary

This chapter presents novel bathymetry, backscatter, ROV imagery and petrological data from six large seamounts on the Southwest Indian Ridge crest. These data are used to identify morphological features in order to assess the tectonic, volcanic and erosional processes occurring on these seamounts. The key points are as follows:

- Bathymetry data, backscatter data, ROV imagery and petrological data were used to identify morphological features across six seamounts including volcanic ridges representing flank rift zones, volcanic cones, lava flows, slope failures, carbonate wave cut platforms and slope failures.

- Morphological and petrological data indicate that two of the seamounts (Middle of What and Vera Seamounts) formed in the neo-volcanic axis, while Coral Seamount, Melville Bank and Sapmer Bank formed, off-axis, in their current tectonic settings

- Flank rift zones (FRZs) are identified on the seamounts and classified into three types: (*i*) long narrow ridges interpreted as having a dyke core and growing through propagation of the dyke away from the edifice; (*ii*) broad ridges formed

by repeated point eruptions from a series of eruption centres on the edge of the main edifice; (*iii*) poorly developed proto-ridges, either type 1 or type 2 ridges in an early stage of development.

- Analysis of flank rift zone orientations show volcanic ridge emplacement is controlled by lithospheric stresses associated with the local tectonic setting, specifically the proximity to the ridge axis and transform or fracture zone.

- A melt migration mechanism is proposed to account for the off-axis volcanism occurring on the ridge crest. It is hypothesised that small packets of magma accumulate along the impermeable boundary at the top of the melting column and are buoyantly driven upslope from areas of anomalously thick crust observed on seismic data to areas of thinner crust. Large faults rooted in the brittle-ductile transition provide conduits through which magma may ascend to the surface.

- The development of flank rift zones on the edifice is controlled by edifice height. Seamounts above 2000 m showing well developed flank rift zones. This is attributed to an increase in the lithostatic pressure at the base of the melt column promoting lateral intrusion.

- The edifice volume shows a positive correlation with flank rift zone length, unlike other studies in which edifice height is proposed as the governing factor. This suggests that the availability of magma supply is a limiting factor at these seamounts.

- Two main types of slope failure are identified on the seamounts (*i*) major slope failures, which significantly indent the seamount edifice; (*ii*) small gully structures, which do not alter the geometry of the seamount.

- Slope failure profiles could be distinguished from volcanic unfailed flanks using the exponential, b, coefficient and RMS errors of an exponential function fitted to the profiles with the exception of one anomalous profile.

- The slope failure profiles exhibited morphological features associated with both slumping and debris avalanche processes. These features are attributed to a two-stage failure process in which slumping along deep seated faults is followed by collapse of the surficial material on the over steepened slope.
- The precise causes of any given slope failure are uncertain, however slope gradient, edifice height and lithology appear to be consistent factors across the seamounts.

Chapter 5

Seamount Distribution

Seamounts are topographic rises on the seafloor, which have limited lateral extent and generally have circular or sub circular bases (Koppers and Watts, 2010). Early definitions of seamounts arose from those observed in intraplate settings and had elevations in excess of 1000 m (Menard, 1963). Since then, however, seamounts have been identified in a wide variety of tectonic settings, some of the smallest located on the mid-ocean ridge crests with elevations as low as 50 m (Smith and Cann, 1990).

Studies of seamount distribution generally fall into two categories: (1) local studies using high resolution multibeam bathymetry over a relatively small area (e.g. Smith and Cann, 1992; Batiza and Vanko, 1984; Behn et al., 2004); (2) global studies using satellite derived bathymetry or gravity data (e.g. Wessel, 2001; Kitchingman and Lai, 2004; Kim and Wessel, 2011) and shipboard bathymetry data (Hillier and Watts, 2007). This chapter is, therefore, split into two separate studies. The first study focusses on the detection of small seamounts (as small as 50 m tall) within the axial valley. This study is limited to areas with complete swath bathymetry of the axial valley, which consist of four Sections along the ridge. The second study focusses on the detection of large seamounts (greater than 300 m tall) on the ridge crest and flanks. This study uses a combination of swath and satellite derived bathymetry, and provides a means to examine the variation in volcanic activity across the ridge as a whole, as well

as comparisons with other spreading centres. A modified basal outlining algorithm (MBOA), developed by Bohnenstiehl et al. (2012) is used to detect volcanic seamount structures in the axial valley as well as on the ridge crest and surrounding flanks.

5.1 The Modified Basal Outlining Algorithm

The aim of the Modified Basal Outlining Algorithm (MBOA), which was developed by Bohnenstiehl et al. (2012), is to identify seamount edifices and subsequently re-evaluate the basal contour of the seamount, thus providing more accurate estimations of seamount height, volume and area. This is particularly important for seamounts in areas of rough topography, as the algorithm is able to isolate seamounts from surrounding features such as fault scarps and fracture zones.

The modified basal outlining algorithm initially identifies closed contours from gridded bathymetry data. The contouring interval, which affects the minimum seamount elevation that can be detected, may be specified. These contours are then selected or rejected based on a series of specified parameters:

1. Closed contours which exceed a specified maximum diameter or are below a minimum diameter are rejected, removing large plateaus and small knolls.

2. Closed contours that do not enclose at least two other contours are rejected due to insufficient positive relief.

3. Closed contours for which a best fitting ellipse (determined using least squares) exceeds a specified ellipticity ratio are rejected. This removes fault generated abyssal hill topography, which tends to be more elongate than volcanic seamounts.

4. Closed contours for which the mean error between the basal contour and best fitting ellipse exceeds a specified error, are rejected. The error is calculated as the radial separation between the basal contour and best fitting ellipse, normalised for the radius of the ellipse for that azimuth. These are then averaged across all

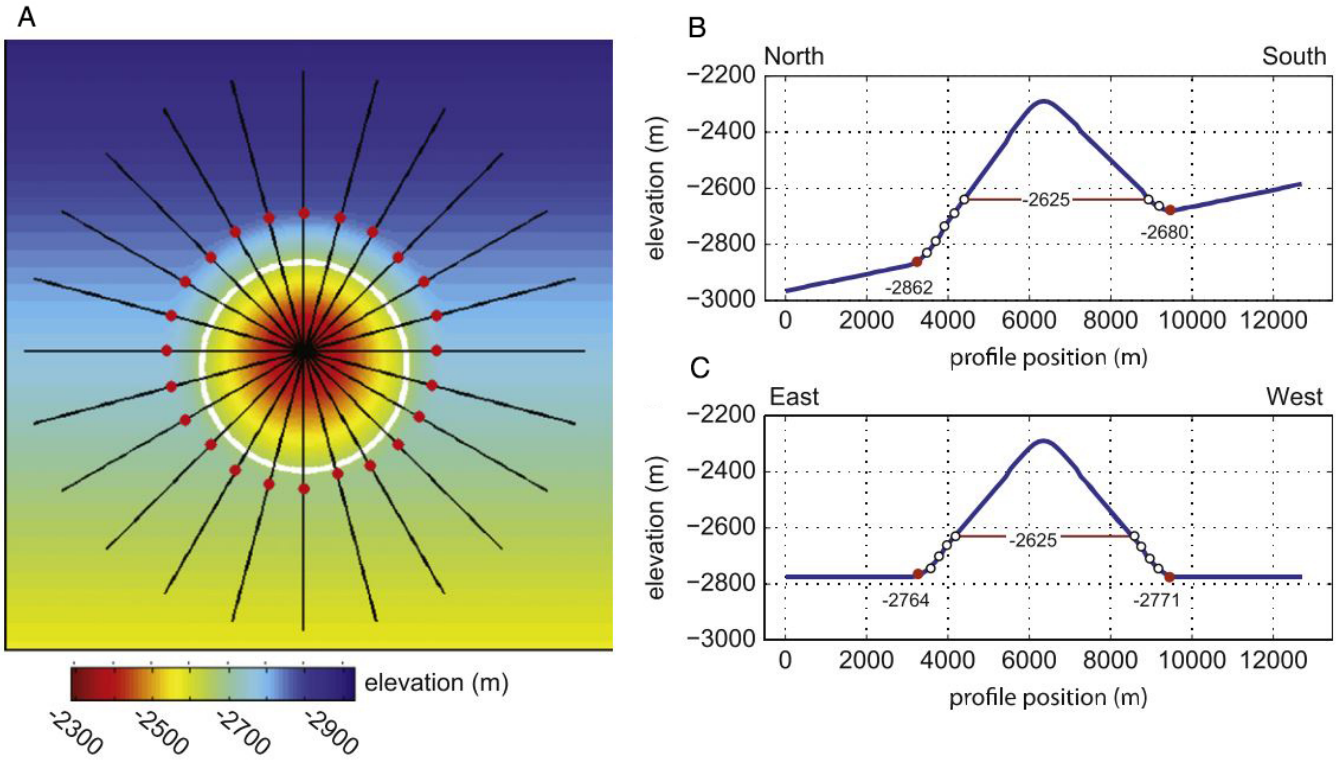


Figure 5.1: Reproduced from Bohnenstiehl et al. (2012). Panel A shows the locations of topographic profiles passing through the topographic peak, distributed azimuthally. Panels B and C show N-S and E-W profiles. White circles show the incremented steps as the basal contour is modified down slope. Red circles show the termination point of the basal contour modification for these profiles.

the azimuths.

5. Closed contours which have a slope that fails to fall within a specified range of gradients are rejected. The slope is calculated by approximating the seamount to a circular cone where the basal area is defined by the planimetric area within the basal contour, and the height is defined by the maximum elevation in within the basal contour. The slope is therefore given by $tan^{-1}\left(\frac{\text{height}}{\text{basal radius}}\right)$

6. Closed contours which are enclosed in another closed contour are rejected so that each topographic high is represented by a single basal contour.

The remaining closed contours each define a single topographic high. The basal contour is then modified to produce a more accurate basal outline, which takes into account the complex morphology of the seamount and surrounding topography.

1. Topographic profiles passing through the topographic peak are constructed, distributed azimuthally as shown in Figure 5.1.

2. For each profile the intersection of the initial basal contour and the topographic profile is identified and acts as an initial starting point.

3. For each profile the basal contour point is incrementally stepped downslope in the forward direction, the reverse direction, and then both forward and reverse directions simultaneously.

4. Following incrementation the new seamount profile is assessed against a series of geometric criteria to determine if the new profile better describes the edifice. The primary geometric criteria used to determine this is the ratio of the cross section area, A, to the outlining perimeter, O. It has been shown that the A/O ratio of a cross section through a seamount generally increases until the profile extends beyond the base of the seamount edifice (Hillier, 2008). The outlining contour is migrated downslope until the A/O ratio fails to increase. This is repeated in the reverse profile direction, and finally once more in both directions simultaneously for each profile.

5. In addition to the A/O, a number of parameters including maximum slope, distance from peak, and the fractional difference in basal height between the forward and reverse direction profiles are checked after each migration to prevent unreasonable edifice boundaries. The migration halted if these parameters are violated.

6. This is repeated for each of the azimuthally distributed profiles resulting in a new irregular basal outline, which cross cuts the contours. This is then smoothed using a median filter to produce the final basal outline.

The modified basal outline is then used for calculations of height, volume and area and represents the seamount edifice more accurately than the original basal contour. The volume and height are calculated relative to a non-planar basal surface, which passes through the modified basal outline. This technique was applied to bathymetry grids

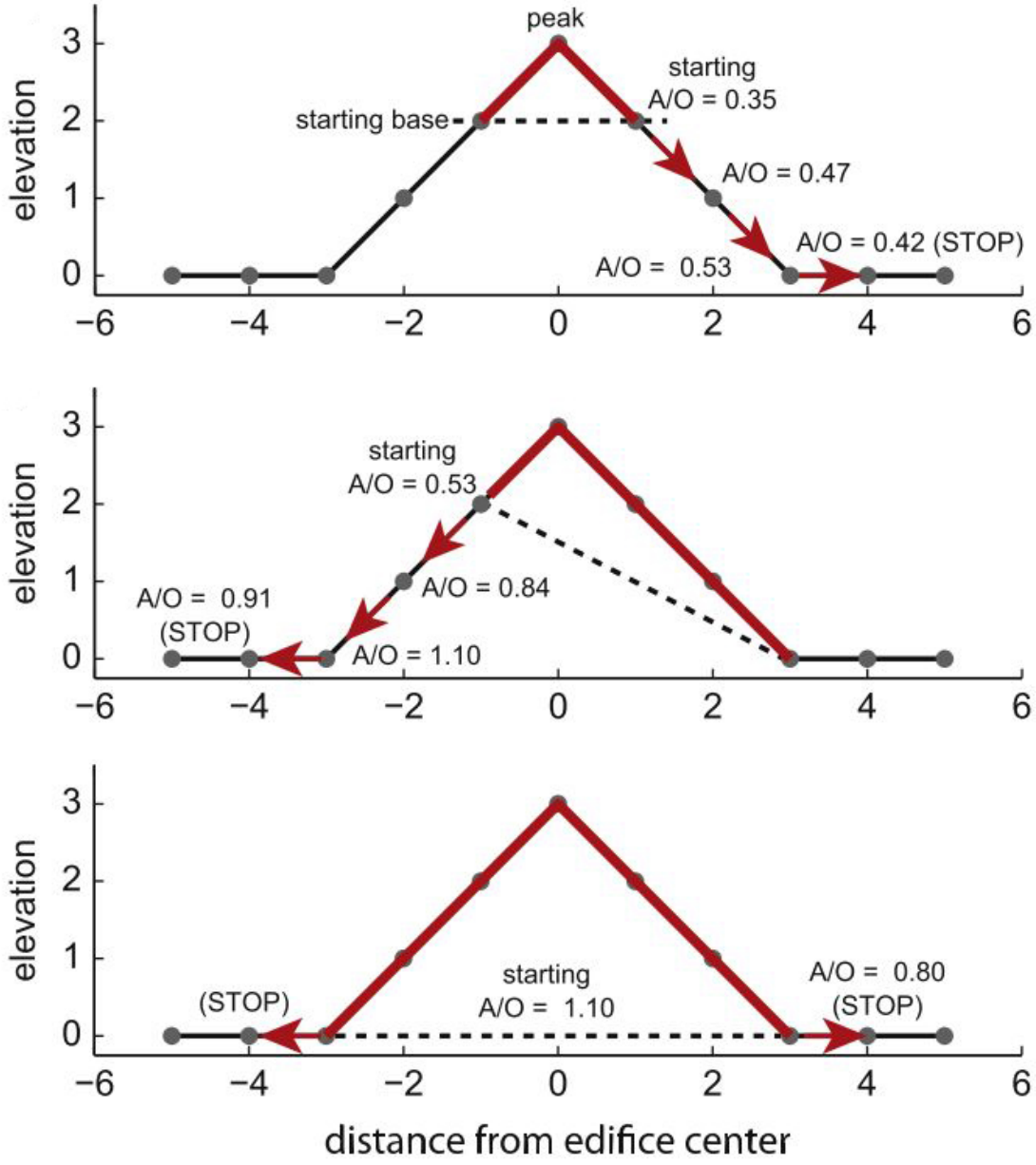


Figure 5.2: Reproduced from Bohnenstiehl et al. (2012). Schematic diagram showing the incrementation of the basal contour, and the subsequent changes in the ratio of the cross sectional area and outlining perimeter, which is primarily used to determine the location of the base of the seamount.

across the SWIR and surrounding area in two separate studies. The first study focusses on the detected of small seamounts (at least 50 m tall) within the axial valley. The second study focusses on the detection of large seamounts (greater than 300 m tall) on the ridge crest and flanks.

5.2 Axial Valley Floor Seamounts

This study aims to identify small seamounts (greater than 50 m tall) on the axial valley floor across four different Sections of the ridge: the oblique Section (10° E to 16 E), the orthogonal Section (16° E to 25° E), the central Section (46° E to 52° E) and the eastern Section (56° E to 61° E). There are a number similar studies which use swath bathymetry to detect small axial valley seamounts on the MAR (Smith and Cann, 1990, 1992), Galapagos spreading centre (Behn et al., 2004) and Gakkel Ridge (Cochran, 2008). Mendel and Sauter (1997) conducted a similar study on the easternmost part of the SWIR between 57° E and 70° E. This overlaps slightly with the eastern Section of this study.

5.2.1 Data and Methods

The Sections of the ridge with complete swath bathymetry coverage used for this study are illustrated in Figure 5.3.

The bathymetry data were gridded at an interval of 50 m, and the analysis conducted on boxes spanning 0.2° longitude for computational efficiency. All seamounts within the boxes were analysed and the axial valley floor seamounts subsequently distinguished based on their location compared to the bounding axial valley walls. Figure 5.4 shows an example of the seamounts detected on several segments on the orthogonal Section; each seamount is represented by a white circle of fixed diameter. The map is contoured at 250 m so seamounts between 50 m and 100 m may not be visible on the bathymetry.

For this study the algorithm was tested and calibrated using an area of the MAR between 24° N and 30° N, which has been the location of numerous bathymetric, gravity and seismic studies (e.g. Lin et al., 1990; Sempere et al., 1993; Smith and Cann, 1990). Seamount distribution studies have been carried out using bathymetry and side-scan sonar (Smith et al., 1995) and it has been used to calibrate closed contour seamount detection algorithms in other studies (e.g. Behn et al., 2004; Cochran, 2008), providing

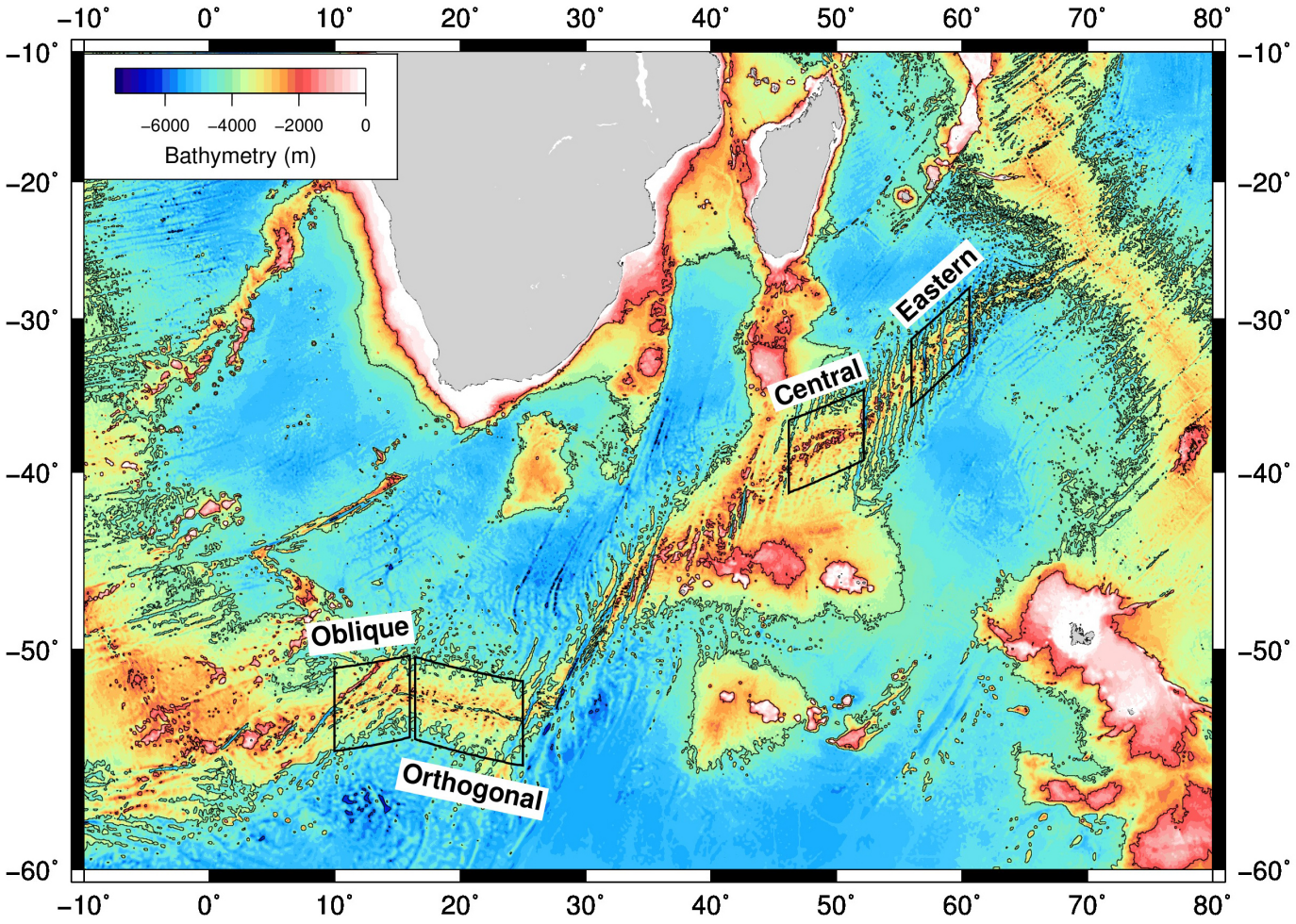


Figure 5.3: Bathymetric map showing location of four study areas: oblique, orthogonal, central, eastern. Study areas are outlined by black boxes. Bathymetry data is derived from the GEBCO 2014 30'' x 30'' global bathymetry grid (IOC et al., 2003) and contoured at 2000 m.

a basis for comparison and calibration. Shipboard bathymetry between 24° N and 30° N was gridded at an interval of 50 m. Behn et al. (2004) showed that a contour interval of 10 m and maximum aspect ratio of 2 (elliptical ratio of 0.5) were sufficient to distinguish volcanic edifices from tectonic highs in the axial inner valley. Figure 5.5 shows the bathymetry of a Section of the MAR axial valley between 25.5° N and 27.5° N and the locations of the identified seamounts greater than 50 m in height. These are classified into axial valley floor seamounts (red circles) and rim flank seamounts (white circles).

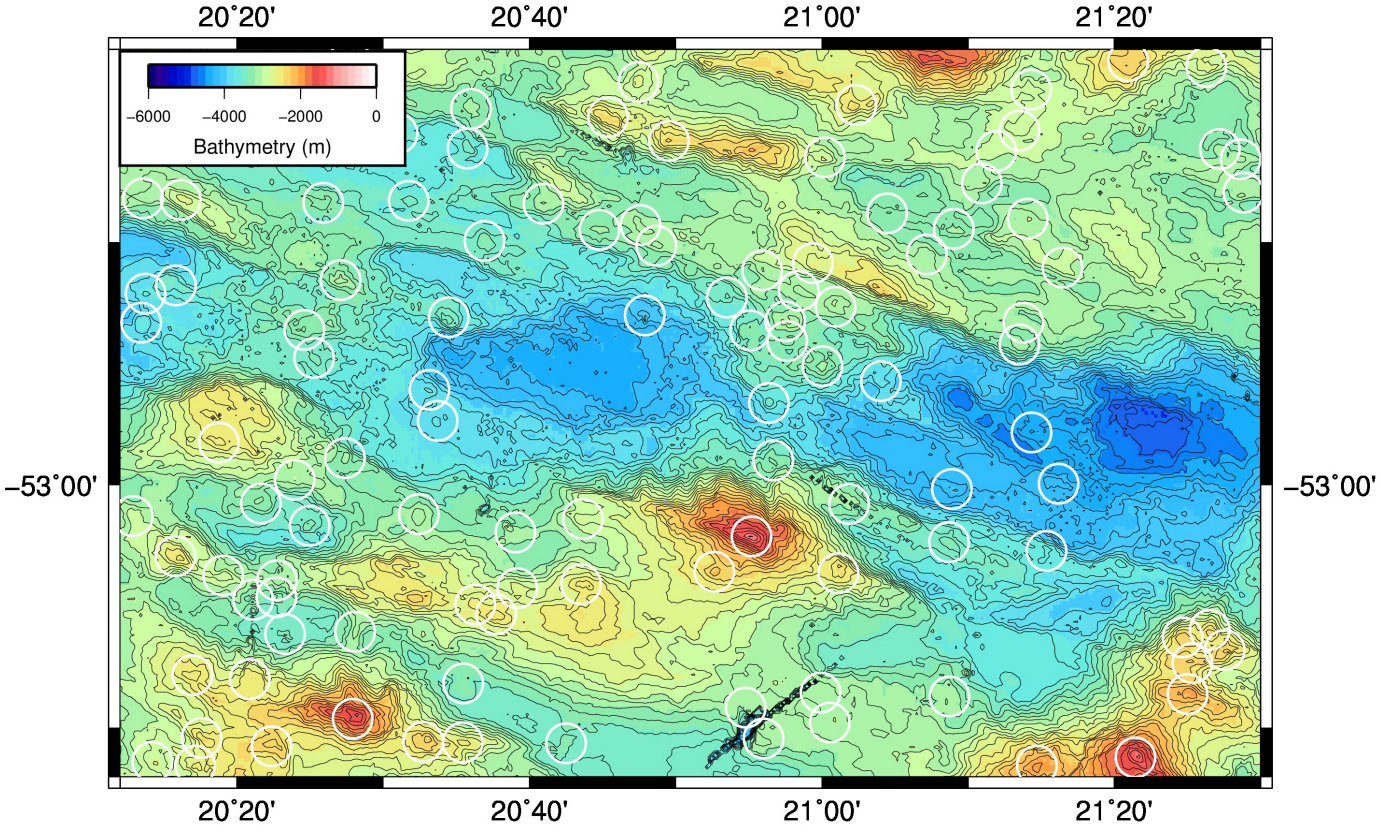


Figure 5.4: Bathymetric map of the axial valley gridded at 50 m using swath bathymetry. White circles of fixed diameter are used to show the locations of seamounts detected which are greater than 50 m in height. The map is contoured at 250 m so seamounts between 50 and 100 m may not be clearly visible on the bathymetry.

A total of 437 seamounts, which had a relief (vertical distance between the basal contour and seamount peak) greater than 50 m, were identified on the axial valley floor between 24° N and 30° N. These were identified over an area of 7192.4 km^2, giving a seamount density of 60.76 seamounts per 1000 km ^{2}. This seamount density lies between the estimates of 80 and 55.5 per 1000 km^2 made by Smith and Cann (1992) and Cochran (2008). The variation in estimated seamount densities between these studies is most likely due to differences between closed contouring algorithm methodologies and manual side-scan sonar identification, as well as differences in the definition of the axial valley floor boundaries.

Seamount populations have previously been characterised by their cumulative height-

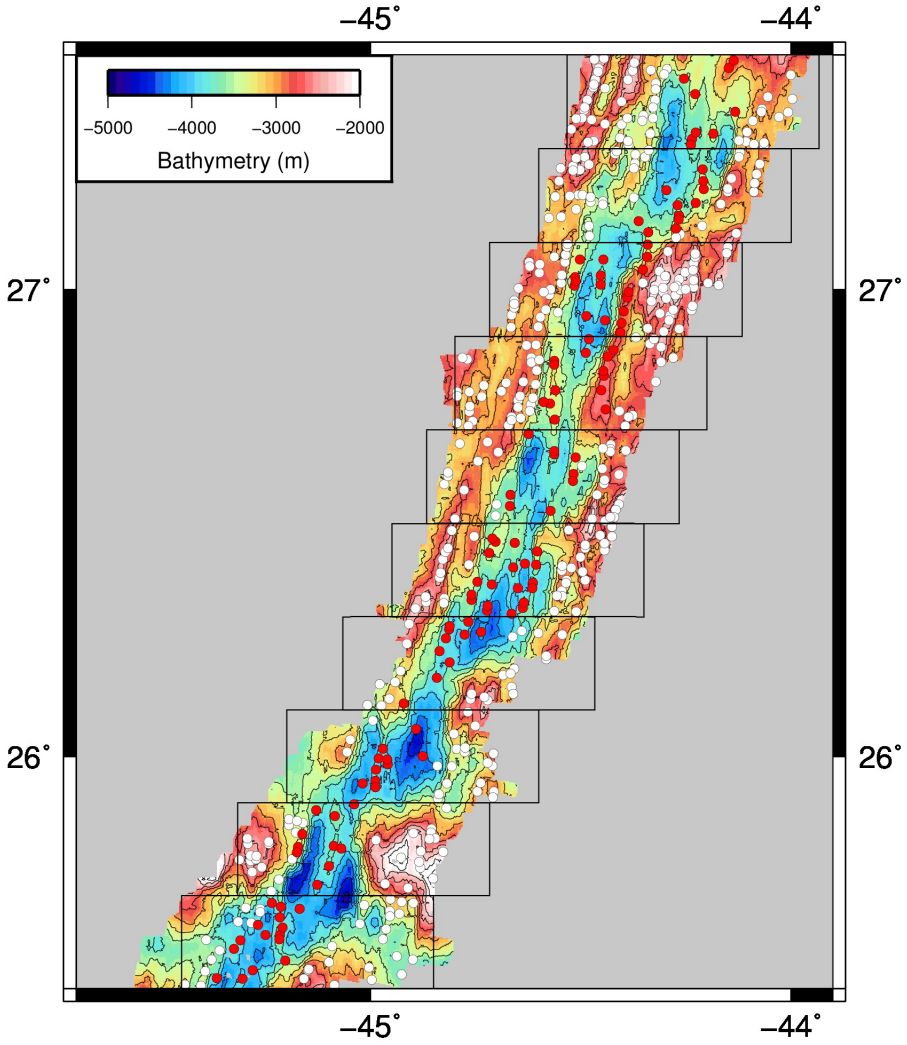


Figure 5.5: Bathymetric map of the MAR axial valley and flanking highs between 25.5° and 27.5° N gridded at 50 m derived from multibeam bathymetry. This represents a subset of the entire analysis area which extends between 24° and 30° N. Black boxes show the areas in which the MBOA was used to detect seamounts. Red circles show the locations of seamounts detected on the axial valley floor greater than 50 m in height. White circles show the location of seamounts detected on the flanking highs greater than 50 m in height. The bathymetry is contoured at 250 m.

frequency, which has shown that the height distribution follows an exponential pattern (Jordan et al., 1983). Since the height distribution does not follow a Gaussian distribution, a non-linear least squares model is not suitable; Smith and Jordan (1988) showed that a maximum likelihood model is the most appropriate way to characterise the seamount populations. Maximum likelihood estimates parameters based on the

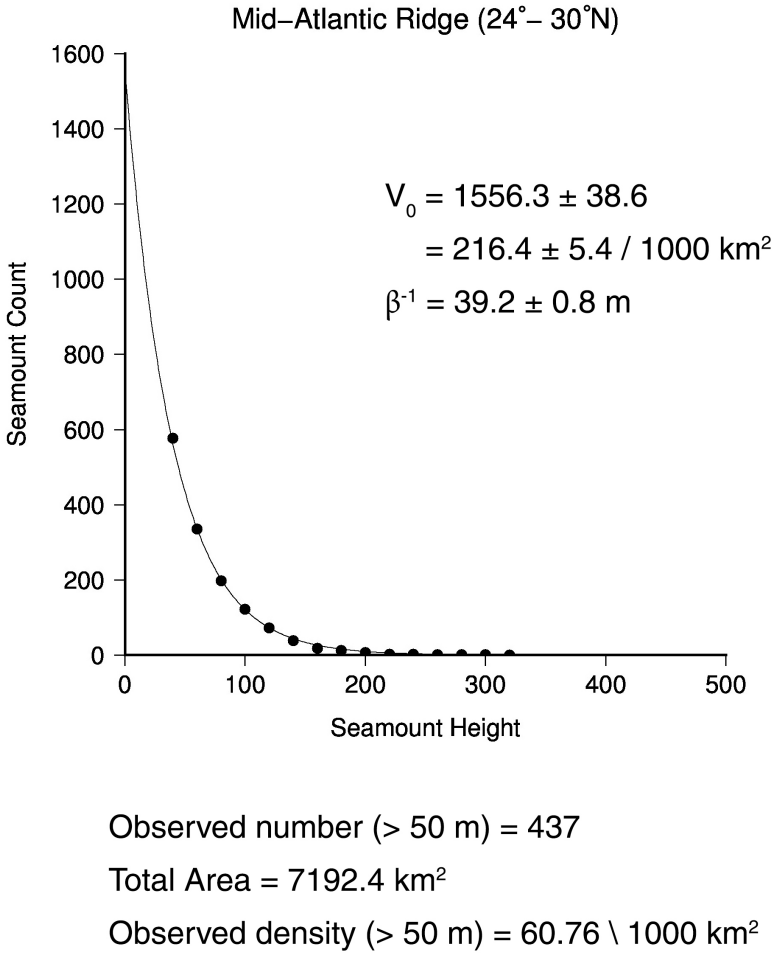


Figure 5.6: Cumulative count of seamounts plotted against height for the axial valley floor of the MAR from 24° N to 30° N. Black solid circles show the observed height distribution, black line shows the maximum likelihood model fit to the data.

probability of those parameters reproducing the observed data. The model assumes that the number of seamounts, v, per unit area is given by

$$v(H) = v_0 e^{-\beta H} \tag{5.1}$$

for seamounts greater than or equal to height, H. v_0 is the average number of seamounts per unit area and β^{-1} is defined as the characteristic height of the seamount population. Figure 5.6 shows the cumulative height distribution of the seamount population for the MAR between 24° and 30° N.

The data is represented by the black dots, while the black line represents the maximum likelihood model fit. The data shows a generally good fit to the exponential model. Slight deviations from the model at seamount heights greater than 130 m are attributed to the inherent randomness in the small number of tall seamounts present. The maximum likelihood fit provides estimates of v_0 and β values. The v_0 value provides information on the total number of seamounts with height greater than 0 m detected; however it assumes that there are a large number of small seamounts present which are unresolvable on the swath bathymetry. As a result the v_0 gives an impression of a greater number of seamounts than may be observed, and consequently the observed number of seamounts per unit area (number of seamounts detected over 50 m in height) will be used as a more representative indicator of the seamount density in a given region. The v_0 and β values are useful for comparing the results from this study with other studies of the same region. In order to compare the v_0 values they have been normalised by area. Table 5.1 shows the seamount population characteristics estimated using the maximum likelihood model on the MAR between 24° N and 30° N.

Table 5.1: Seamount population statistics for different studies between 24° N and 30° N on the axial valley floor of the Mid-Atlantic Ridge

Study	**Observed number (greater than 50 m tall)**	**Observed density (per 1000 km ^{2})**	**Total no. of seamounts (per 1000 km ^{2}), v_0**	**Characteristic Height, β^{-1} (m)**
This study	437	60.8	216.4 ± 5.4	39.2 ± 0.8
Cochran (2008)	399	55.5	242.7 ± 9.4	42.1 ± 1.6
Behn et al. (2004)	455	-	144±7	40±2
Smith and Cann (1992)	481	80	195±9	58.1±1.6

The observed number of seamounts over 50 m in height, observed seamount density and v_0 values obtained from this study for the MAR region are similar to previously obtained values. The characteristic height of 39.2 m is very close to the characteristic height values of 42.1 m and 40 m obtained by Cochran (2008) and Behn et al. (2004).

5.2.2 Results

Oblique Section

Figure 5.7 shows the location of seamounts in the inner axial valley floor of the oblique Section (see Figure 5.3), which have a maximum height (maximum height difference between the highest point and a point on the basal contour) greater than 50 m.

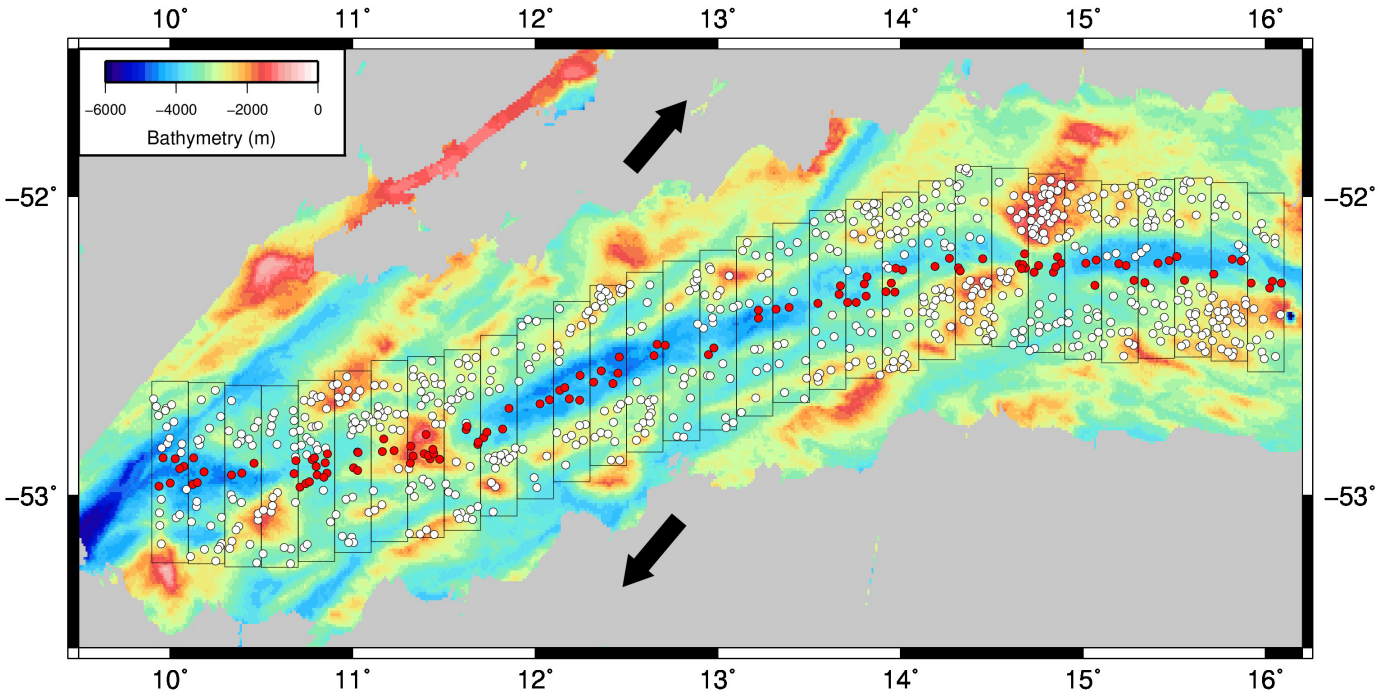


Figure 5.7: Bathymetry map of the oblique Section based on multibeam bathymetry. Black boxes outline the areas used in the analysis to detect seamounts. Red circles show the locations of seamounts with height greater than 50 m in the axial valley floor. White circles show the location of seamounts with height greater than 50 m on the rim flanks. Bathymetry data was used to identify the limits of the axial valley floor to calculate the observed seamount densities.

This analysis identified 119 seamounts within the oblique axial valley floor over an area of 6211.2 km^2, giving an observed average density of 19.2 per 1000 km ^{2}. This density is 31.6 % of that observed on the MAR axial valley floor and the second lowest density observed out of the four Sections of the SWIR in this study.

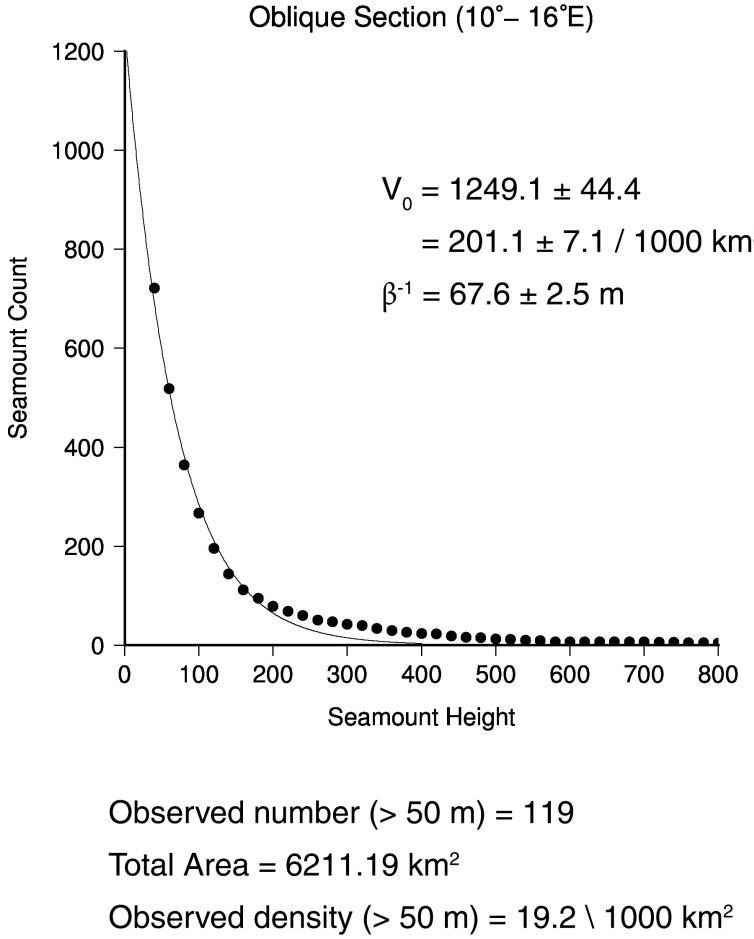


Figure 5.8: Cumulative count of seamounts plotted against height for the axial valley floor of the oblique Section. Black solid circles show the observed height distribution, black line shows the maximum likelihood model fit to the data.

Figure 5.8 shows the height distribution for the seamount population on the oblique Section. This seamount population has a characteristic height (β^{-1}) of 67.6 m, which is the tallest out of all studies on the SWIR and approximately 1.7 times the height observed at the MAR. This larger characteristic height is attributed to two factors. The first is that the MBOA adjusts the initial basal contour downwards to produce a more

accurate basal contour, which increases the seamount height compared to traditional closed contour methods. Calibration with the area on the MAR suggests, however, that this effect is minimal. The second is that the colder thermal regime at the ultra-slow spreading SWIR produces a stronger lithosphere, capable of supporting taller seamounts. Seamounts emplaced on weaker lithosphere are smaller due to greater flexural subsidence, whereas on the stronger lithosphere of the SWIR, more of the seamount edifice remains visible.

The greater characteristic seamount height compared to the MAR is evident in the large number of seamounts between 200 m and 500 m tall, causing the seamount population to deviate from the exponential model. The total seamount volume represented by a seamount population, and therefore magma supply, is a product of the seamount density and seamount height. Assuming a constant height to basal radius ratio between the SWIR and the MAR, the magma supply at the oblique Section is approximately 54 % that of the MAR. This is primarily due to the low seamount density at the SWIR, despite the greater characteristic height.

The seamount distribution is not uniform along the oblique Section. Figure 5.9 compares the distribution of seamounts along the axial valley with axial depth. Bathymetric and sampling studies along the oblique Section (e.g. Dick et al., 2003; Standish et al., 2008) have been used to split the Section into amagmatic segments, characterised by deep wide axial valleys, punctuated by two magmatic segments, characterised by shallow saddles, centred on 11.3° E and 14.7° E. We would expect the greatest seamount density to be observed at these magmatic segments, however that is not the case. Inspection of the axial bathymetry shows that these segments are dominated by large seamounts, which fill the axial valley. Seamounts detected on these segments using the MBOA represent parasitic cones on these large seamounts, and therefore do not represent the actual magma supply. This is further supported by the increase in seamount numbers in the shallow areas immediately surrounding these magmatic segments, suggesting the melt is focussed towards these segments. The amagmatic segments, which

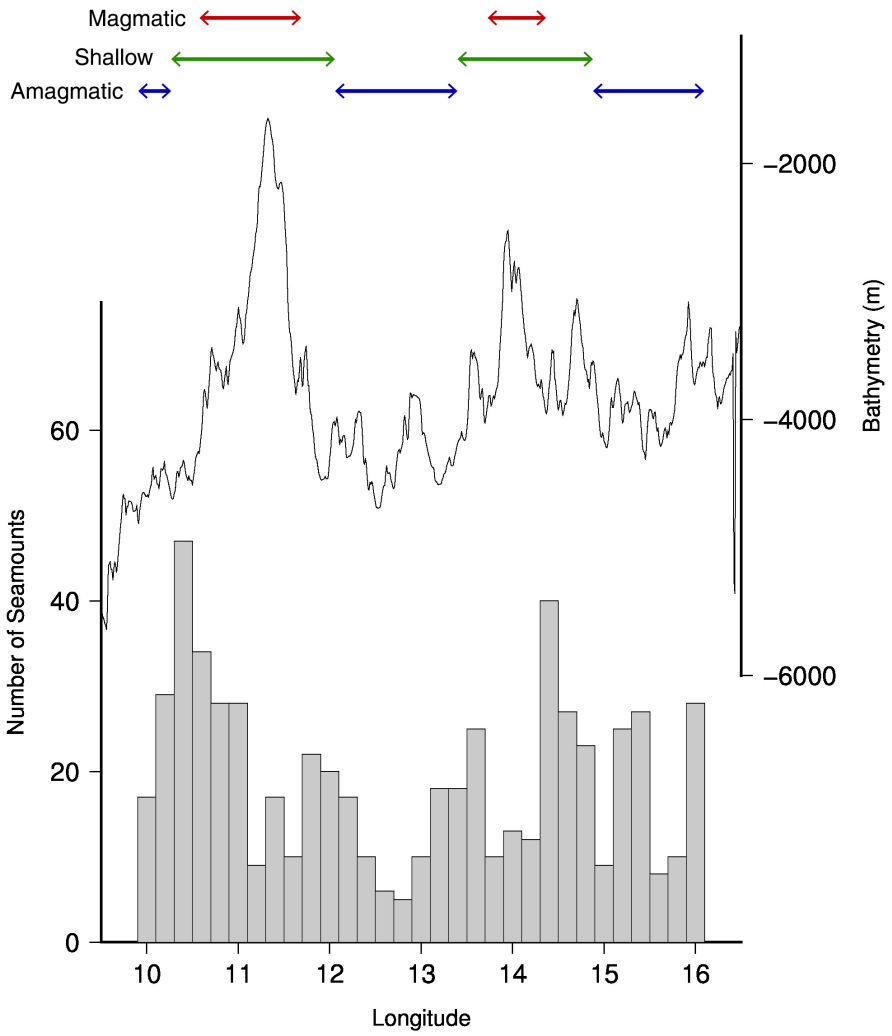
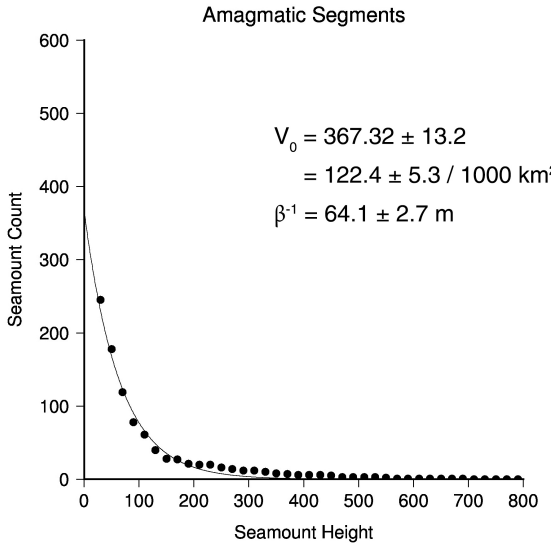


Figure 5.9: Seamount distribution along the axial valley of the oblique Section. Lower graph shows the number of seamounts binned in intervals of 0.2° longitude. Upper graph shows the axial bathymetry along zero-age.

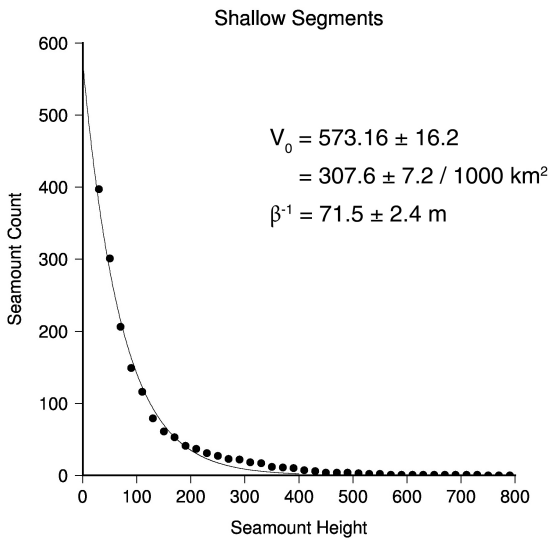
have greater axial depths, are generally represented by a low seamount density, consistent with the observations of Dick et al. (2003).

The differences between the seamount populations on the different segment types in this Section are made clear by looking at the population statistics for each type of segment. Swath bathymetry, mantle Bouguer anomalies (see chapter 3) and lithological sampling by Dick et al. (2003) were used to divide the oblique Section into three segment types: (1) Amagmatic segments, characterised by deep wide axial valleys and tectonised



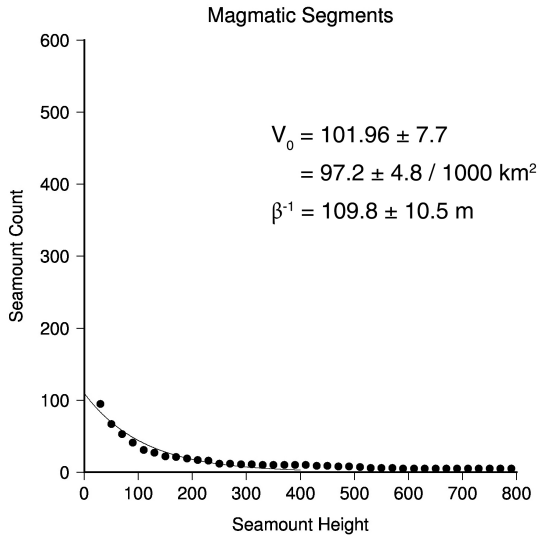
Observed number (> 50 m) = 39
Total Area = 3002.07 km²
Observed density (> 50 m) = 12.9 \ 1000 km²

(a) Amagmatic segments



Observed number (> 50 m) = 48
Total Area = 1863.35 km²
Observed density (> 50 m) = 25.8 \ 1000 km²

(b) Shallow segments



Observed number (> 50 m) = 26
Total Area = 1138.7 km²
Observed density (> 50 m) = 22.8 \ 1000 km²

(c) Magmatic segments

Figure 5.10: Cumulative count of seamounts plotted against height for the axial valley floor of the three segments types in the oblique Section, a) Amagmatic, b) Shallow c) Magmatic. Black solid circles show the observed height distribution, black line shows the maximum likelihood model fit to the data.

structure; (2) Magmatic segments, characterised by extremely shallow axial depths caused partial magmatic filling of axial valley; (3) Shallow segments, characterised by shallow axial depths and narrow hourglass shaped axial valleys, though the axial valleys are not filled. Figure 5.10 shows the seamount population statistics of these three segment types.

The amagmatic segments have the lowest observed seamount density of 12.9/1000 km^2, 67% of the total Section seamount density. These segments also have the lowest characteristic height, which, along with the low seamount density, suggests a significant reduction in melt supply at these segments. The shallow segments have the highest observed seamount density of 25.8/1000 km^2 and a characteristic height of 71.5 m indicating a greater melt supply than at the amagmatic segments. The observed seamount density is still significantly lower than that observed at the MAR, so this should still be considered part of a melt-poor system. The magmatic segments where we would expect a greater observed seamount density and increased characteristic height, exhibit a lower seamount density than the adjacent shallow segments. This is due to the filling or partial filling of the axial valley with volcanic material, forming large seamount structures spanning the axial valley width. The 'seamounts' detected are therefore more likely to be parasitic cones leading to a lower seamount density than expected. The characteristic height of 109.8 m is greater than either of the other Sections, though the height distribution suggests that this is derived more from a lack of small seamounts that a particular abundance of large seamounts. It does, however, support the increase in melt supply at these segments.

Orthogonal Section

Figure 5.11 shows the locations of seamounts with height greater than 50 m detected within the axial valley of the orthogonal Section (between 16 ° E and 25° E).

The analysis identified 243 seamounts in this Section over an area of 9020.97 km^2, giving an observed seamount density of 26.9/1000 km^2. This is greater than the seamount

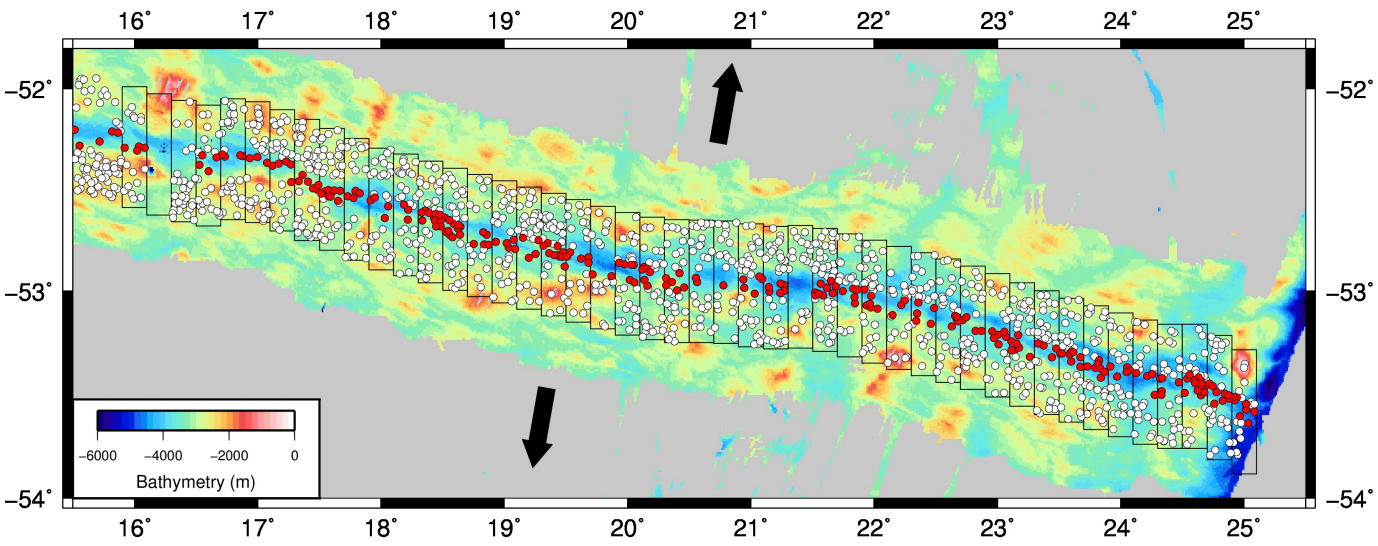


Figure 5.11: Bathymetry map of the orthogonal Section based on multibeam bathymetry. Black boxes outline the areas used in the analysis to detect seamounts. Red circles show the locations of seamounts with height greater than 50 m in the axial valley floor. White circles show the location of seamounts with height greater than 50 m on the rim flanks.

density observed on the oblique Section, but still only 44% that of the MAR. The seamount density for this Section is similar to that of the shallow segments on the oblique Section, suggesting that the orthogonal Section represents an intermediate melt supply, though still melt-poor compared to the mid-ocean ridge system. Figure 5.12 shows the seamount height distribution of the orthogonal Section seamount population, which yields a characteristic height of 55.4 m, shorter than the oblique Section though taller than the seamounts on the MAR.

The population statistics show that the orthogonal Section, like the oblique Section, has a lower seamount density than the MAR, though the characteristic height is greater. Assuming a constant height to basal radius between the SWIR and the MAR, the magma supply at the orthogonal Section is approximately 63 % that of the MAR.

The distribution pattern along this Section is different from that across the oblique Section. Where the oblique Section was split into different segments with distinct seamount populations, the distribution is more consistent between segments along the orthogonal Section. Figure 5.13 shows the distribution along the axial valley with

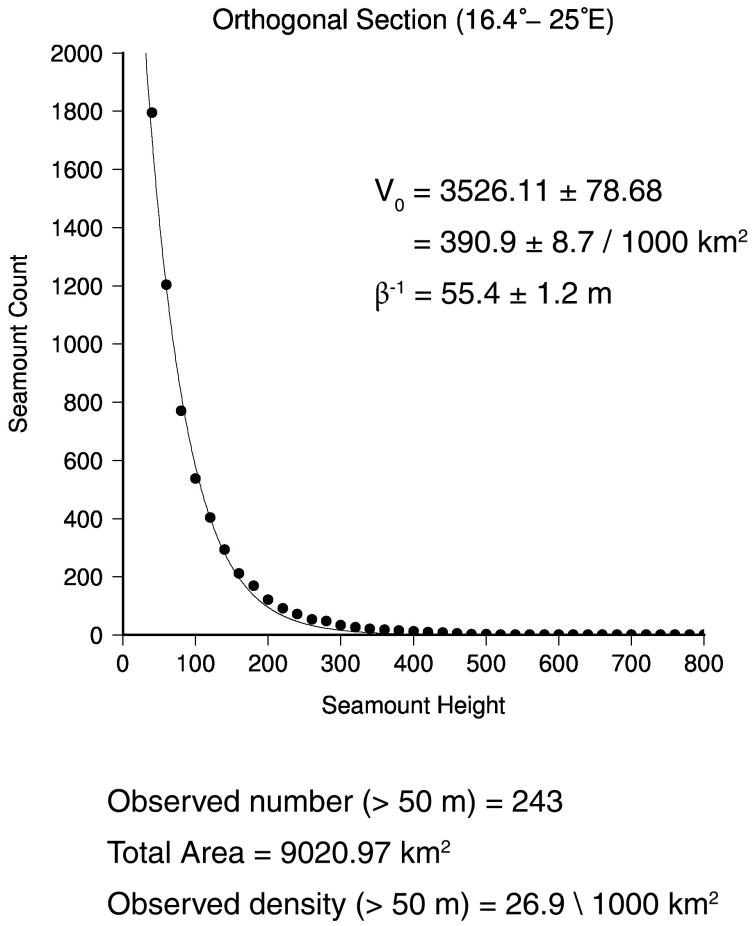


Figure 5.12: Cumulative count of seamounts plotted against height for the axial valley floor of the orthogonal Section. Black solid circles show the observed height distribution, black line shows the maximum likelihood model fit to the data.

longitude compared to the axial bathymetry.

There is a notable broad increase in seamount numbers towards the centre of the Section. Short wavelength changes in seamount numbers are superimposed along this longer wavelength pattern. These shorter wavelength patterns may correspond to individual segments, in which case we would expect an increase towards the centre of the segment due to melt migration away from the bounding discontinuities, as has been observed on the MAR (e.g. Lin et al., 1990; Tolstoy et al., 1993).

In order to test this, the spatial distribution of the seamounts within each segment was analysed. For each seamount the distance between the edifice and the discontinuity

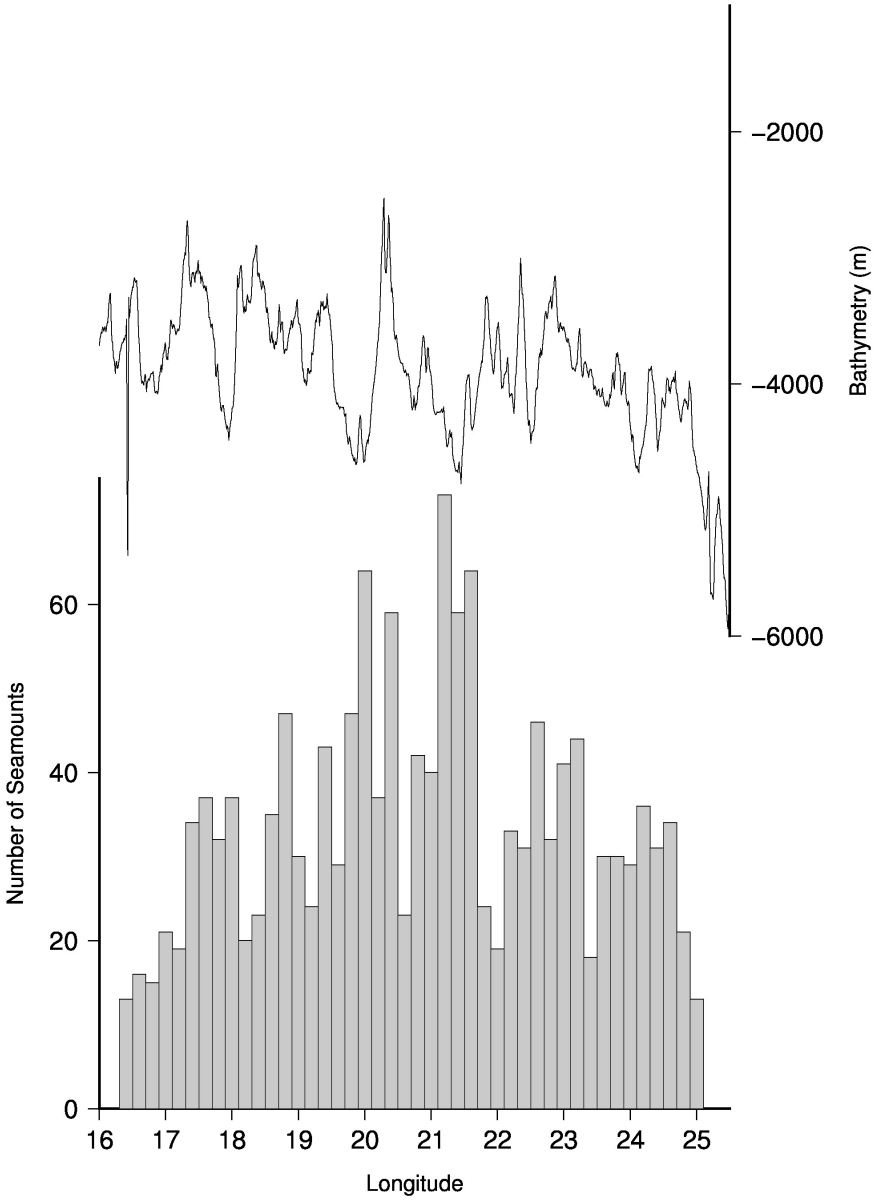


Figure 5.13: Seamount distribution along the axial valley of the orthogonal Section. Lower graph shows the number of seamounts binned in intervals of 0.2° longitude. Upper graph shows the axial bathymetry along zero-age crust.

immediately to the west was calculated. This distance was then divided by the total length of that segment and multiplied by 360° to form a phase angle, which is a non-dimensional representation of the seamounts position within the segment. An angle of 0° corresponds to the discontinuity, while an angle of 180° corresponds to the centre of the segment. Therefore, a large number of seamounts with angles between 90° and 270°

indicate a high concentration of seamounts at the centre of the segment; conversely a large number of seamounts with angles between 0° and 90°, and 270° and 360° indicate high a concentration of seamounts near the segment ends. This approach allows us to compare the seamount spatial distribution for segments of different length. Figure 5.14 shows the phase angle distribution for seamounts in the inner valley of the orthogonal Section.

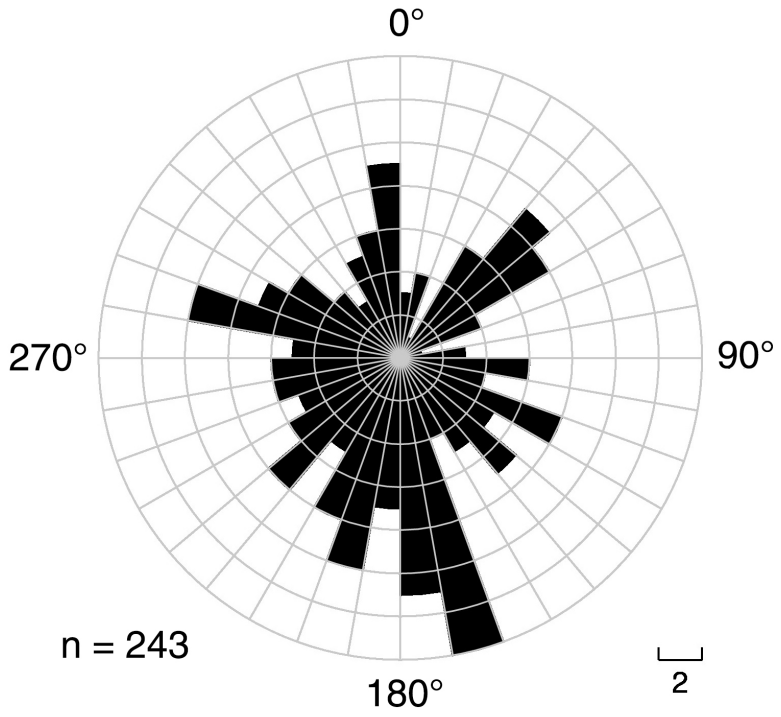


Figure 5.14: Polar histogram of the seamount phase angles, which form a non-dimensional representation of the seamount position with respect to the segment centre and bounding discontinuities. An angle of 0° corresponds to the discontinuity, while an angle of 180° corresponds to the centre of the segment.

The phase angle distribution shows a greater number of edifices between 90° and 270° i.e. the two segment quarters either side of the segment centre, than between 270° and 360°, and 0° and 90°. There is a particularly large concentration of seamounts between 160° and 200° corresponding to the central ninth of the ridge segment. These results suggest that, for this Section of the ridge, the melt generated beneath any given segment migrates towards the centre of the segment, increasing the local melt supply

at the segment centre, and therefore the number of seamounts formed.

Central Section

Figure 5.15 shows the location of seamounts, with heights greater than 50 m, within the axial valley floor of the central region, between 46.1° E and 52.3° E. In contrast to the orthogonal and oblique Sections, where swath bathymetry extended off axis, the swath bathymetry coverage is limited to the axial valley in parts of this Section.

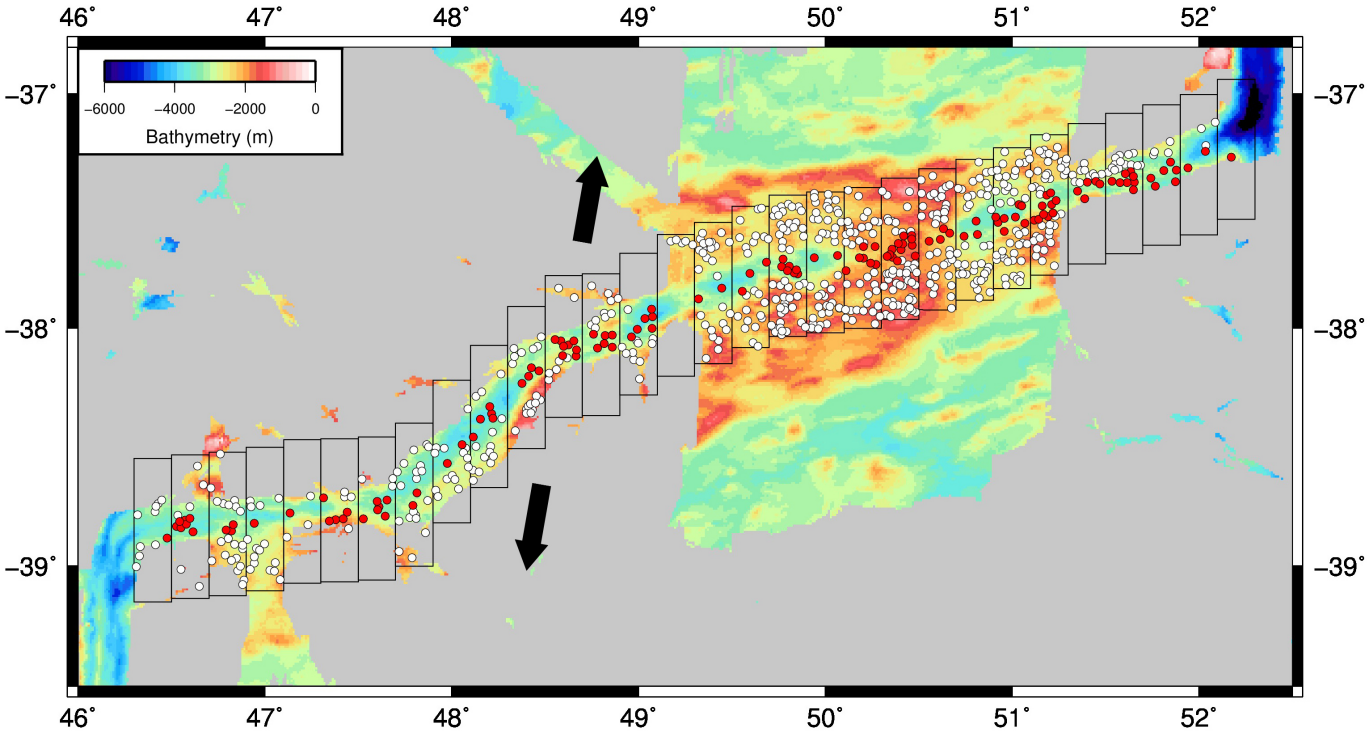


Figure 5.15: Bathymetry map of the central Section based on multibeam bathymetry. Black boxes outline the areas used in the analysis to detect seamounts. Red circles show the locations of seamounts with height greater than 50 m in the axial valley floor. White circles show the location of seamounts with height greater than 50 m on the rim flanks.

The analysis identified 138 seamounts over an area of 8370.04 km ^{2}, giving an observed seamount density of 16.5/1000 km^2, the lowest density out of the four Sections. This is, perhaps, contrary to what would be expected since this central Section of the ridge corresponds to the eastern part of a broad rise, which is influenced by the Marion and

Crozet hotspots (Georgen et al., 2001; Sauter et al., 2009).

In contrast to the sparse seamounts in the axial valley, there are abundant volcanic edifices on the flanking highs, which are broader than at any other point along the SWIR. Figure 5.16 shows the seamount height distribution for the central Section which has a characteristic height of 65.2 m. This height is similar to other Sections of the ridge.

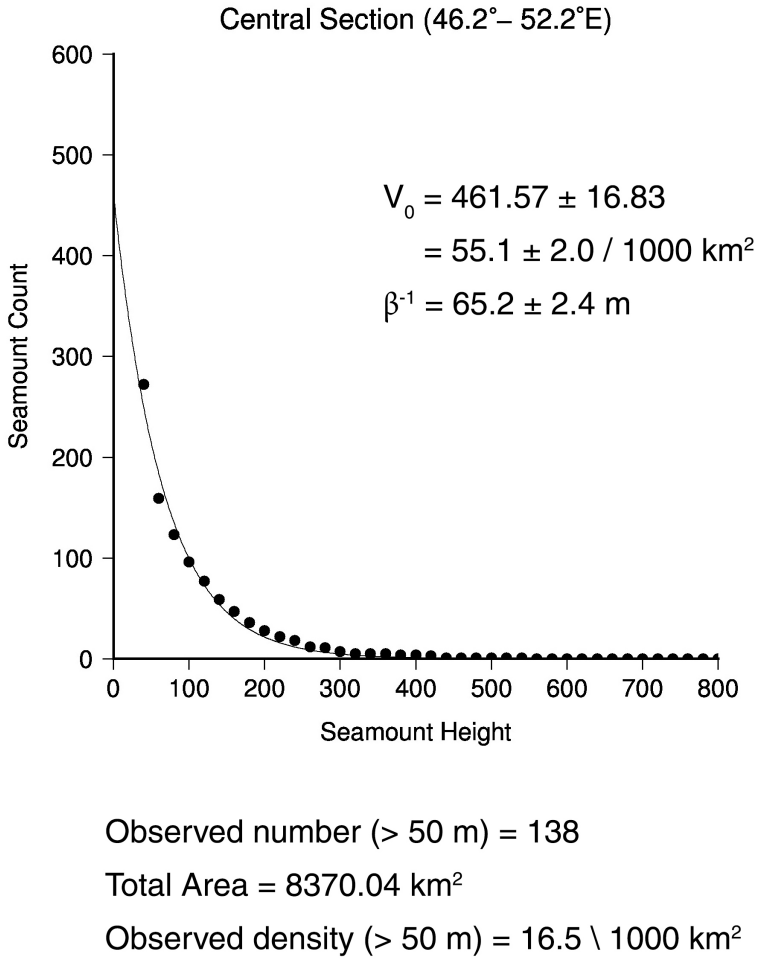


Figure 5.16: Cumulative count of seamounts plotted against height for the axial valley floor of the central Section. Black solid circles show the observed height distribution, black line shows the maximum likelihood model fit to the data.

The distribution of axial valley seamounts shown in Figure 5.15 is not consistent, but instead forms small clusters of concentrated edifices, separated by areas of sparse isolated edifices. This may be due to small scale segmentation, as was found at the

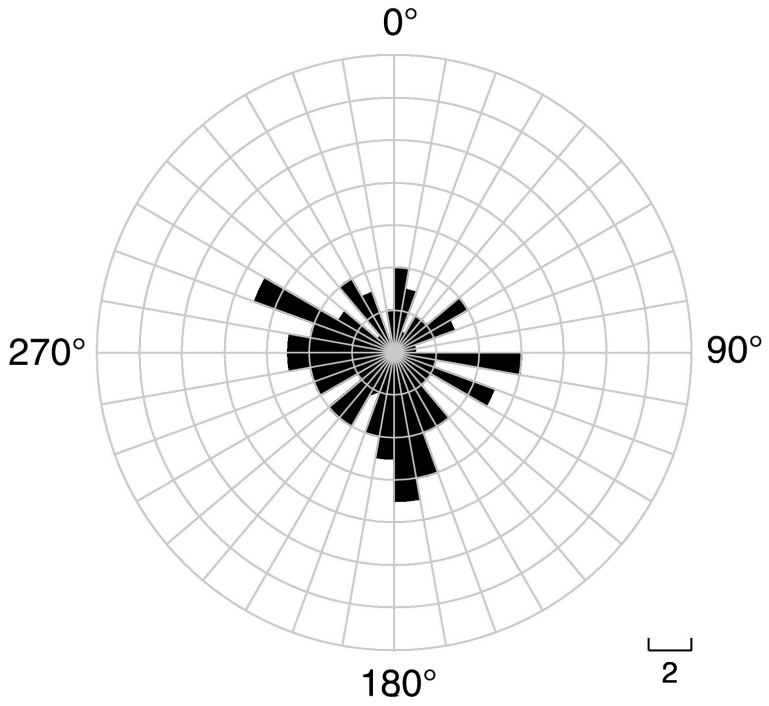


Figure 5.17: Polar histogram of the seamount phase angles, which form a non-dimensional representation of the seamount position with respect to the segment centre and bounding discontinuities. An angle of 0° corresponds to the discontinuity, while an angle of 180° corresponds to the centre of the segment.

orthogonal Section. The phase distribution of these seamounts, representing the distribution within the segments, (Figure 5.17) shows a larger proportion of seamounts present in the central part of the segments with very few seamounts adjacent to the discontinuities. As seen at segments on the orthogonal Section, there is a particularly large concentration of seamounts close to the centre of the segment, supporting the presence of melt migration towards the centre of segments.

Figure 5.18 shows the distribution of seamounts compared to the axial bathymetry. The seamount distribution clearly shows six magmatic centres, which correspond to highs on the bathymetry. However, based on bathymetry and mantle Bouguer anomalies the number of segments exceeds the number of magmatic centres, meaning that while some segments appear to be magmatically robust, others have sparse evidence of magmatism.

The majority of the seamounts found in the magmatically sparse Sections are located

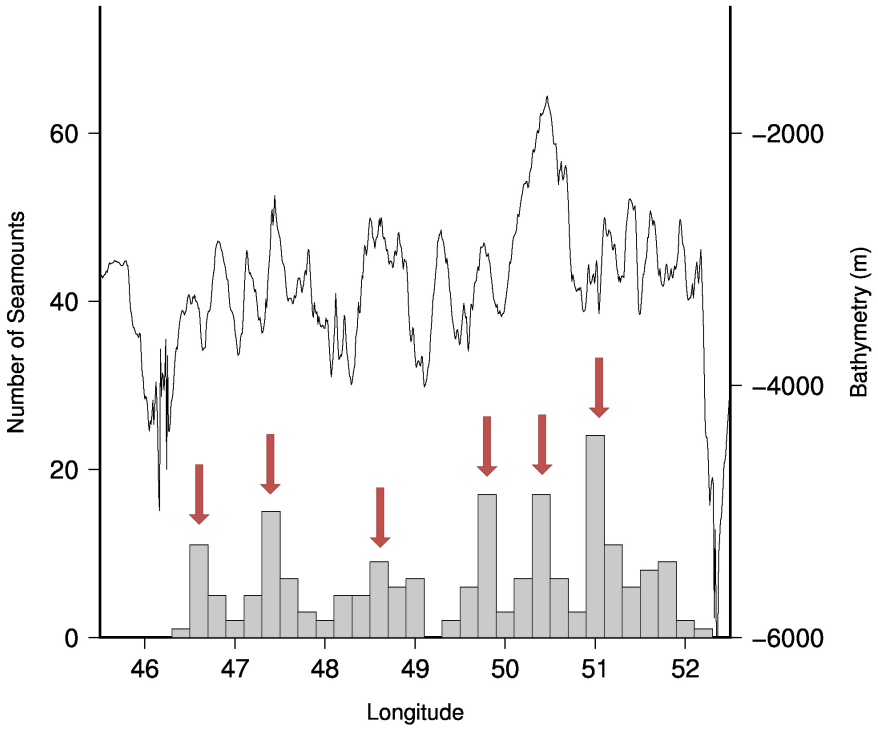


Figure 5.18: Seamount distribution along the axial valley of the central Section. Lower graph shows the number of seamounts binned in intervals of 0.2° longitude. Upper graph shows the axial bathymetry along zero-age crust.

on the edge of the axial valley floor away from the neovolcanic zone, which is assumed to lie in the centre of the axial valley. This is similar to the observations made in areas of sparse magmatism on the ultra-slow Gakkel ridge by Cochran (2008). These observations may indicate that the magmatism in these regions is caused by the ascendance of magma along the large normal faults forming the axial valley morphology. These faults, which outcrop at the surface at the edge of the axial valleys, form lines of weakness, which act as magma conduits causing isolated volcanoes to form.

Eastern Section

Figure 5.19 shows the location of seamounts over 50 m in height in the axial valley floor of the eastern Section, between 55.9° E and 60.7° E. Unlike the other study areas, this Section of the SWIR has transform discontinuities which have unique tectonic

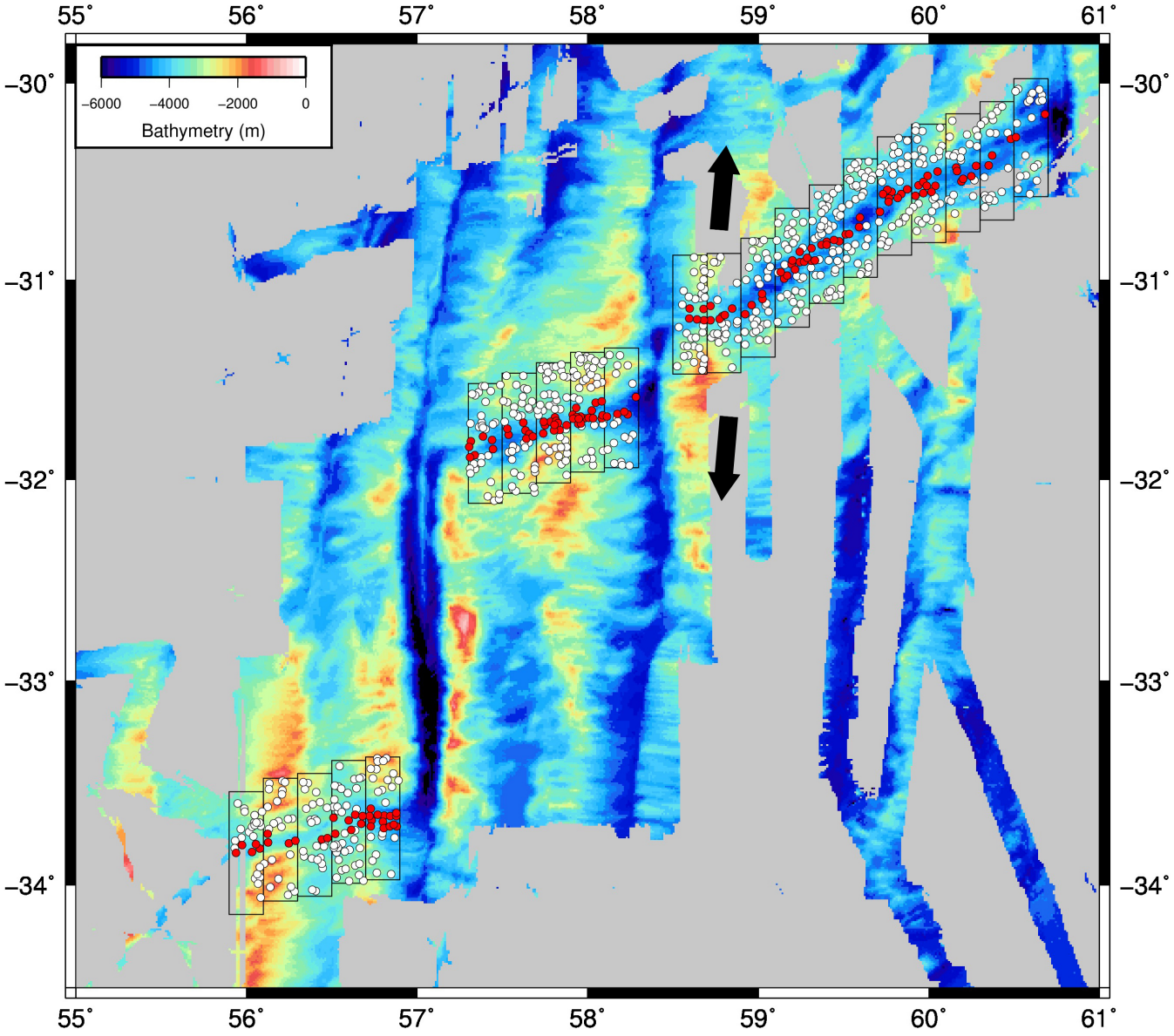


Figure 5.19: Bathymetry map of the eastern Section based on multibeam bathymetry. Black boxes outline the areas used in the analysis to detect seamounts. Red circles show the locations of seamounts with height greater than 50 m in the axial valley floor. White circles show the location of seamounts with height greater than 50 m on the rim flanks.

morphologies. In order to avoid rough small scale morphology resulting from these transform features being identified as volcanic seamounts, the transform regions were excluded from the analysis.

The analysis identified 144 seamounts over 50 m in height over an area of 3760.13 km^2,

giving an observed density of 38.3/1000 km^2. This is the highest observed density out of all the Sections studied, however it is still only 63% of that observed at the MAR. The height distribution gives a characteristic height of 65.2 m, similar to other Sections on the ridge.

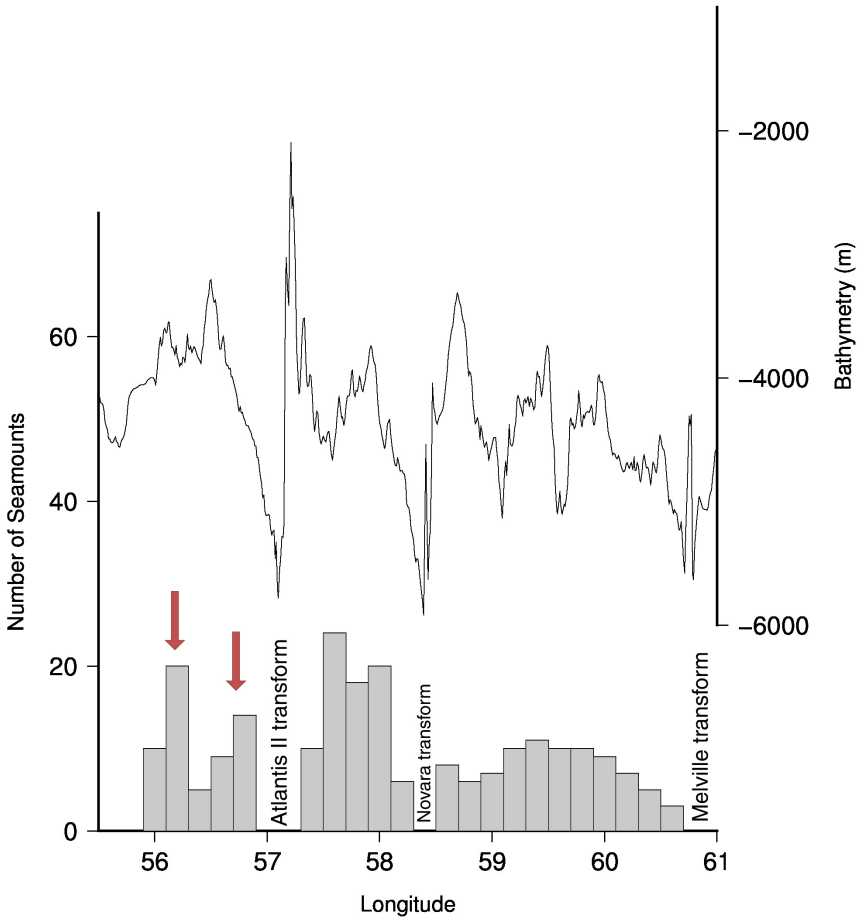


Figure 5.20: Seamount distribution along the axial valley of the eastern Section. Lower graph shows the number of seamounts binned in intervals of 0.2° longitude. Upper graph shows the axial bathymetry along zero-age crust.

Figure 5.20 shows the distribution of seamounts along the axis. The regions with no seamounts between 56.9° E and 57.3° E , and 58.3° E and 58.5° E are areas of no data due to the Atlantis II and Novara transform faults respectively. There is evidence of variation on a segment scale to the west of the Atlantis II transforms, where abundant seamount clusters correspond with axial valley and off axis bathymetric highs. In

contrast, sparse seamounts correspond to off axis bathymetric lows, which represent non-transform discontinuities. This suggests that melt is migrating towards segment centres as seen elsewhere on the ridge. To the east of the Atlantis II transform, the broad seamount distribution increases away from the transforms, but does not correspond to the smaller scale segmentation. This suggests that melt migration processes are less active to the east of the Atlantis II transform.

5.2.3 Discussion

Orthogonal Section

The orthogonal Section is morphologically similar to the MAR, with localised point source eruptions forming seamounts similar to those described by Smith and Cann (1990, 1992). The distribution of these seamounts within the axial valley suggests that they formed in the central neovolcanic zone This is assumed to be the location of the neovolcanic zone, which, following the model on the MAR, is likely to be supplied with magma by feeder dykes. Along axis variation shows segment scale melt migration towards segment centres as observed at the MAR (Tolstoy et al., 1993), leading to concentrated clusters of seamounts over bathymetric highs. Though these morphological features give a similar appearance to that observed on the MAR, the seamount density for this Section is 44% of that at the MAR. In this respect, it is similar to the western volcanic zone on the Gakkel ridge described by Cochran (2008), though unlike the western volcanic zone, the orthogonal Section has a much greater characteristic height than the MAR. Despite the taller seamounts, the lower observed seamount density means that this Section of the ridge has a significantly lower volume of erupted lava than an equivalent area along the MAR. This low melt production is reflected in the geochemistry of basalts sampled from this Section, which lie within the $Na_{8.0}$ vs $Fe_{8.0}$ global array of Klein and Langmuir (1987) but reflect a lower extent of melting (Standish et al., 2008).

Overall, compared to the MAR, the orthogonal Section is magma poor, however there is sufficient magma supply to maintain a similar morphology to the MAR, indicating that the processes of melt generation and propagation to the surface are similar, despite the differences in magma budget.

Oblique Section

The oblique Section has a very different morphology to the orthogonal Section; this is reflected in the seamount distribution. The oblique Section consists of anomalously deep oblique segments separated by shallower segments culminating in two strongly magmatic centres at 11.3° E and 14.7° E. The seamount density increases at these shallow segments surrounding the volcanic centres, though it decreases over the volcanic centres themselves. This is due to the large volcanic edifices filling the axial valley at these locations, which are not detected by the algorithm which is calibrated to detect small valley floor seamounts. The 'seamounts' detected over these volcanic centres are actually parasitic cones on the larger volcanic edifices. In contrast the oblique deep segments have a lower seamount density, and form isolated seamounts lacking the clusters observed at the volcanic centres. These observations strongly support the presence of strong melt focussing, with the majority of the melt generated beneath the oblique Sections migrating towards the volcanic centres. This mechanism is supported by geochemical evidence from basalts dredged from the volcanic centres, which show an enriched MORB signature despite the high degree of partial melting (Standish et al., 2008).

The presence of some seamounts in the oblique segments suggests that some lava is erupted at the seafloor, though rock dredges of the axial valley floor by Dick et al. (2003) suggest that the amount of basalt lavas is greatly reduced compared to other areas of the ridge. In other sparsely magmatic Sections on the ridge the seamounts are primarily located along faults at the edge of the axial valley. In contrast, the seamounts in these oblique segments are distributed evenly across the axial valley. This does not,

however, preclude the use of faults as magma conduits. Detailed mapping of this axial valley by Dick et al. (2003) showed that the axial valley floor in these segments is highly tectonised and dominated by faulting, forming tectonically generated crustal blocks. It is likely that these faults act as conduits for the limited eruptions occurring on these segments. It should be noted that, due to the rough seafloor morphology in these segments, there is a higher probability of the algorithm picking a tectonically generated high as a volcanic seamount, leading to an increase in the apparent seamount density.

Overall, the seamount population in this region is very different from the MAR or orthogonal Section. It has strong similarities with the seamount population of the eastern volcanic zone on the Gakkel ridge described by Cochran (2008). This suggests that the volcanic morphology and the melt focussing mechanisms associated with them may be a characteristic of a melt-poor end-member of ultra-slow spreading ridges.

Central Section

The central Section has the lowest observed seamount density out of the four Sections. This is, perhaps, contrary to what would be expected since this central Section of the ridge corresponds to the eastern part of a broad rise, called the Marion rise. This rise has been attributed to the influence of the Marion hotspot, which is located 250 km off the ridge axis. The central Section, where the seamount counting analysis was performed, is separated from the Marion hotspot by several transform faults, which reduce the hotspot influence (Georgen et al., 2001). In contrast, the axial highs bounding the axial valley are broad and have a high seamount density. Sauter et al. (2009) suggested that these broad axial rim mountains and the volcanic centre at 50.5° E may be attributed to a melting anomaly caused by the Crozet hotspot. The influence of hotspots on mid-ocean ridges causes an increase in the mantle temperature and degree of partial melting (Ito et al., 2003), both of which are evidenced by large scale geophysical and geochemical variations along the SWIR in this region due to the Marion

hotspot (see chapter 3). The increase in partial melting, and therefore magma budget, should be reflected by an increase in the observed seamount density; however this is not the case. Behn et al. (2004) observed a similar decrease in seamount abundance at the Galapagos spreading centre approaching the Galapagos hotspot. He attributed this to a change in the eruption style: from point source eruptions forming pillow lavas and seamounts in the region outside the influence of the hotspot, to fissure eruptions forming sheet and lobate flows near the hotspot due to the increase in magma supply. However, a number of observations do not support this mechanism at the SWIR. The general axial morphology in the central Section, though shallower than other areas of the ridge, does not resemble the transition from axial valley to axial high observed at the Galapagos hotspot. This suggests that although the degree of partial melting is greater than elsewhere on the SWIR, it is not sufficient to produce morphologies characteristic of fast spreading ridges, such as fissure eruptions forming sheet flows.

In the areas of sparse seamounts, the distribution of the seamounts within the axial valley tends towards the edges of the axial valley. The formation of seamounts along the traces of the normal faults, which bound the axial valley, suggests that magma is migrating upwards along the faults, which act as conduits. This is consistent with other sparsely magmatic areas observed elsewhere on the ridge, and similar observations have been made at the sparsely magmatic zone on the Gakkel ridge (Cochran, 2008).

The along axis seamount distribution shows six distinct volcanic centres, fewer than the number of segments defined by axial bathymetry and gravity. This suggests that the melt focussing mechanisms observed at the oblique Section are also occurring at the central Section, though to a lesser degree. This forms the observed pattern of clustered seamounts at volcanic segments, separated by sparsely magmatic areas. In this Section of the ridge, the length of the sparsely magmatic segments is larger than that of the volcanic segments, which are very short, resulting in a low average seamount density. Overall, the seamount population in this Section shows similar characteristics to the oblique Section, though the melt focussing takes place over a shorter distance.

Eastern Section

The eastern Section has the highest observed seamount density out of the four Sections, despite this Section of the ridge having a deeper axial depth than the central part of the ridge, indicating a reduction in melt supply. The along ridge distribution, particularly east of the Atlantis II transform, shows a more even distribution and lacks evidence of strong melt migration on a segment scale. Previous studies of bathymetry and gravity (e.g. Cannat et al., 1999) have shown that the closely spaced Atlantis II, Novara and Melville transforms form a significant boundary between the relatively magma rich central Section of the SWIR and extremely magma poor easternmost SWIR. The reduction in melt migration mechanisms may be due to a decrease in magma supply across the Atlantis II transform. It is this even distribution of seamounts which leads to the high seamount density, since the seamount density for any given part of the eastern Section is similar to the segment centres elsewhere on the ridge. This suggests an increase in the melt supply in direct contradiction with large scale geophysical and geochemical evidence (Sauter and Cannat, 2010). The reason for this may be related to the large number of closely spaced transform faults in this region. Detailed bathymetric mapping of the segments and discontinuities in this region (e.g. Hosford et al., 2003) has shown that there are a large number of normal and oblique faults resulting from the large transform faults and non-transform discontinuities. These faults may provide an increase in the number of available conduits for magma to ascend to the surface, increasing the number of points of seamount nucleation, leading to a larger number of seamounts.

5.2.4 Patterns of Magmatism

The observations over the four study areas show three main factors affecting the seamount population on the axial valley floor: the degree of partial melting, the availability of magma conduits, and the degree of focussed upwelling and melt migration.

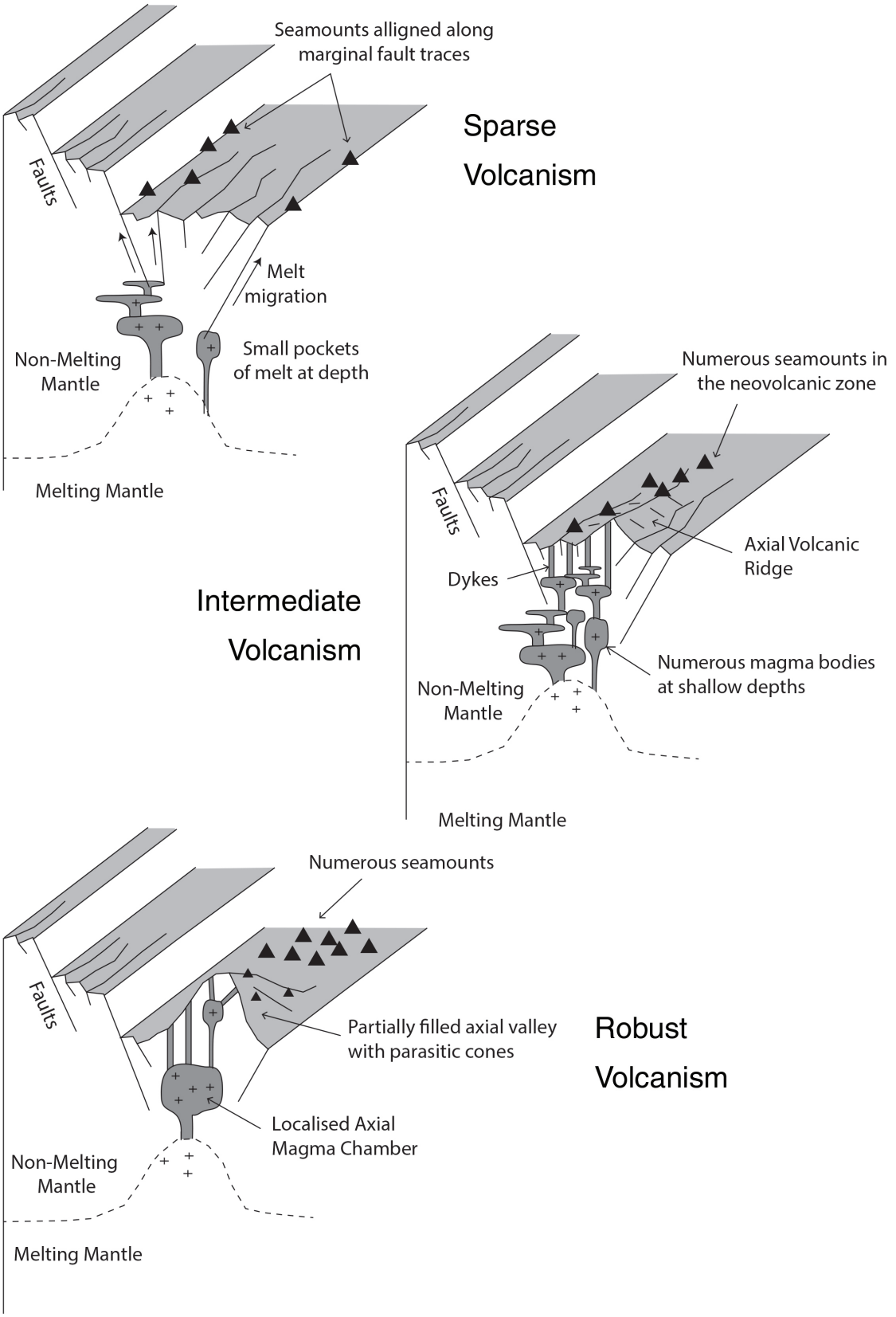


Figure 5.21: Schematic block diagrams illustrating the three different styles of volcanism observed on different areas of the SWIR axial valley.

Figure 5.21 shows schematic illustrations of the axial valley for sparsely volcanic, intermediate volcanic, and robustly volcanic zones. At sparsely volcanic areas, which have low degrees of partial melting, the conduit availability governs the distribution of seamounts in the axial valley. Major faults, which are able to tap deep magma pockets, form conduits along which melt can reach the surface, forming sparse linear seamount chains. In areas with intermediate degrees of partial melting, the seamounts are formed by localised point source eruptions, similar to those observed at the MAR (Smith and Cann, 1990). These are, therefore, attributed to a similar sub-axial structure of Smith et al. (1995), consisting of a series of magma bodies, which accumulate at different depths and are then tapped by dykes. A small number of areas show very robust volcanism, forming partially filled axial valleys with sporadic parasitic cones leading to an apparently lower seamount density compared to the surrounding areas. Seismic studies on the magmatically robust segment centred on 50.5° E (Jian et al., 2017) have presented evidence for an axial magma chamber under this Section of the ridge. There is insufficient seismic data at other robustly magmatic segments to confirm this; however it is likely that the increase in degree of partial melting and the melt focussing mechanisms proposed for these segments, produces large bodies of magma within the crust, providing the source for the excess volcanism observed.

5.3 Ridge Flank Seamounts

The second part of this study is focussed on large seamounts (greater than 300 m in height) on the ridge crest and flanks of the Southwest Indian Ridge. This provides a measure of the volcanic activity along the whole of the ridge and allows comparison between the SWIR and other spreading centres with different spreading rates.

5.3.1 Data and Methods

The data used for this study is an integration of shipboard and satellite derived bathymetry (see chapter 2 for details) gridded at 1 km intervals. This grid resolution precludes seamounts below a height of ∼200 m as the basal radii are not sufficient large to be resolved. Searching for the seamounts on the ridge crest and flanks introduces a number of challenges which are not present in the axial valley. The flanks of slow and ultra-slow spreading ridges are characterised by tectonically generated abyssal hills, therefore the algorithm must be able to distinguish between volcanic edifices and abyssal hill structures. There are few previous studies locating large seamounts on ridge crests, particularly in an ultra-slow spreading ridge, therefore there are few studies with which to compare or calibrate the results. The algorithm was, therefore, tested on several sections of the ridge and the sensitivities of the seamount distribution results to different parameters were analysed. The final parameters were then applied to the Southwest Indian region and the results compared with subsets of global studies such as those of Hillier and Watts (2007) and Wessel (2001).

Parameter Testing

Previous testing of the MBOA (Howell et al., 2012) was undertaken on a continental cinder cone volcanic field in which volcanic cones are superimposed on minimal background topography. At the SWIR the background topography is extremely variable due to faulting and transform structures, many of which are of comparable amplitude to volcanic seamounts. Therefore, in addition to detecting topographic highs, the algorithm must also be able to filter volcanic edifices from abyssal hill topography, transverse ridges and oceanic core complexes. This is achieved by using a series of parameters, including contour interval, maximum basal contour dimension, ellipticity and geometric irregularity, to distinguish between typical submarine volcanic seamounts and other topographic highs. The parameters used in the algorithm are summarised in table 5.2.

Table 5.2: Input parameters for the Modified Basal Outlining Algorithm

Symbol	**Parameter**
C	Contouring interval used to find initial basal contours
C_0	Start level of contouring calculated as minimum elevation in grid rounded to the nearest multiple of C_0
D	Maximum dimension for a basal contour to be considered a seamount
E	Maximum elliptical ratio of best fitting elliptical model of a basal contour for it to be considered a seamount
E_{fit}	Threshold misfit to the best fitting elliptical model of a basal contour for it to be considered a seamount
$Slope_{min}$	Minimum slope for the topographic high to be considered a seamount
$Slope_{max}$	Maximum slope for the topographic high to be considered a seamount

Two areas of the Southwest Indian Ridge from 15° to 22° E and 48° to 52° S and 40° to 47° E and 37° to 48° S were used to test the sensitivity and importance of each of the parameters. The first topographic sample consists of an orthogonally spreading mid-segment area of the ridge. The second topographic sample consists of a series of fracture zones and hotspot related topography.

A minimum, maximum and base case value for each parameter is proposed in order to distinguish volcanic seamounts from background topography. The base case value is the value deemed the most geological reasonable parameter, while the maximum and minimum values are the most extreme values that are still considered geologically plausible. One-at-a-time (OAAT) sensitivity analysis is performed for the different input parameters. This involves varying one parameter between the minimum and maximum values whilst holding all other parameters fixed at the base case values.

These are displayed in graphical form to show the change in the different outputs caused by the change in the investigated parameter. The importance index, sensitivity index and elasticity index for each parameter-output pair is also calculated. The range, base case values, mean and standard deviation of each input parameter are listed in table 5.3.

Table 5.3: Input parameter statistics

Input Parameter	**Minimum**	**Maximum**	**Base Case**	**Mean**	**Standard Deviation**
Contour Interval (m)	25	300	150	153.57	102.5
Maximum Basal Dimension (km)	14	80	35	44	24.82
Elliptical Ratio (km/km)	0.1333	0.833	0.5	0.289	0.409
Elliptical Fit	0.2	0.8	0.4	0.5	0.258
Minimum H-R Ratio [=tan(slope)] (m/m)	0.034921 [=tan(2)]	0.17633 [=tan(10)]	0.052408 [=tan(3)]	0.084215 [=tan(4.81)]	0.055094 [=tan(3.15)]

Consider a generalised model with several independent variables given by $\bar{X} = X_1 \dots X_k$

where k is the number of input parameters, and several dependant variables given by $\bar{Y} = Y_1 \dots Y_n$ where n is the number of different model outputs and $\bar{Y} = f(X)$.

Following this notation, the importance index (Hoffman and Gardner, 1983), which is the variance of the input parameter divided by the variance of the output, for a specific pair of input parameter (X_i) and output (Y_j), is given by

$$I_{i,j} = \frac{\frac{\Sigma(X_i - \bar{X}_i)^2}{k-1}}{\frac{\Sigma(Y_j - \bar{Y}_j)^2}{n-1}} \tag{5.2}$$

The importance index provides an indication of which parameters contribute more strongly to the uncertainty of the output due to uncertainty of the input parameter. The sensitivity index (Hoffman and Gardner, 1983) is given by

$$S_{i,j} = \frac{\partial Y_j}{\partial X_i} \tag{5.3}$$

The sensitivity index shows the factor by which the model output Y_j changes due to a small change in the input parameter X_i. The greater the sensitivity index, the greater the change in output caused by a small change in the input parameters. One problem with interpreting sensitivity indexes is that since different output variables have different units, it is not possible to sensibly compare sensitivity indexes. These can be converted into proportional changes of the input parameter and output by calculating the elasticity index, which is dimensionless and therefore comparable between different output variables. The elasticity index is given by

$$E_{i,j} = \frac{\partial Y_j}{\partial X_i} \cdot \frac{X_{ibase}}{Y_{jbase}} \tag{5.4}$$

where X_{ibase} and Y_{jbase} are the base case for input parameter X_i and the output where all input parameters are set to their base case values. The resultant importance, sensitivity and elasticity indexes are listed in table 5.4.

Table 5.4: Importance, sensitivity and elasticity indexes from one-at-time sensitivity analysis on the input parameters for the Modified Basal Outlining Algorithm

		Input Parameters				
Outputs	Sensitivity Analysis	Contour Interval (m)	Maximum Basal Dimension (km)	Elliptical Ratio (km/km)	Elliptical Fit	Minimum Height-Radius Ratio [=tan(slope)] (m/m)
Total Count	Importance Index	1.2177	0.230197	0.599316	0.00383643	0.947576
	Sensitivity Index	-0.941555	0.940318	-196.8	12.5	-1470.44
	Elasticity Index	-1.14824	0.26757	-0.799999	0.0406503	-0.417474
Average Height	Importance Index	0.176632	0.00708041	0.00960478	0.000448424	0.0202949
	Sensitivity Index	0.00229516	0.0014909	-0.126384	0.0333617	2.44809
	Elasticity Index	0.377029	0.0571462	-0.0692044	0.0146143	0.0936235
Total Height	Importance Index	0.532972	0.271455	0.639615	0.00654854	0.8214
	Sensitivity Index	-0.504964	0.97845	-185.137	15.2892	-1194.25
	Elasticity Index	-0.674399	0.304911	-0.824194	0.0544514	-0.371318
Average Volume	Importance Index	0.229819	0.533679	0.0349851	0.000324105	0.438543

	Sensitivity Index	0.59213	3.16203	-1.6174	-3.6325	-1802.97
	Elasticity Index	0.440455	0.548817	-0.0040104	-0.0072054	-0.312225
Total Volume	Importance Index	0.413834	0.733021	0.596095	0.0024517	1.88161
	Sensitivity Index	-86.1308	461.801	-34487.2	2119.58	-403063
	Elasticity Index	-0.520881	0.651646	-0.69521	0.0341822	-0.567477
Average Ellipticity	Importance Index	0.00106611	0.000100635	0.0211796	5.91E-05	0.000558058
	Sensitivity Index	0.000153855	-0.000175555	0.248663	-0.00875833	-0.499075
	Elasticity Index	0.0325936	-0.00867781	0.175595	-0.0049478	-0.024614
Azimuthal Range	Importance Index	0.00104212	0.0040645	0.00402327	0	0.138602
	Sensitivity Index	-0.00971778	0.0346571	-8.11327	0	-74.4504
	Elasticity Index	-0.0170847	0.014217	-0.047546	0	-0.0304721

The sensitivity, importance and elasticity indexes were used to eliminate parameters for which variation in the input does not have a great impact on the algorithm outputs. It is important to consider both the importance index, which provides an indication of how uncertainties in the input parameters affect the output results, and the elasticity index, which is an indicator of how small changes in an input parameter affects the output results. The sensitivity index was not considered as it is not possible to compare these

between different outputs with different units, however the elasticity index provides, in effect, a normalised sensitivity index. Any parameters with average importance indexes and sensitivity indexes below a threshold of 0.02 were discounted from further sensitivity analysis and the parameters set to the base case value. The threshold value of 0.02 was chosen as it is equivalent to changes in output of less than 5 %. Figure 5.22 shows an example of the variations in algorithm outputs with variation of one of the excluded input parameters.

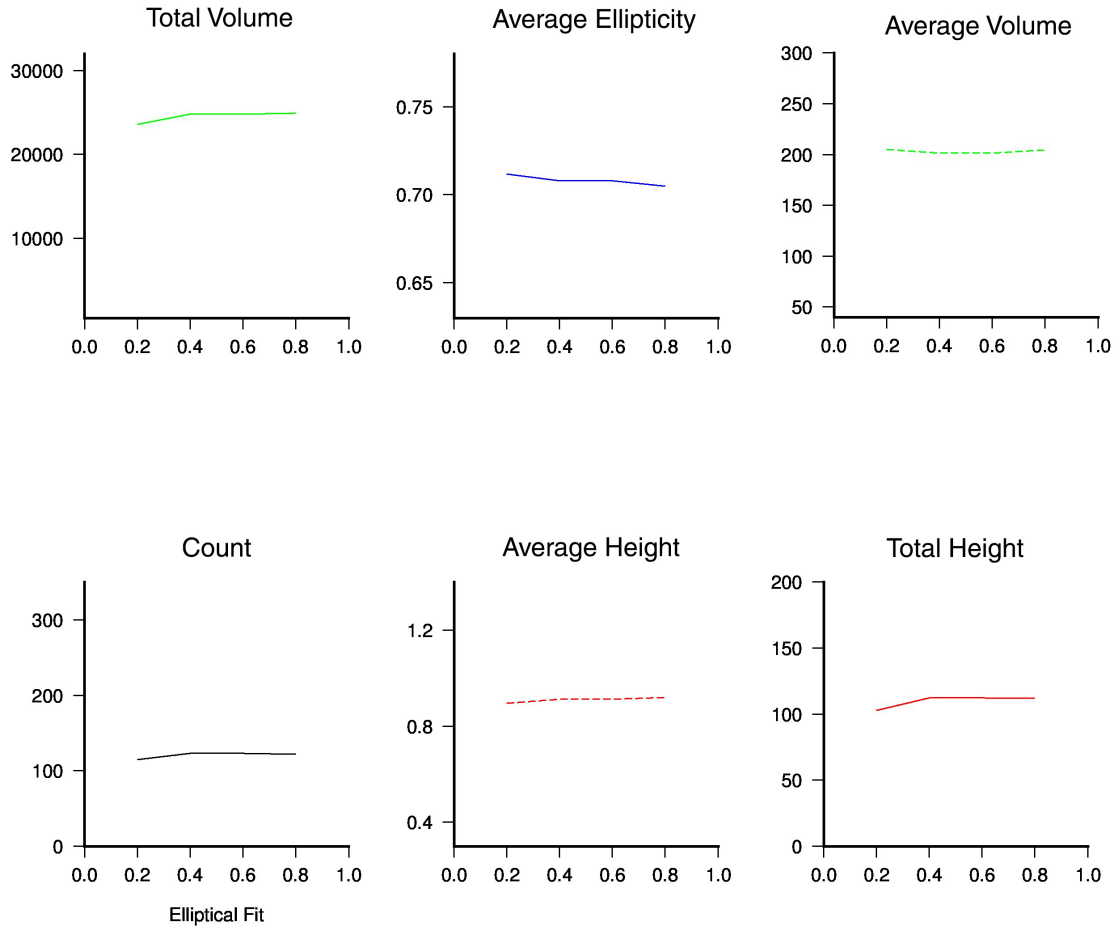


Figure 5.22: Series of graphs showing the variation in different output parameters due to varying the e-fit, while other parameters are held at base case values. The output parameters measured are (a) seamount number (b) average seamount height (c) total seamount height (d) total seamount volume (e) average seamount ellipticity, calculated using the ratio of the long and short axes (f) average seamount volume

The figure shows minimal variation in output when the input parameter is varied, con-

firming that these parameters do not require further analysis. The following parameters were excluded from further analysis and their values set to their base case value: e-fit, maximum slope, initial start contour. The final values used for these parameters are listed in table 5.5. The remaining parameters, which are deemed to have a significant effect on the output results, are discussed in more detail in the following sections.

Contour Interval

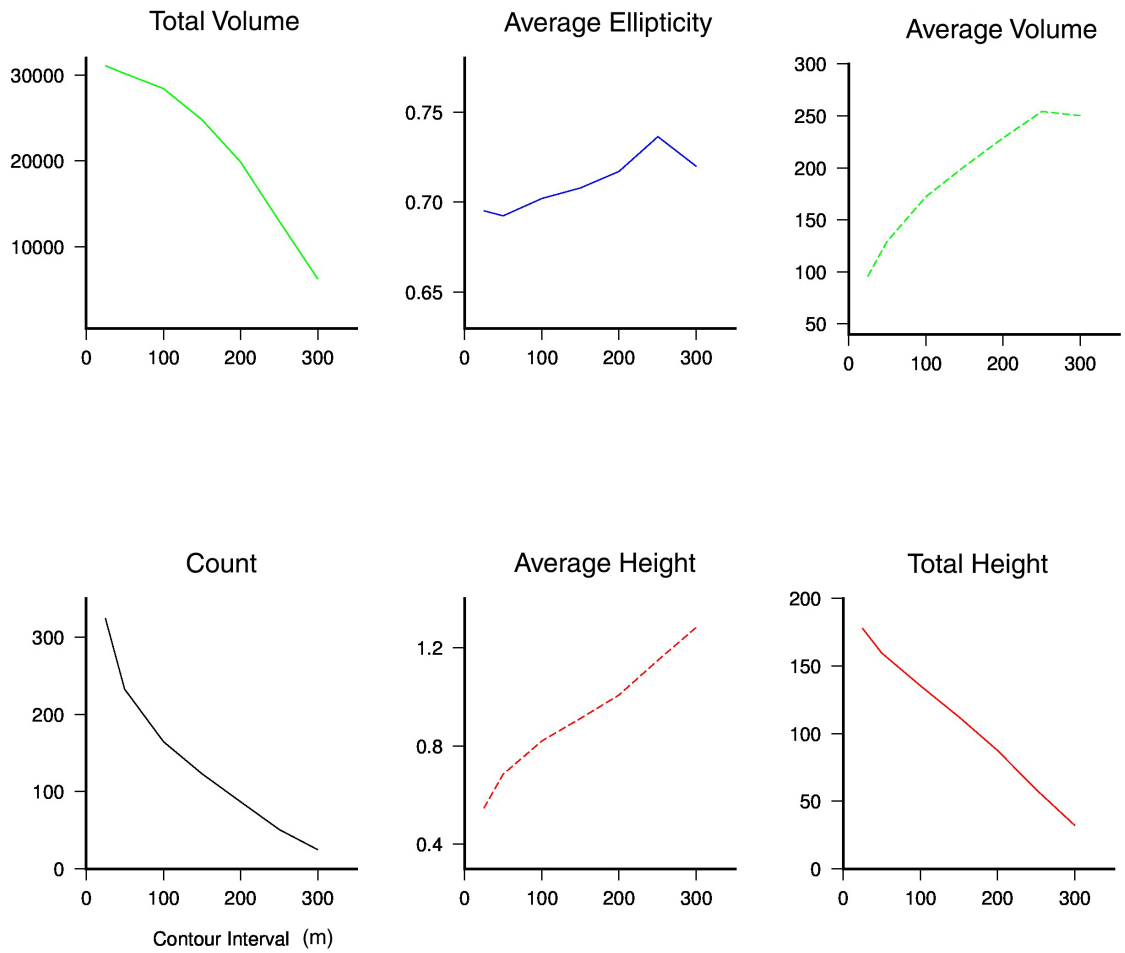


Figure 5.23: Series of graphs showing the variation in different output parameters due to varying the contour interval, while other parameters are held at base case values. The output parameters measured are (a) seamount number (b) average seamount height (c) total seamount height (d) total seamount volume (e) average seamount ellipticity, calculated using the ratio of the long and short axes (f) average seamount volume (g) range of azimuths exhibited by the best fitting ellipses

The contour interval defines the interval in metres at which the topographic grid is

contoured prior to locating closed contours. This governs the threshold height below which seamounts are not detected. The contour interval is approximately 0.5 to 0.35 times the threshold height. This threshold height is important for distinguishing between volcanic seamounts and tectonic abyssal hill structures. Goff (1991) showed that average abyssal hill height on the MAR varied between 105 m ± 20 m to 299 m ± 33 m, and were consistently shorter on the fast spreading EPR. Taking the maximum height threshold of abyssal hill topography from the MAR, the base case contour value was initially set at 150 m to exclude abyssal hill topography. Figure 5.23 shows the variation in the different outputs when the contour interval is varied above and below the base case value.

The number of seamounts detected increases with decreasing contour interval as the threshold detection height decreases. The rate of increase in the number of seamounts detected increases for a contour interval below 100 m (approximating a threshold detection height of 200 m). This is interpreted as the inclusion of abyssal hill topography for contour intervals below 100 m. This is consistent with the decrease in average volume and average elliptical ratio with decreasing contour intervals, indicating that the edifices being added are small volume edifices with a high degree of ellipticity. While this height threshold excludes abyssal hill topography, it also excludes smaller mid-ocean ridge volcanic seamounts.

Maximum Basal Dimension

The maximum basal dimension is the maximum distance threshold in kilometres for any two points on an initially selected closed contour, in order for it to be considered a valid basal contour. This removes the closed contours defining large plateau and ridge structures.

The minimum and maximum values used for testing were derived from base diameter-height ratios for typical seamounts which vary between 2 and 11.5 (Wessel, 2001) and the maximum height of seamounts in the ocean which is ∼7 km. Combining these leads to a basal diameter range between 14 km and 40 km. The base case value was

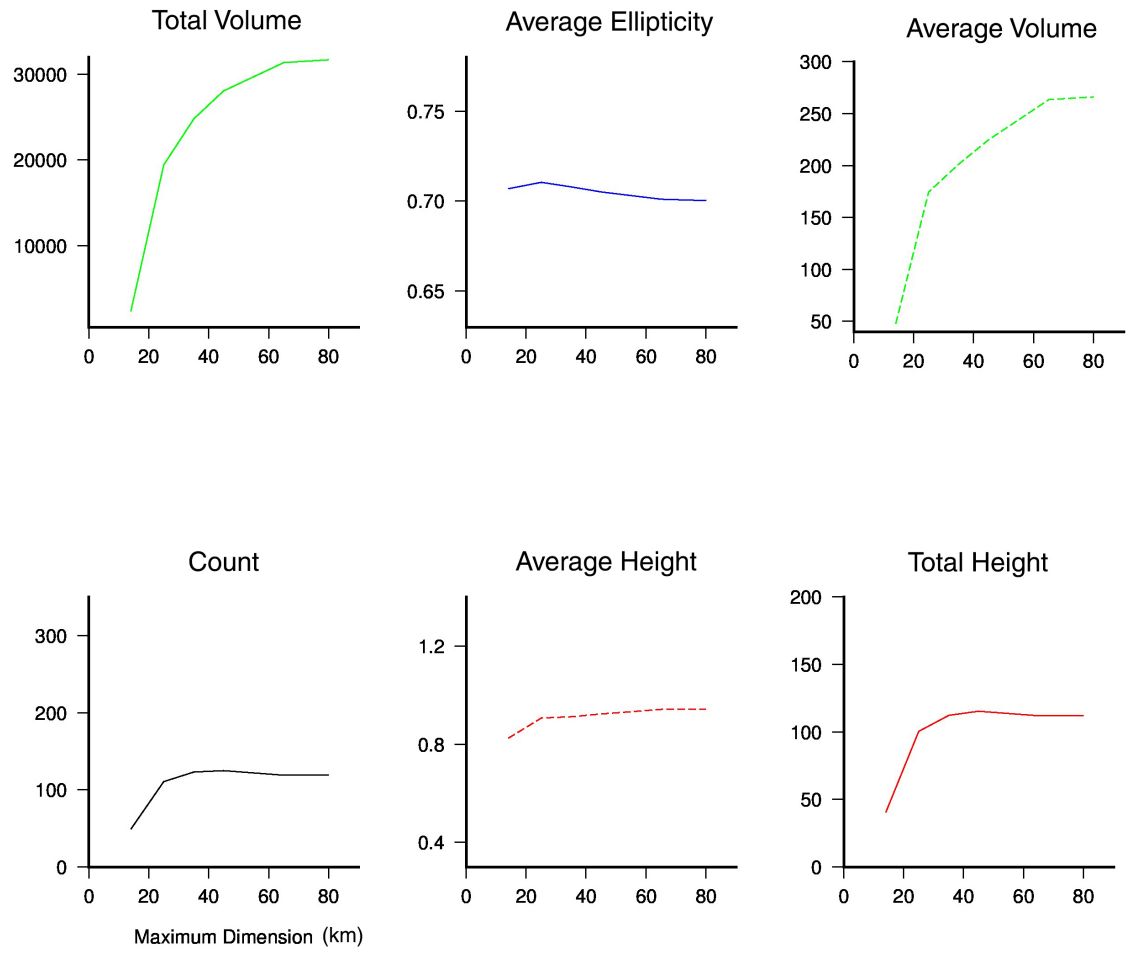


Figure 5.24: Series of graphs showing the variation in different output parameters due to varying the maximum basal dimension, while other parameters are held at base case values. The output parameters measured are (a) seamount number (b) average seamount height (c) total seamount height (d) total seamount volume (e) average seamount ellipticity, calculated using the ratio of the long and short axes (f) average seamount volume (g) range of azimuths exhibited by the best fitting ellipses

set as 35 km based on the seamounts investigated in chapter 4. Figure 5.24 shows the variation in the different outputs when the maximum basal dimension is varied above and below the base case value.

Variation in the maximum basal dimension has a large effect on the average and total volume output: as edifice basal radius increases, volume increases at a greater rate. Interestingly, the number of seamounts detected and the height of those seamounts decreases sharply at maximum basal dimensions lower than 30 km, but plateau between

35 and 80 km. This indicates that for maximum basal dimensions above 35 km, the same edifices are being selected but are being defined by a larger basal contour. For cases where the top of section of a seamount is selected by the algorithm, the subsequent downslope modification of the basal contour ensures that the whole seamount edifice is picked. Therefore, we want to select the minimum basal dimension that does not exclude any seamounts. Based on the trends in the seamount count and seamount height this threshold is ∼35 km. Therefore the maximum basal dimension is set as 35 km.

Elliptical Ratio

The elliptical ratio is the ratio of the long axis to the short axis of a best fit ellipse, fitted to the basal contour using a least squares fitting method. Small mid-ocean ridge seamounts are roughly circular in shape (Batiza, 1982; Smith and Cann, 1990), however as demonstrated in chapter 4 large seamounts may have irregular morphologies. A base case elliptical ratio of 0.5 is used, which equates to a maximum aspect ratio of 2, similar to that used to distinguish between volcanic and tectonic edifices in other seamount distribution studies (e.g. Behn et al., 2004; Cochran, 2008). The elliptical ratio is a useful tool in separating volcanic seamounts from ridges (though these are partially screened out by the maximum basal dimension requirements) and abyssal hill topography. In particular the separation of abyssal hill topography from volcanic seamounts due solely to the elliptical ratio threshold would remove the necessity of a high height detection threshold introduced by the contour interval. This would allow the algorithm to detect small seamounts currently screened out in order to remove abyssal hill topography. Figure 5.25 shows the variation in the different outputs when the elliptical ratio is varied above and below the base case value.

The number of seamounts detected decreases with increasing elliptical ratio (more circular), which is due to the removal of transverse ridges and abyssal hill topography. The average height and volume remain constant except at very high elliptical ratios due to a low sample size. The average elliptical ratio for abyssal hill topography on the

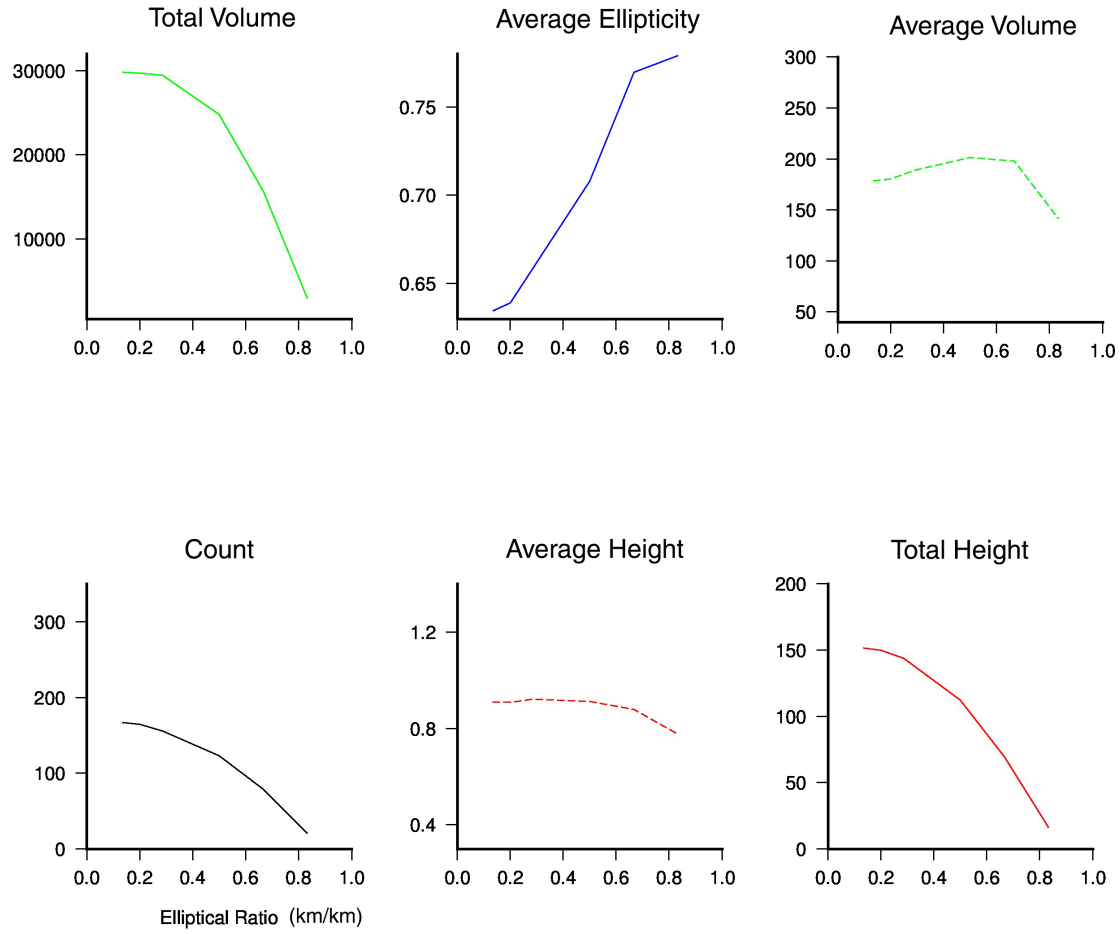


Figure 5.25: Series of graphs showing the variation in different output parameters due to varying the maximum elliptical ratio, while other parameters are held at base case values. The output parameters measured are (a) seamount number (b) average seamount height (c) total seamount height (d) total seamount volume (e) average seamount ellipticity, calculated using the ratio of the long and short axes (f) average seamount volume (g) range of azimuths exhibited by the best fitting ellipses

MAR (Goff, 1991) is between 0.227 and 0.526 with an average of 0.353. The threshold for the elliptical ratio is therefore set to 0.5.

Minimum Slope

The minimum slope is the minimum slope gradient for an edifice determined from the radius to height ratio. This parameter is useful to remove the background seafloor topographic undulations, such as those due to the breakup of the axial rim mountains as they move off axis or sedimentary deposits. The base case was set to a slope of

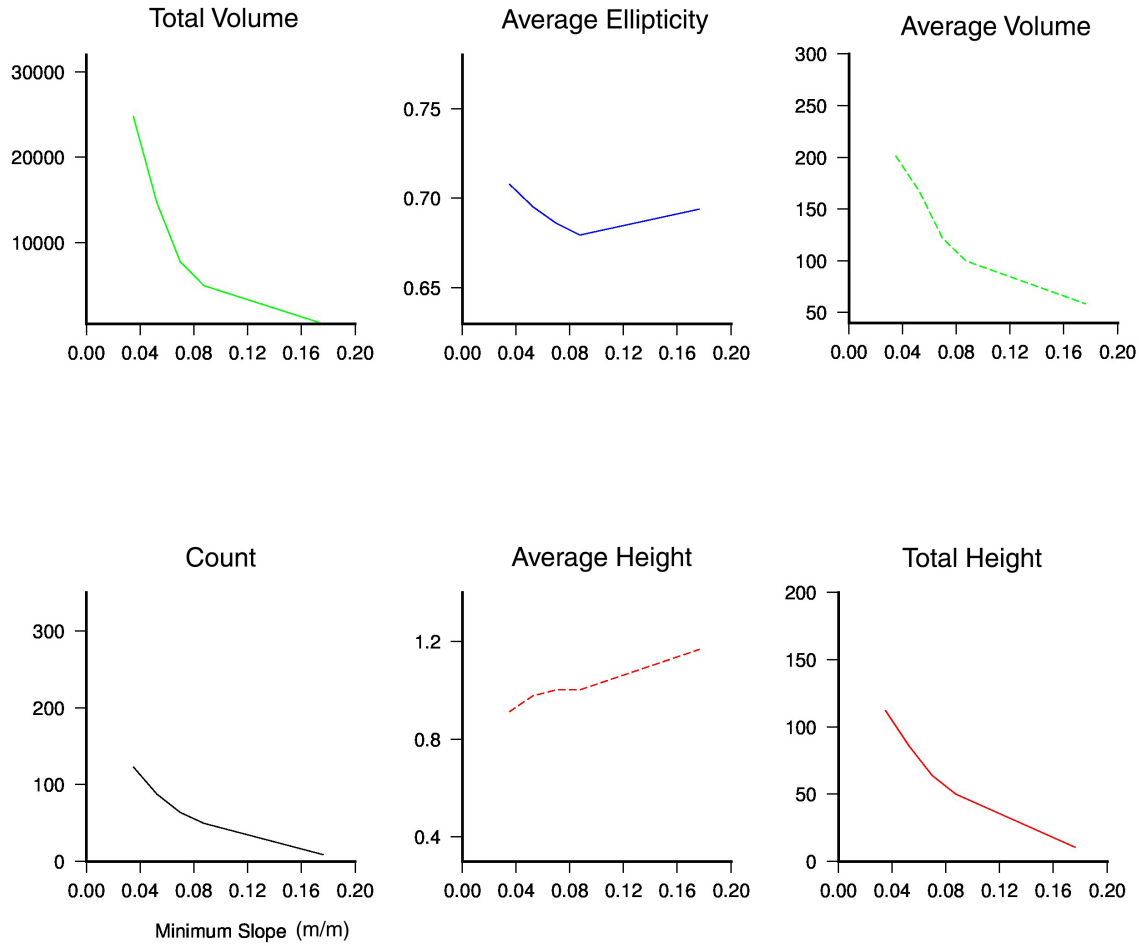


Figure 5.26: Series of graphs showing the variation in different output parameters due to varying the minimum slope threshold, while other parameters are held at base case values. The minimum slope threshold is expressed in the graphs as minimum height-radius ratio i.e. $tan(slope)$. The output parameters measured are (a) seamount number (b) average seamount height (c) total seamount height (d) total seamount volume (e) average seamount ellipticity, calculated using the ratio of the long and short axes (f) average seamount volume (g) range of azimuths exhibited by the best fitting ellipses

2°. Figure 5.26 shows the variation in the different outputs when the minimum slope threshold is varied above and below the base case value (tan 3°).

The seamount volume shows a sharp decrease as the slope increases from 2° to 3°. This is interpreted as the removal of the background topography with very gentle slopes and relatively long wavelengths, which has a large impact on the estimation of volume. The number of seamounts also decreases rapidly initially, becoming less rapid with increasing slope threshold. Since this parameter is designed to eliminate

the background topographic undulations, the parameter is set to the lowest number following the rapid initial decrease. Therefore the minimum slope is set to 3°.

Final Parameter Values

The final parameters used are listed in table 5.5.

Table 5.5: Final values selected as input parameters for the Modified Basal Outlining Algorithm

Parameter	**Symbol**	**Value**
Contour Interval	C	150 m
Contour Start Level	C_0	25 m
Maximum Basal Dimension	D	35 km
Maximum Elliptical Ratio	E	0.5
E-Fit	E_{fit}	0.4
Minimum Slope	$Slope_{min}$	3°
Maximum Slope	$Slope_{max}$	60°

Smooth seafloor

The easternmost part of the SWIR between the Melville transform (61° E) and the Rodriguez Triple Junction (70° E) has a different seafloor morphology compared to the rest of the ridge. This seafloor type, called 'smooth seafloor', was classified by Cannat et al. (2006) using extensive off-axis bathymetry, gravity, magnetic and side-scan sonar data. Unlike the magmatic and tectonic ridges found elsewhere on the flanks of the SWIR, the seafloor in this section consists of smooth rounded ridges, with no volcanic cones or scarps. The small number of volcanic cones was confirmed on the basis of small scale morphology and substrate characteristics determined from side-scan sonar studies (Sauter et al., 2004). The round topped morphology of these

ridges are, however, indistinguishable from gently sloping volcanic edifices elsewhere on the ridge based on bathymetry data alone. While testing on other parts of the ridge has shown that edifices which fit the parameters used in the MBOA are statistically likely to be seamounts, on the easternmost part of the SWIR this is not the case. In addition to this problem, oceanic core complexes, which are tectonically generated highs due to exhumation of the seafloor along normal faults, are abundant in this region (Ildefonse et al., 2007). These oceanic core complexes are characterised by corrugated fault surfaces, which distinguish them from volcanic edifices, however these are not distinguishable using the MBOA. Therefore, the MBOA was not applied to the ridge eastwards of the Melville transform (61° E) as the results would not be representative of the seamount abundance. This area of the ridge has been well established as a melt-poor endmember of the Southwest Indian Ridge through numerous studies. This also removes the need to distinguish between volcanic edifices which formed on the Southwest Indian Ridge, from those which formed on the adjacent Southeast Indian Ridge and Central Indian Ridge.

Effect of grid size

For reasons of computational efficiency, the bathymetry grids were cut into smaller subgrids to which the MBOA was applied. Since this study is locating large seamount edifices, there is a possibility that seamounts which lie on the join between two grid boxes would be missed. The loss of seamounts along the grid margins was investigated using synthetic topography consisting of a plane with superimposed Gaussian shaped seamounts (for more information see chapter 6). The number of seamounts detected by the algorithm for the full grid (20° x 20°) was first established. The algorithm was then applied to the same synthetic topography, split into different sized, and the number of seamounts detected was recorded. The degree to which seamount edifice along grid margins are missed is illustrated for different grid size in Figure 5.27.

The results of the different grid sizes shows a sharp decline in the number of seamounts

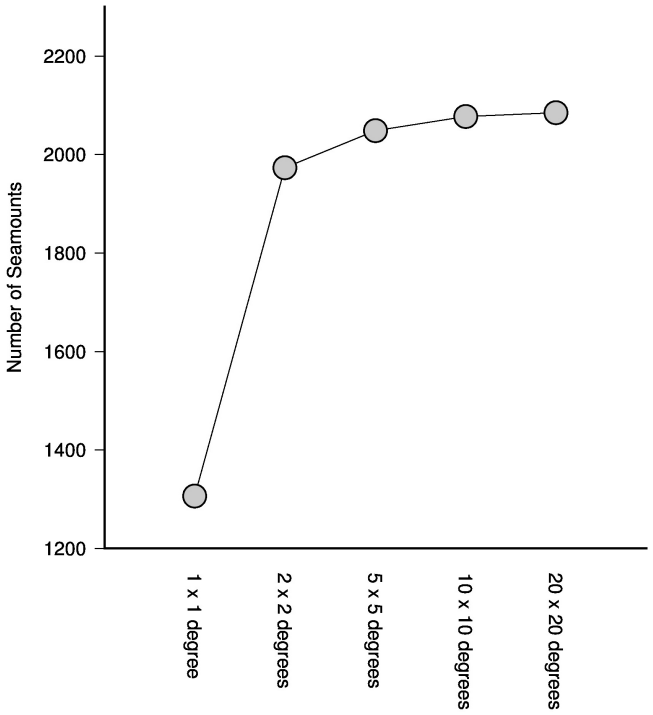


Figure 5.27: Graph illustrating the number of seamounts detected for the same synthetic grid split up into different size grids. The number of seamounts lost along the margin is equal to the difference between the number of detected seamounts for the grid being investigated and the full grid (20° x 20°)

detected using a grid size of 1° x 1° and to a lesser extent using a grid size of 2° x 2°. The final grid size chosen was 5° x 5°, in order to balance computational efficiency and the output accuracy. The resulting outputs for each grid were combined to produce two databases: (1) modified basal outlines for each seamount (2) centroid location, volume, height, perimeter, planar area, best fit ellipse axes, best fit ellipse orientation, for each seamount.

5.3.2 Results

There are very few studies of large seamounts on mid-ocean ridge crest, and no directly comparable studies along the SWIR. Therefore the MBOA was applied to the Southwest Indian region between 60° S, 10° W and 25° S, 70° E using the parameters determined above. The results of this analysis were then compared with subsets of

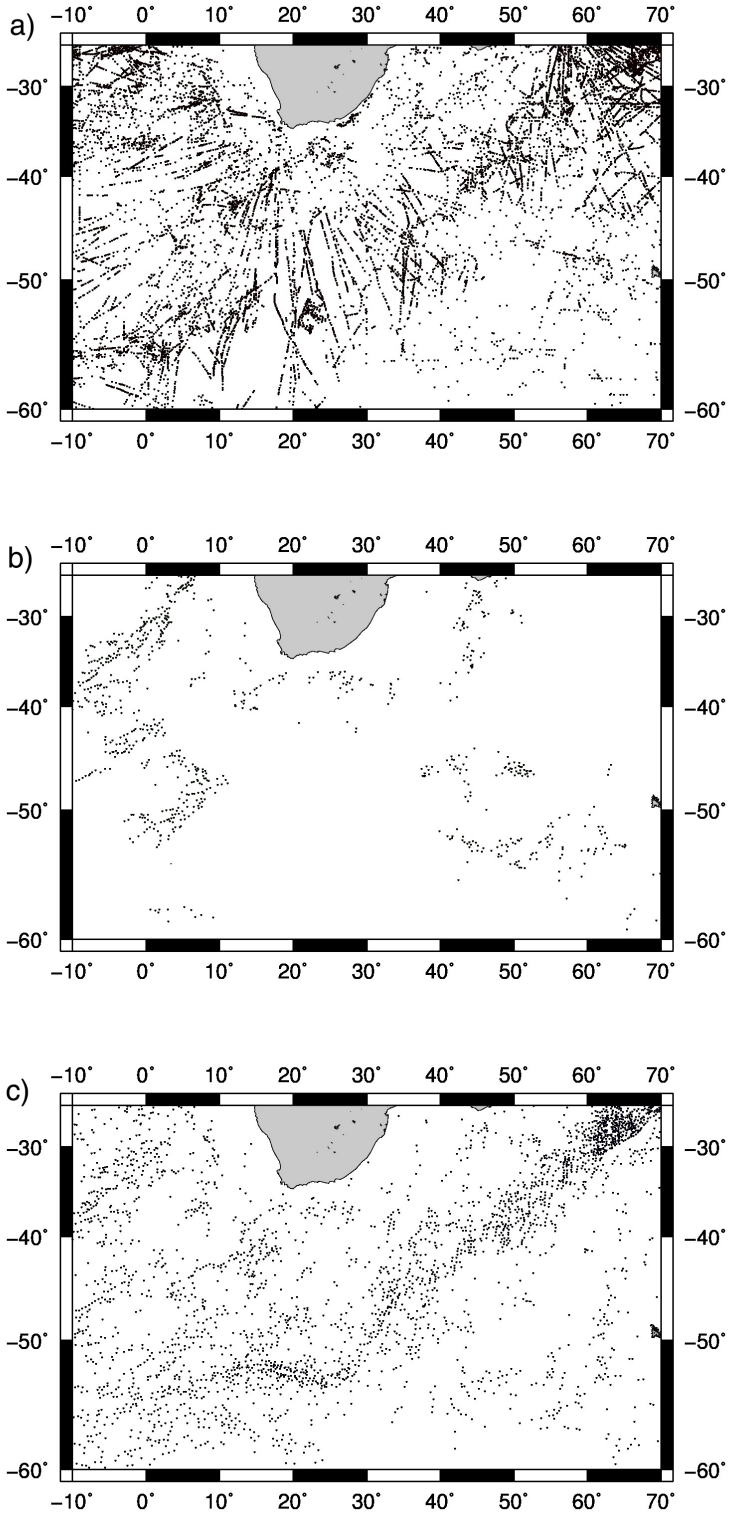


Figure 5.28: Maps showing locations of seamounts located in the SWIR region from (a) Hillier and Watts (2007) (0.1 to 6.7 km in height), (b) Wessel (2001) (2 to 7 km in height), (c) this study (∼0.3 to 7 km in height). The seamount locations from the other two studies were sampled from global data sets.

several global studies.

Figure 5.28 shows the distribution of seamounts from the MBOA, Hillier and Watts (2007) study, which used shiptrack bathymetry, and Wessel (2001) study, which used satellite gravity data. The distribution shows that the majority of the seamounts detected are located along the mid-ocean ridge crest. The reduction in seamount density away from the ridge axis is most likely due to increased sediment cover, and seamounts breaking up as they move off axis. Comparison of the three seamount distributions shows that the results of the shiptrack bathymetry study of Hillier and Watts (2007) have the greatest similarities to the seamount distribution found in this study. The seamounts picked using satellite gravity by Wessel (2001) are restricted to heights greater than $\sim$1.5 km, and therefore do not show the majority of the mid-ocean ridge seamounts.

Figure 5.29 shows the height-frequency distributions for the Southwest Indian Ridge region (-10 to 70° E, 25 to 60° S) for this study (blue line) and the study by Hillier and Watts (2007) (red line). The Hillier and Watts (2007) study was based solely on shiptrack data and then corrected for seafloor coverage, and so provides a good study for comparison since the methodologies and data are both different. The distribution for this study shows excellent agreement with the Southwest Indian subset of a global seamount study of Hillier and Watts (2007). The deviation for seamount heights $<$300 m is due to the contour interval used for the MBOA, meaning seamounts below 300 m in height are not detected in order to eliminate abyssal hill topography. This study shows a slightly higher number of seamounts for seamount heights $>$300 m. This is because this study utilises gridded swath bathymetry, which is able to resolve seamounts better than the single beam data used in the Hillier and Watts (2007) study. The deviation in the height distribution for seamount heights $>$4 km is most likely due to the inclusion of oceanic islands in this study, which are not detectable on shiptrack bathymetry. The good agreement between these two studies suggests that the MBOA, and the chosen parameters, are successfully picking seamounts in the Southwest Indian Region.

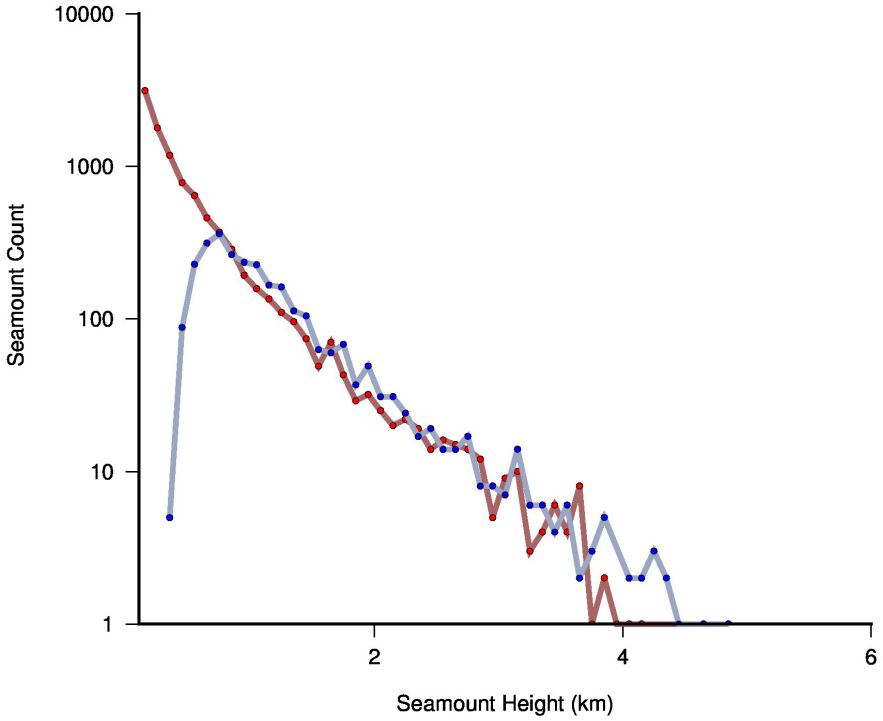


Figure 5.29: Log number of seamounts plotted against height for the Southwest Indian Ridge region (-10 to 70° E, 25 to 60° S).Blue line shows the results from this study. Red line shows the results from a subset of the global study of Hillier and Watts (2007) taken over the same SWIR region.

Along Ridge Variation

The relationship between large off-axis seamounts and processes occurring at mid-ocean ridges has not been well established. These flank rim seamounts may be split into two main types, those that form in the axial valley and subsequently move off axis due to seafloor spreading, and those that form off the ridge axis. For the purposes of this study it is assumed that all the seamounts on the ridge crest on crust younger than 5 Ma were formed in the axial valley, and subsequently moved off axis. This is likely to lead to overestimations in the magma budget of the ridge; however the variation in seamount abundance should provide an indication of the relative changes in magma budget along the ridge. Large seamounts (greater than 300 m tall), unlike the very small axial valley seamounts, require a period of sustained magma injection to form. It

is therefore reasonable to assume that areas of high abundance of these large seamounts are indicative of old volcanic centres on the ridge. These volcanic centres require an increase in the magma supply, which may be achieved through regional effects such as an increase in partial melting, or local melt-focussing mechanisms. The number and volume of seamounts on the ridge flanks, therefore, provide an indication of the time-integrated magma budget along the ridge. It should be noted that seamount populations studies (e.g. Behn et al., 2004) have shown that there is an increased degree of inherent frequency randomness with increasing seamount height, which may introduce anomalous results since the number of seamounts analysed are relatively small.

Figure 5.30 shows the distribution of seamounts binned in 1° increments along the ridge axis for crustal ages between 0 and 5 Ma, though the algorithm parameters exclude the small seamounts situated on young crust from this analysis.

The number of seamounts varies between 0 and 13 along any given 1° bin within 5 Ma of the volcanic axis (shown in panel A of Figure 5.30). This number reflects the degree of nucleation of seamounts, however a higher number of seamounts does not necessarily indicate a higher magma flux, as the seamounts vary in size. The trend in number of the seamounts along the ridge shows areas of increased seamount abundance between 16° E to 25° E (Section C, the orthogonal Section) and in the area around the Atlantis II transform fault (55° E to 61° E). These results are consistent with the high density of small seamounts in the axial valley floor of these areas, as described in section 5.2.2. The large number of edifices in these parts of the ridge indicates a greater number of locations at which magma reaches the surface in sufficient volumes and over a short time period, in order to produce a volcanic edifice. This indicates a greater number of magma pathways between the magma source at depth and the surface, as well as a greater melt supply in these regions.

The increased seamount abundance in the area between 16° E and 25° E (the orthogonal Section) may be due to the variation in effective spreading rate along the Southwest

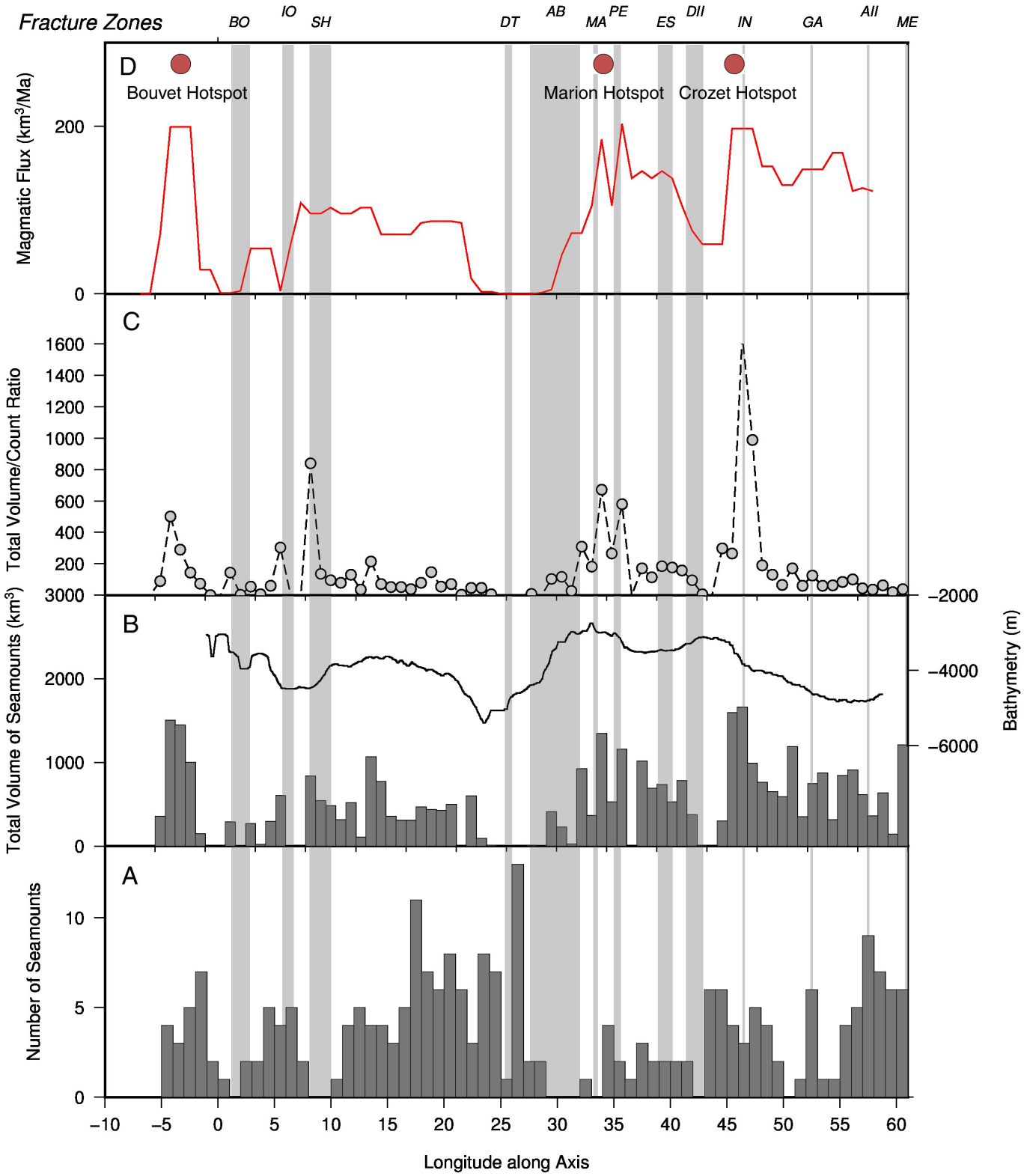


Figure 5.30: Profiles of seamount counting statistics along the ridge crest of the Southwest Indian Ridge. Panel A shows the number of seamounts binned in 1° intervals. Panel B shows the total volume of seamounts binned in 1° intervals. Panel C shows the total volume-seamount count ratio for each 1° bin. Panel D shows the magmatic flux calculated by integrating the total seamount volume over the crustal age. This assumes that all seamounts formed on zero-age crust.

Indian Ridge. The orthogonal Section is one of the few Sections of the SWIR where the effective spreading rate is equal to the full spreading rate, due to orthogonal spreading. This has two implications. The first is that the increase in spreading rate has a large effect on the height of the melt column. The ultra-slow spreading rates of the Southwest Indian Ridge mean that it lies on the edge of the rapid reduction in predicted melt supply for very slow spreading rates, according to the models of Bown and White (1994) and Reid and Jackson (1981). Therefore, a small increase in the spreading rate relative to other Sections of the ridge causes a greater relative increase in the melt than would result from an incremental spreading rate change at faster spreading ridges. In addition to the increase in melt supply, this increase in spreading rate also increases the extensional stresses experienced by the lithosphere in the axial valley, leading to an increased number of cracks and fissures Macdonald (1982). Smith and Cann (1992) proposed that these fissures form the main magma conduits for volcanism in the axial valley of the MAR, which are fed from small discrete magma bodies within the crust, producing a large number of small seamounts. The presence of MAR-like morphology in the axial valley of this Section, observed in section 5.2.2, suggests that similar mechanisms are occurring on this Section of the SWIR, and that the increase in fissure density permits the nucleation of a greater number of seamounts.

In contrast, the area around the Atlantis II transform coincides with a west to east decrease in degree of partial melting, based on large scale geochemical and geophysical trends (see chapter 3). Since the observed increase in the number of seamounts is not related to an increased melt supply, there must be an increase in magma conduits and pathways for the limited supply to reach the surface. This is an area with a large number of closely spaced transform faults, as well as large oblique non-transform discontinuities. This highly tectonised region provides a large number of zones of weakness in the lithosphere along fracture zone and non-transform discontinuity traces. Swath bathymetry of this region shows a large number of seamounts forming parallel to the N-S trending fracture zone traces, similar to those observed at the East Pacific Rise (Batiza, 1982). These seamounts are likely to have formed off-axis through the

ascendance of magma along large faults and zones of weakness within these transform structures.

The seamount count between 33° E and 42° E is generally lower than the rest of the ridge, indicating fewer large seamounts on the flanks. This is, perhaps, contrary to the expected trend since this region forms part of the Marion rise and is influenced by the Marion hotspot, which is situated 250 km off the ridge axis. Geochemical and geophysical trends along the ridge axis (see chapter 3) are consistent with increased partial melting in this region; however the seamount abundance appears to be comparatively low. While this low seamount abundance appears to directly contradict the increased magma supply, comparison of the seamount abundance and total volume of those seamounts shows that for the region between 33° E and 42° E there are a smaller number of large volume seamounts. This suggests that there has been a longer period of sustained magmatism in discrete locations, forming these large volume seamounts. Observations of the axial valley seamount abundance pattern in this region (see section 5.2.2) showed that melt was being focussed from a number of segments to a smaller number of distinct volcanic centres. The effect of concentrating the magma supply, in addition to the increased degree of partial melting resulting from the hotspot influence, may be responsible for the small number of large seamounts.

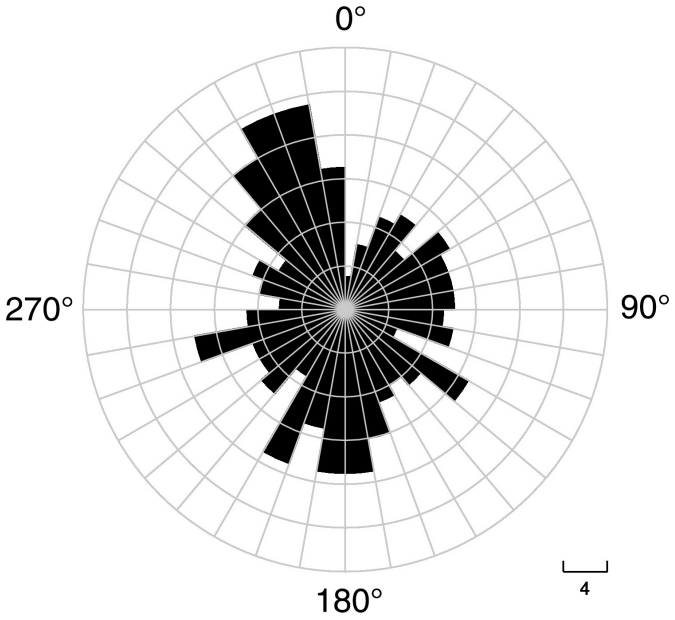
The total volume of seamounts binned in 1° bins within 5 Ma of the axis provides a better indication of the time-integrated magmatic flux of the ridge. The seamount volumes are estimated by defining a non-planar surface, which is constrained to pass through the modified basal contour, and then integrating between this surface and the seamount surface. Testing of this methodology at the Springerville volcanic field showed that this methodology increased the accuracy of edifice volume estimates (Howell et al., 2012). This is particularly important on the rough morphology of the SWIR, where the edifice must be distinguished from the surrounding topography. The seamount volume is an indicator of the magma supply along the ridge, therefore the volume for each edifice was divided by the crustal age of the seamount, in order to provide a rough

estimate of the magmatic flux (shown in panel D of Figure 5.30). This assumes that all of the seamounts formed on zero-age and therefore is designed to serve as a general indicator only. The magmatic flux shows a rough positive correlation with the axial bathymetric profile (shown in panel B). Areas of anomalously shallow bathymetry, such as those centred on -4° E, 34° E and 47° E all correspond to higher magmatic flux. Areas of deep bathymetry, such as those centred on 5° E and 25° E, generally show lower magmatic fluxes, though these are less clear than the highs. These shallow regions with high magmatic flux closely coincide with the locations of the Bouvet, Marion and Crozet hotspots (though the Crozet hotspot is located ∼1000 km off the axis). The increases in magmatic flux in close proximity to the Marion and Bouvet hotspots are likely due to the increased degree of partial melting caused by the influx of hot, low density material towards the ridge from the hotspot. The region around the Marion hotspot shows a broad area of increased magmatism, which is consistent with the broad bathymetric rise, and suggests a broad area of influence. In contrast, the region around the Bouvet hotspot shows a more localised increase in magmatism, suggesting that the influence of this hotspot is more focussed. The increase in magmatic flux at 47° E may be due to a melting anomaly caused by the Crozet hotspot, as suggested by Sauter et al. (2009), however this is difficult to prove. Other areas of the ridge, such as the orthogonal Section, show an intermediate magmatic flux compared to the extreme highs and lows elsewhere on the ridge. These observations are consistent with the long wavelength geochemical and geophysical trends described in chapter 3.

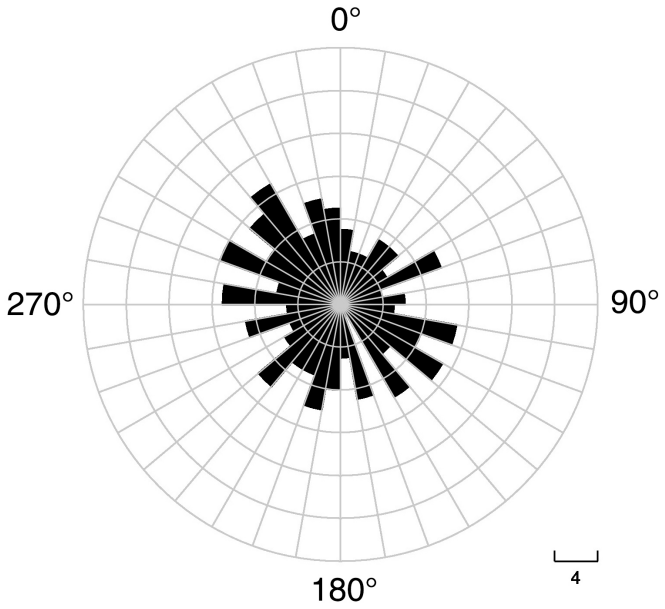
The total volume of seamounts along the ridge does not always correlate with the number of seamounts, as discussed for the area between 33° E and 42° E. It is therefore useful to calculate the volume/count ratio, which indicates areas of the ridge which exhibit particularly small number of large, isolated volcanoes compared with those that have a large number of small volcanoes. This ratio shows four notable peaks at -4° E, 8° E, 34°-36° E, and 46° E, indicating a small number of very large seamounts at these locations. With the exception of the westernmost peak, these all correspond to the location of transform faults. The systematic variation in large seamount abundance

with proximity to transform faults was investigated using the phase distribution method described in 5.2.2. The phase angle is a non-dimensional representation of a seamount's position within a segment. An angle of 0° corresponds to the discontinuity, while an angle of 180° corresponds to the centre of the segment. Therefore, a large number of seamounts with angles between 90° and 270° indicate a concentration of seamounts at the centre of the segment; conversely a large number of seamounts with angles between 0° and 90°, and 270° and 360° indicate a concentration of seamounts near the segment ends. Figure 5.31 shows (*a*) the phase distribution of seamounts where segment boundaries are defined by transform faults and for comparison (*b*) the phase distribution of seamounts if transform boundaries are ignored.

The phase distribution in which transform boundaries are ignored produces a reasonably even distribution, with no particularly preferences towards the segment centre or the segment ends. The phase distribution for transform segments, in contrast, shows a large number of seamounts located between 320° and 360°, i.e. in the ninth of the segment immediately to the west of a transform fault and accompanying fracture zone trace. There is also an increase in the very centre of the segment (around 180°) which may be attributed to the effect of melt migration away from the transforms towards the centre of the segment. The most likely explanation for the increase in seamount abundance adjacent to the transform boundaries is the presence of so called 'leaky transforms'. These were proposed by Batiza (1981) to be the source or off-axis volcanism in the Pacific, and have been used to explain linear formations of seamounts near the East Pacific Rise (Batiza, 1982). These leaky transforms form a zone of weakness in the lithosphere permitting the migration of magma to the surface. Once a magma conduit has been established, thermal considerations make further injections and eruptions of magma more likely, providing the sustained magmatism required to build a seamount. The reason behind the preference for seamounts to form to the west of the transform boundaries as opposed to the east is unclear; morphological studies across transform boundaries have shown that they are asymmetric, therefore it may be due to the inherent structure of the fracture zone.



(a) Phase distribution including transform discontinuities



(b) Phase distribution neglecting transform discontinuities

Figure 5.31: Polar histogram of the seamount phase angles, which form a non-dimensional representation of the seamount position with respect to the segment centre and bounding discontinuities. (a) includes transform discontinuities (b) does not include transform discontinuities. An angle of 0° corresponds to the discontinuity, while an angle of 180° corresponds to the centre of the segment.

Variation with Spreading Rate

Previous studies on the East Pacific Rise (e.g. Lonsdale, 1977; Macdonald et al., 1988) and Mid-Atlantic Ridge (e.g. Smith and Cann, 1992; Smith et al., 1995) have shown that the abundance of on axis seamounts is a strong function of spreading rate. Studies of small seamounts on the spreading axis have shown a greater abundance at slow spreading rates, where volcanism is dominated by point sources forming seamounts, while at fast spreading ridges, fissure eruptions lead to sheet flows which do not form seamounts. This has been further confirmed by studies over intermediate spreading ridges, which show that as the axial morphology changes from an axial valley to an axial high, the abundance of seamounts decreases (Behn et al., 2004). These studies were concerned with small mid-ocean ridge seamounts. This section aims to determine if this relationship is reflected in the larger seamounts (>300 m tall) on the ridge flanks.

The modified basal outlining algorithm was applied to boxes along the crest of the Mid-Atlantic Ridge and East Pacific Rise using the same parameters as used in this large seamount study. These parameters were not thoroughly tested on the different morphologies of these two ridges; therefore these results are intended only to provide a broad indication of seamount abundance. The resulting seamount abundances and total volumes were binned in 1° increments (of latitude for the MAR and EPR, and longitude for the SWIR). The change in the actual distance presented by 1° of latitude at the equator and high latitudes is not deemed significant enough to affect the broad changes in volcanism along the ridge. The along-axis distributions of these three ridges are compared in Figure 5.32.

These results show a clear positive correlation between spreading rate and seamount abundance, in contrast to the results from studies using smaller seamounts. The South-west Indian Ridge has the fewest seamounts and lowest total seamount volume, followed by the Mid-Atlantic Ridge and the East Pacific Rise, which has the most seamounts and highest seamount volume. Batiza (1981) showed that the number of seamounts in the Pacific increased with crustal age as new off-axis seamounts are formed. This may

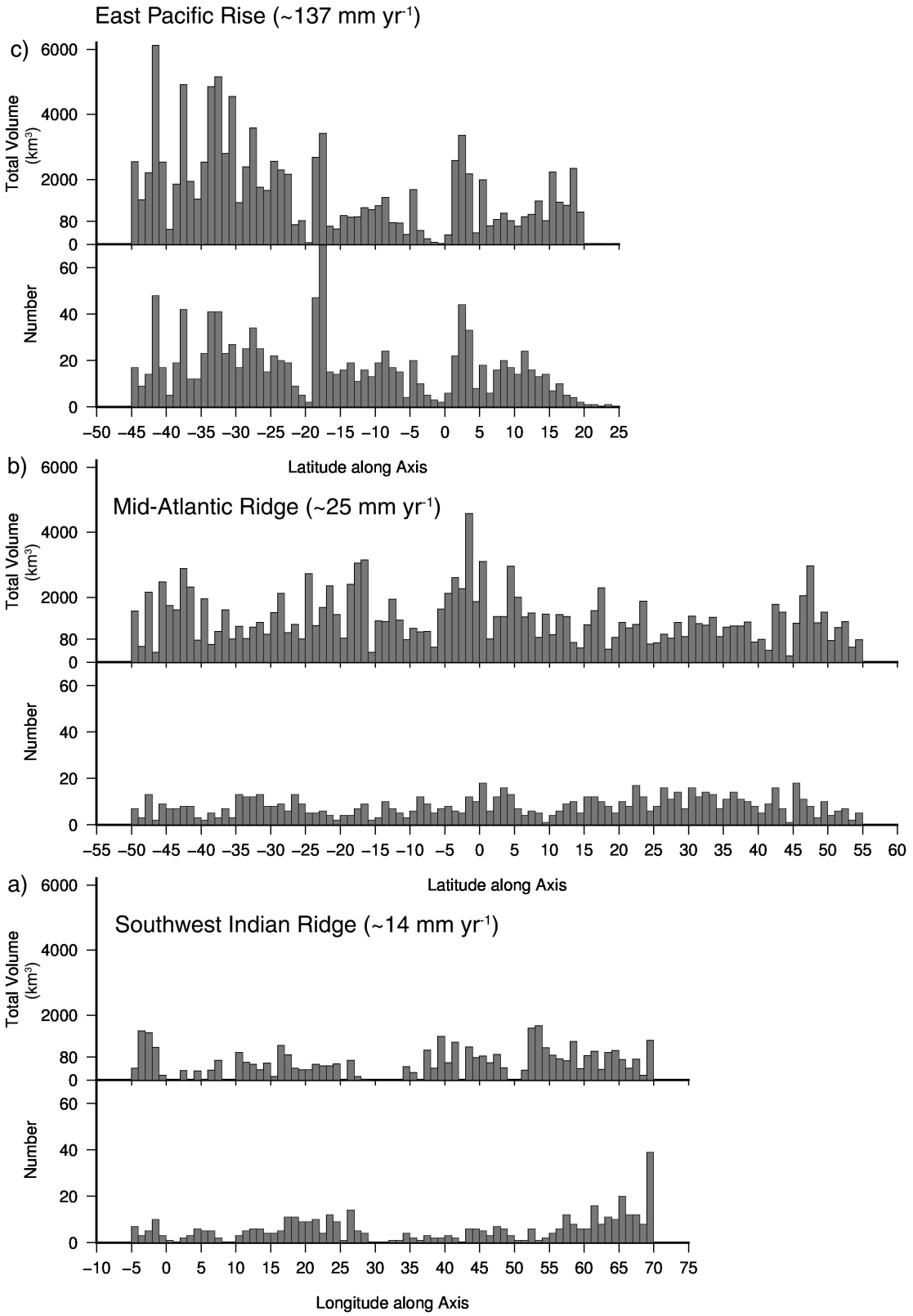


Figure 5.32: Seamount number and total volume binned in 1° increments of longitude (SWIR) or latitude (EPR and MAR) for (a) Southwest Indian Ridge (b) Mid-Atlantic Ridge (c) East Pacific Rise.

help to explain the difference between the seamount populations within the axial valley and ridge flanks. While the number of seamounts forming on the axial rise at the EPR are small, the addition of off-axis seamounts, particularly along zones of weakness such as fracture zones, increases the seamount density on the ridge flanks. In contrast, at the Mid-Atlantic Ridge, the majority of the seamounts form in the axial valley. This produces a greater seamount density in the axial valley, but fewer seamounts on the flanks, since many of these small seamounts break up as they move out of the axial valley to form abyssal hills. The Southwest Indian Ridge appears to follow the same trend as the Mid-Atlantic Ridge, with the majority of the seamounts forming in the axial valley and then being transported off axis. The difference in seamount abundance and volume between the SWIR and the MAR may be attributed to the difference in melt supply, as demonstrated by the axial valley seamount densities in section 5.2.2. The lack of testing of the MBOA on the MAR and EPR flanks precludes detailed analysis of the along-axis trends of these ridges.

5.4 Chapter Summary

This chapter presents two studies of seamount distribution along the Southwest Indian ridge. The first study investigates the distribution of small seamounts in the axial valley of four study areas, based on shipboard bathymetry. The second study investigates the distribution of large seamounts on the ridge flanks, based on integrated shipboard and satellite bathymetry. The key points are as follows:

- The Modified Basal Outlining Algorithm (MBOA) is used to identify seamounts in the axial valley of the SWIR at four study locations using multibeam bathymetry.
- The algorithm was tested and calibrated using a well-studied area of the MAR between 24° N and 30° N. This yielded similar results to previous seamount counting studies and provided a basis for comparison between the SWIR and MAR.

- Compared to the MAR, all Sections of the SWIR had lower seamount abundances, though greater characteristic heights. These are attributed to the lower melt supply predicted at ultra-slow spreading rates and a colder stronger lithosphere, which is able to support taller seamounts in the axial valley.

- The seamount population characteristics for the four different study areas showed a range of values, though a number of consistent features were identified.

- In magmatically sparse areas, seamounts form in the edges of the axial valley or along fault lines, indicating that these faults are used as magma conduits to the surface. This suggests that the conduit availability is the governing factor on seamount abundance in these areas.

- In highly magmatic areas, where the axial valley had become filled with volcanic material, the MBOA detected only parasitic cones on the large seamounts, producing an apparently low density despite the high magma supply.

- Segment-scale melt migration towards the centre of segments was observed at some Sections, but not all. These segments generally displayed a similar morphology to the MAR, but lacked the large scale melt focussing in other Sections of the ridge.

- Large scale melt focussing mechanisms were present on the oblique and central Sections of the ridge, forming alternating magmatically sparse and magmatically rich areas.

- The MBOA was tested on the flanks of the SWIR in order to detect large seamounts. Sensitivity analysis was used to select parameters that are able to remove the background abyssal hill topography of the SWIR, whilst detecting the volcanic seamounts.

- The results of this analysis was compared with the global seamount distribution study of Hillier and Watts (2007) and showed good agreement, suggesting that the MBOA is successful in picking volcanic seamounts from rough background

topography.

- The MBOA was applied to the ridge crest and the seamount abundance and volume calculated, and the distribution in 1° bins along the ridge was analysed.
- Variations in the along-ridge abundance showed that small changes in the effective spreading rate had large impacts on the seamount abundance. This is due to the range of spreading rates exhibited by the SWIR, which span a rapid change in predicted melt supply following the models of Bown and White (1994) and Reid and Jackson (1981).
- An increase in the number of large seamounts at transform faults was attributed to the presence of leaky transform faults. These form zones of weakness, which are then exploited as magma pathways. There is a preference for seamounts to preferentially form on the western margin of fracture zones, though it is not clear why.
- The variations in estimated magmatic flux along the ridge show a positive correlation with the axial bathymetry. Two highs in the magmatic flux correspond to areas of the ridge influenced by the Marion and Bouvet hotspot plumes, as the influx of material from the hotspots increases the magmatic flux over those areas of the ridge.
- Comparison of ridge flank seamount populations between the SWIR, MAR and EPR show a systematic increase in both seamount abundance and volume with increasing spreading rate. This is attributed to the greater rate of off-axis volcanism at the EPR, and the destruction of small seamounts at the MAR and SWIR as they move out of the axial valley.

Chapter 6

Admittance and Elastic Thickness

During the late 1950s and early 1960s, the advent of surface ship gravimeters permitted the first detailed marine gravity surveys. Talwani et al. (1961) performed the first comprehensive marine gravity study of a mid-ocean ridge, the Reykjanes Ridge. He showed that the free-air anomaly over the ridge averaged to zero, while the Bouguer anomaly, which is corrected for the effects of topography, comprised a broad low, which reflects the low density, hot upwelling region beneath the ridge.

Comparisons of topography and gravity over ridge crests (e.g. Watts, 1982) have shown a strong correlation between topography and free-air gravity, however a residual isostatic anomaly low over the rift valley shows that the ridge is not compensated by crustal thinning. Free-air gravity anomalies at the Labrador (Kristofferson and Talwani, 1977) and Coral (Weissel and Watts, 1979) Seas, which stopped spreading over 40 Myr ago, show strong similarities to those observed over active rifts. These observations suggest that stresses in the lithosphere are supported elastically, and may be maintained for long periods of time (Watts, 1982).

Early admittance studies by McKenzie and Bowin (1976) examined the relationship between gravity and bathymetry along profiles in the Atlantic Ocean, including one across the Mid-Atlantic Ridge. They concluded that their results could be explained

by an elastic plate model with a thickness of ∼10 km. This is much lower than elastic thickness estimates using loads on older crust (e.g. Watts, 1978). McKenzie and Bowin (1976) suggested that the topography sampled in the profile was created at the ridge axis, where the isotherms are shallower, and then frozen in as the newly formed crust moved off axis. These 2D admittance techniques were applied to a series of profiles along the Mid-Atlantic Ridge and East Pacific Rise by Cochran (1979), who suggested that the elastic thickness decreases with increasing spreading rate. At a similar time, McNutt (1979) applied the admittance technique to 3D gridded data at the Juan de Fuca ridge, yielding an elastic thickness of ∼2 km.

Previous admittance studies on the Southwest Indian Ridge consist of a single 2D profile study across the ridge crest, yielding elastic thicknesses of 2 km to 5 km (Watts et al., 1985), and two studies of intra-plate volcanic topography to the south of the ridge (Goslin and Diament, 1987; Diament et al., 1986).

This chapter aims to extend the elastic thickness studies over mid-ocean ridge crests in the following ways:

- Conduct a series of synthetic tests to elucidate the sources of error within 3D window admittance techniques.

- Determine best fit elastic thicknesses for Southwest Indian Ridge, which has not been subject to previous spectral analysis along the whole ridge.

- Incorporate windowed admittance techniques in 3D and modern datasets to areas on the Mid-Atlantic and East Pacific Rise in which previously only 2D profiles were used for spectral analysis.

- Using the new results from the ultra-slow spreading SWIR, slow spreading MAR and fast spreading EPR, re-examine the relationship between elastic thickness and spreading rate.

6.1 Isostatic Models

The term isostasy is used to describe the equilibrium state toward which the crust and mantle tend in the absence of disturbing forces (Watts, 2001). The loading or unloading of topography on the Earth's surface disturbs this equilibrium, causing an isostatic response in order to compensate for the mass excess or deficit, and return the system to equilibrium. A number of isostatic models have been proposed to explain the response of the lithosphere to loading.

Airy Isostasy

Airy viewed the Earth as having a crust overlying a fluid mantle of greater density. He suggested that mass excesses, such as mountains, were compensated by a low density crustal root extending into the fluid mantle (Airy, 1855). In the Airy model, which was quantified by Heiskanen (1931), the depth of this thickened crust is directly proportional to the height of the overlying topography.

For a simple single layer, uniform density crustal model, the thickness of a crustal root, r, overlying a topographic height, h, is then given by (Heiskanen, 1931)

$$r = \frac{h\rho_c}{\rho_m - \rho_c} \tag{6.1}$$

where ρ_c and ρ_m are the densities of the crust and mantle respectively.

In the case of ocean basins, the water replaces the crust at the surface creating a mass deficit and therefore crustal thinning, r, over water depth, h, given by (Heiskanen, 1931)

$$r = \frac{h(\rho_c - \rho_w)}{\rho_m - \rho_c} \tag{6.2}$$

where ρ_w is the density of the water.

Pratt Isostasy

In contrast, Pratt proposed that the compensations for surface topography came from lateral density variations within the crust, which are directly proportional to the height of the overlying topography (Pratt, 1859). The depth to the base of the crust remains consistent in this model, and is the depth at which all pressures are equal, called the depth of compensation. In the Pratt model, which was quantified by Hayford (1909), the density of the crust, ρ, underlying a topographic height, h, is given by

$$\rho = \frac{\rho_0 D_c}{D_c + h} \tag{6.3}$$

where ρ_0 is the density of the topography and D_c is the depth of compensation. In the case of oceans, the density of the crust, ρ, underlying water depth, h, is given by (Hayford, 1909)

$$\rho = \frac{\rho_0 D_c + \rho_w h}{D_c + h} \tag{6.4}$$

Flexural Isostasy

The Airy and Pratt models consider isostatic compensation to occur locally as a consequence of crustal blocks floating on a fluid mantle (Fisher, 1889). In contrast, flexural isostatic models take into account the inherent strength and rigidity of the lithosphere. This is a modification of the Airy model whereby the underlying density distribution is controlled by the strength of the lithosphere (Gunn, 1943). In the flexural isostatic model the excess mass of the load is balanced by a mass deficit at depth, and a flexural depression is created as in the Airy model. The finite strength of the lithosphere means that the deformation is not locally confined, but is distributed across a radius of regionality, R, defined by Vening Meinesz (1931) as

$$R = 2.905\beta \tag{6.5}$$

where β is a three-dimensional flexural parameter which is dependant on the flexural rigidity, D, given by

$$\beta = \left[\frac{D}{(\rho_m - \rho_{infill})g}\right]^{\frac{1}{4}} \tag{6.6}$$

where g is the acceleration due to gravity, and ρ_m and ρ_{infill} are the densities of the mantle and material infilling the flexural depression respectively.

Vening-Meinesz modelled the flexure of an elastic plate over an inviscid mantle when a topographic load is applied. The thickness of this plate, called the elastic thickness (T_e), does not represent any particular stratum in the lithosphere, but is instead a geometric analogue of the integrated strength of the lithosphere (Burov and Diament, 1995; Kirby, 2014).

6.1.1 Elastic Plate Model

The behaviour of the lithosphere in response to loading is governed by its rheological properties. Modelling the behaviour of complex crustal rheology with few constraints, particularly in continental settings, is challenging. The elastic plate model was used by Walcott (1970), who assumed that during loading the lithosphere behaves as a plate with a perfectly elastic rheology, emplaced on an inviscid mantle. This is, of course, a simplification since rocks undergo brittle failure at low temperature, and deform in a ductile manner at high temperatures(Kirby, 1980); however over loading timescales of tens of millions of years, the behaviour of the lithosphere approximates that of a thin elastic plate (Burov and Watts, 2006; Burov, 2011).

The elastic plate model makes the following assumptions:

- The plate thickness (elastic thickness) is small compared to the radius of curvature
- The deflections under loading are small compared to the thickness of the plate
- The plane stress boundary condition is applied, so that the vertical stress, σ_y, is

equal to 0

In considering the flexure of an elastic plate, we can simplify the problem by considering the flexure of an elastic beam of unit width, (see Figure 6.1), provided that the stresses and strains that act on the beam as part of a plate are taken into account (Timoshenko, 1958).

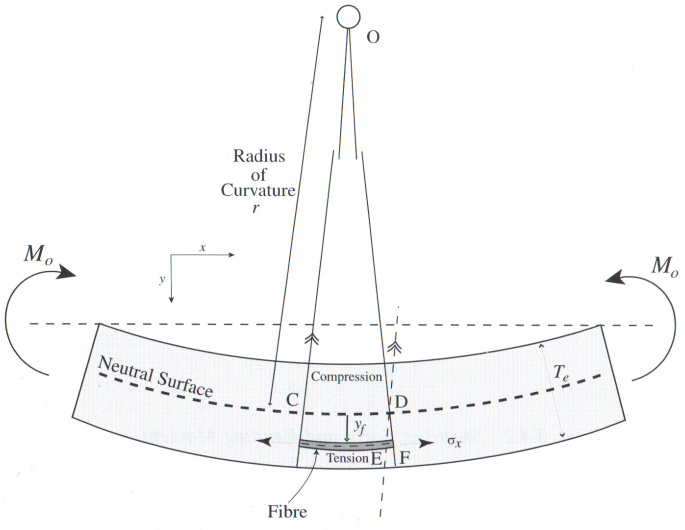


Figure 6.1: Schematic diagram illustrating the flexure of an elastic beam due to bending moments applied at either end of the beam. Adapted from Watts (2001).

There are two quantities which must be determined to evaluate the flexure of an elastic beam: the bending moment, M, and the vertical shear force, V.

Figure 6.2 illustrates the stresses experienced by an element of a cross section of a beam with a height of dy and a unit width.

The moment that acts on the element, dM, about the neutral surface of the beam is given by

$$\begin{aligned} \text{moment} &= \text{stress x area x distance} \\ dM &= \sigma_x \quad dy \cdot 1.0 \quad y_f \\ &= \frac{E y_f^2}{r(1-\nu^2)} \quad dy \end{aligned} \tag{6.7}$$

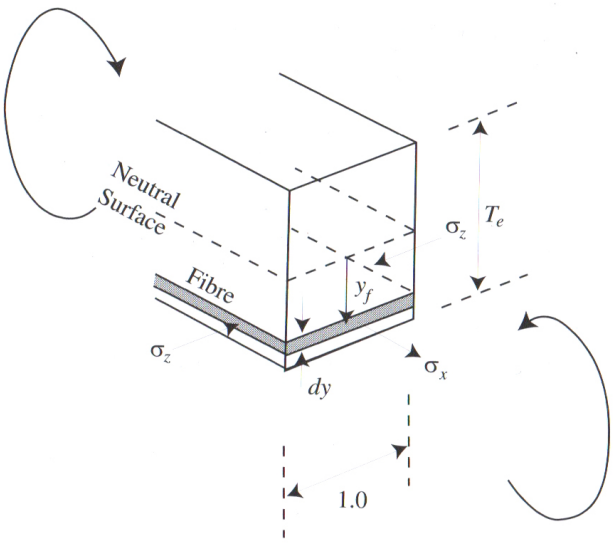


Figure 6.2: Schematic diagram illustrating the stresses experienced by an element of a cross section of a flexed beam. Adapted from Watts (2001).

where σ_x is the stress component in the x direction, y_f is the distance from the element to the neutral surface, E is the Young's modulus, r is the radius of curvature and ν is Poissons's ratio. The total bending moment is obtained via depth integration of the element moments over the thickness of the plate, T_e.

$$\begin{aligned} M &= \frac{E}{r(1-\nu^2)} \int_{\frac{T_e}{2}}^{\frac{-T_e}{2}} y_f^2 \quad dy \\ &= \frac{-ET_e^3}{12(1-\nu^2)} \frac{1}{r} \\ &= -\frac{D}{r} \end{aligned} \tag{6.8}$$

where D is defined as the flexural rigidity of the plate and given by

$$D = \frac{ET_e^3}{12(1-\nu^2)} \tag{6.9}$$

The radius of the curvature, in the Cartesian coordinate system shown in Figure 6.1, is given by

$$\frac{1}{r} = \frac{\frac{d^2y}{dx^2}}{[1 + (\frac{dy}{dx})^2]^{\frac{3}{2}}} \tag{6.10}$$

where $\frac{1}{r} \rightarrow \frac{d^2y}{dx^2}$ for small deflections. Substituting this into equation 6.8 gives

$$M = -D\left[\frac{d^2y}{dx^2}\right] \tag{6.11}$$

Once the bending moment has been defined, the vertical shear force can be defined by considering the moments acting on an element of beam width, dx, as seen in Figure 6.3.

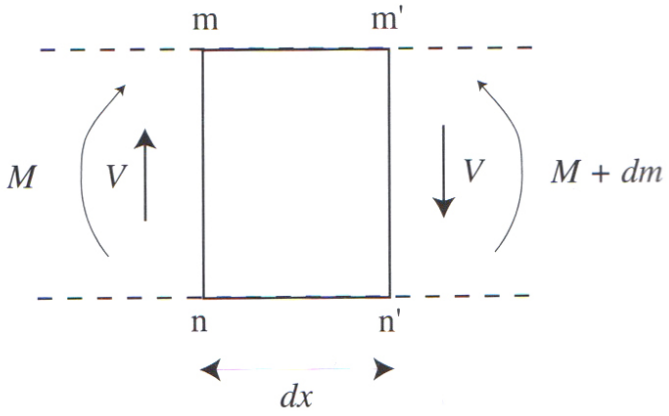


Figure 6.3: Schematic diagram illustrating the moments acting on an element of the beam and the shear forces acting on the boundary of the element. Adapted from Watts (2001).

Assuming that the element is of negligible mass, the shear forces acting on each boundary of the element will be equal. The bending moment, M, increases by dM which is given by

$$\begin{aligned} dM &= V dx \\ \therefore V &= \frac{dM}{dx} \end{aligned} \tag{6.12}$$

We can now consider the force balance of applying a force of q per unit area to the surface of an element of beam width, dx, simulating that of a load due to infill of the

flexural depression. We also apply a force of p per unit area to the base of the element, simulating the buoyant response from the displacement of the underlying substratum, as seen in Figure 6.4.

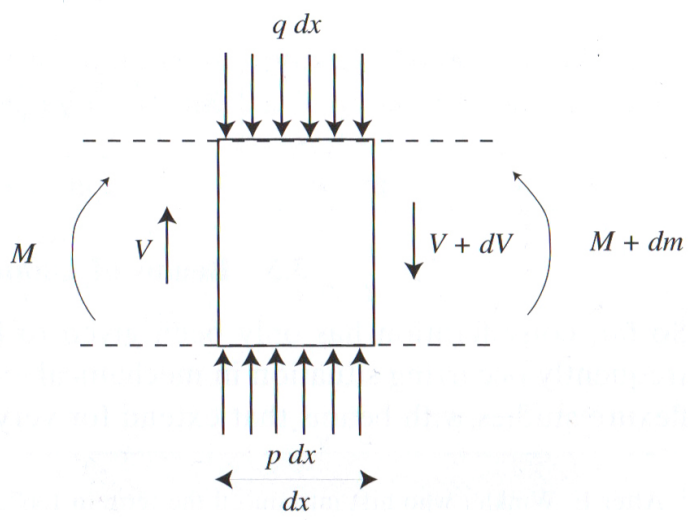


Figure 6.4: Schematic diagram illustrating the forces applied to the top and bottom of the element of the beam. Adapted from Watts (2001).

This force balance is given by

$$\begin{aligned} qdx \cdot 1.0 + (V + dV) - pdx \cdot 1.0 - V = 0 \\ p - q = \frac{dV}{dx} \\ p - q = \frac{d^2M}{dx^2} \end{aligned} \tag{6.13}$$

Substituting equation 6.11 into equation 6.13 gives

$$D\frac{d^4y}{dx^4} + p - q = 0 \tag{6.14}$$

This is the general equation for the deflection of an elastic beam.

Modelling the flexural effect of more complex non-linear loads requires a three-dimensional approach. Two orthogonal bending moments, M_x and M_z, and the twisting moment, M_{xz}, are obtained by depth integration of the bending stress, as for the elastic beam,

giving

$$M_x = -D\left(\frac{\partial^2 y(\bar{r})}{\partial x^2} + \frac{\partial^2 y(\bar{r})}{\partial z^2}\right) \tag{6.15}$$

$$M_z = -D\left(\frac{\partial^2 y(\bar{r})}{\partial z^2} + \frac{\partial^2 y(\bar{r})}{\partial x^2}\right) \tag{6.16}$$

$$M_{xz} = -D(1-\nu)\frac{\partial^2 y(\bar{r})}{\partial x \partial z} \tag{6.17}$$

where Poisson's ratio is assumed to be isotropic and $\bar{r}$ is the projection of the position vector onto the x-z plane. These moments may be substituted into the partial differential equation that relates the moments to the applied surface load, q, and buoyant basal force, p, to give the full differential equation for flexure of a thin elastic plate of variable thickness T_e. This is given by

$$\nabla^2(D\nabla^2 y(\bar{r})) = (1-\nu)\left(\frac{\partial^2 D}{\partial x^2}\frac{\partial^2 y(\bar{r})}{\partial z^2} - 2\frac{\partial^2 D}{\partial x \partial z}\frac{\partial^2 y(\bar{r})}{\partial x \partial z} + \frac{\partial^2 D}{\partial z^2}\frac{\partial^2 y(\bar{r})}{\partial x^2}\right) \tag{6.18}$$

where ∇^2 is the 2D Laplacian differential operator. By assuming uniform flexural rigidity, D, equation 6.18 becomes

$$\begin{aligned} D\left[\frac{\partial^4 y(\bar{r})}{\partial x^4} + 2\frac{\partial^4 y(\bar{r})}{\partial x^4 \partial z^4} + \frac{\partial^4 y(\bar{r})}{\partial z^4}\right] + p(\bar{r}) - q(\bar{r}) = 0 \\ D \cdot \nabla^4 y(\bar{r}) + p(\bar{r}) - q(\bar{r}) = 0 \end{aligned} \tag{6.19}$$

which is equivalent in form to equation 6.14.

The force applied to the surface of the plate, $q(\bar{r})$, is generated by the topographic load

and the material infilling the flexural depression. This is given by

$$q(\bar{r}) = -(\rho_c - \rho_w)gh_0(\bar{r}) - (\rho_{infill} - \rho_w)gy(\bar{r}) \tag{6.20}$$

where $h_0(\bar{r})$ and $y(\bar{r})$ are the heights of the topographic load and flexure respectively, and ρ_c, ρ_w, ρ_{infill}, and ρ_m are the densities of the crust, water, infill material and mantle respectively.

The force applied to the base of the plate $p(\bar{r})$ is generated by the mantle and is given by

$$p(\bar{r}) = (\rho_m - \rho_c)gy(\bar{r}) \tag{6.21}$$

Substituting these into equation 6.19 gives

$$D \cdot \nabla^4 y(\bar{r}) + (\rho_m - \rho_c)gy(\bar{r}) - (\rho_c - \rho_w)gh_0(\bar{r}) - (\rho_{infill} - \rho_w)gy(\bar{r}) = 0 \tag{6.22}$$

Since the measured topography $h(\bar{r})$ comprises two parts, the load topography, $h_0(\bar{r})$, and the plate flexure, $y(\bar{r})$, we can express the topographic load in terms of the observed topography and plate flexure, which gives

$$D \cdot \nabla^4 y(\bar{r}) + \big[\rho_m - \rho_c\big]gy(\bar{r}) - \big[\rho_c - \rho_w\big]g\big(h(\bar{r}) - y(\bar{r})\big) - \big[\rho_{infill} - \rho_w\big]gy(\bar{r}) = 0 \tag{6.23}$$

The analysis is greatly simplified by taking the Fourier transform of equation 6.23

$$Dk^4\mathbf{Y}(\bar{k}) + \big[\rho_m - \rho_c\big]g\mathbf{Y}(\bar{k}) - \big[\rho_c - \rho_w\big]g\big(\mathbf{H}(\bar{k}) - \mathbf{Y}(\bar{k})\big) - \big[\rho_{infill} - \rho_w\big]g\mathbf{Y}(\bar{k}) = 0 \tag{6.24}$$

where $\bar{k}$ is the wave vector and the Fourier transform terms are of the form

$$\mathbf{Y}(\bar{k}) = \int_S y(\bar{r})e^{(2\pi i\bar{k}\cdot\bar{r})}dS \tag{6.25}$$

where S is the surface of the plate.

Equation 6.24 can be rearranged to give the equation relating the flexure, $\mathbf{Y}(\bar{k})$, to the observed topography, $\mathbf{H}(\bar{k})$, for the simple crustal model shown in Figure 6.5.

$$\begin{aligned}\mathbf{Y}(\bar{k}) &= -\left[\frac{\rho_c - \rho_w}{\rho_m - \rho_{infill}}\right]\left[1 + \frac{D\bar{k}^4}{(\rho_m - \rho_{infill})g}\right]^{-1}\mathbf{H}(\bar{k}) \\ &= -\frac{\rho_c - \rho_w}{\rho_m - \rho_{infill}}\Phi_e(\bar{k})\mathbf{H}(\bar{k})\end{aligned} \tag{6.26}$$

where

$$\Phi_e(\bar{k}) = \left[1 + \frac{D\bar{k}^4}{(\rho_m - \rho_{infill})g}\right]^{-1} \tag{6.27}$$

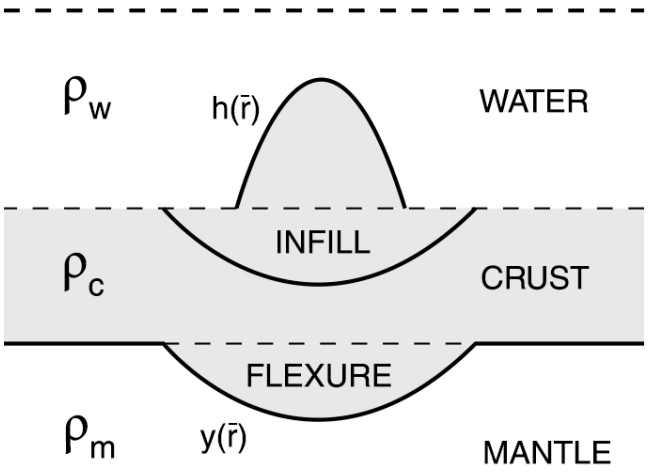


Figure 6.5: Schematic diagram illustrating the simple crustal model used for the relationship between topography and flexure, given in equation 6.26.

Equation 6.26 gives the relationship between flexure, $\mathbf{Y}(\bar{k})$, and flexural rigidity, D, and consequently elastic thickness, T_e. Measurements of flexure from surface loading, therefore, allow us to estimate T_e. It is, however, difficult to directly observe flexure without detailed seismic observations (e.g. Watts and Ten Brink, 1989). Therefore, we use a parameter which is sensitive to both the load and the resultant flexure: the free-air gravity anomaly.

6.1.2 Modelling Gravity Anomalies

Gravity anomalies are sensitive to the flexure produced by loading and easily observable both at sea and on land, therefore they provide a means to study the flexure of the lithosphere. The flexure of the lithosphere under vertical loading causes deformation of surfaces of density contrast, such as the Moho. These deformations lead to density excesses and deficits, which cause gravity anomalies.

Parker (1972) has shown that, to the first order the Fourier transform of the gravity anomaly, $\Delta g_P(\bar{r})$, at point P is related to the Fourier transform of the gravity anomaly, $\Delta g_Q(\bar{r})$, at point Q is given by

$$\Delta \mathbf{g}_P(\bar{k}) = e^{-|\bar{k}|p} \Delta \mathbf{g}_Q(\bar{k}) \tag{6.28}$$

where p is the height of P above Q. Using Green's equivalent layer theorem we can replace the gravity anomaly, $\Delta g_Q(\bar{r})$, with an equivalent surface mass distribution on the same place, $\mathbf{M}_Q(\bar{k})$, that is given by (Watts, 2001)

$$\mathbf{M}_Q(\bar{k}) = \frac{\Delta \mathbf{g}_Q(\bar{k})}{2\pi G} \tag{6.29}$$

$\mathbf{M}_Q(\bar{k})$ can be expressed in terms of the Fourier transform of a topographic surface of density contrast, $\Delta\rho$, such that

$$\Delta \mathbf{g}_Q(\bar{k}) = 2\pi G \Delta\rho \mathbf{H}(\bar{k}) \tag{6.30}$$

where $\mathbf{H}(\bar{k})$ is the Fourier transform of the topographic surface. Combining equations 6.28 and 6.30 gives an equation for calculating the gravity anomaly due to an undulating interface of uniform density contrast in the wave domain.

$$\Delta \mathbf{g}_P(\bar{k}) = e^{-|\bar{k}|p} 2\pi G \Delta\rho \mathbf{H}(\bar{k}) \tag{6.31}$$

6.1.3 Gravitational Admittance

The gravitational admittance, $\mathbf{Z}(\bar{k})$, is the wavenumber parameter that modifies the topography in order to produce the gravity anomaly (Watts, 2001). The gravitational admittance in its simplest form, calculated in three dimensions, is given by (e.g. Dorman and Lewis, 1970)

$$\mathbf{Z}(\bar{k}) = \frac{\Delta\mathbf{g}(\bar{k})}{\mathbf{H}(\bar{k})} \tag{6.32}$$

where $\Delta\mathbf{g}(\bar{k})$ and $\mathbf{H}(\bar{k})$ are the Fourier transforms of the gravity anomaly, $\Delta g(\bar{r})$, and topography, $h(\bar{r})$, respectively, and are dependent on the wave vector which is given by

$$|\bar{k}| = \sqrt{k_x^2 + k_y^2} \tag{6.33}$$

From Parker's equation (Equation 6.28) to the first order, the Fourier transform of the gravity anomaly measured at sea level due to seafloor topography is given by

$$\Delta\mathbf{g}_H(\bar{k}) = 2\pi G(\rho_c - \rho_w)\mathbf{H}(\bar{k})e^{-|\bar{k}|d} \tag{6.34}$$

where ρ_c is the density of the topography, ρ_w is the density of seawater and d is the mean water depth. Combining equations 6.32 and 6.34 gives an equation for the theoretical admittance for uncompensated topography

$$\mathbf{Z}(\bar{k})_{uncomp} = 2\pi G(\rho_c - \rho_w)e^{-|\bar{k}|d} \tag{6.35}$$

In addition to the admittance resulting from the relationship between the gravity anomaly and topography attributed to the seafloor topography, we wish to express the admittance in the case of lithospheric flexure in response to the seafloor topography. Figure 6.6 shows a simple crustal model which undergoes flexure due to loading.

Assuming that the load and material that infills the flexure has the same density as the crust and that the crust is of uniform density, the Fourier transform of the gravity

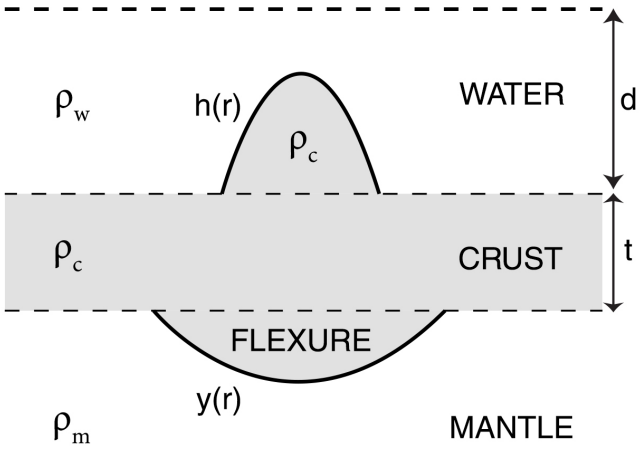


Figure 6.6: Schematic diagram illustrating the simple crustal model used to derive the equations for gravitation admittance due to flexure.

anomaly due to flexure measured at sea level is given by

$$\Delta \mathbf{g}_{flex}(\bar{k})_H = 2\pi G(\rho_m - \rho_c)\mathbf{Y}(\bar{k})e^{-|\bar{k}|(d+t)} \tag{6.36}$$

where t is the crustal thickness. Substituting equation 6.26 in to 6.36 gives us the Fourier transform of the combined gravity anomaly in terms of the Fourier transform of the topography

$$\Delta \mathbf{g}(\bar{k})_{total} = 2\pi G(\rho_c - \rho_w)\mathbf{H}(\bar{k})e^{-|\bar{k}|d}(1 - \phi'_e(\bar{k})e^{-kt}) \tag{6.37}$$

Substituting this into equation 6.32 gives us the theoretical admittance for a simple flexural isostatic model

$$\mathbf{Z}(\bar{k})_{flexure} = 2\pi G(\rho_c - \rho_w)e^{-|\bar{k}|d}(1 - \phi'_e(\bar{k})e^{-kt}) \tag{6.38}$$

This may be applied to a more complex model by including the gravity contributions from multiple crustal layers and the contribution of the material infilling the flexural depression (see section 6.2.1).

Equation 6.38 provides a theoretical expression for the admittance, which is dependent

on the flexural rigidity, D, and consequently the elastic thickness, T_e. By comparing the observed admittance with the theoretical admittance calculated using a range of $T_e's$ we can determine the best fit T_e.

As stated in equation 6.32, the observed admittance is calculated using the Fourier transforms of the observed topography and gravity anomaly, however in reality a number of modifications are first made to the data. Firstly, the Fourier transforms of the topography and gravity anomaly are multiplied by the complex conjugate to remove uncorrelated noise (McNutt, 1979). Secondly, the data undergoes annular averaging, which has the duel effect of removing noise, since it is not expected to be annularly coherent, and converting the two dimensional admittance, $\mathbf{Z}(\bar{k})$, into the one dimensional admittance, $\mathbf{Z}(k_r)$ (e.g. McNutt, 1979). The annuli are spaced logarithmically so that equal amounts of information are present in each annulus (Banks et al., 1977).

$$\mathbf{Z}(k_r) = \frac{\langle \Delta\mathbf{g}(\bar{k}) \cdot \mathbf{H}^*(\bar{k}) \rangle}{\langle \mathbf{H}(\bar{k}) \cdot \mathbf{H}^*(\bar{k}) \rangle} \tag{6.39}$$

where $\langle\rangle$ indicates annular averaging of the spectra, * denotes the complex conjugate and k_r is the one dimensional radial wavenumber.

It is useful, at this stage, to define two additional spectral parameters: the coherence, γ^2, and the phase, Φ_z. The coherence is a measure of the correlation between the topography and gravity anomaly and is calculated using the ratio of cross power spectrum to auto power spectra

$$\gamma^2(\bar{k}) = \frac{S_{H\Delta g}(k)^2}{S_{HH}(k) S_{\Delta g \Delta g}(k)} \tag{6.40}$$

where $S_{H\Delta g}$ is the cross-spectrum of the gravity anomaly and topography while S_{HH} and $S_{\Delta g \Delta g}$ are the auto-power spectra of the topography and gravity respectively. The phase of the admittance, Φ_z, is given by

$$e^{-i2\Phi_z(\bar{k})} = \frac{\mathbf{Z}(\bar{k})}{\mathbf{Z}^*(\bar{k})} \tag{6.41}$$

where the * denotes the complex conjugate. The phase should be close to 0 within the wavelengths of high coherence since, although the admittance is complex, it is expected to be real. It has been suggested, however, that the 360° annular averaging may remove the imaginary part of the admittance (Kirby, 2014).

The coherence is also used to estimate the error in the admittance, which is given by (Munk and Cartwright, 1966)

$$Z_{error})(k_r) = \sqrt{|\frac{1}{n(k_r)}\big(\frac{1}{\gamma^2(k_r)} - 1\big)|} \tag{6.42}$$

where $n(k_r)$ is the number of estimates in the annular waveband, and $\gamma^2(k_r)$ is the coherence between the gravity and bathymetry spectra. This estimate of the admittance error is used to calculate the error bars for the isostatic response functions later in this chapter.

Figure 6.7 shows an example of admittance, coherence and phase of the admittance for a 9° x 9° window on the Southwest Indian Ridge. This was calculated using the GEBCO 2014 30'' x 30'' grid, based on shiptrack bathymetry, and the Sandwell and Smith v.23.1 free-air predicted gravity grid derived from satellite altimetry. At short wavelengths the water depth attenuates the gravity effect of the topography, leading to a decrease in the admittance as well as increasing noise. At long wavelengths the isostatic compensation competes with the gravity effect of the topography, leading to a decrease in the admittance. The coherence is useful in determining the wavelengths at which the observed gravity anomaly is caused by the sea-floor topography (McKenzie and Bowin, 1976; Watts, 1978). The coherence approaches 0 at short and very long wavelengths, while at intermediate wavelengths, at which most of the free-air gravity anomaly is caused by the topography, the coherence approaches 1. The phase is expected to be close to 0 within the wavelengths of high coherence, and reflects the increasing noise at shorter wavelengths.

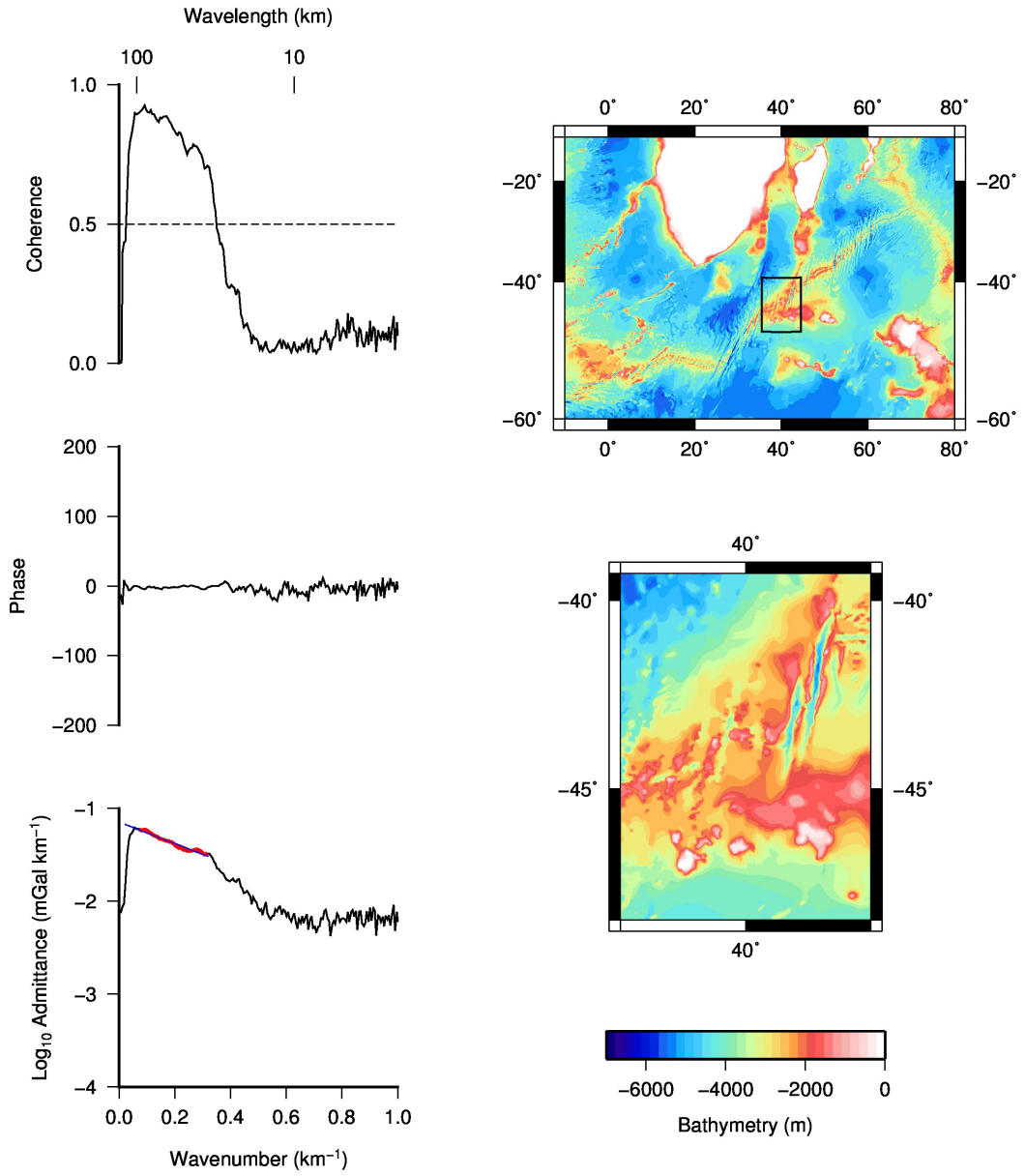


Figure 6.7: The coherence, phase and admittance determined from the spectral analysis of bathymetry and free-air gravity anomalies for a window on the Southwest Indian Ridge crest. The inset shows the location and topographic features of the window. The red points on the admittance graph show the data used to estimate the slope. The blue line shows the best fit slope.

6.1.4 Determination of Best Fit Elastic Thickness

We can determine the best fit elastic thickness, T_e, by comparing the theoretical admittance (given in equation 6.38) for a range of $T_e s$ with the observed admittance. The

theoretical admittance depends on water depth and crustal density. We can determine the best fit mean water depth, d, and crustal density, ρ_c, from the slope and intercept of the part of the admittance spectrum that reflects the uncompensated topography. Taking the log of both sides of the one dimensional form of equation 6.38 gives

$$log_{10}\mathbf{Z}(k_r) = -kdlog_{10}e + log_{10}(2\pi G(\rho_c - \rho_w)) \tag{6.43}$$

Therefore a log-linear plot of $\mathbf{Z}(k_r)$ against k_r has a slope of $0.4335d$ and an intercept on the $\mathbf{Z}(k_r)$ axis of $log_{10}[2\pi G(\rho_c - \rho_w)]$. In a deep marine basin setting, the water depth and crustal densities can be assumed to be relatively consistent between admittance windows, however at a ridge crest these parameters have greater variation.

Instead we can define a wavenumber parameter that modifies the gravity effect of the topography to produce the gravity anomaly, and is also independent of the water depth and crustal density, called the isostatic response function (IRF). The theoretical IRF, $\phi_e(k_r)$, is given by the ratio of the total gravity anomaly (Equation 6.37) to the gravity anomaly generated by the topography (Equation 6.34). For a simple case of flexure (see Figure 6.6) this is given by

$$\begin{aligned}\phi_e(k_r) &= \frac{\Delta g(\bar{k})_{total}}{\Delta g(\bar{k})_{topo}} \\ &= \frac{2\pi G(\rho_c - \rho_w)\mathbf{H}(\bar{k})e^{-|\bar{k}|d}(1 - \phi'_e(\bar{k})e^{-kt}}{2\pi G(\rho_c - \rho_w)\mathbf{H}(\bar{k})e^{-|\bar{k}|d}} \\ &= (1 - \Phi_e{}'e^{-|\bar{k}|t})\end{aligned} \tag{6.44}$$

The isostatic response function allows us to compare the state of isostasy across different windows since it is independent of water depth. The dependence on crustal thickness is assumed to have a negligible effect at mid-ocean ridges, however it should be noted that unlike faster spreading ridges, seismic and petrological evidence indicate heterogeneous crustal thicknesses at the Southwest Indian Ridge (Li et al., 2015). The observed IRF can be calculated from the observed admittance, $\mathbf{Z}(\bar{k})$, as shown by

combining equations 6.34 and 6.32

$$\begin{aligned}\phi_e(k_r) &= \frac{\Delta g(\bar{k})_{total}}{\Delta g(\bar{k})_{topo}} \\ &= \frac{\Delta g(\bar{k})_{total}}{2\pi G(\rho_c - \rho_w)\mathbf{H}(\bar{k})e^{-|\bar{k}|d}} \\ &= \frac{\mathbf{Z}(\bar{k})}{2\pi G(\rho_c - \rho_w)e^{-|\bar{k}|d}}\end{aligned} \tag{6.45}$$

By comparing the observed IRF to theoretical IRFs for a range of T_e, the best fit T_e is determined through least squares fitting. Prior to this, the coherence, γ^2, (equation 6.40) is used to determine the portions of the spectrum that are dominated by the relationship between the surface topography and gravity anomaly. Only wavebands which correspond to a coherence threshold of 0.5 or greater were used in the least squares fitting. The observed IRF was compared with the theoretical IRF over the selected waveband for a range of T_e between 0 and 40 km. The RMS error between the observed and theoretical IRF was calculated for each theoretical input T_e and the best fit estimated from the minimum RMS error (see Figure 6.8). The RMS error minimum may be well or poorly defined, leading to smaller or greater uncertainties in the best fit T_e. In order to quantify this variation, upper and lower bounds are calculated using a constant difference cut off of 20% of the minimum RMS error value, above the RMS error minima.

6.2 Synthetic Testing

The windowed admittance method was tested using synthetic bathymetry and gravity data, in order to determine the accuracy of T_e recovery using different gridding projections and window sizes. These tests are also used to calculate the systematic biases resulting from the windowing function which is previously discussed by Kalnins and Watts (2009), and the effects on the admittance of the gravity effect of the ridge

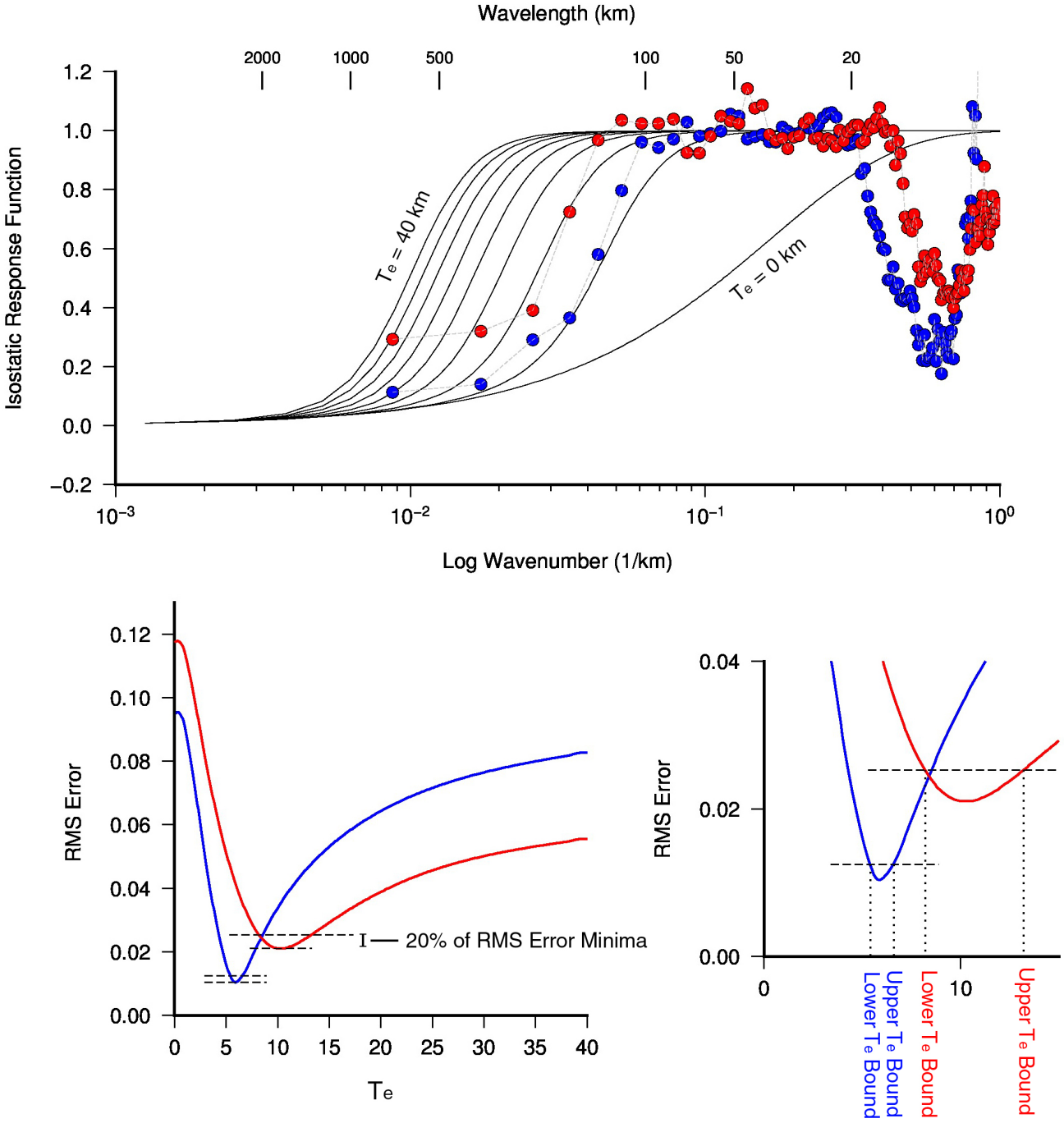


Figure 6.8: Top panel shows the IRFs for two different windows (centred on 15° E and 65° E at the ridge axis) with different T_e in blue and red. The black lines are the theoretical flexural IRFs for T_e between 0 and 40 km. The bottom left panel shows the RMS error minima used to determine best fit T_e. The bottom right panel shows an enlarged image of the RMS minima illustrating the constant difference cut off of 20% of the minimum RMS error value, which is used to determine upper and lower bonds for the best fit T_e

topography and its compensation.

6.2.1 Synthetic Data

Synthetic Bathymetry

Synthetic bathymetry data was constructed following the method of Kalnins (2011) in order to produce a number of randomly distributed seamounts on a basal seafloor surface. These data are designed to be representative of typical deep ocean seafloor topography created at a mid-ocean ridge. Seismic reflection studies (Watts and Ten Brink, 1989) and gravitational admittance studies (Watts, 1978) have shown that volcanic seamounts and oceanic islands are constructional features, which load the oceanic crust and lithosphere. These studies show that the subsequent flexural structures and gravity anomalies may be explained by a simple model in which the seamounts load an elastic plate that overlies an inviscid substratum (Watts, 1978). We use this relationship between seamount loading and lithospheric flexure to justify the use of seamounts as topographic loads for synthetic testing.

Figure 6.9 shows the synthetic bathymetry, which was constructing by assuming a base depth of 6000 m, on to which seamount structures were imposed. The seamount edifice shape is constructed using a Gaussian distribution and are assumed to be radially symmetrical. The distribution of seamount height range between 0.15 and 5.95 km, and is based on the height-frequency data for seamounts in the Southwest Indian region shown in Figure 5.29 in Chapter 5. These seamount heights were then binned at 100 m intervals and the output seamount heights randomly varied within each 100 m bin. In order to ensure that there are a sufficient number of seamounts to load the elastic plate, the model produces a minimum of one seamount per bin, however this means that the number of large seamounts is slightly over estimated with respect to the height-frequency distribution observed in chapter 5. These slightly higher concentrations of larger seamounts are, however, useful in simulating topography typical of hotspot-ridge

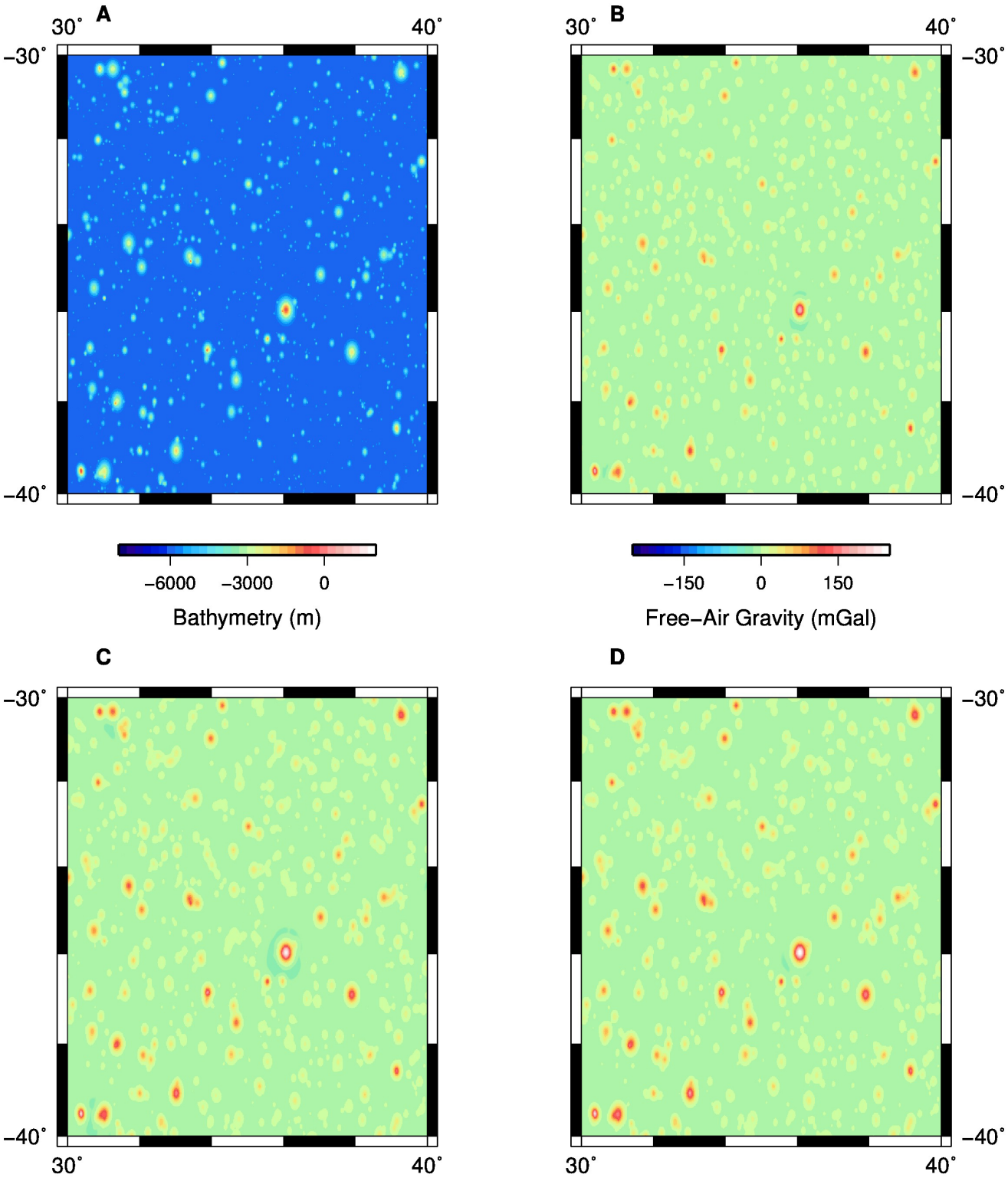


Figure 6.9: Panel A shows a sample of synthetic bathymetry. Panels B, C and D show the corresponding gravity data for T_e of 2 km, 6 km and 10 km respectively.

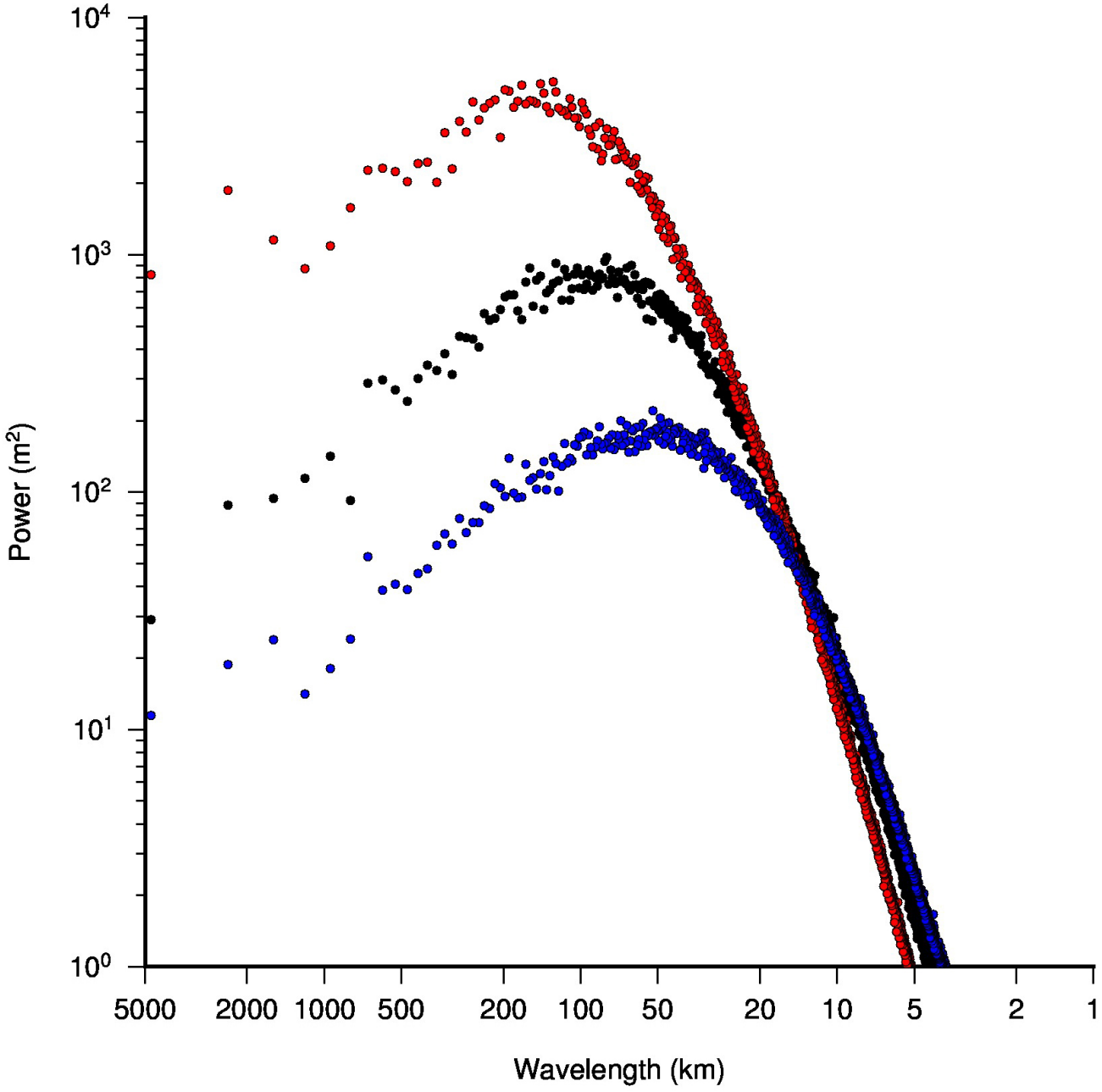


Figure 6.10: Power spectra for the topography of synthetic bathymetry using base-height ratios between 2 and 11.7 (black), between 1 and 5.85 (blue) and between 3 and 23.4 (red).

interaction. The magnitude of the basal radius for each seamount was constructed using randomly varying ratios of basal radius to height. These radius-height ratios were varied between 2:1 and 11.7:1, which are typical of oceanic seamounts (Wessel, 2001).

Seamounts are relatively narrow loads compared to the elastic thickness of the plate. To ensure that the wavelength of the load was sufficient to produce observable flexure, the power spectra of the topography and gravity were calculated in the radial direction using GMT's `grdfft`. Figure 6.10 shows that the power spectra for all the synthetic topography grids peak between wavelengths of 20 and 500 km, which is within the diagnostic waveband of flexure (Watts, 2001). In addition, a series of synthetic bathymetry grids with the seamount topography width increased by a factor of 2 and 3 were constructed and the gravitational admittance calculated. Comparison of the admittance of the narrower and wider seamounts showed no significant differences in the recovery of input T_e.

The free-air gravity and topography grids were padded by 5° to avoid edge effects when calculating the gravitational admittance. To simulate real shipboard bathymetric data, normally distributed random noise with a standard deviation of 12 m was added to each point on the grid, in order to imitate instrumental error. This was determined from the noise observed in the power spectra for real topography data at short wavelengths.

Synthetic Free-Air Gravity Anomaly

The free-air gravity anomaly is sensitive to the flexure of the lithosphere under loading and therefore dependant on the T_e. In order to test the T_e retrieval of the windowed admittance technique, synthetic free-air gravity anomaly data was calculated for a range of fixed T_e between 2 km and 14 km in 4 km increments. While these T_e values are low when compared to global oceanic T_e studies (Watts, 1978) they are typical of mid-ocean ridge crests (Cochran, 1979).

Figure 6.11 shows the crustal model used to calculate the gravity anomaly, which is a two layer model with an upper crust of density, ρ_2, overlying a lower crust of density, ρ_3, where $\rho_3 > \rho_2$. The layer thicknesses and densities used in the model are summarised in table 6.1. This model differs from the single layer, 6 km thick crustal model used to calculate the admittance, in order to ensure that the results are model independent.

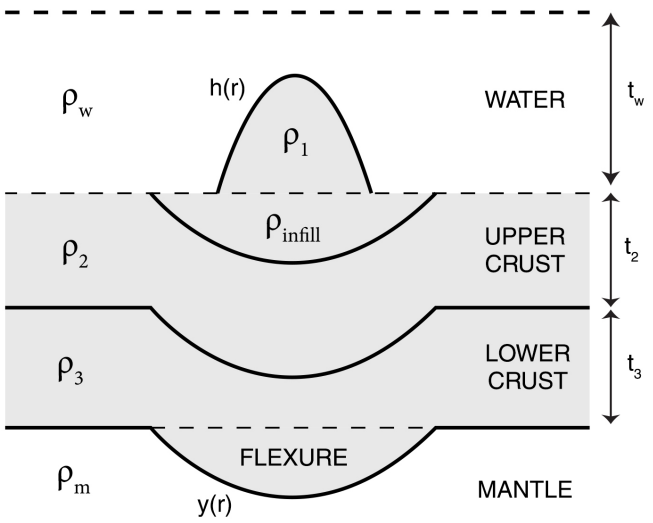


Figure 6.11: Schematic diagram illustrating the two layer crustal model used to calculate the gravity anomaly for the topography and flexed synthetic surfaces.

The gravity anomaly is calculated in two stages. In the first stage the load is emplaced on an elastic plate of thickness, T_e, and the resultant flexure calculated using the previously derived equation relating topography and flexure (equation 6.26).

$$\mathbf{Y}(\bar{k}) = -\frac{\rho_c - \rho_w}{\rho_m - \rho_{infill}}\Phi_e(\bar{k})\mathbf{H}(\bar{k}) \tag{6.46}$$

In the second stage Parker's equation (a linear approximation of which is given in equation 6.28) is used to determine the gravity anomaly contribution of the load and resultant flexed surfaces of density contrast. The full Parker equation is given by

$$\Delta\mathbf{g}(\bar{k}) = 2\Delta\rho e^{-|\bar{k}|}\sum_{n=1}^{\infty}\frac{|\bar{k}|^{n-1}}{n!}\mathbf{H}(\bar{k}) \tag{6.47}$$

where n is the order. This calculation was carried out to fourth order approximations, which are sufficient to imitate shipboard gravity data. The resultant grids show free-air gravity anomalies associated with the flexure due to seamount loading, which broaden with increasing T_e.

Table 6.1: Layer thicknesses and densities used in crustal model

Parameter	**Notation**	**Value**
Thickness of upper crust	t_1	2.0 km
Thickness of lower crust	t_2	4.0 km
Density of seawater	ρ_w	1030 kg m^{-3}
Density of load infill	ρ_{infill}	2670 kg m^{-3}
Density of upper crust	ρ_2	2800 kg m^{-3}
Density of lower crust	ρ_3	2900 kg m^{-3}
Density of mantle	ρ_m	3330 kg m^{-3}

Random noise was added to the gravity data to simulate the typical misfit between shipboard and satellite data. Sandwell and Smith (2008) showed misfits of 2.5 to 4 mGal therefore a random error standard deviation of 4 mGal was added.

6.2.2 Synthetic T_e Recovery

The windowed admittance technique was carried out on the synthetic data for a number of windows at different T_e to determine the accuracy of the method. A number of parameters including data projection and window size were varied in order to determine the parameter values which produce the most accurate T_e recovery.

Data Projection

Synthetic bathymetry and gravity data were initially produced using a Mercator projection, which is a cylindrical conformal map projection with no distortion along the equator. The distortion increases with latitude, becoming very large in polar regions. The Southwest Indian Ridge region ranges between 60° S and 20° S, and as a result the degree of distortion created by the map projection changes between admittance windows. A series of 9° x 9° windows were sampled from the synthetic data, centred on latitudes ranging between 25° S and 55° S in 5° increments. The admittance technique,

(described in section 6.1.4) was used to determine best fitting T_e for each window, which was compared with the input T_e for the synthetic topography.

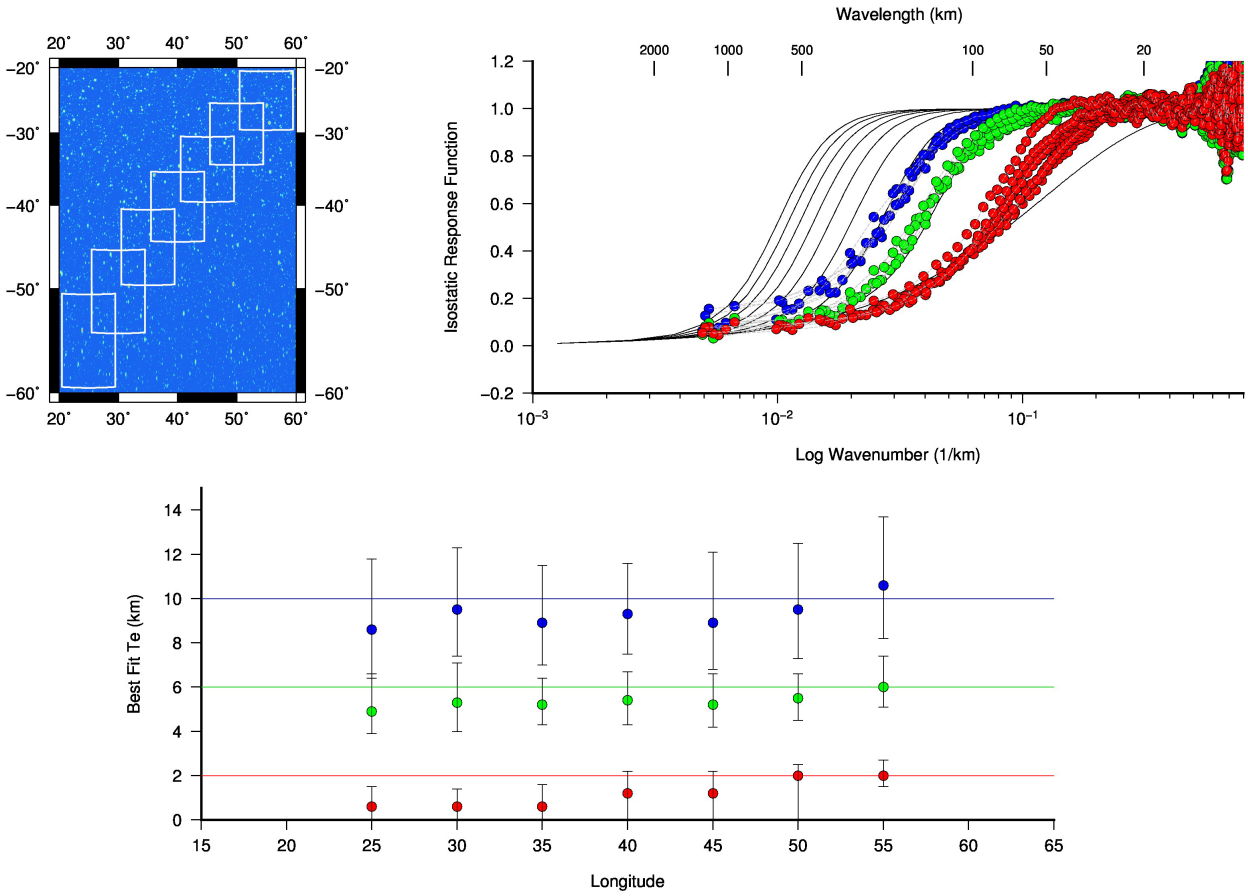


Figure 6.12: Isostatic response functions and best fit T_e from least squares fitting for windows with a Mercator projection. Top left panel shows the position of the windows and the variation in window size with latitude. Top right panel shows the IRFs for synthetic T_e of 2 km (red), 6 km (green) and 10 km (blue). Bottom panel shows the recovered T_e (solid circles) compared to the input T_e (coloured lines) for synthetic T_e of 2 km (red), 6 km (green) and 10 km (blue). Error bars are derived from the RMS errors as detailed in Figure 6.8.

Figure 6.12 shows the T_e retrieval for input T_e of 2, 6 and 10 km across different latitudes. The recovered T_e shows an increasing underestimation of T_e with increasing latitude, the reasons for which are two-fold. Firstly, the window dimensions do not remain consistent between different windows; a 9° x 9° window at a latitude of 25°S is 939 km x 1003 km, whereas a 9° x 9° window at a latitude of 55°S is 643 km x 998 km.

This decrease in effective window size with increasing latitude reduces the ability to resolve the long wavelength signatures at higher latitudes. Secondly, this difference in the N-S and E-W dimensions within a given window introduces distortions within the window, which has an effect on the annular averaging used during the calculation of the admittance. The annular averaging process converts the two-dimensional admittance $\mathbf{Z}(\bar{k})$, into the one dimensional admittance, $\mathbf{Z}(k_r)$. However, during annular averaging, when the increment size between wavenumbers in the x and y direction are calculated, they are not the same. This difference in kx_{inc} and ky_{inc} causes the amount of information within an annulus to vary depending on the azimuth, introducing distortions in the admittance.

In order to remove the distortion introduced by the Mercator data projection, Vincenty's formula (Vincenty, 1975) was used to produce a series of equal area grids measuring 1000 km x 1000 km. The inverse method is used to find the geodesic distance in kilometres between two points (ϕ_1, L_1) and (ϕ_2, L_2) where ϕ is the latitude and L is the longitude of points 1 and 2 respectively. The notation used in Vincenty's formula is given in table 6.2. Following the method of Bessel (1825) the geodesic latitude and longitude is mapped onto an auxiliary sphere as reduced (or parametric) latitude and longitude (U_1, λ_1) and (U_2, λ_2). The difference in longitude on the auxiliary sphere (λ) is given by

$$\lambda = L + (1 - C) f sin\alpha\sigma + C sin\sigma[cos(2\sigma_m) + C cos\sigma(-1 + 2cos^2(2\sigma_m))] \tag{6.48}$$

where

$$cos(2\sigma_m) = cos\sigma - \frac{2 sinU_1 sinU_2}{cos^2\alpha} \tag{6.49}$$

and

$$C = \frac{f}{16} cos^2\alpha[4 + f(4 - 3cos^2\alpha)] \tag{6.50}$$

These equations are iteratively evaluated until λ converges to the desired degree of accuracy, in this case 10^{-12} which corresponds to $\sim$0.06 mm. This iterative solution

may fail to converge for nearly antipodal points; however this does not apply in this case.

Once λ has been obtained it is used to evaluate the ellipsoidal distance, s, between the two points, where s is given by

$$\begin{aligned} s = bA(\sigma[Bsin\sigma cos(2\sigma_m)+\frac{1}{4}B[cos\sigma(-1+2cos^2(2\sigma_m)) \\ -\frac{1}{6}Bcos(2\sigma_m)(-3+4sin^2\sigma)(-3+4cos^2(2\sigma_m))] \end{aligned} \tag{6.51}$$

where b is the semi-minor axis of the ellipsoid, and A and B are series expressions evaluated using λ.

Table 6.2: Notation for Vincenty's Formula

Notation	Parameter
L	Difference in longitude of the two points
f	Flattening of the ellipsoid
α	Azimuth at the equator
σ	Arc length between the two points on the auxiliary sphere

The geometric constraints of the oblate spheroid are taken from the GRS80 reference ellipsoid. The resulting geodesic distances are accurate to within 0.015 mm, much greater than needed for this purpose. In order to apply these formulae to the bathymetry and gravity data, a 19° x 19° grid was input into array M, with elements $m_{i,j} = (z, x, y)$ where z represents the latitude, x represents the longitude, and y represents the bathymetry or free-air gravity anomaly.

$$M_{i,j} = \begin{pmatrix} m_{1,1} & m_{1,2} & \cdots & m_{1,nx} \\ m_{2,1} & m_{2,2} & \cdots & m_{2,nx} \\ \vdots & \vdots & \ddots & \cdots \\ m_{nz,1} & m_{nz,2} & \cdots & m_{nz,nx} \end{pmatrix} \tag{6.52}$$

The size of the input grid is unimportant except that it must be sufficiently large to

be cut to the desired window size following conversion to the new projection.

The geodesic distance is calculated using Vincenty' s formula (Equation 6.51) between pairs of co-ordinates along the top row of the array so that

$$s_n = m_{1,n+1} \bowtie m_{1,n} \text{ for } n = 1 \rightarrow nx \tag{6.53}$$

where nx is the array length in the x-direction and $\bowtie$ indicates the application of Vincenty's formula to the x components of each pair.

This is repeated for each row of the array and output to a matrix of distances between points in the z direction. These distances are then accumulated in the x direction starting in one corner to produce a matrix of relative distances in the x direction from column 1 to each point in the matrix. This method is then repeated for the z direction. The resulting matrices of distance to the origin in the z and x directions are combined to produce an array Q of absolute distances from one corner to each data point in the array in km, and the corresponding bathymetric or gravity anomaly data value. Finally the mean values of the distances in the x and z directions are subtracted from the x and z components of each point in the array respectively. This produces a rectangular array with the origin at the centre.

The new array is resampled at a 2 km interval and gridded to form an equal area grid which is then cut to the desired window size.

Figure 6.13 shows the T_e recovery for T_e of 2, 6 and 10 km across different latitudes. The T_e retrieval at 2 km is excellent and the underestimation observed using the Mercator projection has been removed. For higher T_e (6 km and 10 km), an underestimation is still observed. This is attributed to the systematic bias created by the windowing effect (Kalnins and Watts, 2009), which will be discussed and corrected for in the next section.

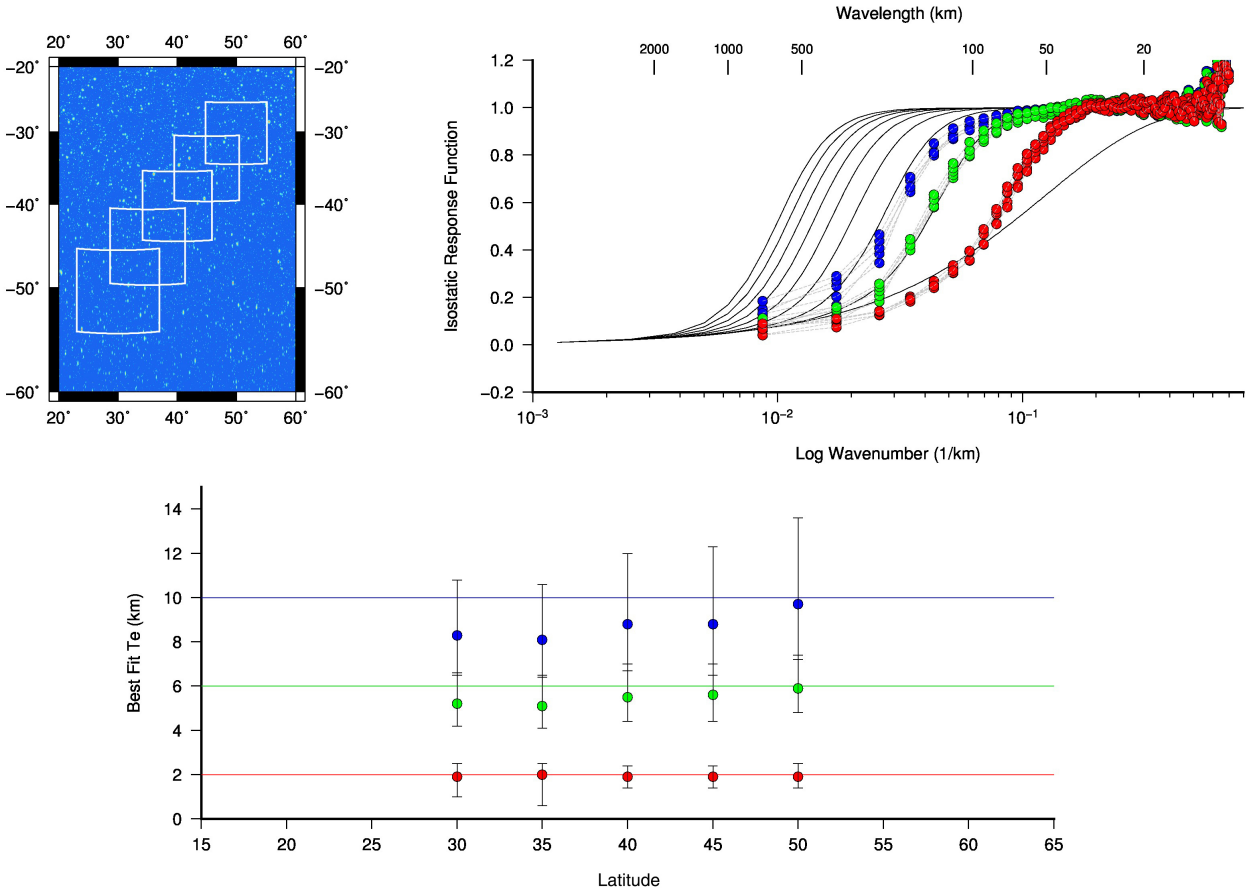


Figure 6.13: Isostatic response functions and best fit T_e from least squares fitting for windows with an equal area projection. Top left panel shows the position of the windows. Top right panel shows the IRFs for synthetic T_e of 2 km (red), 6 km (green) and 10 km (blue). Bottom panel shows the recovered T_e (solid circles) compared to the input T_e (coloured lines) for synthetic T_e of 2 km (red), 6 km (green) and 10 km (blue). Error bars are derived from the RMS errors as detailed in Figure 6.8.

Finite Windowing Bias Correction

Previous studies of T_e on both the continents (Pérez-Gussinyé et al., 2004) and oceans (Simons et al., 2000; Kalnins and Watts, 2009) have shown that windowing techniques introduce a systematic underestimation in T_e. The application of a finite window to the data has the effect of convolving the bathymetry and free-air gravity with a windowing function prior to the calculation of admittance. The observed admittance becomes

(Kalnins and Watts, 2009)

$$Z(k) = \frac{[\Delta \mathbf{g}(\bar{k}) * \mathbf{W}(\bar{k})] \cdot [\mathbf{H}(\bar{k}) * \mathbf{W}(\bar{k})]^*}{[\mathbf{H}(\bar{k}) * \mathbf{W}(\bar{k})] \cdot [\mathbf{H}(\bar{k}) * \mathbf{W}(\bar{k})]^*} \tag{6.54}$$

where $\mathbf{W}$ is the spectral representation of the windowing function, $*$ represents convolution and * represents the complex conjugate. The systematic underestimation is due to the finite nature of the window, used to estimate the observed admittance, causing the long wavelength signals to be artificially shortened. In contrast, the theoretical admittance assumes an infinite window size, which causes the observed admittance to become displaced relative to theoretical admittance and the best fit T_e to be downward biased (Simons and Olhede, 2013). This bias is predictable, therefore an empirical correction value can be calculated by comparing recovered T_e with a range of input T_e for synthetic data.

Figure 6.14 shows the systematic underestimation of T_e, which increases with increasing input T_e, due to finite window size. Best fit T_e for a series of 1000 km x 1000 km windows sampled from synthetic data were averaged to predict the deviation from the theoretical curve. The resultant data points were fitted for T_e between 2 km and 14 km using a cubic model and a least square fitting routine. This fitted cubic equation was used to derive an equation for corrected T_e.

$$Te_{corr} = -0.00260896T_e^3 + 0.0566633T_e^2 + 0.866869T_e + 0.139914 \tag{6.55}$$

A comparison between this correction model and that used by Kalnins and Watts (2009) show good agreement at T_e between 6 km and 12 km, however at low T_e (<6 km) the models differ. This is due to differences in the scope of the two studies. Kalnins and Watts (2009) were estimating T_e in the west-central Pacific ocean, where average T_e is ∼25 km. Calculations of bias corrections for the global study included data for $T_e = 0$, which are upward biased due to linear approximations of Parker's equation (Equation 6.28). This causes the recovered T_e for very low input T_e to become upward

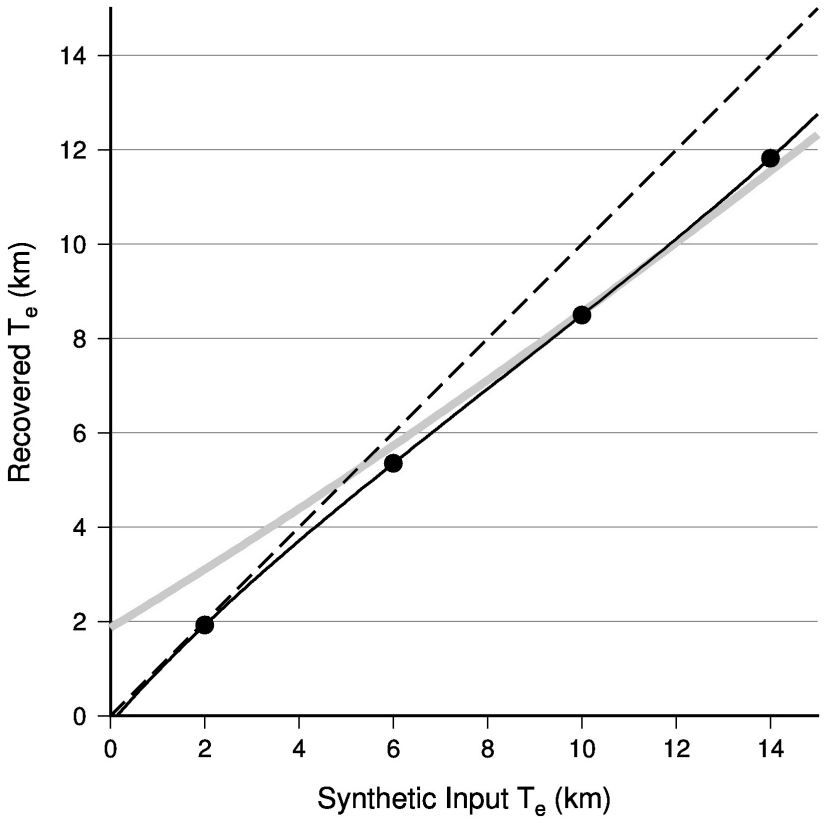


Figure 6.14: Comparison of synthetic input T_e and recovered T_e illustrating the systematic underestimation of T_e, which increases with T_e. Dotted line shows the relationship between synthetic input and recovered T_e if the T_e is recovered perfectly. The black dots show the average recovered T_e over a series of windows for a given synthetic input T_e. The black line shows the fit of the cubic equation describing the downward bias. The grey line shows the bias curve used in Kalnins and Watts (2009).

biased. While this is insignificant for admittance studies on older lithosphere, it has a greater effect on this study, which focuses on mid-ocean ridge crests with very low T_e (Cochran, 1979). The anomalous results for $T_e = 0$ are therefore excluded from the bias correction fitting, removing the distortion at low T_e. The slight deviation at high T_e (>14 km) results from the fact that the model used in this study is unconstrained above 14 km since the T_e on the ridge crest is not expected to exceed this value.

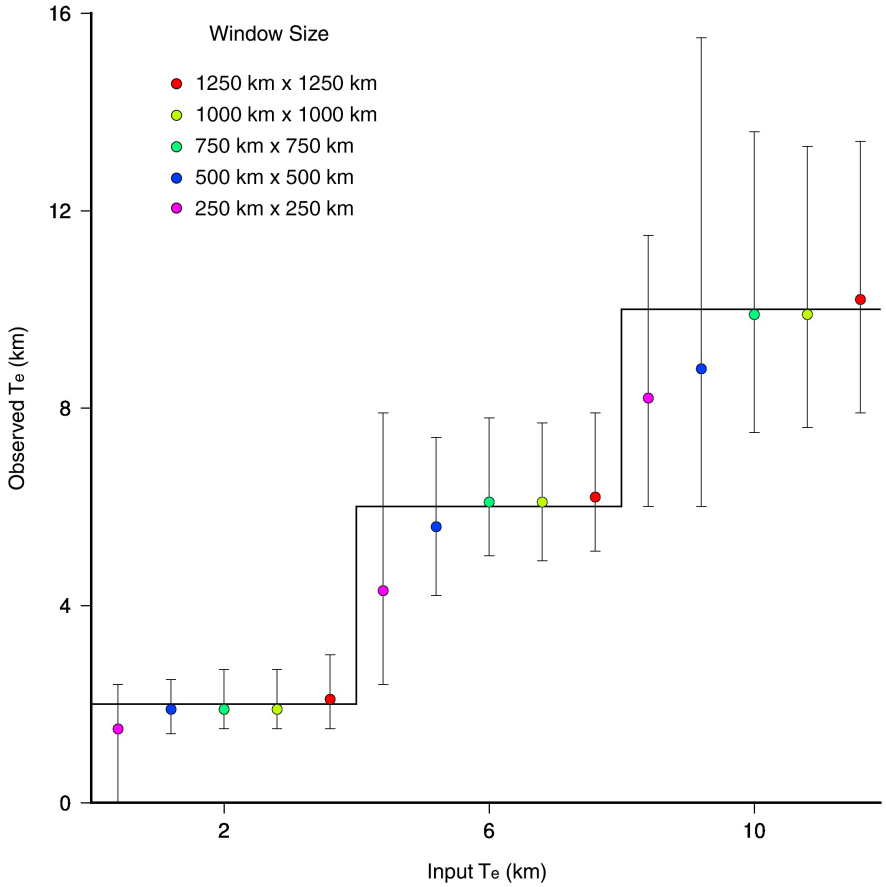


Figure 6.15: Figure showing the difference between input T_e and recovered T_e using synthetic topography and gravity for different window sizes. The solid black line shows the input T_e. The five coloured circles show the recovered T_e for the same input T_e using different window sizes.

Window Size

Previous T_e studies have shown that the choice of window size has an important effect on recovered T_e (Kirby, 2014; Kalnins and Watts, 2009).

Figure 6.15 shows the variation in recovered T_e for different window sizes for synthetic data for T_e between 2 km and 10 km. At low input T_e (T_e=2 km) recovered T_e for all window sizes except 250 km x 250 km shows excellent agreement with the synthetic T_e. For input T_e of 6 km or higher, window sizes of 500 km x 500 km and 250 km x 250 km fail to accurately recover T_e. This is attributed to a failure to capture the flexural response at higher input T_e as the wavelength of the flexural response exceeds the

window size. These synthetic tests show that the T_e recovery improves with increasing window size, however, when working on real bathymetry data, this is balanced by the risk of including multiple tectonic provinces in a single window. Windows of 1000 km x 1000 km were selected as the smallest window which resolved T_e well for input T_e up to 14 km.

Tapering Method

One of the problems with spectral estimates using the Fast Fourier Transform method is that of spectral leakage (McNutt, 1983). Spectral leakage occurs when the power of one harmonic leaks into adjacent harmonics, causing biases in the power of these harmonics (Kirby, 2014). This effect arises from a variety of processes, particularly the occurrence of the Gibbs phenomenon at the edge of the data when it is truncated due to finite windowing (Simons and Olhede, 2013). Methods used to minimise this spectral leakage have included zero-padding the data, applying tapers to the data edges, detrending and mirroring the data along the edges (McNutt, 1983; Diament et al., 1986). Traditional studies of oceanic admittance have used single cosine tapers which are sufficient to prevent the edge effects arising from the Gibbs phenomenon; however it does not minimise spectral leakage. The use of a single taper means the spectrum of the taper can bias the spectral estimate of the data. This study uses a multitaper approach (Thomson, 1982; Pérez-Gussinyé et al., 2004; McKenzie, 1977) in which multiple Slepian tapers (Slepian, 1978) are used to produce a weighted average of the spectra across all the tapers. Since Slepian tapers have the property of being orthogonal, the spectra from the different tapers may be considered independent. The weighted average of these spectra therefore provide minimal spectral leakage. The effect of different tapering methods have been previously investigated (Simons et al., 2000) and outside the scope of this study.

6.2.3 Admittance of the Ridge

Since this study focuses on admittance along and across a mid-ocean ridge crest, synthetic testing was carried out to determine the effect of the ridge on the spectral admittance. A synthetic ridge topography was constructed using the plate cooling model of Parsons and Sclater (1977) at a full spreading rate of 14 mm yr^{-1}. This ridge topography was combined with the synthetic seamount topography to produce a synthetic ridge crest with small wavelength topography superimposed.

Figure 6.16 shows that the elastic thicknesses recovered from the synthetic ridge crest show an increase in T_e of approximately 0.8 km across the apex of the ridge. This is attributed to the bathymetric change caused by thermal subsidence as the crust moves away from the axis and the Pratt isostatic compensation. These synthetic tests were repeated using ridge topography based on spreading rates typical of the Mid-Atlantic Ridge (25 mm yr^{-1}) and the East Pacific Rise (140 mm yr^{-1}). The resultant recovered T_e for a model with an input T_e of 2 km are shown in Figure 6.16. The slow spreading rate shows a similar increase in recovered T_e over the ridge crest of approximately 0.6 km, while the fast spreading ridge shows no change in T_e.

Investigation of this effect for different input synthetic T_e shows that it remains constant up to T_e of 14 km. In order to account for this effect, a synthetic ridge topography calculated using the thermal plate cooling model (Parsons and Sclater, 1977) was removed from the observed bathymetry and gravity data, prior to the calculation of observed admittance. However, this introduced spurious data artifacts into both the gravity and bathymetry. Therefore an empirical correction for this 'ridge admittance' was applied to the recovered T_e over the Southwest Indian (-0.8 km) and Mid-Atlantic (-0.6 km) ridge crests in this study.

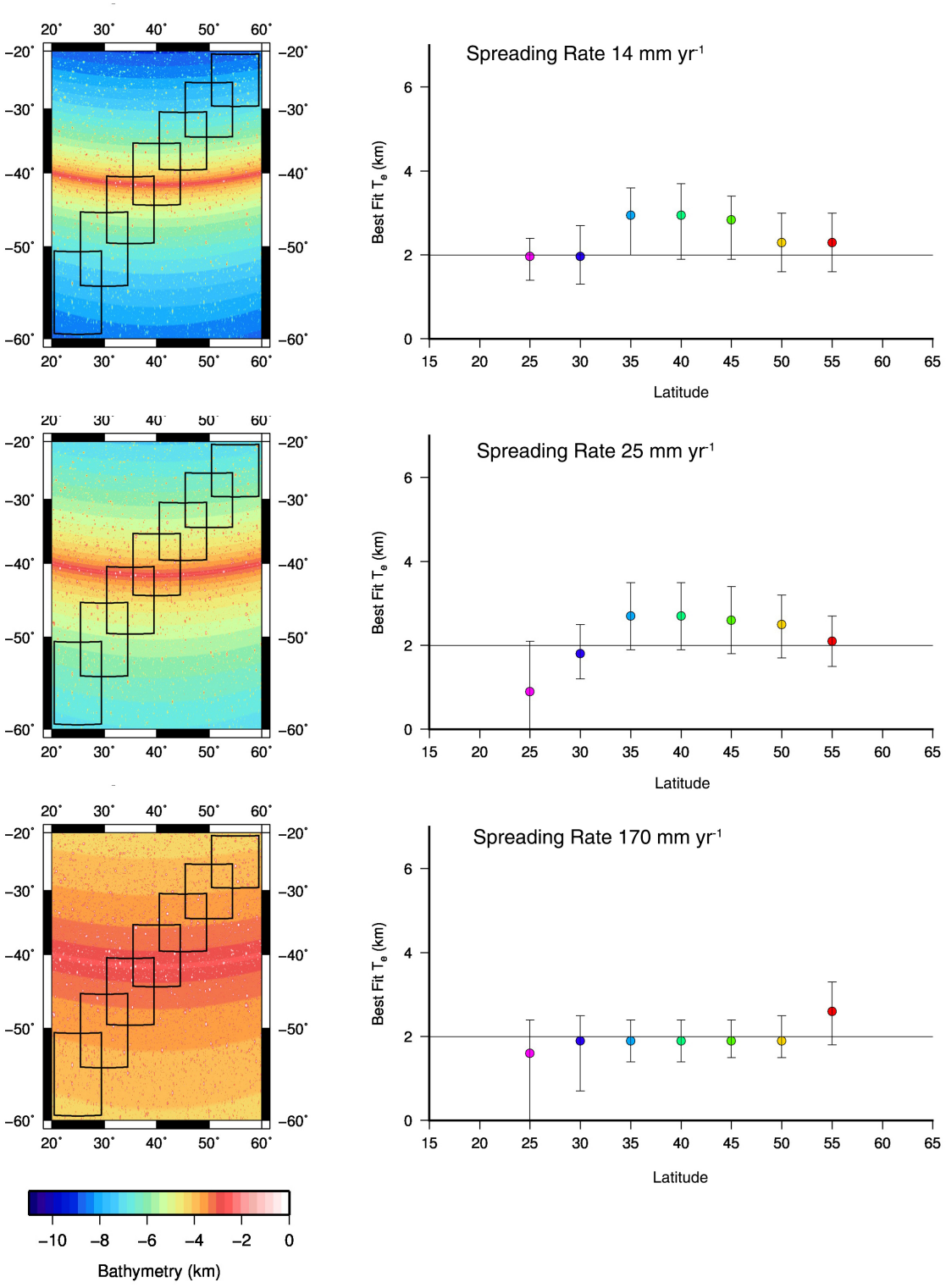


Figure 6.16: Comparison of input synthetic T_e and recovered T_e for windows over a synthetic ridge. The top panel shows results for a synthetic ridge with a spreading rate of 14 mm yr^{-1} typical of the SWIR. The top panel shows results for a synthetic ridge with a spreading rate of 25 mm yr^{-1} typical of the MAR. The top panel shows results for a synthetic ridge with a spreading rate of 140 mm yr^{-1} typical of the EPR.

6.3 Admittance Results

6.3.1 Isostatic Response Functions

The gravitational admittance was calculated for a series of 1000 km x 1000 km windows centred on the ridge axis between 0 ° E and 70° E in 5 ° increments of longitude. Figure 6.17 shows the locations of the windows along the ridge.

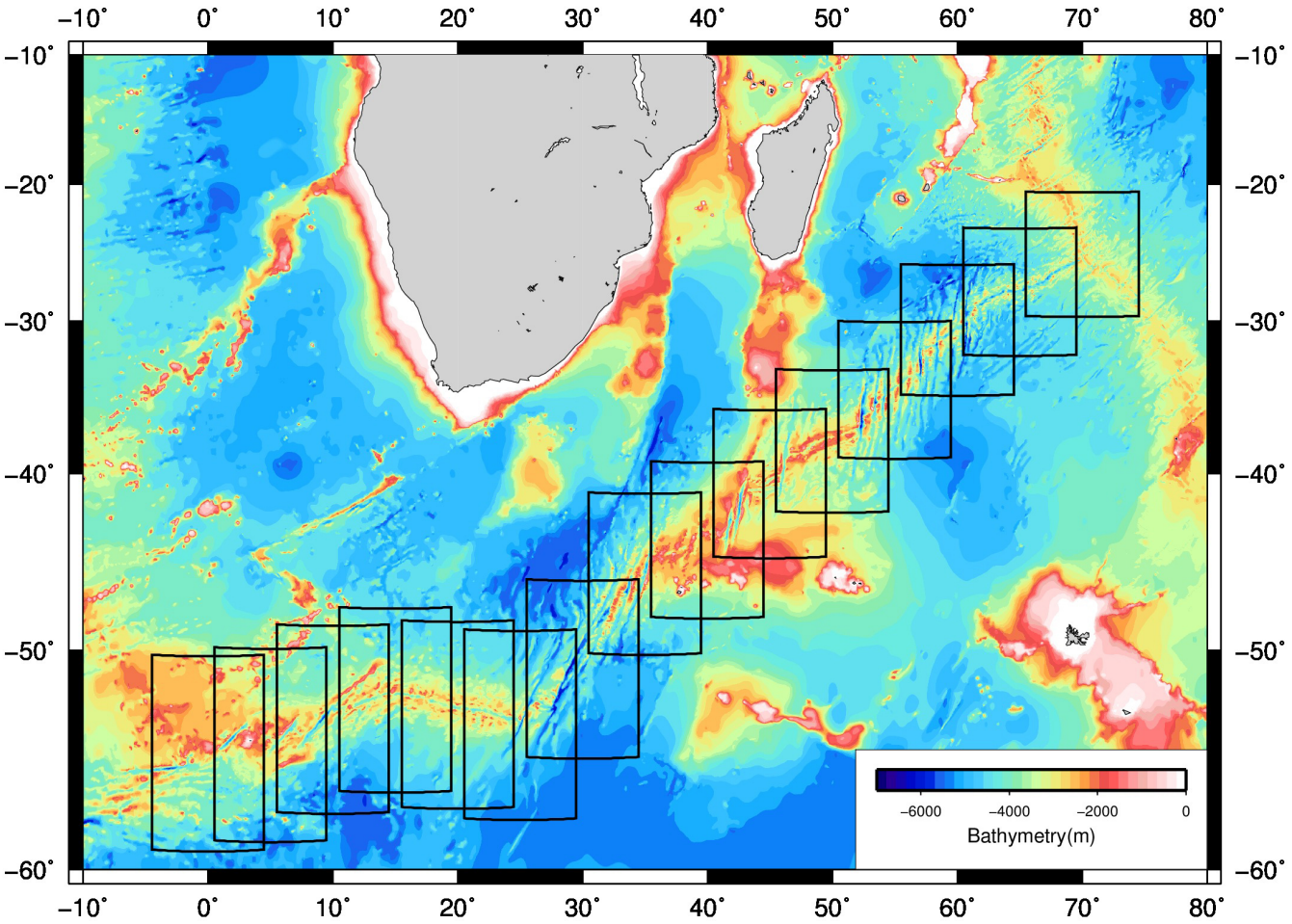


Figure 6.17: Bathymetry map sampled from the GEBCO 2014 30'' x 30'' grid. The locations of the admittance windows on the Southwest Indian Ridge are outlined in black

As discussed in section 6.1.4, the gravitational admittance was used to calculate the isostatic response function for each window, in order to make comparisons between different windows with different mean water depths. The error bars on the isostatic

response functions are calculated using the estimated error in the admittance given in equation 6.42. Upper and lower bounding IRFs are calculated by the addition or subtraction respectively of the admittance error to the observed admittance, prior to the calculation of the IRFs.

The isostatic response functions for the windows along the Southwest Indian ridge crest were fitted against the theoretical IRFs based on flexural isostasy given by equation 6.44, in order to determine best fit T_e using least squares fitting. A visual comparison of the observed and theoretical IRF indicates the variation in the fit across different wavelengths.

Figure 6.18 shows four observed IRFs for windows along the SWIR. As expected from equation 6.44, at short wavelengths the calculated IRF $\rightarrow 1$, since the topography is supported by the strength of the lithosphere. At long wavelengths the calculated IRF $\rightarrow 0$, as the topography is isostatically compensated irrespective of the strength of the lithosphere. The roll over at mid-wavelengths is due to flexure, and the position and nature of this roll over provides information on the elastic thickness and nature of isostasy.

The black lines in Figure 6.18 show the fit of the four observed IRFs to the theoretical flexural IRF, calculated using the best fit T_e from least square fitting. The top two IRFs show a good fit to the flexural model at T_e of 3.3 km and 8.3 km respectively. The bottom two IRFs, however, show a significant departure from the flexural model at long wavelengths. This long wavelength departure occurs, to different degrees, in 11 out of the 15 windows. These positive long wavelength IRF values, which are equivalent to gravitational admittances between 8 mGal/km and 19 mGal/km, have been observed in previous studies (e.g. McKenzie, 1977), and have been attributed to dynamic topography supported by mantle convective forces (McKenzie, 2010).

In order to improve the fit of the theoretical IRF to the observed IRF, a combined flexural-convective IRF model is calculated. This model requires the contribution of mantle-convective forces to the gravitational admittance to be determined. McKenzie

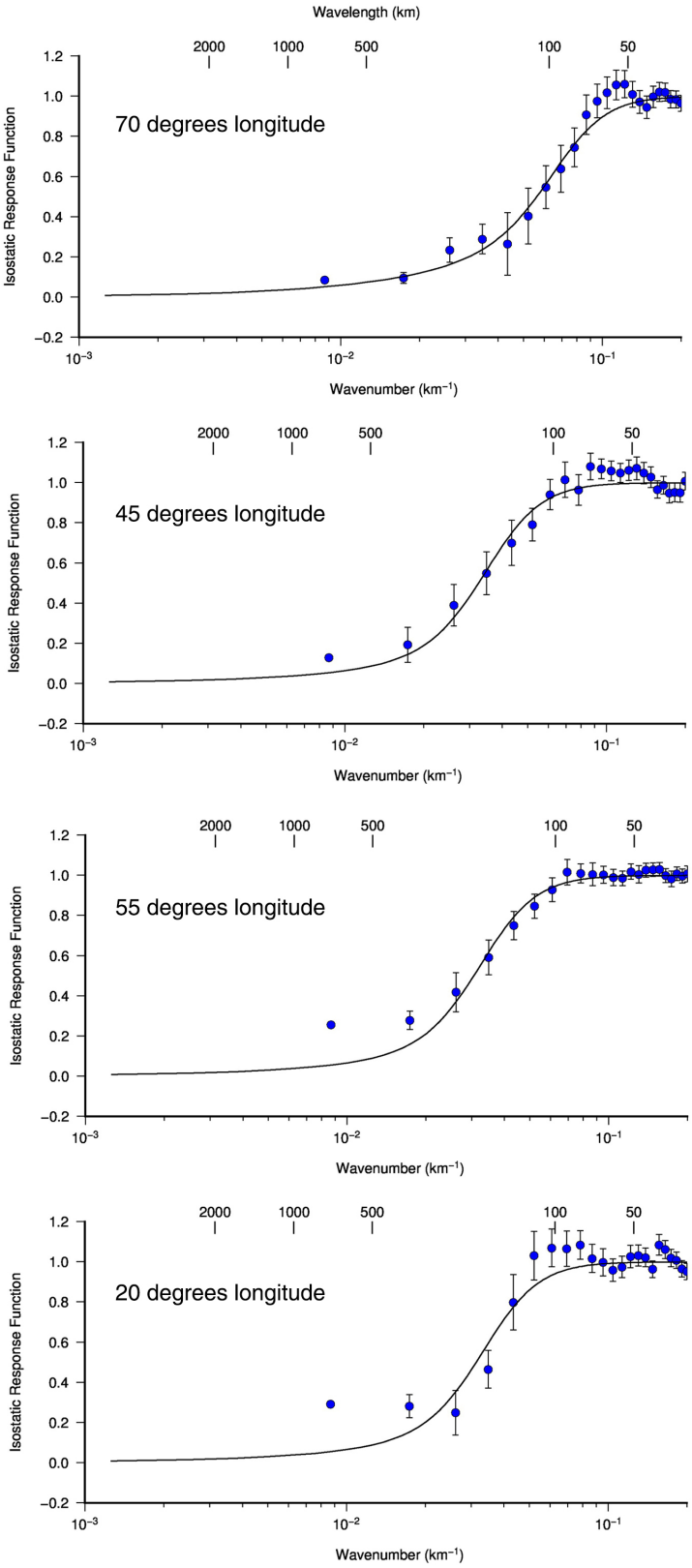


Figure 6.18: Fit of theoretical flexure model to observed IRF data for 4 different windows on the SWIR. The raw data is represented by the blue dots, the error bars are determined using the admittance error. The solid black line is the theoretical flexural model with the best fit T_e determined by least squares fitting.

(2010) calculated theoretical admittance due to mantle convection, Z_c, based on a simple lithospheric model.

$$Z_c = \frac{\Delta g_a + \Delta g_l + \Delta g_T}{\zeta_a + \zeta_T} \tag{6.56}$$

where Δg_a is the gravity contribution from the topography, ζ_a, due to variations in the temperature of the asthenosphere, Δg_l is the gravity contribution from the thermal expansion of the lithosphere and Δg_T is the gravity contribution from the topography, ζ_T, due to variations in the temperature of the lithosphere.

In this study, we have increased the complexity of the model to include the gravity contributions from density contrasts between the water-crust boundary, crust-mantle boundary and the effect of water depth. The model consists of an elastic layer of thickness T_e which overlies a viscous fluid half space. The model parameters are listed in table 6.3 and illustrated in Figure 6.19. The elastic layer affects the surface deformation due to convection of the underlying viscous fluid. The elastic deformation of a thin sheet subjected to a load is given in equation 6.19.

In this case, the load is the stress exerted by the fluid on the plate. The normal stress exerted by the fluid on the base of the plate, σ_{yy}, is obtained by solving the equation for Stokes flow in half space.

$$0 = \eta \nabla^2 \bar{u} - \rho g \hat{y} - \nabla P \tag{6.57}$$

where η is the dynamic viscosity, $\bar{u} = (v, 0, w)$ is the velocity, ρ is the density of the fluid, $\hat{y}$ is a unit vector in the $+y$ direction (upwards) and P is the fluid pressure. This normal stress, σ_{yy}, consists of two terms, the stress due to the deflection of the stream lines as they approach the surface, and the pressure within the fluid.

$$\sigma_{yy(y=0)} = -P_{(y=0)} + 2\eta \left(\frac{\partial w}{\partial y} \right)_{y=0} \tag{6.58}$$

The fluid pressure term may be split into two parts, a hydrostatic part: $P_0 = \rho g y$,

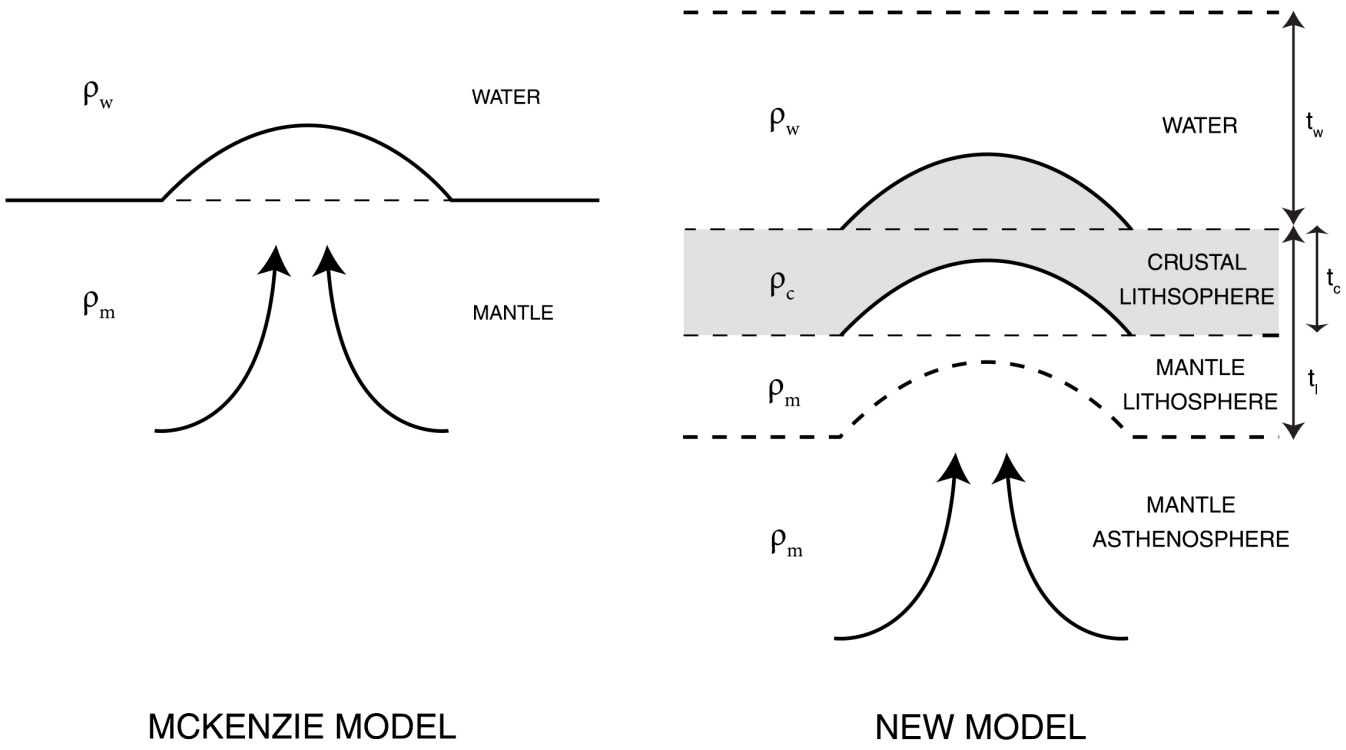


Figure 6.19: Comparison of the McKenzie (2010) model and the model used in this study.

and a thermal expansion part: P_1. From Stokes equation (equation 6.57), the pressure caused by thermal expansion is given by

$$\partial_x P_1 = -\eta \partial_y \nabla^2 \psi \tag{6.59}$$

where ψ is the stream function, given by

$$\bar{u} = \left(\frac{-\partial \psi}{\partial y}, 0, \frac{-\partial \psi}{\partial x} \right) \tag{6.60}$$

The non-hydrostatic stress field in a viscous fluid is given by

$$\bar{g} \times \nabla \rho = \eta \nabla^2 (\nabla \times \bar{u}) \tag{6.61}$$

Table 6.3: Parameters used in combined flexure-convection model

Parameter	**Notation**	**Value**
Elastic thickness	T_e	Fitted for
Lithosphere Thickness	T_l	Fitted for
Weight of convective contribution	γ	Fitted for
Crustal Thickness	T_c	6.0 km
Water Depth	T_w	4.0 km
Density of Mantle	ρ_m	3300 kg m^{-3}
Density of Crust	ρ_c	2670 kg m^{-3}
Density of Seawater	ρ_w	1030 kg m^{-3}
Thermal Expansion Coefficient	α	4×10^{-5} K^{-1}
Young's Modulus	E	10^{11} kg m^{-1} s^{-2}
Poisson's Ratio	ν	0.25
Thermal perturbation	T_0	$100K$
Gravitational Constant	G	6.67×10^{-11} m^3 kg^{-1} s^{-2}

and may be rearranged to give

$$\nabla^4 \psi = \frac{-g}{\eta} \partial_x \rho \tag{6.62}$$

The horizontal density variations are due to thermal expansion. Therefore, assuming no heat advection the pressure variations may be related to temperature variations such that

$$\partial_x \rho = \alpha \rho_m \partial_x T \tag{6.63}$$

where α is the thermal expansion coefficient and T is the temperature. If a surface temperature of $T_0 cos kx$ is imposed at $y = 0$, the steady state temperature of the half space is given by

$$T(x, y) = T_0 e^{ky} cos kx \tag{6.64}$$

where T_0 is a constant. Combining equations 6.62, 6.63, and 6.64 gives

$$\psi = \frac{\rho_m g \alpha T_0}{8\eta k} y^2 e^{ky} sinkx \tag{6.65}$$

And substituting this into the equation for the normal stress (equation 6.58) gives

$$\sigma_{yy(y=0)} = -\frac{3\rho_m g \alpha T_0}{4k} coskx \tag{6.66}$$

We then apply this stress as a load to the elastic plate using the flexure equation (equation 6.19) derived in section 6.1.1, which gives the topographic contribution due to the upward flexure of the plate from convection, ζ.

$$\begin{aligned} \zeta &= \frac{3\rho_m \alpha T_0}{4k(\rho_m - \rho_w)(1+F)} coskx \\ &\text{where} \\ F &= \frac{Dk^4}{g(\rho_m - \rho_w)} \end{aligned} \tag{6.67}$$

The resulting gravity anomaly is given by

$$\begin{aligned} \Delta g_{flexure} =& 2\pi G \Delta\rho \zeta \\ =& \frac{3\pi G \rho_m \alpha T_0}{2k(1+F)} coskx \end{aligned} \tag{6.68}$$

In addition to the topographic contribution caused by the thermal expansion of the rock due to convection, the thermal expansion changes the density of the rock itself. This reduction in density produces a negative gravity anomaly given by

$$\Delta g_{thermal} = -\frac{2\pi G \rho_m \alpha T_0}{2k} coskx \tag{6.69}$$

These two gravity anomalies may now be applied to the different boundaries in the model in figure 6.19. The lithosphere-asthenosphere boundary (LAB) has no density contrast, therefore the only gravity anomaly is due to thermal expansion of the rock.

$$\Delta g_{thermal,LAB} = -2\pi G\left[\frac{\rho_m \alpha T_0 e^{-k(t_l+t_w)}}{2k} coskx\right] \tag{6.70}$$

The crust-mantle boundary (Moho) has a density contrast; therefore the gravity anomaly for this boundary consists of the flexure of this boundary and the thermal expansion of the non-convecting mantle lithosphere beneath.

$$\Delta g_{flexure,moho} = 2\pi G\left[(\rho_m - \rho_c)\zeta_a e^{-k(t_c+t_w)}\right] \tag{6.71}$$

The temperature in the half space is given by equation 6.64, which is bound at y=0. This lithosphere is bound on both sides with the following temperature

$$T(x,z) = \frac{T_0 sinhk((t_l - t_c) - (y - t_c))}{sinhk(t_l - t_c)} coskx \tag{6.72}$$

The thermal expansion for the non-convecting mantle lithosphere at the Moho is given by

$$\Delta g_{thermal,moho} = -\frac{2\pi G\rho_m \alpha T_0 e^{-k(t_l-t_c)}}{2k}\left[\frac{k(t_l - t_c)e^{k(t_l-t_c)}}{sinhk(t_l - t_c)} - 1\right] coskxe^{-k(t_c+tw)} \tag{6.73}$$

The crust-water boundary (topo) has a density contrast; therefore the gravity anomaly for this boundary consists of the flexure of this boundary and the thermal expansion of the crustal lithosphere beneath.

$$\Delta g_{flexure,topo} = 2\pi G\left[(\rho_c - \rho_w)\zeta_a e^{-k(t_w)}\right] \tag{6.74}$$

The gravity anomaly due to the thermal expansion of the crustal lithosphere is given

by

$$\Delta g_{thermal,topo} = -2\pi G\rho_c\alpha T_0 e^{-kt_l}\left[\frac{k(t_l)e^{k(t_l}}{sinhk(t_l)} - 1\right]coskxe^{-k(t_w)} - \left[-\frac{2\pi G\rho_c\alpha T_0 e^{-k(t_l-t_c)}}{2k}\left[\frac{k(t_l-t_c)e^{k(t_l-t_c)}}{sinhk(t_l-t_c)} - 1\right]coskxe^{-k(t_c+tw)}\right] \tag{6.75}$$

The admittance is given by the ratio of the sum of the gravity anomalies to the sum of the topographic contributions

$$Z_c = \frac{\Delta g_{thermal,LAB} + \Delta g_{flexure,moho} + \Delta g_{thermal,moho} + \Delta g_{flexure,topo}\Delta g_{thermal,topo}}{\zeta_{flexure}} \tag{6.76}$$

The observed admittance is a combination of the admittance due to flexure at short wavelengths and the admittance due to dynamic support from mantle convection at long wavelengths (McKenzie, 1977). However, difficulties arise in producing a model combining these two effects, since the admittance spectra cannot be combined using simple addition. By assuming that dynamic support only occurs at long wavelengths and that flexural isostasy only operates at short wavelengths, we can combine these two signals without having to add them together. McKenzie (2010) assumed a threshold of 500 km, beyond which convective admittance had a coherence of 1 and flexural admittance had a coherence of 0. Instead of defining an absolute threshold, we use the flexural response function, which is dependent on the T_e, to define a smooth transition function. The flexural response function, ϕ, is a wavenumber parameter, which varies between 0 and 1 and defines the wavelengths at which flexural isostasy occurs. It varies from 1 at long wavelengths to 0 at short wavelengths and is given by

$$\phi = \left[1 + \frac{Dk^4}{g(\rho_m - \rho_c)}\right]^{-1} \tag{6.77}$$

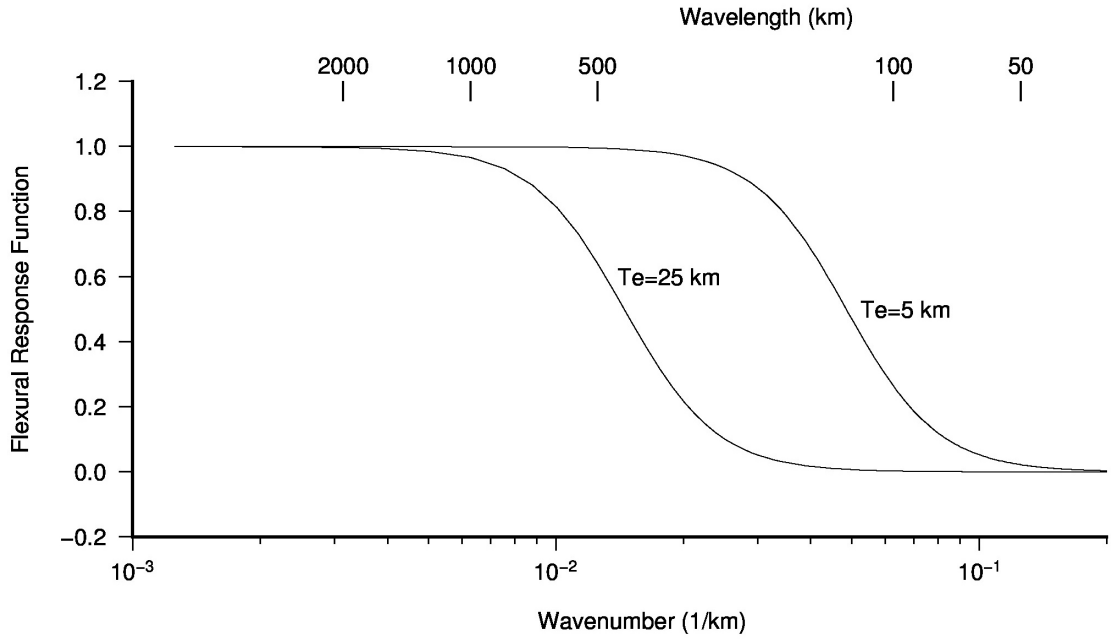


Figure 6.20: Flexural response function, $\phi(k)$

Finally, a weighting factor, γ, is used to reflect the degree to which the admittance due to convection contributes to the combined IRF based on the model fitting. The final combined IRF model is given by

$$\phi_e = Z_c \gamma \phi + Z_f (1 - \gamma \phi) \tag{6.78}$$

There are two mains sources of misfit, shown in Figure 6.18, between the elastic plate model and the observed IRFs: (1) long wavelength positive anomalies (2) steep mid-wavelength rollover with a sharp transition to the long wavelength anomaly. The fit using the new combined model is shown in Figure 6.21. Both sources of misfit described above are reduced using the combined flexure-convection model, particularly those at long wavelength. Observed IRFs for which the flexural model produced a good fit show very little change in the fit between the flexural and combined flexure-convection model, as would be expected. The change in the fit for the combined flexure-convection model results in minor changes in elastic thickness recovery along the ridge (discussed

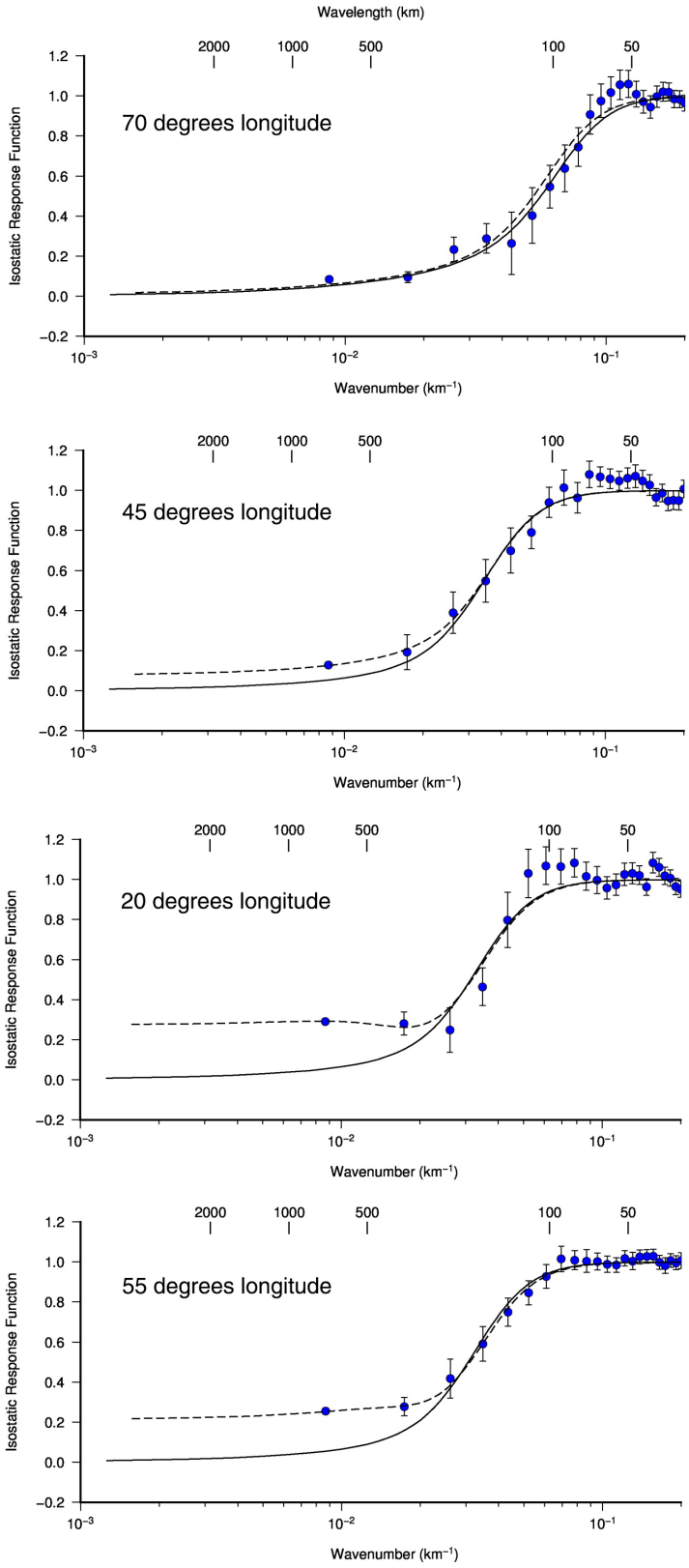


Figure 6.21: Fit of theoretical flexure-convection model to observed IRF data for 4 different windows on the SWIR. The raw data is represented by the blue dots, the error bars are determined using the admittance error. The solid black line is the theoretical flexural model with the best fit T_e determined by least squares fitting. The dotted black line is the new combined flexure-convection model.

further in section 6.3.2).

The combined flexure-convection model also fits for the thickness of the non-convecting lithospheric lid, t_l, and degree of contribution of mantle forces at the long wavelength, γ. The thickness of the non-convecting lithospheric lid varies between 31 km and 97 km along the ridge, with the majority of these lid thicknesses between 50 km and 80 km, as would be expected in an oceanic setting (Bown and White, 1994). Figure 6.22 shows that the lid thickness has a strong positive correlation with the recovered T_e, where high T_e is associated with high lid thickness and low T_e is associated with low lid thickness. This reflects the changes in the depth of isotherms along the ridge, which govern both the T_e and non-convecting lithospheric thickness.

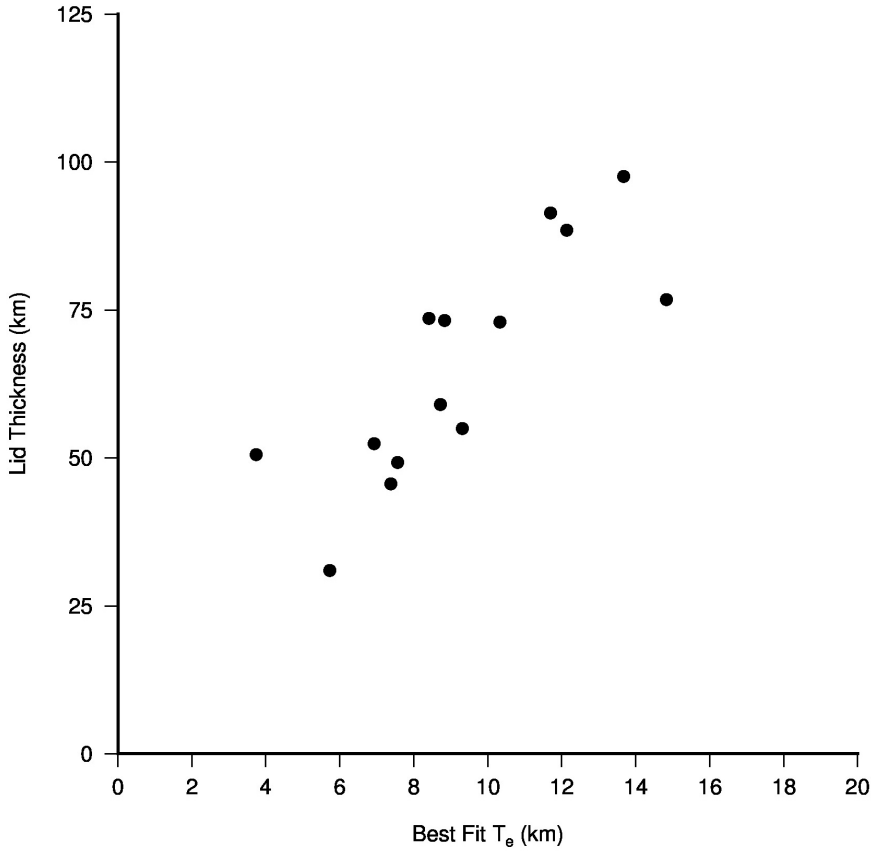


Figure 6.22: Relationship between best fit T_e and lithospheric lid thickness for the windows along the Southwest Indian Ridge.

A number of IRFs show deviation from the model at short wavelengths; in particular the IRFs for windows over the triple junctions show a lower IRF than the model at short wavelengths (see Figure 6.23). High coherence at the corresponding wavenumbers indicate that these result from the observed topography and gravity, and are not a result of the periodic noise which occurs at short wavelengths. This deviation represents the contamination of the IRF by tectonic provinces with different T_e. The lower T_e at short wavelength are caused by the signatures of the South American-Antarctic Ridge and the Central and Southeast Indian ridges, which have a lower T_e due to their higher spreading rate (Cochran et al., 1997; Cochran, 1979).

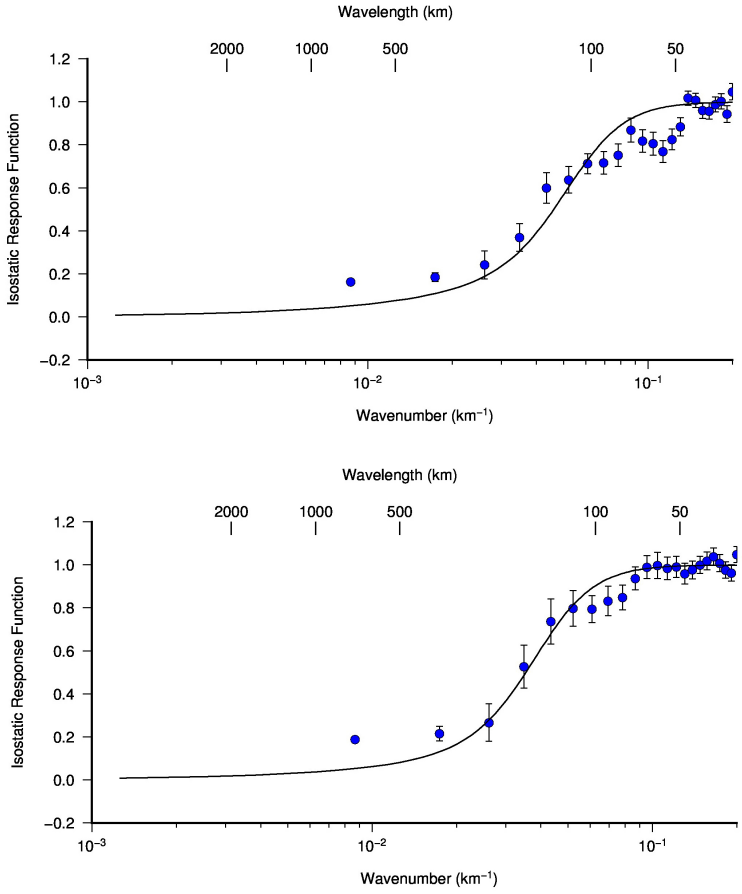


Figure 6.23: Isostatic response functions for windows at 0° and 5° longitude. Blue circles show the observed data, black shows the flexural model fit. Error bars are determined using the admittance error.

6.3.2 Recovered T_e

The majority of the topography sampled by the admittance windows (see Figure 6.17) on the Southwest Indian Ridge is generated at the spreading centre, and so provides information on the elastic thickness of the ridge crest. Possible sources of contamination, which we would expect to affect the recovered T_e along the SWIR include the Bouvet, Marion and Crozet hotspot topography, the aseismic Madgascar ridge and other mid-ocean ridges.

Figure 6.24 shows the recovered T_e, using an elastic plate model expressing the flexure of the lithosphere on the lower graph, and the recovered T_e using the combined flexure-convection model on the upper graph. The broad pattern of increasing T_e away from the Bouvet and Rodriguez triple junctions and local increases and decreases in T_e in the central part of the ridge are reflected in both methods. The combined flexure-convection shows on average slightly higher T_e than a purely flexural model, as well as greater variation in the T_e within the central part of the ridge.

The variation in T_e along the ridge correlates to changes in the geological structures and tectonic provinces on the SWIR. The lowest T_e values correlate to the presence of faster spreading ridge crests within the windows at the two triple junctions. At the Bouvet triple junction, the SWIR intersects with the South American Antarctic Ridge (SAAR) and the southernmost part of the Mid-Atlantic Ridge (MAR), which have average full spreading rates of 18 mm yr^{-1} and 32 mm yr^{-1} (Demets et al., 2010) respectively. At the Rodriguez triple junction the SWIR intersects with the Central Indian Ridge (CIR) and Southeast Indian Ridge (SEIR), which have average full spreading rates of 49 mm yr^{-1} and 58 mm yr^{-1} respectively (Demets et al., 2010). The spreading rate along the SWIR is relatively constant with an average full spreading rate of 14 mm yr^{-1}, with the exception of the region between 10° E and 16° E. This part of the ridge has an effective full spreading rate of 7.6 mm yr^{-1} (see chapter 3) and coincides with an increase in the T_e relative to the surrounding Sections. This pattern of decreasing T_e with increasing spreading rate is consistent with the work of Cochran (1979), and is

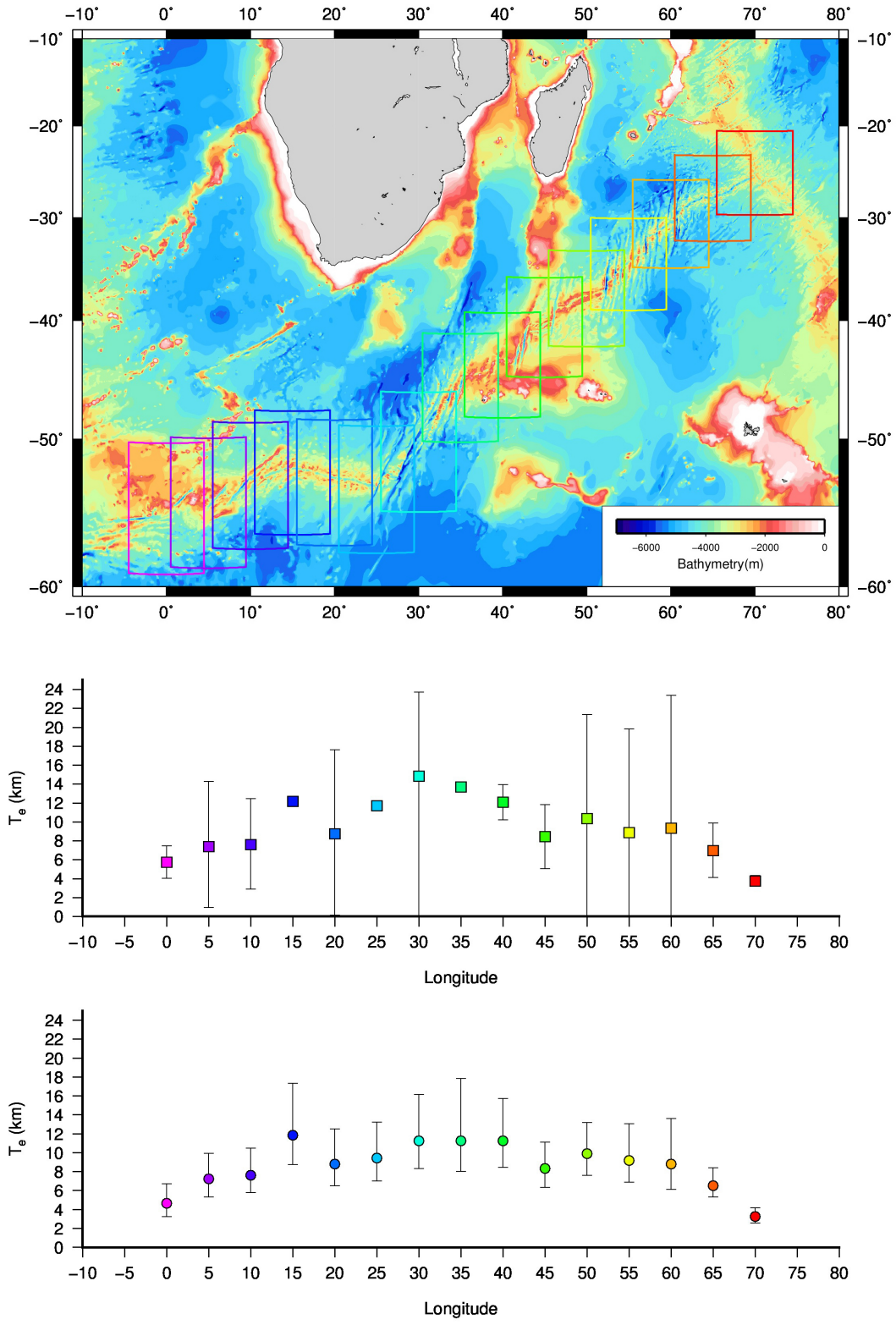


Figure 6.24: Variation in elastic thickness along the Southwest Indian Ridge crest. Top panel shows the position of the windows. Upper graph shows the best fit T_e using the combined flexure-convection model. Lower graph shows the best fit T_e using the purely flexural model.

discussed further in section 6.3.3. The highest T_e value correlates to the window centred on the Andrew Bains - Du Toit fracture zone system, which offsets the SWIR by 750 km in total. The increased T_e over the fracture zone system is attributed to colder and therefore stronger lithosphere due to the juxtaposition of old and young lithosphere. The slight decrease in T_e between 40° E and 50° E coincides with the Marion rise, Marion hotspot topography and the aseismic Madagascar ridge. This decrease is small compared to the errors, and is therefore not as robust as the variation associated with spreading rate. The origin of the Marion rise has been attributed to dynamic support from the Marion hotpot (Georgen et al., 2001); alternatively it has been suggested that the rise is supported by a buoyant geochemically depleted upper mantle, due to the passage of the African superplume (Zhou and Dick, 2013). Recent seismic studies (Li et al., 2015) indicate the presence of heterogeneous crustal thicknesses reaching up to 9.5 km, suggesting the presence of a robust magmatic system. The lower T_e in this region is consistent with a weakening of the lithosphere caused by crustal thickening, as well as thermal perturbations caused by the influence of an active hotspot on a mid-ocean ridge. Areas unperturbed by hotspots interaction and other ridge crests show T_e between 7 and 12 km, lower than those attributed to intraplate settings (Watts, 1978) but higher than those attributed to faster spreading ridges (e.g. Cochran, 1979; McNutt, 1979). The relationship between T_e and spreading rate is discussed further in the next section.

6.3.3 Comparison with other Mid Ocean Ridges

Admittance calculations were carried out on a number of admittance windows along the Mid-Atlantic Ridge (MAR) and East Pacific Rise (EPR) in order to compare the admittance between different mid-ocean ridge crests with different spreading rates. These admittance calculations were carried out using the same method as that used on the SWIR, including the use of an equal area projection, finite windowing corrections and a 1000 km x 1000 km window size.

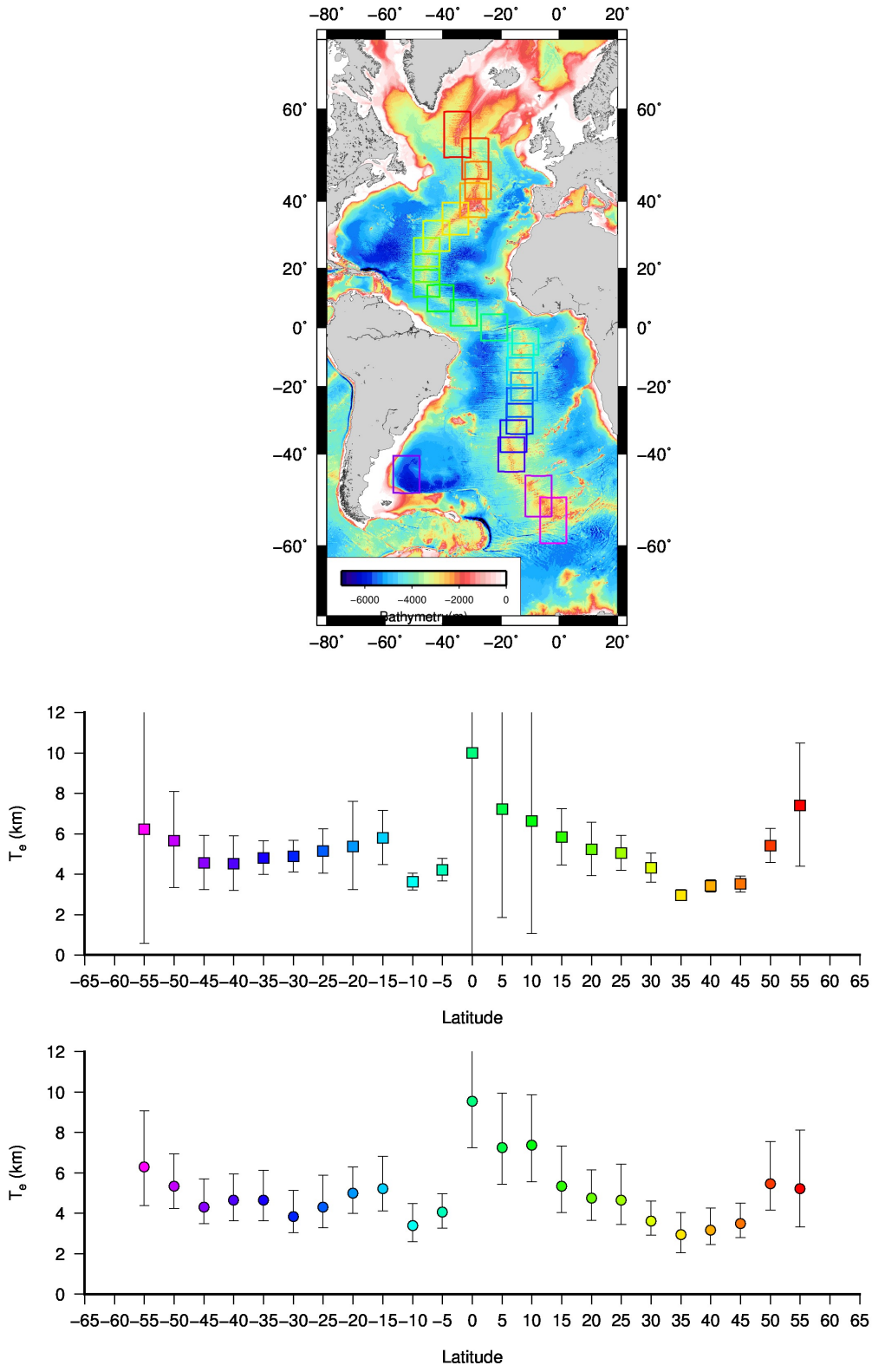


Figure 6.25: Variation in elastic thickness along the Mid-Atlantic Ridge crest. Top panel shows the position of the windows. Upper graph shows the best fit T_e using the combined flexure-convection model. Lower graph shows the best fit T_e using the purely flexural model.

Mid-Atlantic Ridge

Figure 6.25 shows the best fit T_e for the Mid-Atlantic ridge between 55° N and 55° S. The T_e varies between 2.9 km and 10 km, which is lower than those at the SWIR, even taking into account the error estimates. The T_e in the South Atlantic is relatively constant at 4.8 km, however a significant localised high T_e was recovered for the admittance window centred on 0° N. This window contains the Romanche fracture zone which offsets the MAR by 900 km. As with the Andrew Bains fracture zone on the SWIR; the older, colder, more rigid lithosphere brought into contact with the ridge axis by the transform fault causes a localised increase in T_e. The northern part of the MAR has a more variable range of T_e (between 2.9 km and 7.4 km), which reflects the more varied tectonic provinces. The South Atlantic region of the MAR is spreading at a faster rate (31.8 mm yr^{-1} (Demets et al., 2010)) than the Northern Atlantic region (22.8 mm yr^{-1} (Demets et al., 2010)). We would therefore expect the elastic thicknesses to be higher over the North Atlantic than the South Atlantic, however on average this is not the case. The southern and northern most edges of the North Atlantic region have relatively high T_e of ∼7.5 km, but there is a significant decrease in T_e to an average of ∼3.5 km between 35° N and 45° N. The decrease in T_e is attributed to the Azores hotspot which lies 100 km to 200 km east of the Mid Atlantic Ridge axis. The elastic thicknesses for this region show good agreement with previous studies which recovered T_e between 3 km and 6 km (Luis and Neves, 2006). Gravity studies have shown that interaction between the hotspot and the ridge between 4 and 10 Ma have caused increased crustal thickness (Detrick et al., 1995), which weakens the lithosphere leading to lower T_e.

East Pacific Rise

Figure 6.26 shows the best fit T_e for the East Pacific Rise between 0° N and 35° S. The admittance was calculated for windows north of the equator, however recovering T_e was problematic due to contamination by continental crust. The T_e varies between

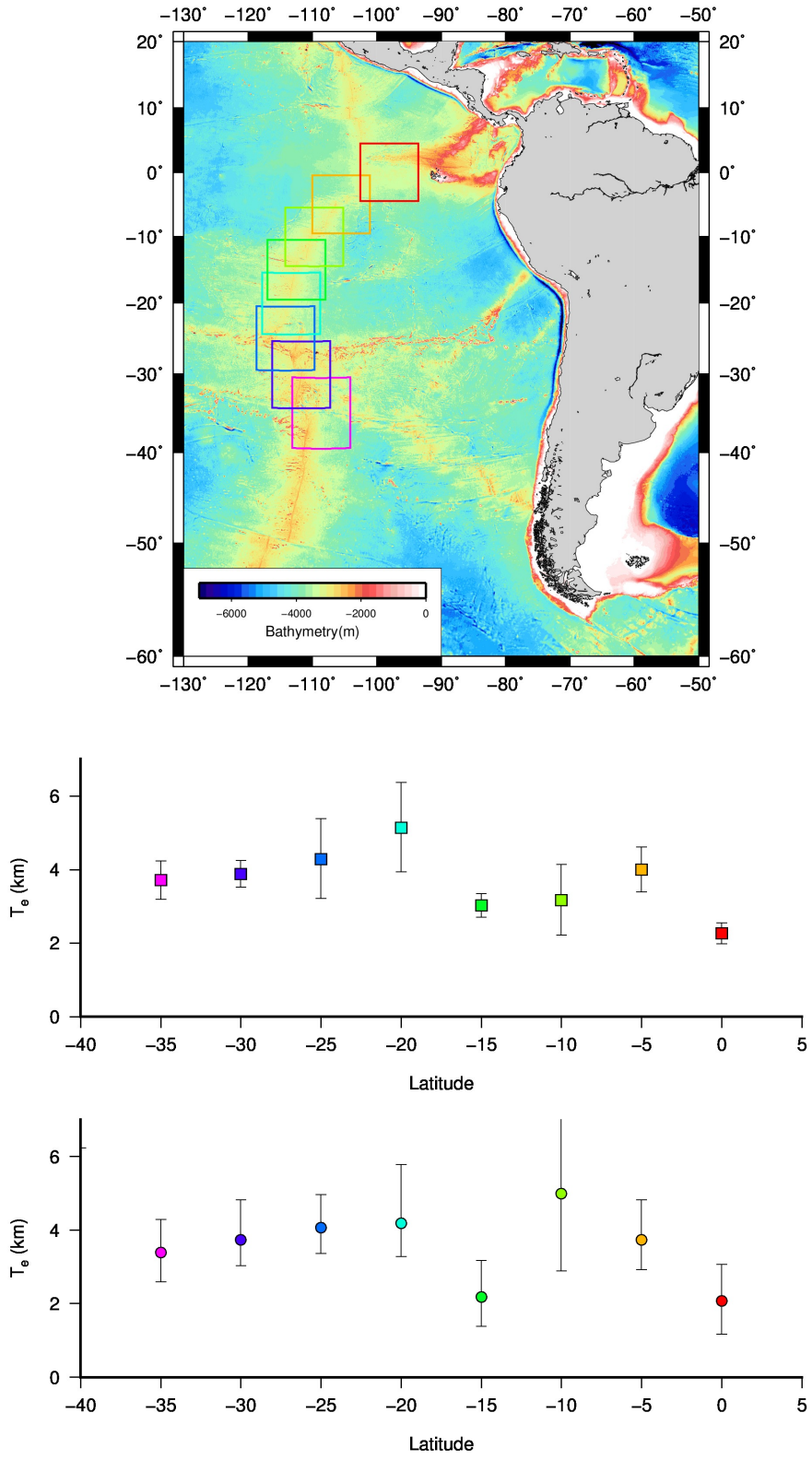


Figure 6.26: Variation in elastic thickness along the East Pacific Rise. Top panel shows the position of the windows. Upper graph shows the best fit T_e using the combined flexure-convection model. Lower graph shows the best fit T_e using the purely flexural model.

2.2 km and 5.1 km, which is lower than those at the SWIR or at the MAR.

The T_e along the East Pacific Rise is slightly higher in the south (20° S to 35° S) than to the north (15° S to 0° N). This is attributed to decrease in spreading rate between the Pacific-Nazca spreading margin in the north ($\sim$170 mm yr^{-1}) and the Pacific-Antarctic spreading margin in the south ($\sim$103 mm yr^{-1}) (Demets et al., 2010). Geochemical data from Miocene basaltic crust (23 Ma to 7 Ma) drilled at the EPR between 3° S and 7° S (Geldmacher et al., 2013) demonstrate the influence of the Galapagos hotspot on the East Pacific Rise in the past. This region has the lowest T_e on the EPR, despite the contamination from the slower spreading Galapagos spreading centre. This may reflect the past influence of the Galapagos hotspot, though this is not certain. The Easter hotspot lies 350 km off the EPR axis at 25° S, however there is no reduction in observed T_e in this region. This may be due to the more complex plate tectonic configuration over this region of the ridge, which includes the Easter and Juan Fernandez microplates.

Figure 6.27 shows the relationship between recovered T_e and spreading rate. The comparison of T_e across these three ridges, as well as data from intermediate spreading ridges (Luttrell and Sandwell, 2012), shows a clear spreading rate dependence. Higher elastic thicknesses were recovered from ridges with slower spreading rates than those with faster spreading rates. This confirms the relationship proposed by Cochran (1979). The change in elastic thickness with spreading rate is attributed to changes in the thermal structure. Following the assumption by Cochran (1979) that the depth to the elastic thickness follows the 450° isotherm, this would suggest that the Southwest Indian Ridge has a colder thermal structure, which is in agreement with geodynamic models (Gente et al., 2003).

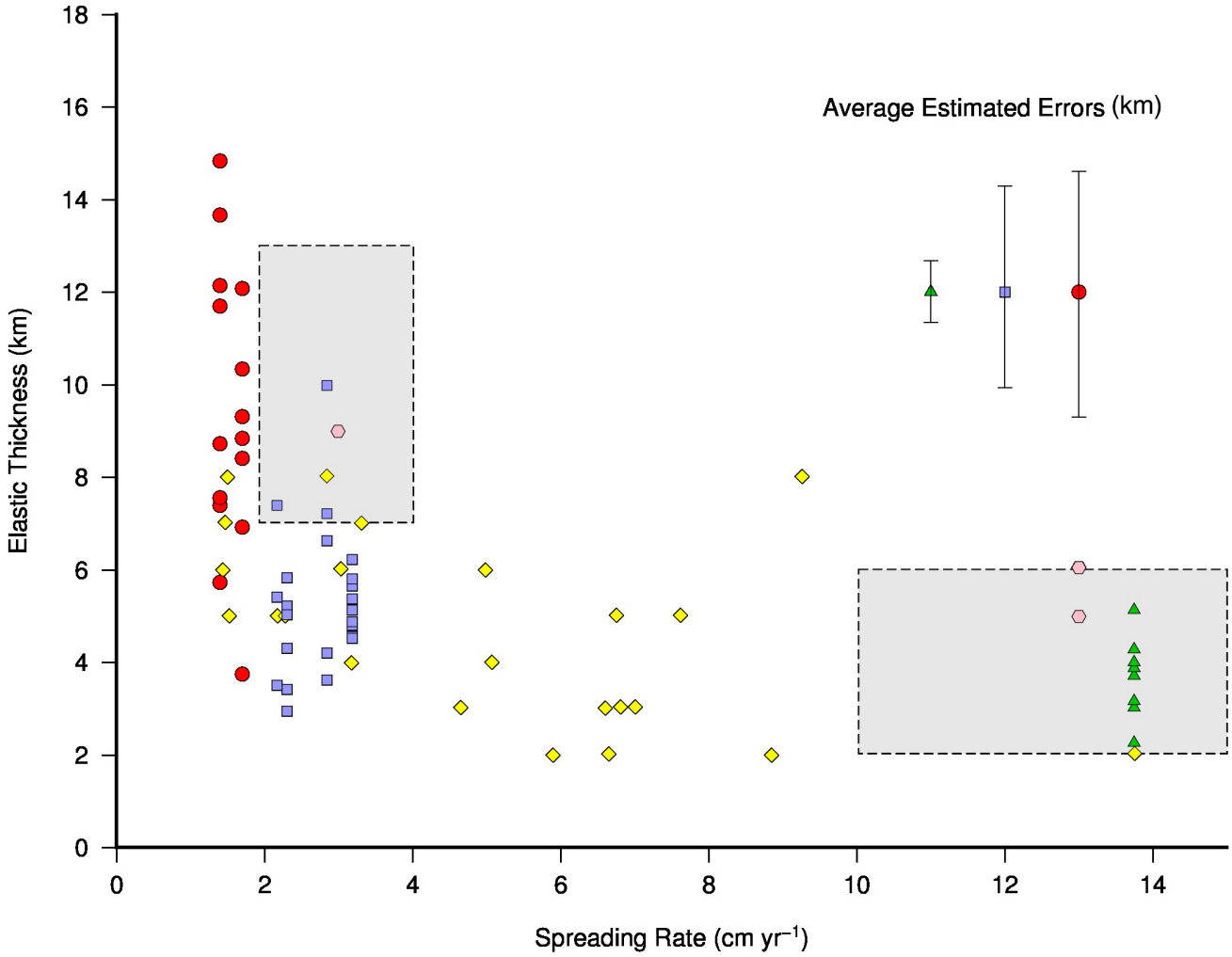


Figure 6.27: Comparison of best fit T_e and spreading rate. Red circles - SWIR, blue squares - MAR, green triangles - EPR, pink circles - data for the MAR and EPR from Cochran (1979), yellow diamonds - data for a global set of ridges from Luttrell and Sandwell (2012). Grey boxes show the range expected for the MAR and EPR from Cochran (1979).

6.4 Chapter Summary

This chapter presents the results of an elastic thickness analysis on the Southwest Indian Ridge and other mid-ocean ridge crests around the globe. The key points are as follows:

- Synthetic bathymetry and gravity data were constructed in order to test the windowed admittance method. These were used to assess the accuracy of T_e recovery for low T_e and identify method parameters, which affect the T_e recovery.

- Synthetic testing was used to show that the projection method used for the bathymetry and gravity data was a source of systematic error. While T_e at low latitudes was recovered well, at high latitudes T_e was systematically underestimated. Vincenty's formula was used to create equal area grids and remove this effect.

- Synthetic testing was used to show that the finite nature of the window caused a systematic bias causing T_e to be underestimated. This effect increased with increasing T_e and was corrected for using an empirical correction determined from synthetic testing.

- The addition of ridge topography, based on the plate cooling model, to the synthetic bathymetry showed that the ridge itself had a spectral admittance due to thermal subsidence. This admittance was present for ultra-slow and slow spreading rates, but absent at fast spreading rates. This was corrected for using an empirical correction determined from the synthetic tests.

- The admittance for 15 windows along the Southwest Indian Ridge crest was calculated. This admittance was used to calculate isostatic response functions for each window, allowing different windows to be compared more easily.

- A flexural model, derived from elastic plate theory, was fitted to the observed IRFs using least squares fitting to determine the best fit T_e. Two main sources of misfit were identified: long wavelength positive anomalies and mid-wavelength rollover.

- A combined flexural-convection model was derived from the equations of McKenzie (2010) and fitted to the observed IRFs using least squares fitting. This model reduced the misfits observed between the flexural model and the IRFs, particu-

larly at the long wavelengths.

- The T_e derived from both models were compared and the pattern along the ridge examined. The best fit elastic thicknesses derived from comparison between theoretical and observed isostatic response functions show an average between 7 km and 12 km. The elastic thicknesses were reduced (between 4 km and 6 km) over the Rodriguez and Bouvet triple junction, and elevated over the slower spreading oblique Section; both of which were attributed to a spreading rate dependence. A slight reduction in the elastic thickness coincides with the location of the Marion hostpot, though this is not definitive.

- Windowed admittance was calculated for the Mid-Atlantic and East Pacific Rises, and the best fit T_e estimated using least squares fitting. Comparison of the admittance for the different ridge crests showed a systematic increase in T_e with decreasing spreading rate. This is attributed to the shallow isotherms at faster spreading rates compared to slow spreading rates.

Chapter 7

Conclusions

In this thesis, we have conducted a series of integrated geophysical studies with the aim of better understanding the tectonic and volcanic processes occurring on the ultra-slow spreading Southwest Indian Ridge. We have presented novel bathymetry, gravity and video imagery data, and combined this with existing shiptrack and satellite data.

Previous studies on the Southwest Indian Ridge have focussed on the eastern and western parts of the ridge, which exhibited anomalous mid-ocean ridge morphologies. We have used data along the length of the ridge crest to study the morphological variation and note the following key points:

1. Long wavelength variations in along-axis bathymetry, free-air gravity anomalies, mantle Bouguer anomalies, shear wave velocities and $Na_{8.0}$ are well correlated. These variations are interpreted as changes in the mantle density and crustal thickness caused by (*i*) The influence of the Marion and Bouvet hotspots; (*ii*) Changes in the effective spreading rate due to spreading obliquity.

2. Systematic variation in the shape and size of the axial valley, established using ensemble averaging, is correlated with axial valley depth and the best fit elastic thickness (a proxy for lithospheric strength). This is used to show that the thermal structure of the sub axial lithosphere is the governing factor for the

rheology, which in turn governs the lithospheric strength and shape of the axial valley through the classic wedge model.

3. Significant morphological variation occurs on a segment scale. Along-axis bathymetry and gravity anomalies are used to divide the ridge into segments, separated by transform and non-transform discontinuities. These segments are separated into four different groups, which have different inferred crustal structure and melt migration mechanisms. The distribution of these different segment groups on the ridge is influenced by the long wavelength trends in the mantle and crustal structure.

Large oceanic islands, such as Hawaii and the Canary islands have been the subject of morphological studies, which have been used to infer the magmatic, tectonic and morphological processes occurring at these islands. We have applied these same principles to five large seamounts and an oceanic core complex, situated on the flanks of the Southwest Indian Ridge. Novel bathymetry, gravity, ROV imagery and lithological samples are used to identify constructive and erosional morphological features on each of the seamounts, and we note the following key points:

1. Flank rift zones are well developed on 5 out of the 6 seamounts. An edifice height threshold of 2 km is proposed, with seamounts above this height showing well developed rift zones. The length of these flank rift zones is correlated with edifice volume, indicating that the magma supply is the limiting factor for flank rift zone length.

2. The orientation of the flank rift zones is strongly controlled by the local tectonic setting of the seamount, specifically the proximity of the seamount to transform faults and the ridge axis. The orientation of flank rift zones, evidence of truncated summit morphology and substrate data are used to show that two of the seamounts formed on the axis, while the others formed off axis. A melt migration process is proposed in which isolated magma pockets are tapped by deep seated faults in order to produce off axis volcanism.

3. A number of slope failures are identified across the seamounts using exponential fitting and variation in seamount slope. The morphological evidence suggests a combination of slumping and debris avalanche processes. The precise cause of any given slope failure is uncertain based on the data available, however slope gradient, edifice height and lithology type may all be contributing factors.

The distribution of seamounts along the mid-ocean ridge crest has been used to establish the patterns of magmatism on many ridges including the East Pacific Rise, Mid-Atlantic Ridge, Galapagos spreading centre and Gakkel Ridge. Seamount distribution on the SWIR has been studied in the easternmost part only. We used shipboard and satellite bathymetry to study seamount distribution over the length of the ridge and note the following key points:

1. Comparison of seamount distribution along a section of the MAR using the Modified Basal Outlining Algorithm (MBOA) and other seamount counting methods shows that the MBOA is successful in identifying seamounts from swath bathymetry on the axial valley floor. The seamount population within the SWIR axial valley seamount populations show a lower observed density than on the MAR, though the characteristic height is taller. These differences are attributed to greater magma supply and weaker crust at the faster spreading MAR, caused by shallower isotherms.

2. The seamount populations at the SWIR are characterised into three types: (*i*) Magmatically sparse areas with seamounts found at the axial valley margins in association with faulting (*ii*) Magmatically intermediate areas in which there are numerous seamounts forming in the neovolcanic zone (*iii*) Magmatically robust areas in which the axial valley is partial filled and seamounts form parasitic cones on large volcanic structures. The variation in magmatism along the ridge is attributed to strong melt focussing over several segments and melt migration towards the segment centres.

3. Comparison of the seamount population statistics calculated using the MBOA

show excellent agreement with those of a global study using shipboard bathymetry data.

4. Variation in the number of seamounts and total seamount volume show that the seamount distribution is governed by the effective spreading rate, presence of transform faults and location of hotspots. Increases in the estimated magmatic flux closely coincide with the locations of the Bouvet, Marion and Crozet hotspots.

5. Comparison of the Southwest Indian Ridge, Mid-Atlantic Ridge and East Pacific Rise flank seamount distribution shows that both the number and volume of seamounts increases with spreading rate. This is attributed to the increase in magma supply at faster spreading ridges and the greater degree of off axis volcanism at the EPR compared to the SWIR.

Admittance studies provide a means to assess the lithospheric strength in the oceans. We used gravity and bathymetry data to conduct 3D admittance studies across a series of windows along the ridge and we note the following key points:

1. Synthetic testing of the 3D windowed admittance method shows a number of sources of error. A Mercator projection produces distortion in the bathymetry and gravity grids at high latitudes, leading to systematic underestimation in retrieved elastic thickness. An equal area projection removes this distortion and the resulting underestimation. The finite nature of the admittance windows causes a systematic underestimation, which is corrected using an empirical correction determined from synthetic testing. Finally, the admittance of the ridge topography caused by thermal subsidence caused an increase in the recovered elastic thickness at ultra-slow and slow spreading ridges.

2. Comparison of isostatic response functions calculated from the observed admittance and theoretical admittance based on a flexural isostatic model show considerable misfits at long wavelengths, which are attributed to dynamic topography

from mantle convection. A combined flexural-convection model is derived, which reduces these misfits.

3. The best fit elastic thicknesses over the SWIR vary on average between 7 and 12 km. The elastic thicknesses are reduced (between 4 and 6 km) over the Rodriguez and Bouvet Triple Junctions, and elevated over the slower spreading oblique section. This illustrates a spreading rate dependence in which the elastic thickness increases with decreasing spreading rate. A slight reduction in the elastic thickness coincides with the location of the Marion hotspot, though this elastic thickness reduction is within error.

4. Comparison of best fit elastic thicknesses between the Southwest Indian Ridge, Mid-Atlantic Ridge and East Pacific Rise show a clear spreading rate dependence. The elastic thicknesses decrease with increasing spreading rate, which is attributed to the shallow isotherms at faster spreading ridges leading to a weaker lithosphere.

7.1 Future Work

Many of the bathymetry and gravity observations in this thesis are used to make inferences about the crustal thickness and mantle densities beneath the ridge. The different contributions to the gravity anomaly from the crust and mantle are uncertain without constraints on the crustal thickness through seismic studies. A number of seismic refraction and tomographic experiments have been carried out on the SWIR including:

- Seismic refraction experiments at 66°E (Müller et al., 1997; Minshull et al., 2006)
- Seismic refraction experiments at 57°E at Atlantic Bank oceanic core complex (Müller et al., 1997; Muller et al., 2000)

- Seismic refraction and tomography at 49°E at the Dragon Flag vent field and oceanic core complex (Li et al., 2015; Zhao et al., 2013; Jian et al., 2017)
- Microseismicity studies from OBS passive seismology at the melt poor oblique and eastern sections (Schmid and Schlindwein, 2016; Schlindwein, 2012)

These studies reveal a wide range of crustal thicknesses between 9.5 km and 2 km, however they are all centred on anomalous segments. The majority of the studies are conducted over Group IV type segments (see chapter 3), which are the melt-poor endmembers on the SWIR, or over oceanic core complexes, which are anomalous tectonic structures. One experiment (Li et al., 2015; Jian et al., 2017) is conducted over a Group I type segment, which are the melt-rich endmembers on the SWIR, and have anomalously shallow axial topography. We have shown in chapter 3 that the majority of the segments on the ridge are Group II and Group III type segments, the structure of which has yet to be established using seismic experiments. Therefore, proposed future work should include a seismic experiment on non-anomalous ridge segments, which are representative of the ridge as a whole in order to establish the differences in crustal structure between the SWIR and other ridges.

Seamounts are characterised by localised upwelling, swift currents and a relatively shallow habitat which form favourable environmental conditions for the formation of diverse zoological benthic assemblages (Samadi et al., 2007). Large suspension feeders such as corals, sponges and crinoids are present on the six seamounts described in chapter 4, which form a distinct structural framework on the substrate of large areas of the seamount. The growth of these seamount invertebrates may be very slow, leading to long lifespans (Andrews et al., 2005). We therefore propose that future work could explore the relationship between the spatial distribution of these benthic species and the geological processes occurring on the seamount. These processes include the locations of volcanic eruptions and slope failures, which determine factors such as the substrate type, slope gradient and large scale morphology, which would affect the local currents.

Bibliography

Acosta, J., Uchupi, E., Smith, D., Muñoz, A., Herranz, P., Palomo, C., Llanes, P., Ballesteros, M. and Group, Z. W. (2003), Comparison of volcanic rifts on La Palma and El Hierro , Canary Islands and the Island of Hawaii, *Marine Geophysical Researches* **24**, 59–90.

Adams, E. W., Schlager, W. and Wattel, E. (1998), Submarine slopes with an exponential curvature, *Sedimentary Geology* **117**, 135–141.

Airy, G. B. (1855), On the Computation of the Effect of the Attraction of Mountain-Masses, as Disturbing the Apparent Astronomical Latitude of Stations in Geodetic Surveys, *Philosophical Transactions of the Royal Society of London* **145**, 101–104.

Andrews, A. H., Cailliet, G. M., Kerr, L. A., Coale, K. H., Lundstrom, C. and De Vogelaere, A. P. (2005), Investigations of age and growth for three deep-sea corals from the Davidson Seamount off central California, *in* A. Freiwald and J. M. Roberts, eds, 'Cold-Water Corals and Ecosystems', Springer-Verlag, Berlin/Heidelberg, pp. 1021–1038.

Applanix (n.d.), 'POSMV Specifications'.
URL: *http://www.applanix.com/products/marine/pos-mv.html*

Artyushkov, E. V. (1973), Stresses in the lithosphere caused by crustal thickness inhomogeneities, *Journal of Geophysical Research* **78**(32), 7675–7708.

Baines, G. A., Cheadle, M. J., Dick, H. J., Hosford Scheirer, A., John, B. E., Kusznir, N. J. and Matsumoto, T. (2003), Mechanism for generating the anomalous uplift of oceanic core complexes: Atlantis Bank, southwest Indian Ridge, *Geology* **31**(12), 1105–1108.

Banks, R. J., Parker, R. L. and Huestis, S. P. (1977), Isostatic compensation on a regional scale: Local versus regional mechanisms, *Geophysical Journal Royal Astronomical Society* **51**, 431–452.

Barruol, G. (2013), RHUM-RUM Marion Dufresne MD192 cruise report Sept - Oct 2012, Technical report.

Bassett, D. and Watts, A. (2015), Gravity anomalies, crustal structure, and seismicity at subduction zones: 1. Seafloor roughness and subducting relief, *Geochemistry Geophysics Geosystems* **16**, 1508–1540.

Bates, C. C., Gaskell, T. F. and Rice, R. B. (1982), *Geophysics in the Affairs of Man*, Pergamon Press.

Batiza, R. (1981), Lithospheric Age Dependence of Off-ridge Volcano Production in the North Pacific, *Geophysical Research Letters* **8**, 853–856.

Batiza, R. (1982), Abundances, distribution and sizes of volcanoes in the Pacific Ocean and implications for the origin of non-hotspot volcanoes, *Earth and Planetary Science Letters* **60**, 195–206.

Batiza, R. and Vanko, D. (1984), Volcanic development of small oceanic central volcanoes on the flanks of the East Pacific Rise inferred from narrow beam echo sounder surveys, *Marine Geology* **54**, 53–90.

Batiza, R. and White, J. (2000), Submarine lavas and hyaloclasite, *in* H. Sigurdsson, ed., 'Encyclopedia of Volcanoes', Academic Press, San Diego, pp. 361–381.

Behn, M. D., Sinton, J. M. and Detrick, R. S. (2004), Effect of the Galápagos hotspot on seafloor volcanism along the Galápagos Spreading Center (90.9-97.6W), *Earth and Planetary Science Letters* **217**(3-4), 331–347.

Behn, M., Lin, J. and Zuber, M. (2002), Evidence for weak oceanic transform faults, *Geophysical Research Letters* **29**(24), 2207.

Bessel, F. W. (1825), The calculation of longitude and latitude from geodesic measurements, *Astronomische Nachrichten* **331**(8), 852–861.

Binard, N., Hekinian, R., Cheminee, J. L. and Stoffers, P. (1992), Styles of Eruptive Activity on Intraplate Volcanos in the Society and Austral Hot-Spot Regions: Bathymetry, Petrology, and Submersible Observations, *Journal of Geophysical Research* **97**(B10), 13999–14015.

Bird, P. (2003), An updated digital model of plate boundaries, *Geochemistry Geophysics Geosystems* **4**(3), 1027.

Blondel, P. and Murton, B. J. (1997), *Handbook of Seafloor Sonar Imagery*.

Bloxham, J. and Gubbins, D. (1985), The secular variation of the Earth's magnetic field, *Nature* **317**(6040), 777–781.

Bohnenstiehl, D. R., Howell, J. K., White, S. M. and Hey, R. N. (2012), A modified basal outlining algorithm for identifying topographic highs from gridded elevation data , Part 1: Motivation and methods, *Computers and Geosciences* **49**, 308–314.

Bonatti, E. (1978), Vertical tectonism in oceanic fracture zones, *Earth and Planetary Science Letters* **37**, 369–379.

Born, G., Dunne, J. and Lame, D. (1979), Seasat Mission Overview, *Science* **204**(4400), 1405–1406.

Bown, J. W. and White, R. S. (1994), Variation with spreading rate of oceanic crustal thickness and geochemistry, *Earth and Planetary Science Letters* **121**, 435–449.

Bronner, A., Sauter, D., Munschy, M., Carlut, J., Searle, R., Cannat, M. and Manatschal, G. (2014), Magnetic signature of large exhumed mantle domains of the Southwest Indian Ridge results from a deep-tow geophysical survey over 0 to 11 Ma old seafloor, *Solid Earth* **5**(1), 339–354.

Bullard, E. C. (1936), Gravity measurements in East Africa, *Philosophical Transactions of the Royal Society* **235**, 445–531.

Bullard, E. C. and Mason, R. G. (1963), The magnetic field over the oceans, *in* 'The Sea: The Earth Beneath the Sea', pp. 175–217.

Burov, E. B. (2011), Rheology and strength of the lithosphere, *Marine and Petroleum Geology* pp. 1–42.

Burov, E. B. and Watts, A. B. (2006), The long-term strength of continental lithosphere : jelly sandwich or crème brûlée ?, *GSA Today* **16**(1), 4–10.

Burov, E. and Diament, M. (1995), The effective elastic thickness (Te) of continental lithosphere: What does it really mean?, *Journal of Geophysical Research* **100**, 3905–3927.

Canales, P. J., Detrick, S., Hooft, E. E. and Naar, F. (1997), Variations in axial morphology along the Galápagos spreading center and the influence of the Galápagos hotspot, *Journal of Geophysical Research* **102**(B12), 27341–27354.

Cannat, M., Rommevaux-Jestin, C. and Fujimoto, H. (2003), Melt supply variations to a magma-poor ultra-slow spreading ridge (Southwest Indian Ridge 61 to 69E), *Geochemistry, Geophysics, Geosystems* **4**(8), 9104.

Cannat, M., Rommevaux-jestin, C., Sauter, D., Deplus, C. and Mendel, V. (1999), Formation of the axial relief at the very slow spreading Southwest Indian Ridge (49 to 69E), *Journal of Geophysical Research* **104**, 22823–22843.

Cannat, M., Sauter, D., Bezos, A., Meyzen, C., Humler, E. and Le Rigoleur, M. (2008), Spreading rate, spreading obliquity, and melt supply at the ultraslow spreading Southwest Indian Ridge, *Geochemistry Geophysics Geosystems* **9**(4), 1–26.

Cannat, M., Sauter, D., Mendel, V., Ruellan, E., Okino, K., Escartin, J., Combier, V. and Baala, M. (2006), Modes of seafloor generation at a melt-poor ultraslow-spreading ridge, *Geological Society of America* **34**(7), 605–608.

Carpine-Lancre, J., Fisher, R., Harper, B., Hunter, P., Jones, M., Kerr, A., Laughton, A., Ritchie, S., Scott, D. and Whitmarsh, M. (2003), *The History of GEBCO 1903-2003*.

Carracedo, J. C. (1994), The Canary Islands: an example of structural control on the growth of large oceanic-island volcanoes, *Journal of Volcanology and Geothermal Research* **60**, 225–241.

Chapman, M. E. and Talwani, M. (1982), Geoid anomalies over deep sea trenches, *Geophysical Journal of the Royal Astronomical Society* **68**(2), 349–369.

Chen, Y. and Jason Morgan, W. (1990), A Nonlinear Rheology Model for Mid-Ocean Ridge Axis Topography, *Journal of Geophysical Research* **95**(B11), 17,583–17,604.

Choi, E.-s., Lavier, L. and Gurnis, M. (2008), Thermomechanics of mid-ocean ridge segmentation, *Physics of the Earth and Planetary Interiors* **171**, 374–386.

Chu, D. and Gordon, R. G. (1999), Evidence for motion between Nubia and Somalia along the Southwest Indian ridge, *Nature* **398**(March), 64–67.

Clague, D. A., Moore, J. G. and Reynolds, J. R. (2000), Formation of submarine flat-topped volcanic cones in Hawai'i, *Bulletin of Volcanology* **62**, 214–233.

Cochran, J. R. (1979), An Analysis of Isostasy in the World's Oceans 2. Midocean Ridge Crests, *Journal of Geophysical Research* **84**(B9), 4713–4729.

Cochran, J. R. (2008), Seamount volcanism along the Gakkel Ridge , Arctic Ocean, *Geophysical Journal International* **174**, 1153–1173.

Cochran, J. R., Kurras, G., Edwards, M. H. and Coakley, B. J. (2003), The Gakkel Ridge: Bathymetry, gravity anomalies, and crustal accretion at extremely slow spreading rates, *Journal of Geophysical Research* **108**(B2).

Cochran, J. R., Sempere, J.-C. and SEIR-scientific Team (1997), The Southeast Indian Ridge between 88E and 118E : Gravity anomalies and crustal accretion at intermediate spreading rates, *Journal of Geophysical Research* **102**(B7), 15463–15487.

De Chabalier, J.-b. and Avouac, J.-p. (1994), Kinematics of the Asal Rift (Djibouti) Determined from the Deformation of Fieale Volcano, *Science* **265**, 1629–1776.

Debayle, E., Kennett, B. and Priestley, K. (2005), Global azimuthal seismic anisotropy and the unique plate-motion deformation of Australia, *Nature* **433**(February), 509–512.

Demets, C., Gordon, R. G. and Argus, D. F. (2010), Geologically current plate motions, *Geophys. J. Int.* **181**, 1–80.

Detrick, R. S., Needham, H. D. and Renard, V. (1995), Gravity anomalies and crustal thickness variations along the Mid-Atlantic Ridge between 33N and 40N, *Journal of Geophysical Research* **100**, 3767–3787.

Diament, M., Jean-Claude, S. and Ahmed, H. (1986), Isostasy of the Northern Bay of Biscay continental margin, *Geophysical Journal International* **86**, 893–907.

Dick, H. J. B., Lin, J. and Schouten, H. (2003), An ultraslow-spreading class of ocean ridge., *Nature* **426**, 405–12.

Dick, H. J. B., Schouten, H., Meyer, P. S., Gallo, D. G., Bergh, H., Tyce, R., Patriat, P., Johnson, K. T. M., Snow, J. and Fisher, A. (1991), Tectonic Evolution of the Atlantis I I Fracture Zone, *proceedings of the Ocean Drilling Program, Scientific Results* **118**, 359–398.

Dick, H. J., Natland, J. H., Alt, J. C., Bach, W., Bideau, D., Gee, S., Haggas, S., Hertogen, J. G. H., Hirth, G., Martin, P., Ildefonse, B., Iturrino, G. J., John, B. E., Kelley, D. S., Kikawa, E., Kingdon, A., Leroux, P. J., Maeda, J., Meyer, P. S., Miller, D. J., Naslund, H. R., Niu, Y.-l., Robinson, P. T., Snow, J., Stephen, R. A., Trimby, P. W., Worm, H.-u. and Yoshinobu, A. (2000), A long in situ section of the lower ocean crust: results of ODP Leg 176 drilling at the Southwest Indian Ridge, *Earth and Planetary Science Letters* **179**, 31–51.

Dixon, T. H., Naraghi, M., McNutt, M. K. and Smith, S. M. (1983), Bathymetric prediction from SEASAT altimeter data, *Journal of Geophysical Research* **88**(C3), 1563–1571.

Dorman, L. M. and Lewis, B. T. R. (1970), Experimental Isostasy: 1. Theory of the Determination of the Earth's Isostatic Response to a Concentrated Load, *Journal of Geophysical Research* **75**(17), 3357–3365.

Duchossois, G. (1991), The ERS-1 mission objecives, *ESA bulletin* **65**, 16–25.

Duncan, R. A. (1981), Hotspots in the Southern Oceans - an absolute frame of reference for motion of the Gondwana continents, *Tectonophysics* **74**(1-2), 29–42.

Egedal, J. (1947), The magnetic diurnal variation of the horizontal force near the magnetic equator, *Journal of Geophysical Research* **52**(4), 449–451.

Elsworth, D. and Voight, B. (1995), Dike intrusion as a trigger for large earthquakes and the failure of volcano flanks, *Journal of Geophysical Research* **100**(B4), 6005–60024.

Eotvos, R. (1919), Experimenteller Nachweis der Schwereanderung, due ein auf normal geformte Erdoberflache in ostlichen order westlichen Richtung bewegter Corper durch dieser Bewegung erleidet, *Ann. d. Phys.* **59**, 743–752.

Escartín, J., Soule, S. A., Cannat, M., Fornari, D. J., Düünür, D. and Garcia, R. (2014), Lucky Strike seamount: Implications for the emplacement and rifting of segment-centered volcanoes at slow spreading mid-ocean ridges, *Geochemistry, Geophysics, Geosystems* **15**(11), 4157–4179.

Fialko, Y. A. and Rubin, A. M. (1998), Thermodynamics of lateral dike propagation: Implications for crustal accretion at slow spreading mid-ocean ridges, *Journal of Geophysical Research-Solid Earth* **103**(B2), 2501–2514.

Fisher, O. (1889), *Physics of the Earth's Crust*, Macmillan and Company.

Fiske, R. and Jackson, E. (1972), Orientation and growth of Hawaiian volcanic rifts: the affect of regional structure and gravitational stresses, *Proceedings of the Royal Society of London* **329**, 299–326.

Font, L., Murton, B. J., Roberts, S. and Tindle, A. G. (2007), Variations in Melt Productivity and Melting Conditions along SWIR (70 E - 49 E): Evidence from Olivine-hosted and Plagioclase-hosted Melt Inclusions, *Journal of Petrology* **48**(8), 1471–1494.

Fornari, D. J. and Ryan, W. B. F. (1984), The Evolution of Craters and Calderas on Young Seamounts: Insights from Sea Marc 1 and Sea Beam Sonar Surveys of a Small Seamount Group near the Axis of the East Pacific Rise at ˜ 10N, *Journal of Geophysical Research* **89**(B13), 11069–11083.

Fornari, D. J., Ryan, W. B. F. and Fox, P. J. (1985), Sea-floor lava fields on the East Pacific Rise., *Geology* **13**(6), 413–416.

Fujita, K. and Sleep, N. H. (1978), Membrane stresses near mid-ocean ridge-transform intersections, *Tectonophysics* **50**(2-3), 207–221.

Gee, M. J. R., Watts, A. B., Masson, D. G., Neil, C. and Mitchell, N. C. (2001), Landslides and the evolution of El Hierro in the Canary Islands, *Marine Geology* **177**(3-4), 271–293.

Geldmacher, J., Höfig, T. H., Hauff, F., Hoernle, K., Garbe-Schönberg, D. and Wilson, D. S. (2013), Influence of the Galápagos hotspot on the East Pacific Rise during Miocene superfast spreading, *Geology* **41**(2), 183–186.

Gente, P., Dyment, J., Maia, M. and Goslin, J. (2003), Interaction between the Mid-Atlantic Ridge and the Azores hot spot during the last 85 Myr: Emplacement and rifting of the hot spot-derived plateaus, *Geochemistry, Geophysics, Geosystems* **4**(10), 8514.

Georgen, J. E., Lin, J. and Dick, H. J. B. (2001), Evidence from gravity anomalies for interactions of the Marion and Bouvet hotspots with the Southwest Indian Ridge : effects of transform offsets, *Earth and Planetary Science Letters* **187**, 283–300.

Goff, J. A. (1991), A Global and Regional Stochastic Analysis of Near-Ridge Abyssal Hill Morphology, *Journal of Geophysical Research* **96**(B13), 21713–21737.

Goslin, J. and Diament, M. (1987), Mechanical and thermal isostatic response of the Del Cano Rise and Crozet Bank (southern Indian Ocean) from altimetry data, *Earth and Planetary Science Letters* **84**, 285–294.

Grace (2013), Gravity Recovery and Climate Experiment, *The University of Texas* pp. 1–5.

Gracia, E., Bideau, D., Hekinian, R. and Lagabrielle, Y. (1999), Detailed geological mapping of two contrasting second-order segments of the Mid-Atlantic Ridge between Oceanographer and Hayes fracture zones (33 30'N- 35N), *Journal of Geophysical Research* **104**(B10), 22903–22921.

Gregg, T. K. P. and Fink, J. H. (1995), Quantification of submarine lava-flow morphology through analog experiments, *Geology* **23**(1), 73–76.

Grindlay, N. R., Fox, P. J., Macdonald, K. C. and Barabara, S. (1991), Second-Order Ridge Axis Discontinuities in the South Atlantic : Morphology , Structure, and Evolution, *Marine Geophysical Researches* **13**, 21–49.

Grindlay, N. R., Madsen, J. A., Rommevaux-jestin, C. and Sclater, J. (1998), A different pattern of ridge segmentation and mantle Bouguer gravity anomalies along the ultra-slow spreading Southwest Indian Ridge (1530'E to 25E), *Earth and Planetary Science Letters* **161**, 243–253.

Gudmundsson, A. (1995), Stress fields associated with oceanic transform faults, *Earth and Planetary Science Letters* **136**, 603–614.

Gunn, R. (1943), A quantitive evaluation of the influence on the lithosphere on the anomalies of gravity, *Journal of the Franklin Institute* **236**, 47–65.

Hampton, M. A., Lee, H. J. and Locat, J. (1996), Submarine landslides, *Reviews of Geophysics* **34**(1), 33–59.

Haxby, W. F., Karner, G. D., LaBrecque, J. L. and Weissel, J. K. (1983), Digital images of combined oceanic and continental data sets and their use in tectonic studies, *Eos, Transactions American Geophysical Union* **64**(52).

Hayford, J. F. (1909), *Geodesy: The Figure of the Earth and Isostasy from Measurements in the United States*, US Government Printing Office.

Heezen, B. C. (1960), The Rift in the Ocean Floor, *Scientific American* **203**(4), 98–110.

Heiskanen, W. (1931), Isostatic tables for the reduction of gravimetric observations calculated on the basis of Airy's hypothesis, *Bulletin Geodesique* **30**(1), 110–153.

Hess, H. H. (1946), Drowned ancient islands of the Pacific basin, *Tectonophysics* pp. 772–791.

Hillier, J. K. (2008), Seamount detection and isolation with a modified wavelet transform, *Basin Research* **20**(4), 555–573.

Hillier, J. K. and Watts, A. B. (2007), Global distribution of seamounts from ship-track bathymetry data, *Geophysical Research Letters* **34**, 1–5.

Hoffman, F. O. and Gardner, H. (1983), Evaluation of uncertainties in environmental radiological assessment models, *in* 'Radiological Assessments: A Textbook on Environmental Dose Assessment', p. 11.

Hooft, E. and Detrick, R. (1993), The role of density in the accumulation of basaltic melts at mid-ocena ridges, *Geophysical Research Letters* **20**(6), 423–426.

Hosford, A., Tivey, M., Matsumoto, T., Dick, H., Schouten, H. and Kinoshita, H. (2003), Crustal magnetization and accretion at the Southwest Indian Ridge near the Atlantis II fracture zone, 0 25 Ma, *Journal of Geophysical Research* **108**(B3), 1–23.

Howell, J. K., White, S. M. and Bohnenstiehl, D. R. (2012), A modified basal outlining algorithm for identifying topographic highs in gridded elevation data , part 2 : Application to Springerville Volcanic Field, *Computers and Geosciences* **49**, 315–322.

Huang, P. Y. and Solomon, S. C. (1987), Centroid depths and mechanisms of mid-

ocean ridge earthquakes in the Indian Ocean, Gulf of Aden, and Red Sea, *Journal of Geophysical Research* **92**(B2), 1361–1382.

Ildefonse, B., Blackman, D. K., John, B. E., Ohara, Y., Miller, D. J. and MacLeod, C. J. (2007), Oceanic core complexes and crustal accretion at slow-speading ridges, *Geology* **35**(7), 623–626.

IOC, IHO and BODC (2003), Centeneary Edition of the GEBCO Digital Atlas, published on behalf of the International Oceanographic Commission and the International Hydrographic Organisation as part of the General Bathymetric Chart of the Oceans, British Oceanographic Data Centre, Liv.

Ito, G., Lin, J. and Graham, D. (2003), Observational and theoretical studies of the dynamics of mantle plume-mid-ocean ridge interaction, *Reviews of Geophysics* **41**(4).

Jackson, H., Reid, I. and Falconer, R. K. H. (1982), Crustal Structure Near the Arctic Mid-Ocean Ridge, **87**(B3), 1773–1783.

Janney, P. E., Roex, A. P. L. E. and Carlson, R. W. (2005), Hafnium Isotope and Trace Element Constraints on the Nature of Mantle Heterogeneity beneath the Central Southwest Indian Ridge (13 E to 47 E), *Journal of Petrology* **46**(12), 2427–2464.

Jian, H., Singh, S. C., Chen, Y. J. and Li, J. (2017), Evidence of an axial magma chamber beneath the ultraslowspreading Southwest Indian Ridge, *Geology* **45**(2), 143–146.

Johnson, D. and Nurminen, J. (2007), *The History of Seafaring:Navigating the World's Oceans*, 1st edn, Conway.

Johnson, H. P. and Embley, R. W. (1990), Axial Seamount: An Active Ridge Axis Volcano on the Central Juan De Fuca Ridge, *Journal of Geophysical Research* **95**(B8), 12,689–12,696.

Jokat, W., Ritzmann, O., Schmidt-Aursch, M. C., Drachev, S., Gauger, S. and Snow, J. (2003), Geophysical evidence for reduced melt production on the Arctic ultraslow Gakkel mid-ocean ridge, *Nature* **423**, 962–965.

Jones, E. J. W. (1999), *Marine Geophysics*, Wiley.

Jordan, T. H., Menard, H. W. and Smith, D. K. (1983), Density and size distribution of seamounts in the eastern pacific inferred from wide-beam sounding data, *Journal of Geophysical Research* **88**(B12), 10508–10518.

Kalnins, L. M. (2011), Spatial Variations in the Effective Elastic Thickness of the Lithosphere and their Tectonic Implications, PhD thesis.

Kalnins, L. M. and Watts, A. B. (2009), Spatial variations in effective elastic thickness in the Western Pacific Ocean and their implications for Mesozoic volcanism, *Earth and Planetary Science Letters* **286**, 89–100.

Karson, J. A. and Dick, H. J. B. (1983), Tectonics of ridge-transform intersections at the Kane fracture zone, *Marine Geophysical Researches* **6**(1), 51–98.

Keating, B. and McGuire, W. (2000), Island Edifice Failures and Associated Tsunami Hazards, *Pure and Applied Geophysics* **157**, 899–955.

Kelemen, P., Kikawa, E., Miller, D. J., Ildefonse, B. and Godard, M. (2007), Leg 209 summary: processes in a 20-km-thick conductive boundary layer beneath the Mid-Atlantic Ridge, 14-16N, *proceedings of the Ocean Drilling Program, Scientific Results* **209**, 1–33.

Kim, S.-s. and Wessel, P. (2011), New global seamount census from altimetry-derived gravity data, *Geophysical Journal International* **186**, 615–631.

Kinoshita, J., Dick, H. J. and Yokosuka/Shinkai 6500 Scientific Party (2001), MODE '98 Leg 4 Cruise Report, Technical report.

Kirby, J. F. (2014), Estimation of the effective elastic thickness of the lithosphere using inverse spectral methods: The state of the art, *Tectonophysics* **631**, 87–116.

Kirby, S. H. (1980), Tectonic stresses in the lithosphere: constraints provided by the experimental deformation of rocks, *J Geophys Res* **85**, 6353–6363.

Kitchingman, A. and Lai, S. (2004), Inferences on potential seamount locations from mid- resolution bathymetric data, *in* T. Morato and D. Pauly, eds, 'Seamounts: Biodiversity and Fisheries', pp. 7–12.

Klein, E. and Langmuir, C. H. (1987), Global correlations of ocean ridge basalt chemistry with axial depth and crustal thickness, *Journal of Geophysical Research* **92**(B8), 8089–8115.

Kokelaar, P. (1986), Magma-water interactions in subaqueous and emergent basaltic volcanism, *Bulletin of Volcanology* **48**, 275–289.

Kong, L. S. L., Solomon, S. C. and Purdy, G. M. (1992), Microearthquake characteristics of a mid-ocean ridge along-axis high, *Journal of Geophysical Research* **97**(B2), 1659–1685.

Kongsberg (n.d.), 'SIMRAD EM120 Specifications'.

Koppers, A. and Watts, A. B. (2010), Intraplate Seamounts as a Window into Deep Earth Processes, *Oceanography* **23**(1), 42–57.

Kristofferson, Y. and Talwani, M. (1977), Extinct triple junction south of Greenland relative to North America, *Geological Society of America* **88**, 103–1049.

Kuo, B.-y. and Forsyth, D. W. (1988), Gravity Anomalies of the Ridge-Transform System in the South Atlantic Between 31 and 34.5 S : Upwelling Centers and Variations in Crustal Thickness, *Marine Geophysical Researches* **10**, 205–232.

Kurz, M. D., Roex, A. P. L. E. and Dick, H. J. B. (1998), Isotope geochemistry of the oceanic mantle near the Bouvet triple junction, *Geochimica et Cosmochimica Acta* **62**(5), 841–852.

LaCoste, L. J. B. (1959), Surface ship gravity measurements on the Texas A. and M. College ship the 'Hidalgo', *Geophysics* **24**, 309–322.

le Roex, A. P., Dick, H. J. B. and Watkins, R. T. (1992), Petrogenesis of anomalous K-enriched MORB from the Southwest Indian Ridge: 1153E to 1438E, *Contributions to Mineralogy and Petrology* **110**, 253–268.

Li, J., Jian, H., Chen, Y. J., Singh, S. C., Ruan, A., Qiu, X., Zhao, M., Wang, X., Niu, X., Ni, J. and Zhang, J. (2015), Seismic observation of an extremely magmatic accretion at the ultraslow spreading Southwest Indian Ridge, *Geophysical Research Letters* **42**, 2656–2663.

Ligi, M., Bonatti, E., Bortoluzzi, G., Carrara, G., Fabretti, P., Penitenti, D., Gilod, D., Peyve, S., Skolotnev, S. and Turko, N. (1997), Death and Transfiguration of a Triple Junction in the South Atlantic, *Science* **276**(April), 243–245.

Lin, J. and Phipps Morgan, J. (1992), The spreading rate dependence of three-dimentional mid-ocean ridge gravity structure, *Geophysical Research Letters* **19**(1), 13–16.

Lin, J., Purdy, G., Schouten, H., Sempéré, J.-C. and Zervas, C. (1990), Evidence from gravity data for focused magmatic accretion along the Mid-Atlantic Ridge, *Nature* **344**, 627–632.

Lonsdale, P. F. (1977), Structural Geomorphology of a Fast Spreading Rise Crest: The East Pacific Rise Near 3 25'S, *Marine Geophysical Researches* **3**, 251–293.

Luis, J. F. and Neves, M. C. (2006), The isostatic compensation of the Azores Plateau : A 3D admittance and coherence analysis, *Journal of Volcanology and Geothermal Research* **156**, 10–22.

Luongo, G., Cubellis, E., Obrizzo, F. and Petrazzuoli, S. M. (1991), A physical model for the origin of volcanism of the Tyrrhenian margin: the case of Neapolitan area, *Journal of Volcanology and Geothermal Research* **48**, 173–185.

Luttrell, K. and Sandwell, D. (2012), Constraints on 3-D stress in the crust from support of mid-ocean ridge topography, *Journal of Geophysical Research* **117**, 1–19.

Macdonald, K. (1982), Mid-Ocean Rifges: Fine Scale Tectonic, Volcanic and Hydrothermal Processes Within the Plate Boundary Zone, *Ann. Rev. Earth Planet. Sci.* **10**, 155–190.

Macdonald, K. C., Fox, P. J., Perram, L. J., Eisen, M. F., Haymon, R. M., Miller, S. P., Carbotte, S. M., Cormier, M. H. and Shor, A. N. (1988), A new view of the mid-ocean ridge from the behavious of ridge-axis discontinuities, *Nature* **335**, 217–225.

Macdonald, K., Luyendyk, B. P., Mudie, J. D. and Spiess, F. N. (1975), Near-bottom geophysical study of the Mid-Atlantic Ridge median velley near 37N: Preliminary observations, *Geology* pp. 211–216.

Macdonald, K. and Sempere, J.-C. (1984), East Pacific Rise From Siqueiros to 0rozco

Fracture Zones: Along-Strike Continuity of Axial Neovolcanic Zone and Structure and Evolution of Overlapping Spreading Centers, *Journal of Geophysical Research* **89**(B7), 6049–6069.

Macleod, C. J., Dick, H. J. B., Allerton, S., Robinson, P. T., Coogan, L. A., Edwards, S. J., Galley, A., Gillis, J. M., Hirth, G., Hunter, A. G., Hutchinson, D., Kvassnes, A. J., Natland, J. H., Salisbury, M., Schandl, E. S., Stakes, D. S., Thompson, G. M. and Tivey, M. (1998), Geological mapping of sloe-spreading lower oceanic crust: A deep-towed video and wireline rock drilling survey of Atlantis Bank (ODP Site 735, Southwest Indian Ridge), *InterRidge news* **7**(2), 39–43.

MacLeod, C. J., Searle, R. C., Murton, B. J., Casey, J. F., Mallows, C., Unsworth, S. C., Achenbach, K. L. and Harris, M. (2009), Life cycle of oceanic core complexes, *Earth and Planetary Science Letters* **287**(3-4), 333–344.

Madsen, J. A., Forsyth, D. W. and Detrick, R. S. (1984), A New Isostatic Model for the East Pacific Rise Crest, *Journal of Geophysical Research* **89**(B12), 9997–10015.

Malinverno, A. (1990), A Quantitative Study of the Axial Topography of the Mid-Atlantic Ridge, *Journal of Geophysical Research* **95**(B3), 2645–2660.

Malinverno, A. (1993), Transition between a valley and a high at the axis of mid-ocean ridges, *Geology* **21**, 639–642.

Marine Magnetics Corp (2007), SeaSPY Technical Application Guide rev1.4, Technical report.

Marks, K. M. and Smith, W. H. F. (2006), An evaluation of publicly available global bathymetry grids, *Marine Geophysical Researches* **27**(1), 19–34.

Masson, D. G., Watts, A. B., Gee, M. J. R., Urgeles, R., Mitchell, N. C., Le Bas, T. P. and Canals, M. (2002), Slope failures on the flanks of the western Canary Islands, *Earth Science Reviews* **57**, 1–35.

Matsumoto, T., Miyashita, S., Arai, S., Morishita, T., Maeda, J.-i., Kumagai, H., Ohtomo, Y. and Dick, H. J. B. (2003), 'Magmatism and Crust-mantle Boundary on the Ultra-slow Spreading Ridge as Observed in Atlantis Bank, Southwest Indian Ridge'.

McGuire, W. J. (1996), Volcano instability: a review of contemporary themes, *Geological Society, London, Special Publications* **110**(1), 1–23.

McKenzie, D. (2010), The influence of dynamically supported topography on estimates of Te, *Earth and Planetary Science Letters* **295**, 127–138.

McKenzie, D. and Bowin, C. (1976), The relationship between bathymetry and gravity in the Atlantic Ocean, *Journal of Geophysical Research* **81**(11), 1903–1915.

McKenzie, D. P. (1977), Surface deformation , gravity anomalies and convection, *Geophysical Journal of the Royal Astronomical Society* **48**, 211–238.

McNutt, M. (1979), Compensation of Oceanic Topography : An Application of the Response Function Technique to the Surveyor Area, *Journal of Geophysical Research* **84**(B13), 7589–7598.

McNutt, M. (1983), Influence of plate subduction on isostatic compensation in northern California, *Tectonics* **2**(4), 399–415.

Menard, H. (1960), The East Pacific Rise, *Science* **132**(3441), 1737–1746.

Menard, H. (1963), Oceanic islands, seamounts, guyots and atolls, *in* 'The sea 3', pp. 365–385.

Mendel, V., Munschy, M. and Sauter, D. (2005), MODMAG , a MATLAB program to model marine magnetic anomalies, *Computers and Geosciences* **31**, 589–597.

Mendel, V. and Sauter, D. (1997), Seamount volcanism at the super slow-spreading Southwest Indian Ridge between 57 E and 70 E, *Geology* **25**(2), 99–102.

Mendel, V., Sauter, D., Parson, L. and Vanney, J.-r. (1997), Segmentation and Morphotectonic Variations Along a Super Slow-Spreading CenterThe Southwest Indian Ridge(57E-70E), *Marine Geophysical Researches* **19**, 505–533.

Meyer, P. S., Dick, H. J. B. and Thompson, G. (1989), Cumulate gabbros from the Southwest Indian Ridge, 54S-7 16' E: implications for magmatic processes at a slow spreading ridge, *Contributions to Mineralogy and Petrology* **103**(1), 44–63.

Meyzen, C. M., Toplis, M. J., Humler, E., Ludden, J. N. and Mével, C. (2003), A discontinuity in mantle composition beneath the southwest Indian ridge., *Nature* **421**, 731–3.

Micro-G LaCoste (n.d.), Air-Sea Gravity System II, Technical report.

Minshull, T. A., Muller, M. R. and White, R. S. (2006), Crustal structure of the Southwest Indian Ridge at 66E: Seismic constraints, *Geophysical Journal International* **166**(1), 135–147.

Mitchell, N. C. (1993), A Model for Attenutation of Backcatter due to Sediment Acumulations and Its Application to Determine Sedment Thicknesses with GLORIA Sirescan Sonar, *Journal of Geophysical Research* **98**(B12), 22,477–22,493.

Mitchell, N. C. (2001), Transition from cicular to stellate forms of submarine volcanoes, *Journal of Geophysical Research* **106**(B2), 1987–2003.

Mitchell, N. C. (2003), Susceptibility of mid-ocean ridge volcanic islands and seamounts to large-scale landsliding, *Journal of Geophysical Research* **108**(B8).

Mitchell, N. C. and Livermore, R. A. (1998), Spiess Ridge: An axial high on the slow spreading Southwest Indian Ridge, *Journal of Geophysical Research* **103**(B7), 15457–15471.

Mitchell, N. C., Masson, D. G., Watts, A. B., Gee, M. J. R. and Urgeles, R. (2002), The morphology of the submarine flanks of volcanic ocean islands A comparative study

of the Canary and Hawaiian hotspot islands, *Journal of Volcanology and Geothermal Research* **115**, 83–107.

Moore, J., Clague, D. A., Holcomb, R., Lipman, P., Normark, W. R. and Torresan, M. E. (1989), Prodigious Submarine Landslides on the Hawaiian Ridge, *Journal of Geophysical Research* **94**(B12), 17465–17484.

Moore, J. G. and Fiske, R. S. (1969), Volcanic substructure inferred from dredge samples and ocean-bottom photographs, Hawaii, *Bulletin of the Geological Society of America* **80**(7), 1191–1202.

Moore, J. G. and Normark, W. R. (1994), Giant Hawaiian Landslides, *Annual Review of Earth and Planetary Sciences* **22**, 119–144.

Morgan, J. (1981), 13. Hotspot tracks and the opening of the Atlantic and Indian Oceans, *in* 'The Oceanic Lithosphere', p. 443.

Muller, M. R., Minshull, T. A. and White, R. S. (1999), Segmentation and melt supply at the Southwest Indian Ridge, *Geology* **27**(10), 867–870.

Muller, M. R., Minshull, T. A. and White, R. S. (2000), Crustal structure of the Southwest Indian Ridge at the Atlantis II Fracture Zone, *Journal of Geophysical Research* **105**(B11), 25809–25828.

Müller, R. D., Roest, W. R., Royer, J. Y., Gahagan, L. M. and Sclater, J. G. (1997), Digital isochrons of the world's ocean floor, *Journal of Geophysical Research* **102**(B2), 3211–3214.

Munk, W. H. and Cartwright, D. E. (1966), Tidal Spectroscopy and Prediction, *Philosophical Transactions of the Royal Society A: Mathematical, Physical and Engineering Sciences* **259**(1105), 533–581.

Murray, J. and Hjort, J. (1912), *The Depths of the Ocean*.

Nakamura, K. (1977), Volcanoes as possible indicators of tectonic stress orientation - principle and proposal, *Journal of Volcanology and Geothermal Research* **2**(1), 1–16.

Needham, J. (1994), *The Shorter Science and Civilisation in China*, Vol. 4.

Neumann, A. and Forsyth, W. (1993), The paradox of the Axial Profile: Isostatic Compensation Along the Axis of the Mid-Atlantic Ridge?, *Journal of Geophysical Research* **98**(B10), 17,891–17,910.

Neves, M. C., Bott, M. H. P. and Searle, R. C. (2004), *Patterns of stress at midocean ridges and their offsets due to seafloor subsidence*, Vol. 386.

Newmark, N. M. (1965), Effects of Earthquakes on Dams and Embankments, *Géotechnique* **15**(2), 139–160.

Olive, J.-A., Behn, M. D. and Tucholke, B. E. (2010), The structure of oceanic core complexes controlled by the depth distribution of magma emplacement, *Nature Geoscience* **3**(7), 491–495.

Palmiotto, C., Corda, L., Ligi, M., Cipriani, A., Dick, H. J., Douville, E., Gasperini, L., Montagna, P., Thil, F., Borsetti, A. M., Balestra, B. and Bonatti, E. (2013), Non-volcanic tectonic islands in ancient and modern oceans, *Geochemistry, Geophysics, Geosystems* **14**(10), 4698–4717.

Parker, R. L. (1972), The rapid calculation of potential anomalies, *Geophysical Journal of the Royal Astronomical Society* **31**, 447–455.

Parmentier, E. and Haxby, W. (1986), Thermal stresses in the oceanic lithosphere-Evidence from geoid anomalies at fracture zones, *Journal of Geophysical Research* **91**(B7), 7193–7204.

Parsons, B. and Sclater, J. G. (1977), An Analysis of the Variation of Ocean Floor Bathymetry and Heat Flow with Age, *Journal of Geophysical Research* **82**(5), 803–827.

Patriat, P., Sauter, D., Munschy, M. and Parson, L. (1997), A Survey of the Southwest Indian Ridge Axis Between Atlantis II Fracture Zone and the Indian Ocean Triple Junction: Regional Setting and Large Scale Segmentation, *Marine Geophysical Researches* **19**, 457–480.

Pérez-Gussinyé, M., Lowry, A. R., Watts, A. B. and Velicogna, I. (2004), On the recovery of effective elastic thickness using spectral methods: Examples from synthetic data and from the Fennoscandian Shield, *Journal of Geophysical Research* **109**, 1–20.

Phipps Morgan, J., Parmentier, E. and Lin, J. (1987), Mechanisms for the Origin of Mif-Ocean Ridge Axial Topography: Implications for the Thermal and Mechanical Structure of Accreting Plate Boundaries, *Journal of Geophysical Research* **92**(B12), 12,823–12,836.

Phipps Morgan, J. and Parmentier, E. M. (1984), Lithospheric stress near a ridgetransform intersection, *Geophysical Research Letters* **11**(2), 113–116.

Pockalny, R. A., Gente, P. and Buck, R. (1996), Oceanic transverse ridges: A flexural response to fracture-zone-normal extension, *Geology* **24**(1), 71–74.

Pratt, J. H. (1859), On the Deflection of the Plumb-Line in India, Caused by the Attraction of the Himmalaya Mountains and of the Elevated Regions Beyond; and Its Modification by the Compensating Effect of a Deficiency of Matter below the Mountain Mass, *Philosophical Transactions of the Royal Society* **149**, 745–778.

Priestley, K. and Mckenzie, D. (2013), The relationship between shear wave velocity, temperature, attenuation and viscosity in the shallow part of the mantle, *Earth and Planetary Science Letters* **381**, 78–91.

Purdy, G. M., Kong, L. S. L., Christeson, G. L. and Solomon, S. C. (1992), Relationship between spreading rate and the seismic structure of mid ocean ridges, *Nature* **355**, 815–817.

Raitt, R. W. (1963), The Crustal Rocks, *in* 'The sea 3', Interscience Publishers, New York, pp. 85–102.

Ramsey, N. (1950), The internal diamagnetic field correction in measurements of the proton magnetic moment, *Physical Review* **77**(4), 567.

Reid, I. and Jackson, H. (1981), Oceanic spreading rate and crustal thickness, *Marine Geophysical Researches* **5**, 165–172.

Rogers, A., Baco, A., Griffiths, H., Hart, T. and Hall-Spencer, J. (2007), Corals on Seamounts, *in* 'Seamounts: ecology, fisheries and conservation', Blackwell Publishing Ltd, Oxford, pp. 141–169.

Ruch, J., Wang, T., Xu, W., Hensch, M. and Jónsson, S. (2016), Oblique rift opening revealed by reoccurring magma injection in central Iceland, *Nature Communications* **7**, 1–7.

Ryan, M. (1987), Neutral buoyancy and the mechanical evolution of magmatic systems, *in* B. Mysen, ed., 'Magmatic Processes: Physciochemical Processes', Geochemical Society, University Park, PA, pp. 259–288.

Ryan, M. P., Koyanagi, R. Y. and Fiske, R. S. (1981), Modeling the Three-Dimensional Structure of Macroscopic Magma Transport Systems: Application to Kilauea Volcano, Hawaii, *Journal of Geophysical Research* **86**(B8), 7111–7129.

Samadi, S., Schlacher, T. and Richer De Forges, B. (2007), Seamount Benthos, *in* 'Seamounts: Ecology, Fisheries & Conservation', pp. 117–140.

Sandwell, D. T. (1984), Thermomechanical evolution of Oceanic Fracture Zones, *Journal of Geophysical Research* **89**(B13), 11401–11413.

Sandwell, D. T. (1986), Thermal Stress and the Spacings of Transform Faults, *Journal of Geophysical Research* **91**(B6), 6405–6417.

Sandwell, D. T. and Smith, W. H. F. (1997), Marine gravity anomaly from Geosat and ERS 1 satellite altimetry, *Journal of Geophysical Research* **102**(B5), 10.039–10.054.

Sandwell, D. T. and Smith, W. H. F. (2008), 'README 18.1 for Global Marine Gravity'.
URL: *ftp://topex.ucsd.edu/pub/global_topo_1min/README_V18.1.txt*

Sandwell, D. T. and Smith, W. H. F. (2009), Global marine gravity from retracked Geosat and ERS-1 altimetry: Ridge segmentation versus spreading rate, *Journal of Geophysical Research: Solid Earth* **114**(1).

Sauter, D. and Cannat, M. (2010), The Ultraslow Spreading Southwest Indian Ridge, *Geophysical Monograph Series* **188**, 153–173.

Sauter, D., Cannat, M. and Mendel, V. (2008), Magnetization of 026.5 Ma seafloor at the ultraslow spreading Southwest Indian Ridge, 6167E, *Geochemistry Geophysics Geosystems* **9**(4), 1–23.

Sauter, D., Cannat, M., Meyzen, C., Bezos, A., Patriat, P., Humler, E. and Debayle, E. (2009), Propagation of a melting anomaly along the ultraslow Southwest Indian

Ridge between 46 E and 52 20' E : interaction with the Crozet hotspot?, *Geophysical Journal International* **179**, 687–699.

Sauter, D., Mendel, V., Rommevaux-jestin, C., Parson, L. M., Fujimoto, H., Mevel, C., Cannat, M. and Tamaki, K. (2004), Focused magmatism versus amagmatic spreading along the ultra-slow spreading Southwest Indian Ridge: Evidence from TOBI side scan sonar imagery, *Geochemistry Geophysics Geosystems* **5**(10), 1–20.

Sauter, D., Patriat, P., Rommevaux-Jestin, C., Cannat, M. and Briais, A. (2001), The Southwest Indian Ridge between 4915'E and 57E: focused accretion and magma redistribution, *Earth and Planetary Science Letters* **192**(3), 303–317.

Schlindwein, V. (2012), Teleseismic earthquake swarms at ultraslow spreading ridges: Indicator for dyke intrusions?, *Geophysical Journal International* **190**(1), 442–456.

Schlindwein, V. and Schmid, F. (2016), Mid-ocean-ridge seismicity reveals extreme types of ocean lithosphere, *Nature* **535**, 276–279.

Schmid, F. and Schlindwein, V. (2016), Microearthquake activity, lithospheric structure, and deformation modes at an amagmatic ultraslow spreading Southwest Indian Ridge segment, *Geochemistry, Geophysics, Geosystems* **17**(7), 2905–2921.

Schouten, H. and White, R. S. (1980), Zero-offset fracture zones, *Geology* **8**(4), 175–179.

Sclater, J. G., Bowin, C. O., Hey, R., Hoskins, H., Peirce, J., Phillips, J. and Tapscott, C. (1976), The Bouvet triple junction, *Journal of Geophysical Research* **81**(11), 1857–1869.

Searle, R. C. and Bralee, A. V. (2007), Asymmetric generation of oceanic crust at the ultra-slow spreading Southwest Indian Ridge, 64E, *Geochemistry Geophysics Geosystems* **8**(5), 1–28.

Searle, R. C., Keeton, J. A., Owens, R. B., White, R. S., Mecklenburgh, R., Parsons, B. and Lee, S. M. (1998), The Reykjanes Ridge: structure and tectonics of a hot-spot-influenced, slow-spreading ridge, from multibeam bathymetry, gravity and magnetic investigations, *Earth and Planetary Science Letters* **160**, 463–478.

Sempere, J.-C., Lin, J., Brown, H. S., Schouten, H. and Purdy, G. M. (1993), Segmentation and Morphotectonic Variations Along a Slow-Spreading Center: The Mid-Atlantic Ridge (24 00' N - 30 40' N), *Marine Geophysical Researches* **15**, 153–200.

Severinghaus, J. P. and Macdonald, K. C. (1988), High inside corners at ridge-transform intersections, *Marine Geophysical Researches* **9**(4), 353–367.

Seyler, M. (2003), Evidence for major-element heterogeneity in the mantle source of abyssal peridotites from the Southwest Indian Ridge (52 to 68E), *Geochemistry Geophysics Geosystems* **4**(2), n/a–n/a.

Siebert, L. (1984), Large Volcanic Debrus Avalanches: Characteristics of Source Areas, Deposits and Associated Eruptions, *Journal of Volcanology and Geothermal Research* **22**, 163–197.

Simons, F. J. and Olhede, S. C. (2013), Maximum-likelihood estimation of lithospheric flexural rigidity, initial-loading fraction and load correlation, under isotropy, *Geophysical Journal International* **193**(3), 1300–1342.

Simons, F. J., Zuber, M. and Korenaga, J. (2000), "Isostatic response of the Australian lithosphere: Estimation of effective elastic thickness and anisotropy using multitaper spectral analysis, *Journal of Geophysical Research* **105**, 19163–19184.

Sleep, N. H. (1969), Sensitivity of heat flow and gravity to the mechanism of sea-floor spreading, *Journal of Geophysical Research* **74**(2), 542–548.

Slepian, D. (1978), Prolate spheroidal wave functions, Fourier analysis, and uncertaintyV: The discrete case, *Bell Labs Technical Journal* **57**, 1371–1430.

Small, C. (1995), Observations of ridge-hotspot interactions in the Southern Ocean, *Journal of Geophysical Research* **100**(B9), 17931–17946.

Small, C. (1998), Global Systematics of Mid-Ocean Ridge Morphology, *Geophysical Monograph Series* **106**, 1–25.

Smith, D. K. and Cann, J. R. (1990), 'Hundreds of small volcanoes on the median valley floor of the Mid-Atlantic Ridge at 24-30N'.

Smith, D. K., Cann, J. R., Dougherty, M. E., Lin, J., Spencer, S., Macleod, C., Keeton, J., Mcallister, E., Brooks, B., Pascoe, R. and Robertson, W. (1995), Mid-Atlantic Ridge volcanism from deep-towed side-scan sonar images, 25-29N, *Journal of Volcanology and Geothermal Research* **67**, 233–262.

Smith, D. K. and Jordan, T. H. (1988), 'Seamount Statistics in the Pacific Ocean'.

Smith, D. K., Kong, L., Johnson, K. T. M. and Reynolds, J. R. (2002), Volcanic morphology of the submarine Puna Ridge, Kilauea Volcano, *in* E. Takahashi, P. Lipman, M. O. Garcia, J. Naka and S. Aramaki, eds, 'Hawaiian volcanoes: deep underwater perspectives', American Geophysical Union, Washington DC, pp. 125–142.

Smith, K. and Cann, R. (1992), The role of seamount volcanism in crustal construction at the mid-atlantic ridge (24-30 N), *Journal of Geophysical Research* **97**(B2), 1645–1658.

Smith, P. A. (1937), The Submarine Topography of Bogoslof, *Geographical Review* **27**(4), 630–636.

Smith, W. (1993), On the Accuracy of Digital Bathymetric Data, *Journal of Geophysical Research* **98**(B6), 9591–9603.

Smith, W. and Sandwell, D. (2004), Conventional Bathymetry, Bathymetry from Space, and Geodetic Altimetry, *Oceanography* **17**(1), 8–23.

Snow, J. and Edmonds, H. N. (2007), Ultraslow-spreading ridges. Rapid Paradigm Changes, *Oceanography* **20**(1), 90–101.

Sparks, D. W. and Parmentier, E. (1994), Chapter 4 The Generation and Migration of Partial Melt beneath Oceanic Spreading Centers, pp. 55–76.

Standish, J. J., Dick, H. J. B., Michael, P. J., Melson, W. G. and Hearn, T. O. (2008), chemistry and the importance of process versus source, *Geochemistry Geophysics Geosystems* **9**(5).

Standish, J. J. and Sims, K. W. W. (2010), Young off-axis volcanism along the ultraslow-spreading Southwest Indian Ridge, *Nature Geoscience* **3**(4), 286–292.

Stanley, H. R. (1979), The Geos 3 Project, *Journal of Geophysical Research* **84**(B8), 3779–3783.

Talwani, M., Early, W. L. L. X. P. and Hayes, D. E. (1966), Continuous Analog Computation and Recording of Cross-Coupling and Off-Leveling Errors, *Journal of Geophysical Research* **71**(8), 2079–2090.

Talwani, M., Heezen, B. C. and Worzel, J. L. (1961), Gravity Anomalies, Physiography, and Crustal Structure of the Mid-Atlantic Ridge, *Publications of the Bureau Seismology International* **22**, 81–111.

Tapponnier, P. and Francheteau, J. (1978), Necking of the lithosphere and the mechanics of slowly accreting plate boundaries, *Journal of Geophysical Research* **83**(B8), 3955–3970.

Thebault, E., Finlay, C., Beggan, C., Alken, P., Aubert, J., Barrois, O. and Betrand, F. (2015), International Geomagnetic Reference Field: the 12th generation, *Earth, Planets and Space* **67**(79).

Theberge, A. E. (1989), Sounding Pole to Sea Beam, *in* 'Technical Papers 1989 ASPRS/ACSM Annual Convention: Surveying and Cartography', pp. 334–346.
URL: *http://www.photolib.noaa.gov/cgs/sound.html*

Thomson, D. (1982), Spectrum estimation and harmonic analysis, *Proceedings of the IEEE* **70**, 1055–1096.

Timoshenko, S. (1958), *Strength of materials. Part II. Advanced theory and problems*, Van Nostrand Co., New York.

Tisseau, M. and Patriat, P. (1981), Identification des anomalies magnétiques sur les dorsales à faible taux d'expansion: Méthode des taux fictifs, *Earth and Planetary Science Letters* **52**(2), 381–396.

Tolstoy, M., Harding, A. J. and Orcutt, J. A. (1993), Crustal Thickness on the Mid-Atlantic Ridge: Bull's Eye Gravity Anomalies and Focused Accretion, *Science* **262**(October), 726–729.

Tooney, D., Solomon, S. and Purdy, G. (1988), Microearthquakes beneath median valley of Mid-Atlantic Ridge near 23N: Tomography and Tectonics, *Journal of Geophysical Research* **93**(B8), 9093–9112.

Turcotte, D. (1974), Are transform faults thermal contraction cracks?, *Journal of Geophysical Research* **79**(47), 2573–2577.

van Wyk de Vries, B. and Merle, O. (1996), The effect of volcanic constructs on rift fault patterns, *Geology* **24**(7), 643–646.

Varnes, D. (1978), Slope Movement Types and Processes, pp. 11–33.

Vening Meinesz, F. (1931), Une nouvelle methode pour la reduction isostatique regionale de lintensite de la pesanteur, *Bulletin Geodesique* **29**(1), 33–51.

Vening Meinesz, F. (1950), Les graben africains, resultant de compression ou de tension dans la croute terrestre, *Inst. R. Colonial Belge Bull.* **21**, 539–552.

Vening Meinesz, F. A. (1929), *Theory and practice of pendulum observations at sea*, J. Waltman, Jr.

Vestine, E. H. (1960), The survey of geomagnetic field in space, *Trans. Amer. Geophys. Un.* **41**, 4–21.

Vincenty, T. (1975), Direct and Inverse Solutions of Geodesics on the Ellipsoid with Application of Nested Equations, *Survey Review XXII* **176**, 88–93.

Vogt, P. R. and Smoot, N. C. (1984), The Geisha Guyots: Multibeam Bathymetry and Morphometric Interpretation, *Journal of Geophysical Research* **89**(B13), 11085–11107.

Walcott, R. (1970), Flexural rigidity, thickness and viscosity of the lithosphere, *Journal of Geophysical Research* **75**, 3941–3953.

Walter, T. R., Troll, V. R., Cailleau, B., Belousov, A., Schmincke, H. U., Amelung, F. and Bogaard, P. (2005), Rift zone reorganization through flank instability in ocean island volcanoes: An example from Tenerife, Canary Islands, *Bulletin of Volcanology* **67**(4), 281–291.

Watts, A. B. (1978), An Analysis of Isostasy in the World's Oceans 1. Hawaiian-Emperor Seamount Chain, *Journal of Geophysical Research* **83**(B12), 5989–6004.

Watts, A. B. (1982), Gravity anomalies over Oceanic rifts, Continental and Oceanic Rifts, *Geodynamic Series 8* pp. 99–106.

Watts, A. B. (2001), *Isostasy and Flexure of the Lithosphere*, Cambridge University Press, Cambridge.

Watts, A. B., Cochran, J. R., Patriat, P. and Doucoure, M. (1985), A bathymetry and altimetry profile across the Southwest Indian Ridge crest at 31S latitude, *Earth and Planetary Science Letters* **73**, 129–139.

Watts, A. B. and Masson, D. G. (1995), A giant landslide on the north flank of Tenerife, Canary Islands, *Journal of Geophysical Research* **100**(B12), 24,487–24,498.

Watts, A. B. and Ten Brink, U. (1989), Crustal Structure, Flexure, and Subsidence

History of the Hawaiian Islands, *Journal of Geophysical Research* **94**(B8), 10473–10500.

Weissel, J. K. and Watts, A. B. (1979), Tectonic Evolution of the Coral Sea Basin, *Journal of Geophysical Research* **84**, 4572–4582.

Wessel, P. (2001), Global distribution of seamounts inferred from gridded Geosat/ERS-1 altimetry, *Journal of Geophysical Research* **106**(B9), 19431–19441.

Wessel, P. and Smith, W. (1991), Free software helps map and display data, *Eos Transactions, AGU* **72**(41), 441.

Wolfe, C. J., Purdy, G. M., Toomey, D. R. and Solomon, S. C. (1995), Microearthquake characteristics and crustal velocity structure at 29N on the Mid-Atlantic Ridge: The architecture of a slow spreading segment, *Journal of Geophysical Research* **100**(B12), 24449–24472.

Worzel, J. L. (1959), Continuous gravity measurements on a surface ship with the Graf Sea Gravimeter, *Journal of Geophysical Research* **64**, 1299–1315.

Worzel, J. L. and Harrison, J. C. (1963), Gravity at Sea, *in* 'The Sea: The Earth Beneath the Sea', Interscience Publishers, pp. 134–174.

Zhao, M., Qiu, X., Li, J., Sauter, D., Ruan, A., Chen, J., Cannat, M., Singh, S., Zhang, J., Wu, Z. and Niu, X. (2013), Three-dimensional seismic structure of the Dragon Flag oceanic core complex at the ultraslow spreading Southwest Indian Ridge (4939E), *Geochemistry, Geophysics, Geosystems* **14**(10), 4544–4563.

Zhou, H. and Dick, H. J. B. (2013), Thin crust as evidence for depleted mantle supporting the Marion Rise, *Nature* **494**, 195–200.